Chemical evolution of the Large Magellanic Cloud

Mathieu van Der Swaelmen

UNIVERSITÉ DE NICE SOPHIA-ANTIPOLIS — UFR Sciences

École Doctorale Sciences Fondamentales et Appliquées

THESE DE DOCTORAT

pour obetnir le titre de

Docteur en Sciences
de l'Univeristé de Nice Sophia-Antipolis

Spécialité : Sciences de l'univers

présentée et soutenue par

Mathieu Van der swaelmen

Évolution chimique du Grand Nuage de Magellan

Thèse dirigée par

Directrice de thèse	**Sophie Maurogordato**
Co-directrices de thèse	**Vanessa Hill**
	Francesca Primas

soutenue publiquement le 12 avril 2013

JURY

Présidente	Beatriz Barbuy	IAG, Universidade de São Paulo (Brésil)
Rapporteurs	Pascale Jablonka	Observatoire de Paris
	Bertrand Plez	Laboratoire Univers et Particules de Montpellier
Examinateur	Piercarlo Bonifacio	Observatoire de Paris
Directrice	Sophie Maurogordato	Observatoire de la Côte d'Azur
Co-directrices	Vanessa Hill	Observatoire de la Côte d'Azur
	Francesca Primas	European Southern Observatory (Allemagne)

Évolution chimique du Grand Nuage de Magellan

Mathieu Van der swaelmen

Laboratoire Lagrange — UMR 7293
Observatoire de la Côte d'Azur
Boulevard de l'Observatoire
BP 4229
F-06304 NICE Cedex 4 (FRANCE)
Tél : 04 92 00 30 11
Fax : 04 92 00 30 33

Évolution chimique du Grand Nuage de Magellan

Résumé : Malgré des années de travaux théoriques et observationnels intensifs, nous sommes toujours loin d'une complète compréhension de l'univers proche, la Voie Lactée (MW) et ses galaxies voisines. Parmi les satellites de la MW, le Petit et le Grand Nuage de Magellan (LMC) sont particulièrement intéressant puisqu'ils forment le plus proche exemple de galaxies en interaction gravitationnelle et hydrodynamique, et partant, constituent un laboratoire unique pour étudier les effets des marées et l'échange de matière sur l'évolution chimique et l'histoire de la formation stellaire d'une galaxie. Le LMC est une galaxie de petite masse barrée à disque, prototype des galaxies riches en gaz que l'on pense jouer un rôle important dans la construction des grandes galaxies dans le cadre du ΛCDM. De plus, avec sa métallicité actuelle d'environ le tiers de la métallicité solaire, le chemin d'enrichissement chimique suivi par le LMC donne un grand poids aux yields des générations stellaires pauvres en métaux, ce qui fait du LMC un environnement idéal pour étudier la nucléosynthèse aux basses métallicités.

Ce travail de doctorat vise à: 1) caractériser chimiquement la population de la barre du LMC, 2) comparer les tendances des éléments de la MW et du LMC et interpréter les différences ou ressemblance en termes d'évolution chimique et/ou de processus nucléosynthétiques (contraintes sur les sites et les processus nucléosynthétiques), 3) comparer l'évolution chimique de la barre et du disque interne du LMC et interpréter les différence ou ressemblance dans le contexte de la formation de la barre.

Nos résultats montrent que l'histoire chimique du LMC a connu un forte contribution des supernovae de type I ainsi qu'un fort enrichissement en éléments *s* par les vents d'étoiles AGB pauvres en métaux. Par rapport à la MW, les étoiles massives ont eu une contribution plus petite à l'enrichissement chimique du LMC. Les différences observées entre la barre et le disque parlent en faveur d'un épisode de formation stellaire accrue il y a quelques Gyr, ayant lieu dans les zones centrales du LMC et conduisant à la formation de la barre. Ceci est en accord avec les histoires de la formation stellaire récemment dérivées.

Mots-clés : Étoiles: abondances — Galaxies: Nuages de Magellan — Galaxies: abondances — Galaxies: évolution

Chemical evolution of the Large Magellanic Cloud

Abstract: Despite decades of intensive observational and theoretical work, we are still far from a complete and clear understanding of the nearby universe, the Milky Way (MW) and its neighbours. Among the satellites of the MW, the Small and Large Magellanic Cloud (LMC) are of particular interest since they form the closest example of galaxies in gravitational and hydrodynamical interaction, and therefore constitute a unique laboratory to study the effect of tides and matter exchange on the chemical evolution and star formation history of a galaxy. The LMC is a low-mass barred disc galaxy, prototypical of gas-rich galaxies that are thought to play an important role in the build-up of large galaxies in the ΛCDM framework. Furthermore, with its present day metallicity of only third of solar, the chemical enrichment path followed by the LMC gives a heavy weight to the yields of metal-poor stellar generations, which makes the LMC an ideal environment to study nucleosynthesis at low metallicities.

This thesis work aims at: 1) chemically characterizing the LMC bar population, 2) comparing the elemental trends of the MW and the LMC and interpreting the differences or similarities in terms of chemical evolution and/or nucleosynthesis processes (constraints on the nucleosynthetic sites and processes), 3) comparing the chemical evolution of the LMC bar and inner disc and interpreting the differences or similarities between the LMC bar and inner disc in the context of the bar formation.

Our results show that the chemical history of the LMC experienced a strong contribution from type Ia supernovae as well as a strong *s*-process enrichment from metal-poor AGB winds. Massive stars made a smaller contribution to the chemical enrichment compared to the MW. The observed differences between the bar and the disc speak in favour of an episode of enhanced star formation a few Gyr ago, occurring in the central parts of the LMC and leading to the formation of the bar. This is in agreement with recently derived star formation histories.

Keywords: Stars: abundances — Galaxies: Magellanic Clouds — Galaxies: abundances — Galaxies: evolution

Évolution chimique du Grand Nuage de Magellan

Abrégé: Malgré des années de travaux théoriques et observationnels intensifs, nous sommes toujours loin d'une complète compréhension de l'univers proche, la Voie Lactée (MW) et ses galaxies voisines. Parmi les satellites de la MW, le Petit et le Grand Nuage de Magellan (LMC) sont particulièrement intéressant puisqu'ils forment le plus proche exemple de galaxies en interaction gravitationnelle et hydrodynamique, et partant, constituent un laboratoire unique pour étudier les effets des marées et l'échange de matière sur l'évolution chimique et l'histoire de la formation stellaire d'une galaxie. Le LMC est une galaxie de petite masse barrée à disque, prototype des galaxies riches en gaz que l'on pense jouer un rôle important dans la construction des grandes galaxies dans le cadre du ΛCDM. De plus, avec sa métallicité actuelle d'environ le tiers de la métallicité solaire, le chemin d'enrichissement chimique suivi par le LMC donne un grand poids aux yields des générations stellaires pauvres en métaux, ce qui fait du LMC un environnement idéal pour étudier la nucléosynthèse aux basses métallicités.

Ce travail de doctorat vise à: 1) caractériser chimiquement la population de la barre du LMC, 2) comparer les tendances des éléments de la MW et du LMC et interpréter les différences ou ressemblance en termes d'évolution chimique et/ou de processus nucléosynthétiques (contraintes sur les sites et les processus nucléosynthétiques), 3) comparer l'évolution chimique de la barre et du disque interne du LMC et interpréter les différence ou ressemblance dans le contexte de la formation de la barre.

Nous avons obtenu des spectres à haute résolution et à signal-sur-bruit intermédiaire avec FLAMES/GIRAFFE à l'ESO/VLT et j'ai effectué une analyse chimique détaillée de 106 et 58 étoiles de champ géantes rouges appartenant au LMC (la plupart plus vieille que 1 Gyr), et située respectivement dans la barre et le disque LMC. J'ai mené la réduction de données avec un soin particulier : j'ai utilisé le pipeline GIRAFFE de l'ESO pour le correction du biais et du courant d'obscurité, la calibration en longueur d'onde, l'extraction de spectre et la correction du champ plat et j'ai développé mes propres outils pour effectuer la soustraction du ciel, la correction en vitesse radiale et la co-addition des spectres. J'ai mis au point des pipelines semi-automatiques pour déterminer les paramètres stellaires de nos étoiles de la barre et du disque du LMC et pour dériver leur composition chimique atmosphérique (en utilisant à la fois les largeurs équivalentes et l'ajustement des raies d'absorption). Pour valider mes procédures de détermination des paramètres stellaires et de mesures d'abondance, j'ai mené des tests intensifs en utilisant Arcturus, une étoile géante du disque épais de la MW moyennement pauvre en métaux. Grâce à la grande couverture en longueur d'onde de nos spectres, j'ai mesuré

des abondances chimiques pour 17 ions appartenant aux éléments α, éléments impairs légers, éléments du pic du fer, aux éléments s et r.

Nous trouvons que les rapports des éléments α [Mg/Fe] et [O/Fe] sont plus faibles dans le LMC que dans la MW tandis que le LMC a des rapports [Si/Fe], [Ca/Fe], et [Ti/Fe] similaires à eux de la MW. Pour les éléments lourds, [Ba, La/Eu] présente une forte croissance lorsque la métallicité augmente à partir de [Fe/H] ≈ -0.8 dex, et le LMC a des rapports [Y + Zr/Ba + La] plus faibles que ceux de la MW. Cu est presque constant sur tout le domaine de métallicité et est plus petit d'environ 0.5 dex dans le LMC par rapport à la MW. La barre et le disque interne du LMC présentent des différences dans leurs rapports [α/Fe] (dispersion légèrement plus grande pour la barre dans l'intervalle de métallicité $[-1, -0.5]$), leurs Eu (la tendance de la barre est au-dessus de celle du disque pour [Fe/H] ≥ -0.5 dex), leur Y et Zr, leur Na et leur V (décalage entre les distributions de la barre et du disque).

Nos résultats montrent que l'histoire chimique du LMC a connu un forte contribution des supernovae de type I ainsi qu'un fort enrichissement en éléments s par les vents d'étoiles AGB pauvres en métaux. Par rapport à la MW, les étoiles massives ont eu une contribution plus petite à l'enrichissement chimique du LMC. Les différences observées entre la barre et le disque parlent en faveur d'un épisode de formation stellaire accrue il y a quelques Gyr, ayant lieu dans les zones centrales du LMC et conduisant à la formation de la barre. Ceci est en accord avec les histoires de la formation stellaire récemment dérivées.

Chemical evolution of the Large Magellanic Cloud

Summary: Despite decades of intensive observational and theoretical work, we are still far from a complete and clear understanding of the nearby universe, the Milky Way (MW) and its neighbours. Among the satellites of the MW, the Small and Large Magellanic Cloud (LMC) are of particular interest since they form the closest example of galaxies in gravitational and hydrodynamical interaction, and therefore constitute a unique laboratory to study the effect of tides and matter exchange on the chemical evolution and star formation history of a galaxy. The LMC is a low-mass barred disc galaxy, prototypical of gas-rich galaxies that are thought to play an important role in the build-up of large galaxies in the ΛCDM framework. Furthermore, with its present day metallicity of only third of solar, the chemical enrichment path followed by the LMC gives a heavy weight to the yields of metal-poor stellar generations, which makes the LMC an ideal environment to study nucleosynthesis at low metallicities.

This thesis work aims at: 1) chemically characterizing the LMC bar population, 2) comparing the elemental trends of the MW and the LMC and interpreting the differences or similarities in terms of chemical evolution and/or nucleosynthesis processes (constraints on the nucleosynthetic sites and processes), 3) comparing the chemical evolution of the LMC bar and inner disc and interpreting the differences or similarities between the LMC bar and inner disc in the context of the bar formation.

We obtained high-resolution and mid signal-to-noise ratio spectra with FLAMES/GIRAFFE at ESO/VLT and I performed a detailed chemical analysis of 106 and 58 LMC field red giant stars (mostly older than 1 Gyr), located in the bar and the disc of the LMC respectively. I carefully carried out the data reduction: I used the ESO GIRAFFE pipeline for the bias and dark current correction, wavelength calibration, spectrum extraction and flat fielding and I developed my own tools to perform sky subtraction, radial velocity correction and spectrum co-addition. I set up semi-automated pipelines to determine the stellar parameters of our LMC bar and disc stars and to derive their photospheric chemical composition (using both equivalent widths and absorption line fitting). To validate my stellar parameter determinations and abundance measurement procedures, I performed thorough tests using the well-known mildly metal-poor Milky-Way thick disc giant Arcturus. Thanks to the large wavelength coverage of our spectra, I measured elemental abundances for 17 ions belonging to α-, light odd, iron-peak, s- and r-elements.

We find that the α-element ratios [Mg/Fe] and [O/Fe] are lower in the LMC than in the MW while the LMC has similar [Si/Fe], [Ca/Fe], and [Ti/Fe] to the MW. As for the heavy elements, [Ba, La/Eu] exhibit a strong increase

with increasing metallicity starting from [Fe/H] ≈ -0.8 dex, and the LMC has lower [Y + Zr/Ba + La] ratios than the MW. Cu is almost constant over all metallicities and about 0.5 dex lower in the LMC than in the MW. The LMC bar and inner disc exhibit differences in their [α/Fe] (slightly larger scatter for the bar in the metallicity range $[-1, -0.5]$), their Eu (the bar trend is above the disc trend for [Fe/H] ≥ -0.5 dex), their Y and Zr, their Na and their V (offset between the bar and the disc distributions).

Our results show that the chemical history of the LMC experienced a strong contribution from type Ia supernovae as well as a strong *s*-process enrichment from metal-poor AGB winds. Massive stars made a smaller contribution to the chemical enrichment compared to the MW. The observed differences between the bar and the disc speak in favour of an episode of enhanced star formation a few Gyr ago, occurring in the central parts of the LMC and leading to the formation of the bar. This is in agreement with recently derived star formation histories.

Contents

List of Figures

List of Tables

Chapter 1

Introduction

Contents

1.1 The Large Magellanic Cloud in a cosmological context

1.1.1 The Large Magellanic Cloud within the Local Group

The large-scale structure of the universe does not exhibit a random and uniform distribution of galaxies: in fact, galaxies form complex filamentary structures throughout the universe. According to the Λ *cold dark matter (ΛCDM) model* (also called the *standard model*), when the universe cooled, primordial inhomogeneities of matter density have grown and led to the formation of clumps of dark matter and gas along thin filamentary structures, distributed around large void spaces. Then, gas collapsed within the potential well of dark matter haloes and formed galaxies. Thus, dark matter filaments gave birth to the large-scale structures, known today as *galaxy super-clusters*, which host isolated galaxies and small to large associations of gravitationally tightly or loosely bound galaxies, called respectively *galaxy clusters* and *galaxy groups*.

Our Galaxy, the *Milky Way (MW)*, is one member of the *Local Group (LG)* (Fig. 1.1), which itself is a member of the *Local Super-cluster* — or *Virgo Super-cluster* — (whose main member is the *Virgo cluster*). The two main galaxy members, i.e. the more massive galaxies, of the Local Group are the *Andromeda Galaxy* (M31) and the MW, and are thought to have their own system of satellites. The LG offers a broad variety of galaxy types: *barred spiral galaxies* (MW and M31), *spiral*

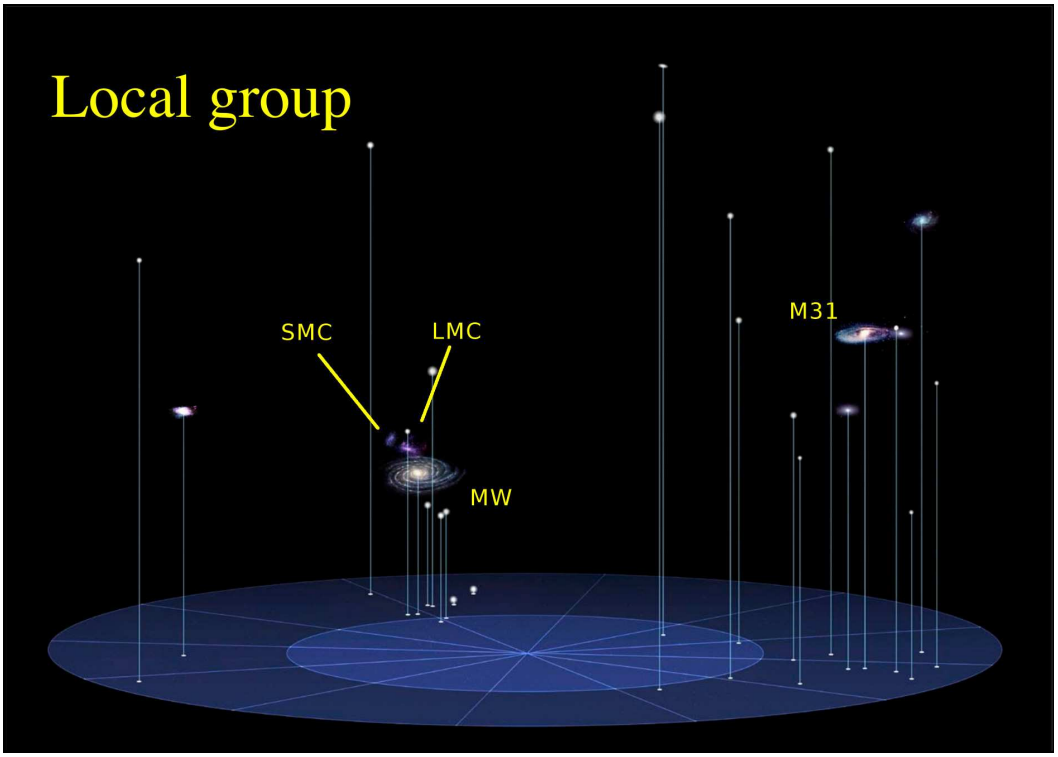

Figure 1.1: **The Local Group.** The Milky Way, Small Magellanic Cloud, Large Magellanic Cloud and M31 are shown.

galaxy (the *Triangulum Galaxy*, also known as M33[1]), *irregular galaxies* (e.g., MW's companions: the Large and Small Magellanic Clouds), *dwarf elliptical galaxies* and *dwarf spheroidal (dSph)* galaxies (e.g., Andromeda's companion: M32, NGC 147 etc.; MW's companions: Fornax, Sagittarius, Sculptor etc.) and likely a long string of *ultra-faint dwarf galaxies*.

The Small Magellanic Cloud (SMC) and Large Magellanic Cloud (LMC) — and Andromeda Galaxy — are the only galaxies visible for the naked eyes. Shining in the Southern skies (Fig. 1.2), the two Clouds were unknown to Europeans until the first expeditions of the 16th century. On the other hand, while they were probably known by Southern inhabitants since pre-historical times (e.g., reference to the Clouds in Australian aborigines' culture), the oldest written mention dates back to 964: Al Sufi, a Persian astronomer, reported in his book, *Book of Fixed Stars*, the presence of "a white ox" in the sky (Westerlund, 1997; Frommert & Kronberg, 2006, 2007). At the end of the 15th century and in the early 16th century, the first European explorers reported the existence of the two Clouds in the Southern skies. Descriptions by Italian explorers Peter Martyr d'Anghiera and Andrea Corsa,

[1]In fact, the Triangulum Galaxy is one of the four most massive galaxies of the LG, less massive and smaller than Andromeda and the MW, and of comparable size and mass to the MW. Doubts remain on whether it is a gravitationally bound companion of Andromeda, i.e. part of Andromeda's satellite system, or a more isolated galaxy

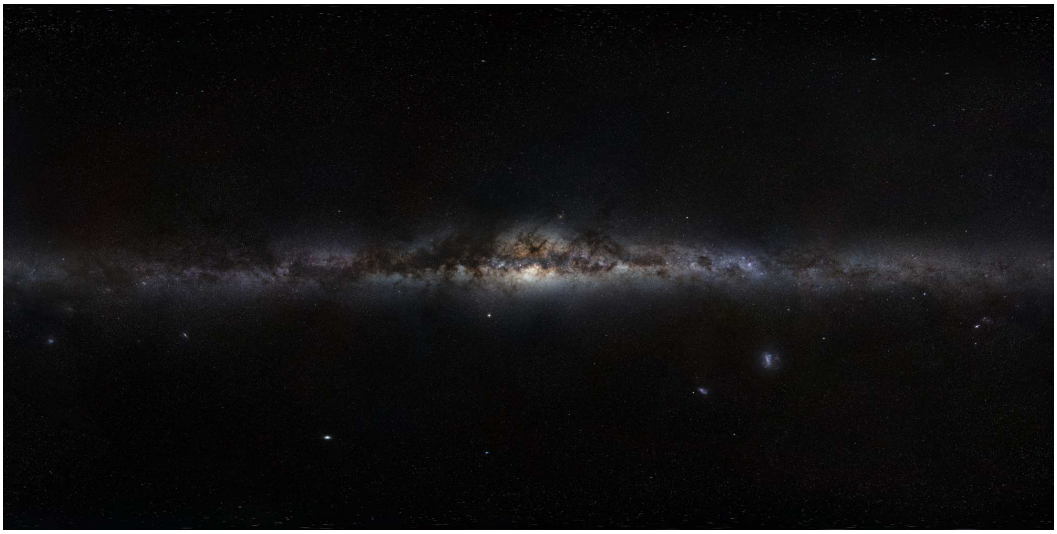

Figure 1.2: **The Milky Way and its two companions the Small Magellanic Cloud and the Large Magellanic Cloud.** The two Clouds are visible in the Southern hemisphere of the MW. *Credits:* ESO/Serge Brunier

and later, Amerigo Vespucci, bring to mind the SMC and LMC. Later, after the first circumnavigation of the globe between 1519 and 1522, initiated by Ferdinand Magellan, Antonio Pigafetta — one of the expedition's survivor — gave a clever interpretation of the two Clouds as small clusters of stars. And eventually, history has associated the two Clouds to Magellan's name. The SMC and LMC are galaxies in the vicinity of the MW: they are the second and third closest satellites of the MW (resp. at 50 kpc and 63 kpc), after the Sagittarius dwarf spheroidal (at 16 kpc, which is in a merging process with the MW). The LMC is the fourth most massive galaxy in the LG. First classified as irregular galaxies in the Hubble classification, the discovery of MC-like galaxies (i.e. sharing similar morphological features; see Sec. 1.2) in the deep sky (e.g., de Vaucouleurs, 1964; de Vaucouleurs et al., 1968; de Vaucouleurs & Freeman, 1972) motivated to consider the LMC as the prototype of a new spiral class, Barred Magellanic spiral (SBm).

1.1.2 LMC-like galaxies in a ΛCDM context

The ΛCDM is the current preferred theoretical framework to study the formation of large-scale structures in the universe. However, the predicted number of dwarf satellites is larger than what is locally observed (e.g., Klypin et al., 1999; Moore et al., 1999): the discovery of ultra-faint dwarf galaxies around the MW has started the solving of the problem. Another problem is that ΛCDM simulations predict a rare occurrence of LMC-like galaxies around MW-like galaxies, and worse, MC-like binary systems around MW-like galaxies are even rarer. We shall therefore wonder whether our Galaxy is atypical (i.e. the ΛCDM framework is right and LMC-like satellites are rare) or whether it is typical (i.e. the ΛCDM framework is wrong and

LMC-like satellites are frequent). James & Ivory (2011) used Hα narrow-band imaging to search for star-forming satellite galaxies around 143 luminous spiral galaxies and conclude that LMC analogues are rare. Robotham et al. (2012) use data gathered for the GAMA project (multi-wavelength spectroscopic galaxy survey; Driver et al., 2011) to estimate the frequency of MC analogues around MW-like galaxies. They found that there are: (1) 12 % chance to find a LMC-like companion within a projected separation of 70 kpc, (2) $\sim$ 4 % chance to find two companions at least as massive as the SMC, (3) 0.4 % chance to find an exact MC analogue. These observational facts are in agreement with recent ΛCDM simulations, for instance: Boylan-Kolchin et al. (2011) find that 20-32 % of MW-mass haloes host an LMC analogue and 10-25 % per cent host an SMC analogue; Tollerud et al. (2011) predict that 10 % of MW-like galaxies host an LMC-like satellite within 50 kpc. In fact, the differences between the quoted percentages can be explained by how MW, SMC and LMC analogues are defined and selected (halo mass of the MW-like host, distance ranges where the satellites are looked for etc.). However, models predict LMC-like satellites too red (i.e., too old) compared to our LMC (the LMC is bluer which is explained by its dominant young and intermediate-age stars): the predicted frequency of LMC-like satellite is even lower when the colour is taken into account. Thus, observations and models strongly suggest that our Galaxy is atypical due to the presence of two close and relatively massive satellites, the SMC and LMC, hosting a dominant young and intermediate-age population.

1.2 The Large Magellanic Cloud: morphology, interaction history and chemical evolution

Despite decades of intensive observational and theoretical works, we are still far from a complete and clear understanding of our close universe, the MW and its neighbours. Among the satellites of the MW, the SMC and the LMC are of particular interest since they form the closest example of galaxies in gravitational and chemical interactions and, therefore, constitute a unique laboratory to study the effect of gravitational tides and matter exchange on the chemical evolution and the star formation history of a galaxy. In this section, I propose a review of the main observational features of the LMC, how they can be explained theoretically or by dynamical modelling and emphasise still open questions. Although the study of the SMC is beyond the scope of this thesis work, I will briefly compare the two Clouds when it is particularly relevant.

1.2.1 Morphology and kinematics

Overview The LMC is an almost face-on, gas-rich galaxy with regions of active stellar formation located at 50 kpc (Alves, 2004a). It has a mass of $10^{10} M_{\odot}$ (van der Marel et al., 2002), which is intermediate between massive spirals and dwarf galaxies. And if a face-on appearance is ideal to disentangle the different structures and sample them, the cost is to make the vertical information hardly recoverable (e.g., see below the problem of the bar location). It is observationally clear that

the LMC has a luminous off-centre prominent bar-like structure that is probably embedded in a disc (e.g., Cioni et al., 2000), and a single (embryonic) stellar spiral arm (where stellar formation occurs; e.g., Harris & Zaritsky, 2009); on the other hand, the existence of an (extended) old stellar halo (similar to that of the MW) is still matter of debate (Alves, 2004b; Majewski et al., 2009; Minniti et al., 2003; Pejcha & Stanek, 2009; Subramaniam & Subramanian, 2009a). Because of its off-centre bar and its single spiral arm, the LMC is said to be doubly asymmetric. A detailed look shows that the LMC morphology (and more generally the morphology of the MC system) is very complicated and indicates a tumultuous history, fruits of gravitational interactions with its nearest neighbour the SMC, and more recently with the MW. Indeed, even if doubts remain on the dynamical scenario linking the MW and the Magellanic Clouds (MCs) and on how long the SMC and LMC have shared a common history, it is widely accepted that some morphological features of both Clouds (Fig. 1.3) are the stigmata of the recent interaction history, for instance:

- the Magellanic Bridge (MB), made of gas and stars, connects the LMC and the SMC and illustrate the matter exchange between the two Clouds;
- the LMC disc (Nikolaev et al., 2004) and bar (Subramaniam, 2003) are found to be warped;
- the Magellanic Stream (MS) extending over 150° (Mathewson et al., 1974; Wannier & Wrixon, 1972) and the Leading Arm (LA) (Putman et al., 1998), which are leading and trailing streams of neutral hydrogen gas whose origin (ram pressure, tidal interactions) remains unclear (e.g., Besla et al., 2010; Diaz & Bekki, 2012; Gardiner & Noguchi, 1996).

Gas distribution Luks & Rohlfs (1992) showed that the neutral hydrogen has a symmetric rotation field and is distributed in a flat disc. Kim et al. (1998) with a high-resolution survey, confirmed this feature: the H I distribution in the LMC exhibits a well-organised rotation field on large scales (Fig. 1.4). Also, their H I map clearly shows the presence of spiral arm-like features, which were already identified as areas of stellar activity. However, the LMC spiral arm-like features are not similar in nature to what is found in the MW. Indeed, Dixon & Ford (1972) early argued that they unlikely originate in density waves, and it was later confirmed by theoretical works of Colin & Athanassoula (1989), Dottori et al. (1996) and Gardiner et al. (1998). Gardiner et al. (1998) showed that without bar perturbation, spiral features may appear but are transient structures that quickly vanish (timescales $< 50\,\mathrm{Myr}$) while the presence of an off-centre bar influences the distribution of gas and the stellar activity and generates an asymmetrical spiral structure. On small and meso-scales, Kim et al. (1998) showed that the H I distribution exhibits a turbulent and fractal structure with filaments, H I holes and shells (Fig. 1.4). Staveley-Smith et al. (2003) extended the Kim et al. (1998) study. They determined a total H I mass of $4.8 \times 10^8\,\mathrm{M}_\odot$, with 75 % of the mass contained within a radius of 3.5 kpc. They also found that spiral features channel gas into the MB, MS and LA.

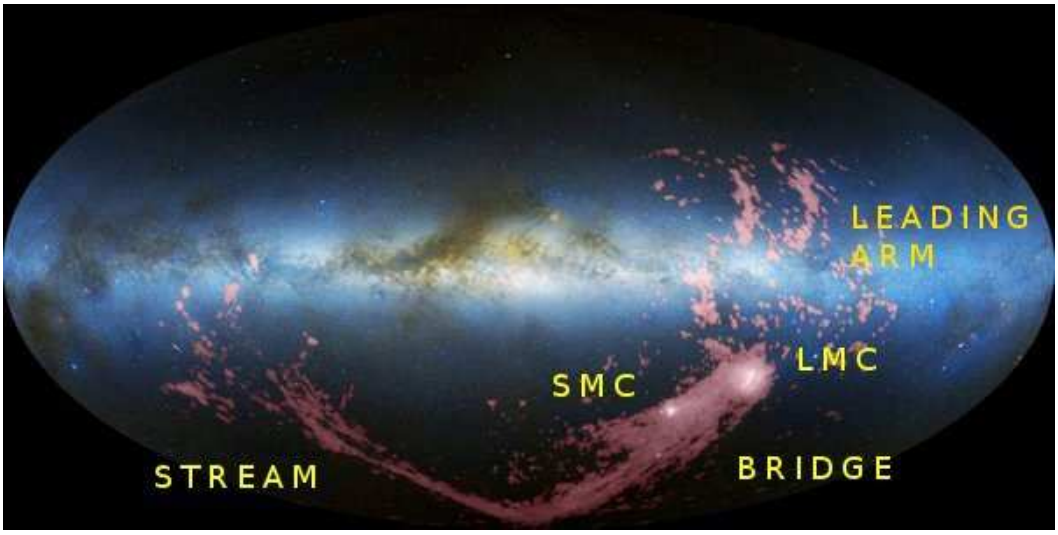

Figure 1.3: **The Small Magellanic Cloud, the Large Magellanic Cloud, the Magellanic Bridge, the Magellanic Stream and the Leading Arm.** We clearly see the MB connecting the two Clouds, the extended MS circling the MW and the LA. Red: neutral hydrogen. *Credits:* Nidever et al. (2010)

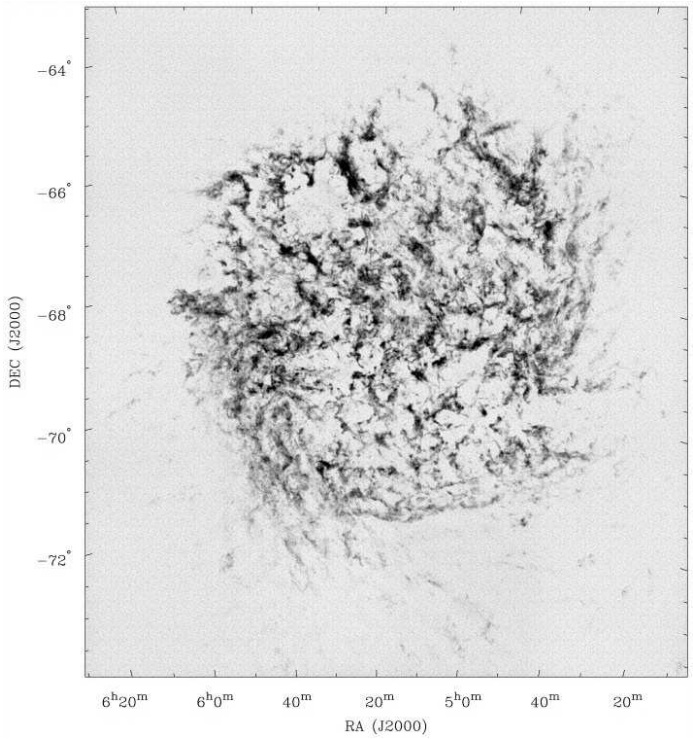

Figure 1.4: **The LMC neutral hydrogen distribution.** The LMC gaseous disc is well-organised on large scales; on smaller scales, we can identify turbulent and floculent features, filaments, HI holes and shells. *Credits:* Kim et al. (1998)

The LMC bar The LMC bar (Fig. 1.5) is a structure with a cigar-like shape and is one of the most intriguing features. As mentioned, the bar is off-centre, i.e. the bar centroid is not aligned with the disc centroid nor with the rotational centre of the gas (van der Marel & Cioni, 2001). The geometry and location of the bar has been often questioned. Subramaniam (2003), Lah et al. (2005) and Koerwer (2009) reported that the bar is warped. Zhao & Evans (2000) argued that instead of being in-plane and off-centre, the LMC bar is misaligned with the LMC disc plane, and the bar and disc centroids are offset both in the sky plane and along the line of sight. They proposed two scenarios: the so-called bar is a small unvirialised LMC companion, originating in the proto-MC, that has survived up to present days and is seen as a bar due to projection effects, or the bar belongs to the LMC but is misaligned. Their scenarios require young structures since in the first case, the small companion would have quickly spiraled onto the LMC centre (few 100 Myr) and in the second case, dynamical frictions should have quickly enforced coplanarity (few 100 Myr). However, Nikolaev et al. (2004) proposed (based on RR Lyrae distances) that the LMC bar lies above the disc plane, at a distance of at least 0.5 kpc and Haschke et al. (2012a) also claim that the bar is levitating at some 5 kpc in front of the plane (again based on RR Lyrae distances; let us note that, in their study, they could not not confirm this feature from Cepheids distances). On the other hand, Subramaniam & Subramanian (2009b) claim that their study (based on red clump stars distances) rules out the possibility of a protruding bar in front of the LMC disc plane. In order to explain the origin of the asymmetric, off-centre and levitating features, Zaritsky (2004) showed that all can be explained by a tri-axial stellar bulge embedded in a highly obscuring thin disc.

The LMC bar hosts young to old stars (the bar appears in infrared images tracing old stars, see Fig. 1.5); however, the bulk of young and intermediate-age LMC stars are found in the central regions of the LMC, especially the bar. Last notable remark, the bar is absent from the gas maps (H I: Kim et al., 1998; Staveley-Smith et al., 2003; CO: Mizuno et al., 2001). The bar is not the site of ongoing strong stellar activity: 30 Doradus (the Tarantula nebula[2]), the most active star forming region of the LG, lies outside the bar (Fig. 1.5) and maybe above the LMC plane (Kennicutt et al., 1995; Walborn, 1991); Constellation III, another active star forming region, is even farther away from the bar (Fig. 1.5). The origin and nature of the bar will be further discussed in Section 1.2.5.

The LMC disc The LMC disc (see left panel of Fig. 1.5) has an exponential profile with a scale-length ~ 1.4 kpc (van der Marel, 2001; van der Marel & Cioni, 2001), is warped (Nikolaev et al., 2004) and extends up to, at least 7 kpc for Gallart et al. (2004) and even up to 16 kpc for Saha et al. (2010). The disc hosts spiral arm-like features, seen in the stellar and gas distributions. A thickening of the disc has been proposed by Weinberg (2000) and can be due to dynamical interactions with the MW halo, but due to the face-on geometry of the LMC, this thickening is hard to observe directly. Carrera et al. (2011, 2008b) reported that the velocity dispersion

[2]First thought to be a star, it was called 30 Doradus until Nicolas Louis de Lacaille discovered its being a nebula

Figure 1.5: **The Large Magellanic Cloud in the visible (left panel) and the near infrared (right panel).** In the left panel, we clearly see the bar and MB connecting the two Clouds. The bluest areas are the site of star formation. In particular, we can remark two active star forming regions: the Tarantula nebula, above the Eastern edge of the bar and the Constellation III, in the Northern, close to the spiral arm feature. In the right panel, we see the old population distributed in a well-defined disc and in the central bar. *Credits:* ESO (left panel); IPAC (Massachusetts; right panel)

decreases with increasing radius (as expected for an exponential profile), except for the bar (using data from Cole et al., 2005) and their outermost fields at 9 kpc: the bar exhibits a lower velocity dispersion than their innermost disc field while an enhanced velocity dispersion is observed for their outermost disc fields compared to the disc fields at smaller galactocentric distances. Although, the statistics is small for the outermost fields, it could be the sign of disc thickening in the outer regions of the LMC. Carrera et al. (2011, 2008b) also reported that the most metal-poor stars (which tend to be the oldest stars) have a velocity dispersions slightly higher ($25\,\mathrm{km\,s^{-1}}$) than the most metal-rich stars (which tend to be the youngest stars) ($20\,\mathrm{km\,s^{-1}}$): the LMC disc could thicken as time goes by. Another explanation is that the increase of the velocity dispersion with radius is the sign of a changing disc/halo ratio.

The LMC stellar halo The quest for an LMC stellar halo has also been a long standing issue. Minniti et al. (2003) found that RR Lyrae in the inner regions of the LMC have a large velocity dispersion and deduced that they belong to an old stellar halo and Pejcha & Stanek (2009) reconstructed a 3D map of the LMC stellar halo using distance measurement of RRab Lyrae stars. However, Freeman (1999), Alves (2004b) and Subramaniam & Subramanian (2009a) discussed the fact that RR Lyrae are really tracing a stellar halo: they found that RR Lyrae exhibit a hot kinematics but the surface density profile of the so-defined halo is very similar to that of the disc (such feature is not observed for MW disc and halo). Long period variables and globular cluster (GC) have also been used as halo tracers: long period variables have a hot kinematics but not enough to be a purely pressure supported population while GC have a disc kinematics (Olszewski et al., 1996). Majewski

et al. (2009) discuss the possibility of an extended LMC stellar halo found at very large galactocentric radius (Nidever et al., 2011 discuss of the existence of a similar structure for the SMC).

1.2.2 Stellar populations: observational facts

1.2.2.1 Globular clusters

GC are among the most studied astrophysical objects in the MW, SMC and LMC since they were thought to host a single stellar population, with homogeneous chemical composition and it was easy to derive ages from color-magnitude diagram (CMD) using main-sequence turn-offs[3]. Da Costa (1991); Olszewski et al. (1996) reviewed our knowledge and understanding of the GC systems in the SMC and LMC and the main facts are summed up hereafter.

Geisler et al. (2003) call the LMC a "star cluster factory": the LMC has the highest specific frequency of clusters in the LG (van den Bergh, 1998). Hodge (1988a) estimated the number of LMC GC to about 4200 (Bica et al., 1999 found 6559 extended objects in the LMC: 2577 clusters, 2883 emission-free associations and 1199 nebulae) while Hodge (1986) estimated the number of SMC GC to about 2000 (Bica & Schmitt, 1995 found 1188 extended objects in the SMC and the MB: 554 clusters, 343 emission-free associations and 291 nebulae). Both LMC and MW formed at early epoch (i.e. during the very first Gyr of the galaxy life) massive GC that form today a $\sim$ 12 to 13 Gyr-old metal-poor population. However, while both LMC and MW lost the ability to form GC about 12 Gyr ago, the LMC re-ignited the formation of GC $\lessapprox 4$ Gyr ago. This led to the definition of the so-called *age gap*, i.e. a period of more than 8 Gyr (from $\sim$ 4 to 12 Gyr ago) during which no or almost no GC have been formed in the LMC. A long quest for LMC GC falling in this age range has proven to be unsuccessful, the only candidate being the enigmatic ESO121-SC03 (Mateo et al., 1986). Questions have been raised about the accuracy of ages, possible biases in or incompleteness of the studied samples: e.g., magnitude limited observations leading to miss the faintest GC (fading of the GC because of stellar evolution; Elson & Fall, 1988) or disruptive processes leading to the destruction of GC. However, Hodge (1988b) showed that the dissolution timescales of GC in the LMC is five to ten times longer than in the MW and Da Costa (1991); Olszewski et al. (1991) argued that it is unlikely that those two mechanisms could conspire to make such a distribution. And as for the accuracy of ages, numerous studies have improved the determination of ages e.g., Bica et al., 1998; Geisler et al., 1997, 2003; Piatti et al., 2003, 2002; Rich et al., 2001 and confirmed the borders of the age gap. Olszewski et al. (1991) notice that the age gap correlates with a metallicity gap: the intermediate-age GC are more metal-rich ([Fe/H] $\gtrapprox -1.0$ dex, with a mean metallicity around -0.5 dex) and the oldest are

[3]Since then, it appears that GC are much more complicated objects than previously thought showing self-enrichment and having multiple stellar populations, the most famous example being the over-studied ω Centauri, a MW GC hosting multiple stellar populations (e.g., Bedin et al., 2004; Ferraro et al., 2004b; Pancino et al., 2000, 2011, 2003; Romano et al., 2010b; Villanova et al., 2007). Besides, multiple stellar populations have also been found in LMC GC (e.g., Mackey et al., 2008; Milone et al., 2013, 2009).

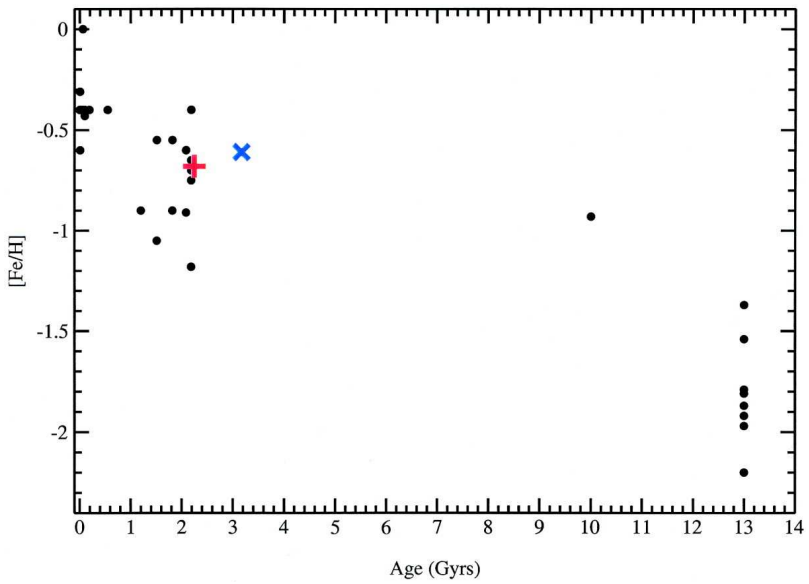

Figure 1.6: **The LMC GC AMR.** We clearly see the age gap separating the very populated group of young and intermediate-age LMC clusters, on the one hand, and the scarcely populated group of old LMC clusters. The only cluster found in the age gap is the remote ESO121-SC03. *Credits:* Rich et al. (2001)

more metal-poor ([Fe/H] ≈ -2.0 dex). Both intermediate-age and old LMC GC exhibit a disc kinematics (Olszewski et al., 1996); let us note that unlike LMC, most of the old GC of the MW belong to the halo.

On the other hand, the SMC started the formation of GC about 10 Gyr ago, i.e. later than the LMC and MW, and has never stopped since then (Da Costa, 1991; Olszewski et al., 1996). In particular, the SMC has formed numerous cluster during the LMC age gap. Amazingly the age-metallicity relation (AMR) derived for SMC and LMC GC exhibit a relative good match (Piatti et al., 2002) at old and intermediate age. Rich et al. (2000), based on a limited sample of GC, discussed the possibility of a similar age gap in the SMC GC distribution: they claim that SMC GC formed in two main events 8 Gyr and 2 Gyr ago. However, Rafelski & Zaritsky (2005) conclude that there is no evidence for an equivalent age gap in the SMC GC distribution.

The differences between the two Clouds in the GC population has led to various interpretations. For instance, Da Costa (1991) claim that the high number of GC between 1 and 3 Gyr in the LMC compared to the SMC is a sign that the cause of the re-ignition is internal, otherwise if it were due to an external cause like tidal interactions, it should have had the same effect in the two MC. Relying on Lin & Richer (1992), Olszewski et al. (1996) suggested that ESO121-SC03 has been accreted from the SMC since ESO121-SC03 has similar age and metallicity to SMC GC. Olszewski et al. (1996) pointed the fact that mutual tidal interactions between the two Clouds and different GC formation histories are not incompatible: because of the difference of mass between the two Clouds, the tidal interactions of the LMC

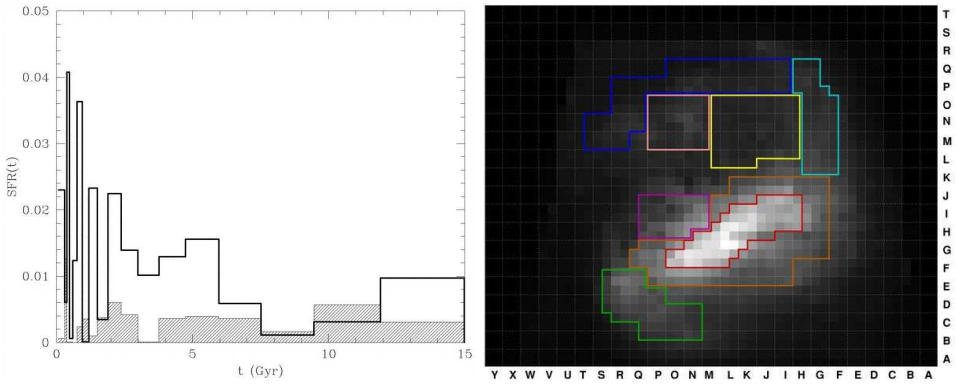

Figure 1.7: **Left panel: The LMC SFH in the bar and the disc.** Thick line histogram: LMC bar; shaded histogram: LMC disc. *Credits:* Smecker-Hane et al. (2002). **Right panel: Star-count map of the LMC.** The gray intensity is proportional to the number of stars present in that region. Red line: the LMC bar; magenta line: Tarantula nebula; pink line: Constellation III. We see that the bar hosts a huge number of stars compared to the other regions of the LMC, mostly young and intermediate-age stars. *Credits:* Harris & Zaritsky (2009)

could have been enough to maintain a continuous GC formation in the SMC, while only close encounters between the two Clouds could have triggered the re-ignition of the GC formation in the LMC.

1.2.2.2 Field stars

Star formation histories Many authors (Holtzman et al., 1999; Olsen, 1999; Smecker-Hane et al., 2002) have derived star formation histories for field stars from deep CMD obtained with the Hubble Space Telescope (HST) and showed that there is no field counterpart to the LMC GC age gap, i.e. there was star formation at all epochs. Harris & Zaritsky (2001) found a quiescent epoch (which does not mean absence of star formation) between 12 and 5 Gyr ago. Smecker-Hane et al. (2002) have derived from deep CMD the star formation history (SFH) for field stars located in the LMC bar and the inner part of the LMC disc (Fig. 1.7). They show that the SFH of the bar and the inner disc were similar at old epochs (between 7 and 14 Gyr); but while the SFH of the inner disc has remained rather constant until now, the bar has experienced a dramatic increase of its SFH, 6 to 4 Gyr and 2 to 1 Gyr ago.

Harris & Zaritsky (2009) performed for the first time an extensive spatial mapping of the SFH of the LMC albeit from much shallower CMD. Confirming and extending previous studies, they built the following picture: the LMC underwent an initial burst of star formation, followed by a quiescent period between 12 and 5 Gyr ago, and then the star formation resumed and has persisted at a significantly higher rate up to present day. In addition, the global pattern of the LMC SFH exhibits several enhanced episodes of star formation in the LMC at 12 Myr, 100 Myr, 500 Myr and 2 Gyr. The AMR for both LMC GC and field stars (Harris & Zaritsky,

2009) are very similar at old and intermediate ages (the comparison is not relevant during the age gap): it suggests a tight coupling of these two modes of star formation along the whole history of the LMC, with a rapid chemical enrichment over the last 5 Gyr (increased by 0.5 dex).

Comparing their detailed SFH for the LMC to that of the SMC, Harris & Zaritsky (2004) and Harris & Zaritsky (2009) found a relatively good correlation between some enhanced episodes of star formation, supporting the idea that close encounters between the two Clouds had influenced the stellar activity in both SMC and LMC: three peaks at 100 Myr, 500 Myr and 2.5 Gyr in the LMC SFH and three peaks at 60 Myr, 400 Myr and 2-3 Gyr in the SMC SFH. In addition, they remark that the global shape of the SFH of both Clouds is very similar with an initial burst, followed by a quiescent period and then a re-ignition of the stellar activity 3 and 5 Gyr ago for the SMC and LMC respectively. They interpreted these similarities within the frame of a shared history of the two Clouds through a long term (at least several Gyr) binary interaction, rather than a three body (SMC–LMC–MW) interaction: new proper measurements of the MC by Kallivayalil et al. (2006b) seem to rule out scenarios involving multiple encounters between the three galaxies and favoured rather first capture models.

Thanks to their spatially resolved mapping of the LMC, Harris & Zaritsky (2009) could also discuss the SFH of particular regions of the LMC. For instance, they showed that 30 Doradus and Constellation III are very recent star forming regions: their star formation rate (SFR) was at a low level until a few 10 Myr ago. The region of strongest interest for this thesis work is the LMC bar. Harris & Zaritsky (2009) claim that the bar has been part of the LMC for most of its history. In their Figure 8, they detect a star formation in the bar at the beginning, $\sim$ 14 Gyr ago, and "nothing" until 6 Gyr ago (the quiescent epoch). Then, stellar formation seems to be re-ignited in the central regions of the LMC: some strong central events of star formation between 6 Gyr and 4 Gyr, $\sim$ 500 Myr and $\sim$ 100 Myr ago map the shape of the bar while the central event of star formation 2.5 Gyr ago does not. Harris & Zaritsky (2009) confirmed what was found by Smecker-Hane et al. (2002): unlike the disc, the central regions of the LMC experienced a strong stellar activity during the last $\sim$ 6 Gyr.

Age and metallicity gradients Hidalgo et al. (2003) and Skillman et al. (2003) (see also Robles-Valdez et al., 2013; Zhang et al., 2012 for observational findings and Pipino et al., 2006 for theoretical predictions) showed that the star formation is suppressed in the outer edge of dwarf irregulars and preferentially concentrated towards the centre of this kind of galaxies. Hidalgo et al. (2003) discuss two formation scenarios called *halo/disc scenario* or *shrinking scenario* to explain this fading of the star formation towards the outer regions. In the first scenario, a first star formation occurs during the early phase of the galaxy formation, then the gas is swept by supernova explosions and the star formation is temporarily paused; after a galaxy restructuring (formation of a halo), star formation re-starts in a disc phase. In the second scenario, the star forming region progressively shrinks as the galaxy ages and the ratio of young to old stars increases towards the centre. To discriminate between the two scenarios, Hidalgo et al. (2003) suggests to look at

the relative fraction of young or intermediate-age stars to old stars, the metallicity mixture and the kinematics of stars: a halo phase requires old, low-metallicity, kinematically hot stars while the shrinking disc scenario allows for a significant fraction of intermediate-age stars in the outskirts of the galaxy (i.e., the outskirts are not exclusively made of old population).

Gallart et al. (2008) suggest that the LMC experienced such an *outside-in formation* of its disc in contrast with the *inside-out formation* predicted by ΛCDM hydrodynamical simulations for the built-up of the disc of large galaxies (e.g., observations of abundance gradients: Janes, 1979; Mayor, 1976; Panagia & Tosi, 1980; Shaver et al., 1983; chemical evolution of discs: Chiappini et al., 1997, 2001; Prantzos & Boissier, 2000; cosmological simulations: Pilkington et al., 2012; Roškar et al., 2008). In their four LMC fields located between radii of 3 to 6 kpc, Gallart et al. (2008) found a coeval old population while the age of the youngest component of the dominant stellar population increases with the galactocentric distance (from 100 Myr to 1.5 Gyr). The shrinking of the star forming region is supported by the colour functions that point an enhanced star formation in the three innermost fields 4 Gyr ago. In addition, the age gradient correlates with H I map by Staveley-Smith et al. (2003) where the innermost fields correspond to highest H I density columns: the gas disappears progressively from the outer towards inner regions, which halts the star formation activity. Furthermore, the kinematics of LMC disc stars are too low to be that of halo stars even in fields as far as 8-9 kpc from the LMC centre (e.g., Carrera et al., 2011, 2008b; Gallart et al., 2004). However, we have to keep in mind that these results do not rule out the possibility of radial migrations, which can produce similar effects (i.e. the young populations form in the inner region, then migrate towards the outer edge).

Carrera et al. (2008a) (13 SMC fields) and Carrera et al. (2011, 2008b) (resp. 4 and 6 LMC fields) derived metallicities, ages and kinematics from the infrared Ca II triplet (CaT) for hundreds of red giant branch (RGB) field stars at different locations in the disc of the SMC and LMC respectively, aiming at finding age or metallicity gradients. Carrera et al. (2011, 2008b) confirmed and extended results of Gallart et al. (2008): the age gradient exists up to 9 kpc across the LMC disc and in different spatial directions. A metallicity gradient appears beyond a galactic radius of 7 kpc: it does not reveal a different chemical enrichment but is instead explained by the age gradient. Indeed, the outward-decreasing ratio of (young or) intermediate-age (which tend to be more metal-rich) to old stars (which tend to be more metal-poor) implies an outward-decreasing ratio of metal-rich to metal-poor stars, hence a metallicity gradient. Carrera et al. (2011) checked this fact in two ways: first, the mean metallicity of the 10 % most metal-poor stars is constant with radius while the mean metallicity of the 10 % most metal-rich stars is constant up to $\sim$ 6 kpc and then decreases; second, the derived AMR for all the fields studied in Carrera et al. (2011, 2008b) are statistically identical (differences could be hidden in the large errors on ages), i.e. all fields experienced the same chemical enrichment. The results for SMC fields in Carrera et al. (2008a) are very similar: a metallicity gradient is found across the SMC disc and is explained by an age gradient; no significant variation of the AMR, i.e. the chemical enrichment, is detected along the galactic radius; the increase of the age of the youngest population with increasing

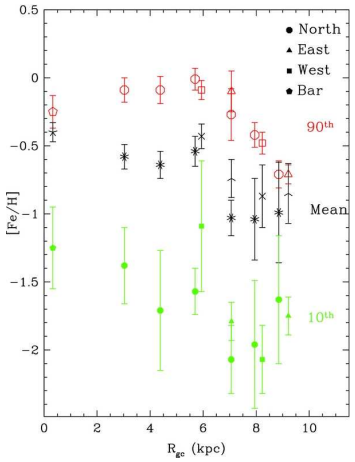

Figure 1.8: **Left panel: Metallicity gradient along the LMC radius.** Metallicity obtained from the Ca II triplet metallicity index by Carrera et al. (2011, 2008b) for RGB stars at various location on the LMC disc. Green symbols: mean metallicity of the 10 % most metal-poor stars; black symbols: mean metallicity of the full sample; red symbols: mean metallicity of the 10 % most metal-rich stars. A metallicity gradient appears from 6 kpc onwards among the most metal-rich population while the metallicity gradient remains flat for the most metal-poor population. This metallicity gradient is interpreted as an age gradient. *Credits:* Carrera et al. (2011, 2008b)

radius supports the scenario of an outside-in formation of the SMC disc as well.

Cole et al. (2005) derived metallicity, ages and kinematics for 373 RGB stars located in the LMC bar. The AMR for their bar field exhibits a rapid increase at ancient times reaching -1 dex in ~ 4 Gyr, then a steady increase of ~ 0.5 dex over the last ~ 10 Gyr (reaching a mean metallicity of ~ -0.45 dex). Cole et al. (2005) remark that the metallicity of their LMC bar field has doubled between the epoch 6–8 Gyr ago (mean metallicity of ~ -0.72 dex), on the one hand, and the epoch 3–6 Gyr (mean metallicity of ~ -0.46 dex). Consistently, with results of Smecker-Hane et al. (2002) (who find a enhanced stellar activity in the LMC bar compared to the disc), Cole et al. (2005) find that 90 % of the stars are younger than 6 Gyr, the median for the sample is 2 Gyr.

1.2.2.3 Detailed chemical abundances

The very first detailed high-resolution determination of chemical abundances in the atmosphere of LMC stars were performed on Cepheids or supergiant stars in both SMC (Spite et al., 1989: three supergiants; Russell & Bessell, 1989: eight supergiants; Luck & Lambert, 1992: seven Cepheids or supergiant stars; Hill, 1997; Hill et al., 1997: six supergiants; Hill, 1999: six supergiants; Venn, 1999: ten supergiants) and LMC (Russell & Bessell, 1989: eight supergiants; Luck & Lambert, 1992: seven Cepheids or supergiant stars; Hill, 1995: nine supergiants). Despite the low statistics, those studies brought interesting results. They showed that [α/Fe] of

SMC/LMC supergiants is similar to that of MW supergiants, i.e. below the MW disc stars of the same metallicity as the SMC/LMC. And Luck & Lambert (1992) and Hill (1995) derived a striking result: the chemical composition of supergiants stars, i.e. very young stars likely formed with the $\sim$ present day chemical composition of the Clouds, exhibit enhanced abundances in Ba and Eu. This feature is not seen in the MW counterpart of those LMC supergiants and was not expected from the nucleosynthesis theory and yields predictions.

Those early studies relied on a very few number of stars (below ten), which is clearly not enough to draw strong and general conclusions on the chemical enrichment of the LMC, and they required luminous targets, as supergiants which are young stars and do not allow the probing of ancient epochs. In fact, the *galactic archaeology*, which consists in chemically and kinematically tagging stars in order to identify and characterise stellar populations, is a powerful tool helping in reconstructing the past history of a given galactic environment but requires deep high-resolution observations and large datasets. The application of galactic archaeology techniques was already complicated for the MW and it became much more challenging when applied to external galaxies like the SMC or LMC. Thus the needs in observation time and detection sensitivities have drastically increased. The first scientific jump has been brought by the advent of eight-meter class telescopes (e.g., the VLT), which allows the observation of fainter and distant sources. The second jump has been brought by the development of multi-fibres spectroscopy (e.g., FLAMES). This has led to the first compilation of large datasets, which once *homogeneously analysed*, allow to pull out statistically significant and homogeneous results and thus formulate solid interpretations.

In this vein, recent high-resolution detailed abundances of LMC RGB stars have been published for GC stars (Johnson et al., 2006: ten RGB stars in four old GC; Mucciarelli et al., 2008: 27 stars in three young GC; Mucciarelli et al., 2010: 18 stars in three old GC; Mucciarelli et al., 2011: 30 stars of NGC 1866) and field stars (Pompéia et al., 2008: 59 field disc stars; Lapenna et al., 2012: 89 field disc stars). Mucciarelli et al. (2008) confirmed the unexpected enhanced Ba, La and Eu abundances in metal-rich stars. Pompéia et al. (2008) provided for the first time a detailed chemical analysis of a large sample of LMC RGB stars located in the LMC disc, $\sim 2^\circ$ South of the LMC bar. Pompéia et al. (2008) were able to derive abundances for 16 different elements, sampling the main nucleosynthetic elemental families (i.e. α-, iron-peak, s- and r-elements) and showed that asymptotic giant branch (AGB) winds and type Ia supernova (SNIa) played a major role in the chemical evolution of the LMC disc. Lapenna et al. (2012) measured the α content (O, Mg, Si) of 89 stars in a field close to the LMC globular cluster NGC 1786, some 3° North-West of the bar. In Chapter 5, I will compare and discuss the detailed chemical abundances obtained in Chapter 4 for our LMC bar and disc fields to those previous studies.

1.2.3 Possible chemical evolution scenarios

The derived SFH (Harris & Zaritsky, 2009; Smecker-Hane et al., 2002) for LMC field stars and AMR for LMC GC (e.g., Piatti et al., 2002) and field stars (Carrera

et al., 2011, 2008b; Cole et al., 2005) can help to build a first vision of the chemical evolution of the LMC.

Carrera et al. (2011, 2008b) noticed that the AMR derived for all their LMC disc fields are statistically identical, and in the following we will consider a unique AMR for the whole LMC disc. The AMR of the LMC bar and disc are similar for old ages (see comparison in Carrera et al., 2008b), exhibiting a rapid increase over the first 4 Gyr: the bar reached a mean metallicity of ~ -1 dex while the disc reached a mean metallicity of ~ -0.8 dex. Then, the AMR of the disc flattens, leading to a slow chemical enrichment: between 10 and 3-4 Gyr ago, the mean metallicity of the disc increased by 0.2 dex. Finally, the disc experienced a fast episode of chemical enrichment the last $\sim 3-4$ Gyr during which the mean metallicity jumped from ~ -0.6 dex to ~ -0.2 dex. On the other hand, after the initial increase of its metallicity, the LMC bar experienced a downturn in the rate of the chemical enrichment and kept an approximate constant enrichment rate over the last 10 Gyr (with a possible slight steepening around 6-5 Gyr ago).

A crude comparison of the LMC bar AMR to the theoretical AMR proposed by Pagel & Tautvaisiene (1998) for a bursty (two bursts 14 and 3 Gyr ago) and a smooth chemical evolution of the LMC fails: the smooth model seems to better reproduce the chemistry at intermediate ages (younger than 5 Gyr) while the bursty model seems to better reproduce the behaviour at old epochs (older than ~ 7 Gyr). However, Cole et al. (2005) suggest that the class of bursty models is more promising to reconcile the AMR of old and young/intermediate-age stars (e.g., by tuning the time of the second burst).

The AMR of the LMC bar and disc may appear surprising when one remembers that the SFH of the bar experienced a violent increase about 6 and 2 Gyr ago while that of the disc remained constant (Smecker-Hane et al., 2002). However, Carrera et al. (2008b) showed that it can be understood by invoking infalls and outflows of gas (e.g., infall of metal-poor gas from the SMC or infall of pre-enriched material from the disc + outflow), which helps to reproduce the AMR over the last Gyr. Tsujimoto et al. (1995) and Bekki & Tsujimoto (2012a) have also published chemical evolution models for the LMC, testing various parameters like the ratio of SNIa and type II supernova (SNII), the slope of the initial mass function (IMF), gas loss due to supernova (SN) explosions etc. Based on the results of this thesis work, I will further discuss the chemical evolution of the LMC and some of the above models in Chapter 5.

1.2.4 Possible dynamical scenarios

As underlined in the previous sections, the histories of the MW, SMC and LMC have been intimately linked — at least over the last Gyr — and the challenge of dynamical evolution modelling is to reproduce *simultaneously* and *as best as possible* most of the morphological and dynamical features of these three galaxies. Because of lower computational power, early works were interested in reproducing a few number of characteristics. For instance, Murai & Fujimoto (1980) or Lin & Lynden-Bell (1982) attempted to explain the origin of the MS via tidal debris using a MW with a massive halo and a long-lived SMC–LMC binary system performing

several close encounters with our Galaxy. Gardiner & Noguchi (1996) succeeded in modelling the formation of the MS and the LA during a close encounter of the three galaxies 1.5 Gyr ago, and the formation of a tidal tail and the MB during a close encounter between the two Clouds 200 Myr ago. Let us note that, in their simulations, Gardiner & Noguchi (1996) modelled only the SMC with self-gravitating particles while the MW and the LMC were represented by static spherical potentials. The improvement of computational capabilities has allowed more sophisticated hydrodynamical simulations which properly model the three galaxies, allow to follow the gas and stellar components of each galaxy separately etc.

Until 2005-2006, models were based on two assumptions: (1) the SMC and the LMC are a long-lived binary system, (2) the MW, SMC and LMC are a long-term interacting system and the three galaxies have experienced several close encounters. Bekki et al. (2004b) and Bekki & Chiba (2005) showed that when dynamical frictions between the two Clouds are taken into account, the binary system cannot remain for the last 13 Gyr. Therefore, they claim that the SMC and LMC were born as separate entities and that the dynamical coupling occurred recently (in their model, 4 Gyr ago). However, Kallivayalil et al. (2006b) determined the proper motions of the two Clouds to a higher precision (thanks to HST images on a ten year baseline) and their results (i.e. higher velocities) have turned upside down these well-established vision. According to the new proper motions, fundamental questions have been revived: Kallivayalil et al. (2006a) question whether the SMC and LMC form a bound system while Besla et al. (2007) wonder whether the MC are on their first capture onto the MW. This new proposed framework is more challenging to explain the formation of the MS and LA: while previous dynamical simulations assumed several pericenter passages of the two Clouds, the new proper motions require to form the leading and trailing streams within a single passage of the Clouds about the MW. For instance, Bekki (2011) show that the single and first close encounter ~ 2 Gyr ago between the LMC and the MW lead to the formation of short stream-like structures and claim that at least two pericenter passages are needed to reproduce the MS and the LA (i.e., the first close encounter occurred 4 Gyr ago). On the other hand, as noted by Besla et al. (2007), a recent first close encounter (i.e. 2-3 Gyr ago) is a convenient assumption to explain the recent observed enhanced star formation in the LMC. In the following, I will briefly describe some dynamical models.

Bekki et al. (2004b) and Bekki & Chiba (2005) performed N-body simulations of the LMC, taking into account gravitational interactions with both MW and SMC. Since dynamical frictions between the two Clouds should prevent a long-lived binary system, Bekki et al. (2004b) and Bekki & Chiba (2005) assume that the LMC and SMC were born as separate entities and that the dynamical coupling occurred 4 Gyr ago for the first time. This assumption offers a convenient framework to explain the different GC histories of the two Clouds (age gap for the LMC, delayed start of the GC formation for the SMC). In their model, the LMC formed far from the MW so that the MW gravitational field could not maintain the GC formation while the SMC was closer to the MW and formed GC from 10 Gyr ago up to now. Thus, the re-ignition of the GC formation in the LMC could be the sign of a recent SMC–LMC coupling. Indeed, the first close encounter 4 Gyr ago has initiated a period of strong

tidal interactions between the two Clouds, provoking shocks and compression of gas clouds, leading to the formation of a new generation of GC (e.g., see Bekki et al., 2004a for the formation of GC from cloud-cloud collisions). To explain the difference between the field SFH and the GC history, they argue that field star formation is more sensitive to tidal interactions than GC formation, and therefore, can begin earlier, i.e. when the SMC and LMC are farther from each other. In their model, the tidal capture of the SMC by the LMC began 6-7 Gyr ago and initiated an era of enhanced (field) star formation, the culmination of this intense activity occurring ~ 4 Gyr ago with the first SMC–LMC collision (i.e. close encounter) which produced the intermediate-age clusters and raised the metallicity of the LMC by a factor of three. The two Clouds have experienced four close encounters over the last ~ 4 Gyr and several pericenter passages about the MW over the last 10 Gyr (independently and then quasi-simultaneously after the first collision of the two Clouds). The tidal interactions with the MW and/or the SMC has sustained the field star formation in the LMC (especially the last ~ 4 Gyr) and has created the LMC bar (i.e. the bar did not form spontaneously from disc instabilities), has thickened the LMC disc by tidal heating and has created a stellar halo by spatial redistribution of the stars located in the outer edge of the LMC disc.

Motivated by the results of Kallivayalil et al. (2006b) on the MC proper motions, Besla et al. (2007) explore the scenario of a first capture of the LMC onto the MW. They underline weaknesses of scenarios based on multiple pericenter passages. Particularly, the recent increase observed in the SFH of the LMC is explained by a close encounter with the MW; however, it is surprising and difficult to understand that the the previous passages did not produce similar effects. Thus, their best orbital model predicts an LMC 1 Mpc away from the MW ~ 5 Gyr ago while a bound orbit would require a much more massive MW than what is observed today. In addition, van den Bergh (2006) performed a morphological comparison of the MW and Andromeda satellites and claim a remote origin for the SMC and LMC which appear as "outliers" (they are gas-rich while all the other satellites are gas-poor). If a first capture scenario is convenient in certain respects, it revives the question of the MS and LA, as underlined above. However, Besla et al. (2010) succeeded in forming the MS and LA using only SMC–LMC interactions, i.e. without the aid of the MW and thus consistently with a first capture scenario (see also Diaz & Bekki, 2011, 2012). More recently, Besla et al. (2012) presented sophisticated simulations within the framework of a first capture scenario and tested two models (model 1: the SMC and LMC experienced two close encounters, but the SMC never gets closer than 20 kpc to the LMC; model 2: the SMC and LMC experienced three close encounters, the last one being a direct collision less than 0.5 Gyr ago) aiming at reproducing all the morphological and dynamical patterns: at the beginning, the MC are a binary pair, evolving in isolation until their first passage close to the MW. Their model 2 fulfils most of the requirements (Fig. 1.9): a leading arm, a 150° trailing stream, a bridge (hosting star formation) between the two Clouds, offset gas and disc centroids for the LMC, an asymmetric off-centre LMC bar absent from the gas (see also Sec. 1.2.5), a single spiral-arm hosting star formation and an elliptical warped LMC stellar disc; it fails however at reproducing the mass and morphological peculiarities (bifurcation) of the MS and the current SFR in the LMC

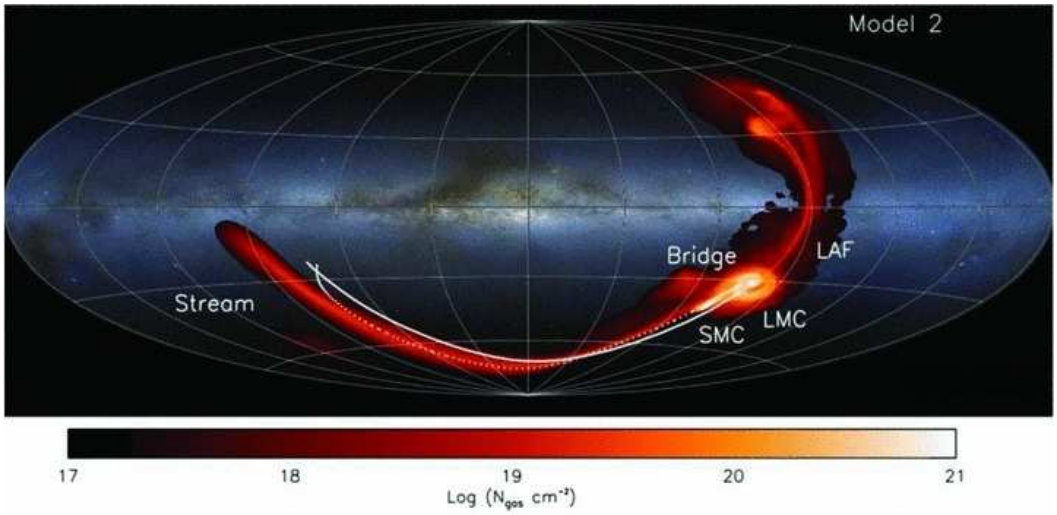

Figure 1.9: **Dynamical modelling of the MW, the SMC and the LMC.** Final state of Model 2 proposed by Besla et al. (2012). The colour codes the hydrogen density. We can identify the main morphological features listed previously: the MB, MS and the LA. This model gives a final (i.e. current) state extremely close to what is shown in Figure 1.3. *Credits:* Besla et al. (2012)

and the SMC.

1.2.5 Insights on the nature and origin of the LMC bar

As I explained in Section 1.2.1, the LMC bar is an enigmatic structure, with amazing properties: asymmetric and warped geometry, with a centroid off-centre with respect to those of the underlying stellar disc and gas disc, maybe misaligned with respect to and/or located in front of the disc plane. Deciphering the nature and the origin of the so-called LMC bar is one of the main items in the wish list of astronomers interested in the LMC. Below, I will discuss three cases: Zaritsky (2004) geometrical solution, the scenario of dynamically-driven bar and the scenario of burst-born bar. In each case, the bar is assumed to be coplanar[4].

Zaritsky (2004) proposed an attractive solution — a tri-axial stellar bulge embedded in a highly obscuring thin disc — which aims at reproducing all the quoted features. Unfortunately, this solution is not completely satisfactory since it requires a strong reddening (or a very inclined disc which has equivalent effect), which is not supported by several reddening maps of the LMC (see Chapter 3). And if this were the case, one would still have to understand the origin of such a stellar bulge (driven by a dynamical instability in the past or similar to early-type bulges?). In addition to the reddening problem, Cole et al. (2005) measured radial velocities for 373 RGB field stars located in the LMC bar and found a velocity dispersion

[4]The likely link (e.g., Gardiner et al., 1998) between the presence of the bar and the spiral arm-like features in the LMC does not speak in favour of a levitating bar.

$\sim 25\,\mathrm{km\,s^{-1}}$ for their sample, i.e. lower than those expected for a bulge. However, the velocity dispersion of Cole et al. (2005) LMC bar stars is not uniform with respect to the metallicity: the 5 % most metal-rich stars have a velocity dispersion of $\sim 17\,\mathrm{km\,s^{-1}}$ while the 5 % most metal-poor stars a velocity dispersion of $\sim 41\,\mathrm{km\,s^{-1}}$, i.e. the most metal-poor population is kinematically hotter than the most metal-rich one and resembles, in that sense, to a bulge or a halo component. However, as noted by Cole et al. (2005), it is unlikely that the formation of the bar/bulge had preferentially heated metal-poor disc stars.

The LMC bar is often thought as a dynamically-driven bar, i.e. a structure driven by disc instabilities like the one found at the centre of the MW. Physics of bars (formation, dissolution, renewal, effects on the gas etc.) in disc galaxies has been broadly studied: Combes & Sanders (1981), Colin & Athanassoula (1989), Combes et al. (1990), Combes & Elmegreen (1993), Sellwood & Wilkinson (1993), Bournaud & Combes (2002), Regan & Teuben (2004), Kormendy & Kennicutt (2004) etc. For instance, the channelling of gas towards the central regions due to the bar torques is expected but no signatures of the LMC bar have been found in the gas distribution, which strongly weakens the scenario of a dynamically-driven bar. Another possibility could be that, indeed, gas has been driven towards the inner regions and completely turned into stars, which would explain why we do not see a central gas over-density. However it seems unlikely that such a dramatic event would have left such a well-organised disc of gas: indeed, we should anyway expect some signatures in the present-day distributions, like gas-free spaces in or around the central regions. Another interesting point is that bars may be short-lived because of the central mass concentration and destroy themselves within 1-2 Gyr (Athanassoula et al., 2005; Bournaud et al., 2005). Yet, Harris & Zaritsky (2009) find that the LMC bar has existed during most of the LMC lifetime (the SFH traces the LMC bar even at old epochs). Simulations (e.g., Bournaud & Combes, 2002) have shown that the formation of bars can be a recurrent process: bars can vanish and be renewed a couple of times over a Hubble time. Therefore, we could imagine that we are observing a second occurrence of a bar structure in the LMC. However, at each renewal, the bar is expected to be weaker than the previous time; the prominence of the current bar seems to be contradictory (in other words, the previous bar structure should have been even more marked). If we assume that we have a dynamically-driven bar, one still has to explain why it is asymmetric, warped and off-centre. The model 2 in Besla et al. (2012) explains the asymmetric off-centre bar: as the LMC disc is bar unstable, the bar is present from the beginning; it becomes asymmetric off-centre due to a close encounter of the LMC and SMC a few Myr ago.

Instead of being the result of dynamical instabilities, the LMC bar can also be a stellar over-density provoked by a recent and violent stellar burst and embedded in the LMC disc. Observational facts support the scenario of a *burst-born bar*: the SFH of the LMC bar derived by Smecker-Hane et al. (2002) exhibits a dramatic increase over the last Gyr, compared to what is seen for the disc, which implies that a huge number of stars have been recently formed; consistently, Cole et al. (2005) find that 90 % of their RGB sample located in the LMC bar are younger than 6 Gyr. In addition, one may also wonder whether a burst-born bar would have

an imprint on the gas distribution and if the effects would be different than those of a dynamically-driven bar? For instance, Gardiner et al. (1998) showed that an asymmetric off-centre bar will create a single spiral arm in the disc and one has to wonder whether an asymmetric off-centre burst-born bar will also trigger the formation of a spiral arm feature. In the inner regions, we can expect that the gas distribution feels the self-gravity of the burst-born bar; however, the effect should be weaker than for a dynamically-driven bar since the burst-born bar forms within the disc without involving *a priori* a dramatic reorganisation of orbits. Kim et al. (1998) claim that they found evidences of gas streams along the bar contour. Thus, if the scenario of a burst-born bar seems to be more in-line with the observations (and compatible with the outside-in formation of the disc), one still has to explain what triggered the formation of the stellar burst and the morphological features of this stellar over-density (cigar-shape, asymmetry, off-centre location, warp). Bekki et al. (2004b) and Bekki & Chiba (2005) showed that tidal interactions (between the two Clouds and the MW) can trigger the formation of the asymmetric off-centre bar. In their model, the successive close encounters between the LMC and SMC starting ~ 4 Gyr ago build up the bar. Thus, in their models, Bekki & Chiba (2005) need the SMC to explain the origin of the bar. Yet, LMC-like galaxies (i.e. with an asymmetric off-centre bar) have been observed without an SMC-like companion (Wilcots & Prescott, 2004). So Bekki (2009) proposed also a collision with a dark satellite to explain the origin of the LMC bar without using the SMC.

1.3 Aims and structure of this thesis work

As emphasised in the previous sections, numerous questions on the origin, formation and (dynamical and chemical) evolution of the LMC are still unanswered. In order to shed new lights on the chemical evolution of the LMC, an international collaboration has been initiated aiming at the chemical tagging of LMC populations and the first results on the LMC inner disc were published in Pompéia et al. (2008). As part of this project, my thesis work offers the detailed chemical analysis of a sample of RGB stars located in the LMC bar, as well as a homogeneous re-analysis of the Pompéia et al. (2008) LMC disc sample, and aims at:

1. chemically characterising the LMC bar population;

2. comparing the elemental trends of the MW and the LMC and interpreting the differences or similarities in terms of chemical evolution and/or nucleosynthesis processes (constraints on the nucleosynthetic sites and processes);

3. comparing the chemical evolution of the LMC bar and inner disc and interpreting the differences or similarities between the LMC bar and inner disc in the context of the bar formation.

In Chapter 2, I will describe the LMC bar and inner disc samples, describe the data reduction applied to the LMC bar spectra and determine the radial velocities of our LMC bar and inner disc stars. Compared to small samples of ≈ 10

stars, allowing a manual analysis, and to large huge datasets (e.g., Gaia-ESO survey, APOGEE, HERMES, GAIA) of hundreds/thousands of stars, requiring a fully automated handling (e.g., Bailer-Jones, 2011; Kordopatis et al., 2011; Recio-Blanco et al., 2006), our samples are of intermediate size (of the order of 100 stars), i.e. large enough to derive statistically strong results but still of thinkable size to be carefully analysed in a semi-manual fashion. Therefore, in Chapters 3 and 4, I will present the semi-automated pipelines I set up to determine the stellar parameters of our LMC bar and disc stars and to derive their photospheric chemical composition. In Chapter 5, I will confront the results for our two LMC fields, compare them to the LMC and MW literature and propose an interpretation of our findings. Finally, in Chapter 6, I will give a summary of my thesis work and make suggestions for future works.

Chapter 2

Observations & data processing

Contents

2.1 Observations

2.1.1 The FLAMES/GIRAFFE spectrograph

The Fibre Large Array Multi Element Spectrograph (FLAMES) is an ESO facility, born from an international collaboration (ESO, Laboratoire GEPI de l'Observatoire de Paris–Meudon, Observatoire de Genève–Lausanne, and the Anglo Australian Observatory) and mounted in 2002 at the Nasmyth platform of the Kueyen UT2 of the Very Large Telescope (VLT) (Paranal, Chile). This multi-object facility has a field of view of 25′ and allows to record spectra at intermediate or high resolution. FLAMES is formed of a fibre positioner OzPoz, the medium-to-high resolution optical spectrograph GIRAFFE and a link to the red arm of the échelle high resolution spectrograph UVES. The two spectrographs can be used separately or in combined mode (e.g., eight targets are observed at high resolution with UVES and 135 targets observed at lower resolution with GIRAFFE).

[1] http://www.eso.org/public/images/eso-paranal-33/
[2] http://www.eso.org/sci/facilities/paranal/instruments/flames/doc/SPIE_ESO.ps.gz

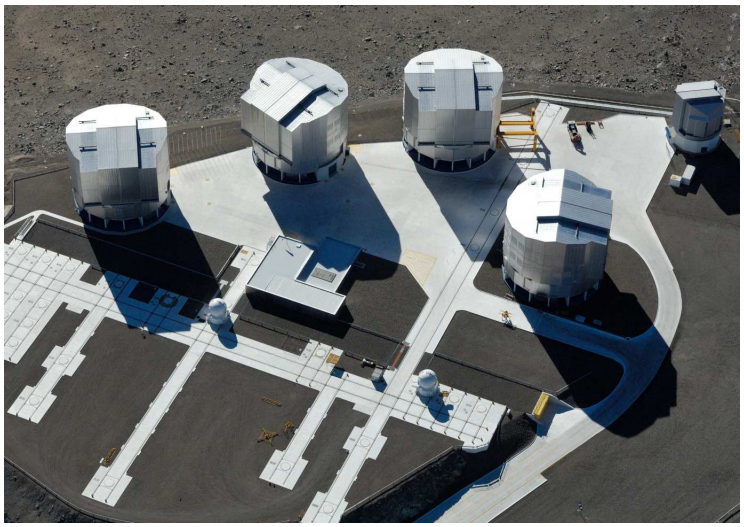

Figure 2.1: The Very Large Telescope. Are visible: the four unit telescopes (UTs) (from left to right: Antu, Kueyen, Melipal and Yepun), two auxiliary telescopes (ATs), the AT tracks and the VST (top left). *Credits:* ESO[1]

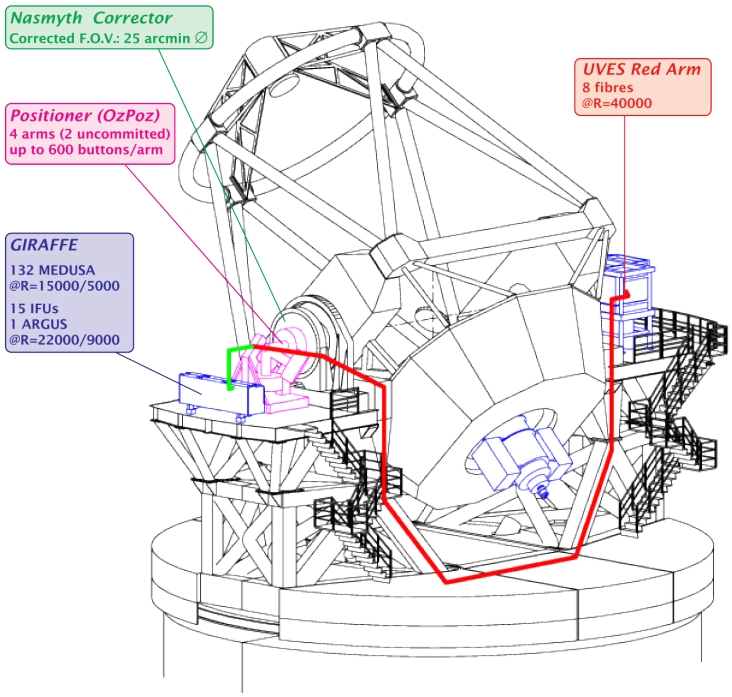

Figure 2.2: Schematic drawing of UT2 showing all FLAMES components: the Nasmyth corrector, the OzPoz fibre positioner, the GIRAFFE spectrograph and the link to the red arm. *Credits:* Pasquini et al. (2000)[2]

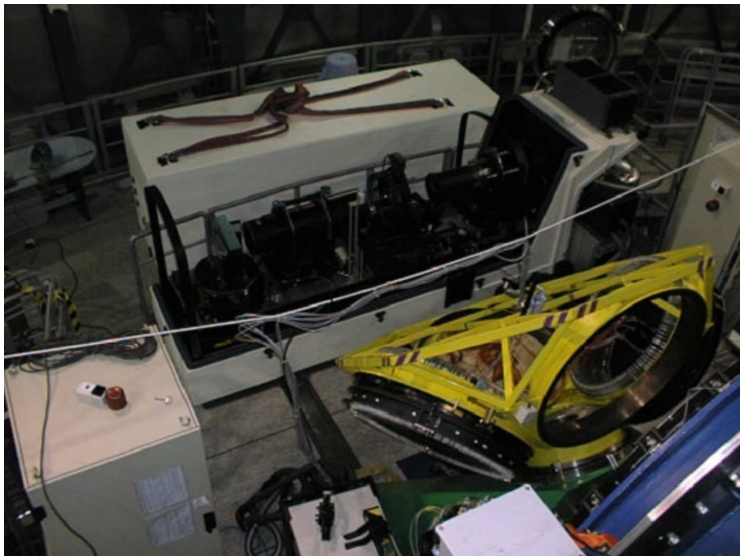

Figure 2.3: Top view of the Nasmyth platform A of UT2. **Picture background:** GIRAFFE is opened and exhibit its opto-mechanical components (picture background). **Picture foreground:** the OzPoz fibre positioner (yellow structure). *Credits:* Kaufer et al. (2012)

GIRAFFE This spectrograph has been designed and built by the GEPI (Observatoire de Paris–Meudon). Its two gratings (600 lines mm^{-1} and 316 lines mm^{-1}) allow low and high resolution spectroscopy ($R \sim 5600-8000$ and $R \sim 11\,000-30\,000$, respectively). Spectra from 3790 Å to 9000 Å can be obtained thanks to 32 filters, eight for the low resolution mode and 24 for the high resolution mode. A GIRAFFE setting is the combination of a filter, a grating and a grating order. GIRAFFE can be operated in three different modes: MEDUSA, IFU or ARGUS. IFU and ARGUS are arrays of fibres and are used to collect spectra of extended object (galaxies, nebula etc.) while MEDUSA is suited for non-resolved targets like stars of the Milky Way (MW) or of distant galaxies. GIRAFFE is equipped with a 2148×4096 CCD camera, whose pixels are 15 µm squares. In MEDUSA mode, up to 135 objects can be observed simultaneously (the fibres have a diameter of 1.2″).

OzPoz The fibre positioner is made of two plates (MEDUSA 1 and MEDUSA 2) where the fibres are mechanically placed according to the astronomical coordinates of the targets. The plates are mounted on a rotating platform, and while one is observing, the second is prepared for the next observing block, which avoids the waste of precious observing time. The fibre positioner also hosts the calibration lamps used to obtain flat-field frames and wavelength calibration frames (Sec. 2.2.1.1, 2.2.1.3).

[3] http://www.eso.org/sci/facilities/paranal/instruments/flames/inst/OzPoz.html and http://www.eso.org/sci/facilities/paranal/instruments/flames/inst/Giraffe.html

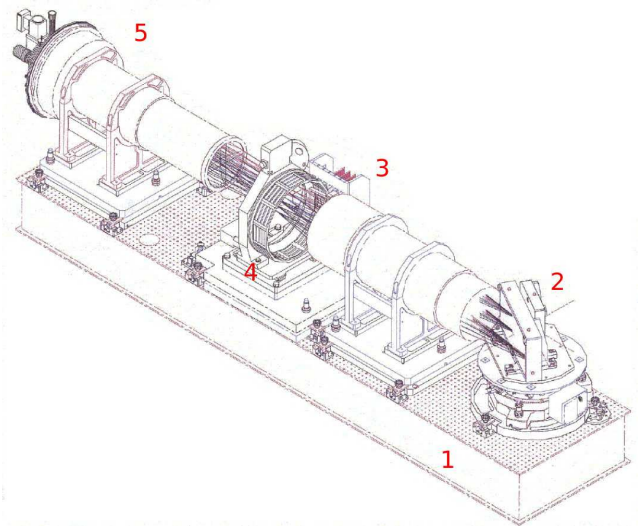

Figure 2.4: GIRAFFE optical table: (1) optical table; (2) LR & HR gratings; (3) slits; (4) filter wheel; (5) CCD. *Credits:* Pasquini et al. (2000)

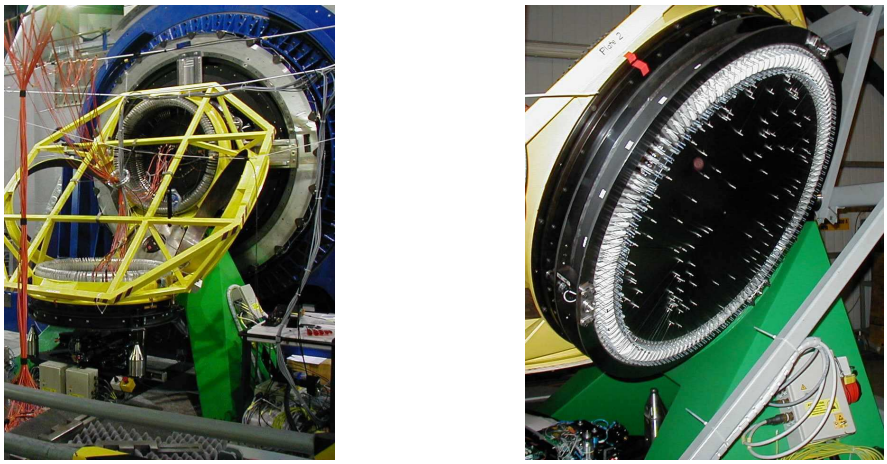

(a) OzPoz (b) An OzPoz plate

Figure 2.5: **Left panel:** The OzPoz fibres positioner at the Nasmyth focus: one plate is looking towards the telescope, the other is facing the ground. The Nasmyth corrector (blue structure) is also visible: it is a system of lenses allowing the exploitation of the full field of view (25′). **Right panel:** Back view of an OzPoz plate: fibres are mechanically positioned and attached with magnetic buttons. *Credits:* ESO[3]

Principle of CCD imaging The coupled-charged device (CCD) is one of the main element of the spectrograph: this sensor is the device used to convert photons emitted by the stars into electric current. Each time a photon hits a photo-site or pixel of the CCD two-dimensional array, an electron-hole pair is created in the semi-conductor (photo-active) material by photoelectric effect. The number of created electrons is proportional to the number of incoming photons, i.e. the exposure time: as long as photons rain onto the parallel register (pixels matrix), charges are trapped in the potential well of the photo-site and accumulate. When the image recording stops, the photo-charges are sequentially read out and the pixels are reset: the electrons of each row are first vertically shifted towards the serial register, then they are horizontally shifted towards the output node, where the charge is amplified and converted into a voltage.

2.1.2 The LMC bar sample

Cole et al. (2005) observed 373 red giant branch (RGB) stars in the field of the Large Magellanic Cloud (LMC) bar (centre coordinates: $(\alpha_{\rm bar}, \delta_{\rm bar}) = (5.402\,{\rm h}, -69.7543°)$) and derived radial velocities and metallicities from low-resolution infrared Ca II triplet (CaT) spectra. We used their metallicity distribution to select 113 RGB stars belonging to the LMC bar, taking care to sample as evenly as possible the whole metallicity range from $[{\rm Fe/H}]_{\rm CaT} = -1.69\,{\rm dex}$ to $[{\rm Fe/H}]_{\rm CaT} = 0.14\,{\rm dex}$. Indeed, since metal-poor stars ($[{\rm Fe/H}] \leq -1.0\,{\rm dex}$) are rare, a random selection would not provide enough metal-poor stars; hence this metallicity selection, a necessary precaution to trace the early epochs of the LMC history (which over-populate the low-metallicity tail of the metallicity distribution). Figures 2.6a, 2.6b and 2.6c show respectively the location of the 373 stars from Cole et al. (2005) and our 113 targets on a $(V-I), I$ color-magnitude diagram (CMD), the metallicity distribution function and the radial velocity distribution of these two samples. We obtained high resolution spectra of our 113 stars at VLT/ESO with the FLAMES/GIRAFFE multi-fibre spectrograph (Pasquini et al., 2002). In order to measure numerous elemental abundances, we used three setups HR11 ($\lambda_{\rm central} = 572.8\,{\rm nm}$, $R_{\lambda_{\rm central}} \simeq 24\,200$), HR13 ($\lambda_{\rm central} = 627.3\,{\rm nm}$, $R_{\lambda_{\rm central}} \simeq 22\,500$) and HR14[4] ($\lambda_{\rm central} = 651.5\,{\rm nm}$, $R_{\lambda_{\rm central}} \simeq 17\,740$), covering a total of ≈ 1000 Å. The spectra thus cover lines belonging to the α- (Ca, O, Mg, Ti, Si), iron-peak (Sc, V, Cr, Co, Ni, Cu), s-process and r-process elements (Ba, La, Zr, Y, Eu). Thanks to the MEDUSA mode of the GIRAFFE spectrograph up to 135 objects can be observed simultaneously in a single exposure. For our purposes, around 10 to 20 fibres were allocated to sky positions and the other remaining fibres were devoted to the observation of LMC bar stars. In addition, three hot (O–B type) stars in the LMC were allocated to fibres, to allow an accurate correction for telluric absorption lines (Sec. 2.2.2.2). Table 2.1 lists the observations (service mode), the dates and the total exposure times. Table 2.5 gives, for our LMC bar stars, their 2MASS identifiers, VI magnitudes from Szymanski (2005); Udalski et al. (1997, 2000), JHK magnitudes from Skrutskie et al. (2006), $[{\rm Fe/H}]_{\rm CaT}$ and $v_{\rm rad,CaT}$

[4] In fact, there are two setups HR14: HR14A (the one we used) and HR14B. HR14B has a larger resolution than HR14A but a smaller wavelength coverage.

Table 2.1: For each setup, the exposures, the total exposure times and the observation dates are given.

Setups	#	Total exp. time	Dates
HR11	10	7 h 42 min	2006-10-[6, 7, 10, 26]
			2006-11-[8, 22]
HR13	5	5 h 50 min	2004-01-15
			2004-02-[16, 21]
			2004-03-26
HR14	4	4 h 08 min	2004-02-[16, 17, 18, 20]

from Cole et al. (2005) (and corresponding 1-σ errors).

2.1.3 The LMC inner disc sample: re-analysis of Pompeia et al.

Pompéia et al. (2008) has chemically analysed 59 RGB stars located in the LMC disc (hereafter, referred as the inner disc sample; centre coordinates: $(\alpha_{\rm disc01}, \delta_{\rm disc01}) = (5.206\,{\rm h}, -71.222^\circ)$), $\sim 2^\circ$ South of the LMC bar. A low resolution survey (Smecker-Hane et al., Private communication; see also Pompéia et al., 2008) allowed to select LMC inner disc stars in order to sample the low-metallicity tail of the metallicity distribution function. Figures 2.7a, 2.7b and 2.7c show respectively the location of the 114 stars from Smecker-Hane et al. (Private communication) and the 67 stars from Pompéia et al. (2008) on a $(V-I), I$ CMD, the metallicity distribution function and the radial velocity distribution of these two samples. As for the LMC bar stars, the LMC inner disc stars have been observed with GIRAFFE using the setups HR11, HR13 and HR14[5]. In order to homogeneously compare the LMC bar and inner disc samples, I will re-analyse Pompéia et al. (2008) sample (re-determination of both stellar parameters and abundances). To this end, in Chapters 3 and 4, I will use equivalent width (EW) and (already) reduced spectra of Pompéia et al. (2008) and apply my pipelines. Table 2.6 gives, for the LMC disc stars, their identifiers, VI magnitudes from Smecker-Hane et al. (2002), JHK magnitudes from Skrutskie et al. (2006), $[{\rm Fe/H}]_{\rm CaT}$ and $v_{\rm rad,CaT}$ from Smecker-Hane et al. (Private communication) (and corresponding 1-σ errors).

2.2 Data processing

Before using the astronomical data for science purposes, we have to process them through a number of codified steps — the data reduction cascade —, which will turn raw data into reduced data (Baranne et al., 1996; Hall et al., 1994; Melo & Smoker, 2009). The data reduction aims at: correcting the recorded spectroscopic frames for the instrumental signatures (CCD, optical system) or at least, minimising them; extracting two-dimensional spectra and collapsing them into one-dimensional spectra; calibrating the extracted spectra into wavelength; removing the sky contribution; correcting wavelengths for radial velocities; eventually, co-adding multiple

[5] Precisely, HR14B (see Footnote 4).

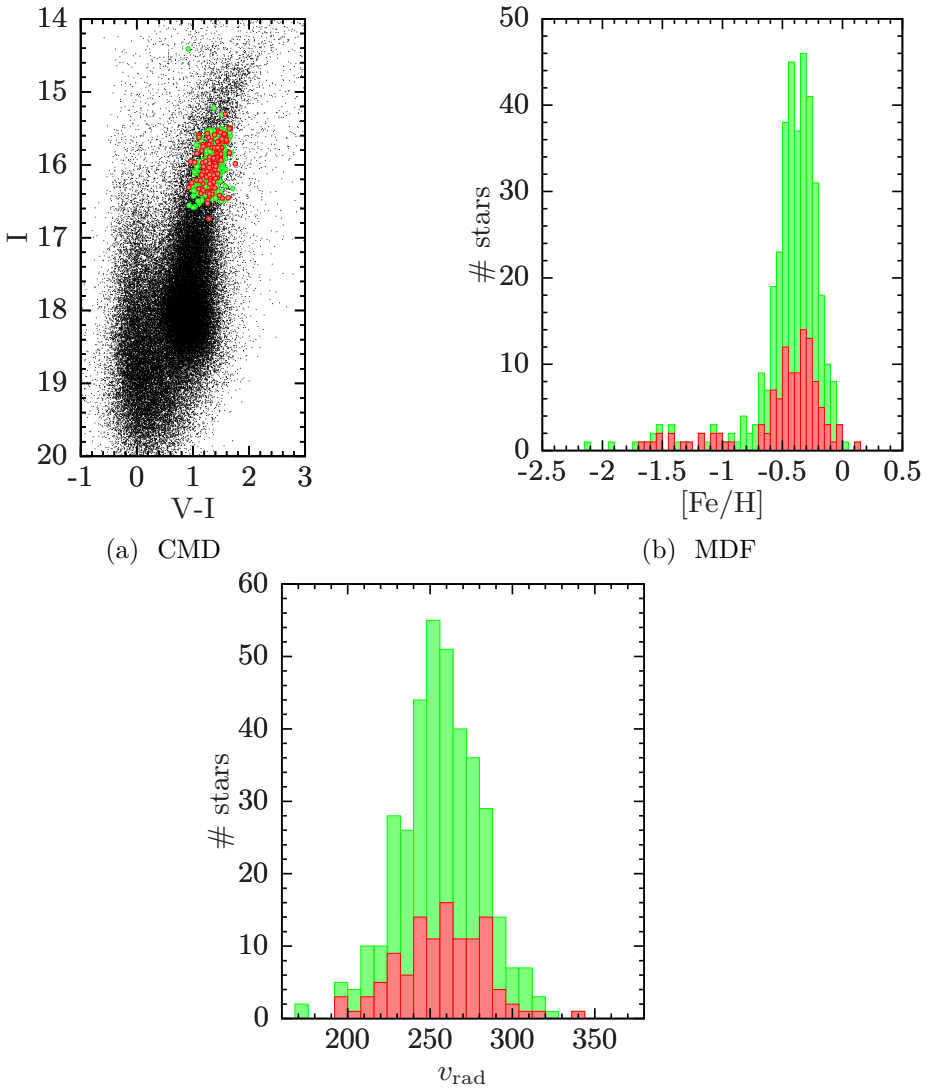

(a) CMD

(b) MDF

(c) Radial velocities distribution

Figure 2.6: **Top left panel:** Colour-magnitude $(\mathrm{V}-\mathrm{I}, \mathrm{I})$ diagram. Red filled circles: our selected RGB stars; green filled circles: Cole et al. (2005) RGB sample; black tiny dots: Zaritsky et al. (2004) catalogue (stars within 0.20° about the centre of the LMC bar field). For the first two datasets, V and I magnitudes are OGLE-III photometry (Szymanski, 2005; Udalski et al., 1997, 2000). **Top right panel:** Metallicity distribution function (dex). Red bars: our selected RGB stars; green bars: Cole et al. (2005) RGB sample. Metallicities are those derived from the infrared CaT index by Cole et al. (2005). **Bottom panel:** Radial velocities distribution ($\mathrm{km\,s^{-1}}$). Red bars: our selected RGB stars; green bars: Cole et al. (2005) RGB sample. Radial velocities are those derived from infrared CaT low-resolution spectra by Cole et al. (2005). The total Cole et al. (2005) distribution has a mean metallicity $\langle[\mathrm{Fe/H}]_{\mathrm{CaT}}\rangle = -0.45\,\mathrm{dex}$ (with a standard deviation $\sigma\left([\mathrm{Fe/H}]_{\mathrm{CaT}}\right) = 0.31\,\mathrm{dex}$) and a mean radial velocity $v_{\rm rad} = 257\,\mathrm{km\,s^{-1}}$ (with a standard deviation $\sigma\left(v_{\rm rad}\right) = 25\,\mathrm{km\,s^{-1}}$).

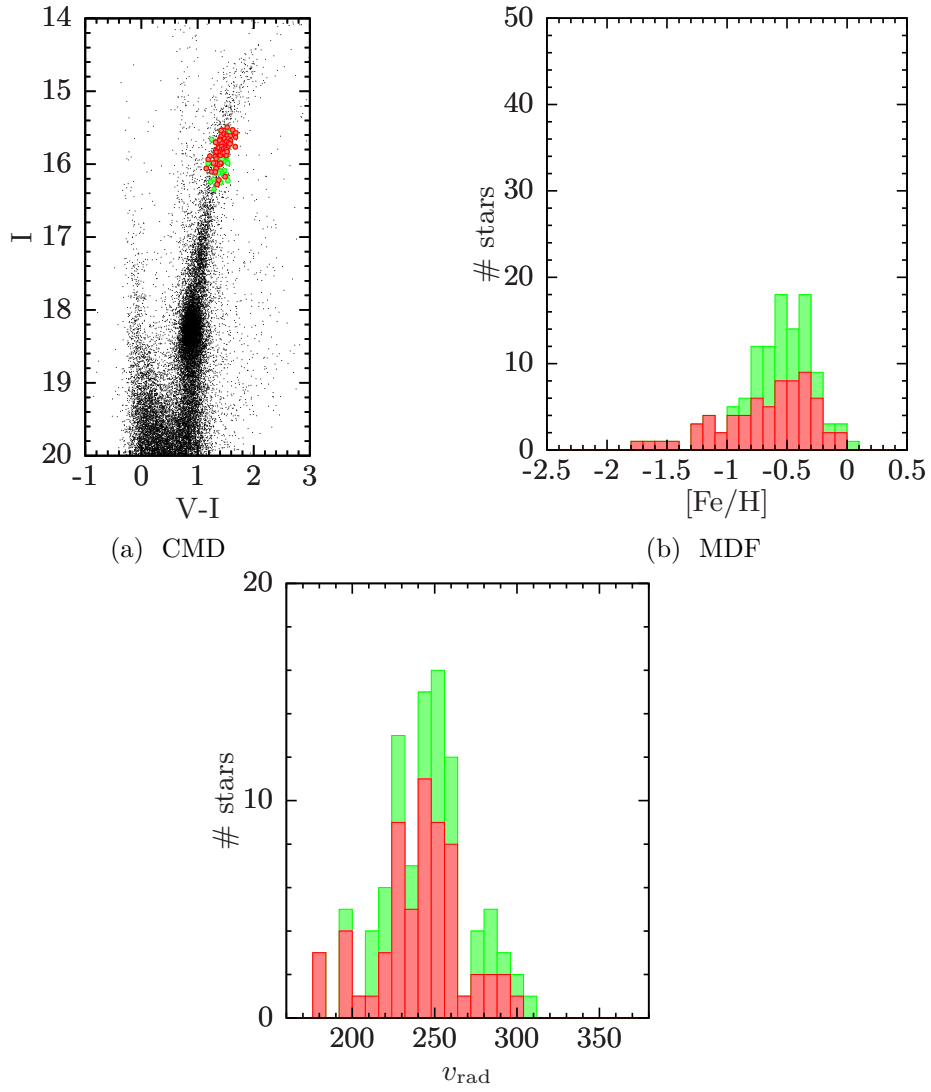

(a) CMD

(b) MDF

(c) Radial velocities distribution

Figure 2.7: **Top left panel:** Colour-magnitude (V−I, I) diagram. Red filled circles: Pompéia et al. (2008) RGB stars; green filled circles: Smecker-Hane et al. (2002) RGB sample; black tiny dots: Zaritsky et al. (2004) catalogue (stars within 0.20° about the centre of the LMC inner disc field). For the first two datasets, V and I magnitudes are CTIO photometry from Smecker-Hane et al. (2002). **Top right panel:** Metallicity distribution function (dex). Red bars: Pompéia et al. (2008) RGB stars; green bars: Smecker-Hane et al. (Private communication) RGB sample. Metallicities are those derived from the infrared CaT index by Smecker-Hane et al. (Private communication). **Bottom panel:** Radial velocities distribution ($\mathrm{km\,s^{-1}}$). Red bars: Pompéia et al. (2008) RGB stars; green bars: Smecker-Hane et al. (Private communication) RGB sample. Radial velocities are those derived from infrared CaT low-resolution spectra by Smecker-Hane et al. (Private communication). The total Smecker-Hane et al. (Private communication) distribution has a mean metallicity $\langle [\mathrm{Fe/H}]_{\mathrm{CaT}} \rangle = -0.60\,\mathrm{dex}$ (with a standard deviation $\sigma\,([\mathrm{Fe/H}]_{\mathrm{CaT}}) = 0.33\,\mathrm{dex}$) and a mean radial velocity $\langle v_{\rm rad} \rangle = 244\,\mathrm{km\,s^{-1}}$ (with a standard deviation $\sigma\,(v_{\rm rad}) = 27\,\mathrm{km\,s^{-1}}$).

observations (if any) of the same star. We carried out the first three steps of the data reduction with the help of the ESO GIRAFFE pipeline (v2.8.1, released on 02/09/2009), built upon the Geneva GIRAFFE pipeline described in (Blecha et al., 2000) and part of the *esorex* framework[6], and I developed my own tools to perform sky subtraction, radial velocity correction and spectrum co-addition. To successfully perform the data reduction, a number of frames, called *calibration frames*, are needed in addition to the science record. In the following subsections, I will review the different steps of the data reduction, recall why they are necessary and how they are carried out.

2.2.1 Extraction of astronomical spectra

2.2.1.1 Instrumental signatures

Electronics artifacts Even if no light is applied to the CCD chip and the integration time is null, the measured current is not null (or equivalently the intensity frame is not null): there is always a residual signal due to the electronics (the bias level is the electric pre-charge to activate the pixels) and read-out process themselves (read-out noise due to junctions, parasite voltage, pixel-to-pixel offsets, downloading process etc.). This is called the *bias* and has to be accounted for in the final science raw frame. Thus a zero-length (or infinitely short) exposure is obtained with shutter closed: this provides the *bias frame* $B(i,j)$ (where i and j denote the pixel position on the chip). As the residual signal is an additive effect, the bias correction simply consists in subtracting the bias frame to the science raw frame. As any physical measurement, the recording of bias frame is accompanied with noise, which will be injected into the science frame when subtracting. To minimise this effect, we record a few number of bias frames; then the routine *gimasterbias* of the GIRAFFE pipeline combines (mean, median, k-σ clipping etc.) them in a *master bias frame* $B_{\text{master}}(i,j)$ in order to improve the signal-to-noise ratio (S/N ratio). Figures 2.8a and 2.8b show respectively an example of bias and master bias frame.

Dark current The temperature of the CCD detector is responsible for thermal excitation of electrons in the semi-conductor material constituting the photo sites. If an electron gets enough energy, it will cross the band gap between the valence and the conduction bands: consequently, electron-hole pairs are stochastically generated and the electrons are trapped by the electric well of the pixel. Hence a weak electric current, called *dark current*. As soon as the integration time is non null (time-dependency), thermally generated electrons accumulate in the pixel and produce a non-null intensity map, even if no light falls onto the CCD chip. This will affect our science frames and has to be corrected for. As the dark current strongly depends on temperature, the first mean to drastically reduce it is to cool the detector. This technical solution will not completely prevent thermal noise, and in addition, owing to manufacturing imperfections, the dark current generated will differ from pixel to pixel. Therefore, we record a *dark frame* $D(i,j)$ with shutter closed and with an exposure time similar to that used for the science targets in order to map the

[6]Pipeline available at http://www.eso.org/sci/software/pipelines/.

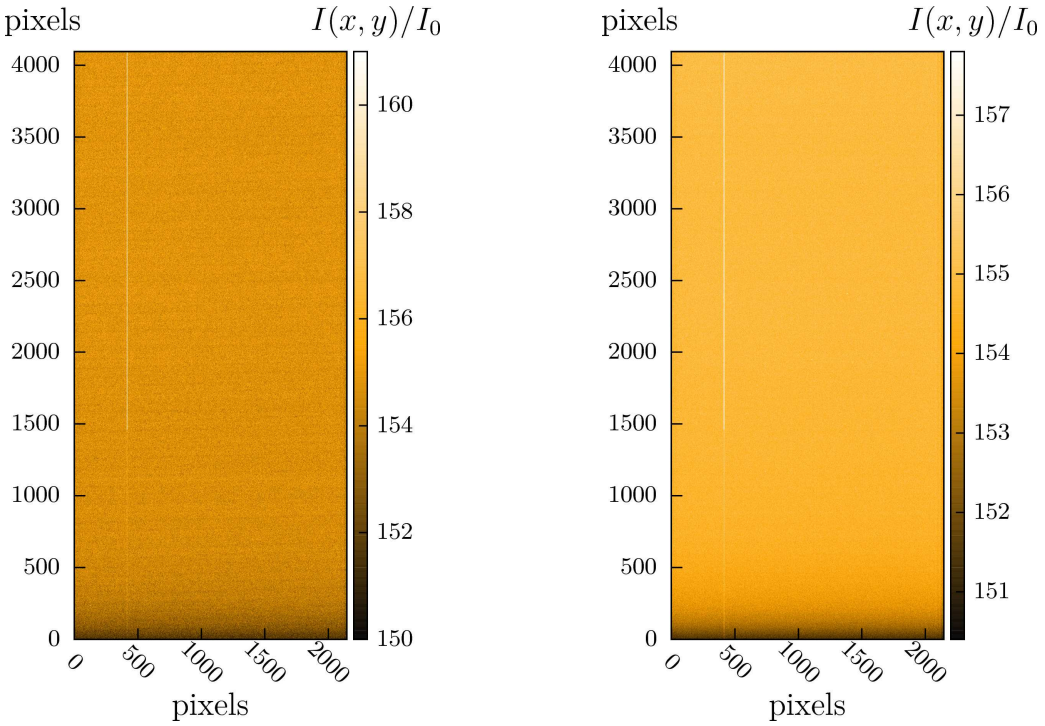

(a) Bias frame

(b) Master bias frame

Figure 2.8: **Left panel:** Bias frame. **Right panel:** Master bias frame. As expected, the S/N ratio is improved from the single bias frame to the master bias frame.

thermal signal across the CCD array. Like the electronic bias, the dark current is an additive effect and the dark correction simply consists in subtracting the dark frame to the science raw frame.

A dark frame will measure two components the electronic bias and the dark current. It may appear useless to record bias frames, since dark frames can correct the two effects simultaneously. However, while the dark current scales with time, the electronic bias does not. So, if the exposure time used for the dark frame and for the science frame are different, we have to scale the dark frame in time (e.g., by assuming a linear time-dependency) before subtracting it to the science frame. Thus, the master bias frame is needed to de-bias the dark frame and to permit time-scaling. Furthermore, as the generation of electron-hole pairs is a random process, described by a Poisson distribution, the dark current at a given pixel will fluctuate around a mean value. To reduce the shot noise in the dark frame and limit the introduction of additional noise in the science frame, we record a number of dark frames; then the routine *gimasterdark* de-bias and combines them in a (de-biased) *master dark frame* $D_{\mathrm{master}}(i, j)$. Thus, when we subtract the master dark frame to the science raw frame, only the mean dark current level will be removed: the operation will leave the shot noise (of the dark current) in the science frame, and will further bring the additional noise of the master dark frame, leading to a slight decrease of the S/N ratio. Figures 2.9a shows an example of dark frame; Figures 2.9b and 2.9c show CCD defects, cosmic hits and the CCD glow (see below § "Bad pixels", "Scattered light" and "Cosmic ray events"). Figures 2.10a and 2.10b show an example of master dark frame before and after the bias correction.

Flat-field Before reaching the CCD pixels, the light which enters the telescope travels through the optical system of the spectrograph: fibres, slit, lenses, filters, grating etc. Energy losses may occur along the path light. In particular, the fibres are not strictly identical and will not transmit the light with the same efficiency. Similarly, the pixels constituting the CCD have a wavelength-dependent quantum efficiency (percentage of incoming photons converted into electrons). Even if we were to illuminate the CCD chip with a monochromatic radiation, we would observe small variations in the pixel response since the pixels are not strictly identical. Finally, optical patterns (fringing, vignetting, artifacts made by dust etc.) may exist and introduce spatial variations of the intensity of the light arriving on the CCD. In order to handle those transmission inhomogeneities, we record a third calibration frame, the *flat-field frame* $F(i, j)$. It is called flat-field because it requires a uniform illumination of the CCD. Here, since we are doing spectroscopy, it means that we use a luminous source whose spectrum is a pure continuum, i.e. without emission or absorption lines. The energy distribution has also to be as uniform (in wavelength) as possible; otherwise, we will introduce the spectral signature of the lamp in the astronomical data. For GIRAFFE, flat-field frames are obtained with a tungsten lamp whose light goes through the whole optical system after the telescope and field corrector (Kaufer et al., 2012). As the transmission inhomogeneities are a multiplicative effect, the correction is done by dividing the de-biased dark-subtracted science frame by the de-biased dark-subtracted flat-field frame. As for the bias and dark frame, it is important to minimise the noise (mainly photon noise) in the flat-

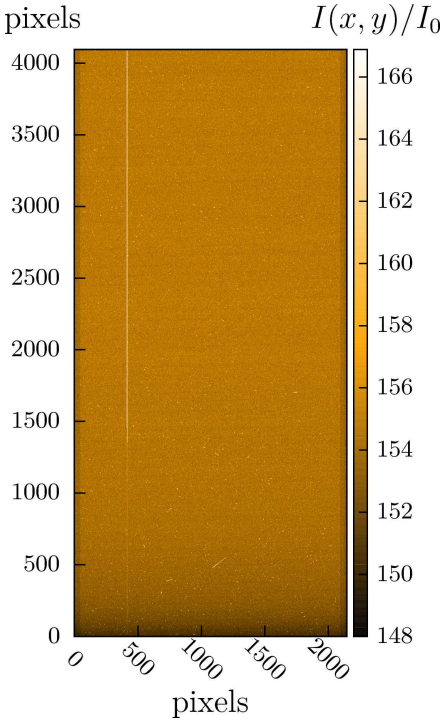

(a) Whole dark frame

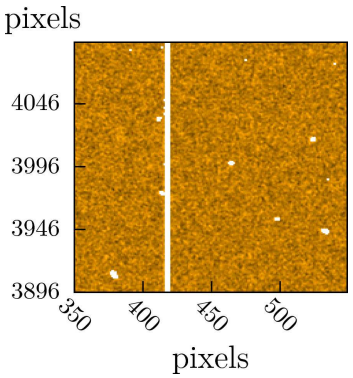

(b) Hot columns & spurious pixels

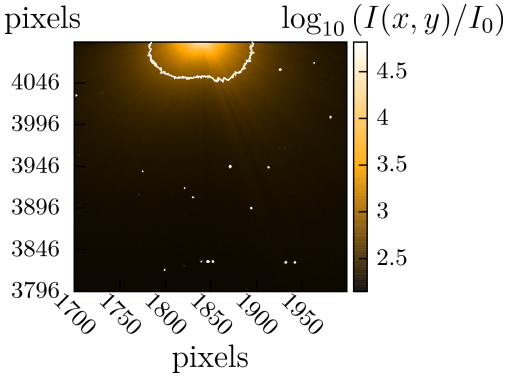

(c) CCD glow

Figure 2.9: **Left panel:** Whole dark frame taken in January 2004. The colour bar indicates the intensity in linear scale. We see that the CCD has a low and uniform intensity. **Upper right panel:** Zoom-in on the previous dark frame. If a dark frame is essentially "dark", it may exhibit some hot pixels: here, we see a stripe of hot pixel columns (thick bright vertical line) and tiny bright areas due to cosmic rays or CCD defects (false colour to emphasise the effects). **Lower right panel:** Zoom-in on a dark frame (colours in logarithmic scale) taken in January 2007. The so-called CCD glow, located in the upper left corner of the "Bruce" CCD (replaced in May 2008 by the "Carreras" CCD), is visible. The white curve is the isopleth where the intensity equals 1 % of the maximum intensity. The intensity of the glow has *suddenly* varied in time after maintenance operations: it is absent from the 2004 dark frame but present in this dark frame.

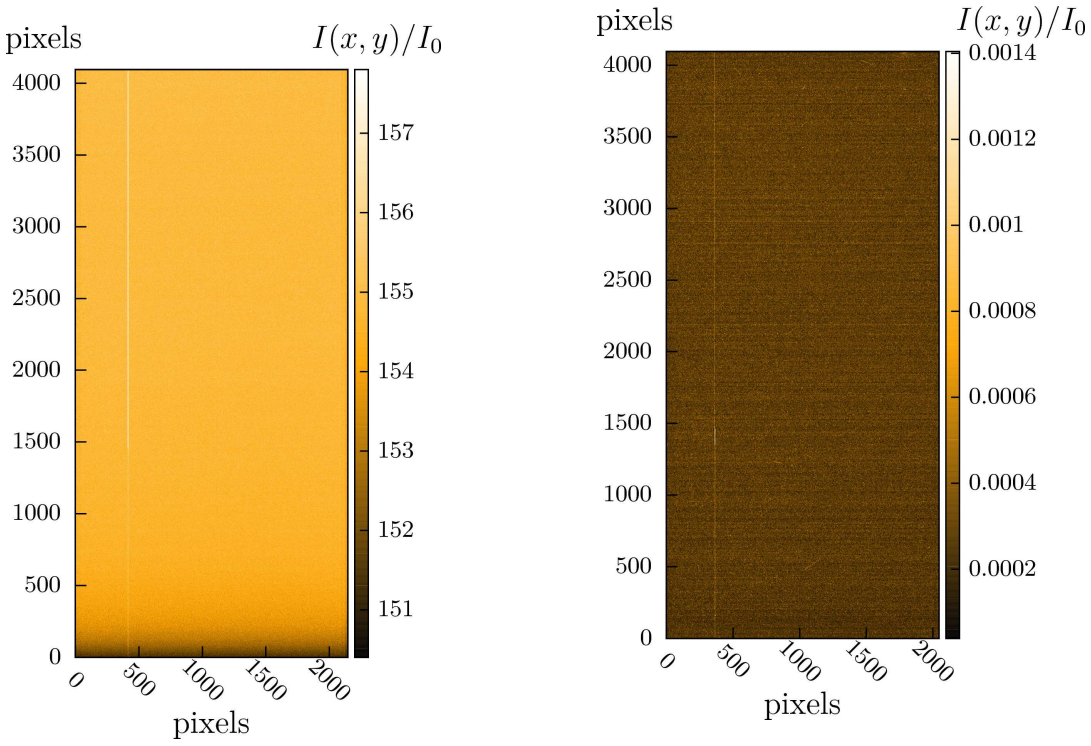

(a) Biased master dark frame

(b) Master dark frame

Figure 2.10: **Left panel:** Biased master dark frame. **Right panel:** Master dark frame. We see that the dark current is very low and that most of the signal present in a raw dark frame is indeed the bias signal. With the new GIRAFFE CCD, the dark current is so low that dark frames are no longer needed. The dark frame has a size 2148×4096 while the master dark frame has a size 2048×4096: the over-scan region (first and last 50 columns) have been stripped out.

field frame in order to not decrease the S/N ratio of the astronomical spectra. This is achieved by recording a number of flat-field frames (three frames, typically) that will be combine into a *master flat-field frame* $F_{\text{master}}(i, j)$ by the routine *gimasterflat*. Within the frame of multi-fibre spectroscopy, the flat-field frame has a second role: it allows the fibre localisation, and so, the spectrum extraction (Sec. 2.2.1.2), by providing the trace of all the fibres onto the CCD. To this end, it is therefore important that the light of the tungsten lamp travels through the whole optical system (i.e. fibres + slit + lenses + grating). Figure 2.11a shows an example of flat-field frame, Figure 2.11b the localisation of the glow and Figure 2.11c the fibre centroids and widths (see Sec. 2.2.1.2).

Bad pixels Pixels are called "bad" when they do not respond as expected. They can be the results of the CCD manufacturing (variation of the pixel sensitivity across the chip, imperfections etc.) or appear when the device ages. *Hot pixels* have higher dark current rate and quickly saturate during the exposure; they appear as bright dots in the frames. *Cold* and *dead pixels* exhibit a lower quantum efficiency and have little or no sensitivity to the incoming light; they will produce dark dots in the frames. Because of the read-out process, a bad pixel may corrupt the signal along the column and create *dark columns* (the transfer of charges from top-to-bottom pixels is temporarily stopped by a strong potential well), *bright columns* (a very hot pixel injects extra electrons when it receives the charges from upper pixels; Fig. 2.9b) or *bright trails* (a pixel with a poor charge-transfer efficiency will release its electrons at a slow rate and will contaminate the electrons pool of upper pixels when they go through it). The GIRAFFE pipeline uses a *bad pixel map* to flag and handle bad pixels. Correcting defective pixels is only possible when the effects involve very few pixels: for instance, the pipeline can interpolate the signal using adjacent valid pixels. In fact, the GIRAFFE pipeline skips bad pixels and weights valid pixels accordingly to compensate. When a part of a column (fibres are aligned with columns) is concerned, the signal is unfortunately lost. In the dark frame of Figure 2.9b, we can see the three bright columns of the "Bruce" FLAMES CCD; their coordinates are 368, 369 and 370 and correspond to the fibre 24: the signal of this fibre is corrupted and cannot be fixed (GIRAFFE Quality Control group, 2012).

Scattered light In a multi-object spectrograph, the area between two adjacent projections of fibres on the CCD chip is not completely dark, even after the removal of the electronic bias and the dark current component: the luminous pollution, or *scattered light*, originates in internal reflections and affects the whole CCD. The routine *giscience* of the GIRAFFE pipeline tries to correct the flat-field and science frames for this additive effect (Melo & Smoker, 2009), but the scattered light is not reported as a major issue when FLAMES is used in the MEDUSA mode (GIRAFFE Quality Control group, 2012).

The first CCD (called "Bruce") which equipped the GIRAFFE spectrograph had a defect in the upper left corner causing the appearance of a particular contaminating feature, proportional to the observing time, called *glow* in dark or science frames (Fig. 2.9c). This feature was due to the light emitted by a faint diode and

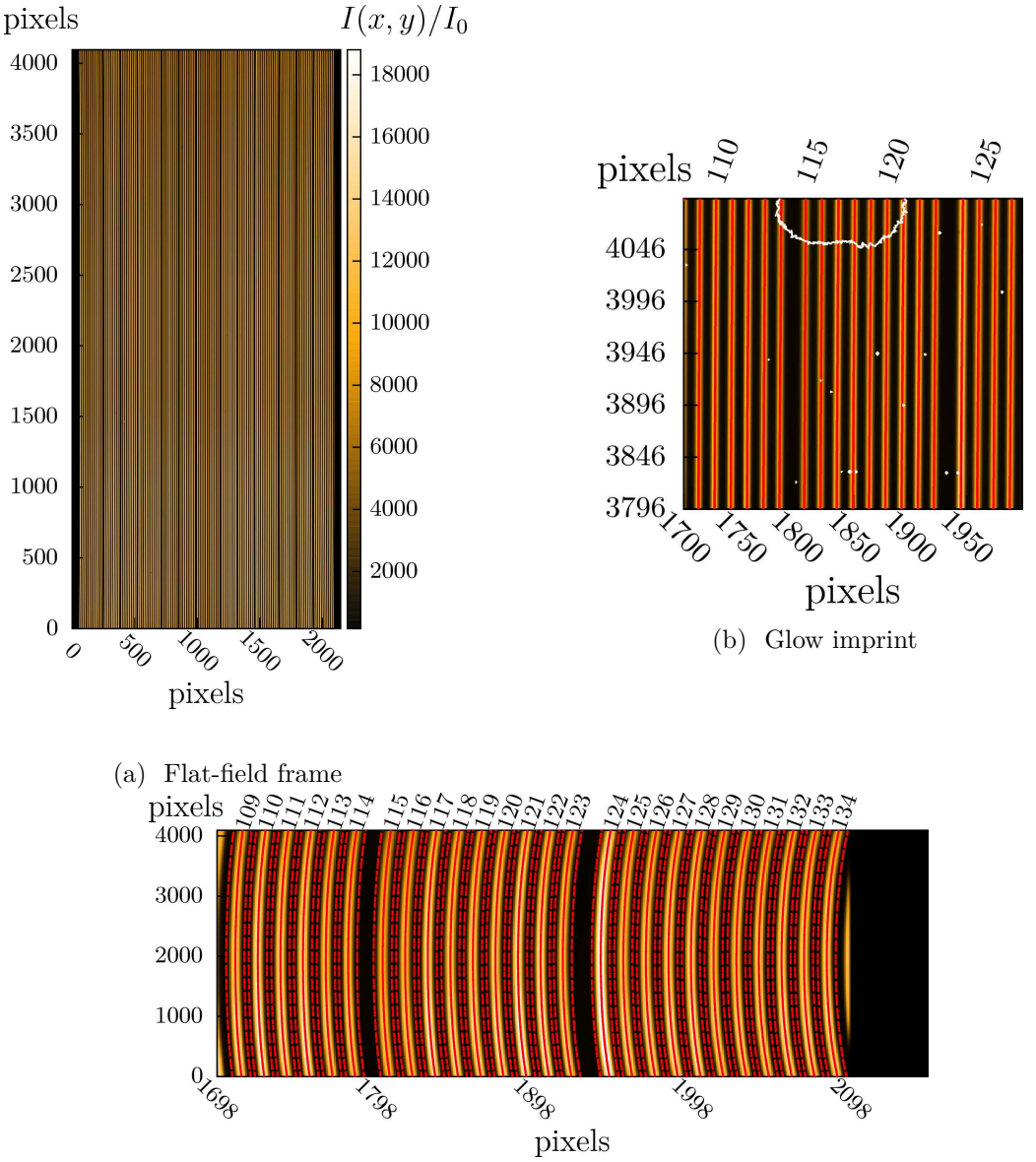

(a) Flat-field frame

(b) Glow imprint

(c) Fibre localisation

Figure 2.11: **Upper left panel:** Flat-field frame. The 135 vertical bright lines are the projection of the fibres onto the CCD. **Upper right panel:** Glow imprint over a flat-field frame (isopleth of Fig. 2.9c). In this example, the glow mainly affects the red part of the spectra from fibres 114 to 122. **Bottom panel:** In multi-fibre spectroscopy, flat-field frames have a second role: they allows the fibre localisation (centroid + width). The red solid line is the fibre centroid and the red dashed lines represents the width of the fibre as detected by the GIRAFFE pipeline.

provoked intensity jumps in the reddest part of spectra from approximately fibres 110 to 130. As the phenomenon was rather stable in time, it should have been possible to correct it by using dark frames recorded close in time with the science data. Unfortunately, in our case, because of long exposure times, many pixels (those closer to the CCD edge) became saturated and it was no longer possible to recover the spectral information. When our science frames are affected by the glow, we decided to exclude the altered part of concerned spectra (Sec. 2.2.5).

Cosmic ray events High-energy particles will light on a pixel (or sometimes, a small cluster of pixels) when they are absorb by the semi-conductor metal. Generally, the pixels will saturate and appear very bright since a huge number of electrons will be freed. Those high-energy particles may originate in cosmic radiation (SNe explosions etc.) or in background Earth radioactivity, but are often called *cosmic ray hits*. As for thermally generated electrons, electrons produced by cosmic ray hits are indistinguishable from photo-charges and represent another noise source in the astronomical data. But, as they hit the CCD surface randomly, it is possible to remove them with the help of multiple exposure: e.g., if we combine a number of dark (or bias, or flat-field) frames using the median, pixels affected by cosmic rays will appear as outliers and will be naturally removed. We removed cosmic rays from science frames during the co-addition of spectra (Sec. 2.2.5).

2.2.1.2 Spectra extraction

In multi-object spectroscopy, the spectra of many different targets are projected side-by-side onto the CCD and recorded simultaneously. In addition, spectra are recorded in a two-dimensional format: they extend over several pixels along the spatial direction. A particular operation of the data reduction is therefore devoted to localising the image of each fibre onto the CCD surface (to separate the target two-dimensional spectra) and then collapsing the spectra (to obtain a one-dimensional spectrum per fibre).

Fibre localisation The GIRAFFE pipeline performs the fibre localisation during the creation of the master flat-field frame. As the flat-field frame is obtained with a bright light source having a featureless spectrum, the trace of the fibres on the CCD is well defined at all wavelengths (i.e. at all pixels). For each row (i.e. along the spatial direction), the routine identifies the position of the fibres by fitting a Gaussian profile: at a given row, the centre and width of the fibres are recorded. Then, the procedure is repeated for all the CCD rows in order to build the fibre profile along the dispersion direction.

Spectrum extraction Once the localisation and the width of the fibres are known, the object spectrum extraction is feasible. The GIRAFFE pipeline offers the summation extraction or the optimal extraction (in fact, there are two different implementations of an optimal extraction method). The summation extraction consists in averaging the fluxes vertically in order to build the one-dimensional spectra. The optimal extraction (Horne, 1986; Robertson, 1986) is a more sophisticated

algorithm aiming at improving the S/N ratio of the extracted spectra: it weights the fluxes along the spatial direction by their own S/N ratio (the pixels receiving less light have a smaller photon count and thus exhibit a lower S/N ratio). The optimal extraction algorithm implemented in the GIRAFFE pipeline has also the ability to remove cosmic rays from spectra. Nevertheless, the extraction of spectra via the optimal method turned out to be unstable for some of our observations and introduced curvature at the blue/red edges of the spectra. Therefore, we preferred to use the summation method.

Flat-fielding: a remark The mathematically correct way of flat-fielding the science raw frame would be to divide it by the flat-field frame pixel-by-pixel. It would require to illuminate uniformly (in intensity) the fibre profile along the spatial direction. Unfortunately, it is not possible and the intensity in the spatial direction drops towards the edge of the fibre profile, implying a decrease of the S/N ratio. If we were to divide the science raw frame by the flat-field frame pixel-by-pixel, we would distort the spectra far from the fibre centre. A solution to avoid this is to extract the flat-field spectra and the science spectra *before* flat-fielding. We can note that when the extraction combines the pixels vertically (i.e. pixels that have been illuminated by radiations of same wavelength), the pixel-to-pixel variations of wavelength sensitivity are averaged. Then, the flat-field spectra, different from a fibre to another, are normalised to compensate for the fibre relative transmission. However, it is worth noticing that for GIRAFFE, the fibre relative transmission is extremely stable (GIRAFFE Quality Control group, 2011). After extracting the spectra, the routine *giscience* divides the extracted science spectra by the extracted normalised flat-field spectra.

2.2.1.3 Wavelength calibration

After extraction and flat-fielding, the science spectra have to be wavelength calibrated which allows to map the pixel space to the wavelength space. To this end, a fourth calibration file is recorded, called *wavelength calibration frame* or *arc frame*. The fibres are illuminated by a lamp producing a spectrum whose numerous and narrow emission lines have well-known wavelengths. Such an emission spectrum is obtained with a hollow-cathode lamp, containing a gas ionised by a high voltage; e.g., in GIRAFFE, a Th–Ar lamp is used. The emission spectra are injected into the fibres, follow the full optical path of the spectrograph and are recorded onto the CCD. The wavelength calibration frame is then de-biased, dark-subtracted, and extracted by the routine *giwavecalibration* (using the fibre localisation and width determined previously). For each fibre, the emission lines are searched in the spectrum; faint, blended or non-Gaussian lines are rejected while the remaining lines are identified thanks to a catalogue and their position (i, j) on the CCD is determined. The residual between the positions predicted by the GIRAFFE optical model and those measured is fitted by a Chebychev polynomial and the final dispersion solution is computed for each fibre by the routine *giwavecalibration*. Finally, the science spectra are wavelength calibrated thanks to the dispersion solution. Figure 2.12 show the dispersion solution for three fibres; Figures 2.13a and 2.13c show the

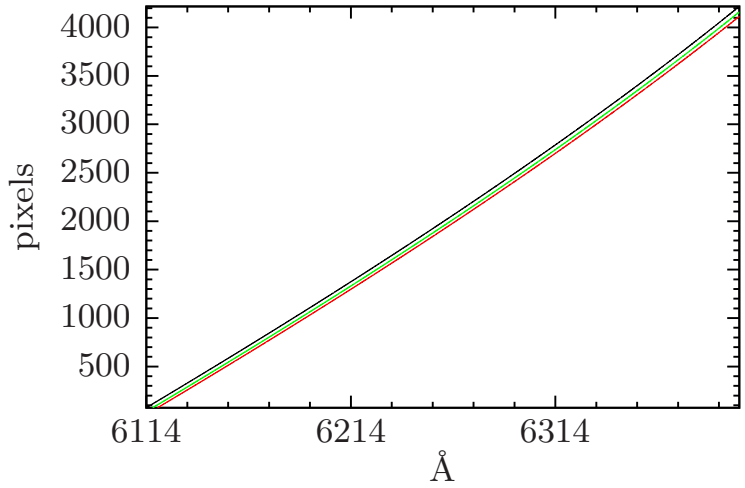

Figure 2.12: Dispersion solution for three fibres 1 (black line), 61 (red line) and 121 (green line). The dispersion solution is not linear (pixels are larger at higher wavelengths) and is different from a fibre to another.

emission spectra before and after the wavelength calibration: after calibration, the emission lines are aligned from fibre-to-fibre and appear as a straight line (along the spatial direction), revealing the quality of the calibration.

GIRAFFE offers the possibility to perform a simultaneous calibration: when the science exposure is recorded, five fibres, called *SimCal fibres*, are fed with the light of the Th–Ar lamp. Then, when the routine *giscience* reduces the science spectra and calibrate them in wavelength using the dispersion solution, it uses the information carried by the SimCal fibres to correct the wavelengths (by applying a wavelength offset to all the fibres, the offset being either constant or linearly increasing). This additional wavelength correction is useful to correct for a residual wavelength drift: wavelength calibration frames are recorded during daytime, and when science frames are recorded, mechanical vibrations (due to the change of slit, of filter, of grating) or change of optical indices (due to atmospheric temperature or pressure variations) may have change the light path, and therefore, the dispersion solution (spectrograph drifts in GIRAFFE high resolution mode have been observed to be of the order of few hundred $\mathrm{m\,s^{-1}}$; e.g., see Platais et al., 2007).

2.2.1.4 Putting it all together

The science raw frame $R(i,j)$ recorded on the CCD is given by the data reduction equation as follows:

$$R(i,j) = B(i,j) + D(i,j) + F(i,j) \times \left[\tilde{S}_\star(i,j) + S_{\mathrm{sky}}(i,j)\right] \tag{2.1}$$

where (i,j) are the pixel coordinates on the CCD matrix, B is the electronic bias D is the dark current, F is the flat-field, $\tilde{S}_\star$ is the star spectrum and S_{sky} is the sky spectrum. As explained in previous sections, in practise, we do not have access to the actual functions B, D, F but only to an estimate. The routines *gimasterbias*, *gimasterdark*, *gimasterflat* of the GIRAFFE pipeline compute the master bias

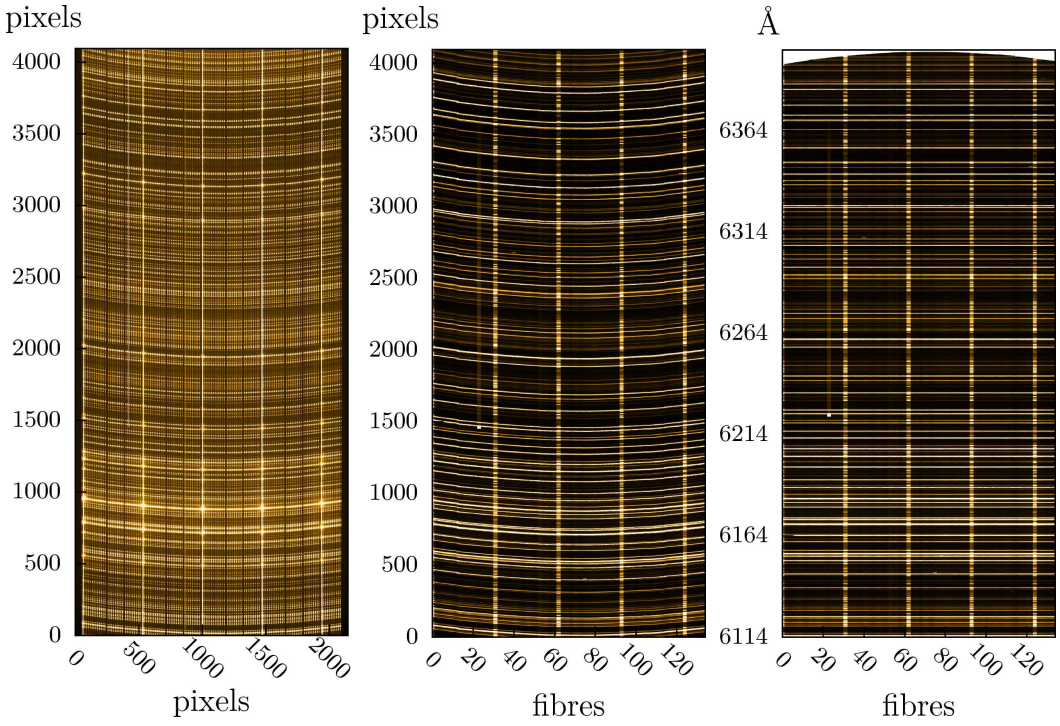

(a) Raw arc frame (b) Extracted arc frame (c) Rebinned arc frame

Figure 2.13: **From left to right panel:** Raw, extracted and rebinned wavelength-calibrated arc frame. The first picture shows that the dispersion solution changes from a fibre to another since the bright dots (i.e. emission lines) are not aligned horizontally. Once the fibres have been localised, spectrum extraction is possible: the two-dimensional spectra are turned into one-dimensional spectra. The size of the extracted frame is then 135×4096. With the dispersion solution, spectra can be wavelength calibrated: in the third frame, emission lines are now horizontally aligned. The GIRAFFE pipeline performs also a rebinning: for instance, for HR13, the final frame size is 135×5800.

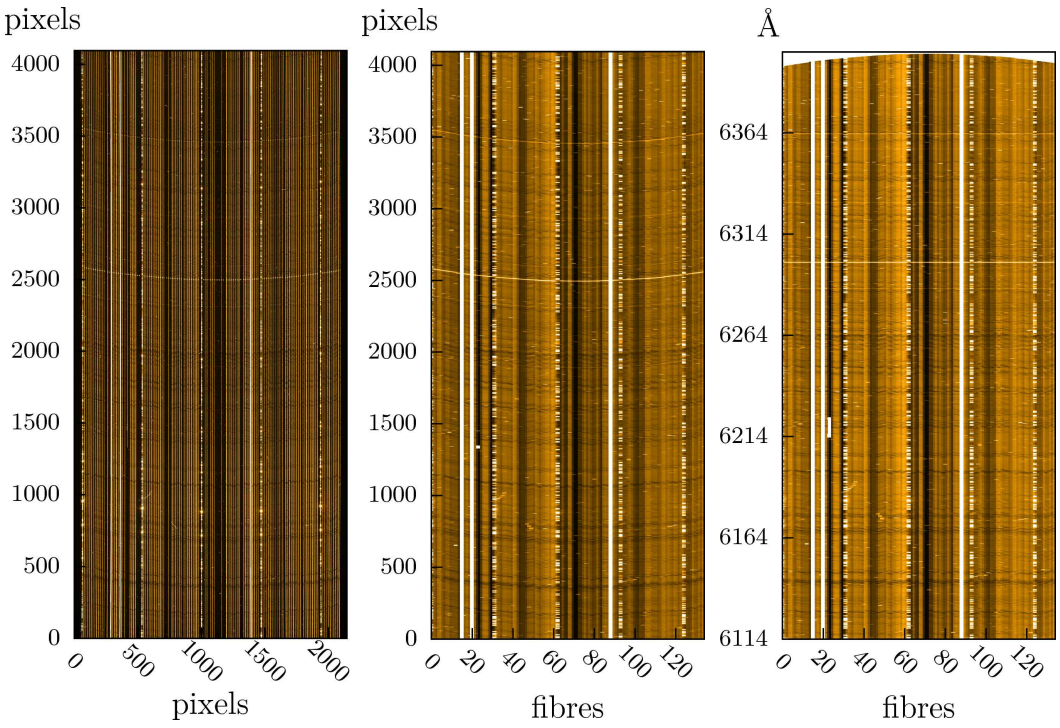

(a) Raw science frame (b) Extracted science frame (c) Rebinned science frame

Figure 2.14: **From left to right panel:** Raw, extracted and rebinned wavelength-calibrated science frame. Five fibres exhibit strong emission lines (bright dots): they are the *SimCal* fibres used to correct for small wavelength shifts due to the spectrograph drift. Sky emission lines becomes straight horizontal lines while stellar absorption lines remain wiggly because all stars do not have the same $v_{\rm rad}$.

$B_{\rm master}$, the master dark $D_{\rm master}$ (after de-biasing individual dark frames), and the master flat-field $F_{\rm master}$ (after de-biasing and dark-subtracting individual flat-field frames) respectively. Equation 2.1 thus becomes:

$$R(i,j) = B_{\rm master}(i,j) + D_{\rm master}(i,j) + F_{\rm master}(i,j) \times \left[\tilde{S}_\star(i,j) + S_{\rm sky}(i,j)\right] \quad (2.2)$$

The routine *giscience* computes $S_{\rm obs}(i,j) = \tilde{S}_\star(i,j) + S_{\rm sky}(i,j)$ as follows:

$$\begin{aligned} S_{\rm obs}(i,j) &= \tilde{S}_\star(i,j) + S_{\rm sky}(i,j) \\ &= \frac{\mathcal{E}\left[R(i',j') - B_{\rm master}(i',j') - D_{\rm master}(i',j')\right]}{\mathcal{E}\left[F_{\rm master}(i',j')\right]} \end{aligned} \quad (2.3)$$

where $\mathcal{E}$ denotes the spectrum extraction, (i',j') are the pixel coordinates on the CCD matrix, i is the fibre number of the extracted spectrum and j the pixel number of the extracted spectrum along the dispersion solution. Eventually, the routine *giscience* uses the dispersion solution provided by the routine *giwavecalibration* to calibrate the reduced spectra in wavelength. Figure 2.14a show a raw science frame while Figures 2.14b and 2.14c show the result of the data reduction work-flow.

2.2.2 Effects of the atmosphere

As shown by Eq. 2.3, the reduced spectra are not the stellar spectra $S_\star$. Indeed, the light emitted by stars goes through the Earth atmosphere which has its own emissivity $S_{\rm sky}$ and absorption coefficient $t_{\rm atm}(\lambda)$, and therefore, we record $S_{\rm obs}(\lambda) = \tilde{S}_\star(\lambda) + S_{\rm sky}(\lambda)$, where $\tilde{S}_\star(\lambda) = t_{\rm atm}(\lambda) S_\star(\lambda)$.

2.2.2.1 Sky continuum and emission lines

The *sky background* $S_{\rm sky}$ is an additional (polluting) light, recorded simultaneously to the science light; it has a continuum and emission lines component. The Earth atmosphere is the main contributor to the sky background. Indeed, even during the night, the Earth atmosphere radiates and this *atmosphere brightness* is due to: thermal continuum, airglow (upper atmosphere), emission lines (de-excitation of atoms and molecules in the Earth atmosphere) etc. Other sources responsible for the sky background are: moonlight, zodiacal light (sunlight scattered or reflected by interplanetary dust particles), integrated light of faint objects (non-resolved stars, distant galaxies), and diffuse Galactic light (Galactic starlight scattered or reflected by interstellar dust).

The sky background is an additive effect and has to be accurately removed from the recorded spectra to allow accurate abundance measurements. The sky subtraction is a tricky question. To isolate the sky component, we have to observe a blank region of the sky, i.e. a region free of stars. Because of possible spatial dependency of the sky emission, this region should be close to the science target to sample the same portion of the atmosphere. And due to possible time-dependency, we should record the sky spectrum simultaneously to the science spectrum. For our observations, the first constraint (spatial dependency) is released since the sky emission can be considered constant over the GIRAFFE field of view ($\theta \approx 25'$).

Concerning the time-dependency, in multi-object spectroscopy, it is always possible to devote a number of fibres to record the sky spectrum simultaneously to the science exposure.

As described in Section 2.1.2, in our observing program we allocated around 10 to 20 fibres to sky positions. As for the bias, dark or flat-field frames, the question of noise arises: the sky fluxes are marred by various sources of noise, especially the photon noise, and we have to minimise this, otherwise we will decrease the S/N ratio of the stellar spectra. One possibility is to carefully combine the different sky spectra and form a *master sky spectrum*. I adopted the following strategy. I visually sorted out the sky spectra to check for their quality and discarded those showing spectral contamination or defects: jump in fluxes due to polluting light (stellar light, CCD glow, simultaneous calibration lamp) or a CCD defect. After this quality selection, we ended up with a handful of sky spectra (at least five to eight) in most cases. As the selected sky spectra exhibit the same continuum level (testifying of the spatial stability of the atmosphere layers), I averaged them with k-σ clipping rejection and subtracted the resulting master sky to each stellar spectrum. This procedure was applied to each stellar spectrum (i.e. to each observation of the 113 bar stars and for each setup). Thus, after this step, we are left with:

$$\begin{aligned} \tilde{S}_\star(\lambda) &= t_{\rm atm}(\lambda) S_\star(\lambda) \\ &= S_{\rm obs}(\lambda) - S_{\rm sky,master}(\lambda) \end{aligned} \tag{2.4}$$

Figure 2.15 (top panel) shows a spectrum before and after sky-subtraction.

2.2.2.2 Telluric absorption bands

The last step to access to the stellar spectrum is to correct for the atmosphere absorption, which is a multiplicative effect. Molecules of the Earth atmosphere (especially O_2, H_2O in our wavelength domain) may absorb the stellar light as it crosses the atmosphere layers and give birth to *telluric absorption bands* in the stellar spectrum.

For our purposes, we are concerned by the absorption occurring around 6300 Å and contaminating an oxygen line. Among the two oxygen lines (at 6300 Å and 6363 Å) that are available in the optical wavelength range, the first is the strongest line and is more appropriate to abundance measurement. Unfortunately, it is in a region contaminated by atmospheric spectral features caused by O_2 (from 6270 Å to 6330 Å). To measure abundance reliably, it is mandatory to correct for the telluric lines. To this end, a usual technique to retrieve the atmosphere transmission coefficient consists in observing hot fast rotating stars whose spectrum is (almost) free of stellar spectral features[7] and contains only the telluric absorption bands. We observed three hot stars simultaneously to our science targets for that purpose: 05235121-6934233, 05235885-6952357, 05242945-6937236 and I inspected the spectra of the three stars. As the star 05235885-6952357 showed the broadest stellar spectral features and the highest S/N ratio, we used its spectrum for a telluric correction: in the wavelength region [6270 Å, 6330 Å], after scaling the continuum level

[7] Most of absorption lines are so broadened by the rotation (see Chapter 4) that they vanish from the stellar spectrum.

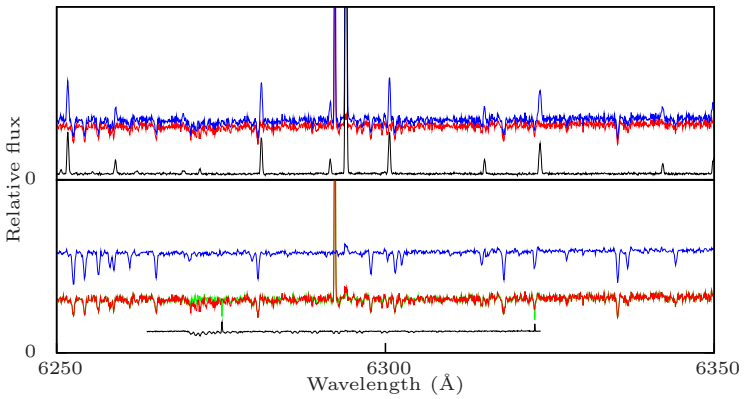

Figure 2.15: **Top panel:** an example of raw spectrum (blue) for the star 05244301-6943412 and the corresponding master sky (black) we used to obtain the sky-subtracted spectrum (red). In the red spectrum sky emission lines have been correctly removed. A cosmic ray remains at $\sim$ 6290 Å. **Bottom panel:** the sky-subtracted spectrum of 05244301-6943412 before (red) and after (green) the correction for the telluric lines. The spectrum of the fast rotator is plotted in black to show the position of telluric features. The blue spectrum is the co-added spectrum: the k-σ clipping has removed the remaining cosmic rays and the signal-to-noise ratio is clearly improved compared to the single exposure. All spectra are plotted in the same scale, except for the fast rotator spectrum (it has been scaled for legibility).

of the hot fast rotating star (absorption proportional to the input flux), I divided our individual stellar spectra by the hot star spectrum. We checked that no discontinuities were introduced. For our purposes, apart from this region, we considered that $t_{\rm atm}(\lambda) = 1$. Figure 2.15 (bottom panel) shows a spectrum before and after correction for telluric bands.

2.2.3 Noise and signal-to-noise ratio measurements

During an ideal photon detection, only photons from the source (the star) are detected. Since photon arrivals are a random process following a Poisson probability distribution, statistical fluctuations affect the photon count: if $n_\star$ is the mean number of incoming photons per pixel per second, then the variance is given by $n_\star$ and the S/N ratio per pixel is:

$$\mathrm{S/N} = \frac{n_\star \Delta t}{\sqrt{n_\star \Delta t}} = \sqrt{n_\star \Delta t} \tag{2.5}$$

where Δt is the integration time. However, Sections 2.2.1.1 and 2.2.2 showed that the signal recorded by a CCD pixel is built up by the bias, dark current (shot noise), star and sky photons (shot noise), and in addition, since the quantum efficiency is not 1, not all incoming photons are converted into electrons by a CCD pixel.

Therefore, the S/N ratio per pixel is given by the *CCD equation*:

$$\mathrm{S/N} = \frac{n_\star Q_\mathrm{E}(\lambda)\Delta t}{\sqrt{(n_\star + n_\mathrm{sky})Q_\mathrm{E}(\lambda)\Delta t + n_\mathrm{dark}\Delta t + \sigma_{bias}^2}} \tag{2.6}$$

where $Q_\mathrm{E}(\lambda)$ is the quantum efficiency ($\mathrm{e^-}$/photon), $n_\star$ the mean number of incoming star photons (photon/s/pix), n_sky the mean number of incoming sky photons (photon/s/pix), n_dark the mean number of dark electrons ($\mathrm{e^-}$/s/pix), σ_{bias} the read-out noise (r.m.s $\mathrm{e^-}$/pix; for GIRAFFE CCD: $3\,\mathrm{e^-}$/pix). Two regimes are defined:

- *read-noise limited regime*: ${\sigma_{bias}}^2 \gg \{n_\star Q_\mathrm{E}(\lambda)\Delta t, n_\mathrm{sky}Q_\mathrm{E}(\lambda)\Delta t, n_\mathrm{dark}\Delta t\}$ and Equation 2.6 becomes:

  $$\mathrm{S/N} \approx \frac{n_\star Q_\mathrm{E}(\lambda)}{\sigma_{bias}}\Delta t \tag{2.7}$$

  The S/N ratio increases linearly with the integration time.

- *photon-noise limited regime*: ${\sigma_{bias}}^2 \ll \{n_\star Q_\mathrm{E}(\lambda)\Delta t, n_\mathrm{sky}Q_\mathrm{E}(\lambda)\Delta t, n_\mathrm{dark}\Delta t\}$ and Equation 2.6 becomes:

  $$\mathrm{S/N} \approx \frac{n_\star Q_\mathrm{E}(\lambda)}{\sqrt{(n_\star + n_\mathrm{sky})Q_\mathrm{E}(\lambda) + n_\mathrm{dark}}}\sqrt{\Delta t} \tag{2.8}$$

  and if the dark current is negligible:

  $$\mathrm{S/N} \approx \frac{n_\star Q_\mathrm{E}(\lambda)}{\sqrt{(n_\star + n_\mathrm{sky})Q_\mathrm{E}(\lambda)}}\sqrt{\Delta t} \tag{2.9}$$

  The S/N ratio increases with the square root of the integration time. Two extreme cases:

  $$\begin{aligned} \text{object dominated}: &\quad \mathrm{S/N} \approx \sqrt{n_\star Q_\mathrm{E}(\lambda)\Delta t} \\ \text{background dominated}: &\quad \mathrm{S/N} \approx \frac{n_\star}{\sqrt{n_\mathrm{sky}}}\sqrt{Q_\mathrm{E}(\lambda)\Delta t} \end{aligned}$$

  Thus, for faint sources, the S/N ratio is inversely proportional to the sky noise. As shown in Fig. 2.15, our observations are object dominated. In both cases, if $\Delta t_\mathrm{long} = k\Delta t_\mathrm{short}$, it is formally equivalent to perform a single long exposure with integration Δt_long or average k short exposures with integration time Δt_short: $\mathrm{S/N_{long}} = \mathrm{S/N_{mean}} = \sqrt{k}\mathrm{S/N_{short}}$. However, averaging k short exposures gives better results because it allows cosmic hits removal (Sec. 2.2.5). The different exposures can also be median-combined: it yields a lower S/N ratio ($\mathrm{S/N_{median}} = \sqrt{2k/\pi}\mathrm{S/N_{short}} < \mathrm{S/N_{mean}}$) but it is more robust to outliers.

The GIRAFFE pipeline keeps track of the error along the data reduction: if Equation 2.6 gives the S/N ratio for a pixel of the raw frame, the successive data reduction steps make the expression of the S/N ratio for an extracted pixel more

complicated (errors have to be propagated when frames are combined, subtracted or divided). To compute the S/N ratio, I used the error spectrum produced by the ESO GIRAFFE pipeline, so that the S/N ratio at pixel i is given by:

$$\mathrm{S/N}_i = \frac{\mathrm{flux}_i}{\mathrm{error}_i} \tag{2.10}$$

Actually, this estimator of the S/N ratio is not accurate and likely underestimates the S/N ratio. Indeed, when pixels are rebinned by the pipeline, they become correlated; nevertheless, the error propagation does not take into account this correlation, and therefore, the errors are overestimated and the S/N ratio underestimated. However, it is still a good index to compare the quality of a spectrum to another and we will use it during spectrum co-addition[8] (Sec. 2.2.5).

2.2.4 Radial velocities measurements

We obtained multiple observations of the same star in a given setup: 10 exposures with HR11, 5 exposures with HR13 and 4 exposures with HR14, which represents a total of more than 2000 spectra. Having multiple observations is of great importance since it allows to combine the different spectra, and thus improve the S/N ratio (the noise decreases and cosmic ray events can be removed). But as the observations are performed at different dates, we can not combine them straightforwardly, but we first have to correct them for relative radial velocities (or at least apply barycentric corrections).

2.2.4.1 Method to determine the radial velocities

Radial velocity measurements rely on the Doppler–Fizeau effect, which provokes a wavelength shift $\Delta\lambda = \lambda - \lambda_0$ between the emitted λ_0 and received λ wavelengths (Gullberg & Lindegren, 2002; Lindegren & Dravins, 2003). For the light travelling in the vacuum at speed c, the wavelength shift depends only on the relative velocity $\overrightarrow{v_{\mathrm{rel}}}$ between the emitter and the receiver:

$$\frac{\lambda}{\lambda_0} = \frac{1+\beta\cos\theta}{\sqrt{1-\beta^2}} \quad \text{with} \quad \beta = \frac{v_{\mathrm{rel}}}{c} = \frac{\|\overrightarrow{v_{\mathrm{rel}}}\|}{c} \tag{2.11}$$

where θ is the angle in the receiver frame between the direction of photon propagation and $\overrightarrow{v_{\mathrm{rel}}}$. For our purposes, v_{rel} is the relative velocity between the Earth and the observed star and is of the order of a few hundred $\mathrm{km\,s^{-1}}$, i.e. $v_{\mathrm{rel}} \ll c$. Equation 2.11 can be approximated by:

$$\frac{\lambda}{\lambda_0} \approx 1 + \beta\cos\theta = 1 + \frac{v_{\mathrm{rel}}\cos\theta}{c} \tag{2.12}$$

hence, with $v = v_{\mathrm{rel}}\cos\theta$ the relative radial velocity (i.e. line-of-sight component):

$$\frac{\Delta\lambda}{\lambda_0} = \frac{\lambda-\lambda_0}{\lambda_0} = \frac{v}{c} \tag{2.13}$$

[8] We used the pipeline error products to propagate the errors after sky-subtraction and telluric absorption correction.

If the star is receding from the Earth, $v > 0$, $\Delta\lambda > 0$ and the wavelength is redshifted. It is possible to use a set of identified absorption lines to measure v with Equation 2.13 by comparing the recorded wavelength to the rest wavelength of the transition (laboratory measurement); a precise estimate of v is then obtained by averaging the velocities derived from each line. However, for the sake of automation, I wrote a cross-correlation routine using my own Gaussian masks to perform the radial velocity measurement. In order to build Gaussian masks resembling our spectra in terms of stellar parameters (temperature, gravity, metallicity, microturbulent velocity) and spectral resolution, I used a set of our LMC spectra: in each spectrum, I selected a high number (≥ 30) of strong spectral features (iron, calcium etc. lines), fitted them with a Gaussian profile, computed an average absorption line profile, and then I built a mask for each setup. The two-pass cross-correlation routine compares the observed spectrum to the mask and works as follows:

1. The stellar spectrum is normalised to 1.0 by a low-order polynomial; fluxes higher than 1.1 (likely cosmic ray hits) are trimmed out.

2. A first pass uses a coarse grid ($\Delta v = 2\,\mathrm{km\,s^{-1}}$) covering the range $[-400\,\mathrm{km\,s^{-1}}, 400\,\mathrm{km\,s^{-1}}]$ to compute the cross-correlation function of the stellar spectrum and the Gaussian mask.

3. A Gaussian fit is applied to the function and returns the position v_{peak} and the width σ_{peak} of the cross-correlation peak.

4. A second pass computes the cross-correlation function over a finer grid ($\Delta v = 0.1\,\mathrm{km\,s^{-1}}$) covering the range $[v_{\mathrm{peak}} - \sigma_{\mathrm{peak}}, v_{\mathrm{peak}} + \sigma_{\mathrm{peak}}]$.

5. A parabola is fitted to the peak of the cross-correlation curve in order to find the final radial velocity.

Figure 2.16 displays an example of a cross-correlation function and the parabolic fit used to determine the radial velocity.

The cross-correlation routine returns the relative radial velocity, i.e. measured in the Earth frame; to correct it for the Earth motion and obtain the barycentric velocity v_{rad} (i.e. measured relative to solar system barycentre), I used the MIDAS[9] task *barycor* to compute the barycentric correction v_{Earth} (Table 2.2): $v_{\mathrm{rad}} = v + v_{\mathrm{Earth}}$. In fact, to recover the actual radial velocity of a star, two other terms should be taken into account: gravitational redshift which is caused by the star gravitational well and equally affects absorption lines (Pasquini et al., 2011) and convective shifts which is due to convective motions in stellar photospheres and affects lines depending on the depth at which they form (weaker lines form in deeper photospheric layers and tend to be more blue-shifted than strong lines; Allende Prieto et al., 2002; Asplund et al., 2000; Chiavassa et al., 2011). However, we neglected those effects since they are small (a few hundred $\mathrm{m\,s^{-1}}$) and likely comparable to the uncertainty on a single radial velocity measurement.

[9] Available at http://www.eso.org/sci/software/esomidas/.

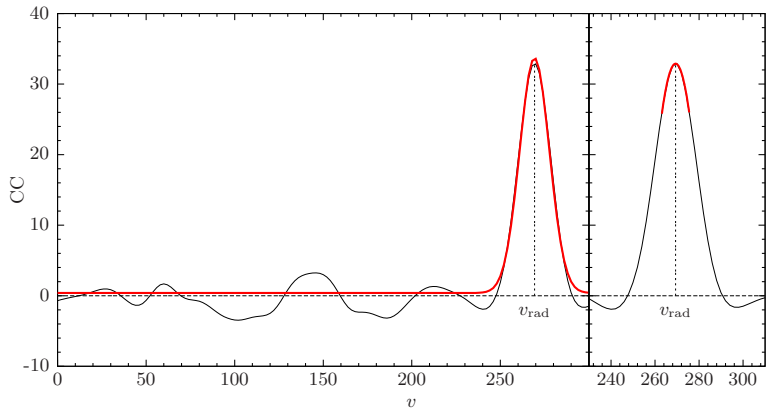

Figure 2.16: **Left panel:** Example of radial velocity determination from a cross-correlation function (black line). We first used a Gaussian fit (red thick line) to locate the position of the maximum and then defined a smaller velocity range (Gaussian fit FWHM) and compute the cross-correlation function over a finer grid to improve the determination of the radial velocity.. **Right panel:** Zoom-in on the maximum of the cross-correlation function and its parabolic fit (red thick line).

Table 2.2: Barycentric corrections for LMC bar stars computed with the MIDAS task *barycor*. Observations are identified by their ESO OB ID.

HR11		HR13		HR14	
ESO OB ID	$v_{\rm Earth}$ $\mathrm{km\,s^{-1}}$	ESO OB ID	$v_{\rm Earth}$ $\mathrm{km\,s^{-1}}$	ESO OB ID	$v_{\rm Earth}$ $\mathrm{km\,s^{-1}}$
243392	−2.31156	148164	0.49120	148166	0.75219
243393	−2.06151	148173	1.85711	148168	0.60711
243394	−2.03249	148174	0.67664	148169	0.51737
243395	−2.11123	148175	0.70996	148170	0.45909
243396	−2.14178	148176	−0.80428		
243397	−2.34669				
243438	−1.47898				
243439	−2.26194				
243440	−2.37914				
243441	−2.23058				

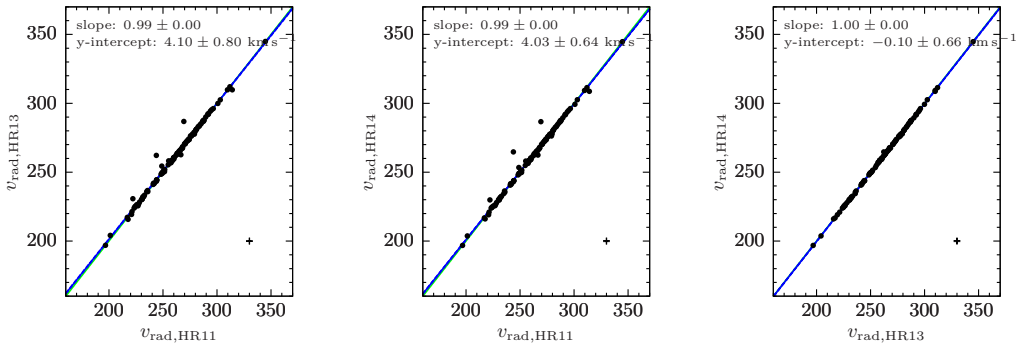

(a) HR13 vs. HR11 (b) HR14 vs. HR11 (c) HR14 vs. HR13

Figure 2.17: **From left to right panel:** HR13 vs. HR11, HR14 vs. HR11, HR14 vs. HR13. The median error bar is 0.2, 0.3 and 0.4 km s^{-1} for HR11, HR13 and HR14 respectively (cross in the bottom right corner). In the first two figures, the points outside the 1-to-1 relation are the suspected pulsating or binary stars. As explained, the agreement between HR13 and HR14 is excellent for all stars, even those whose $v_{\rm rad}$ varies, since observations were at the same epoch. Green solid line: 1-to-1 relation (hidden by the linear fit); blue solid line: linear fit to the data (fit parameters and their error are given in the plots).

2.2.4.2 Radial velocity measurements for the LMC bar sample

Identifying suspicious spectra Using a k-σ clipping ($k = 2$) rejection (over the radial velocity) allowed me to point out suspicious spectra requiring a special investigation, and I discarded them if justified (e.g., low S/N ratio leading to a poor determination of the radial velocity). For instance, in the setup HR14, for the star 05231321-6946382, I measured four radial velocities: 270.2 km s^{-1}, 270.3 km s^{-1}, 270.5 km s^{-1} and 275.4 km s^{-1}; based on the above procedure, I flagged the observation leading to a velocity of 275.4 km s^{-1}. Indeed, the fourth estimate is at a distance 1.7σ of the mean, which happens $\sim 10\,\%$ of the time; as we have four measurements, we expect 0.4 (< 0.5) of them to be at 1.7σ of the mean; statistically, it is safe to removed it from the analysis. Besides, the poor S/N ratio of the last observation (~ 2) leads to a higher error on $v_{\rm rad}$ from this frame and explains the disagreement between the velocities, and thus brings another justification to discard this observation. I only excluded a few spectra with this test.

Setup-to-setup variations In order to detect any systematic effect (from one setup to the other) or possible variations of the radial velocity, I computed a mean barycentric radial velocity for each star in each setup (*without* k-σ clipping since poor radial velocity determinations are already discarded). For a given setup s, I used the $\rm N_s$ estimates to compute the mean radial velocity $v_{{\rm rad},s}$. As the setup HR11 provides the highest number of exposures, the sample standard deviation of the radial velocity distribution is better defined; so I employed it to estimate the precision on a single velocity measurement by computing the mean of the standard deviations and found 0.6 km s^{-1}. Finally, I computed conservatively the error on a

mean radial velocity as follows:

$$e_{\mathrm{rad},s} = \max\left(\sqrt{\frac{\widehat{\mathrm{Var}}\left[v_{\mathrm{rad},s}\right]}{\mathrm{N}_s}}, \frac{0.6}{\sqrt{\mathrm{N}_s}}\right) \tag{2.14}$$

where $\widehat{\mathrm{Var}}\left[X\right] = \left(\widehat{\mathrm{Std}}\left[X\right]\right)^2$ is the unbiased sample variance. Figures 2.17a, 2.17b and 2.17c compare the mean radial velocities per setup.

I performed a T-test to compare $v_{\mathrm{rad,HR11}}$, $v_{\mathrm{rad,HR13}}$, and $v_{\mathrm{rad,HR14}}$, taken two by two. The T-test hypotheses are:

- H_0: the two mean radial velocities are equal.
- H_1: they are different; significance level: 1 %.
- Hypothesis of equal variance, since the variances, given by $(e_{\mathrm{rad},s})^2$, are similar from a setup to another.

For 103 bar stars (91 % of the sample), the T-test concluded that the three mean radial velocities are equal at the significance level of 1 %. For those stars, we have:

- $\langle v_{\mathrm{rad,HR11}} - v_{\mathrm{rad,HR13}} \rangle = -0.1\,\mathrm{km\,s^{-1}}$, $\widehat{\mathrm{Std}}\left(v_{\mathrm{rad,HR11}} - v_{\mathrm{rad,HR13}}\right) = 0.6\,\mathrm{km\,s^{-1}}$
- $\langle v_{\mathrm{rad,HR11}} - v_{\mathrm{rad,HR14}} \rangle = 0.3\,\mathrm{km\,s^{-1}}$, $\widehat{\mathrm{Std}}\left(v_{\mathrm{rad,HR11}} - v_{\mathrm{rad,HR14}}\right) = 0.7\,\mathrm{km\,s^{-1}}$
- $\langle v_{\mathrm{rad,HR13}} - v_{\mathrm{rad,HR14}} \rangle = 0.4\,\mathrm{km\,s^{-1}}$, $\widehat{\mathrm{Std}}\left(v_{\mathrm{rad,HR13}} - v_{\mathrm{rad,HR14}}\right) = 0.3\,\mathrm{km\,s^{-1}}$

The standard deviation of the differences are comparable to the combined median errors (e.g., for HR11 and HR13, $\sqrt{0.2^2 + 0.3^2} = 0.4\,\mathrm{km\,s^{-1}} \sim 0.6\,\mathrm{km\,s^{-1}}$), and therefore, are explainable by the random noise. There is a small offset from a setup to another, which can be due to the quality of the wavelength calibration, the mismatch between spectra and Gaussian masks, the level of S/N ratio, the resolution etc. which vary from one setup to another. Remarkably, although the *SimCal* light was turned off for the setup HR11 (i.e. no additional wavelength correction), the offset between HR11 and HR13 (resp. HR11 and HR14) is very small.

Detecting time-variations This T-test also allows to identify individual outliers that show true time variations of v_{rad}. For 10 stars reported in Table 2.3, at least one of the three T-tests failed. We remark that for all reported cases, the radial velocities measured for HR13 and HR14 agree rather well, while the radial velocity measured for HR11 is discrepant with the two others. The stars 05240482-6948280, 05254540-6940531, and 05224448-6954402 show the most dramatic disagreement with differences of about 8, 17, 18 $\mathrm{km\,s^{-1}}$ (resp.) between HR11 and HR13 or between HR11 and HR14. The mean observation epoch and the time extent of the observing program are given in the last columns of the Table 2.3. The observations in HR13 and HR14 were run at similar epoch while those in HR11 were carried out two years later: those discrepancies probably reveal a true radial velocity variation, due to an internal stellar variability or a binary system. Figure 2.18 displays the radial velocity curves for the five stars with the most extreme variations. The period of variation seems to be large, which is expected for giant stars.

Table 2.3: Mean radial velocities and standard deviation about the mean, mean observing epoch $\langle \mathrm{MJD} \rangle$ and its extent $\mathrm{MJD_{max}} - \mathrm{MJD_{min}}$ for stars showing a disagreement in their mean radial velocities from one setup to another. For HR13, there are more than two months between the first and the last observation; for stars with a variable v_{rad}, it explains the high values of the standard deviation observed for this setup.

2MASS ID	HR11			HR13			HR14		
	v_{rad} $\mathrm{km\,s^{-1}}$	$\sigma(v_{\mathrm{rad}})$ $\mathrm{km\,s^{-1}}$	#	v_{rad} $\mathrm{km\,s^{-1}}$	$\sigma(v_{\mathrm{rad}})$ $\mathrm{km\,s^{-1}}$	#	v_{rad} $\mathrm{km\,s^{-1}}$	$\sigma(v_{\mathrm{rad}})$ $\mathrm{km\,s^{-1}}$	#
05223316-6951389	220.9	0.9	8	219.3	0.8	5	219.1	0.6	4
05224448-6954402	243.8	5.2	9	262.2	8.0	5	264.7	1.2	4
05230867-6956329	266.6	0.6	7	262.7	1.2	5	262.4	0.6	4
05231074-6939184	201.2	0.6	9	204.1	0.6	5	203.7	0.6	4
05231091-6942374	248.9	1.4	9	254.4	3.9	5	253.4	0.7	4
05240482-6948280	222.1	1.9	9	230.7	4.1	5	229.9	0.6	4
05240604-6942380	255.3	0.7	8	258.2	0.6	5	258.1	0.6	4
05240613-6953529	217.7	1.2	9	215.8	0.6	5	216.1	0.7	4
05254540-6940531	269.3	2.6	9	286.8	1.4	5	286.7	0.6	4
05255801-6937309	257.5	0.6	9	256.9	0.6	5	256.4	0.6	4
$\langle \mathrm{MJD} \rangle$ (d)	54045.347			53054.700			53053.109		
$\mathrm{MJD_{max}} - \mathrm{MJD_{min}}$ (d)	82.94			71.84			4.86		

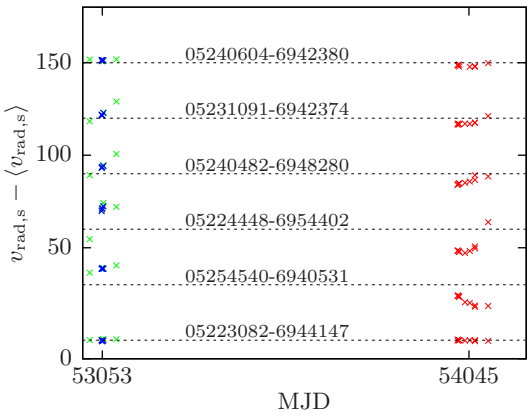

Figure 2.18: Radial velocity curves for six stars. The relative radial velocities $v_{\mathrm{rad},s} - \langle v_{\mathrm{rad},s} \rangle$ determined for each exposure are plotted as a function of MJD for five stars where the T-test failed and we suspect a variability in the radial velocity. The curves were shifted for legibility (the solid line represents the offset). The bottom curve (star 05223082-6944147) is a star with no radial velocity variability and shown here for reference. Red: HR11, green: HR13, blue: HR14 (for HR13 data and HR14 data obtained at the same epoch, the green crosses are below the blue ones).

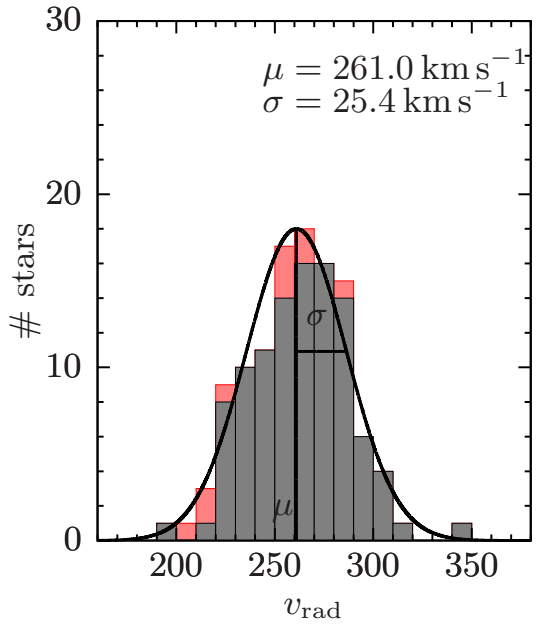

Figure 2.19: Distribution of the radial velocities of the LMC bar stars. The histogram overplotted in red denote the stars for which we suspect a radial velocity variability. The mean and the standard deviation of the distribution are respectively $261\,\mathrm{km\,s^{-1}}$ and $25\,\mathrm{km\,s^{-1}}$. A Gaussian curve $(\mu;\sigma)$ is plotted over the histogram.

Tables 2.7 to 2.9 give the mean radial velocities per setup (with 1-σ errors, 95 % confidence interval and number of independent measurements) and Table 2.10 provides the weighted mean radial velocity defined by:

$$\langle v_{\mathrm{rad}} \rangle = \sum_s \omega_s v_{\mathrm{rad},s} \quad \text{with} \quad \begin{cases} \rho_s = \dfrac{1}{{e_{\mathrm{rad},s}}^2} \\ \omega_s = \dfrac{\rho_s}{\sum_s \rho_s} \end{cases} \tag{2.15}$$

where the sum is over the three setups s and provides the associated error defined by:

$$e_{\mathrm{rad}} = \sqrt{\sum_s \omega_s^2 {e_{\mathrm{rad},s}}^2} \tag{2.16}$$

The median error on the final radial velocity is $\sim 0.2\,\mathrm{km\,s^{-1}}$. Figure 2.19 shows the distribution of the radial velocities in the LMC bar; the mean $\hat{\mu}$ of the $\langle v_{\mathrm{rad}} \rangle$ distribution is $261\,\mathrm{km\,s^{-1}}$ and the standard deviation $\hat{\sigma}$ of the distribution is $25\,\mathrm{km\,s^{-1}}$, in good agreement with values reported in Cole et al. (2005) ($\hat{\mu}_{\mathrm{Cole}} = 257\,\mathrm{km\,s^{-1}}$, $\hat{\sigma}_{\mathrm{Cole}} = 24.7\,\mathrm{km\,s^{-1}}$).

Comparison to CaT radial velocities Figure 2.20 shows the comparison between the high-resolution mean radial velocities $\langle v_{\mathrm{rad}} \rangle$ (this work) and those derived from infrared CaT low-resolution spectra by Cole et al. (2005) $v_{\mathrm{rad,CaT}}$. We found

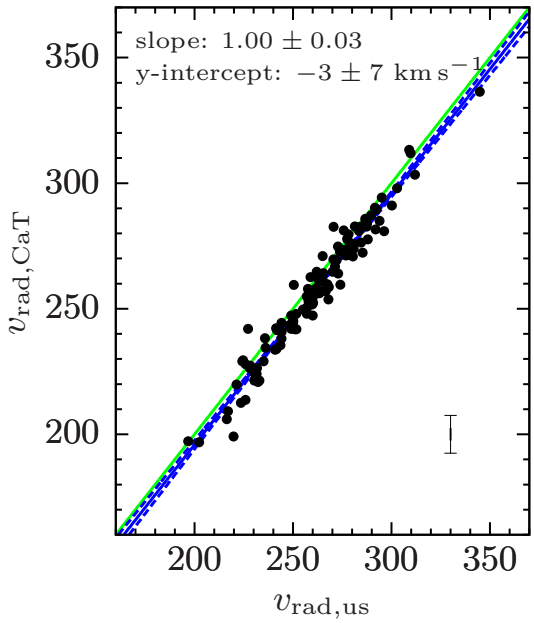

Figure 2.20: CaT vs. HR radial velocities. The median error on $\langle v_{\rm rad} \rangle$ (resp. $v_{\rm rad,CaT}$) is $0.2\,{\rm km\,s^{-1}}$ (resp. $7.5\,{\rm km\,s^{-1}}$). In the mean, $v_{\rm rad,CaT}$ is $\sim 4\,{\rm km\,s^{-1}}$ lower than $\langle v_{\rm rad} \rangle$. Green solid line: 1-to-1 relation; blue solid line: linear fit to the data (fit parameters and their error are given in the plots); blue dashed lines: lines obtained after adding or subtracting errors to fit parameters.

$\langle \langle v_{\rm rad} \rangle - v_{\rm rad,CaT} \rangle = 4.2\,{\rm km\,s^{-1}}$, with a standard deviation $5.4\,{\rm km\,s^{-1}}$. Thus, in the mean, CaT radial velocities are slightly underestimated: the low-resolution spectra are from FORS2/VLT which has no *SimCal* lamp and a stability no better than 5 to $10\,{\rm km\,s^{-1}}$. The median error on $v_{\rm rad,CaT}$ is $7.5\,{\rm km\,s^{-1}}$ and explains the standard deviation of the differences.

2.2.4.3 Re-determination of the radial velocities for the LMC inner disc sample

Applying the cross-correlation routine The LMC inner disc spectra I worked on have been only wavelength corrected for the Earth motion $v_{\rm Earth}$: therefore, I applied my cross-correlation routine to HR11, HR13 and HR14 spectra in order to re-determine the radial velocities. As I have only one estimate for radial velocities of LMC inner disc stars (spectra already co-added), I assumed an error on $v_{\rm rad}$ of $0.6\,{\rm km\,s^{-1}}$ (Sec. 2.2.4). We found a good agreement from one setup to another:

- $\langle v_{\rm rad,HR11} - v_{\rm rad,HR13} \rangle = 0.3\,{\rm km\,s^{-1}}$, $\widehat{\rm Std}\,(v_{\rm rad,HR11} - v_{\rm rad,HR13}) = 0.9\,{\rm km\,s^{-1}}$
- $\langle v_{\rm rad,HR11} - v_{\rm rad,HR14} \rangle = 0.3\,{\rm km\,s^{-1}}$, $\widehat{\rm Std}\,(v_{\rm rad,HR11} - v_{\rm rad,HR14}) = 0.7\,{\rm km\,s^{-1}}$
- $\langle v_{\rm rad,HR13} - v_{\rm rad,HR14} \rangle = 0.1\,{\rm km\,s^{-1}}$, $\widehat{\rm Std}\,(v_{\rm rad,HR13} - v_{\rm rad,HR14}) = 0.5\,{\rm km\,s^{-1}}$

Figures 2.21a, 2.21b and 2.21c compare the mean radial velocities per setup.

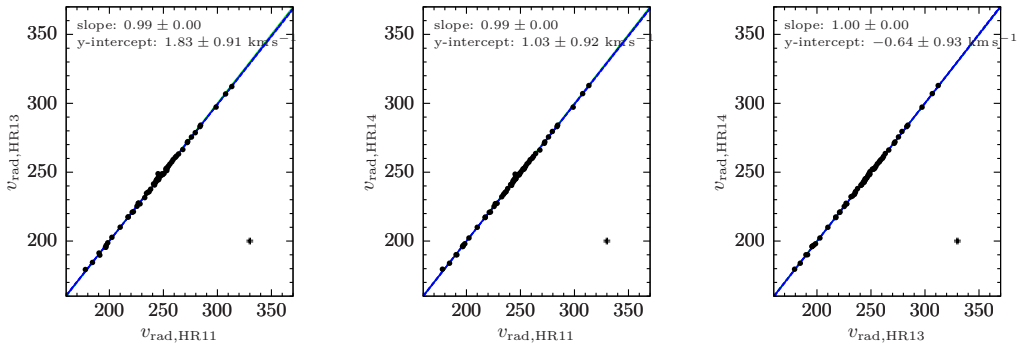

(a) HR13 vs. HR11 (b) HR14 vs. HR11 (c) HR14 vs. HR13

Figure 2.21: **From left to right panel:** HR13 vs. HR11, HR14 vs. HR11, HR14 vs. HR13. The median error bar is $0.6\,\mathrm{km\,s^{-1}}$ for all stars (cross in the bottom right corner). Green solid line: 1-to-1 relation (hidden by the linear fit); blue solid line: linear fit to the data (fit parameters and their error are given in the plots).

Table 2.11 provides the mean radial velocity and its error defined by Equations 2.15 and 2.16. The median error on the final radial velocity is $\sim 0.3\,\mathrm{km\,s^{-1}}$. Figure 2.22 shows the distribution of the radial velocities in the LMC inner disc; the mean $\hat{\mu}$ of the $\langle v_{\rm rad}\rangle$ distribution is $242.2\,\mathrm{km\,s^{-1}}$ and the standard deviation $\hat{\sigma}$ of the distribution is $27.7\,\mathrm{km\,s^{-1}}$, in good agreement with values reported in Smecker-Hane et al. (Private communication) ($\hat{\mu}_{\rm SmeckerHane} = 244\,\mathrm{km\,s^{-1}}$, $\hat{\sigma}_{\rm SmeckerHane} = 27\,\mathrm{km\,s^{-1}}$).

Comparison to Pompeia et al. Figure 2.23a presents the comparison between mean radial velocities $\langle v_{\rm rad}\rangle$ (this work) and those derived by Pompéia et al. (2008) $v_{\rm rad,Pompeia}$. As no error is provided for radial velocities in Pompéia et al. (2008), we assumed an error of $0.6\,\mathrm{km\,s^{-1}}$ for all stars. We found an excellent agreement, within error bars, between the two sets of radial velocities: $\langle\langle v_{\rm rad}\rangle - v_{\rm rad,Pompeia}\rangle = 1.6\,\mathrm{km\,s^{-1}}$, with a standard deviation $0.8\,\mathrm{km\,s^{-1}}$.

Comparison to CaT radial velocities Figure 2.23b shows the comparison between the high-resolution mean radial velocities $\langle v_{\rm rad}\rangle$ (this work) and those derived from the infrared CaT index by Smecker-Hane et al. (Private communication) $v_{\rm rad,CaT}$. We found $\langle\langle v_{\rm rad}\rangle - v_{\rm rad,CaT}\rangle = 2.8\,\mathrm{km\,s^{-1}}$, with a standard deviation $7.7\,\mathrm{km\,s^{-1}}$. Thus, as for bar stars, in the mean, CaT radial velocities are slightly underestimated (low-resolution spectra from HYDRA/CTIO with no *SimCal*). The median error on $v_{\rm rad,CaT}$ is $5.5\,\mathrm{km\,s^{-1}}$ and explains the dispersion of the differences.

2.2.5 Co-addition of spectra and signal-to-noise ratio

With radial velocities in hand, all observations of a given star can be registered in the same frame (e.g., the frame of the star using v determined in Sec. 2.2.4) and then co-added. Since this last step of the data reduction aims at improving the S/N

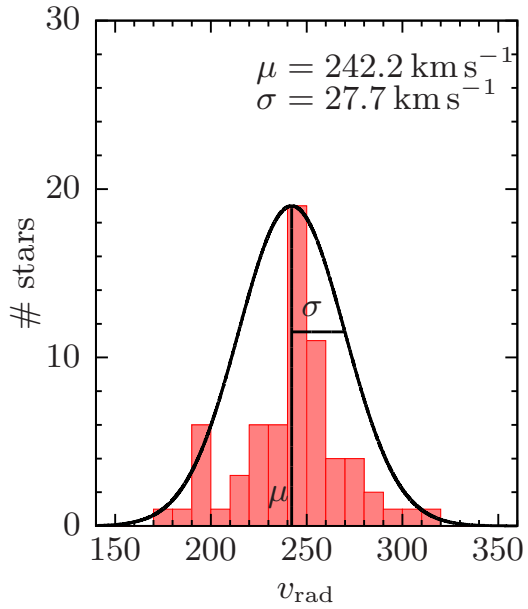

Figure 2.22: Distribution of the radial velocities of the LMC bar stars. The histogram overplotted in red denote the stars for which we suspect a radial velocity variability. The mean and the standard deviation of the distribution are respectively $261\,\mathrm{km\,s^{-1}}$ and $25\,\mathrm{km\,s^{-1}}$. A Gaussian curve $(\mu;\sigma)$ is plotted over the histogram.

ratio and at removing spurious pixels, it has to be done carefully and requires some quality checks (e.g., at least, to check the S/N ratio of individual observations).

Signal-to-noise ratio Before co-adding multiple exposures, we selected the spectra according to their median S/N ratio, requiring it to be higher than ~ 3.

CCD glow and SimCal fibres Some observations were taken with the old FLAMES CCD, affected by the so-called glow (a polluting light in one corner of the CCD shown in Fig. 2.9c); when necessary, we removed the part of a given spectrum altered by this extra source of light. Observations with HR13 and HR14 were made with the simultaneous calibration lamp turned on. However, some well-known strong emission lines of the Th–Ar gas leak and contaminate the stellar light of the ~ 5 science fibres adjacent to a given SimCal fibre; we removed these wavelength regions when needed.

Co-addition and S/N ratio of LMC bar stars Once all exposures of the same star were in the same frame, we averaged them with k-σ clipping rejection (over the fluxes at a given wavelength) to clean for cosmic rays and increase S/N ratio. Figure 2.15 (bottom panel) compares a co-added spectra to one of the single spectra used in the co-addition: the improvement of the S/N ratio is clearly visible. We ended with a typical final S/N ratio of around 25 for HR11, 40 for HR13 and 48 for HR14. Table 2.4 lists the typical lowest, the median and the typical highest values of S/N ratio as well as an empirically corrected S/N ratio (see Sec. 2.3.3).

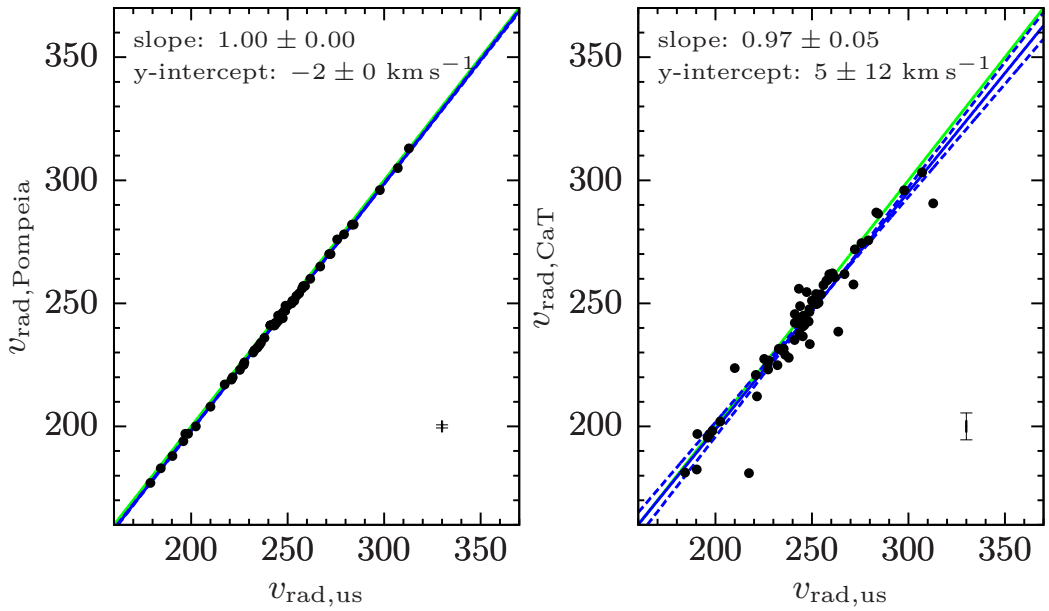

(a) Pompeia et al. vs. us (b) CaT vs. HR

Figure 2.23: **Left panel:** Pompeia et al. vs. HR radial velocities. The median error on $\langle v_{\rm rad} \rangle$ (resp. $v_{\rm rad,Pompeia}$) is 0.3 km s^{-1} (resp. 0.6 km s^{-1}). In the mean, $v_{\rm rad,Pompeia}$ is ~ 2 km s^{-1} lower than $\langle v_{\rm rad} \rangle$. **Right panel:** CaT vs. HR radial velocities. The median error on $\langle v_{\rm rad} \rangle$ (resp. $v_{\rm rad,CaT}$) is 0.3 km s^{-1} (resp. 5.5 km s^{-1}). In the mean, $v_{\rm rad,CaT}$ is ~ 3 km s^{-1} lower than $\langle v_{\rm rad} \rangle$. Green solid line: 1-to-1 relation; blue solid line: linear fit to the data (fit parameters and their error are given in the plots); blue dashed lines: lines obtained after adding or subtracting errors to fit parameters.

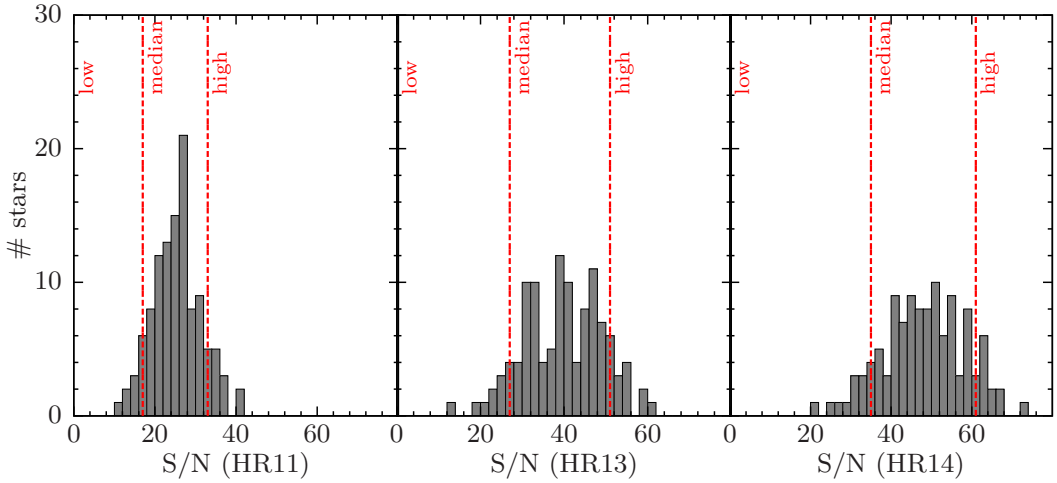

Figure 2.24: S/N ratio histograms for LMC bar stars for HR11, HR13 and HR14. Red dashed lines defines the low, median and high quality S/N ratio regime.

Table 2.12 gives for each LMC bar star the median S/N ratio per setup and the quality flag (see Sec. 2.3.3) and Figure 2.24 shows the S/N ratio histograms for each setup.

S/N **ratio of LMC bar stars** For LMC disc stars, I worked on the co-added spectra and did not have the corresponding error spectra to compute a median S/N ratio. In Section 4.2.5.2, I will use LMC bar stars to build an empirical calibration (between S/N ratio and $\hat{T}^2_{\rm nominal}$) and use this calibration to estimate the S/N ratio for LMC disc stars. Table 2.13 gives for each LMC disc star the calibrated S/N ratio per setup and the quality flag and Figure 2.25 shows the S/N ratio histograms for each setup.

2.3 Arcturus as a benchmark star

2.3.1 Principle and aims of differential chemical analysis

Chemical analysis methods are legion: they rely upon different tools and different databases (code of spectrum synthesis, library of stellar model atmospheres, atomic and molecular data etc.) which can introduce systematic effects from a method to another. In order to control any systematic effect that could hamper the comparison of our derived abundances to literature measurements, we have tested and applied our methods to the well-known mildly metal-poor Milky-Way thick disc giant Arcturus (HD 124897, α Boo). Indeed, well-known stars such as the Sun, or the giant stars μLeo or Arcturus are often chosen (*e.g.,* Alves-Brito et al., 2010; Lecureur et al., 2007; Meléndez et al., 2009; Ramírez et al., 2009; Worley et al., 2009) as reference stars for differential analysis, since the literature is broad and provides a good knowledge of their stellar parameters and atmospheric chemical composition (from

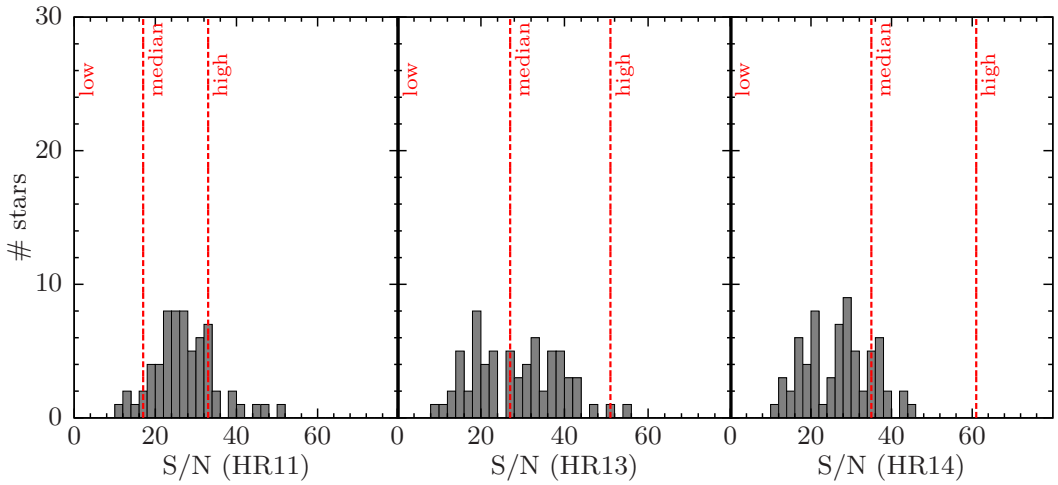

Figure 2.25: S/N ratio histograms for LMC inner disc stars for HR11, HR13 and HR14. Red dashed lines defines the low, median and high quality S/N ratio regime.

independent and less model-dependent methods). Arcturus, with $T_{eff} = 4286\,K$, $\log g = 1.66$ and $[Fe/H] = -0.52\,dex$ (Ramírez & Allende Prieto, 2011, and see references therein), is very similar to the stars of our LMC sample, hence the choice of this star as a benchmark for our sample.

2.3.2 Preparation of Arcturus GIRAFFE-like spectra

We sliced the Hinkle et al. (2000) spectral atlas of Arcturus (high resolution $R \sim 150\,000$, high S/N ratio ~ 1000) into three pieces to simulate an HR11 (550 nm to 589 nm), an HR13 (609 nm to 641 nm) and an HR14 (629 nm to 671 nm) spectrum. We then degraded the resolution (according to the setup, see Sec. 2.1.2) and sampling of these spectra to reach a best quality spectrum for each setup (referred to as {low-resolution, low sampling, ∞ S/N } in the following). We finally added Gaussian noise according to the typical noise encountered in our LMC sample for each setup, to match four assumptions of S/N ratio: an ∞ S/N, which is the original quality of the Hinkle et al. (2000) atlas; a high S/N, which corresponds to the median of the ninth decile of the S/N ratio distribution (the best 10% of the sample); a median S/N, which corresponds to the $\sim$ median of the S/N ratio distribution; a low S/N, which corresponds to the median of the first decile of the S/N ratio distribution (the worse 10% of the sample).

2.3.3 Discussion on signal-to-noise ratio measurements

As explained in Section 2.2.3, the S/N ratio computed from the GIRAFFE pipeline products (as the ratio of the flux over its propagated error) is likely underestimated. Indeed, if we inject in our {low-resolution, low sampling, ∞ S/N } Arcturus spectrum a Gaussian noise described by the variance ${\sigma_{noise}}^2$, and if we compare this noisy spectrum to a GIRAFFE LMC spectrum with a S/N = ${\sigma_{noise}}^{-1}$ (measured as

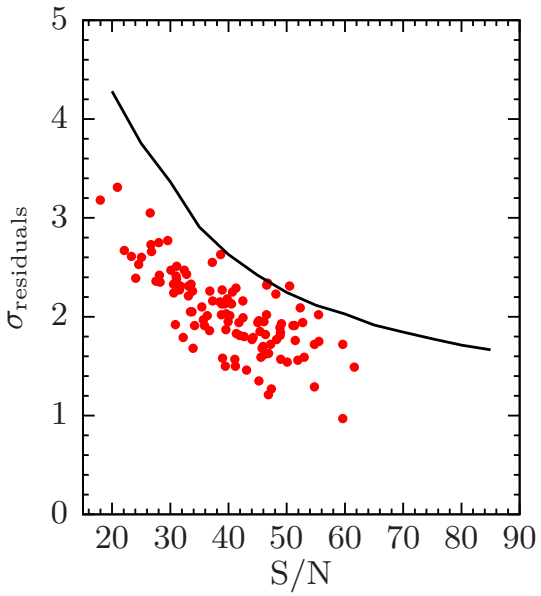

Figure 2.26: $\sigma_{\rm residual}$ vs. S/N. Black solid line: we measured $\sigma_{\rm residual}$ of the Arcturus HR13 spectrum for different values of artificially added noise ${\sigma_{\rm noise}}^2 = ({\rm S/N})^{-2}$; red dots: LMC HR13 spectra. For Arcturus with artificial noise, $\sigma_{\rm residual} \simeq 2$ when S/N $\simeq 55$ while for our LMC spectra, $\sigma_{\rm residual} \simeq 2$ when S/N $\simeq 40$.

described in Sec. 2.2.3), the quality of the GIRAFFE spectrum will appear better than the quality of the noisy Arcturus spectrum. In order to empirically find a correspondence between the measured S/N and the genuine S/N, we employed the automated tool DAOSPEC (Stetson & Pancino, 2008), designed to measure EW: when it performs this task, the software splits the input spectrum S into a fitted continuum component C_f and a fitted line component L_f and returns a number $\sigma_{\rm residual}$ called "relative flux dispersion in residual spectrum", which is the dispersion (expressed in percentage) of:

$$\frac{|S_i - (C_{f\,i} + L_{f\,i})|}{C_{f\,i}} \tag{2.17}$$

where i is the pixel index. Therefore, $\sigma_{\rm residual}$ depends on the S/N ratio, with an observed dependency as shown in Figure 2.26. The saturation of the residuals at high values of S/N ratio is probably due to the residual not being dominated by the noise anymore but by the mismatch (between the observed absorption lines and the fitted profiles). For each setup and S/N ratio regime (low, median or high) observed in our LMC spectra, we investigated various values of ${\sigma_{\rm noise}}^2$ until the $\sigma_{\rm residual}$ approximately matched the targeted S/N ratio. Table 2.4 gives for each setup, the values of S/N ratio (measured and corrected values) corresponding to the qualifiers high, median, and low.

Thus we added a Gaussian noise (with zero-mean and variance ${\sigma_{\rm noise}}^2 = ({\rm S/N}^*)^{-2}$) in the three {low-resolution, low sampling, ∞ S/N } spectra according to S/N ratio values listed in Table 2.4. We drew 101 realisations

Table 2.4: Values of S/N ratio corresponding to the qualifiers high (best 10% of the sample), median and low (worse 10% of the sample). S/N is the measured with the pipeline products and S/N* is the empirically corrected .

Qualifier	HR11		HR13		HR14	
	S/N	S/N*	S/N	S/N*	S/N	S/N*
low	16	25	24	35	31	35
median	25	40	40	55	48	60
high	36	55	55	75	64	75

for each high, median and low S/N ratio version of the Arcturus spectra. In the following, we will employ the single ∞ S/N, the 101 high S/N, the 101 median S/N, and the 101 low S/N spectra when we determine the stellar parameters (Chapter 3) and when we measure the chemical abundances (Chapter 4).

2.4 Large tables

Table 2.5: Photometry, CaT metallicity and radial velocity of LMC bar stars. 2MASS identifiers, VI magnitudes from Szymanski (2005); Udalski et al. (1997, 2000), JHK magnitudes from Skrutskie et al. (2006), $[Fe/H]_{CaT}$ and $v_{rad,CaT}$ from Cole et al. (2005). Errors are provided for each quantity.

2MASS ID	V	σ (V)	I	σ (I)	J	σ (J)	H	σ (H)	K	σ (K)	$[Fe/H]_{CaT}$	σ ($[Fe/H]_{CaT}$)	$v_{rad,CaT}$	$\sigma\left(v_{rad,CaT}\right)$
	mag	mag	mag	mag	mag	mag	mag	mag	mag	mag	dex	dex	$km\,s^{-1}$	$km\,s^{-1}$
05223082-6944147	17.228	0.031	15.674	0.022	14.526	0.043	13.709	0.043	13.565	0.042	-0.14	0.14	245.2	7.5
05223112-6945292	17.163	0.021	15.579	0.014	14.434	0.046	13.639	0.055	13.487	0.045	-0.41	0.14	261.6	7.6
05223186-6947159	17.450	0.030	16.065	0.022	15.101	0.056	14.321	0.059	14.127	0.080	-0.35	0.14	266.8	7.6
05223309-6946595	17.106	0.037	15.764	0.017	14.838	0.048	14.079	0.059	14.161	0.086	-0.40	0.14	254.4	7.4
05223316-6951389	17.664	0.024	16.317	0.019	15.460	0.074	14.656	0.074	14.573	0.118	-1.69	0.15	199.1	7.6
05223318-6937044	17.492	0.024	16.181	0.018	15.264	0.061	14.542	0.066	14.450	0.106	-0.18	0.14	247.3	7.6
05223416-6944433	17.411	0.046	16.169	0.018	15.442	0.085	14.811	0.098	14.555	0.103	-1.05	0.12	221.6	7.5
05223487-6938057	17.455	0.017	16.061	0.014	15.208	0.064	14.300	0.083	14.256	0.085	-0.37	0.13	209.2	7.5
05223506-6937279	17.372	0.039	15.886	0.020	14.900	0.057	14.108	0.058	14.033	0.074	-0.34	0.14	258.6	7.5
05223557-6943373	17.439	0.023	16.257	0.015	15.487	0.085	14.781	0.098	14.650	0.136	-1.28	0.11	227.9	7.6
05223701-6936166	16.898	0.031	15.719	0.012	14.885	0.048	14.380	0.058	14.118	0.087	-0.35	0.14	256.2	7.6
05223787-6954562	17.487	0.019	15.836	0.016	14.688	0.048	13.888	0.048	13.714	0.061	0.14	0.15	251.7	7.6
05223895-6945007	16.976	0.013	15.588	0.014	14.631	0.032	13.865	0.040	13.644	0.058	-0.42	0.14	227.3	7.5
05223988-6946110	16.992	0.013	15.534	0.012	14.542	0.037	13.687	0.041	13.569	0.052	-0.51	0.13	220.8	7.5
05224062-6953310	17.350	0.016	15.874	0.015	14.747	0.047	14.015	0.060	13.899	0.063	-0.35	0.14	233.7	7.5
05224164-6935518	17.590	0.013	16.217	0.012	15.425	0.070	14.523	0.079	14.066	NaN	-0.30	0.14	258.8	7.5
05224195-6941099	17.316	0.014	15.868	0.015	14.835	0.051	13.974	0.069	14.050	0.072	-0.31	0.14	281.6	7.4
05224240-6940567	16.917	0.021	15.957	0.018	15.313	0.084	14.757	0.091	14.637	0.121	-0.28	0.14	273.4	7.7
05224276-6940109	16.986	0.016	15.668	0.012	14.741	0.045	13.966	0.051	13.826	0.063	-0.58	0.13	241.8	7.6
05224309-6940275	17.266	0.025	15.789	0.017	14.696	0.037	13.903	0.043	13.899	0.062	-0.28	0.14	313.3	7.4
05224321-6952397	17.392	0.016	15.993	0.012	15.012	0.061	14.268	0.057	14.125	0.081	-0.40	0.15	221.4	7.4
05224448-6954402	17.482	0.020	16.327	0.016	15.350	0.053	14.707	0.086	14.570	0.105	-0.92	0.13	264.7	7.5
05224854-6940010	17.984	0.017	16.458	0.013	15.401	0.074	14.490	0.074	14.368	0.107	-0.05	0.15	224.0	7.6
05225062-6936580	17.334	0.021	16.089	0.019	15.100	0.069	14.473	0.070	14.307	0.090	-0.36	0.14	257.3	7.5
05225069-6955486	17.438	0.031	15.938	0.015	14.854	0.043	14.130	0.056	13.909	0.064	-0.30	0.14	259.6	7.7
05225632-6942269	17.151	0.015	15.974	0.014	15.128	0.061	14.433	0.074	14.384	0.095	-1.19	0.13	280.9	7.6
05225877-6938172	17.536	0.023	16.355	0.015	15.548	0.083	14.863	0.126	14.444	NaN	-0.48	0.14	213.7	7.4
05225980-6954368	17.893	0.021	16.420	0.017	15.357	0.069	14.468	0.060	14.432	0.106	-0.96	0.12	229.1	7.9
05230009-6935251	17.234	0.016	15.808	0.013	14.807	0.051	14.061	0.053	13.958	0.061	-0.20	0.15	285.0	7.4
05230011-6946353	17.240	0.012	16.310	0.012	15.539	0.060	15.175	0.118	14.953	0.155	-0.44	0.14	247.3	7.5
05230203-6935557	17.252	0.017	15.997	0.012	15.147	0.065	14.416	0.055	14.320	0.087	-1.10	0.11	251.9	7.5
05230230-6939587	17.293	0.017	15.931	0.014	14.783	0.084	14.055	0.088	13.912	0.084	-0.57	0.13	272.3	7.4
05230353-6952441	17.350	0.019	15.851	0.014	14.709	0.059	13.945	0.050	13.846	0.064	-0.33	0.14	336.4	7.6
05230370-6944219	17.600	0.027	16.256	0.023	15.269	0.071	14.417	0.103	14.399	0.120	-1.41	0.11	276.4	7.5
05230589-6944122	16.696	0.015	15.590	0.015	14.761	0.063	14.225	0.079	14.232	0.099	-0.50	0.13	248.0	7.5
05230606-6951113	17.742	0.067	15.985	0.016	14.803	0.043	14.003	0.042	13.871	0.062	-0.16	0.14	273.9	7.6
05230647-6944394	17.282	0.022	16.212	0.019	15.374	0.069	14.816	0.070	14.657	0.116	-1.55	0.10	238.3	7.7
05230776-6946082	16.964	0.015	15.722	0.012	14.852	0.047	14.194	0.051	14.040	0.076	-1.10	0.12	279.6	7.5
05230867-6956329	18.028	0.017	16.741	0.017	15.890	0.103	14.913	0.086	14.683	NaN	-0.44	0.14	264.2	7.4
05231074-6939184	16.980	0.014	15.720	0.011	14.709	0.045	14.094	0.048	14.040	0.076	-1.33	0.11	196.8	7.5
05231091-6942374	16.910	0.015	15.625	0.012	14.488	0.065	13.811	0.061	13.750	0.057	-0.46	0.13	241.8	7.4
05231221-6938166	17.182	0.016	15.954	0.014	14.865	0.050	14.304	0.050	14.226	0.081	-0.05	0.15	275.8	7.4
05231315-6945212	17.212	0.016	16.023	0.014	15.056	0.101	14.410	0.093	14.240	0.099	-0.50	0.13	281.0	7.5
05231321-6946382	17.128	0.017	15.588	0.011	14.443	0.043	13.697	0.042	13.462	0.056	-0.34	0.14	282.6	7.6
05231411-6948546	17.169	0.025	15.496	0.014	14.243	0.036	13.457	0.029	13.306	0.040	-0.28	0.14	311.9	7.5

Continued on next page

2MASS ID	V	σ (V)	I	σ (I)	J	σ (J)	H	σ (H)	K	σ (K)	$[Fe/H]_{CaT}$	σ ($[Fe/H]_{CaT}$)	$v_{rad,CaT}$	$\sigma\left(v_{rad,CaT}\right)$
	mag	mag	mag	mag	mag	mag	mag	mag	mag	mag	dex	dex	$km\,s^{-1}$	$km\,s^{-1}$
05231484-6950196	17.439	0.016	16.108	0.012	15.117	0.051	14.370	0.067	14.319	0.088	-0.31	0.16	257.0	7.4
05231562-6955430	17.275	0.024	15.674	0.016	14.546	0.074	13.688	0.065	13.566	0.079	-0.34	0.14	303.4	7.4
05231631-6942507	17.153	0.015	15.763	0.010	14.680	0.045	14.000	0.049	13.832	0.062	-0.31	0.14	282.8	7.5
05231634-6951332	17.612	0.045	16.172	0.017	15.299	0.114	14.435	0.088	14.475	0.119	-0.46	0.13	254.7	7.4
05231962-6943309	17.227	0.012	16.247	0.012	15.543	0.096	15.114	0.105	14.628	NaN	-0.48	0.14	252.4	7.5
05232020-6954561	16.881	0.020	15.303	0.017	14.187	0.065	13.407	0.061	13.256	0.067	-0.44	0.14	212.5	7.5
05232148-6952155	17.284	0.018	15.770	0.013	14.743	0.050	13.862	0.037	13.747	0.059	-0.36	0.14	284.0	7.5
05232181-6945429	17.329	0.013	16.040	0.012	15.133	0.065	14.462	0.071	14.124	0.079	-0.58	0.13	277.8	7.5
05232554-6943388	17.293	0.019	16.142	0.012	15.319	0.063	14.492	0.061	14.479	0.098	-0.52	0.14	242.0	7.5
05232624-6943558	17.278	0.019	15.853	0.012	14.876	0.059	13.520	NaN	13.293	NaN	-0.29	0.14	219.8	7.6
05232680-6953109	17.282	0.013	15.981	0.017	15.152	0.050	14.373	0.056	14.317	0.085	-1.42	0.13	253.7	8.6
05232845-6944158	17.226	0.017	15.784	0.015	14.726	0.055	14.045	0.057	13.955	0.076	-0.20	0.14	281.2	7.5
05232892-6947486	17.342	0.028	15.970	0.018	15.063	0.056	14.264	0.051	14.285	0.091	-0.48	0.13	271.0	7.5
05233236-6948257	17.749	0.027	16.487	0.022	15.515	0.077	14.834	0.080	14.468	0.104	-1.04	0.12	229.1	7.5
05235653-6947387	16.933	0.024	15.750	0.017	14.868	0.065	14.179	0.050	14.290	0.083	-0.58	0.15	244.4	7.7
05235851-6945519	17.321	0.019	15.882	0.011	14.799	0.047	14.109	0.071	13.909	0.082	-0.23	0.15	285.8	7.5
05240317-6953036	17.723	0.018	16.427	0.012	15.532	0.068	14.827	0.078	14.542	0.103	-0.36	0.14	260.9	7.7
05240482-6948280	17.536	0.025	16.223	0.029	15.409	0.083	14.605	0.073	14.517	0.103	-0.55	0.14	226.3	7.6
05240604-6942380	18.082	0.017	16.452	0.013	15.396	0.065	14.421	0.061	14.304	0.089	-0.23	0.15	254.9	7.5
05240613-6953529	17.538	0.022	16.395	0.014	15.390	0.060	14.883	0.077	14.745	0.122	-1.59	0.11	206.0	7.7
05240672-6947130	17.642	0.030	16.363	0.016	15.478	0.083	14.882	0.091	14.633	0.129	-0.29	0.14	270.8	7.6
05240803-6956250	17.387	0.011	15.977	0.010	14.984	0.048	14.334	0.047	14.141	0.074	-0.28	0.14	224.8	7.6
05240830-6944428	17.140	0.029	15.584	0.019	14.469	0.036	13.664	0.036	13.534	0.047	-0.39	0.14	282.3	7.5
05241033-6944374	17.405	0.018	15.988	0.018	14.918	0.074	14.170	0.074	13.987	0.083	-0.29	0.14	289.6	7.5
05241341-6945303	17.285	0.014	15.891	0.013	14.866	0.056	14.049	0.050	14.076	0.075	-0.51	0.14	242.0	7.5
05241479-6946323	16.997	0.014	15.967	0.012	15.260	0.062	14.853	0.092	14.644	0.119	-0.30	0.14	261.6	7.5
05241699-6942158	17.366	0.016	15.977	0.013	15.002	0.047	14.258	0.044	14.253	0.077	-0.21	0.14	247.9	7.5
05241794-6951317	17.748	0.027	16.402	0.024	15.289	0.067	14.518	0.058	14.508	0.104	-0.25	0.14	271.2	7.6
05242161-6942097	17.321	0.016	15.900	0.012	14.995	0.057	14.133	0.053	14.058	0.063	-0.57	0.14	256.6	7.5
05242198-6943579	17.231	0.015	15.759	0.013	14.656	0.042	13.918	0.044	13.708	0.057	-0.22	0.14	259.5	7.5
05242240-6944344	17.281	0.018	15.764	0.018	14.734	0.043	13.851	0.036	13.781	0.059	-0.34	0.14	221.4	7.5
05242409-6942051	17.138	0.019	15.671	0.012	14.561	0.052	13.871	0.057	13.740	0.071	-0.42	0.14	262.6	7.6
05242542-6955188	17.188	0.026	15.892	0.015	15.048	0.076	14.341	0.069	14.049	0.076	-0.42	0.13	240.9	7.6
05242687-6943577	16.730	0.015	15.620	0.013	14.850	0.043	14.263	0.050	14.326	0.090	-0.33	0.14	262.3	7.5
05242702-6956445	17.606	0.013	16.233	0.013	15.410	0.099	14.565	0.090	14.442	0.116	-0.54	0.13	235.5	7.5
05242811-6947467	17.302	0.017	15.927	0.015	14.926	0.056	14.153	0.047	14.089	0.076	-0.46	0.14	283.7	7.5
05243272-6955362	17.044	0.019	15.555	0.014	14.451	0.035	13.775	0.046	13.524	0.050	-0.58	0.13	272.7	7.7
05243734-6945496	17.641	0.015	16.380	0.016	15.734	0.121	14.712	0.078	14.884	0.154	-0.26	0.15	241.5	7.5
05243901-6948426	17.006	0.015	15.718	0.013	14.546	NaN	14.157	0.067	13.927	NaN	-0.54	0.13	253.0	7.5
05244189-6954427	17.644	0.021	16.301	0.017	15.457	0.077	14.647	0.075	14.682	0.117	-0.35	0.14	234.0	7.5
05244210-6942596	17.787	0.017	16.528	0.013	15.626	0.088	15.064	0.110	14.878	NaN	-0.69	0.13	259.7	7.6
05244301-6943412	16.825	0.017	15.569	0.013	14.676	0.038	14.034	0.039	13.974	0.059	-1.54	0.10	291.1	7.5
05244340-6950004	17.708	0.016	16.317	0.012	15.425	0.077	14.502	0.055	14.444	0.090	-0.13	0.16	294.3	7.6
05244408-6942423	16.967	0.011	15.806	0.011	14.936	0.048	14.308	0.054	14.283	0.081	-1.19	0.12	298.0	7.5
05244600-6946017	17.507	0.020	16.141	0.013	15.266	0.061	14.590	0.080	14.280	0.090	-0.24	0.15	229.5	7.5
05244637-6947340	17.283	0.013	16.100	0.014	15.401	0.070	14.686	0.074	14.585	0.103	-0.47	0.14	257.9	7.5
05244698-6956141	17.564	0.016	16.122	0.011	15.158	0.059	14.485	0.055	14.446	0.092	-0.32	0.14	226.4	7.4
05244878-6948359	17.121	0.018	15.681	0.013	14.721	0.032	13.887	0.055	13.839	0.054	-0.25	0.14	234.5	7.7
05244976-6943230	17.201	0.014	15.731	0.012	14.632	0.047	13.893	0.053	13.795	0.053	-0.49	0.13	269.3	7.5
05245212-6948184	17.379	0.025	16.015	0.020	15.070	0.085	14.450	0.062	14.215	0.070	-0.36	0.15	274.8	7.5
05245859-6952257	17.686	0.014	16.396	0.015	15.700	0.082	14.896	0.083	14.625	0.106	-0.68	0.13	197.2	7.7
05252428-6939311	17.265	0.010	15.792	0.011	14.761	0.036	14.016	0.029	13.722	0.050	-0.12	0.14	258.3	7.5

Continued on next page

2MASS ID	V	σ (V)	I	σ (I)	J	σ (J)	H	σ (H)	K	σ (K)	$[Fe/H]_{CaT}$	σ ($[Fe/H]_{CaT}$)	$v_{rad,CaT}$	$\sigma\left(v_{rad,CaT}\right)$
	mag	mag	mag	mag	mag	mag	mag	mag	mag	mag	dex	dex	$km\,s^{-1}$	$km\,s^{-1}$
05252899-6939078	17.347	0.013	16.213	0.012	15.364	0.065	14.841	0.081	14.702	0.116	-0.43	0.14	249.7	7.5
05253039-6940288	17.432	0.017	16.135	0.016	15.196	0.049	14.550	0.061	14.315	0.071	-0.29	0.14	264.0	7.6
05253040-6936261	17.314	0.014	15.922	0.014	14.815	0.059	14.076	0.051	13.886	0.064	-0.70	0.12	277.6	7.4
05253235-6943137	17.298	0.012	16.138	0.017	15.291	0.072	14.640	0.072	14.521	0.106	-1.64	0.12	271.4	7.5
05253522-6937078	17.153	0.014	15.764	0.016	14.682	0.047	13.952	0.042	13.863	0.055	-0.47	0.19	282.7	7.4
05254540-6940531	17.563	0.027	16.262	0.018	15.303	0.058	14.551	0.057	14.551	0.100	-0.21	0.14	276.4	7.5
05254864-6940501	17.426	0.016	16.016	0.018	14.951	0.072	14.307	0.073	13.984	0.070	-0.41	0.14	243.5	7.5
05255000-6942466	17.254	0.034	15.657	0.016	14.687	0.058	13.886	0.052	13.794	0.060	-0.37	0.14	238.1	7.6
05255267-6943155	17.137	0.017	15.576	0.013	14.439	0.043	13.642	0.038	13.550	0.041	-0.18	0.14	269.6	7.6
05255625-6941243	16.912	0.011	15.844	0.015	14.986	0.050	14.416	0.049	14.384	0.095	-0.49	0.14	282.7	7.5
05255801-6937309	17.163	0.018	15.645	0.015	14.550	0.051	13.785	0.058	13.704	0.064	-0.30	0.14	250.4	7.5
05255812-6942522	17.588	0.025	16.183	0.010	15.141	0.056	14.572	0.057	14.428	0.089	-0.10	0.15	244.6	7.5
05260124-6939268	17.278	0.014	15.908	0.010	14.955	0.045	14.122	0.038	13.903	0.062	-0.62	0.13	287.2	7.5
05260720-6942342	17.435	0.017	16.330	0.017	15.617	0.083	14.836	0.077	14.785	0.120	-0.61	0.13	290.2	7.5
05260784-6938341	17.209	0.032	15.764	0.015	14.657	0.049	13.943	0.044	13.662	0.053	-0.56	0.13	242.2	7.6
05261339-6940590	17.150	0.019	15.503	0.016	14.333	0.035	13.559	0.027	13.337	0.039	-0.04	0.15	264.7	7.6

Table 2.6: Photometry, CaT metallicity and radial velocity of LMC inner disc stars. Identifiers, VI magnitudes from Smecker-Hane et al. (2002), JHK magnitudes from Skrutskie et al. (2006), $[Fe/H]_{CaT}$ and $v_{rad,CaT}$ from Smecker-Hane et al. (2002). Errors are provided for each quantity.

ID	V	σ (V)	I	σ (I)	J	σ (J)	H	σ (H)	K	σ (K)	$[Fe/H]_{CaT}$	σ ($[Fe/H]_{CaT}$)	$v_{rad,CaT}$	$\sigma\left(v_{rad,CaT}\right)$
	mag	mag	mag	mag	mag	mag	mag	mag	mag	mag	dex	dex	$km\,s^{-1}$	$km\,s^{-1}$
0499-LMCDisc01	17.023	0.007	15.699	0.004	14.655	0.035	13.869	0.027	13.674	0.040	-0.44	0.18	212.2	3.5
0512-LMCDisc01	16.994	0.004	15.539	0.002	14.450	0.032	13.615	0.043	13.536	0.040	-0.78	0.15	247.6	2.8
0522-LMCDisc01	17.005	0.004	15.537	0.003	14.345	0.040	13.722	0.047	13.436	0.043	-0.37	0.18	271.9	3.9
0533-LMCDisc01	16.958	0.004	15.537	0.003	14.454	0.035	13.743	0.036	13.608	0.043	-0.43	0.20	236.6	10.0
0534-LMCDisc01	17.111	0.004	15.890	0.002	14.710	0.035	14.039	0.042	13.951	0.054	-1.11	0.16	254.6	13.5
0546-LMCDisc01	17.041	0.005	15.619	0.004	14.568	0.033	13.859	0.041	13.653	0.050	-0.91	0.15	260.6	2.8
0548-LMCDisc01	17.095	0.007	15.680	0.005	14.503	0.029	13.678	0.035	13.547	0.047	-0.31	0.19	246.5	3.3
0564-LMCDisc01	17.127	0.003	15.935	0.003	14.889	0.045	14.397	0.063	14.272	0.079	-1.76	0.19	196.9	11.0
0565-LMCDisc01	17.061	0.003	15.585	0.002	14.491	0.032	13.697	0.039	13.500	0.048	-0.60	0.17	237.7	5.1
0576-LMCDisc01	17.132	0.003	15.806	0.002	14.661	0.039	13.980	0.048	13.643	0.043	-1.03	0.14	303.2	2.7
0593-LMCDisc01	17.168	0.003	15.688	0.002	14.495	0.029	13.667	0.028	13.557	0.039	-0.58	0.20	229.1	7.6
0599-LMCDisc01	17.174	0.005	15.756	0.003	14.532	0.036	13.744	0.032	13.645	0.034	-0.71	0.16	241.9	3.1
0601-LMCDisc01	17.112	0.004	15.673	0.003	14.590	0.034	13.900	0.035	13.788	0.056	-0.77	0.20	248.9	7.1
0606-LMCDisc01	17.152	0.003	15.791	0.002	14.704	0.037	13.976	0.051	13.896	0.057	-1.63	0.08	181.2	5.5
0611-LMCDisc01	17.122	0.004	15.603	0.002	14.496	0.036	13.713	0.036	13.589	0.049	-0.42	0.18	245.0	2.6
0614-LMCDisc01	17.023	0.045	15.492	0.007	14.414	0.037	13.675	0.043	13.404	0.048	-0.71	0.26	255.9	11.4
0620-LMCDisc01	17.205	0.003	15.790	0.002	14.632	0.037	13.893	0.040	13.881	0.063	-0.28	0.19	198.2	3.4
0625-LMCDisc01	17.144	0.004	15.614	0.003	14.464	0.024	13.678	0.038	13.464	0.046	-0.86	0.16	243.3	6.6
0629-LMCDisc01	17.140	0.004	15.766	0.002	14.711	0.033	14.030	0.040	13.819	0.052	-0.97	0.19	182.5	9.4
0631-LMCDisc01	17.054	0.004	15.655	0.003	14.672	0.051	13.968	0.047	13.680	0.064	-0.90	0.19	259.2	11.1
0633-LMCDisc01	17.131	0.003	15.647	0.002	14.547	0.037	13.763	0.046	13.708	0.054	-1.21	0.25	195.4	10.9
0640-LMCDisc01	17.154	0.004	15.772	0.003	14.755	0.054	13.945	0.037	13.815	0.045	-0.82	0.13	220.9	7.1
0646-LMCDisc01	17.071	0.007	15.674	0.005	14.681	0.033	14.008	0.048	13.926	0.068	-0.66	0.25	227.9	9.9
0651-LMCDisc01	17.152	0.007	15.713	0.005	14.666	0.036	13.924	0.049	13.740	0.054	-0.51	0.18	242.6	5.4
0655-LMCDisc01	17.202	0.004	15.674	0.002	14.546	0.037	13.786	0.040	13.641	0.051	-0.66	0.18	226.8	5.3
0656-LMCDisc01	17.191	0.004	15.758	0.003	14.659	0.036	13.958	0.053	13.737	0.054	-0.56	0.20	231.5	7.5
0658-LMCDisc01	17.229	0.003	15.797	0.002	14.730	0.061	13.959	0.057	13.704	0.056	-0.40	0.19	231.5	5.0
0664-LMCDisc01	17.156	0.004	15.529	0.002	14.390	0.029	13.565	0.021	13.385	0.034	-0.58	0.17	249.7	5.1
0666-LMCDisc01	17.167	0.005	15.833	0.003	14.766	0.036	14.212	0.058	14.004	0.070	-1.02	0.11	225.6	5.3
0671-LMCDisc01	17.197	0.004	15.705	0.003	14.568	0.027	13.837	0.042	13.621	0.049	-0.55	0.12	251.1	4.5
0672-LMCDisc01	17.193	0.003	15.611	0.002	14.454	0.035	13.579	0.035	13.452	0.037	-0.38	0.18	250.2	2.3
0679-LMCDisc01	17.203	0.004	15.653	0.003	14.504	0.037	13.700	0.032	13.591	0.050	-0.34	0.19	253.7	3.3
0690-LMCDisc01	17.266	0.005	15.678	0.002	14.400	0.035	13.552	0.029	13.418	0.039	-0.23	0.19	295.9	2.9
0699-LMCDisc01	17.214	0.006	16.058	0.005	15.089	0.053	14.470	0.035	14.591	0.091	-1.15	0.21	224.9	14.2
0700-LMCDisc01	17.284	0.004	15.821	0.002	14.729	0.039	13.909	0.045	13.682	0.049	-0.37	0.22	286.4	9.7
0701-LMCDisc01	17.214	0.004	15.693	0.003	14.607	0.040	13.745	0.034	13.599	0.046	-0.33	0.25	261.8	6.6
0705-LMCDisc01	17.215	0.005	15.886	0.004	14.878	0.047	14.147	0.047	14.025	0.071	-0.72	0.18	NaN	NaN
0706-LMCDisc01	17.208	0.004	15.894	0.003	14.960	0.045	14.198	0.051	14.106	0.071	-0.47	0.19	NaN	NaN
0710-LMCDisc01	17.308	0.007	15.762	0.004	14.425	0.030	13.631	0.022	13.427	0.029	-0.65	0.16	261.9	3.6
0720-LMCDisc01	17.314	0.003	15.984	0.002	14.922	0.043	14.227	0.050	14.327	0.092	-0.90	0.15	202.0	6.0
0721-LMCDisc01	17.253	0.007	15.784	0.006	14.567	0.045	13.803	0.042	13.613	0.052	-0.58	0.17	250.4	3.4
0728-LMCDisc01	17.249	0.004	15.836	0.002	14.805	0.038	13.964	0.047	13.969	0.067	-0.80	0.19	257.7	5.8
0731-LMCDisc01	17.255	0.004	15.593	0.003	14.376	0.032	13.524	0.030	13.401	0.044	-0.23	0.22	275.6	6.0
0748-LMCDisc01	17.279	0.004	15.781	0.003	14.794	0.040	13.964	0.047	13.802	0.056	-0.17	0.20	227.4	4.7
0752-LMCDisc01	17.320	0.003	15.801	0.002	14.523	0.037	13.831	0.037	13.619	0.056	-0.08	0.21	223.1	4.3

Continued on next page

ID	V	σ (V)	I	σ (I)	J	σ (J)	H	σ (H)	K	σ (K)	$[Fe/H]_{CaT}$	σ ($[Fe/H]_{CaT}$)	$v_{rad,CaT}$	$\sigma\left(v_{rad,CaT}\right)$
	mag	mag	mag	mag	mag	mag	mag	mag	mag	mag	dex	dex	$km\,s^{-1}$	$km\,s^{-1}$
0756-LMCDisc01	17.251	0.004	15.568	0.002	14.377	0.036	13.499	0.025	13.331	0.034	-0.46	0.17	257.4	3.5
0758-LMCDisc01	17.269	0.005	15.983	0.004	15.036	0.057	14.383	0.075	14.339	0.095	-1.22	0.15	259.5	7.9
0766-LMCDisc01	17.343	0.003	15.861	0.002	14.705	0.044	13.924	0.054	13.828	0.063	-0.46	0.14	286.9	4.5
0773-LMCDisc01	17.264	0.008	15.707	0.005	14.599	0.050	13.702	NaN	13.487	NaN	-0.51	0.13	230.9	4.0
0775-LMCDisc01	17.261	0.005	15.927	0.004	14.836	0.048	14.324	0.052	14.110	0.070	-1.28	0.23	245.6	11.1
0776-LMCDisc01	17.287	0.004	15.877	0.003	14.843	0.036	14.273	0.064	14.042	0.065	-0.75	0.12	235.1	5.5
0782-LMCDisc01	17.291	0.004	15.844	0.003	14.784	0.032	13.994	0.051	13.804	0.051	-0.34	0.26	233.4	13.3
0789-LMCDisc01	17.310	0.009	15.629	0.006	14.340	0.033	13.495	0.034	13.270	0.043	-0.36	0.13	240.5	4.0
0790-LMCDisc01	17.301	0.004	15.721	0.003	14.527	0.032	13.655	0.037	13.512	0.049	-0.45	0.19	241.1	5.5
0793-LMCDisc01	17.319	0.004	15.843	0.003	14.761	0.036	13.927	0.053	13.820	0.062	-0.53	0.18	242.1	3.1
0808-LMCDisc01	17.360	0.004	16.105	0.002	15.210	0.049	14.622	0.058	14.465	0.080	-1.50	0.13	NaN	NaN
0834-LMCDisc01	17.355	0.009	15.828	0.007	14.659	0.024	13.807	0.043	13.768	0.057	-0.64	0.17	196.8	7.2
0835-LMCDisc01	17.434	0.003	15.760	0.002	14.402	0.035	13.592	0.040	13.430	0.042	-0.36	0.15	262.2	2.7
0854-LMCDisc01	17.415	0.004	15.997	0.003	14.936	0.038	14.163	0.051	14.095	0.069	-0.10	0.21	290.6	8.8
0855-LMCDisc01	17.393	0.004	16.001	0.003	14.921	0.035	14.160	0.040	14.004	0.071	-0.02	0.22	181.0	55.9
0859-LMCDisc01	17.397	0.006	15.883	0.004	14.717	0.037	14.051	0.048	13.805	0.058	-0.22	0.20	NaN	NaN
0879-LMCDisc01	17.390	0.008	16.057	0.004	NaN	NaN	NaN	NaN	NaN	NaN	-1.14	0.15	253.8	9.7
0900-LMCDisc01	17.400	0.007	15.983	0.004	14.956	0.036	14.154	0.049	14.021	0.058	-0.27	0.19	274.5	4.6
0937-LMCDisc01	17.426	0.008	16.108	0.005	14.909	0.039	14.194	0.053	13.919	0.055	-1.40	0.18	238.5	13.4
1055-LMCDisc01	17.599	0.004	16.219	0.002	15.092	0.052	14.350	0.060	14.190	0.074	-0.87	0.16	NaN	NaN
1105-LMCDisc01	17.661	0.005	16.170	0.002	14.876	0.045	14.103	0.051	13.932	0.057	-1.15	0.17	243.4	5.0
1118-LMCDisc01	17.628	0.004	16.278	0.002	15.296	0.044	14.515	0.055	14.289	0.076	-0.25	0.27	223.7	14.6

Table 2.7: Mean HR11 radial velocities for LMC bar stars: mean radial velocity, sample standard deviation $\widehat{\mathrm{Std}}\,(v_{\mathrm{rad}})$, corrected sample standard deviation $\widehat{\mathrm{Std}}\,(v_{\mathrm{rad}})^{\star}$ (used afterwards for the statistical analysis), 1-σ error $\sigma\,(v_{\mathrm{rad}})$, 95 % confidence interval and number of independent measurements.

2MASS ID	v_{rad} km s^{-1}	$\widehat{\mathrm{Std}}\,(v_{\mathrm{rad}})$ km s^{-1}	$\widehat{\mathrm{Std}}\,(v_{\mathrm{rad}})^{\star}$ km s^{-1}	$\sigma\,(v_{\mathrm{rad}})$ km s^{-1}	95 % C.I. km s^{-1}	#
05223082-6944147	250.0	0.2	0.6	0.2	0.5	9
05223112-6945292	263.1	0.2	0.6	0.2	0.5	9
05223186-6947159	271.2	0.4	0.6	0.2	0.5	9
05223309-6946595	258.3	0.4	0.6	0.2	0.5	9
05223316-6951389	220.9	0.9	0.9	0.4	0.8	8
05223318-6937044	259.9	0.4	0.6	0.2	0.5	8
05223416-6944433	230.8	1.1	1.1	0.4	0.8	9
05223487-6938057	217.0	0.4	0.6	0.2	0.5	9
05223506-6937279	268.2	0.3	0.6	0.2	0.5	9
05223557-6943373	226.9	1.3	1.3	0.4	1.0	9
05223701-6936166	263.4	0.3	0.6	0.2	0.5	9
05223787-6954562	260.1	0.4	0.6	0.2	0.5	8
05223895-6945007	228.3	0.2	0.6	0.2	0.5	9
05223988-6946110	232.2	0.4	0.6	0.2	0.5	9
05224062-6953310	240.9	0.3	0.6	0.2	0.5	9
05224164-6935518	268.1	0.4	0.6	0.2	0.5	8
05224195-6941099	291.9	0.4	0.6	0.2	0.5	9
05224240-6940567	276.3	0.4	0.6	0.2	0.5	9
05224276-6940109	250.8	0.3	0.6	0.2	0.5	9
05224309-6940275	314.1	4.9	4.9	1.7	3.8	9
05224321-6952397	232.8	0.2	0.6	0.2	0.5	9
05224448-6954402	243.8	5.2	5.2	1.8	4.0	9
05224854-6940010	231.3	0.7	0.7	0.2	0.5	8
05225062-6936580	265.9	0.2	0.6	0.2	0.5	9
05225069-6955486	274.3	0.4	0.6	0.2	0.5	8
05225632-6942269	296.6	1.4	1.4	0.5	1.0	9
05225877-6938172	225.7	0.4	0.6	0.2	0.5	9
05225980-6954368	234.9	0.5	0.6	0.2	0.5	8
05230009-6935251	293.8	0.4	0.6	0.2	0.5	9
05230011-6946353	249.2	0.6	0.6	0.2	0.5	9
05230203-6935557	258.5	1.1	1.1	0.4	0.9	9
05230230-6939587	285.5	0.3	0.6	0.2	0.5	9
05230353-6952441	344.7	0.4	0.6	0.2	0.5	9
05230370-6944219	278.8	1.2	1.2	0.5	1.0	8
05230589-6944122	257.0	0.6	0.6	0.2	0.5	9
05230606-6951113	280.8	0.5	0.6	0.2	0.5	9
05230647-6944394	236.0	1.5	1.5	0.6	1.3	8
05230776-6946082	279.7	2.2	2.2	0.8	1.7	9
05230867-6956329	266.6	0.4	0.6	0.2	0.6	7
05231074-6939184	201.2	0.6	0.6	0.2	0.5	9
05231091-6942374	248.9	1.4	1.4	0.5	1.1	9
05231221-6938166	280.7	0.4	0.6	0.2	0.5	9
05231315-6945212	283.6	0.4	0.6	0.2	0.5	8
05231321-6946382	270.6	0.2	0.6	0.2	0.5	9
05231411-6948546	309.7	0.5	0.6	0.3	0.6	6
05231484-6950196	266.8	0.3	0.6	0.2	0.5	9
05231562-6955430	311.9	0.2	0.6	0.2	0.5	9
05231631-6942507	281.4	0.3	0.6	0.2	0.5	9
05231634-6951332	260.0	0.5	0.6	0.2	0.5	9
05231962-6943309	260.0	0.4	0.6	0.2	0.5	9
05232020-6954561	223.2	0.3	0.6	0.2	0.5	9
05232148-6952155	287.5	0.4	0.6	0.2	0.5	9
05232181-6945429	277.4	0.4	0.6	0.2	0.5	9
05232554-6943388	227.5	0.4	0.6	0.2	0.5	9
05232624-6943558	221.3	0.3	0.6	0.2	0.5	9
05232680-6953109	268.0	0.3	0.6	0.2	0.5	9
05232845-6944158	275.5	0.3	0.6	0.2	0.5	9
05232892-6947486	264.9	0.5	0.6	0.2	0.5	9
05233236-6948257	224.0	0.5	0.6	0.2	0.5	9
05235653-6947387	244.1	0.5	0.6	0.2	0.5	9
05235851-6945519	286.7	0.3	0.6	0.2	0.5	9
05240317-6953036	265.5	0.5	0.6	0.2	0.5	9
05240482-6948280	222.1	1.9	1.9	0.7	1.4	9
05240604-6942380	255.3	0.7	0.7	0.3	0.6	8
05240613-6953529	217.7	1.2	1.2	0.4	0.9	9
05240672-6947130	280.4	0.4	0.6	0.2	0.5	9
05240803-6956250	230.1	0.3	0.6	0.2	0.5	9
05240830-6944428	282.6	0.4	0.6	0.2	0.5	9
05241033-6944374	292.2	0.4	0.6	0.2	0.5	9
05241341-6945303	248.9	0.3	0.6	0.2	0.5	9
05241479-6946323	262.9	0.4	0.6	0.2	0.5	9
05241699-6942158	251.6	0.5	0.6	0.2	0.5	9
05241794-6951317	277.0	0.4	0.6	0.2	0.5	9
05242161-6942097	259.7	0.3	0.6	0.2	0.5	9
05242198-6943579	251.4	0.3	0.6	0.5	1.5	3
05242240-6944344	230.5	0.5	0.6	0.2	0.5	9

Continued on next page

2MASS ID	$v_{\rm rad}$ $\rm km\,s^{-1}$	$\widehat{\rm Std}\,(v_{\rm rad})$ $\rm km\,s^{-1}$	$\widehat{\rm Std}\,(v_{\rm rad})^{\star}$ $\rm km\,s^{-1}$	$\sigma\,(v_{\rm rad})$ $\rm km\,s^{-1}$	95 % C.I. $\rm km\,s^{-1}$	#
05242409-6942051	259.0	0.2	0.6	0.2	0.5	9
05242542-6955188	244.3	0.2	0.6	0.2	0.5	9
05242687-6943577	263.9	0.3	0.6	0.2	0.5	9
05242702-6956445	243.8	0.5	0.6	0.2	0.5	8
05242811-6947467	287.0	0.3	0.6	0.2	0.5	9
05243272-6955362	273.7	0.3	0.6	0.2	0.5	9
05243734-6945496	241.9	0.3	0.6	0.2	0.5	9
05243901-6948426	257.7	0.4	0.6	0.2	0.5	8
05244189-6954427	241.6	0.4	0.6	0.2	0.5	9
05244210-6942596	267.6	0.6	0.6	0.2	0.5	8
05244301-6943412	300.8	1.2	1.2	0.4	0.9	9
05244340-6950004	295.1	0.2	0.6	0.2	0.5	9
05244408-6942423	303.0	0.5	0.6	0.2	0.5	9
05244600-6946017	224.2	0.2	0.6	0.2	0.5	9
05244637-6947340	257.6	0.5	0.6	0.2	0.5	9
05244698-6956141	231.6	0.4	0.6	0.2	0.5	9
05244878-6948359	235.7	0.3	0.6	0.2	0.5	9
05244976-6943230	272.0	0.4	0.6	0.2	0.5	9
05245212-6948184	272.7	0.4	0.6	0.2	0.5	9
05245859-6952257	196.8	0.7	0.7	0.3	0.6	9
05252428-6939311	261.9	0.2	0.6	0.2	0.5	9
05252899-6939078	254.8	0.3	0.6	0.2	0.5	9
05253039-6940288	272.9	0.3	0.6	0.2	0.5	9
05253040-6936261	288.1	0.5	0.6	0.2	0.5	9
05253235-6943137	279.1	2.3	2.3	0.8	1.8	9
05253522-6937078	284.4	0.3	0.6	0.2	0.5	9
05254540-6940531	269.3	2.6	2.6	0.9	2.0	9
05254864-6940501	248.2	0.3	0.6	0.2	0.5	9
05255000-6942466	244.0	0.3	0.6	0.2	0.5	9
05255267-6943155	270.5	0.4	0.6	0.2	0.5	9
05255625-6941243	287.6	0.3	0.6	0.2	0.5	9
05255801-6937309	257.5	0.3	0.6	0.2	0.5	9
05255812-6942522	250.2	0.3	0.6	0.2	0.5	9
05260124-6939268	289.6	0.4	0.6	0.2	0.5	9
05260720-6942342	291.5	0.5	0.6	0.2	0.5	9
05260784-6938341	241.2	0.4	0.6	0.2	0.5	9
05261339-6940590	269.9	0.3	0.6	0.2	0.5	9

Table 2.8: Mean HR13 radial velocities for LMC bar stars (same columns as Table 2.7).

2MASS ID	$v_{\rm rad}$ km s^{-1}	$\widehat{\rm Std}\,(v_{\rm rad})$ km s^{-1}	$\widehat{\rm Std}\,(v_{\rm rad})^{\star}$ km s^{-1}	$\sigma\,(v_{\rm rad})$ km s^{-1}	95 % C.I. km s^{-1}	#
05223082-6944147	250.4	0.2	0.6	0.3	0.7	5
05223112-6945292	262.9	0.4	0.6	0.3	0.7	5
05223186-6947159	271.7	0.4	0.6	0.3	0.7	5
05223309-6946595	258.2	1.1	1.1	0.6	1.4	5
05223316-6951389	219.3	0.8	0.8	0.4	1.0	5
05223318-6937044	260.4	0.4	0.6	0.3	0.7	5
05223416-6944433	230.4	1.1	1.1	0.6	1.4	5
05223487-6938057	217.2	0.3	0.6	0.3	0.7	5
05223506-6937279	268.5	0.3	0.6	0.3	0.7	5
05223557-6943373	225.6	0.2	0.6	0.3	0.7	5
05223701-6936166	263.7	0.4	0.6	0.3	0.7	5
05223787-6954562	259.6	0.4	0.6	0.3	0.7	5
05223895-6945007	228.3	0.2	0.6	0.3	0.7	5
05223988-6946110	232.3	0.2	0.6	0.3	0.7	5
05224062-6953310	241.1	0.4	0.6	0.3	0.7	5
05224164-6935518	267.4	0.2	0.6	0.3	0.7	5
05224195-6941099	292.0	0.3	0.6	0.3	0.7	5
05224240-6940567	276.1	0.1	0.6	0.3	0.7	5
05224276-6940109	251.5	0.2	0.6	0.3	0.7	5
05224309-6940275	309.8	3.7	3.7	1.9	4.6	5
05224321-6952397	233.3	0.5	0.6	0.3	0.7	5
05224448-6954402	262.2	8.0	8.0	4.1	9.9	5
05224854-6940010	232.0	0.2	0.6	0.3	0.7	5
05225062-6936580	265.9	0.3	0.6	0.3	0.7	5
05225069-6955486	273.7	0.3	0.6	0.3	0.7	5
05225632-6942269	296.2	0.3	0.6	0.3	0.7	5
05225877-6938172	226.4	0.5	0.6	0.3	0.7	5
05225980-6954368	235.9	0.8	0.8	0.4	1.0	5
05230009-6935251	294.3	0.4	0.6	0.3	0.7	5
05230011-6946353	249.0	0.4	0.6	0.3	0.7	5
05230203-6935557	258.4	0.5	0.6	0.3	0.7	5
05230230-6939587	285.3	0.3	0.6	0.3	0.7	5
05230353-6952441	344.9	0.3	0.6	0.3	0.7	5
05230370-6944219	279.0	0.6	0.6	0.3	0.8	5
05230589-6944122	256.9	0.5	0.6	0.3	0.7	5
05230606-6951113	281.0	0.3	0.6	0.3	0.7	5
05230647-6944394	235.9	0.2	0.6	0.3	0.7	5
05230776-6946082	279.4	3.3	3.3	1.7	4.1	5
05230867-6956329	262.7	1.2	1.2	0.6	1.5	5
05231074-6939184	204.1	0.4	0.6	0.3	0.7	5
05231091-6942374	254.4	3.9	3.9	2.0	4.8	5
05231221-6938166	281.0	0.2	0.6	0.3	0.7	5
05231315-6945212	283.4	0.1	0.6	0.3	0.7	5
05231321-6946382	270.6	0.4	0.6	0.3	0.7	5
05231411-6948546	309.8	0.3	0.6	0.3	0.7	5
05231484-6950196	266.7	0.3	0.6	0.3	0.7	5
05231562-6955430	312.0	0.2	0.6	0.3	0.7	5
05231631-6942507	281.6	0.2	0.6	0.3	0.7	5
05231634-6951332	260.3	0.6	0.6	0.3	0.7	5
05231962-6943309	260.7	0.5	0.6	0.3	0.7	5
05232020-6954561	223.9	0.3	0.6	0.3	0.7	5
05232148-6952155	287.7	0.2	0.6	0.3	0.7	5
05232181-6945429	277.7	0.4	0.6	0.3	0.7	5
05232554-6943388	226.9	0.3	0.6	0.3	0.7	5
05232624-6943558	221.4	0.6	0.6	0.3	0.7	5
05232680-6953109	268.0	0.4	0.6	0.3	0.7	5
05232845-6944158	276.4	0.3	0.6	0.3	0.7	5
05232892-6947486	265.3	0.4	0.6	0.3	0.7	5
05233236-6948257	224.7	0.5	0.6	0.3	0.7	5
05235653-6947387	244.2	0.2	0.6	0.3	0.7	5
05235851-6945519	286.8	0.3	0.6	0.3	0.7	5
05240317-6953036	265.0	0.3	0.6	0.3	0.7	5
05240482-6948280	230.7	4.1	4.1	2.1	5.1	5
05240604-6942380	258.2	0.4	0.6	0.3	0.7	5
05240613-6953529	215.8	0.4	0.6	0.3	0.7	5
05240672-6947130	280.6	0.3	0.6	0.3	0.7	5
05240803-6956250	230.2	0.5	0.6	0.3	0.7	5
05240830-6944428	283.1	0.6	0.6	0.3	0.7	5
05241033-6944374	292.5	0.4	0.6	0.3	0.7	5
05241341-6945303	249.4	0.4	0.6	0.3	0.7	5
05241479-6946323	263.5	0.6	0.6	0.3	0.7	5
05241699-6942158	251.9	0.3	0.6	0.3	0.7	5
05241794-6951317	277.0	0.2	0.6	0.3	0.7	5
05242161-6942097	260.3	0.2	0.6	0.3	0.7	5
05242198-6943579	250.4	0.6	0.6	0.8	5.4	2
05242240-6944344	230.3	0.3	0.6	0.3	0.7	5
05242409-6942051	258.8	0.4	0.6	0.3	0.7	5
05242542-6955188	244.2	0.6	0.6	0.3	0.7	5
05242687-6943577	264.2	0.3	0.6	0.3	0.7	5
05242702-6956445	243.3	0.3	0.6	0.3	0.7	5

Continued on next page

2MASS ID	v_{rad} $\mathrm{km\,s^{-1}}$	$\widehat{\mathrm{Std}}\,(v_{\mathrm{rad}})$ $\mathrm{km\,s^{-1}}$	$\widehat{\mathrm{Std}}\,(v_{\mathrm{rad}})^{\star}$ $\mathrm{km\,s^{-1}}$	$\sigma\,(v_{\mathrm{rad}})$ $\mathrm{km\,s^{-1}}$	95 % C.I. $\mathrm{km\,s^{-1}}$	#
05242811-6947467	287.1	0.4	0.6	0.3	0.7	5
05243272-6955362	274.1	0.4	0.6	0.3	0.7	5
05243734-6945496	241.9	0.3	0.6	0.3	0.7	5
05243901-6948426	258.4	0.5	0.6	0.3	0.7	5
05244189-6954427	241.7	0.5	0.6	0.3	0.7	5
05244210-6942596	267.4	0.4	0.6	0.3	0.7	5
05244301-6943412	299.9	0.8	0.8	0.4	1.0	5
05244340-6950004	295.3	0.4	0.6	0.3	0.7	5
05244408-6942423	302.5	0.3	0.6	0.3	0.7	5
05244600-6946017	225.2	0.5	0.6	0.3	0.7	5
05244637-6947340	257.8	0.3	0.6	0.3	0.7	5
05244698-6956141	231.9	0.3	0.6	0.3	0.7	5
05244878-6948359	236.7	0.2	0.6	0.3	0.7	5
05244976-6943230	272.4	0.4	0.6	0.3	0.7	5
05245212-6948184	273.0	0.2	0.6	0.3	0.7	5
05245859-6952257	196.9	0.7	0.7	0.4	0.9	5
05252428-6939311	262.1	0.4	0.6	0.3	0.7	5
05252899-6939078	255.4	0.5	0.6	0.3	0.7	5
05253039-6940288	273.0	0.4	0.6	0.3	0.7	5
05253040-6936261	287.8	0.3	0.6	0.3	0.7	5
05253235-6943137	277.6	0.5	0.6	0.3	0.7	5
05253522-6937078	284.5	0.4	0.6	0.3	0.7	5
05254540-6940531	286.8	1.4	1.4	0.7	1.8	5
05254864-6940501	248.5	0.3	0.6	0.3	0.7	5
05255000-6942466	244.5	0.4	0.6	0.3	0.7	5
05255267-6943155	270.7	0.7	0.7	0.4	0.9	5
05255625-6941243	287.0	0.3	0.6	0.3	0.7	5
05255801-6937309	256.9	0.5	0.6	0.3	0.7	5
05255812-6942522	250.0	0.1	0.6	0.3	0.7	5
05260124-6939268	290.1	0.6	0.6	0.3	0.7	5
05260720-6942342	292.2	0.8	0.8	0.4	1.0	5
05260784-6938341	242.0	0.8	0.8	0.4	1.0	5
05261339-6940590	270.6	0.3	0.6	0.3	0.7	5

Table 2.9: Mean HR14 radial velocities for LMC bar stars (same columns as Table 2.7).

2MASS ID	$v_{\rm rad}$ km s^{-1}	$\widehat{\rm Std}\,(v_{\rm rad})$ km s^{-1}	$\widehat{\rm Std}\,(v_{\rm rad})^{\star}$ km s^{-1}	$\sigma\,(v_{\rm rad})$ km s^{-1}	95 % C.I. km s^{-1}	#
05223082-6944147	249.7	0.3	0.6	0.4	1.0	4
05223112-6945292	262.5	0.3	0.6	0.4	1.0	4
05223186-6947159	271.2	0.2	0.6	0.4	1.0	4
05223309-6946595	258.1	0.2	0.6	0.4	1.0	4
05223316-6951389	219.1	0.4	0.6	0.4	1.0	4
05223318-6937044	259.5	0.6	0.6	0.4	1.0	4
05223416-6944433	229.9	0.2	0.6	0.4	1.0	4
05223487-6938057	216.8	0.2	0.6	0.4	1.0	4
05223506-6937279	267.5	0.5	0.6	0.4	1.0	4
05223557-6943373	225.7	0.4	0.6	0.4	1.0	4
05223701-6936166	263.2	0.5	0.6	0.4	1.0	4
05223787-6954562	259.2	0.4	0.6	0.4	1.0	4
05223895-6945007	228.0	0.4	0.6	0.4	1.0	4
05223988-6946110	232.0	0.4	0.6	0.4	1.0	4
05224062-6953310	240.6	0.2	0.6	0.4	1.0	4
05224164-6935518	267.6	0.1	0.6	0.4	1.0	4
05224195-6941099	291.8	0.1	0.6	0.4	1.0	4
05224240-6940567	276.1	0.3	0.6	0.4	1.0	4
05224276-6940109	250.6	0.2	0.6	0.4	1.0	4
05224309-6940275	308.7	0.2	0.6	0.4	1.0	4
05224321-6952397	232.6	0.2	0.6	0.4	1.0	4
05224448-6954402	264.7	1.2	1.2	0.7	1.9	4
05224854-6940010	231.1	0.3	0.6	0.4	1.0	4
05225062-6936580	265.7	0.2	0.6	0.4	1.0	4
05225069-6955486	273.6	0.5	0.6	0.4	1.0	4
05225632-6942269	296.2	0.4	0.6	0.4	1.0	4
05225877-6938172	225.7	0.4	0.6	0.4	1.0	4
05225980-6954368	234.5	0.5	0.6	0.4	1.0	4
05230009-6935251	293.9	0.5	0.6	0.4	1.0	4
05230011-6946353	248.8	0.3	0.6	0.4	1.0	4
05230203-6935557	258.7	0.2	0.6	0.4	1.0	4
05230230-6939587	285.2	0.4	0.6	0.4	1.0	4
05230353-6952441	344.7	0.3	0.6	0.4	1.0	4
05230370-6944219	278.2	0.5	0.6	0.4	1.0	4
05230589-6944122	257.0	0.4	0.6	0.4	1.0	4
05230606-6951113	280.6	0.2	0.6	0.4	1.0	4
05230647-6944394	235.5	0.4	0.6	0.4	1.0	4
05230776-6946082	277.8	0.5	0.6	0.4	1.0	4
05230867-6956329	262.4	0.4	0.6	0.4	1.0	4
05231074-6939184	203.7	0.2	0.6	0.4	1.0	4
05231091-6942374	253.4	0.7	0.7	0.4	1.1	4
05231221-6938166	280.4	0.3	0.6	0.4	1.0	4
05231315-6945212	283.1	0.2	0.6	0.4	1.0	4
05231321-6946382	270.4	0.2	0.6	0.5	1.5	3
05231411-6948546	309.3	0.2	0.6	0.4	1.0	4
05231484-6950196	266.1	0.4	0.6	0.4	1.0	4
05231562-6955430	311.4	0.3	0.6	0.4	1.0	4
05231631-6942507	281.3	0.1	0.6	0.4	1.0	4
05231634-6951332	260.2	0.3	0.6	0.4	1.0	4
05231962-6943309	260.3	0.6	0.6	0.4	1.0	4
05232020-6954561	223.9	0.3	0.6	0.4	1.0	4
05232148-6952155	287.5	0.3	0.6	0.4	1.0	4
05232181-6945429	277.5	0.3	0.6	0.4	1.0	4
05232554-6943388	226.7	0.3	0.6	0.4	1.0	4
05232624-6943558	221.0	0.2	0.6	0.4	1.0	4
05232680-6953109	267.9	0.4	0.6	0.4	1.0	4
05232845-6944158	275.6	0.2	0.6	0.4	1.0	4
05232892-6947486	265.0	0.2	0.6	0.4	1.0	4
05233236-6948257	224.4	0.7	0.7	0.4	1.1	4
05235653-6947387	243.7	0.3	0.6	0.4	1.0	4
05235851-6945519	286.3	0.2	0.6	0.4	1.0	4
05240317-6953036	265.0	0.3	0.6	0.4	1.0	4
05240482-6948280	229.9	0.5	0.6	0.4	1.0	4
05240604-6942380	258.1	0.3	0.6	0.4	1.0	4
05240613-6953529	216.1	0.7	0.7	0.4	1.2	4
05240672-6947130	280.1	0.5	0.6	0.4	1.0	4
05240803-6956250	230.1	0.4	0.6	0.4	1.0	4
05240830-6944428	282.6	0.2	0.6	0.4	1.0	4
05241033-6944374	292.1	0.3	0.6	0.4	1.0	4
05241341-6945303	249.1	0.1	0.6	0.4	1.0	4
05241479-6946323	263.2	0.2	0.6	0.4	1.0	4
05241699-6942158	251.4	0.1	0.6	0.4	1.0	4
05241794-6951317	276.6	0.3	0.6	0.4	1.0	4
05242161-6942097	259.5	0.3	0.6	0.4	1.0	4
05242198-6943579	249.8	0.3	0.6	0.4	1.0	4
05242240-6944344	229.9	0.3	0.6	0.4	1.0	4
05242409-6942051	258.6	0.2	0.6	0.4	1.0	4
05242542-6955188	243.9	0.3	0.6	0.4	1.0	4
05242687-6943577	263.9	0.2	0.6	0.4	1.0	4
05242702-6956445	243.0	0.2	0.6	0.4	1.0	4

Continued on next page

2MASS ID	$v_{\rm rad}$ $\rm km\,s^{-1}$	$\widehat{\rm Std}\,(v_{\rm rad})$ $\rm km\,s^{-1}$	$\widehat{\rm Std}\,(v_{\rm rad})^{\star}$ $\rm km\,s^{-1}$	$\sigma\,(v_{\rm rad})$ $\rm km\,s^{-1}$	95 % C.I. $\rm km\,s^{-1}$	#
05242811-6947467	286.9	0.1	0.6	0.4	1.0	4
05243272-6955362	273.9	0.2	0.6	0.4	1.0	4
05243734-6945496	241.3	0.2	0.6	0.4	1.0	4
05243901-6948426	258.1	0.3	0.6	0.4	1.0	4
05244189-6954427	241.4	0.1	0.6	0.4	1.0	4
05244210-6942596	267.0	0.3	0.6	0.4	1.0	4
05244301-6943412	299.3	1.0	1.0	0.6	1.7	4
05244340-6950004	294.9	0.2	0.6	0.4	1.0	4
05244408-6942423	302.6	0.2	0.6	0.4	1.0	4
05244600-6946017	224.8	0.2	0.6	0.4	1.0	4
05244637-6947340	257.4	0.3	0.6	0.4	1.0	4
05244698-6956141	231.5	0.4	0.6	0.4	1.0	4
05244878-6948359	236.4	0.3	0.6	0.4	1.0	4
05244976-6943230	272.1	0.2	0.6	0.4	1.0	4
05245212-6948184	272.8	0.2	0.6	0.4	1.0	4
05245859-6952257	196.8	0.3	0.6	0.4	1.0	4
05252428-6939311	261.7	0.2	0.6	0.4	1.0	4
05252899-6939078	254.9	0.4	0.6	0.4	1.0	4
05253039-6940288	272.6	0.4	0.6	0.4	1.0	4
05253040-6936261	287.7	0.1	0.6	0.4	1.0	4
05253235-6943137	276.3	0.8	0.8	0.5	1.2	4
05253522-6937078	284.2	0.2	0.6	0.4	1.0	4
05254540-6940531	286.7	0.2	0.6	0.4	1.0	4
05254864-6940501	248.0	0.1	0.6	0.4	1.0	4
05255000-6942466	243.8	0.2	0.6	0.4	1.0	4
05255267-6943155	270.2	0.2	0.6	0.4	1.0	4
05255625-6941243	287.0	0.3	0.6	0.4	1.0	4
05255801-6937309	256.4	0.2	0.6	0.4	1.0	4
05255812-6942522	249.7	0.2	0.6	0.4	1.0	4
05260124-6939268	289.4	0.2	0.6	0.4	1.0	4
05260720-6942342	291.5	0.1	0.6	0.4	1.0	4
05260784-6938341	241.6	0.4	0.6	0.4	1.0	4
05261339-6940590	270.2	0.3	0.6	0.4	1.0	4

Table 2.10: Final mean radial velocities $v_{\rm rad}$ (and errors $e_{\rm rad}$) for LMC bar stars.

2MASS ID	$v_{\rm rad}$ km s^{-1}	$e_{\rm rad}$ km s^{-1}
05223082-6944147	250.1	0.2
05223112-6945292	263.0	0.2
05223186-6947159	271.3	0.2
05223309-6946595	258.3	0.2
05223316-6951389	219.8	0.2
05223318-6937044	260.0	0.2
05223416-6944433	230.4	0.3
05223487-6938057	217.0	0.2
05223506-6937279	268.2	0.2
05223557-6943373	226.0	0.2
05223701-6936166	263.4	0.2
05223787-6954562	259.8	0.2
05223895-6945007	228.3	0.2
05223988-6946110	232.2	0.2
05224062-6953310	240.9	0.2
05224164-6935518	267.8	0.2
05224195-6941099	291.9	0.2
05224240-6940567	276.2	0.2
05224276-6940109	251.0	0.2
05224309-6940275	309.0	0.4
05224321-6952397	232.9	0.2
05224448-6954402	262.0	0.6
05224854-6940010	231.5	0.2
05225062-6936580	265.9	0.2
05225069-6955486	274.0	0.2
05225632-6942269	296.3	0.2
05225877-6938172	225.9	0.2
05225980-6954368	235.0	0.2
05230009-6935251	293.9	0.2
05230011-6946353	249.1	0.2
05230203-6935557	258.5	0.2
05230230-6939587	285.4	0.2
05230353-6952441	344.8	0.2
05230370-6944219	278.7	0.2
05230589-6944122	257.0	0.2
05230606-6951113	280.8	0.2
05230647-6944394	235.8	0.2
05230776-6946082	278.2	0.4
05230867-6956329	265.5	0.2
05231074-6939184	202.3	0.2
05231091-6942374	251.7	0.3
05231221-6938166	280.7	0.2
05231315-6945212	283.5	0.2
05231321-6946382	270.6	0.2
05231411-6948546	309.7	0.2
05231484-6950196	266.7	0.2
05231562-6955430	311.9	0.2
05231631-6942507	281.4	0.2
05231634-6951332	260.1	0.2
05231962-6943309	260.2	0.2
05232020-6954561	223.5	0.2
05232148-6952155	287.6	0.2
05232181-6945429	277.5	0.2
05232554-6943388	227.2	0.2
05232624-6943558	221.3	0.2
05232680-6953109	268.0	0.2
05232845-6944158	275.8	0.2
05232892-6947486	265.0	0.2
05233236-6948257	224.2	0.2
05235653-6947387	244.1	0.2
05235851-6945519	286.7	0.2
05240317-6953036	265.3	0.2
05240482-6948280	228.1	0.3
05240604-6942380	257.0	0.2
05240613-6953529	216.4	0.2
05240672-6947130	280.4	0.2
05240803-6956250	230.1	0.2
05240830-6944428	282.7	0.2
05241033-6944374	292.3	0.2
05241341-6945303	249.1	0.2
05241479-6946323	263.1	0.2
05241699-6942158	251.6	0.2
05241794-6951317	276.9	0.2
05242161-6942097	259.8	0.2
05242198-6943579	250.4	0.3
05242240-6944344	230.4	0.2
05242409-6942051	258.9	0.2
05242542-6955188	244.2	0.2
05242687-6943577	264.0	0.2
05242702-6956445	243.6	0.2
05242811-6947467	287.0	0.2
05243272-6955362	273.8	0.2
05243734-6945496	241.8	0.2
05243901-6948426	257.9	0.2
05244189-6954427	241.6	0.2
05244210-6942596	267.5	0.2
05244301-6943412	300.2	0.3
05244340-6950004	295.1	0.2
05244408-6942423	302.8	0.2
05244600-6946017	224.6	0.2
05244637-6947340	257.6	0.2
05244698-6956141	231.7	0.2
05244878-6948359	236.1	0.2
05244976-6943230	272.1	0.2
05245212-6948184	272.8	0.2
05245859-6952257	196.8	0.2
05252428-6939311	261.9	0.2
05252899-6939078	255.0	0.2
05253039-6940288	272.9	0.2
05253040-6936261	288.0	0.2
05253235-6943137	277.4	0.2
05253522-6937078	284.4	0.2
05254540-6940531	284.5	0.3
05254864-6940501	248.2	0.2
05255000-6942466	244.1	0.2
05255267-6943155	270.5	0.2
05255625-6941243	287.4	0.2
05255801-6937309	257.2	0.2
05255812-6942522	250.1	0.2
05260124-6939268	289.7	0.2
05260720-6942342	291.6	0.2
05260784-6938341	241.4	0.2
05261339-6940590	270.1	0.2

Table 2.11: HR11, HR13, HR14 and final radial velocities of LMC bar stars. For each setups: mean radial velocity, 1-σ error $\sigma\,(v_{\rm rad})$. Last two columns give the final mean $v_{\rm rad}$ and its error $e_{\rm rad}$.

ID	HR11		HR13		HR14		Average	
	$v_{\rm rad}$ km s^{-1}	$\sigma\,(v_{\rm rad})$ km s^{-1}	$v_{\rm rad}$ km s^{-1}	$\sigma\,(v_{\rm rad})$ km s^{-1}	$v_{\rm rad}$ km s^{-1}	$\sigma\,(v_{\rm rad})$	$v_{\rm rad}$ km s^{-1}	$e_{\rm rad}$ km s^{-1}
0499-LMCDisc01	222.2	0.6	221.3	0.6	221.1	0.6	221.5	0.3
0512-LMCDisc01	249.0	0.6	248.4	0.6	248.7	0.6	248.7	0.3
0522-LMCDisc01	272.5	0.6	272.2	0.6	271.9	0.6	272.2	0.3
0533-LMCDisc01	244.8	0.6	245.6	0.6	245.5	0.6	245.3	0.3
0534-LMCDisc01	247.3	0.6	247.2	0.6	247.5	0.6	247.3	0.3
0546-LMCDisc01	262.0	0.6	261.6	0.6	261.4	0.6	261.7	0.3
0548-LMCDisc01	248.7	0.6	248.8	0.6	248.6	0.6	248.7	0.3
0564-LMCDisc01	190.4	0.6	191.3	0.6	190.1	0.6	190.6	0.3
0565-LMCDisc01	243.1	0.6	243.5	0.6	243.5	0.6	243.4	0.3
0576-LMCDisc01	307.6	0.6	306.8	0.6	307.0	0.6	307.1	0.3
0593-LMCDisc01	236.8	0.6	235.8	0.6	236.0	0.6	236.2	0.3
0599-LMCDisc01	242.8	0.6	242.6	0.6	242.4	0.6	242.6	0.3
0601-LMCDisc01	243.8	0.6	244.0	0.6	243.6	0.6	243.8	0.3
0606-LMCDisc01	184.3	0.6	184.5	0.6	183.9	0.6	184.2	0.3
0611-LMCDisc01	245.9	0.6	245.5	0.6	245.5	0.6	245.6	0.3
0614-LMCDisc01†	NaN	NaN	243.7	0.6	242.7	0.6	243.2	0.4
0620-LMCDisc01	198.5	0.6	198.7	0.6	198.0	0.6	198.4	0.3
0625-LMCDisc01	243.6	0.6	244.5	0.6	244.2	0.6	244.1	0.3
0629-LMCDisc01	191.1	0.6	189.8	0.6	190.0	0.6	190.3	0.3
0631-LMCDisc01	257.8	0.6	257.5	0.6	257.3	0.6	257.5	0.3
0633-LMCDisc01	196.4	0.6	195.5	0.6	196.0	0.6	196.0	0.3
0640-LMCDisc01	221.1	0.6	220.9	0.6	220.8	0.6	220.9	0.3
0646-LMCDisc01	238.2	0.6	237.6	0.6	238.1	0.6	238.0	0.3
0651-LMCDisc01	248.8	0.6	248.2	0.6	248.0	0.6	248.3	0.3
0655-LMCDisc01	228.4	0.6	227.0	0.6	227.4	0.6	227.6	0.3
0656-LMCDisc01	235.7	0.6	235.4	0.6	235.2	0.6	235.4	0.3
0658-LMCDisc01†	NaN	NaN	232.9	0.6	232.7	0.6	232.8	0.4
0664-LMCDisc01	252.4	0.6	252.6	0.6	252.3	0.6	252.4	0.3
0666-LMCDisc01	226.7	0.6	227.4	0.6	227.1	0.6	227.1	0.3
0671-LMCDisc01	250.6	0.6	249.1	0.6	250.4	0.6	250.0	0.3
0672-LMCDisc01	253.7	0.6	253.5	0.6	252.9	0.6	253.4	0.3
0679-LMCDisc01	254.7	0.6	254.5	0.6	254.3	0.6	254.5	0.3
0690-LMCDisc01	298.8	0.6	297.3	0.6	297.2	0.6	297.8	0.3
0699-LMCDisc01	232.7	0.6	231.5	0.6	232.2	0.6	232.1	0.3
0700-LMCDisc01	284.4	0.6	284.1	0.6	284.1	0.6	284.2	0.3
0701-LMCDisc01	259.0	0.6	259.1	0.6	259.0	0.6	259.0	0.3
0705-LMCDisc01	252.4	0.6	251.9	0.6	252.1	0.6	252.1	0.3
0706-LMCDisc01	217.3	0.6	217.5	0.6	217.0	0.6	217.3	0.3
0710-LMCDisc01	268.0	0.6	266.5	0.6	266.1	0.6	266.9	0.3
0720-LMCDisc01	202.3	0.6	202.7	0.6	202.2	0.6	202.4	0.3
0721-LMCDisc01	253.3	0.6	252.7	0.6	252.8	0.6	252.9	0.3
0728-LMCDisc01	272.1	0.6	271.5	0.6	271.0	0.6	271.5	0.3
0731-LMCDisc01	279.5	0.6	278.7	0.6	279.5	0.6	279.2	0.3
0748-LMCDisc01	225.6	0.6	225.3	0.6	225.1	0.6	225.3	0.3
0752-LMCDisc01	227.2	0.6	227.6	0.6	227.0	0.6	227.3	0.3
0756-LMCDisc01	256.1	0.6	255.9	0.6	256.0	0.6	256.0	0.3
0758-LMCDisc01†	NaN	NaN	258.1	0.6	258.0	0.6	258.1	0.4
0766-LMCDisc01	283.8	0.6	283.1	0.6	283.1	0.6	283.3	0.3
0773-LMCDisc01	234.3	0.6	234.7	0.6	233.9	0.6	234.3	0.3
0775-LMCDisc01	240.9	0.6	241.5	0.6	241.0	0.6	241.1	0.3
0776-LMCDisc01	241.8	0.6	240.7	0.6	240.5	0.6	241.0	0.3
0782-LMCDisc01	249.5	0.6	248.3	0.6	249.0	0.6	248.9	0.3
0789-LMCDisc01	245.6	0.6	244.5	0.6	245.1	0.6	245.1	0.3
0790-LMCDisc01	245.6	0.6	246.5	0.6	246.2	0.6	246.1	0.3
0793-LMCDisc01	241.4	0.6	241.1	0.6	240.8	0.6	241.1	0.3
0808-LMCDisc01	196.8	0.6	195.6	0.6	196.2	0.6	196.2	0.3
0834-LMCDisc01	197.1	0.6	196.9	0.6	196.9	0.6	197.0	0.3
0835-LMCDisc01	260.9	0.6	260.7	0.6	260.1	0.6	260.6	0.3
0854-LMCDisc01	313.3	0.6	312.2	0.6	312.9	0.6	312.8	0.3
0855-LMCDisc01	217.5	0.6	217.4	0.6	217.4	0.6	217.4	0.3
0859-LMCDisc01	245.0	0.6	248.9	0.6	248.6	0.6	247.5	0.3
0879-LMCDisc01	253.1	0.6	251.2	0.6	252.1	0.6	252.1	0.3
0900-LMCDisc01	276.0	0.6	275.5	0.6	275.6	0.6	275.7	0.3
0937-LMCDisc01	264.0	0.6	263.2	0.6	263.5	0.6	263.6	0.3
1055-LMCDisc01	177.8	0.6	179.3	0.6	179.6	0.6	178.9	0.3
1105-LMCDisc01	245.1	0.6	245.0	0.6	245.0	0.6	245.0	0.3
1118-LMCDisc01	210.0	0.6	210.1	0.6	210.0	0.6	210.0	0.3

† Not observed in HR11.

Table 2.12: Median S/N ratio S/N and quality flags for LMC bar stars.

2MASS ID	HR11		HR13		HR14	
	S/N	Quality	S/N	Quality	S/N	Quality
05223082-6944147	28.7	median	38.9	median	50.6	median
05223112-6945292	32.8	median	48.8	median	59.6	median
05223186-6947159	25.0	median	36.8	median	43.6	median
05223309-6946595	35.1	high	45.0	median	51.0	median
05223316-6951389	19.3	median	27.6	median	38.0	median
05223318-6937044	20.8	median	29.6	median	32.5	low
05223416-6944433	28.0	median	45.2	median	50.7	median
05223487-6938057	22.9	median	31.5	median	30.0	low
05223506-6937279	25.2	median	37.3	median	40.5	median
05223557-6943373	24.8	median	39.0	median	42.5	median
05223701-6936166	30.5	median	42.7	median	44.9	median
05223787-6954562	16.6	low	26.6	low	40.6	median
05223895-6945007	36.5	high	51.1	high	59.3	median
05223988-6946110	31.8	median	45.4	median	54.5	median
05224062-6953310	25.3	median	30.1	median	38.2	median
05224164-6935518	15.6	low	30.6	median	35.5	median
05224195-6941099	27.4	median	40.7	median	47.8	median
05224240-6940567	34.0	high	46.9	median	51.9	median
05224276-6940109	33.6	high	50.1	median	54.1	median
05224309-6940275	27.7	median	38.5	median	41.4	median
05224321-6952397	22.4	median	33.1	median	41.3	median
05224448-6954402	20.0	median	22.1	low	26.2	low
05224854-6940010	16.1	low	28.0	median	31.2	low
05225062-6936580	23.5	median	39.9	median	46.1	median
05225069-6955486	17.4	median	20.9	low	29.5	low
05225632-6942269	29.9	median	43.1	median	45.1	median
05225877-6938172	18.8	median	28.2	median	32.1	low
05225980-6954368	13.2	low	18.0	low	25.2	low
05230009-6935251	24.0	median	39.3	median	42.8	median
05230011-6946353	25.6	median	35.7	median	45.6	median
05230203-6935557	22.0	median	32.2	median	36.6	median
05230230-6939587	27.8	median	44.2	median	50.3	median
05230353-6952441	27.2	median	41.8	median	49.4	median
05230370-6944219	23.8	median	41.1	median	48.4	median
05230589-6944122	40.9	high	59.6	high	66.6	high
05230606-6951113	24.1	median	40.1	median	52.6	median
05230647-6944394	25.6	median	41.2	median	48.8	median
05230776-6946082	35.8	high	54.7	high	59.0	median
05230867-6956329	10.0	low	13.6	low	21.3	low
05231074-6939184	30.0	median	47.4	median	48.4	median
05231091-6942374	35.9	high	54.8	high	63.6	high
05231221-6938166	27.5	median	48.9	median	55.0	median
05231315-6945212	15.3	low	31.6	median	44.2	median
05231321-6946382	29.3	median	51.3	high	56.4	median
05231411-6948546	26.1	median	48.1	median	58.6	median
05231484-6950196	26.1	median	39.6	median	45.4	median
05231562-6955430	24.8	median	38.8	median	52.0	median
05231631-6942507	24.4	median	50.5	median	57.8	median
05231634-6951332	22.2	median	39.6	median	48.0	median
05231962-6943309	24.9	median	41.4	median	53.4	median
05232020-6954561	36.5	high	47.3	median	63.9	high
05232148-6952155	29.6	median	48.9	median	59.4	median
05232181-6945429	27.6	median	46.3	median	53.9	median
05232554-6943388	27.2	median	45.8	median	51.2	median
05232624-6943558	26.9	median	45.2	median	50.9	median
05232680-6953109	29.8	median	45.6	median	51.6	median
05232845-6944158	33.2	high	55.5	high	65.8	high
05232892-6947486	25.7	median	44.0	median	53.8	median
05233236-6948257	18.7	median	33.1	median	34.6	low
05235653-6947387	31.5	median	49.0	median	48.4	median
05235851-6945519	30.9	median	52.3	high	58.6	median
05240317-6953036	21.1	median	31.0	median	40.8	median
05240482-6948280	23.5	median	38.8	median	44.3	median
05240604-6942380	16.9	low	32.8	median	39.4	median
05240613-6953529	24.9	median	33.9	median	42.6	median
05240672-6947130	19.8	median	35.9	median	44.9	median
05240803-6956250	22.9	median	26.7	low	36.5	median
05240830-6944428	33.1	high	55.5	high	64.8	high
05241033-6944374	25.2	median	46.3	median	55.0	median
05241341-6945303	26.6	median	46.5	median	59.3	median
05241479-6946323	35.2	high	51.9	high	61.5	high
05241699-6942158	26.5	median	46.6	median	55.4	median
05241794-6951317	19.1	median	31.1	median	40.2	median
05242161-6942097	27.7	median	48.2	median	56.5	median
05242198-6943579	16.2	low	33.6	median	63.5	high
05242240-6944344	31.0	median	52.7	high	60.7	median
05242409-6942051	30.2	median	51.5	high	62.4	high
05242542-6955188	26.3	median	35.4	median	46.6	median
05242687-6943577	41.9	high	61.6	high	67.0	high
05242702-6956445	15.7	low	23.3	low	31.1	low
05242811-6947467	27.9	median	46.1	median	47.7	median
05243272-6955362	27.6	median	36.7	median	49.6	median
05243734-6945496	21.4	median	36.3	median	42.6	median

Continued on next page

2MASS ID	HR11		HR13		HR14	
	S/N	Quality	S/N	Quality	S/N	Quality
05243901-6948426	29.5	median	46.0	median	62.7	high
05244189-6954427	19.2	median	25.0	low	36.6	median
05244210-6942596	13.6	low	28.1	median	36.6	median
05244301-6943412	37.1	high	59.6	high	73.6	high
05244340-6950004	20.2	median	33.8	median	41.1	median
05244408-6942423	26.0	median	46.8	median	55.7	median
05244600-6946017	22.8	median	37.2	median	46.3	median
05244637-6947340	27.5	median	42.5	median	53.3	median
05244698-6956141	19.2	median	24.6	low	35.1	median
05244878-6948359	33.2	high	49.1	median	59.8	median
05244976-6943230	30.2	median	53.0	high	63.5	high
05245212-6948184	26.0	median	40.5	median	48.4	median
05245859-6952257	19.7	median	30.9	median	37.7	median
05252428-6939311	22.7	median	41.3	median	54.1	median
05252899-6939078	20.4	median	33.5	median	46.3	median
05253039-6940288	20.4	median	39.8	median	47.6	median
05253040-6936261	23.0	median	33.7	median	43.4	median
05253235-6943137	21.7	median	39.4	median	44.6	median
05253522-6937078	26.4	median	31.8	median	43.9	median
05254540-6940531	20.7	median	31.1	median	41.5	median
05254864-6940501	21.9	median	40.2	median	51.3	median
05255000-6942466	28.7	median	42.5	median	55.9	median
05255267-6943155	27.7	median	46.7	median	60.8	median
05255625-6941243	30.5	median	41.9	median	51.2	median
05255801-6937309	22.9	median	32.4	median	45.1	median
05255812-6942522	21.2	median	26.8	low	35.8	median
05260124-6939268	23.4	median	34.2	median	46.2	median
05260720-6942342	17.4	median	24.1	low	33.4	low
05260784-6938341	20.3	median	30.6	median	40.4	median
05261339-6940590	24.7	median	38.6	median	54.2	median

Table 2.13: Calibrated S/N ratio S/N and quality flags for LMC inner disc stars.

ID	HR11		HR13		HR14	
	S/N	Quality	S/N	Quality	S/N	Quality
0499-LMCDisc01	41.0	high	47.0	median	32.0	low
0512-LMCDisc01	24.0	median	38.0	median	36.0	median
0522-LMCDisc01	31.0	median	36.0	median	35.0	median
0533-LMCDisc01	23.0	median	32.0	median	28.0	low
0534-LMCDisc01	46.0	high	51.0	high	37.0	median
0546-LMCDisc01	32.0	median	42.0	median	36.0	median
0548-LMCDisc01	29.0	median	40.0	median	37.0	median
0564-LMCDisc01	22.0	median	18.0	low	15.0	low
0565-LMCDisc01	33.0	high	40.0	median	45.0	median
0576-LMCDisc01	35.0	high	55.0	high	37.0	median
0593-LMCDisc01	27.0	median	32.0	median	25.0	low
0599-LMCDisc01	50.0	high	40.0	median	29.0	low
0601-LMCDisc01	19.0	median	29.0	median	29.0	low
0606-LMCDisc01	26.0	median	33.0	median	26.0	low
0611-LMCDisc01	29.0	median	39.0	median	42.0	median
0614-LMCDisc01	nan	median	17.0	low	15.0	low
0620-LMCDisc01	14.0	low	14.0	low	13.0	low
0625-LMCDisc01	24.0	median	36.0	median	31.0	low
0629-LMCDisc01	33.0	high	34.0	median	36.0	median
0631-LMCDisc01	26.0	median	22.0	low	18.0	low
0633-LMCDisc01	24.0	median	38.0	median	31.0	low
0640-LMCDisc01	27.0	median	21.0	low	21.0	low
0646-LMCDisc01	19.0	median	17.0	low	21.0	low
0651-LMCDisc01	26.0	median	35.0	median	27.0	low
0655-LMCDisc01	26.0	median	37.0	median	28.0	low
0656-LMCDisc01	33.0	high	42.0	median	35.0	median
0658-LMCDisc01	nan	median	15.0	low	12.0	low
0664-LMCDisc01	35.0	high	28.0	median	31.0	low
0666-LMCDisc01	22.0	median	20.0	low	19.0	low
0671-LMCDisc01	25.0	median	20.0	low	28.0	low
0672-LMCDisc01	28.0	median	27.0	median	27.0	low
0679-LMCDisc01	30.0	median	33.0	median	39.0	median
0690-LMCDisc01	25.0	median	22.0	low	27.0	low
0699-LMCDisc01	39.0	high	43.0	median	28.0	low
0700-LMCDisc01	12.0	low	15.0	low	16.0	low
0701-LMCDisc01	22.0	median	19.0	low	20.0	low
0705-LMCDisc01	32.0	median	36.0	median	43.0	median
0706-LMCDisc01	21.0	median	19.0	low	21.0	low
0710-LMCDisc01	31.0	median	31.0	median	29.0	low
0720-LMCDisc01	18.0	median	15.0	low	10.0	low
0721-LMCDisc01	24.0	median	22.0	low	24.0	low
0728-LMCDisc01	27.0	median	32.0	median	20.0	low
0731-LMCDisc01	17.0	median	19.0	low	28.0	low
0748-LMCDisc01	17.0	median	10.0	low	18.0	low
0752-LMCDisc01	30.0	median	32.0	median	39.0	median
0756-LMCDisc01	31.0	median	31.0	median	27.0	low
0758-LMCDisc01	nan	median	9.0	low	12.0	low
0766-LMCDisc01	13.0	low	14.0	low	16.0	low
0773-LMCDisc01	29.0	median	27.0	median	24.0	low
0775-LMCDisc01	32.0	median	38.0	median	32.0	low
0776-LMCDisc01	32.0	median	37.0	median	34.0	low
0782-LMCDisc01	20.0	median	19.0	low	20.0	low
0789-LMCDisc01	25.0	median	21.0	low	27.0	low
0790-LMCDisc01	28.0	median	26.0	low	34.0	low
0793-LMCDisc01	38.0	high	26.0	low	16.0	low
0808-LMCDisc01	45.0	high	39.0	median	27.0	low
0834-LMCDisc01	23.0	median	31.0	median	30.0	low
0835-LMCDisc01	18.0	median	12.0	low	17.0	low
0854-LMCDisc01	22.0	median	19.0	low	35.0	median
0855-LMCDisc01	23.0	median	18.0	low	20.0	low
0859-LMCDisc01	27.0	median	31.0	median	31.0	low
0879-LMCDisc01	11.0	low	13.0	low	17.0	low
0900-LMCDisc01	24.0	median	23.0	low	29.0	low
0937-LMCDisc01	23.0	median	18.0	low	20.0	low
1055-LMCDisc01	31.0	median	29.0	median	23.0	low
1105-LMCDisc01	21.0	median	27.0	median	16.0	low
1118-LMCDisc01	21.0	median	22.0	low	18.0	low

Chapter 3

Stellar parameters determination

Contents

3.1 Introduction

The energy generated by nuclear reactions in the central parts of stars is transported towards the outer layers via radiative transfer (photon diffusion), thermal conduction (electron diffusion) or convection (macroscopic movements of cells of matter). The prevalent mechanism of heat transport varies across the stellar radius (e.g., a solar-like star has a radiative zone around the core, followed by a convective zone) and during the star lifetime (e.g., a solar-like star has a fully-convective envelop when it enters the giant phase). Due to the density of absorbers n (free electrons, atoms) and their cross-section σ_ν, the photon mean free path $l_{\text{photon}} = (n\sigma_\nu)^{-1}$ is extremely small compared to the star diameter (e.g., of the order of 1 cm in

the Sun) in stellar interiors: photons are frequently absorbed or scattered in the plasma and do not escape stars easily. However, l_{photon} increases with increasing radius, and at a certain point, becomes large enough for a photon to escape the star (i.e., l_{photon} becomes comparable to the scale height of the uppermost layer of gas): the star becomes transparent to radiation. This particular region of a star is called the photosphere[1] and is the deepest layer of a stellar atmosphere (above the photosphere, one finds the chromosphere and the corona). Most of ultraviolet, visible and infrared radiations originate in the stellar photosphere and looking at such spectra inform us on the physical conditions and the chemical composition of this layer.

For our purposes, i.e. the chemical tagging of stellar populations of the Large Magellanic Cloud (LMC), absorption lines that populate stellar spectra will be particularly useful since they are the access door to the detailed chemical composition of the photosphere: their presence and their shape tell us about how much of an element is in the stellar photosphere. But to correctly interpret the absorption lines in terms of elemental abundances, one must be able to model the photosphere, i.e. to know the temperature and (gas and electronic) pressure stratification as a function of the depth (most usefully the optical depth). To achieve this, we have to determine a number of physical parameters, called in the following *stellar* or *fundamental parameters*. Four parameters are needed: temperature T_{eff}, surface gravity $\log g$, overall (or global) metallicity [M/H] and microturbulence velocity ξ_{micro}. We adopted an iterative procedure, described in the following sections, to derive the stellar parameters of our LMC bar stars.

3.2 Effective temperature

3.2.1 Definition

The effective temperature T_{eff} of a star is the temperature of a black body which would have the same (absolute) bolometric flux $F_{\text{bb}}^{\text{bol}}$ as the star $F_{\star}^{\text{bol}}$:

$$\begin{aligned} \pi F_{\star}^{\text{bol}} &= \pi F_{\text{bb}}^{\text{bol}} \\ &= \pi \int_0^{+\infty} \frac{2h\nu^3}{c^2} \frac{1}{\mathrm{e}^{\frac{h\nu}{kT_{\text{eff}}}} - 1} \,\mathrm{d}\nu \\ &= \sigma T_{\text{eff}}^4 \end{aligned} \tag{3.1}$$

where σ is the Stefan–Boltzmann constant. A temperature gradient (decreasing outwards) exists within a stellar atmosphere and the effective temperature can be understood as the typical temperature of the layer where the radiation comes from.

The effective temperature is the stellar parameter showing the strongest effect on the atmosphere structure and must therefore be carefully determined. In principle, if we were to measure the apparent bolometric flux $f_{\star}^{\text{bol}}$ and the angular radius $\alpha = R_{\star}/d$ of a star, we could compute T_{eff} since:

$$f_{\star}^{\text{bol}} = \alpha^2 \sigma T_{\text{eff}}^4 \quad \text{(energy conservation)} \tag{3.2}$$

[1] In the following, we will use the terms “atmosphere” and “photosphere” interchangeably.

This method requires both to measure the apparent bolometric flux, which means measuring the energy distribution over the full spectral range and being able to correct for interstellar absorption (if needed), and to measure the stellar radius, which is a complicated task and applied to a few number of (relatively close) stars (interferometry, occultation, binary systems). Although this method is the less model-dependent one, we see the double difficulty to use it. Therefore, other techniques have been developed and some of them will be briefly reviewed in Section 3.2.2.

3.2.2 How to determine effective temperature?

In the following, I present standard methods used to determine an estimate of the effective temperature of a star. These methods can be spectroscopic, i.e. they rely on the study of spectral features (see § "Balmer lines", "Paschen continuum", "Excitation temperature"), or photometric, i.e. they rely on colour indices or more generally, on the relative flux of the stellar continuum at different wavelength (see § "IRFM", "Synthetic colour–temperature calibrations", "Empirical colour–temperature calibrations").

Balmer lines In optical spectra, hydrogen absorption lines of the Balmer series (Hα at 6563 Å; Hβ at 4861 Å; Hγ at 4341 Å; Hδ at 4102 Å) can be used to determine the effective temperature in cool[2] F–G stars (Fuhrmann et al., 1993, 1994; Gehren et al., 2004, 2006; Posbic et al., 2012; van't Veer-Menneret & Megessier, 1996). Hydrogen lines exhibit extended wings, formed in deep layers of the photosphere under local thermodynamic equilibrium (LTE) and whose profile depends strongly on temperature and weakly on gravity and hydrogen or metal abundances. The method is independent of the interstellar reddening, and consists in fitting the wings of these hydrogen lines using a grid of model atmosphere and a code of spectrum synthesis. The success of this method relies on the correct modelling of the broadening (Stark broadening and collisions) and convection (which affects the line formation in deep atmosphere layers; Barklem et al., 2002; Cayrel et al., 2011; Fuhrmann et al., 1993). As the gravity is lower in atmosphere of giant stars than in atmosphere of main-sequence stars, densities are smaller and collisions are less frequent; as a result, the broadening of Balmer lines is weaker and this technique is difficult to use in K giant stars.

Paschen continuum In the wavelength range [4000 Å, 7000 Å], the hydrogen absorption coefficient is dominated by the Paschen continuum, i.e. the bound–free absorption of the hydrogen atom from $n = 3$. The Paschen continuum is very temperature sensitive (weakly affected by the absorption lines in the wavelength domain, weakly affected by non-LTE effects) and is similar to that of black body. Therefore, it can be used as a temperature indicator. The principle of the method is to measure the slope of the Paschen continuum

$$p = \log\left(\frac{F_\star(\lambda = 4000)}{F_\star(\lambda = 7000)}\right) \tag{3.3}$$

[2]Since Balmer lines become gravity sensitive in hot stars, the Balmer discontinuity at 3647 Å is the temperature proxy used for such stars.

and then find the temperature of the black body producing the same slope p. The drawback is that one needs to measure accurately relative fluxes in two widely different wavelength bands. Because of the high number of absorption lines in spectra of cool stars, the slope of the continuum is difficult to measure, and therefore, this technique is unusable for our LMC cool giants.

Excitation (or spectroscopic) temperature Under LTE (i.e. when collisions are the dominant process responsible for the population of energy levels), in a gas of temperature T, the number $n_{r,i}$ of atoms in the ionised stage r and the energy level i and the number $n_{r,j}$ of atoms in the ionised stage r and the energy level j are related through the Boltzmann equation:

$$\frac{n_{r,j}}{n_{r,i}} = \frac{g_{r,j}}{g_{r,i}} \mathrm{e}^{-\frac{\chi_{r,j}-\chi_{r,i}}{k_\mathrm{B}T}} \tag{3.4}$$

where $\chi_{r,i}$ (resp. $\chi_{r,j}$) is the energy of the level i (resp. j) relatively to the fundamental level ($\chi_{r,1} = 0$); $g_{r,i}$ (resp. $g_{r,j}$) is the degeneracy of the level i (resp. j), i.e. the number of quantum state with the same energy level; k_B is the Boltzmann constant. The Boltzmann equation is often rewritten considering the total population n_ion of a given ion:

$$\frac{n_{r,i}}{n_\mathrm{ion}} = \frac{g_{r,i}}{U_\mathrm{ion}(T)} \mathrm{e}^{-\frac{\chi_{r,i}}{k_\mathrm{B}T}} \quad \text{with} \quad U_\mathrm{ion}(T) = \sum_{l=1}^{+\infty} g_{r,l} \mathrm{e}^{-\frac{\chi_{r,l}}{k_\mathrm{B}T}} \tag{3.5}$$

where $U_\mathrm{ion}(T)$ is the ion partition function.

The Boltzmann equation tells us that the population of energy levels depends on temperature at the first order. Therefore, it is possible to use absorption lines of a given species corresponding to different excitation potentials ($\chi_{ex} = \chi_{r,j} - \chi_{r,1} = \chi_{r,j}$) to determine the temperature of the stellar photosphere. Usually, Fe I (or Ca I) absorption lines are used since they are abundant in stellar spectra (a few tens per 100 Å) and often easily measurable. The technique consists in varying the temperature of the atmosphere model and requiring that, in the mean, lines of different χ_{ex} give the same Fe I abundance, i.e. the slope of ([Fe I/H]$|\chi_{ex}$) is null. If the tested temperature is lower than the true temperature, then high (resp. low) energy levels will be less (resp. more) populated than reality and therefore the derived abundance for a given line strength will be higher (resp. lower) than reality, resulting in a positive slope. And reciprocally if the tested temperature is greater than the true temperature. Generally, this is an iterative procedure: at each iteration, T is incremented and the slope of ([Fe I/H]$|\chi_{ex}$) is computed by linear regression; the smallest slope (in absolute value) gives the excitation temperature. As the line strength depends also on the element abundance (which is not known *a priori*), the iteration is made on both T and [Fe I/H] and has also to include a convergence criterion for [Fe I/H]. This model-dependent (model atmosphere, spectrum synthesis) method is often used since it is easily implemented (e.g., Lecureur et al., 2007), quick (possibility to use EW), reddening-free and relatively accurate if enough high-quality Fe I lines are available (role of wavelength coverage, resolution and S/N ratio).

Infrared flux method Blackwell & Shallis (1977); Blackwell et al. (1979) introduced the InfraRed Flux Method (IRFM) to derive simultaneously the angular diameter θ and the effective temperature $T_{\rm eff}$ of a star. The method uses the bolometric flux $f_\star^{\rm bol}$ (arriving on Earth) and a monochromatic flux measured (on Earth) in the infrared $f_{\lambda\star}$ and to find the pair $(\theta, T_{\rm eff})$ satisfying the system:

$$\begin{cases} f_\star^{\rm bol} = \dfrac{\theta^2}{4}\sigma T_{\rm eff}^4 \\ f_{\lambda\star} = \dfrac{\theta^2}{4}\phi\left(\lambda, T_{\rm eff}, \log g, [{\rm Fe/H}]\right) \end{cases} \tag{3.6}$$

where $\phi\left(\lambda, T_{\rm eff}, \log g, [{\rm Fe/H}]\right)$ is the monochromatic flux predicted by the model atmosphere and radiative transfer theory (which is less temperature sensitive in the infrared, compared to the integrated flux). Blackwell et al. (1980) altered the method to get rid of the angular diameter by defining the ratios $R_{\rm obs}$ and $R_{\rm theo}$:

$$\begin{cases} R_{\rm obs} = \dfrac{f_\star^{\rm bol}}{f_{\lambda\star}} \\ R_{\rm theo} = \dfrac{\sigma T_{\rm eff}^4}{\phi\left(\lambda, T_{\rm eff}, \log g, [{\rm Fe/H}]\right)} \end{cases} \tag{3.7}$$

The aim is now to equate $R_{\rm obs}$ which is semi-empirical (e.g., needs of bolometric calibrations) and $R_{\rm theo}$ which relies on atmosphere modelling and spectrum synthesis (see Alonso et al., 1994a, for a detailed discussion). We see that the second equation of the system depends on $\log g$ and [Fe/H]. Those two parameters must be obtained separately: for the surface gravity, a rough classification (separation in dwarf, sub-dwarf, giant stars) is enough while the metallicity seems to have a greater role and have to be carefully taken into account ([Fe/H] can be derived photometrically or spectroscopically) (see Casagrande et al., 2010, for a comparison of photometric scales). The results differ according to the colour bands and in general, several infrared colour indices are used and the different temperature estimates are averaged. The temperature derived with IRFM are accurate (Ramírez & Meléndez, 2005a claim a mean uncertainty of 60 K for giant stars) but it is worth noticing that the dereddening of the photometry can become one of the main source of uncertainty. Examples of use of the IRFM method can be found for dwarf (Alonso et al., 1996a; Casagrande et al., 2006; Ramírez & Meléndez, 2005a) and giant stars (Alonso et al., 1999a; Ramírez & Meléndez, 2005a).

Synthetic colour–temperature calibrations This method is heavily model-dependent since the aim is to compute synthetic colour indices from synthetic spectra. For a given set of fundamental parameters, the corresponding atmosphere model is computed and used for the spectrum synthesis (Bessell et al., 1998; Houdashelt et al., 2000). The theoretical spectrum is then convolved with the filter transmission function and colour indices are determined. Well-known stars of the solar vicinity with direct temperature determination (i.e. for which the angular diameter is known) are used to found the zero-point of synthetic colour–temperature calibrations; but, rigorously speaking, it allows correction for a given metallicity and

may not hold true for other metallicities. The huge advantage of this method is the possibility to explore the whole parameter space ($T_{\rm eff}$, $\log g$, [M/H]) and to have calibrations for any colour system which is harshly possible with real data and empirical colour–temperature calibrations (see § "Empirical colour–temperature calibrations") but the cost is a more model-dependent calibration (model atmosphere, spectrum synthesis, opacities computation, atomic and molecular data).

Empirical colour–temperature calibrations Instead of synthetic colour–temperature calibrations, it is possible to derive empirical colour–temperature calibrations if accurate effective temperatures are already available for a (relatively) large set of stars. The aim is to use the results of (observationally or computationally) expensive methods (e.g., direct determination or IRFM) applied to a finite sample to build simple relations requiring less input data and applicable to any star. It allows to form less model-dependent temperature scales compared to synthetic colour–temperature calibrations but requires that calibrating stars correctly sample the parameter space ($T_{\rm eff}$, $\log g$, [M/H]). As said, effects of metallicity have to be taken into account and therefore, the method consists in adjusting coefficients of an analytical function (polynomial, rational fraction) in the space $(X, [{\rm Fe/H}], T_{\rm eff})$ where X is a colour index. A little drawback is that such relations are valid for a given photometric system, though it could be circumvented by using conversion relations (e.g. Alonso et al., 1994b; Bessell, 2005; Bessell & Brett, 1988), with the risk to introduce small systematic effects. When the colour indices have to be corrected for interstellar extinction, the reddening can dominate the uncertainty on the derived temperature. Examples of empirical colour–temperature calibrations can be found for dwarf (Alonso et al., 1996b; Casagrande et al., 2006; Ramírez & Meléndez, 2005b) and giant stars (Alonso et al., 1999b; Ramírez & Meléndez, 2005b). Since random errors on photometric temperatures (see § "Error budget" in Sec. 3.2.3) were smaller than random errors on spectroscopic temperatures ($\sim 200\,{\rm K}$) and since there is no systematic difference between the two scales, we decided to use photometric calibrations from Ramírez & Meléndez (2005b) to determine the effective temperature of our LMC bar stars and a detailed discussion is provided in Section 3.2.3.

3.2.3 Photometric temperature of our LMC stars

Principle Ramírez & Meléndez (2005b) have derived empirical metallicity–colour–temperature calibrations for giant stars covering approximately the temperature range $[4000\,{\rm K}, 7000\,{\rm K}]$ and the metallicity range $[-3.5\,{\rm dex}, 0.4\,{\rm dex}]$. Their photometric calibrations are provided for 17 colour indices, in eight photometric systems and have the following form:

$$T_{\rm eff} = \frac{5040}{\theta_{\rm eff}\,(X, [{\rm Fe/H}])} + P_{[{\rm Fe/H}]}\,(X) \tag{3.8}$$

where

- $\theta_{\rm eff}\,(X, [{\rm Fe/H}])$ is a polynomial whose coefficients a_i change from one colour

Table 3.1: Reddening law.

$E(V)/E(B-V)$	$E(K)/E(B-V)$	$E(V-I)/E(B-V)$	$E(V-J)/E(B-V)$	$E(V-H)/E(B-V)$	$E(V-K)/E(B-V)$
3.24	0.367	1.30	2.16	2.51	2.70

Table 3.2: Mean difference between the four photometric scales (and standard deviation of the difference) for LMC bar stars.

	$T\left((V_J-J_{2M})_0\right)$ K	$T\left((V_J-H_{2M})_0\right)$ K	$T\left((V_J-K_{2M})_0\right)$ K
$T\left((V_J-I_C)_0\right)$	-40 ± 110	$-95\pm\ 80$	-90 ± 100
$T\left((V_J-J_{2M})_0\right)$	–	-50 ± 110	-50 ± 120
$T\left((V_J-H_{2M})_0\right)$	–	–	10 ± 100

band to another:

$$\theta_{\rm eff}\left(X,[{\rm Fe/H}]\right)=a_0+a_1X+a_2X^2+a_3X[{\rm Fe/H}]+a_4[{\rm Fe/H}]+a_5[{\rm Fe/H}]^2 \quad (3.9)$$

- $P_{[{\rm Fe/H}]}\left(X\right)$ is a polynomial needed to correct for residuals left after the fitting of $\theta_{\rm eff}\left(X,[{\rm Fe/H}]\right)$. For a given colour band, the polynomial coefficients b_i change from a metallicity bin to another:

$$P_{[{\rm Fe/H}]}\left(X\right)=\sum_{k=0}b_kX^k \quad (3.10)$$

The LMC bar sample For our LMC bar stars, visible (V_J and I_C magnitude, from the Optical Gravitational Lensing Experiment (OGLE) catalogue Szymanski, 2005; Udalski et al., 1997, 2000) and infrared (J_{2M}, H_{2M} and K_{2M} magnitude, from the 2MASS catalogue Skrutskie et al., 2006) photometry is available (Table 2.5). So it allows us to form four colour indices — (V_J-I_C), (V_J-J_{2M}), (V_J-H_{2M}) and (V_J-K_{2M}) — for which Ramírez & Meléndez (2005b) provide photometric calibrations, in our photometric systems (so no conversion of magnitude from one photometric system to another is needed). Assuming a reddening $E\left(B-V\right)=0.14$ mag (see Sec. 3.6) and using the reddening law given in Table 3.1, we computed four scales of photometric temperatures from the dereddened colour indices. For the first iteration of our procedure of stellar parameters determination, we used the Ca II triplet (CaT) metallicity index from Cole et al. (2005); from the second iteration on, the spectroscopically derived [Fe I/H] is injected in the photometric calibrations. Table 3.4 provides the final photometric temperatures (and the associated error) for each colour index and the final mean temperature. Figure 3.1 and Table 3.2 show that the agreement between the four photometric temperature scales is very good with a mean difference always smaller than 100 K (in absolute value), therefore we simply averaged the four estimates to form the quantity $T_{\rm phot}$:

$$T_{\rm phot}=\frac{1}{4}\left[T\left(V_J-I_C\right)+T\left(V_J-J_{2M}\right)+T\left(V_J-H_{2M}\right)+T\left(V_J-K_{2M}\right)\right] \quad (3.11)$$

For few stars, it was not possible to compute the four photometric temperatures when one (or more) magnitude was missing or when the colour index was out of the polynomial validity range (for each metallicity bin, $P_{[\mathrm{Fe/H}]}(X)$ is defined over a finite colour index range):

- when one (or more) magnitude was missing, we applied a correction to compensate for the missing photometric temperature. For instance, if $T(\mathrm{V_J} - \mathrm{H_{2M}})$ is missing while $T(\mathrm{V_J} - \mathrm{I_C})$ is available, we replaced $T(\mathrm{V_J} - \mathrm{H_{2M}})$ in Equation 3.11 by $T(\mathrm{V_J} - \mathrm{I_C}) + K_{\mathrm{VI,VH}}$; $K_{\mathrm{VI,VH}}$ was obtained by averaging the quantity $\Delta_{\mathrm{VI,VH}}T$ (using all stars whose photometric temperature is computable):

$$\Delta_{\mathrm{VI,VH}}T = T(\mathrm{V_J} - \mathrm{H_{2M}}) - T(\mathrm{V_J} - \mathrm{I_C}) \tag{3.12}$$

- when the colour index was out of the calibration validity range, instead of Equation 3.8, we used:

$$T'_{\mathrm{eff}} = \frac{5040}{\theta_{\mathrm{eff}}(X, [\mathrm{Fe/H}])} + K_{X,[\mathrm{Fe/H}]} \tag{3.13}$$

where $K_{[\mathrm{Fe/H}]}$ is an offset to compensate the missing polynomial term. For a given metallicity bin and a given colour index, $K_{X,[\mathrm{Fe/H}]}$ was obtained by averaging $\Delta_{X,[\mathrm{Fe/H}]}T$ (using all stars whose photometric temperature is computable):

$$\Delta_{X,[\mathrm{Fe/H}]}T = T_{\mathrm{eff}} - \frac{5040}{\theta_{\mathrm{eff}}(X, [\mathrm{Fe/H}])} \tag{3.14}$$

Thus, $K_{X,[\mathrm{Fe/H}]}$ is the mean effect of the polynomial term.

Error budget The photometric calibrations are subject to, at least, four sources of uncertainties: the dispersion σ_{calib} of the calibration relation itself, the uncertainty σ_{color} of the two magnitudes combined to form the colour index, the uncertainty $\sigma(E(\mathrm{B-V}))$ of the reddening $E(\mathrm{B-V})$, and the uncertainty $\sigma([\mathrm{Fe/H}])$ of the [Fe/H] ratio. The dispersion of the calibration relations can be taken from Ramírez & Meléndez (2005b) (their Table 3); they are smaller than 50 K and account for less than 20 K in the error on the final temperature (for the colour indices we used in this study). The errors on the magnitudes were taken from the OGLE and 2MASS catalogues. The typical error is of the order of 0.05 mag, and the error on the colour index translates in a typical error of ~ 35 K on the final mean T_{phot}. As explained above, we first used the CaT metallicity from Cole et al. (2005) as the initial estimator of the [Fe/H] ratio. Although the CaT metallicity is not a very precise estimator of [Fe/H] (mean error of ~ 0.20 dex), the calibrations are not very sensitive to this parameter (typical error of < 5 K on the final mean T_{phot}). For the reddening, we used $E(\mathrm{B-V}) = 0.14$ mag and a conservative relative error $\sigma(E(\mathrm{B-V})) = 0.07$ mag (see Sec. 3.6). It results in a typical error on the final mean T_{phot} of the order of 130 K. Among the four sources of uncertainty denoted above, the reddening is the least constrained quantity and accounts for most of the final error on the final mean temperature. After propagating all the errors, we end up with a mean error on the mean photometric temperature T_{phot} of about 150 K.

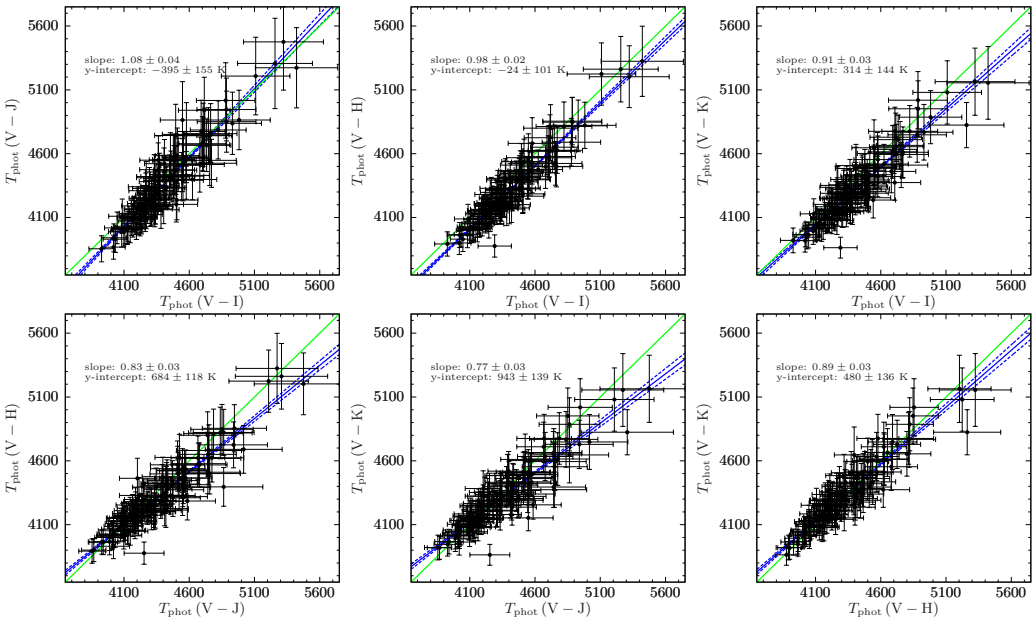

Figure 3.1: Comparison of the four photometric scales for LMC bar stars computed with Ramírez & Meléndez (2005b) photometric calibrations. Green solid line: 1-to-1 relation; blue solid line: linear fit to the data (fit parameters and their error are given in the plots); blue dashed lines: lines obtained after adding or subtracting errors to fit parameters. The slopes of the linear fits are close to 1 in each cases, showing the good agreement between the different photometric scales. The linear fit was performed taking into account correlated x- and y-errors (Monte-Carlo simulations).

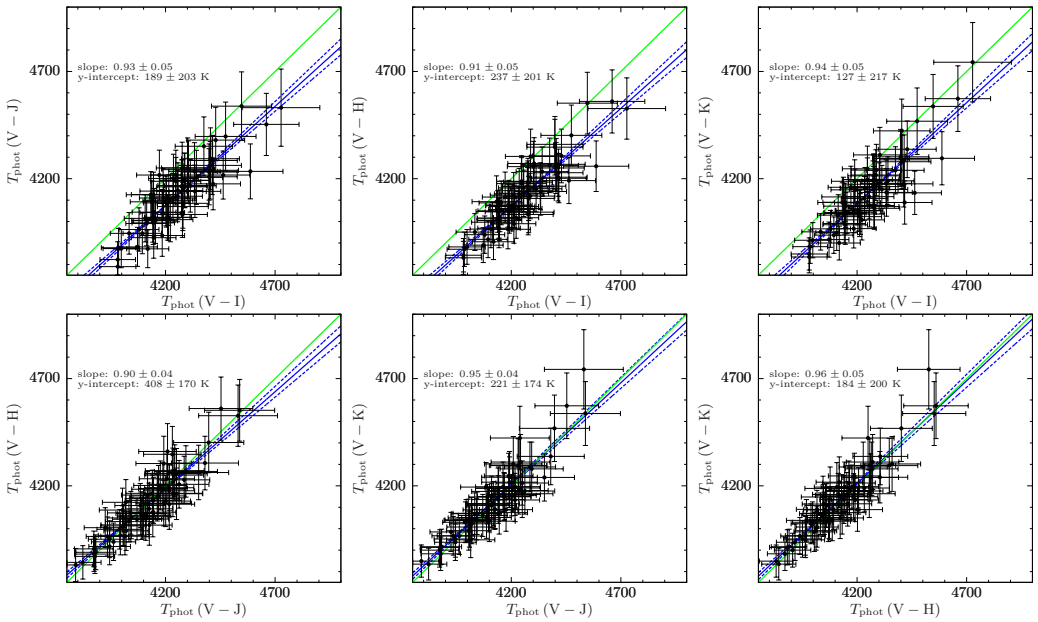

Figure 3.2: Comparison of the four photometric scales for LMC inner disc stars computed with Ramírez & Meléndez (2005b) photometric calibrations. Green solid line: 1-to-1 relation; blue solid line: linear fit to the data (fit parameters and their error are given in the plots); blue dashed lines: lines obtained after adding or subtracting errors to fit parameters. The slopes of the linear fits are close to 1 in each cases, showing the good agreement between the different photometric scales. The linear fit was performed taking into account correlated x- and y-errors (Monte-Carlo simulations).

The LMC inner disc sample In Chapters 4 and 5, we will compare our results for the LMC bar to the results for the LMC inner disc published by Pompéia et al. (2008). In order to remove systematic effects due to differences in the analysis procedures, we re-analysed the 59 stars of the inner disc field and derived a new set of stellar parameters, assuming a reddening $E\,(\mathrm{B}-\mathrm{V}) = 0.12\,\mathrm{mag}$ (computed from Zaritsky et al. (2004) catalogue as for the bar). As for the LMC bar sample, we have VIJHK photometry for LMC inner disc stars (VI magnitudes: Smecker-Hane et al., 2002; JHK magnitudes: Skrutskie et al., 2006). Table 3.5 provides the final photometric temperatures (and the associated error) for each colour index and the final mean temperature. Figure 3.2 compares the four photometric temperature scales; as for the LMC bar stars, the agreement between the four scales is very good. After propagating all the errors, we end up with a mean error on the mean photometric temperature $T_{\rm phot}$ of 100 K. Interestingly, despite the use of different methods, we found a good agreement (Fig. 3.3) between our mean photometric temperatures and the spectroscopic temperatures derived by Pompéia et al. (2008): $\langle T_{\rm spec,Pompeia} - T_{\rm phot} \rangle = -25\,\mathrm{K}$ (r.m.s = 65 K).

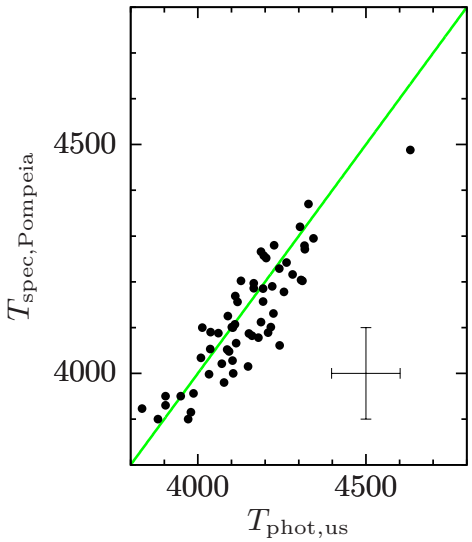

Figure 3.3: Comparison of our photometric temperatures to the spectroscopic temperatures of Pompéia et al. (2008). Green solid line: 1-to-1 relation. Mean error bars are indicated.

3.3 Surface gravity

3.3.1 Definition

A star of mass $M_\star$ and radius $R_\star$ has a surface gravity given by:

$$g = G\frac{M_\star}{{R_\star}^2} \tag{3.15}$$

where G is the gravitational constant, or in logarithmic notation and relatively to the Sun:

$$\log\left[g/g_\odot\right] = \log\left[\frac{M_\star/M_\odot}{(R_\star/R_\odot)^2}\right] \tag{3.16}$$

The gravity is necessary to describe stellar atmosphere and understand the line formation since it acts on the electronic and gas pressures. At a given temperature, a lower gravity implies a lower pressure, hence a lower electronic density: collisions between ions and free electrons are less frequent, and therefore, recombination is less frequent leading to strengthened ionised lines.

From the definition of the surface gravity, we see that two physical quantities are needed for a direct determination: the radius and the mass. As for the radius, the direct measurement of stellar masses is a complicated task. The less-model dependent determination of the mass of a star can be achieved when the star belong to a binary system whose distance is known: the sum and the ratio of the two masses are given by the application of the third Kepler law and the measure of the two semi-major axes (astrometry) or the measure of the radial velocities of the two components (spectroscopy) (e.g. Girard et al., 2000; Pourbaix et al., 2002). Thus

this method is not general since it is applicable to a very narrow category of stellar objects. Standard methods of gravity determination will be briefly introduced in Section 3.3.2.

3.3.2 How to determine surface gravity?

Methods of gravity estimation can be classified into spectroscopic (see § "Ionisation gravity", "Pressure-sensitive lines and molecular equilibrium") and photometric methods (see § "Photometric gravities" "Isochrone gravity")[3].

Ionisation gravity Under LTE, the number $n_{r,i}$ of atoms in the ionised stage r and the energy level i and the number of atoms $n_{r+1,j}$ in the next ionisation stage $r+1$ and the energy level j are related through the Saha equation:

$$\frac{n_{r+1,j}}{n_{r,i}} = \frac{1}{n_e}\left(\frac{2\pi m_e k_\mathrm{B} T}{h^2}\right)^{3/2} \frac{2g_{r+1,j}}{g_{r,i}} \mathrm{e}^{-\frac{\chi_r + \chi_{r+1,j} - \chi_{r,i}}{k_\mathrm{B} T}} \tag{3.17}$$

where n_e is the electron density, m_e the electron mass, h the Planck constant, χ_r the ionisation energy necessary to free an electron in the ground state of stage r, $\chi_{r,i}$ (resp. $\chi_{r+1,j}$) the excitation energy necessary to move an electron in the ground state of stage r (resp. $r+1$) to the energy level i (resp. $j+1$) of stage r (resp. $r+1$). Or, if we consider the total number n_r and n_{r+1} of atoms in the ionisation stages r and $r+1$ (summation over the excitation state):

$$\frac{n_{r+1}}{n_r} = \frac{1}{n_e}\left(\frac{2\pi m_e k_\mathrm{B} T}{h^2}\right)^{3/2} \frac{2U_{r+1}(T)}{U_r(T)} \mathrm{e}^{-\frac{\chi_r}{k_\mathrm{B} T}} \tag{3.18}$$

where $U_r(T)$ (resp. $U_{r+1}(T)$) is the partition function of ion r (resp. $r+1$) given by:

$$U_r(T) = \sum_{l=0}^{+\infty} g_{r,l} \mathrm{e}^{-\frac{\chi_{r,l}}{k_\mathrm{B} T}} \tag{3.19}$$

The Saha equation tells us that the population of ionisation stage depends on the electron density and the temperature. Since the electron density $n_e = P_e/(k_\mathrm{B} T)$, we see that the population fraction of two successive ionisation stage is pressure-sensitive, i.e. can be used as a gravity indicator. Therefore, it is possible to use absorption lines of a given species corresponding to two different ionisation stages. Usually, Fe I and Fe II are the preferred lines in cool F-G-K stars since they are abundant in stellar spectra, easily measurable and (relatively) well-known (in terms of atomic properties). The technique consists in varying the gravity of the atmosphere model and requiring that, in the mean, Fe I and Fe II give the same abundance. At a given temperature, if the tested gravity is lower than the true gravity, then the electron pressure is weaker, the first ionised (resp. neutral) stage will be more (resp. less) populated than reality and therefore the derived Fe II abundances will be lower than Fe I abundances. And reciprocally if the tested gravity is greater than the true

[3] Actually, with the development of asteroseismology, we speak also of seismic gravity, infer ed from stellar oscillations (e.g. Morel & Miglio, 2012).

gravity. The Saha equation exhibits a temperature dependence that cannot be neglected: a change in the temperature can break the ionisation balance. Generally, an iterative procedure is needed in order to converge on a pair $(T_{\rm eff}, \log g)$ satisfying simultaneously the excitation and ionisation balance. As for the excitation criterion, the ionisation criterion is easy to implement (e.g., possibility to use equivalent width (EW)) and necessitates the use of spectrum synthesis code with a grid of model atmospheres. We did not use the ionisation balance to derive the surface gravity of our LMC stars since:

1. the number of available Fe II lines in our wavelength coverage is rather small (between four an six lines) and therefore, prevents us from computing robust Fe II mean abundance.

2. non-LTE effects can affect Fe lines, and if they are not taken into account, they bias the determination of $\log g$ (e.g. Bergemann et al., 2012; Lind et al., 2012).

Pressure-sensitive lines and molecular equilibrium Particular pressure-sensitive spectral features, e.g. the wings of strong metal lines (e.g. Blackwell & Willis, 1977; Edvardsson, 1988; Fossati et al., 2011; Fuhrmann et al., 1997; Thorén et al., 2004) or molecular lines in cool stars (e.g. Bell et al., 1985; Bonnell & Bell, 1993), can also be used as gravity indicator. The quality of the gravity determination relies on the ability to take into account pressure broadening effect in the modelling of line wings. As strong line wings are also sensitive to the metal abundance, the metallicity and abundance of the relevant element are needed to remove the degeneracy. However, those techniques require high signal-to-noise ratio (S/N ratio) and high resolution spectra. In particular, given the resolution and S/N ratio of our GIRAFFE spectra, it cannot be applied to our LMC sample.

Photometric (or trigonometric) gravity A photometric (or trigonometric) gravity is often computed with the following expression:

$$\log\left(\frac{g}{g_\odot}\right) = \log\left(\frac{M}{M_\odot}\right) + 4\log\left(\frac{T_{\rm eff}}{T_{\rm eff\odot}}\right) + 0.4\,(M_{\rm bol} - M_{\rm bol\odot}) \tag{3.20}$$

obtained from the definition of the gravity, of the luminosity[4], of the effective temperature and bolometric magnitude $M_{\rm bol}$[5]. This can be rewritten in terms of apparent magnitude (below, with V magnitude) and distance modulus[6]:

$$\log\left(\frac{g}{g_\odot}\right) = \log\left(\frac{M}{M_\odot}\right) + 4\log\left(\frac{T_{\rm eff}}{T_{\rm eff\odot}}\right) + 0.4m_{\rm V_0} + 0.4BC_{\rm V} \tag{3.21}$$

$$+ 0.4\,(M_{\rm V_0} - m_{\rm V_0}) - 0.4M_{\rm bol\odot} \tag{3.22}$$

where $m_{\rm V_0}$ is the dereddened apparent V magnitude of the star, p its parallax, $BC_{\rm V} = M_{\rm bol} - m_{\rm V_0}$ the bolometric correction in the V band, $M_{\rm bol\odot}$ the solar

[4] $L_\star = 4\pi R_\star^2 \pi F_\star$
[5] $M_{\rm bol} = -2.5\log L_\star + K_{bol}$
[6] $M_{\rm V_0} - m_{\rm V_0} = 5(1 - \log d)$

bolometric magnitude. So the distance of the star, its effective temperature, its apparent V magnitude, and the interstellar extinction have to be known. We see also that the mass enters the equation and is estimated from assumptions on the star age. We avoided the use of the trigonometric formula for our LMC sample, since it forces us to assume the same mass (i.e. the same age) for all the stars of our sample.

Isochrone gravity This method consists in placing a star in the Hertzsprung-Russel diagram (e.g., using $T_{\rm eff}$ and $M_{\rm V}$) and finding the evolutionary track passing through the data point which, in principle, gives us a unique triplet (M, τ, Z) (resp. mass, age and metallicity fraction of the star). It is then possible to derive the surface gravity of the star. However, for giant stars, there exists an age-metallicity degeneracies and several evolutionary tracks can describe the same star (old metal-poor stars and young metal-rich stars sit in the sample place of the CMD). Moreover, Jørgensen & Lindegren (2005); Pont & Eyer (2004) showed that isochrone fitting techniques may suffer from statistical biases (especially, concerning the error propagation), and therefore more sophisticated Bayesian methods have been developed (da Silva et al., 2006). In addition to direct or indirect observational data ($T_{\rm eff}$, $M_{\rm V}$, [Fe/H]), Bayesian methods rely on the choice of a set of evolutionary tracks, an initial mass function (IMF) and an star formation rate (SFR). We decided to use the Bayesian estimation of stellar parameters of da Silva et al. (2006) (see Sec. 3.3.3). Indeed, unlike photometric gravity, the isochrone gravity does not require the star mass and assuming an equal distance for our LMC stars is acceptable since the thickness of the LMC is negligible compared to the distance LMC-Earth. Moreover, comparison of direct and isochrone-based method showed that the latter give reliable results (e.g. Allende Prieto & Lambert, 1999)[7].

3.3.3 Isochrone gravities of our LMC stars

Principle The surface gravities $\log g$ were derived using the Bayesian estimation algorithm[8] of stellar parameters of da Silva et al. (2006), based on Padova evolutionary tracks (Bertelli et al., 1994; Girardi et al., 2000), using constant SFR and IMF from Chabrier (2001). The required input parameters (and their associated errors) are: the effective temperature $T_{\rm eff}$, the iron abundance [Fe/H], the dereddened V magnitude $m_{\rm V_0}$, and the parallax p. We used the photometric temperature $T_{\rm phot}$ defined in Section 3.2.3 as the effective temperature, and the CaT metallicity index (first iteration) or the spectroscopically-derived Fe I abundance (from the second iteration) as an estimate of [Fe/H]. The V magnitude was taken from the OGLE catalogue, and was dereddened using the reddening value given in Section 3.2.3. We assumed the distance modulus of the stars equal to the distance modulus of the LMC, (18.5 ± 0.1) mag (Alves, 2004a), and computed their parallax accordingly: $p = (20 \pm 1) \times 10^{-6}{''}$. The mean error returned by the method on $\log g$ is 0.16 dex for the LMC bar sample and 0.14 dex for the LMC disc sample (including the reddening

[7] Detailed discussions on the gravity determination can be found in Allende Prieto et al. (1999); Bruntt et al. (2010).

[8] Web interface at http://stev.oapd.inaf.it/cgi-bin/param.

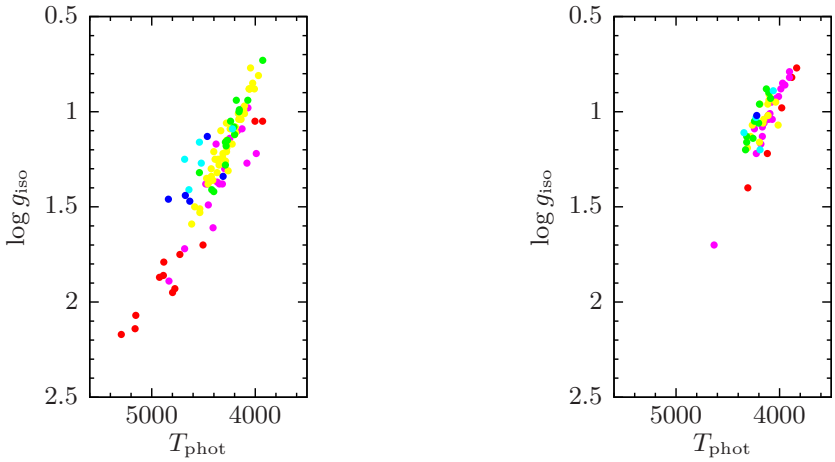

(a) LMC bar (b) LMC inner disc

Figure 3.4: Location of our LMC bar and inner disc stars in the $(T, \log g)$ plane. Blue: $-2\,\mathrm{dex} \leq [\mathrm{Fe\,I/H}] \leq -1.3\,\mathrm{dex}$; cyan: $-1.3\,\mathrm{dex} \leq [\mathrm{Fe\,I/H}] \leq -1.0\,\mathrm{dex}$; green: $-1.0\,\mathrm{dex} \leq [\mathrm{Fe\,I/H}] \leq -0.8\,\mathrm{dex}$; yellow: $-0.8\,\mathrm{dex} \leq [\mathrm{Fe\,I/H}] \leq -0.6\,\mathrm{dex}$; magenta: $-0.6\,\mathrm{dex} \leq [\mathrm{Fe\,I/H}] \leq -0.4\,\mathrm{dex}$; red: $-0.4\,\mathrm{dex} \leq [\mathrm{Fe\,I/H}] \leq 0.0\,\mathrm{dex}$.

conservative error). In addition to the gravity, the Bayesian algorithm returns also the mass and age of the stars.

The LMC bar and inner disc samples Figure 3.4a and 3.4b show respectively the location of our LMC bar and inner disc stars in a $(T, \log g)$ plane, where the metallicity is colour coded. Figure 3.5 compares, for the inner disc sample, our gravities to those derived spectroscopically by Pompéia et al. (2008). Despite the use of different method, we find a good agreement between the two gravity scales: $\langle [\mathrm{Fe\,I/H}]_{\rm Pompeia} - [\mathrm{Fe\,I/H}] \rangle = -0.06\,\mathrm{dex}$ (r.m.s $= 0.15\,\mathrm{dex}$).

3.4 Overall metallicity

3.4.1 Definition

The (non-detailed) chemical composition of a star is usually described in terms of hydrogen, helium and metals because hydrogen and helium are the most abundant chemical elements in stellar material, "metals" being then understood as all the remaining chemical elements. The letters $X = m_{\rm H}/m_{\rm total}$, $Y = m_{\rm He}/m_{\rm total}$ and $Z = 1 - X - Y$ stand for the mass fraction of hydrogen, helium and metals respectively. For instance, Grevesse & Sauval (1998) found $X_\odot = 0.735$, $Y_\odot = 0.248$ and $Z_\odot = 0.017$ for the composition of the solar photosphere. For a star with mass fractions X, Y and Z, the overall metallicity [M/H] is given by:

$$[\mathrm{M/H}] = \log\left(\frac{Z}{Z_\odot}\right) \tag{3.23}$$

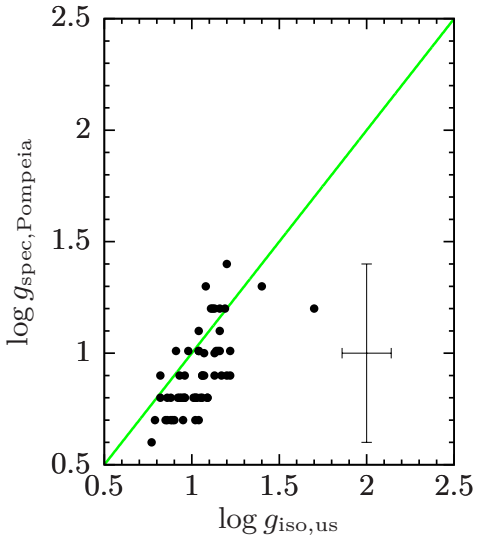

Figure 3.5: Comparison of our isochrone gravities to the spectroscopic gravities of Pompéia et al. (2008). Green solid line: 1-to-1 relation. Mean error bars are indicated.

Thus a star with [M/H] $= -3$ is 1000 more metal-poor than the Sun (i.e. $Z \approx 2 \times 10^{-5}$).

Knowing the metal content of a stellar photosphere is important to properly compute line profiles: since they can be electrons donors, metals (Mg, Ca, Si, Fe etc.) play a role in the opacity and electron density (e.g., H^- continuous absorption in cool stars).

3.4.2 Metallicity of our LMC bar stars

In practise, [M/H] is assimilated to [Fe/H]. [Fe/H] can be estimated using the CaT metallicity index, which relies on the measurement of the EW of the Ca II triplet (8498 Å, 8542 Å, 8662 Å) and the use of empirical calibrations (e.g. Battaglia et al., 2008; Cole et al., 2004). However, such Fe abundances are not precise enough for atmosphere modelling and spectrum synthesis. To obtain more precise [Fe/H], it is customary to average the abundances derived for a set of Fe I lines. Since abundance measurement requires to know all the stellar parameters, the derivation of [Fe/H] is part of an iterative procedure. Our determination of [M/H] was done simultaneously to the determination of the microturbulence velocity (see Sec. 3.5.3).

It is possible to use a more detailed chemical composition for the modelling of the stellar atmosphere or for the radiative transfer. For instance, one can assume a rough value for the α content (e.g., enhanced α for [Fe/H] < -0.5 dex).

3.5 Microturbulence velocity

3.5.1 Definition

Non-thermal motions exist in the gas of stellar atmospheres and cause Doppler broadening of spectral lines. The turbulence, thought to be caused by convection, is called microturbulence when the scale of turbulent motions is small compared to the photon mean free path and is called macroturbulence when the scale of turbulent motions is large compared to the photon mean free path. Therefore, microturbulence changes the local absorption of photons, i.e. changes the strength (EW) of a given line, while macroturbulence modifies the emergent flux, i.e. modifies the line profile at constant EW.

As it modifies line strengths, microturbulence has to be taken into account for spectrum synthesis. Microturbulence has no effect on the total strength of weak lines, since it leaves unchanged the total number of absorbers contributing to the absorption line; nevertheless, it can modify the energy distribution keeping constant the EW, and a weak line becomes shallower and wider. On the other hand, microturbulence changes the behaviour of strong saturated lines. Indeed, assume that, in absence of microturbulence, a line is saturated for a given number of absorbers, i.e. the intensity at the centre of a line reaches a minimum non-zero value (because of the Boltzmann equation, it is not possible to deplete completely the lower level). Then, in presence of microturbulence and for the same number of absorbers, the line will be desaturated since absorbers will now absorb photons at different wavelengths (Doppler shifts): the line strength is changed.

3.5.2 How to determine microturbulence velocity?

From the above definition, a spectroscopic method using absorption lines of different strengths is the only way to measure the microturbulence velocity. The technique consists in varying the microturbulent velocity used in the spectrum synthesis code and requiring that, in the mean, Fe I lines give the same abundance irrespective of the EW. Section 3.5.3 describes the iterative procedure we adopted.

3.5.3 Microturbulence velocity and metallicity of our LMC stars

Principle The overall metallicity and the microturbulent velocity were derived simultaneously by requiring that different Fe I lines of different EW give the same iron abundance [Fe I/H]. We used the automated tool DAOSPEC (Stetson & Pancino, 2008) to measure the equivalent width (EW) W and their associated error, and we used the grid of OSMARCS model atmospheres[9] (Gustafsson et al., 2008) together with the code of spectrum synthesis *turbospectrum* (*turbospectrum* is described in Alvarez & Plez, 1998 and improved along the years by B. Plez) to convert the EW into abundances. Since our stars are giants, atmosphere models and radiative transfer were both in spherical geometry. We built the atmosphere model for a given set of stellar parameters by interpolation onto the OSMARCS grid with the interpolation routine written by Masseron (2006, PhD thesis).

[9] Models available at http://marcs.astro.uu.se.

The iterative procedure is as follows:

1. for a given set of stellar parameters $\{T_{\rm phot}, \log g, \xi_{\rm micro}, [{\rm M/H}]\}$, abundances of around 45 Fe I lines are derived from their EW.

2. the mean [Fe I/H] is computed and compared to the input metallicity; if $|\langle[{\rm Fe\,I/H}]\rangle - [{\rm M/H}]| > 0.01\,{\rm dex}$, then the global metallicity is updated ($[{\rm M/H}] \leftarrow \langle[{\rm Fe\,I/H}]\rangle$) and we go back to step 1. If the convergence is not reached after 10 iterations, we release the previous criterion and increase the threshold by 0.01 dex.

3. the linear regression of [Fe I/H] vs. W' is made, where W' is the reduced equivalent width ($W' = \log W/\lambda$). As said before, the errors on the EW are given by DAOSPEC and are turned into errors on [Fe I/H] abundances by *turbospectrum*. There is no analytical solution to the problem of linear regression with errors on both coordinates, and a few recipes exist to answer this question. Besides, in our cases, the errors of the EW (explanatory variable) and the abundances (dependent variable) are correlated because we used the former to derive the latter. In order to handle as properly as possible the errors on both coordinates, we used a linear regression algorithm based on bootstrapping, as it turns out that the low statistics (number of Fe I lines) dominate the uncertainty on the slope of the regression.

This procedure is repeated for each value of $\xi_{\rm micro}$ in the range $\{1.0, 1.1, \ldots, 2.5\}$ ($\rm km\,s^{-1}$). We then selected the set of parameters which gives a minimum slope, smaller than its error (in absolute value). To accept or reject this best set of stellar parameters, we checked that excitation (in the mean, Fe I lines give the same abundance irrespective of the $\chi_{\rm ex}$) and ionisation (in the mean, Fe I and Fe II lines give the same abundance) equilibria are fulfilled (at least mildly), i.e. we required:

- for the excitation equilibrium: the slope of $(\chi_{\rm ex}|[{\rm Fe\,I/H}])$ is approximately lower than its error;

- for the ionisation equilibrium: $|[{\rm Fe\,II/H}] - [{\rm Fe\,I/H}]| \lessapprox 0.3\,{\rm dex}$ (0.3 dex is six times the mean random uncertainty on [Fe I/H]).

Figures 3.6 to 3.8 illustrate the iterative procedure and the different spectroscopic criteria for the star 05245212-6948184 and different microturbulent velocities (resp. lower than, equal to and higher than the nominal microturbulent velocity). The estimate of the error on the metallicity [M/H] and the microturbulent velocity $\xi_{\rm micro}$ is proposed in Paragraph "Application to Arcturus".

The LMC bar and inner disc samples Tables 3.6 and 3.7 give respectively the final stellar parameters for our LMC bar and inner disc stars. For the LMC bar stars {05223316-6951389, 05225632-6942269, 05225980-6954368, 05224240-6940567, 05232554-6943388, 05244301-6943412, 05253235-6943137} and for the LMC inner disc stars {0564-LMCDisc01, 0706-LMCDisc01, 0721-LMCDisc01, 0758-LMCDisc01, 0790-LMCDisc01, 0808-LMCDisc01, 0835-LMCDisc01, 0879-LMCDisc01, 0937-LMCDisc01} (except for 0758-LMCDisc01, the same stars as in

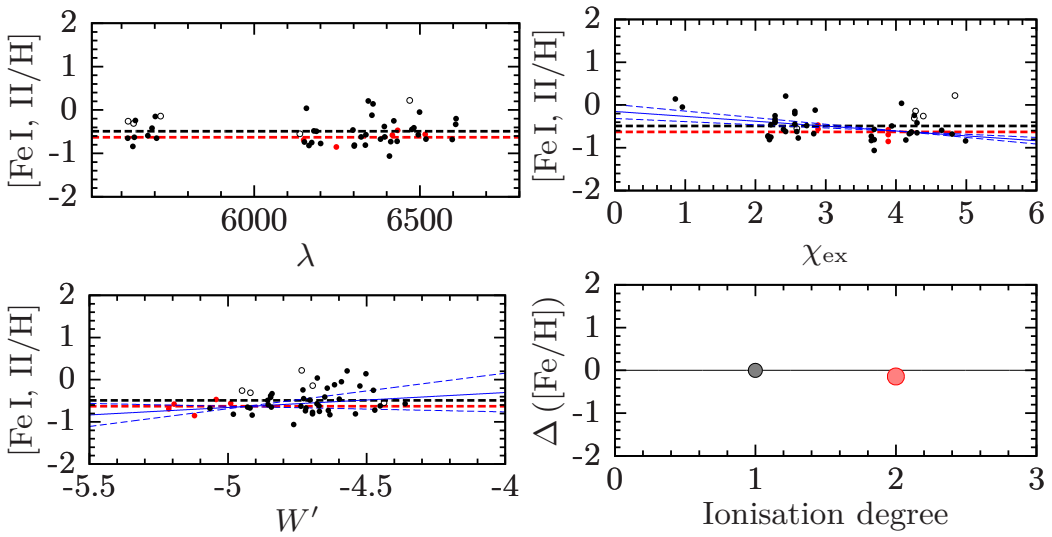

Figure 3.6: Spectroscopic criteria for the star 05245212-6948184 and $\xi_{\mathrm{micro}} = 1.6\,\mathrm{km\,s^{-1}}$. **Top left panel:** [Fe I/H] and [Fe II/H] vs. λ_{line} (wavelength dependency). **Top right panel:** [Fe I/H] and [Fe II/H] vs. χ_{ex} (excitation equilibrium). **Bottom left panel:** [Fe I/H] and [Fe II/H] vs. W' (microturbulent velocity criterion). **Bottom right panel:** $\Delta\,([\mathrm{Fe/H}]) = \langle[\mathrm{Fe\,II/H}]\rangle - \langle[\mathrm{Fe\,I/H}]\rangle$ (ionisation equilibrium). Black dots: Fe I; red dots: Fe II; black dashed thick line: $\langle[\mathrm{Fe\,I/H}]\rangle$; red dashed thick line: $\langle[\mathrm{Fe\,II/H}]\rangle$; blue solid line: linear fit: blue dashed lines: lines obtained after adding or subtracting errors to fit parameters; open symbols: data points rejected by k-σ clipping (not used for the computation of the mean abundance nor the linear fit). For the bottom right panel, the size of the circles is proportional to the error on the mean Fe I and Fe II abundances. In this case, the microturbulent velocity ($1.6\,\mathrm{km\,s^{-1}}$) is smaller than the nominal value ($1.9\,\mathrm{km\,s^{-1}}$): the slope of (W'|[Fe I/H]) is positive; the excitation and ionisation equilibria are broken (resp. negative slope and $\langle[\mathrm{Fe\,II/H}]\rangle < \langle[\mathrm{Fe\,I/H}]\rangle$).

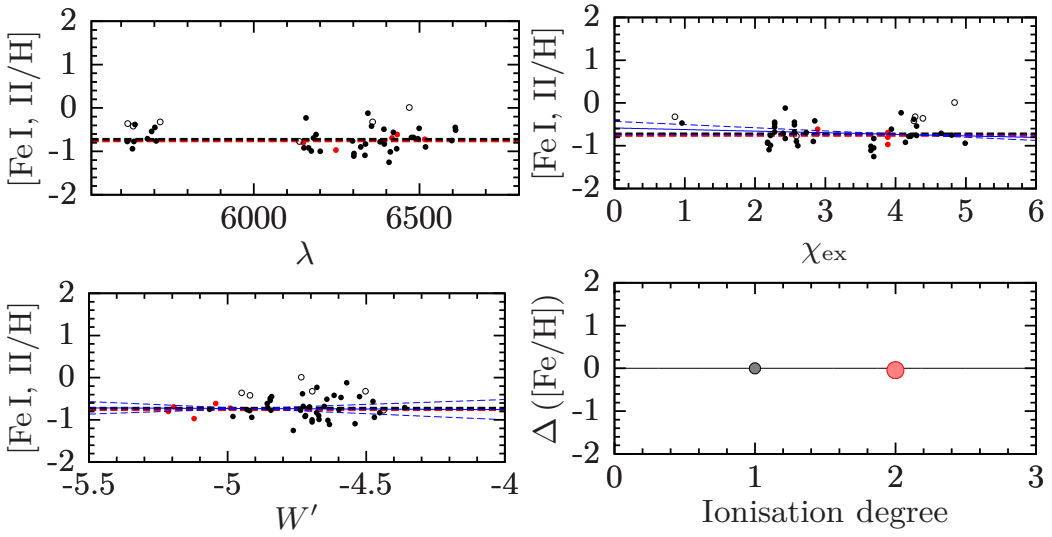

Figure 3.7: Spectroscopic criteria for the star 05245212-6948184 and $\xi_{\mathrm{micro}} = 1.9\,\mathrm{km\,s^{-1}}$. Same legend as Figure 3.6. In this case, the microturbulent velocity is equal to the nominal value ($1.9\,\mathrm{km\,s^{-1}}$): the slope of $(W'|[\mathrm{Fe\,I/H}])$ is almost null; the excitation and ionisation equilibria are fulfilled (resp. null slope and $\langle[\mathrm{Fe\,II/H}]\rangle \approx \langle[\mathrm{Fe\,I/H}]\rangle$).

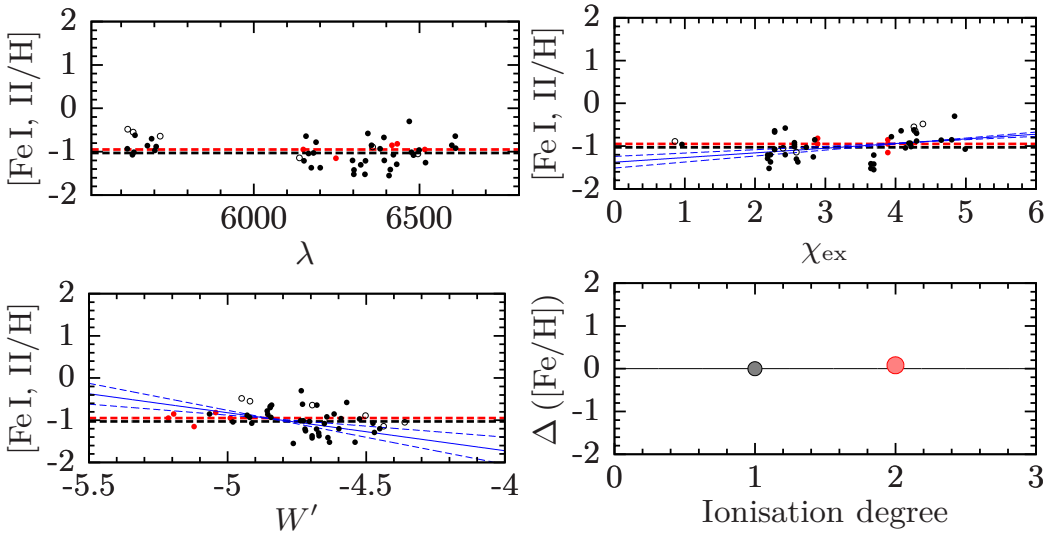

Figure 3.8: Spectroscopic criteria for the star 05245212-6948184 and $\xi_{\mathrm{micro}} = 2.5\,\mathrm{km\,s^{-1}}$. Same legend as Figure 3.6. In this case, the microturbulent velocity ($2.5\,\mathrm{km\,s^{-1}}$) is higher than the nominal value ($1.9\,\mathrm{km\,s^{-1}}$): the slope of $(W'|[\mathrm{Fe\,I/H}])$ is negative; the excitation equilibrium and ionisation equilibria are broken (resp. positive slope and $\langle[\mathrm{Fe\,II/H}]\rangle > \langle[\mathrm{Fe\,I/H}]\rangle$).

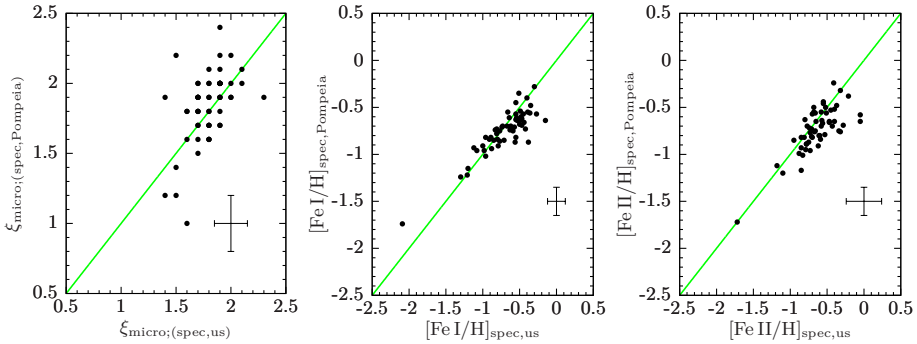

Figure 3.9: Comparison of our spectroscopic microturbulent velocity (left panel), Fe I (middle panel) and Fe II (right panel) abundances to those of Pompéia et al. (2008). Green solid line: 1-to-1 relation. Mean error bars are indicated.

Pompéia et al., 2008), the procedure did not converge onto a satisfactory solution and they were left out the sample. We found a good agreement, within the error bars, between our newly derived microturbulence velocities and iron abundances (Fig. 3.9) and those of Pompéia et al. (2008):

- $\langle \xi_{\rm micro,Pompeia} - \xi_{\rm micro} \rangle = 0.05\,{\rm km\,s^{-1}}$ (r.m.s $= 0.22\,{\rm km\,s^{-1}}$)
- $\langle [{\rm Fe\,I/H}]_{\rm Pompeia} - [{\rm Fe\,I/H}] \rangle = -0.06\,{\rm dex}$ (r.m.s $= 0.15\,{\rm dex}$)
- $\langle [{\rm Fe\,II/H}]_{\rm Pompeia} - [{\rm Fe\,II/H}] \rangle = -0.11\,{\rm dex}$ (r.m.s $= 0.17\,{\rm dex}$)

In Chapter 4, we will use our new set of stellar parameters to re-derive abundances of the LMC inner disc stars.

Application to Arcturus Our set of Arcturus spectra served to perform tests on our iterative procedure giving the overall metallicity [M/H] and the microturbulent velocity $\xi_{\rm micro}$. To this end, we used the effective temperature and the gravity published by Ramírez & Allende Prieto (2011): $T_{\rm eff} = 4286\,{\rm K}$ (spectral energy distribution fitting) and $\log g = 1.66$ (isochrone fitting) and kept them constant and we applied the iterative procedure described in Section 3.5.3 on the 101 realisations of high, median and low S/N ratio version of the Arcturus spectra. Table 3.3 gives the mean [M/H], [Fe I/H], [Fe II/H] and $\xi_{\rm micro}$ and the standard deviation around the mean; results for the ∞ S/N ratio are also given for reference. As could be anticipated, results differ according to S/N ratio, but the differences are mild: the lower the S/N ratio, the higher the metallicity ([Fe I/H], or [Fe II/H]), the higher the difference Δ = [Fe I/H] - [Fe II/H], and the lower the microturbulent velocity. We can notice that the standard deviation around the mean value increases when the S/N ratio decreases, which is again an expected behaviour. Our procedure tends to lead to lower metallicities and higher microturbulent velocity than the reference values in the literature (in fact, in our procedure, the bias in [Fe I/H] varies linearly with the bias in $\xi_{\rm micro}$), although this effect is paradoxically alleviated at the median and low S/N ratio of our LMC sample: Worley et al. (2009) found

Table 3.3: Mean and standard deviation of the distribution of [M/H], [Fe I/H], [Fe II/H] and $\xi_{\rm micro}$ for the 101 realisations of high, median and low S/N ratio version of the Arcturus spectra. The bottom line give the results for the ∞ S/N ratio spectrum.

S/N	$\langle$[M/H]$\rangle$ dex	$\langle$[Fe I/H]$\rangle$ dex	$\langle$[Fe II/H]$\rangle$ dex	$\langle\xi_{\rm micro}\rangle$ km s^{-1}
low	-0.58 ± 0.11	-0.58 ± 0.11	-0.49 ± 0.11	1.82 ± 0.15
median	-0.65 ± 0.06	-0.65 ± 0.06	-0.59 ± 0.07	1.83 ± 0.09
high	-0.69 ± 0.05	-0.69 ± 0.05	-0.63 ± 0.05	1.87 ± 0.07
∞	-0.71	-0.72	-0.70	1.9

[Fe I/H] $= -0.6$ dex and $\xi_{\rm micro} = 1.5$ km s^{-1}; Ramírez & Allende Prieto (2011) found [Fe I/H] $= -0.52$ dex and $\xi_{\rm micro} = 1.74$ km s^{-1}.

Standard deviations reported in Table 3.3 can also be used as an estimator of the (random) error on the determined metallicity and the determined microturbulent velocity in the LMC sample, due to the (random) error on the EW measurements (itself originating in the noise present in the stellar spectra). In the following, we will keep the conservative estimates: $\sigma([{\rm M/H}]) = 0.1$ dex and $\sigma(\xi_{\rm micro}) = 0.15$ km s^{-1}.

3.6 Choice of the reddening

The mapping of the reddening in the LMC has been a longstanding issue, and depending on the targeted stars and the technique used, different reddenings are derived. Zaritsky et al. (2004) published a reddening map of the LMC based on a colour decomposition. We estimated the reddening for our LMC bar field from their catalogue[10]. As all of our stars were not studied by Zaritsky et al. (2004) and as individual reddening values are reported to be too uncertain, we extracted all of the Zaritsky et al. (2004) stars located in our field of view, and computed a median value of the extinction A_V: $A_V = 0.44$ mag, hence a median reddening $E({\rm B-V}) = A_V/3.24 \approx 0.14$ mag (4287 extracted stars). This value of reddening is similar to what was found by Udalski et al. (1999) from red clump (RC) stars (comparison of the observed and the theoretical RC colour): $E({\rm B-V}) \simeq 0.13$ mag in the bar region. Haschke et al. (2012b) have derived optical reddening maps using two different techniques: RC stars and RR Lyrae (comparison of the apparent and the absolute colour, the latter being computed with the period and the metallicity). They found similar results with the two techniques and their reddening map gives $E({\rm B-V}) \simeq 0.06$ mag and $\sigma\left(E({\rm B-V})\right) = 0.05$ mag for our bar field. They found good agreement with other works from Subramaniam (2005) (RC stars) and Pejcha & Stanek (2009) (RR Lyrae). Based on these variations for the reddening in our region, we decided to use a conservative error of 50 %, $\sigma\left(E({\rm B-V})\right) = 0.07$ mag to propagate the errors on our stellar parameters (see Sec. 3.2.3), which covers all the range of possible reddenings in this field.

[10] Online LMC reddening estimator at http://ngala.as.arizona.edu/dennis/lmcext.html.

To investigate further the most probable reddening for our field, we tested the two following hypothesis of reddening: $E(\mathrm{B}-\mathrm{V}) = 0.06\,\mathrm{mag}$ and $E(\mathrm{B}-\mathrm{V}) = 0.14\,\mathrm{mag}$. The choice of the reddening has a strong effect on the photometric temperature scale and somewhat more moderate on the microturbulent velocity (comparable to the typical error on the parameter) and a small effect on the gravity and overall metallicity (lower than the typical error):

- $\langle \mathrm{T_{phot}}[E(\mathrm{B}-\mathrm{V}) = 0.14] - \mathrm{T_{phot}}[E(\mathrm{B}-\mathrm{V}) = 0.06]\rangle = 140\,\mathrm{K}$
  (r.m.s $= 40\,\mathrm{K}$)
- $\langle \log g[E(\mathrm{B}-\mathrm{V}) = 0.14] - \log g[E(\mathrm{B}-\mathrm{V}) = 0.06]\rangle = 0.03$
  (r.m.s $= 0.07$)
- $\langle [\mathrm{M/H}][E(\mathrm{B}-\mathrm{V}) = 0.14] - [\mathrm{M/H}][E(\mathrm{B}-\mathrm{V}) = 0.06]\rangle = -0.02\,\mathrm{dex}$
  (r.m.s $= 0.12\,\mathrm{dex}$)
- $\langle \xi_{\mathrm{micro}}[E(\mathrm{B}-\mathrm{V}) = 0.14] - \xi_{\mathrm{micro}}[E(\mathrm{B}-\mathrm{V}) = 0.06]\rangle = 0.17\,\mathrm{km\,s^{-1}}$
  (r.m.s $= 0.13\,\mathrm{km\,s^{-1}}$)

Figure 3.10 shows the results of the determination of the stellar parameters for the LMC bar stars (first row: $E(\mathrm{B}-\mathrm{V}) = 0.06\,\mathrm{mag}$; second row: $E(\mathrm{B}-\mathrm{V}) = 0.14\,\mathrm{mag}$) and for the median S/N ratio Arcturus spectra (third row). The choice of reddening has a small effect on the distribution of the slopes ([Fe I/H] | $\log(W/\lambda)$) (first column): for $E(\mathrm{B}-\mathrm{V}) = 0.06\,\mathrm{mag}$ and $0.14\,\mathrm{mag}$ respectively, the medians are $-0.008\,\mathrm{dex}$ and $-0.017\,\mathrm{dex}$, the semi-interquartile ranges are $0.037\,\mathrm{dex}$ and $0.030\,\mathrm{dex}$ respectively. We note however that the distribution is narrower when the reddening is higher. Similarly, the effect on the distribution of the slopes ([Fe I/H] | χ_{ex}) (excitation equilibrium, second column) is also small: the medians are similar in both cases and close to zero ($\simeq -0.023\,\mathrm{dex\,eV^{-1}}$), but the distribution is narrower when the reddening is higher: the semi-interquartile ranges are $0.023\,\mathrm{dex\,eV^{-1}}$ and $0.020\,\mathrm{dex\,eV^{-1}}$ for $E(\mathrm{B}-\mathrm{V}) = 0.06\,\mathrm{mag}$ and $0.14\,\mathrm{mag}$ respectively. Whatever the assumed reddening, we see that our photometric scales do not break dramatically the excitation equilibrium and that the highest reddening seems to improve slightly the general trend. The largest effect is observed for the ionisation equilibrium: changing the reddening will shift the distribution of the difference $\Delta(\mathrm{Fe}) = [\mathrm{Fe\,I/H}] - [\mathrm{Fe\,II/H}]$ (ionisation equilibrium, third column). Indeed, the medians are $-0.12\,\mathrm{dex}$ (over-ionisation) and $0.06\,\mathrm{dex}$ (under-ionisation) for $E(\mathrm{B}-\mathrm{V}) = 0.06\,\mathrm{mag}$ and $0.14\,\mathrm{mag}$ respectively, with similar semi-interquartile ranges of $0.12\,\mathrm{dex}$ and $0.11\,\mathrm{dex}$ respectively. The last column of Figure 3.10 shows that the reddening (thus the temperature) has a small effect on the distribution of the standard deviations of Fe I abundances (though the situation improves slightly for $E(\mathrm{B}-\mathrm{V}) = 0.14\,\mathrm{mag}$: smaller median, distribution queue less populated): therefore, the change of reddening has negligible effect on the agreement of Fe I lines (when the pipeline has converged). As the high reddening tends to slightly improve the determination of parameters (distribution of slopes are narrower, the departure from the ionisation equilibrium is reduced), we decided to use this assumption.

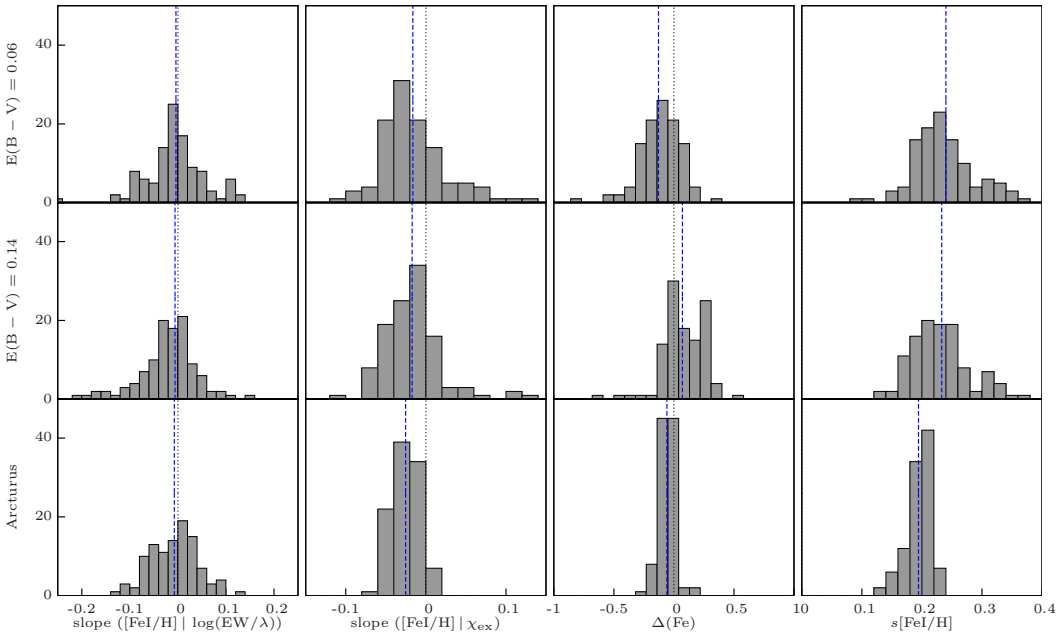

Figure 3.10: Comparison of two reddening assumptions. First and second row: distribution of a given quantity for our LMC stars assuming $E(\mathrm{B}-\mathrm{V}) = 0.06$ mag and $E(\mathrm{B}-\mathrm{V}) = 0.14$ mag respectively. Third row: distribution of a given quantity for the 101 median S/N ratio Arcturus spectra. First column: distributions of the slopes ([Fe I/H] | $\log(W/\lambda)$) (spectroscopic criterion used to derive ξ_{micro}). Second column: distributions of the slopes ([Fe I/H] | χ_{ex}) (excitation equilibrium). Third column: distribution of the difference $\Delta(\mathrm{Fe}) = [\mathrm{Fe\,I/H}] - [\mathrm{Fe\,II/H}]$ (ionisation equilibrium). Fourth column: distribution of the sample standard deviation of [Fe I/H].

We checked that results obtained for the 101 median S/N ratio Arcturus spectra share the same properties: the distribution of the slopes ([Fe I/H] | $\log(W/\lambda)$) is centred around zero; the excitation equilibrium is not exactly fulfilled (the median of the distribution is $-0.024\,\mathrm{dex\,eV^{-1}}$, similar to the median of our LMC sample), and we found a small over-ionisation (the median of Δ(Fe) is -0.05 dex). Therefore, we decided to kept the high reddening values ($E(B-V) = 0.14$ mag for the LMC bar; $E(B-V) = 0.12$ mag for the LMC disc).

3.7 $[Fe/H]_{CaT}$ vs. $[Fe/H]_{spec}$

The top panel of Figure 3.11 compares for both bar and inner disc fields the [Fe I/H] ratio derived from high-resolution spectroscopy to the metallicity derived from the infrared CaT index. The typical error bar on $[Fe/H]_{CaT}$ is 0.1-0.2 dex (Cole et al., 2005), and the typical error bar on $[Fe/H]_{spec}$ is 0.11 dex (quadratic sum of the typical random and systematic errors on the mean Fe abundance). We see a rather good agreement, within the errors, between the two indices up to $[Fe/H]_{CaT} \approx -0.5$ dex; then, for higher $[Fe/H]_{CaT}$, we have $[Fe/H]_{CaT} \geq [Fe/H]_{spec}$. A possible explanation is that for metal-rich stars the continuum placement in the CaT region becomes difficult and leads to poor abundance determinations. Good agreement between CaT metallicities (*e.g.*, Grocholski et al., 2006; Olszewski et al., 1991) and spectroscopic abundances (*e.g.*, Mucciarelli et al., 2008) has been seen for LMC GC with $[Fe/H] = -0.4 \pm 0.1$ and ages around ~ 2 Gyr. Very few to no LMC GC with abundances $[Fe/H] > -0.3$ and ages < 2 Gyr are known, so we have no direct tests of the correspondence between the two methods for LMC stars. A possible contribution to the discrepancy could also be due to the presence of stars in the 0.8-1.2 Gyr age range in the LMC field samples, where the RC magnitude is changing very quickly and few calibrators of the CaT method are available. Based on the trends in the Padova stellar isochrones and with reference to the empirical data in Cole et al. (2004) there might be a bias of order 0.1 dex in the CaT abundances for stars aged ~ 1 Gyr. For the remainder of this paper we take the high-resolution spectroscopic [Fe I/H] to be the true metallicity.

In the metal-poor range, one LMC bar star (05232680-6953109) and four LMC disc stars (0606-LMCDisc01, 0633-LMCDisc01, 0699-LMCDisc01, 1105-LMCDisc01) have very discrepant $[Fe/H]_{CaT}$ and $[Fe/H]_{spec}$ ($|\Delta| \geq 0.4$ dex and $[Fe/H] \lessapprox -0.5$ dex). Except for the disc star 0606-LMCDisc01, we could not find any anomaly in the stellar parameters determination or the abundance measurements. The star 0606-LMCDisc01 with $[Fe/H] = -2.07$ dex has normal α-ratios ($[Ca/Fe] = 0.39$ dex) but overabundant s- and r-ratios ($[Ba/Fe] = 0.57$ dex, $[La/Fe] = 0.51$ dex). This is in agreement with Pompéia et al. (2008) who found $[Fe/H] = -1.74$ dex, $[Ca/Fe] = 0.13$ dex (our LMC disc Ca ratios are 0.1 dex higher in the mean; see Sec. 4.2), $[Ba/Fe] = 0.80$ dex, $[La/Fe] = 0.30$ dex. The high fraction of s-process in this star could be the sign that it is part of a binary system (the s-process elements would have been transfer from a former AGB companion), and therefore, the binarity could explain the disagreement between the CaT and high-resolution [Fe/H].

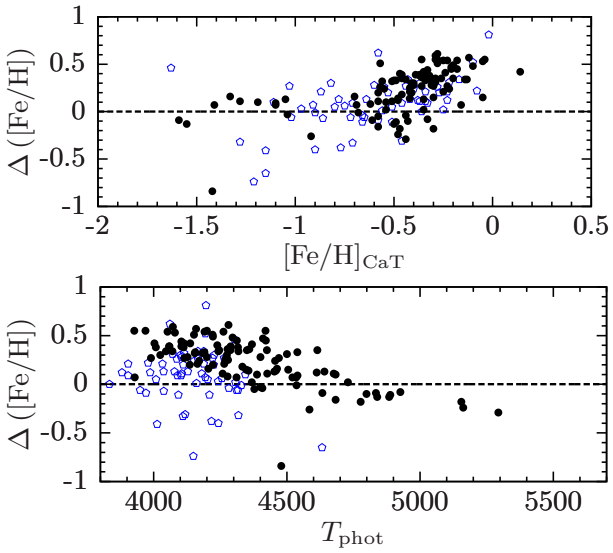

Figure 3.11: **Top panel:** $\Delta([\mathrm{Fe/H}]) = [\mathrm{Fe/H}]_{\mathrm{CaT}} - [\mathrm{Fe/H}]_{\mathrm{spec}}$ **vs.** $[\mathrm{Fe/H}]_{\mathrm{CaT}}$**. Bottom panel:** $\Delta([\mathrm{Fe/H}])$ **vs.** T_{phot}**.** Black filled circles: LMC bar; blue open pentagons: LMC disc.

The bottom panel of Figure 3.11 shows the correlation between $\Delta([\mathrm{Fe/H}]) = [\mathrm{Fe/H}]_{\mathrm{CaT}} - [\mathrm{Fe/H}]_{\mathrm{spec}}$ and T_{phot}. For the coolest stars ($T_{\mathrm{phot}} \lessapprox 4400\,\mathrm{K}$), we observe a difference between our two LMC fields: this difference points towards an age effect.

3.8 Large tables

Table 3.4: Photometric temperature scales for LMC bar stars. For each colour index, $T_{\rm phot}$ and its error. The last columns give the simple mean of the four estimates and the corresponding propagated error.

2MASS ID	$(V_J - I_C)_0$		$(V_J - J_{2M})_0$		$(V_J - H_{2M})_0$		$(V_J - K_{2M})_0$		Average	
	$T_{\rm phot}$	$\sigma\left(T_{\rm phot}\right)$	$T_{\rm phot}$	$\sigma\left(T_{\rm phot}\right)$	$T_{\rm phot}$	$\sigma\left(T_{\rm phot}\right)$	$T_{\rm phot}$	$\sigma\left(T_{\rm phot}\right)$	$T_{\rm phot}$	$\sigma\left(T_{\rm phot}\right)$
	K	K	K	K	K	K	K	K	K	K
05223082-6944147[†]	4126	114	4008	118	4006	103	4021	102	4070	102
05223112-6945292	4099	102	3989	113	4000	103	4011	101	4025	98
05223186-6947159	4345	145	4306	163	4245	132	4213	131	4277	134
05223309-6946595	4410	158	4391	175	4319	141	4484	167	4401	151
05223316-6951389	4407	144	4457	188	4328	145	4368	163	4390	146
05223318-6937044	4460	160	4436	185	4379	148	4410	163	4421	152
05223416-6944433	4578	184	4751	249	4681	201	4554	185	4641	187
05223487-6938057	4332	136	4412	180	4226	135	4294	142	4316	137
05223506-6937279	4209	127	4191	148	4155	122	4203	130	4190	123
05223557-6943373	4691	183	4774	244	4624	190	4614	206	4676	185
05223701-6936166	4719	206	4741	216	4800	184	4655	175	4729	186
05223787-6954562[†]	4022	96	3941	109	3963	98	3967	97	4003	93
05223895-6945007	4340	137	4311	155	4259	128	4208	125	4279	130
05223988-6946110	4247	121	4210	141	4126	114	4150	117	4183	117
05224062-6953310	4223	119	4082	126	4109	116	4134	117	4137	112
05224164-6935518	4364	143	4549	190	4320	148	4153	101	4347	137
05224195-6941099	4256	126	4184	143	4107	117	4252	133	4200	121
05224240-6940567	5322	306	5476	378	5203	242	5164	263	5291	272
05224276-6940109	4449	154	4417	174	4325	137	4323	139	4378	144
05224309-6940275	4222	121	4108	128	4091	112	4184	124	4151	114
05224321-6952397	4324	135	4276	159	4249	130	4249	135	4275	131
05224448-6954402	4757	203	4548	197	4524	171	4511	176	4585	174
05224854-6940010	4159	112	4098	138	4018	109	4045	116	4080	108
05225062-6936580	4577	177	4430	187	4451	157	4421	159	4470	158
05225069-6955486	4190	121	4097	130	4129	118	4092	113	4127	113
05225632-6942269	4701	181	4678	212	4568	172	4634	189	4645	176
05225877-6938172	4707	199	4748	248	4619	202	4374	138	4612	181
05225980-6954368	4246	115	4148	135	4049	110	4124	128	4142	111
05230009-6935251	4286	131	4234	150	4217	126	4246	130	4246	127
05230011-6946353	5422	315	5273	314	5324	275	5155	285	5294	269
05230203-6935557	4555	163	4573	201	4465	155	4491	167	4521	161
05230230-6939587	4383	139	4161	146	4167	130	4173	127	4221	124

Continued on next page

2MASS ID	$(V_J - I_C)_0$		$(V_J - J_{2M})_0$		$(V_J - H_{2M})_0$		$(V_J - K_{2M})_0$		Average	
	$T_{\rm phot}$	$\sigma\left(T_{\rm phot}\right)$	$T_{\rm phot}$	$\sigma\left(T_{\rm phot}\right)$	$T_{\rm phot}$	$\sigma\left(T_{\rm phot}\right)$	$T_{\rm phot}$	$\sigma\left(T_{\rm phot}\right)$	$T_{\rm phot}$	$\sigma\left(T_{\rm phot}\right)$
	K	K	K	K	K	K	K	K	K	K
05230353-6952441	4195	115	4053	125	4066	110	4103	114	4104	108
05230370-6944219	4420	144	4332	164	4201	140	4291	154	4311	135
05230589-6944122	4886	225	4851	239	4847	195	4952	219	4884	205
05230606-6951113†	3928	97	3855	102	3893	95	3921	97	3929	90
05230647-6944394	4931	222	4838	244	4818	202	4768	218	4839	205
05230776-6946082	4578	165	4564	191	4522	160	4497	165	4540	162
05230867-6956329	4508	168	4585	216	4285	148	4255	112	4408	148
05231074-6939184	4552	156	4392	162	4423	148	4486	163	4463	150
05231091-6942374	4505	162	4237	155	4267	133	4323	138	4333	139
05231221-6938166	4625	186	4398	159	4476	152	4519	154	4505	154
05231315-6945212	4681	187	4515	216	4498	170	4461	167	4539	168
05231321-6946382	4147	108	4020	117	4052	107	4016	103	4059	102
05231411-6948546	4020	89	3868	94	3901	91	3919	90	3927	84
05231484-6950196	4427	150	4334	164	4289	137	4351	149	4350	141
05231562-6955430	4082	101	3989	120	3966	102	3994	104	4008	97
05231631-6942507	4337	137	4190	142	4229	127	4215	126	4243	126
05231634-6951332	4270	137	4341	198	4210	137	4337	161	4289	141
05231962-6943309	5257	287	5307	354	5262	257	4824	177	5162	250
05232020-6954561	4107	103	4014	121	4026	107	4036	107	4046	101
05232148-6952155	4177	113	4132	134	4057	107	4085	111	4112	109
05232181-6945429	4497	160	4471	190	4445	156	4291	139	4426	151
05232554-6943388	4764	202	4757	235	4500	160	4594	184	4654	183
05232624-6943558	4291	128	4254	153	3877	87	3864	82	4072	106
05232680-6953109	4478	160	4554	197	4413	148	4470	163	4479	158
05232845-6944158	4265	127	4166	141	4210	126	4247	133	4222	123
05232892-6947486	4364	147	4381	175	4283	134	4398	157	4356	144
05233236-6948257	4542	170	4424	186	4402	155	4237	141	4401	150
05235653-6947387	4708	201	4670	209	4578	161	4775	189	4683	179
05235851-6945519	4270	126	4147	135	4187	127	4157	124	4191	120
05240317-6953036	4484	156	4473	190	4418	156	4305	149	4420	150
05240482-6948280	4456	162	4551	213	4392	151	4425	165	4456	158
05240604-6942380	4047	96	4019	124	3931	97	3964	102	3990	95
05240613-6953529	4770	194	4525	188	4627	181	4611	199	4633	176
05240672-6947130	4516	171	4512	209	4538	176	4435	177	4500	166
05240803-6956250	4311	129	4253	149	4297	134	4261	135	4281	129
05240830-6944428	4131	109	4031	118	4025	104	4047	106	4058	103

Continued on next page

2MASS ID	$(V_J - I_C)_0$		$(V_J - J_{2M})_0$		$(V_J - H_{2M})_0$		$(V_J - K_{2M})_0$		Average	
	$T_{\rm phot}$	$\sigma\left(T_{\rm phot}\right)$	$T_{\rm phot}$	$\sigma\left(T_{\rm phot}\right)$	$T_{\rm phot}$	$\sigma\left(T_{\rm phot}\right)$	$T_{\rm phot}$	$\sigma\left(T_{\rm phot}\right)$	$T_{\rm phot}$	$\sigma\left(T_{\rm phot}\right)$
	K	K	K	K	K	K	K	K	K	K
05241033-6944374	4301	131	4177	147	4171	126	4152	124	4200	122
05241341-6945303	4331	136	4240	152	4174	121	4290	138	4259	129
05241479-6946323	5109	263	5208	304	5224	244	5080	248	5155	245
05241699-6942158	4339	137	4292	157	4261	129	4356	147	4312	135
05241794-6951317	4404	152	4202	150	4175	124	4266	145	4262	131
05242161-6942097	4295	129	4328	164	4203	125	4250	131	4269	129
05242198-6943579	4224	123	4168	119	4137	129	4153	105	4171	112
05242240-6944344	4174	113	4127	131	4052	106	4105	113	4114	109
05242409-6942051	4232	123	4102	131	4154	120	4168	123	4164	116
05242542-6955188	4487	166	4544	210	4465	158	4340	145	4459	158
05242687-6943577	4885	226	4946	246	4855	185	5019	224	4926	210
05242702-6956445	4362	142	4475	210	4311	146	4322	155	4368	147
05242811-6947467	4360	139	4279	156	4230	127	4284	138	4288	132
05243272-6955362	4207	117	4090	125	4150	118	4094	111	4135	111
05243734-6945496	4548	170	4864	300	4396	152	4646	219	4614	185
05243901-6948426	4501	163	4203	138	4463	157	4383	139	4388	144
05244189-6954427	4410	153	4522	189	4373	152	4507	166	4453	151
05244210-6942596	4549	168	4510	208	4569	187	4513	154	4535	166
05244301-6943412	4575	155	4573	175	4534	151	4602	164	4571	155
05244340-6950004	4336	139	4421	171	4214	135	4301	130	4318	133
05244408-6942423	4733	186	4666	206	4623	172	4710	193	4683	180
05244600-6946017	4373	144	4421	182	4405	155	4277	141	4369	144
05244637-6947340	4715	198	4940	259	4725	180	4729	189	4777	192
05244698-6956141	4265	126	4251	154	4281	133	4352	151	4287	132
05244878-6948359	4267	130	4310	139	4194	134	4290	121	4265	125
05244976-6943230	4231	119	4109	129	4125	116	4160	119	4156	114
05245212-6948184	4376	147	4347	181	4394	149	4319	141	4359	143
05245859-6952257	4496	161	4743	244	4511	168	4395	161	4536	168
05252428-6939311	4225	119	4163	135	4164	117	4082	109	4159	114
05252899-6939078	4822	214	4786	228	4813	192	4775	202	4799	194
05253039-6940288	4484	160	4427	177	4434	152	4354	145	4425	150
05253040-6936261	4336	134	4167	140	4169	121	4146	119	4205	121
05253235-6943137	4748	182	4744	216	4651	173	4665	187	4702	175
05253522-6937078	4340	135	4191	140	4193	122	4232	127	4239	124
05254540-6940531	4477	163	4400	178	4331	140	4432	164	4410	151
05254864-6940501	4308	135	4189	150	4254	135	4142	119	4223	125

Continued on next page

2MASS ID	$(V_J - I_C)_0$		$(V_J - J_{2M})_0$		$(V_J - H_{2M})_0$		$(V_J - K_{2M})_0$		Average	
	$T_{\rm phot}$ K	$\sigma\left(T_{\rm phot}\right)$ K	$T_{\rm phot}$ K	$\sigma\left(T_{\rm phot}\right)$ K	$T_{\rm phot}$ K	$\sigma\left(T_{\rm phot}\right)$ K	$T_{\rm phot}$ K	$\sigma\left(T_{\rm phot}\right)$ K	$T_{\rm phot}$ K	$\sigma\left(T_{\rm phot}\right)$ K
05255000-6942466	4087	104	4110	135	4089	114	4129	118	4104	109
05255267-6943155	4124	105	4011	115	4015	103	4058	105	4052	101
05255625-6941243	4982	239	4864	233	4822	181	4886	208	4888	205
05255801-6937309	4168	114	4074	127	4086	113	4132	117	4115	110
05255812-6942522	4315	137	4215	150	4329	140	4324	147	4296	134
05260124-6939268	4367	140	4333	162	4226	124	4180	122	4277	131
05260720-6942342	4879	224	5017	295	4690	187	4748	215	4834	211
05260784-6938341	4264	129	4123	133	4151	119	4077	110	4154	116
05261339-6940590	4034	94	3930	104	3965	96	3946	92	3969	90

† Computation of $T_{\rm phot}$ was not possible for all color indices.

Table 3.5: Photometric temperature scales for LMC inner disc stars. For each colour index, $T_{\rm phot}$ and its error. The last columns give the simple mean of the four estimates and the corresponding propagated error.

ID	$(V_J - I_C)_0$		$(V_J - J_{2M})_0$		$(V_J - H_{2M})_0$		$(V_J - K_{2M})_0$		Average	
	$T_{\rm phot}$ K	$\sigma\left(T_{\rm phot}\right)$ K	$T_{\rm phot}$ K	$\sigma\left(T_{\rm phot}\right)$ K	$T_{\rm phot}$ K	$\sigma\left(T_{\rm phot}\right)$ K	$T_{\rm phot}$ K	$\sigma\left(T_{\rm phot}\right)$ K	$T_{\rm phot}$ K	$\sigma\left(T_{\rm phot}\right)$ K
0499-LMCDisc01	4413	133	4262	136	4207	111	4176	108	4264	117
0512-LMCDisc01	4234	106	4110	114	4061	99	4108	102	4128	99
0522-LMCDisc01	4211	107	4019	107	4123	106	4050	96	4101	97
0533-LMCDisc01	4273	113	4140	121	4165	108	4174	109	4188	107
0534-LMCDisc01	4587	149	4234	128	4258	118	4295	124	4344	124
0546-LMCDisc01	4276	111	4168	122	4184	111	4149	108	4194	107
0548-LMCDisc01	4279	116	4070	112	4044	96	4062	98	4114	100
0564-LMCDisc01	4660	149	4453	145	4560	147	4573	153	4561	139
0565-LMCDisc01	4204	104	4087	113	4072	100	4052	97	4104	97
0576-LMCDisc01	4417	125	4176	121	4202	114	4089	101	4221	109
0593-LMCDisc01	4212	100	4020	101	3990	91	4023	93	4061	90
0599-LMCDisc01	4277	114	4033	107	4033	95	4070	97	4103	98
0601-LMCDisc01	4247	114	4188	111	4188	119	4246	106	4217	106
0606-LMCDisc01	4415	112	4285	117	4228	110	4288	116	4304	107
0611-LMCDisc01	4148	100	4044	110	4050	97	4072	99	4078	95
0614-LMCDisc01	4133	112	4125	108	4093	120	4089	92	4110	101
0620-LMCDisc01	4279	117	4085	116	4108	103	4194	114	4166	106
0625-LMCDisc01	4142	96	4006	102	4013	94	3991	91	4038	90
0629-LMCDisc01	4341	119	4206	126	4233	115	4190	112	4242	112
0631-LMCDisc01	4301	119	4250	140	4256	118	4163	111	4243	115
0633-LMCDisc01	4189	106	4142	105	4077	115	4188	100	4149	100
0640-LMCDisc01	4332	117	4234	134	4165	109	4178	110	4227	111
0646-LMCDisc01	4304	120	4242	134	4271	120	4311	128	4282	118
0651-LMCDisc01	4247	114	4217	116	4177	121	4196	101	4209	106
0655-LMCDisc01†	4138	99	4092	98	4047	97	4115	92	4093	90
0656-LMCDisc01	4255	113	4118	119	4157	110	4116	104	4161	105
0658-LMCDisc01	4257	113	4145	129	4132	108	4075	100	4152	104
0664-LMCDisc01	4034	86	3945	97	3951	86	3952	85	3971	82
0666-LMCDisc01	4399	128	4231	131	4347	130	4294	127	4317	121
0671-LMCDisc01	4185	102	4042	107	4074	100	4044	96	4087	95
0672-LMCDisc01	4079	91	3963	101	3939	87	3966	86	3987	85
0679-LMCDisc01	4114	95	3991	104	3997	92	4030	95	4033	90

Continued on next page

ID	$(V_J - I_C)_0$		$(V_J - J_{2M})_0$		$(V_J - H_{2M})_0$		$(V_J - K_{2M})_0$		Average	
	$T_{\rm phot}$	$\sigma\left(T_{\rm phot}\right)$	$T_{\rm phot}$	$\sigma\left(T_{\rm phot}\right)$	$T_{\rm phot}$	$\sigma\left(T_{\rm phot}\right)$	$T_{\rm phot}$	$\sigma\left(T_{\rm phot}\right)$	$T_{\rm phot}$	$\sigma\left(T_{\rm phot}\right)$
	K	K	K	K	K	K	K	K	K	K
0690-LMCDisc01†	4072	91	3882	91	3890	81	3916	82	3904	80
0699-LMCDisc01	4727	177	4531	180	4527	143	4743	185	4632	162
0700-LMCDisc01	4215	109	4100	118	4070	100	4035	95	4105	99
0701-LMCDisc01†	4145	101	4126	104	4017	94	4090	89	4089	90
0705-LMCDisc01	4405	132	4293	144	4267	120	4279	125	4311	123
0706-LMCDisc01	4429	132	4380	153	4306	125	4337	132	4363	128
0710-LMCDisc01	4119	96	3873	88	3906	83	3900	79	3949	80
0720-LMCDisc01	4404	129	4239	134	4250	119	4423	148	4329	124
0721-LMCDisc01	4222	103	4009	103	4018	96	4008	94	4064	92
0728-LMCDisc01	4286	113	4192	127	4119	106	4217	118	4203	109
0731-LMCDisc01†	3998	83	3874	89	3882	81	3913	82	3881	77
0748-LMCDisc01	4172	104	4217	116	4114	117	4160	98	4166	102
0752-LMCDisc01†	4146	102	3925	96	4005	93	3985	91	3979	89
0756-LMCDisc01	3986	79	3878	90	3871	80	3883	78	3904	75
0758-LMCDisc01	4474	139	4397	160	4402	141	4468	155	4435	137
0766-LMCDisc01†	4191	110	4110	104	4045	99	4148	97	4118	95
0773-LMCDisc01	4107	95	4015	110	3965	87	3948	83	4009	88
0775-LMCDisc01	4399	128	4209	131	4360	130	4302	128	4318	121
0776-LMCDisc01	4288	115	4192	127	4304	127	4240	120	4256	115
0782-LMCDisc01	4236	113	4201	113	4129	119	4156	96	4180	104
0789-LMCDisc01†	3982	81	3823	83	3843	78	3835	74	3834	72
0790-LMCDisc01	4094	88	3945	95	3917	85	3937	85	3973	82
0793-LMCDisc01	4202	105	4096	116	4056	100	4088	103	4111	99
0808-LMCDisc01	4547	137	4538	160	4552	144	4537	149	4543	138
0834-LMCDisc01	4144	97	3994	101	3969	91	4039	97	4037	90
0835-LMCDisc01†	3982	83	3790	79	3831	77	3849	75	3827	71
0854-LMCDisc01	4275	115	4162	125	4144	108	4195	116	4194	109
0855-LMCDisc01	4313	118	4167	123	4153	108	4150	112	4196	108
0859-LMCDisc01	4154	101	4004	106	4087	102	4041	97	4071	94
0879-LMCDisc01†	4399	131	NaN	NaN	NaN	NaN	NaN	NaN	4366	32
0900-LMCDisc01	4276	118	4250	120	4163	120	4213	103	4225	109
0937-LMCDisc01	4463	122	4217	112	4191	107	4134	101	4251	103
1055-LMCDisc01	4334	118	4141	122	4140	110	4136	111	4188	107
1105-LMCDisc01	4185	102	3935	97	3964	91	3967	90	4013	88
1118-LMCDisc01	4375	131	4351	137	4262	127	4239	110	4307	118

† Computation of $T_{\rm phot}$ was not possible for all color indices.

Table 3.6: Final stellar parameters (and associated errors) for LMC bar stars: star identifier, $T_{\rm phot}$, $\log g$, [M/H], $\xi_{\rm micro}$, [Fe I/H], [Fe II/H].

2MASS ID	$T_{\rm phot}$ K	$\sigma(T_{\rm phot})$ K	$\log g$	$\sigma(\log g)$	[M/H] dex	σ([M/H]) dex	$\xi_{\rm micro}$ km s^{-1}	$\sigma(\xi_{\rm micro})$ km s^{-1}	[Fe I/H] dex	σ([Fe I/H]) dex	[Fe II/H] dex	σ([Fe II/H]) dex
05223082-6944147	4070	102	0.98	0.15	-0.49	0.10	1.80	0.15	-0.48	0.04	-0.49	0.15
05223112-6945292	4025	98	0.85	0.14	-0.71	0.10	1.80	0.15	-0.71	0.03	-0.65	0.11
05223186-6947159	4277	134	1.21	0.16	-0.70	0.10	1.90	0.15	-0.71	0.03	-0.78	0.13
05223309-6946595	4401	151	1.21	0.19	-0.68	0.10	2.00	0.15	-0.68	0.03	-0.90	0.10
05223316-6951389	NaN	NaN	NaN	NaN	NaN	NaN	NaN	NaN	NaN	NaN	NaN	NaN
05223318-6937044	4421	152	1.36	0.18	-0.63	0.10	2.40	0.15	-0.63	0.06	-0.87	0.16
05223416-6944433	4641	187	1.41	0.17	-1.18	0.10	1.90	0.15	-1.18	0.03	-1.16	0.06
05223487-6938057	4316	137	1.24	0.16	-0.74	0.10	2.20	0.15	-0.75	0.04	-0.75	0.11
05223506-6937279	4190	123	1.11	0.16	-0.68	0.10	1.90	0.15	-0.67	0.05	-0.70	0.09
05223557-6943373	4676	185	1.44	0.16	-1.40	0.10	1.90	0.15	-1.39	0.03	-1.38	0.09
05223701-6936166	4729	186	1.75	0.14	-0.37	0.10	1.90	0.15	-0.37	0.03	-0.41	0.09
05223787-6954562	4003	93	1.05	0.14	-0.29	0.10	1.70	0.15	-0.28	0.04	-0.31	0.11
05223895-6945007	4279	130	1.06	0.17	-0.66	0.10	2.00	0.15	-0.67	0.03	-0.82	0.07
05223988-6946110	4183	117	0.94	0.16	-0.82	0.10	1.90	0.15	-0.83	0.04	-0.78	0.15
05224062-6953310	4137	112	1.04	0.14	-0.78	0.10	2.10	0.15	-0.77	0.04	-0.75	0.14
05224164-6935518	4347	137	1.38	0.18	-0.44	0.10	1.80	0.15	-0.45	0.03	-0.68	0.13
05224195-6941099	4200	121	1.12	0.16	-0.62	0.10	1.80	0.15	-0.59	0.03	-0.66	0.13
05224240-6940567	NaN	NaN	NaN	NaN	NaN	NaN	NaN	NaN	NaN	NaN	NaN	NaN
05224276-6940109	4378	144	1.17	0.20	-0.57	0.10	1.70	0.15	-0.53	0.03	-0.77	0.04
05224309-6940275	4151	114	1.02	0.15	-0.80	0.10	2.10	0.15	-0.79	0.04	-0.79	0.12
05224321-6952397	4275	131	1.19	0.16	-0.68	0.10	2.00	0.15	-0.70	0.03	-0.80	0.15
05224448-6954402	4585	174	1.50	0.23	-0.66	0.10	1.80	0.15	-0.66	0.03	-0.81	0.17
05224854-6940010	4080	108	1.27	0.12	-0.58	0.10	1.90	0.15	-0.58	0.05	-0.45	0.16
05225062-6936580	4470	158	1.35	0.20	-0.62	0.10	2.00	0.15	-0.63	0.03	-0.91	0.09
05225069-6955486	4127	113	1.09	0.15	-0.58	0.10	1.80	0.15	-0.58	0.05	-0.55	0.19
05225632-6942269	NaN	NaN	NaN	NaN	NaN	NaN	NaN	NaN	NaN	NaN	NaN	NaN
05225877-6938172	4612	181	1.63	0.26	-0.60	0.10	2.00	0.15	-0.60	0.03	-0.83	0.05
05225980-6954368	NaN	NaN	NaN	NaN	NaN	NaN	NaN	NaN	NaN	NaN	NaN	NaN
05230009-6935251	4246	127	1.14	0.17	-0.56	0.10	1.90	0.15	-0.55	0.04	-0.75	0.11
05230011-6946353	5294	269	2.17	0.08	-0.15	0.10	2.30	0.15	-0.15	0.03	-0.43	0.06
05230203-6935557	4521	161	1.27	0.16	-1.17	0.10	1.70	0.15	-1.17	0.03	-1.37	0.10
05230230-6939587	4221	124	1.09	0.13	-1.10	0.10	2.20	0.15	-1.08	0.04	-1.09	0.06
05230353-6952441	4104	108	1.01	0.14	-0.76	0.10	2.00	0.15	-0.77	0.04	-0.66	0.13
05230370-6944219	4311	135	1.34	0.09	-1.50	0.10	1.30	0.15	-1.48	0.02	-1.10	0.11

Continued on next page

2MASS ID	$T_{\rm phot}$ K	$\sigma(T_{\rm phot})$ K	$\log g$	$\sigma(\log g)$	[M/H] dex	σ([M/H]) dex	$\xi_{\rm micro}$ km s^{-1}	$\sigma(\xi_{\rm micro})$ km s^{-1}	[Fe I/H] dex	σ([Fe I/H]) dex	[Fe II/H] dex	σ([Fe II/H]) dex
05230589-6944122	4884	205	1.79	0.14	-0.36	0.10	2.10	0.15	-0.37	0.03	-0.59	0.03
05230606-6951113	3929	90	1.05	0.14	-0.26	0.10	1.50	0.15	-0.23	0.05	-0.13	0.18
05230647-6944394	4839	205	1.46	0.20	-1.43	0.10	1.80	0.15	-1.42	0.02	-1.54	0.05
05230776-6946082	4540	162	1.16	0.17	-1.17	0.10	1.70	0.15	-1.19	0.03	-1.20	0.02
05230867-6956329	4408	148	1.61	0.20	-0.41	0.10	2.10	0.15	-0.40	0.05	-0.45	0.20
05231074-6939184	4463	150	1.13	0.14	-1.49	0.10	1.80	0.15	-1.49	0.02	-1.51	0.07
05231091-6942374	4333	139	1.10	0.19	-0.64	0.10	1.90	0.15	-0.64	0.03	-0.91	0.09
05231221-6938166	4505	154	1.70	0.17	-0.19	0.10	1.70	0.15	-0.20	0.03	-0.15	0.07
05231315-6945212	4539	168	1.32	0.20	-0.82	0.10	1.90	0.15	-0.83	0.05	-1.21	0.12
05231321-6946382	4059	102	0.88	0.14	-0.72	0.10	2.00	0.15	-0.73	0.04	-0.74	0.13
05231411-6948546	3927	84	0.73	0.12	-0.86	0.10	2.10	0.15	-0.83	0.05	-0.55	0.14
05231484-6950196	4350	141	1.28	0.17	-0.66	0.10	2.00	0.15	-0.66	0.04	-0.70	0.10
05231562-6955430	4008	97	0.88	0.13	-0.73	0.10	1.90	0.15	-0.72	0.05	-0.60	0.13
05231631-6942507	4243	126	1.09	0.16	-0.62	0.10	2.10	0.15	-0.65	0.04	-0.66	0.14
05231634-6951332	4289	141	1.28	0.15	-0.84	0.10	2.00	0.15	-0.85	0.03	-0.89	0.07
05231962-6943309	5162	250	2.14	0.09	-0.24	0.10	2.10	0.15	-0.24	0.03	-0.47	0.05
05232020-6954561	4046	101	0.77	0.15	-0.79	0.10	1.80	0.15	-0.78	0.04	-0.74	0.08
05232148-6952155	4112	109	0.99	0.14	-0.74	0.10	2.00	0.15	-0.74	0.03	-0.78	0.14
05232181-6945429	4426	151	1.30	0.18	-0.69	0.10	1.70	0.15	-0.69	0.03	-0.93	0.06
05232554-6943388	NaN	NaN	NaN	NaN	NaN	NaN	NaN	NaN	NaN	NaN	NaN	NaN
05232624-6943558	4072	106	0.94	0.13	-0.88	0.10	2.00	0.15	-0.88	0.03	-0.83	0.10
05232680-6953109	4479	158	1.38	0.22	-0.57	0.10	1.60	0.15	-0.58	0.03	-0.90	0.08
05232845-6944158	4222	123	1.09	0.16	-0.70	0.10	2.00	0.15	-0.69	0.04	-0.87	0.12
05232892-6947486	4356	144	1.26	0.17	-0.61	0.10	1.70	0.15	-0.62	0.03	-0.88	0.05
05233236-6948257	4401	150	1.42	0.14	-0.95	0.10	1.50	0.15	-1.01	0.06	-0.80	0.11
05235653-6947387	4683	179	1.72	0.16	-0.42	0.10	1.80	0.15	-0.42	0.03	-0.62	0.05
05235851-6945519	4191	120	1.08	0.15	-0.78	0.10	2.20	0.15	-0.77	0.03	-0.78	0.12
05240317-6953036	4420	150	1.41	0.15	-0.90	0.10	2.20	0.15	-0.91	0.04	-0.96	0.09
05240482-6948280	4456	158	1.38	0.17	-0.79	0.10	1.80	0.15	-0.79	0.03	-1.03	0.05
05240604-6942380	3990	95	1.22	0.11	-0.49	0.10	1.50	0.15	-0.50	0.05	-0.07	0.06
05240613-6953529	4633	176	1.47	0.14	-1.50	0.10	1.10	0.15	-1.50	0.03	-1.45	0.04
05240672-6947130	4500	166	1.48	0.20	-0.60	0.10	1.90	0.15	-0.60	0.04	-0.72	0.07
05240803-6956250	4281	129	1.18	0.15	-0.90	0.10	2.40	0.15	-0.89	0.04	-0.93	0.14
05240830-6944428	4058	103	0.88	0.14	-0.77	0.10	1.80	0.15	-0.78	0.04	-0.78	0.08
05241033-6944374	4200	122	1.12	0.14	-0.83	0.10	2.00	0.15	-0.84	0.03	-0.89	0.10
05241341-6945303	4259	129	1.15	0.16	-0.60	0.10	1.80	0.15	-0.62	0.04	-0.80	0.06
05241479-6946323	5155	245	2.07	0.09	-0.10	0.10	2.10	0.15	-0.12	0.03	-0.41	0.04
05241699-6942158	4312	135	1.22	0.16	-0.66	0.10	2.20	0.15	-0.66	0.04	-0.89	0.07

Continued on next page

2MASS ID	$T_{\rm phot}$ K	$\sigma(T_{\rm phot})$ K	$\log g$	$\sigma(\log g)$	[M/H] dex	σ([M/H]) dex	$\xi_{\rm micro}$ km s^{-1}	$\sigma(\xi_{\rm micro})$ km s^{-1}	[Fe I/H] dex	σ([Fe I/H]) dex	[Fe II/H] dex	σ([Fe II/H]) dex
05241794-6951317	4262	131	1.31	0.14	-0.78	0.10	1.90	0.15	-0.79	0.04	-0.71	0.08
05242161-6942097	4269	129	1.15	0.15	-0.82	0.10	1.90	0.15	-0.83	0.03	-0.93	0.06
05242198-6943579	4171	112	1.10	0.16	-0.46	0.10	1.70	0.15	-0.46	0.04	-0.76	0.16
05242240-6944344	4114	109	0.99	0.14	-0.75	0.10	2.00	0.15	-0.76	0.04	-0.75	0.12
05242409-6942051	4164	116	1.01	0.16	-0.63	0.10	1.80	0.15	-0.63	0.03	-0.71	0.12
05242542-6955188	4459	158	1.38	0.24	-0.56	0.10	1.90	0.15	-0.56	0.03	-0.77	0.06
05242687-6943577	4926	210	1.87	0.13	-0.25	0.10	2.20	0.15	-0.25	0.03	-0.50	0.04
05242702-6956445	4368	147	1.37	0.17	-0.56	0.10	1.80	0.15	-0.56	0.03	-0.82	0.04
05242811-6947467	4288	132	1.16	0.16	-0.81	0.10	1.90	0.15	-0.81	0.03	-0.99	0.07
05243272-6955362	4135	111	0.92	0.15	-0.80	0.10	1.80	0.15	-0.78	0.04	-0.85	0.04
05243734-6945496	4614	185	1.59	0.24	-0.61	0.10	2.10	0.15	-0.61	0.04	-0.84	0.10
05243901-6948426	4388	144	1.25	0.22	-0.63	0.10	1.70	0.15	-0.64	0.03	-0.65	0.07
05244189-6954427	4453	151	1.49	0.20	-0.47	0.10	1.80	0.15	-0.48	0.03	-0.72	0.10
05244210-6942596	4535	166	1.53	0.18	-0.78	0.10	1.60	0.15	-0.76	0.05	-0.68	0.10
05244301-6943412	NaN	NaN	NaN	NaN	NaN	NaN	NaN	NaN	NaN	NaN	NaN	NaN
05244340-6950004	4318	133	1.38	0.17	-0.48	0.10	1.70	0.15	-0.47	0.03	-0.66	0.12
05244408-6942423	4683	180	1.25	0.19	-1.29	0.10	1.80	0.15	-1.29	0.03	-1.33	0.04
05244600-6946017	4369	144	1.32	0.17	-0.66	0.10	2.20	0.15	-0.65	0.03	-0.83	0.11
05244637-6947340	4777	192	1.93	0.16	-0.29	0.10	2.00	0.15	-0.29	0.03	-0.63	0.04
05244698-6956141	4287	132	1.26	0.15	-0.71	0.10	2.10	0.15	-0.70	0.04	-0.72	0.08
05244878-6948359	4265	125	1.17	0.18	-0.48	0.10	1.80	0.15	-0.46	0.03	-0.73	0.13
05244976-6943230	4156	114	1.00	0.15	-0.83	0.10	1.90	0.15	-0.82	0.03	-0.79	0.07
05245212-6948184	4359	143	1.25	0.17	-0.73	0.10	1.90	0.15	-0.72	0.04	-0.76	0.06
05245859-6952257	4536	168	1.51	0.20	-0.68	0.10	1.90	0.15	-0.67	0.03	-0.56	0.22
05252428-6939311	4159	114	1.04	0.15	-0.70	0.10	2.10	0.15	-0.69	0.04	-0.93	0.12
05252899-6939078	4799	194	1.95	0.17	-0.33	0.10	2.00	0.15	-0.33	0.03	-0.60	0.06
05253039-6940288	4425	150	1.34	0.18	-0.63	0.10	2.10	0.15	-0.64	0.04	-0.84	0.13
05253040-6936261	4205	121	1.08	0.15	-0.85	0.10	1.70	0.15	-0.86	0.03	-0.79	0.10
05253235-6943137	NaN	NaN	NaN	NaN	NaN	NaN	NaN	NaN	NaN	NaN	NaN	NaN
05253522-6937078	4239	124	1.05	0.15	-0.88	0.10	2.30	0.15	-0.87	0.04	-0.76	0.14
05254540-6940531	4410	151	1.36	0.17	-0.69	0.10	2.00	0.15	-0.68	0.04	-0.93	0.05
05254864-6940501	4223	125	1.17	0.16	-0.61	0.10	1.80	0.15	-0.61	0.03	-0.79	0.02
05255000-6942466	4104	109	0.97	0.14	-0.76	0.10	1.90	0.15	-0.76	0.04	-0.80	0.11
05255267-6943155	4052	101	0.88	0.14	-0.72	0.10	2.00	0.15	-0.72	0.04	-0.83	0.08
05255625-6941243	4888	205	1.86	0.14	-0.39	0.10	2.10	0.15	-0.38	0.04	-0.71	0.04
05255801-6937309	4115	110	0.98	0.16	-0.59	0.10	2.00	0.15	-0.57	0.04	-0.69	0.14
05255812-6942522	4296	134	1.30	0.16	-0.58	0.10	1.90	0.15	-0.58	0.04	-0.80	0.06
05260124-6939268	4277	131	1.15	0.16	-0.70	0.10	1.60	0.15	-0.70	0.03	-0.83	0.08

Continued on next page

2MASS ID	$T_{\rm phot}$ K	$\sigma(T_{\rm phot})$ K	$\log g$	$\sigma(\log g)$	[M/H] dex	σ([M/H]) dex	$\xi_{\rm micro}$ km s^{-1}	$\sigma(\xi_{\rm micro})$ km s^{-1}	[Fe I/H] dex	σ([Fe I/H]) dex	[Fe II/H] dex	σ([Fe II/H]) dex
05260720-6942342	4834	211	1.89	0.22	-0.52	0.10	1.80	0.15	-0.52	0.04	-0.52	0.07
05260784-6938341	4154	116	0.99	0.14	-0.88	0.10	1.00	0.15	-0.88	0.05	-0.77	0.20
05261339-6940590	3969	90	0.81	0.14	-0.66	0.10	2.10	0.15	-0.59	0.06	-0.60	0.19

Table 3.7: Final stellar parameters (and associated errors) for LMC inner disc stars: star identifier, $T_{\rm phot}$, $\log g$, [M/H], $\xi_{\rm micro}$, [Fe I/H], [Fe II/H].

ID	$T_{\rm phot}$ K	$\sigma(T_{\rm phot})$ K	$\log g$	$\sigma(\log g)$	[M/H] dex	σ([M/H]) dex	$\xi_{\rm micro}$ km s^{-1}	$\sigma(\xi_{\rm micro})$ km s^{-1}	[Fe I/H] dex	σ([Fe I/H]) dex	[Fe II/H] dex	σ([Fe II/H]) dex
0499-LMCDisc01	4264	117	1.07	0.15	-0.69	0.10	1.90	0.15	-0.71	0.03	-0.78	0.07
0512-LMCDisc01	4128	99	0.88	0.13	-0.91	0.10	1.80	0.15	-0.91	0.03	-0.78	0.04
0522-LMCDisc01	4101	97	0.91	0.15	-0.66	0.10	1.90	0.15	-0.67	0.03	-0.73	0.09
0533-LMCDisc01	4188	107	0.96	0.15	-0.78	0.10	2.10	0.15	-0.77	0.04	-0.81	0.09
0534-LMCDisc01	4344	124	1.11	0.13	-1.21	0.10	1.60	0.15	-1.21	0.02	-1.18	0.08
0546-LMCDisc01	4194	107	0.96	0.14	-0.97	0.10	1.80	0.15	-0.98	0.02	-0.88	0.07
0548-LMCDisc01	4114	100	0.96	0.15	-0.63	0.10	1.90	0.15	-0.63	0.03	-0.61	0.05
0564-LMCDisc01	NaN	NaN	NaN	NaN	NaN	NaN	NaN	NaN	NaN	NaN	NaN	NaN
0565-LMCDisc01	4104	97	0.90	0.14	-0.89	0.10	1.90	0.15	-0.88	0.03	-0.73	0.06
0576-LMCDisc01	4221	109	1.02	0.11	-1.33	0.10	1.80	0.15	-1.30	0.03	-1.10	0.04
0593-LMCDisc01	4061	90	0.89	0.10	-1.19	0.10	2.00	0.15	-1.20	0.02	-0.85	0.07
0599-LMCDisc01	4103	98	0.94	0.13	-0.79	0.10	1.80	0.15	-0.80	0.03	-0.71	0.04
0601-LMCDisc01	4217	106	1.15	0.16	-0.40	0.10	1.90	0.15	-0.39	0.04	-0.55	0.09
0606-LMCDisc01	4304	107	1.09	0.05	-2.07	0.10	1.60	0.15	-2.09	0.02	-1.72	0.08
0611-LMCDisc01	4078	95	0.95	0.15	-0.56	0.10	1.80	0.15	-0.55	0.03	-0.58	0.11
0614-LMCDisc01	4110	101	1.02	0.16	-0.38	0.10	1.50	0.15	-0.38	0.05	-0.59	0.15
0620-LMCDisc01	4166	106	1.08	0.15	-0.57	0.10	1.80	0.15	-0.54	0.05	-0.71	0.09
0625-LMCDisc01	4038	90	0.86	0.13	-0.80	0.10	2.00	0.15	-0.79	0.03	-0.62	0.16
0629-LMCDisc01	4242	112	1.05	0.14	-0.98	0.10	1.90	0.15	-1.00	0.03	-0.79	0.04
0631-LMCDisc01	4243	115	1.09	0.16	-0.49	0.10	1.70	0.15	-0.50	0.04	-0.66	0.09
0633-LMCDisc01	4149	100	1.06	0.15	-0.47	0.10	1.70	0.15	-0.47	0.04	-0.68	0.17
0640-LMCDisc01	4227	111	1.03	0.12	-1.08	0.10	2.30	0.15	-1.12	0.04	-0.85	0.16
0646-LMCDisc01	4282	118	1.13	0.16	-0.62	0.10	1.80	0.15	-0.62	0.04	-0.80	0.08
0651-LMCDisc01	4209	106	1.16	0.16	-0.40	0.10	1.80	0.15	-0.40	0.04	-0.55	0.09
0655-LMCDisc01	4093	90	1.01	0.14	-0.55	0.10	1.90	0.15	-0.55	0.03	-0.52	0.13
0656-LMCDisc01	4161	105	1.06	0.15	-0.61	0.10	1.90	0.15	-0.57	0.04	-0.47	0.15
0658-LMCDisc01	4152	104	1.04	0.15	-0.64	0.10	2.00	0.15	-0.64	0.05	-0.70	0.16
0664-LMCDisc01	3971	82	0.85	0.14	-0.49	0.10	1.80	0.15	-0.49	0.04	-0.37	0.06
0666-LMCDisc01	4317	121	1.13	0.15	-0.96	0.10	1.70	0.15	-0.96	0.03	-0.83	0.05
0671-LMCDisc01	4087	95	0.93	0.13	-0.82	0.10	2.00	0.15	-0.81	0.03	-0.77	0.10
0672-LMCDisc01	3987	85	0.88	0.14	-0.50	0.10	1.70	0.15	-0.50	0.04	-0.47	0.04
0679-LMCDisc01	4033	90	0.93	0.14	-0.57	0.10	1.90	0.15	-0.55	0.04	-0.56	0.02
0690-LMCDisc01	3904	80	0.82	0.14	-0.44	0.10	1.70	0.15	-0.44	0.04	-0.43	0.12
0699-LMCDisc01	4632	162	1.70	0.22	-0.50	0.10	1.50	0.15	-0.50	0.03	-0.58	0.06

Continued on next page

ID	$T_{\rm phot}$ K	$\sigma(T_{\rm phot})$ K	$\log g$	$\sigma(\log g)$	[M/H] dex	σ([M/H]) dex	$\xi_{\rm micro}$ km s^{-1}	$\sigma(\xi_{\rm micro})$ km s^{-1}	[Fe I/H] dex	σ([Fe I/H]) dex	[Fe II/H] dex	σ([Fe II/H]) dex
0700-LMCDisc01	4105	99	1.04	0.15	-0.51	0.10	1.80	0.15	-0.48	0.05	-0.66	0.18
0701-LMCDisc01	4089	90	1.04	0.14	-0.40	0.10	1.80	0.15	-0.42	0.05	-0.40	0.21
0705-LMCDisc01	4311	123	1.19	0.16	-0.66	0.10	1.80	0.15	-0.66	0.03	-0.68	0.04
0706-LMCDisc01	NaN	NaN	NaN	NaN	NaN	NaN	NaN	NaN	NaN	NaN	NaN	NaN
0710-LMCDisc01	3949	80	0.86	0.13	-0.59	0.10	1.70	0.15	-0.59	0.04	-0.45	0.11
0720-LMCDisc01	4329	124	1.20	0.15	-0.89	0.10	1.80	0.15	-0.89	0.03	-0.95	0.11
0721-LMCDisc01	NaN	NaN	NaN	NaN	NaN	NaN	NaN	NaN	NaN	NaN	NaN	NaN
0728-LMCDisc01	4203	109	1.06	0.14	-0.85	0.10	2.10	0.15	-0.85	0.04	-0.67	0.02
0731-LMCDisc01	3881	77	0.82	0.14	-0.35	0.10	1.60	0.15	-0.35	0.04	-0.21	0.10
0748-LMCDisc01	4166	102	1.13	0.15	-0.49	0.10	1.70	0.15	-0.51	0.05	-0.32	0.21
0752-LMCDisc01	3979	89	0.98	0.14	-0.31	0.10	1.70	0.15	-0.30	0.04	-0.41	0.06
0756-LMCDisc01	3904	75	0.79	0.13	-0.55	0.10	1.70	0.15	-0.55	0.04	-0.34	0.07
0758-LMCDisc01	NaN	NaN	NaN	NaN	NaN	NaN	NaN	NaN	NaN	NaN	NaN	NaN
0766-LMCDisc01	4118	95	1.22	0.16	-0.21	0.10	1.40	0.15	-0.15	0.05	-0.05	0.09
0773-LMCDisc01	4009	88	0.92	0.14	-0.57	0.10	1.90	0.15	-0.56	0.04	-0.32	0.14
0775-LMCDisc01	4318	121	1.16	0.14	-0.96	0.10	1.50	0.15	-0.96	0.02	-0.85	0.04
0776-LMCDisc01	4256	115	1.14	0.15	-0.81	0.10	1.90	0.15	-0.81	0.03	-0.74	0.07
0782-LMCDisc01	4180	104	1.17	0.15	-0.50	0.10	1.70	0.15	-0.45	0.04	-0.40	0.10
0789-LMCDisc01	3834	72	0.77	0.13	-0.36	0.10	1.70	0.15	-0.36	0.04	-0.05	0.15
0790-LMCDisc01	NaN	NaN	NaN	NaN	NaN	NaN	NaN	NaN	NaN	NaN	NaN	NaN
0793-LMCDisc01	4111	99	1.02	0.13	-0.74	0.10	1.90	0.15	-0.73	0.03	-0.60	0.08
0808-LMCDisc01	NaN	NaN	NaN	NaN	NaN	NaN	NaN	NaN	NaN	NaN	NaN	NaN
0834-LMCDisc01	4037	90	0.95	0.12	-0.78	0.10	1.90	0.15	-0.77	0.03	-0.53	0.15
0835-LMCDisc01	NaN	NaN	NaN	NaN	NaN	NaN	NaN	NaN	NaN	NaN	NaN	NaN
0854-LMCDisc01	4194	109	1.16	0.15	-0.63	0.10	1.90	0.15	-0.62	0.04	-0.70	0.13
0855-LMCDisc01	4196	108	1.12	0.13	-0.80	0.10	1.90	0.15	-0.83	0.04	-0.71	0.07
0859-LMCDisc01	4071	94	1.04	0.14	-0.55	0.10	1.70	0.15	-0.53	0.04	-0.51	0.10
0879-LMCDisc01	NaN	NaN	NaN	NaN	NaN	NaN	NaN	NaN	NaN	NaN	NaN	NaN
0900-LMCDisc01	4225	109	1.22	0.15	-0.51	0.10	1.90	0.15	-0.47	0.04	-0.57	0.09
0937-LMCDisc01	NaN	NaN	NaN	NaN	NaN	NaN	NaN	NaN	NaN	NaN	NaN	NaN
1055-LMCDisc01	4188	107	1.20	0.10	-1.08	0.10	1.40	0.15	-1.08	0.02	-0.75	0.07
1105-LMCDisc01	4013	88	1.07	0.10	-0.73	0.10	1.70	0.15	-0.74	0.04	-0.28	0.08
1118-LMCDisc01	4307	118	1.40	0.17	-0.26	0.10	1.60	0.15	-0.27	0.04	-0.65	0.12

Chapter 4

Abundance analysis

Contents

4.1 From absorption lines to chemical abundances

4.1.1 Concept

The shape of absorption lines that populate stellar spectra is governed by the quantum characteristics of the radiative transition involved in the absorption (excitation potential, oscillator strength, natural width of energy levels, rotational for molecules, etc.), physical conditions existing in the stellar photosphere (temperature, pressure and density gradients, micro- and macroturbulence, rotation, etc.) and the abundance of the absorbing species (see Sec. 4.1.3 and 4.1.4). Thus, for a given star, once the stellar parameters are known (see Chapter 3) and with the help of atomic and molecular databases, absorption lines can be used as the access door to individual *chemical abundances* (i.e. the quantitative amount of a given element) of elements present in a stellar photosphere (see Sec. 4.2).

4.1.2 Radiative transfer

The radiative transfer equation is:

$$\frac{\mathrm{d}I_\nu}{\mathrm{d}s} = j_\nu - \kappa_\nu I_\nu \tag{4.1}$$

and means that the variation of the specific intensity I_ν over a distance s is due to the energy losses (energy absorbed by the matter) $\kappa_\nu I_\nu$ and the energy gains (energy emitted by the matter) j_ν. κ_ν is called the *absorption coefficient* (*opacity*) and j_ν is called the *emission coefficient*. The radiative transfer equation is often rewritten:

$$\frac{\mathrm{d}I_\nu}{\mathrm{d}\tau_\nu} = S_\nu - I_\nu \tag{4.2}$$

where $S_\nu = j_\nu/\kappa_\nu$ is the *source function* and $\tau_\nu = \int_{\text{path}} \kappa_\nu \, \mathrm{d}s$ is the optical depth. The general solution of Equation 4.2 is:

$$I_\nu(\tau_\nu) = \int_0^{\tau_\nu} S_\nu(t_\nu) \mathrm{e}^{-(\tau_\nu - t_\nu)} \, \mathrm{d}t_\nu + I_\nu(0)\mathrm{e}^{-\tau_\nu} \tag{4.3}$$

Thus to determine the emergent flux in a line, one needs to know S_ν, i.e. j_ν and κ_ν. If we assume local thermodynamic equilibrium (LTE), then S_ν is given by the Planck function. κ_ν is given by the convolution of absorption profiles described in the next section.

4.1.3 Line profile

4.1.3.1 Microscopic effects

The profile of an absorption line, recorded at the focal point of a {telescope + spectrograph} system, has a non-zero width and is the result of multiple broadening mechanisms, briefly recalled hereafter.

Natural (or radiation) broadening An absorption line centred at the wavelength $\lambda_0 = c/\nu_0$ is due to the absorption of photons by an atom excited from an energy level $\chi_{r,i}$ to an energy level $\chi_{r,j}$, such that $\chi_{r,j} - \chi_{r,i} = h\nu_0$ (bound–bound transition). By virtue of the Heisenberg uncertainty principle, each energy level involved in the radiative transition has a non-zero natural width, i.e. the excited atom has a finite lifetime. Therefore, the radiative transition will not happen only at $\lambda_0 = c/\nu_0$ and the probability for a photon with a frequency between ν and $\nu + \mathrm{d}\nu$ to be absorbed is given by a Lorentzian probability density:

$$\mathcal{L}(\nu - \nu_0)\,\mathrm{d}\nu = \frac{1}{\pi} \frac{\Gamma_{\text{rad}}/(4\pi)}{(\nu - \nu_0)^2 + (\Gamma_{\text{rad}}/(4\pi))^2} \,\mathrm{d}\nu \tag{4.4}$$

where Γ_{rad} is the damping constant and is related to the transition probabilities (the larger the transition probability, the larger Γ_{rad}, the shorter the level lifetime and the broader the absorption line). The full width at half maximum is $\Gamma_{\text{rad}}/(2\pi)$. The *oscillator strength* f is equal to the ratio of the predicted (by classical physics) and measured (in laboratory) energy which is absorbed by the line: a quantum treatment is needed to predict the correct amount of absorbed energy.

Collision broadening Collisions between absorbing atoms and surrounding particles (electrons, atoms, ions, molecules) modify, through the Coulomb interaction, the way the photons are absorbed or emitted, and thus the absorption line profile. One classifies the collisional mechanisms depending on the distance between the perturbed (i.e. absorbing atom) and perturbing entities: linear Stark effect, resonance broadening, quadratic Stark effect, Van der Waals broadening. In cool stars, the dominant effect is the Van der Waals broadening (interaction potential $\propto r^{-6}$) due to neutral hydrogen, affecting all lines. It is described by a Lorentzian profile and can be taken into account by replacing $\Gamma_{\rm rad}$ by $\Gamma = \Gamma_{\rm rad} + \Gamma_{\rm col}$. Modelling analytically collisional damping is complicated and one has to resort to approximations (impact or quasi-static approximations).

Doppler (or thermal) broadening Baryonic particles constituting a stellar photosphere are not at rest but are affected by thermal motions. The probability for an absorbing atom to have a velocity between $v = \sqrt{v_x^2 + v_y^2 + v_z^2}$ and $v + \mathrm{d}v$ is given by a Maxwellian probability density:

$$P\left(v\right) \mathrm{d}v_x \, \mathrm{d}v_y \, \mathrm{d}v_z = \left(\frac{m}{2\pi k_{\rm B} T}\right)^{3/2} \mathrm{e}^{-\frac{m}{2k_{\rm B}T}\left(v_x^2+v_y^2+v_z^2\right)} \, \mathrm{d}v_x \, \mathrm{d}v_y \, \mathrm{d}v_z \tag{4.5}$$

or after projection onto the line-of-sight:

$$P\left(\xi\right) \mathrm{d}\xi = \left(\frac{m}{2\pi k_{\rm B} T}\right)^{1/2} \mathrm{e}^{-\frac{m}{2k_{\rm B}T}\xi^2} \, \mathrm{d}\xi \tag{4.6}$$

where T is the kinetic temperature of the gas containing the absorbing atom and m the mass of the absorbing atom. Thermal motions (i.e. sensitive to the photosphere temperature) provoke a Doppler effect, and therefore, modify the absorption line profile: an atom with a velocity ξ along the line-of-sight will see a photon of frequency ν blue-shifted or red-shifted (depending on the motion direction) by $\nu\xi/c$ in its own frame (when $\xi \ll c$). This results in a broadened profile since absorption can occur at a different wavelength from the line centre. The new absorption line profile $\phi\left(\nu - \nu_0\right)$ is given by the convolution of $\mathcal{L}\left(\nu - \nu_0\right)$ by the Maxwellian probability density:

$$\phi\left(\nu - \nu_0\right) = \int_{-\infty}^{+\infty} \mathcal{L}\left(\nu - \nu_0 - \frac{\nu_0}{c}\xi\right) P\left(\xi\right) \mathrm{d}\xi \tag{4.7}$$

If we can neglect the natural broadening (e.g., around the line core) compared to the Doppler broadening, then the line has a Doppler profile given by:

$$\mathcal{D}\left(\nu\right) = \frac{1}{\Delta\nu_{\rm D}\sqrt{\pi}} \mathrm{e}^{-(\nu-\nu_0)^2/(\Delta\nu_{\rm D})^2} \tag{4.8}$$

where $\Delta\nu_{\rm D} = \frac{\nu_0}{c}\sqrt{\frac{2k_{\rm B}T}{m}} = \frac{\nu_0}{c}\xi_{\rm thermal}$ is the Doppler width and $\xi_{\rm thermal}$ is the modal velocity. In the general case, the line has a Voigt profile given by:

$$\phi\left(\nu - \nu_0\right) = \frac{1}{\sqrt{\pi}} \frac{1}{\Delta\nu_{\rm D}} H\left(a, \frac{\nu - \nu_0}{\Delta\nu_{\rm D}}\right) \tag{4.9}$$

where $a = \frac{\Gamma}{(4\pi\Delta\nu_{\rm D})}$ and H is the Voigt function.

Microturbulence broadening Baryonic particles suffer also from non-thermal motions, i.e. turbulence (Sec. 3.5). Microturbulence denotes small-scale motions and is described by the phenomenological parameter $\xi_{\rm micro}$. The microturbulence broadening is described by a Gaussian profile and has to be convolved to the thermal broadening, which is equivalent to replacing $\xi_{\rm thermal}$ by $\sqrt{\xi^2_{\rm thermal} + \xi^2_{\rm micro}}$ in the Doppler width $\Delta\nu_{\rm D} = \frac{\nu_0}{c}\sqrt{\xi^2_{\rm thermal} + \xi^2_{\rm micro}}$.

Other types of broadening Isotopes or hyperfine structure (hfs) cause a broadening of the absorption line: isotopes have slightly different mass, and therefore, the central wavelength describing a given atomic transition is slightly shifted from an isotope to another; the coupling between the nucleus and electronic cloud angular momenta (spin) removes the degeneracy of energy levels and causes an hyperfine splitting, i.e. appearance of new possible transitions. In the abundance analysis, we will take into account the hfs for a number of chemical elements: those with an odd atomic number Z (Sc, V, Co, Cu and Eu) or those with a dominant isotope with odd neutron number (Ba and La).

4.1.3.2 Macroscopic effects

The broadening mechanisms described above act upon microscopic scales: they modify the absorption line profile by modifying the opacity at wavelength λ. There also exist broadening mechanisms acting on macroscopic scales: they modify the absorption without changing the line strength (i.e. without changing the total amount of energy absorbed in the line). To take them into account, one has to convolve the *emerging* flux by the corresponding profile.

Rotation broadening For non-resolved stars, the bulk rotation of gas in stellar photospheres provokes an additional broadening through Doppler effects. It is described by an elliptical and parabolic profile. Giant stars, as those of our samples, are thought to be rather slowly rotating (typically, $\xi_{\rm rot} \lessapprox 5\,{\rm km\,s^{-1}}$; de Medeiros et al., 1996; Gray, 1981; Gray & Toner, 1986).

Macroturbulence broadening Macroturbulence refers to large-scale turbulent motions and provokes also an additional broadening through Doppler effects. It is described by a Gaussian profile of width $\xi_{\rm macro}$. For the giants in our sample, we typically expect $\xi_{\rm macro} \approx 7\,{\rm km\,s^{-1}}$ (Gray & Toner, 1986).

Instrumental broadening The absorption line profile recorded at the focal point of the telescope results from the convolution of the "true" absorption line profile by the instrumental response (the so-called *point spread function* which has a non-zero width because of the finite resolution R of the whole instrument). It is often approximated by a Gaussian function of width $\xi_{\rm instr} = c/R$ (expressed in ${\rm km\,s^{-1}}$). For our FLAMES/GIRAFFE spectra, as R varies from 17 740 to 24 200 (see setup characteristics in Chapter 2), we expect $\xi_{\rm instr}$ between 12 to 17 ${\rm km\,s^{-1}}$.

Broadening applied to our synthetic spectra In Section 4.2.1, we will use synthetic spectra to derive elemental abundances by comparing the shape of synthetic and observed absorption lines. Therefore, it is mandatory to apply a convolution onto the synthesised spectrum to take into account the global broadening effects (the local broadening effects are taken into account when the radiative transfer is done through the model stellar atmosphere).

For our GIRAFFE spectra, the instrumental broadening is clearly the dominant broadening mechanism, and it is possible to obtain a close estimate of $\xi_{\rm instr}$ using the spectrograph characteristics. For instance, for the GIRAFFE setups used for our observational program, we have:

- for HR11, $R \approx 24\,200$, hence $\xi_{\rm instr} \approx 12.4\,{\rm km\,s^{-1}}$.
- for HR13, $R \approx 22\,500$, hence $\xi_{\rm instr} \approx 13.3\,{\rm km\,s^{-1}}$.
- for HR14, $R \approx 17\,740$, hence $\xi_{\rm instr} \approx 16.9\,{\rm km\,s^{-1}}$.

However, applying only the instrumental broadening will not suffice to reproduce the shape of spectral absorption features: even though the instrumental broadening dominates in our spectra, the macroturbulence broadening is not negligible. In fact, to find which broadening has to be applied to the spectrum of a given star, a more efficient solution consists in using a line of an element X for which we *know* the abundance. Indeed, for a given star (i.e. for a fixed set of stellar parameters), for a given perfectly known line of an element X, if we know the abundance of the element X, then the discrepancy between the synthesised and observed line is only due to rotation, macroturbulence and instrumental broadenings. Of course, we are not able to perfectly describe an atomic line and the mismatch between the synthesised and observed line can be due to, for instance, limitations of the line modelling or uncertainties on the input quantum data. Using a relatively large set of lines circumvents this issue since effects of modelling mismatch and uncertainties on quantum data likely cancel out in the average. So in order to determine the parameter $\xi_{\rm tot}$ of the Gaussian convolution applied to our synthesised spectra, we set up the following procedure:

1. for a given star, with stellar parameters $\{T_{\rm phot}, \log g, [{\rm M/H}], \xi_{\rm micro}\}$, observed in the setup s, we compute the corresponding theoretical spectrum over the whole wavelength domain covered by the setup s.
2. we convolve the spectrum by a Gaussian profile with a FWHM $= 2\sqrt{2\ln 2}\xi_{\rm tot}$.
3. we normalise the theoretical spectra and the observed spectrum in the same way and then, for each Fe I line j present in the wavelength range, compute the χ^2 quantity:

$$ {T_j}^2\left(\xi_{\rm tot}\right) = \frac{1}{\sum_{i=1}^{n}\hat{\mathcal{S}}_i}\sum_{i=1}^{n}\hat{\mathcal{S}}_i\left(\mathcal{S}\left([{\rm X/Fe}]\right)_i - \mathcal{O}_i\right)^2 \qquad (4.10) $$

where i is the pixel index, n the number of pixel in the interval I, $\hat{\mathcal{S}}$ the (normalised) theoretical spectrum *without* the element X, $\mathcal{S}\left([{\rm X/Fe}]\right)$ the (normalised) theoretical spectrum for a given value of [X/Fe], and $\mathcal{O}$ the (normalised) observed spectrum. In the above sum, the flux in each pixel is

weighted according to contamination (see also § "Fitting of absorption profiles" for a discussion of the different terms). The length of the interval I is the same for any Fe I line and was chosen to be about twice the typical full width at half maximum (FWHM) (we used the FWHM returned by DAOSPEC, i.e. the FWHM at the central wavelength of the setup), i.e. 0.4 Å for HR11 and HR13, 0.9 Å for HR14. This length guarantees to include both wings of Fe I lines in the computation of ${T_j}^2$, which are very sensitive to the convolution. And we sum the contribution of all Fe I lines:

$$T^2\left(\xi_{\mathrm{tot}}\right) = \sum_{\text{Fe I lines}} {T_j}^2\left(\xi_{\mathrm{tot}}\right) \tag{4.11}$$

We computed T^2 for each value of ξ_{tot} in the range $\{11.0, 11.1, \ldots, 17.9, 18.0\}$ for HR11, $\{12.0, 12.1, \ldots, 19.9, 19.0\}$ for HR13, and $\{15.0, 15.1, \ldots, 21.9, 22.0\}$ for HR14 and, for each star and each setup, we selected ξ_{tot} that minimises T^2. Using the Fe I lines offers two advantages: first, for each star, the Fe I abundance is known (see Sec. 3.5.3) and was derived from the same set of lines (thus homogeneity); second, iron lines are numerous within each setup (6 for HR11, 11 for HR13 and 19 for HR14) and distributed over the whole wavelength range (from 5619 Å to 5717 Å for HR11, from 6151 Å to 6380 Å for HR13 and from 6380 Å to 6609 Å for HR14). Thus, the convolution parameter is robustly determined for the whole wavelength range of a given setup, and therefore, we can safely use any absorption line during the abundance analysis. $\xi_{\mathrm{tot}} = \sqrt{{\xi_{\mathrm{instr}}}^2 + {\xi_{\mathrm{macro}}}^2 + {\xi_{\mathrm{rot}}}^2}$ allows to simultaneously take into account rotation, macroturbulence and instrumental broadenings[1]. Although the rotation broadening has a parabolic profile, it is safe to approximate it by a Gaussian profile for giant stars, since they are affected by a slow rotation only. For ξ_{tot}, we found typical $13.8\,\mathrm{km\,s^{-1}}$ for HR11, $15.4\,\mathrm{km\,s^{-1}}$ for HR13, and $19.3\,\mathrm{km\,s^{-1}}$ for HR14, which is in agreement with expected values (i.e. ξ_{tot} is slightly larger than ξ_{instr}).

4.1.4 Curve of growth

The equivalent width (EW) W is defined by:

$$W \equiv \int_{\mathrm{line}} \frac{F\left(\lambda\right) - F_{\mathrm{c}}\left(\lambda\right)}{F_{\mathrm{c}}\left(\lambda\right)}\,\mathrm{d}\lambda \tag{4.12}$$

and is the area above the line profile and below the continuum. The variation of the EW as a function of the absorber abundance is called the *curve of growth*. This curve is a useful tool to understand the behaviour of absorption lines. Indeed, one distinguishes three regimes:

1. the linear (or Doppler) part: for weak lines, i.e. when the column density of absorbing species is small, the EW is given by:

$$W \propto \frac{\pi \mathrm{e}^2 \lambda_0^2}{m_{\mathrm{e}} c^2} f N \tag{4.13}$$

[1]The three broadenings can be combined since they are homogeneous: this is the advantage of expressing the instrumental broadening as a velocity.

where f is the oscillator strength and N the number of absorber, i.e. EW is proportional to the abundance N: $W \propto N$. The line profile is Gaussian. Let us note that for an atomic line, the relevant quantity is not f but $\log gf$ where g is the statistical weight and is provided to *turbospectrum* through line lists, together with the central wavelength, excitation potential, damping constant and Van der Waals damping factor (see below § "Collision broadening") of the line (and possibly, the quantum description of the radiative transition). It is important to have the most accurate quantum data in order to make accurate abundance measurements: for instance, a bias in $\log gf$ changes the abundance ratio by the same amount, since $\log gf$ is homogeneous to an abundance ratio.

2. the logarithmic (or flat) part: for saturated lines, the EW grows slowly with increasing absorber density: $W \propto \sqrt{\log N}$. The flux in the line core has reached a minimum value (set by the Boltzmann equation) and cannot go deeper, the width of the line slowly increases. The line profile is still Gaussian.

3. the square-root (or damping) part: for strong lines, i.e. when the column density of absorbing species is large, the EW grows faster with increasing absorbing density: $W \propto \sqrt{N}$. The Lorentzian wings drive the evolution of the EW.

It is obvious that measuring chemical abundances will be best done when the studied line is a weak or strong line. If a line is saturated, then a large variation of the absorbing abundance only corresponds to a small variation of the EW. Figures 4.1a and 4.1b show an example of curve of growth for an Fe line, together with its profile at different positions on the curve of growth.

4.1.5 Notation

For a chemical element X, it is customary to define the following astronomical hydrogen-normed abundance scales:

$$\begin{cases} \epsilon(\mathrm{X}) = \dfrac{N_\mathrm{X}}{N_\mathrm{H}} \quad \text{with} \quad N_\mathrm{H} \equiv 10^{12}\,\mathrm{g}^{-1} & (4.14a) \\ A(\mathrm{X}) = \log(\epsilon(\mathrm{X})) + 12 = \log\left(\dfrac{N_\mathrm{X}}{N_\mathrm{H}}\right) + 12 & (4.14b) \\ [\mathrm{X/H}] = \log\left(\dfrac{N_\mathrm{X}}{N_\mathrm{H}}\right) - \log\left(\dfrac{N_\mathrm{X}}{N_\mathrm{H}}\Big|_\odot\right) = \log(\epsilon(\mathrm{X})) - \log(\epsilon_\odot(\mathrm{X})) & (4.14c) \\ \qquad\qquad = A(\mathrm{X}) - A_\odot(\mathrm{X}) \end{cases}$$

where N_X (resp. N_H) is the number density of absorbing X (resp. H) atoms. [X/H] is the bracket notation providing a solar-scaled abundance; the unit is dex[2]. More

[2]Contraction of "decimal exponent".

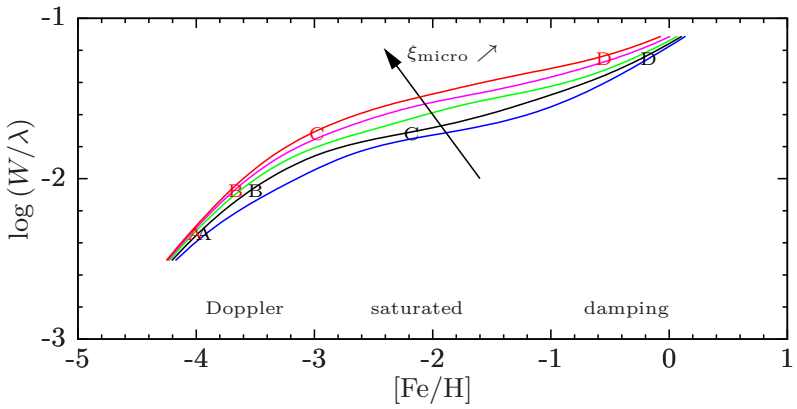

(a) Curve of growth

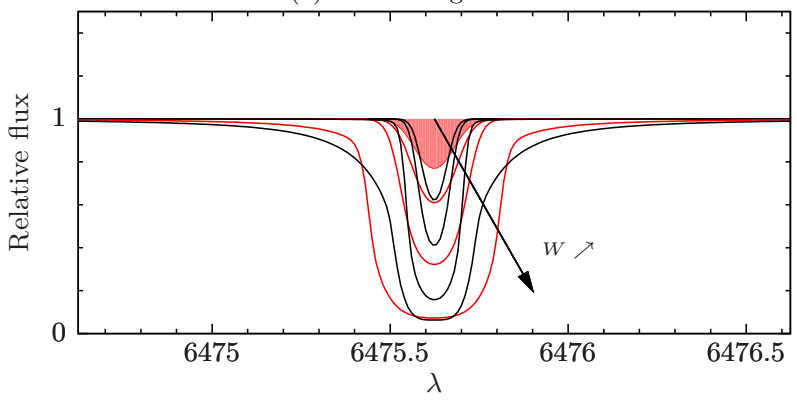

(b) Absorption line profiles

Figure 4.1: **Curves of growth (top panel) and profiles (bottom panel) computed with *turbospectrum* for a Fe line (at** 6475.62 Å**;** $\xi_{\rm ex} = 2\,{\rm eV}$**;** $\log gf = -2$**) and a cool giant star (**$T_{\rm eff} = 4000\,{\rm K}$**,** $\log g = 1$**,** $[{\rm M/H}] = -0.5\,{\rm dex}$**). Top panel: Curves of growth for various microturbulent velocities.** Blue line: $\xi_{micro} = 1.0\,{\rm km\,s^{-1}}$; black line: $\xi_{micro} = 1.5\,{\rm km\,s^{-1}}$; green line: $\xi_{micro} = 2.0\,{\rm km\,s^{-1}}$; magenta line: $\xi_{micro} = 2.5\,{\rm km\,s^{-1}}$; red line: $\xi_{micro} = 3.0\,{\rm km\,s^{-1}}$. The three regimes — Doppler, saturated and damping part — are roughly indicated (the frontiers slightly change from a curve of growth to another). When the microturbulent velocity increases, the shoulder, i.e. the transition between the linear and the flat part, is higher: for a given line and a given star, increasing the microturbulent velocity "delays" (in terms of abundance) the saturation of the line. **Bottom panel: Evolution of the line profile along two curves of growth.** Black solid line: $\xi_{micro} = 1.5\,{\rm km\,s^{-1}}$; red solid line: $\xi_{micro} = 3.0\,{\rm km\,s^{-1}}$; profiles correspond to the save EW each time. For the weakest red line, the equivalent width, i.e. the area between the line and the continuum, is coloured. The four profiles respectively correspond to the positions labelled A, B, C and D in the top panel: at a given position, the equivalent width W is the same for the black and red profiles. At position A, the two lines are on the Doppler part of the curve of growth: when abundance increases (from A to B), the depth of the line quickly increases. At position C, the black line is already on the saturated part while the red line is on the shoulder (because of higher microturbulent velocity): the depth and width of the black line increase slowly with increasing abundance. At position D, the black line is already on the damping part while the red line is still at the beginning: the depth of the black (and red) line is at the maximum allowed by thermodynamics and the growth of the equivalent width is only due to the development of the damping wings.

generally, in the following, abundance ratios will be given in the bracket notation [A/B], where A and B are two different chemical elements (e.g., [Mg/Fe] or [Ba/Eu]), given by the following arithmetic relations:

$$[\mathrm{A/B}] = [\mathrm{A/H}] - [\mathrm{B/H}] = [\mathrm{A/Fe}] - [\mathrm{B/Fe}] \tag{4.15}$$

It is obvious from the above definition that $[\mathrm{A/B}]_{\odot} = 0\,\mathrm{dex}$ for any pair (A, B).

4.2 Abundance analysis of our LMC bar and disc stars

4.2.1 Procedures of abundance measurements

Introduction Abundance measurement needs the computation of the theoretical spectrum corresponding to a set of stellar parameters and a chemical composition and I will use the code of spectrum synthesis *turbospectrum* (Alvarez & Plez, 1998) to perform this task. To compute the emergent flux, *turbospectrum* has to solve the radiative transfer equation (Eq. 4.2) taking into account all chemical species:

- *turbospectrum* is fed with the spherical atmosphere model of the star: the atmosphere is discretised in 56 layers described by an optical depth, a temperature, electronic and gas pressures; for each layer of the atmosphere model, the LTE is assumed and the population of each energy level of each ion can be calculated (Boltzmann and Saha equations);
- *turbospectrum* is fed with the atomic and molecular line lists, which contain the relevant quantum data describing radiative transitions;
- *turbospectrum* compute opacities, assuming a solar composition scaled to the star metallicity (individual abundances can also be set up);
- to compute the synthetic spectrum, *turbospectrum* uses the computed opacities and performs the radiative transfer (in one dimensional spherical geometry) for all atmosphere layers, the output flux of layer $n-1$ being the input flux of layer n;
- eventually, a macroscopic broadening is applied to the synthetic spectrum to take into account instrument response, stellar rotation and macroturbulence.

turbospectrum can be run into modes: "equivalent width" where *turbospectrum* varies the abundance of an element in order to match the input EW and "synthesis" where *turbospectrum* computes a synthetic spectrum in a given wavelength range. In the followings, I will use these two modes to derive the chemical composition of our LMC bar and inner disc stars.

Equivalent width This EW method consists in measuring, for a given element X, the observed equivalent width of a line W_{obs} and comparing it to a theoretical equivalent width W_{theo}, obtained by varying the abundance [X/Fe]. The searched [X/Fe] is the one yielding a match between W_{obs} and W_{theo}. As explained in Section 3.5.3, we used DAOSPEC (Stetson & Pancino, 2008) to measure the EW of

atomic lines. We converted EW into abundances, using *turbospectrum* (in spherical geometry, with LTE spherical radiative transfer) together with the grid of OSMARCS spherical model atmospheres. DAOSPEC requires as input the observed spectrum, a list of lines whose EW will be measured and a configuration file. With an iterative algorithm, DAOSPEC separates the spectrum into a continuum component and an absorption line component (Gaussian profiles), assuming a constant FWHM, and fits a polynomial to the continuum. It determines the central wavelength of all found absorption lines and cross-correlates its list with the input list to identify the lines. Finally, DAOSPEC normalised the spectrum with the fitted continuum and measures on the normalised spectrum the EW of all identified lines. One remark. The advantage to use EW to derive elemental abundances is to rely on area measurements, which are robustly defined quantities. Particularly, unlike the fitting of absorption profiles, knowing the rotation, macroturbulence and instrumental broadening is not needed at all (since these broadenings leave the EW unchanged): thus it avoids the introduction of a new parameter, i.e. a new source of uncertainty (see § "Broadening applied to our synthetic spectra" in Sec. 4.1.3.2).

Fitting of absorption profiles The fitting of absorption profile (Fig. 4.2) consists in computing a grid of theoretical spectra by varying the abundance of an element and comparing them to an observed absorption line of this specific element and search for the best fit, which gives us the abundance. We set up the following procedure:

1. for a given absorption line $\mathcal{L}$ of an element X, with a central wavelength λ_0, we defined a small wavelength interval I in which the profile fitting is performed. The definition of the interval results from the compromise between three contradictory requirements: covering as many pixels as possible, avoiding neighbouring lines and including continuum on both sides. The typical width of the wavelength interval considered ranges from 3 to 5 Å.

2. we compute a grid of theoretical spectra by varying the abundance ratio [X/Fe] with *turbospectrum*, from -1 dex up to 1 dex, by increment of 0.1 dex. We compute the spectra over a wavelength range centred on λ_0 and convolved them by a Gaussian profile to take into account the combined effects of rotation, macroturbulence and instrumental response (see § "Broadening applied to our synthetic spectra" in Sec. 4.1.3.2).

3. we normalise the theoretical spectra and the observed spectrum in the same way and then compute the quantity:

$$T^2\left([\mathrm{X/Fe}]\right) = \frac{1}{\sum_{i=1}^{n}\hat{\mathcal{S}}_i}\sum_{i=1}^{n}\hat{\mathcal{S}}_i\left(\mathcal{S}\left([\mathrm{X/Fe}]\right)_i - \mathcal{O}_i\right)^2 \tag{4.16}$$

where i is the pixel index, n the number of pixel in the interval I, $\hat{\mathcal{S}}$ the (normalised) theoretical spectrum *without* the element X, $\mathcal{S}\left([\mathrm{X/Fe}]\right)$ the (normalised) theoretical spectrum for a given value of [X/Fe], and $\mathcal{O}$ the (normalised) observed spectrum. $\hat{\mathcal{S}}$ allows to weight each pixel by its contamination: if the flux at pixel i is only due to the absorption by the element X, then

$\hat{\mathcal{S}}_i = 1$; if the flux at pixel i is the result of the absorption by the element X and by one or more other chemical entities, then $\hat{\mathcal{S}}_i < 1$. Therefore, the more contaminated, the less it counts in $T^2([\mathrm{X/Fe}])$.

4. T^2 is (generally) a convex function of [X/Fe], the position of the minimum $T^2_{\mathrm{nominal}} = T^2\left([\mathrm{X/Fe}]_{\mathrm{nominal}}\right)$ gives us the best-fit abundance $[\mathrm{X/Fe}]_{\mathrm{nominal}}$. $T^2\left([\mathrm{X/Fe}]\right)$ is not a genuine χ^2 since we do not divide the quadratic difference $\left(\mathcal{S}\left([\mathrm{X/Fe}]\right)_i - \mathcal{O}_i\right)^2$ by the error at pixel i (the errors returned by the pipeline do not take into account the correlation between pixels) but we can still use it to find the best fit.

5. the last step aims at accepting or rejecting the solution. Once again, as $T^2\left([\mathrm{X/Fe}]\right)$ is not a genuine χ^2, we cannot apply usual statistics theorems, and for instance, we cannot associate a probability to the fit based on the χ^2 alone. Therefore, to decide whether the solution has to be rejected, we checked the shape of the T^2 curve thanks to simple geometrical criteria. Indeed, the shape of the T^2 curve is not accidental and reveals the curve of growth of the measured line. For instance, a saturated line is likely to produce a very open curve; a weak line is likely to produce a curve with a well defined minimum, but with a left branch that becomes flat for the smallest abundance; on the other hand, the mismatch between the synthesis and the observed spectrum will influence the value of T^2_{nominal}. So it is easier to work with the normalised T^2 given by:

$$\hat{T}^2\left([\mathrm{X/Fe}]\right) = \frac{T^2\left([\mathrm{X/Fe}]\right) - T^2_{\mathrm{nominal}}}{T^2_{\mathrm{nominal}}} \tag{4.17}$$

Non-detection: as we cover a broad abundance range ([X/Fe] varies from -1 to 1 dex), we expect (in general) a strong variation of T^2 over this interval. A flat T^2 curve (or at least, if the curve has a completely flat left branch) is the symptom of a non-detection of the line. If the line is very weak, then the profile of the absorption line will slightly change from one abundance point of the grid to the next, at least as long as [X/Fe] is small (say $\lessapprox -0.3$ dex). Therefore, $\left(\mathcal{S}\left([\mathrm{X/Fe}]\right)_i - \mathcal{O}_i\right)^2 \approx \mathrm{cst}$, thus $T^2\left([\mathrm{X/Fe}]\right) \approx \mathrm{cst}$. For larger abundances, the line appears in the synthesis and T^2 (or $\hat{T}^2$) steeply increases. We can detect a flat left (right) branch with this criterion: $\hat{T}^2(-1.0) < \epsilon_1$ ($\hat{T}^2(+1.0) < \epsilon_1$, respectively). We empirically fixed ϵ_1 to 4.0. In other words, we require T^2 to be five times as high as T^2_{nominal} at the grid border for the solution to be meaningful. It may happen that the nominal abundance is close to the grid edge; thus the left (right) branch will not be complete and the solution will be mistakenly rejected. So, in that case, we checked the local symmetry of the $\hat{T}^2$ curve around the nominal abundance. If the curve is non-symmetric, the solution is rejected. In the mean, the rejection rate is of about ten lines/star; the rejection is minimum for stars with a metallicity between -1 and -0.5 dex and tends to be higher for metallicities lower than -1.0 dex or larger than -0.5 dex. Figure 4.3 shows examples of $\hat{T}^2$ profiles. Figure 4.10 shows the dependence of $\hat{T}^2$ with S/N (in fact, it is a median relation computed from

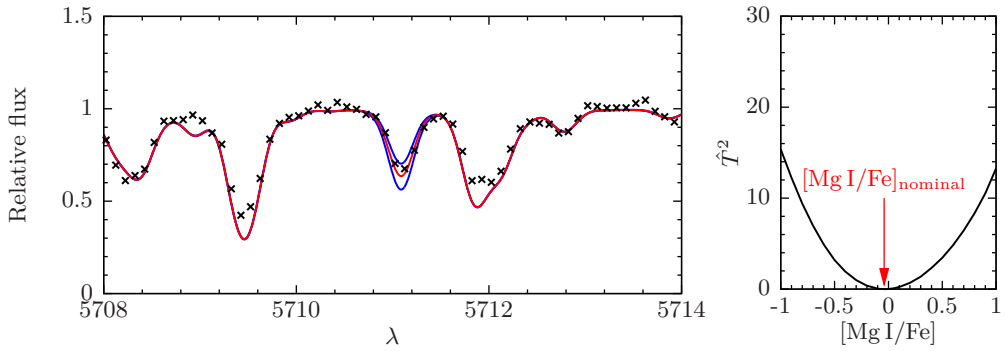

Figure 4.2: **Example of absorption line fitting. Left panel: Spectrum synthesis in the region of the Mg I line at 5711 Å for the star 05243901-6948426.** Black crosses: observed spectrum; red solid line: spectrum for the best-fit abundance $[\mathrm{Mg\,I/Fe}]_{\mathrm{nominal}} = -0.04$ dex; blue solid lines: spectra for $[\mathrm{Mg\,I/Fe}] = -0.20$ dex and $[\mathrm{Mg\,I/Fe}] = 0.10$ dex (i.e. $[\mathrm{Mg\,I/Fe}]_{\mathrm{nominal}} \pm$its random error). **Right panel: Corresponding $\hat{T}^2$ function.** The position of the minimum is indicated by the red arrow.

all T^2_{nominal} for all LMC bar stars; see Sec. 4.2.5.2 for details): as expected, $\hat{T}^2$ varies as a power-law of S/N.

We used the EW or the fitting of absorption profile depending on the line: if the number of lines was high (≥ 5), we privileged the EW; if only few lines were available or if a blend was present or if the element has a hfs, we privileged the fitting of absorption profile.

4.2.2 Line lists: compilation and calibration

List of elements In our broad wavelength coverage, we are in position to measure elemental abundances for 17 elements (the method used, EW or SS, and the number of available lines are given in parenthesis): O I (SS, 1), Mg I (SS, 3), Si I (EW, 3), Ca I (EW, 13), Ti I (EW, 8), Ti II (EW, 3), Na I (SS, 4), Sc II (SS, 6), V I (SS, 12), Cr I (SS, 4), Co I (SS, 3), Ni I (EW, 7), Cu I (SS, 1), Y I (SS, 1), Zr I (SS, 4), Ba II (SS, 2), La II (SS, 3), Eu II (SS, 2).

We compiled the atomic line lists from the line database VALD[3] (Kupka et al., 1999, 2000); for the measured lines, we used the $\log gf$ quoted in Pompéia et al. (2008). We took into account the hfs for Sc II (Wiese et al., 1966: 5640 Å, 5667 Å, 5669 Å, 6245 Å; Martin et al., 1988: 5657 Å, 6604 Å), V I (Martin et al., 1988: 6119 Å, 6135 Å, 6150 Å, 6199 Å, 6224 Å, 6274 Å, 6285 Å, 6292 Å, 6357 Å, 6452 Å, 6531 Å; Kurucz, 1988: 6224 Å), Co I (Fuhr et al., 1988: 5647.240 Å, 6117.000 Å, 6282.600 Å), Cu I (Bielski, 1975: 5782.127 Å), Ba II (Rutten, 1978: 6496.912 Å; no hfs data for 6141.713 Å), La II (Lawler et al., 2001a: 6262.287 Å, 6390.477 Å; no hfs data for 6320.430 Å), and Eu II (Lawler et al., 2001b: 6437.640 Å, 6645.064 Å). We extracted the hfs data from the Kurucz database[4] (Kurucz, 1995) for Sc, V, Co,

[3]Database available at http://www.astro.uu.se/~vald/php/vald.php.
[4]Database available at http://kurucz.harvard.edu.

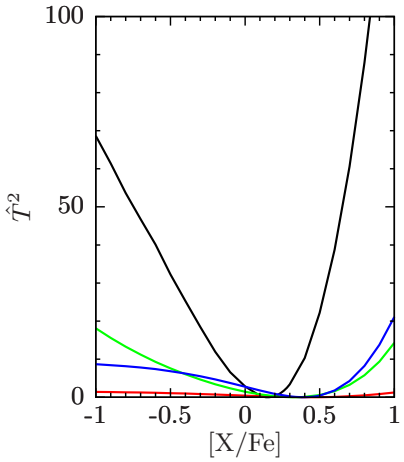

Figure 4.3: **Examples of $\hat{T}^2$ profiles for various lines and stars.** The black profile as a well-defined minimum and is almost symmetric (weak line) while the green profile is very open and has a valley instead of a minimum. The blue profile probably corresponds to a saturated line since the left branch is rather flat; however, the abundance measurement is feasible. The red profile is completely flat: there is no detection.

and Cu; we computed the hyperfine splitting for Ba, La and Eu using the published hyperfine constants (see Sec. 4.2.4 for the cleaning of the line list and Table A.1 for the final list of measured lines). As our stars are cold ($T_{\rm phot} \sim 4500\,{\rm K}$), molecules form in the stellar atmospheres and form absorption lines in the stellar spectra: we included the molecular line lists of $^{12}{\rm C}\,^{14}{\rm N}$, $^{13}{\rm C}\,^{14}{\rm N}$ (Plez, private communication) and TiO (Plez, 1998) in the spectrum synthesis. We consider the solar composition from Grevesse & Sauval (1998). For all our LMC stars, we fixed the carbon and nitrogen abundances: $[{\rm C/Fe}] = -0.65\,{\rm dex}$ and $[{\rm N/Fe}] = 0.3\,{\rm dex}$ (values derived from Smith et al., 2002). For Arcturus, we used $[{\rm C/Fe}] = 0.05\,{\rm dex}$ and $[{\rm N/Fe}] = 0.34\,{\rm dex}$ (Lecureur et al., 2007).

Calibration of the line lists When a line of interest is blended by another chemical species (atom or molecule), the abundance measurement becomes more difficult. Especially, if the absorption profile of the contaminant is poorly predicted (lack of accurate experimental quantum data or reliable theoretical predictions), as it is the case for CN lines. We therefore calibrated a number of CN lines contaminating crucial lines of Y, Zr, Ba, La and Eu using Arcturus.

4.2.3 Application to Arcturus

Protocole In the following, we will derive the abundances for Arcturus so that it will provide the zero-point of our abundance scale. In order to have a unique Arcturus atmosphere model for any signal-to-noise ratio (S/N ratio) hypothesis, we chose as stellar parameters $T_{\rm eff} = 4286\,{\rm K}$, $\log g = 1.66$, $[{\rm M/H}] = -0.65\,{\rm dex}$ and $\xi_{\rm micro} = 1.8\,{\rm km\,s^{-1}}$: the former two are from Ramírez & Allende Prieto (2011) while

Table 4.1: Elemental abundances and errors for our ∞, high, median and low S/N ratio version of the Arcturus spectra as well as abundance ratios (and their errors) published by Ramírez & Allende Prieto (2011) and Worley et al. (2009). The number of lines used and the method to derive the abundances are recalled.

[X/Fe]	∞ S/N ratio	high S/N ratio	median S/N ratio	low S/N ratio	#	Method	Ramirez et al.	Worley et al.
	dex	dex	dex	dex			dex	dex
O I	0.46	0.47 ± 0.03	0.44 ± 0.04	0.41 ± 0.06	1	SS	0.50 ± 0.03	0.57 ± 0.02
Mg I	0.34 ± 0.06	0.33 ± 0.03	0.33 ± 0.04	0.30 ± 0.07	3	SS	0.37 ± 0.03	0.34 ± 0.15
Si I	0.32 ± 0.04	0.33 ± 0.05	0.33 ± 0.06	0.33 ± 0.11	2	EW	0.33 ± 0.04	0.24 ± 0.14
Ca I	0.04 ± 0.04	0.06 ± 0.02	0.05 ± 0.02	0.03 ± 0.04	10	EW	0.11 ± 0.04	0.19 ± 0.06
Ti I	0.36 ± 0.07	0.38 ± 0.02	0.36 ± 0.03	0.34 ± 0.04	8	EW	0.27 ± 0.05	0.35 ± 0.12
Ti II	0.32 ± 0.07	0.33 ± 0.04	0.31 ± 0.04	0.32 ± 0.08	3	EW	0.21 ± 0.04	0.33 ± 0.10
Na I	0.11 ± 0.04	0.11 ± 0.03	0.09 ± 0.04	0.06 ± 0.07	3	SS	0.11 ± 0.03	0.15 ± 0.04
Sc II	0.29 ± 0.02	0.29 ± 0.03	0.27 ± 0.04	0.25 ± 0.07	4	SS	0.23 ± 0.04	0.24 ± 0.01
V I	0.03 ± 0.02	0.03 ± 0.02	0.01 ± 0.02	-0.03 ± 0.03	7	SS	0.20 ± 0.05	-
Cr I	-0.05 ± 0.06	-0.05 ± 0.04	-0.07 ± 0.05	-0.09 ± 0.08	3	SS	-0.05 ± 0.04	-
Co I	0.21 ± 0.11	0.20 ± 0.03	0.19 ± 0.04	0.15 ± 0.07	2	SS	0.09 ± 0.04	-
Ni I	0.08 ± 0.04	0.10 ± 0.03	0.08 ± 0.03	0.07 ± 0.05	6	EW	0.06 ± 0.03	-
Cu I	-0.02	-0.03 ± 0.06	-0.03 ± 0.08	-0.05 ± 0.15	1	SS	-	-
Y I	0.02	0.01 ± 0.07	-0.01 ± 0.08	-0.02 ± 0.13	1	SS	-	0.07 ± 0.24
Zr I	-0.06 ± 0.03	-0.07 ± 0.03	-0.09 ± 0.04	-0.13 ± 0.05	3	SS	-	0.01 ± 0.07
Ba II	-0.18 ± 0.03	-0.16 ± 0.06	-0.18 ± 0.07	-0.22 ± 0.11	2	SS	-	-0.19 ± 0.08
La II	-0.03 ± 0.05	-0.02 ± 0.04	-0.04 ± 0.06	-0.06 ± 0.09	3	SS	-	0.04 ± 0.08
Eu II	0.41 ± 0.02	0.42 ± 0.07	0.40 ± 0.07	0.38 ± 0.18	2	SS	-	0.36 ± 0.04

we determined the latter two in Section 3.5.3 (median S/N ratio hypothesis).

We followed the same procedure described above to derive the abundances for our Arcturus spectra. For the high (respectively median and low) S/N ratio hypothesis, we computed a mean abundance and dispersion (over the 101 realisations) for each individual line of a given element, and then we computed the final mean abundance ratio (over the $N_{\rm lines}$) following the procedure described in Section 4.2.4. The error on the individual line abundance (dispersion over the 101 realisations) was propagated when we computed the final mean abundance. We did the same for the ∞ S/N ratio hypothesis (except for the averaging over the realisations); as we have only one realisation for this S/N ratio assumption, we used the standard error of the mean as an error estimator (hence the lack of error bar when only one line was used). Table 4.1 gives the results for the ∞, high, median and low S/N ratio version of the Arcturus spectra as well as the abundance ratios (and their errors) published by Ramírez & Allende Prieto (2011) and Worley et al. (2009).

Comparison to the literature Chemical differences appeared for two elements: calcium and vanadium. When we first computed [Ca/Fe], we obtained ≈ -0.12 dex which is not the expected ratio for a disc star and is very different from the Ramírez & Allende Prieto (2011) and Worley et al. (2009) ratios. The $\log gf$ we used had been taken from the NIST[5] database and used in Pompéia et al. (2008). We tested two other sets of $\log gf$: the Kurucz $\log gf$ gave also ≈ -0.12 dex (the Kurucz and the NIST $\log gf$ of our Ca I lines are almost equal); the VALD $\log gf$ gave ≈ 0.05 dex, which is closer to the quoted [Ca/Fe]. We decided to keep the VALD $\log gf$ (Drozdowski et al., 1988; Smith, 1981, 1988; Smith & Raggett, 1981) in order to alleviate the disagreement. Vanadium has an hyperfine structure: when we take into

[5]Database available at http://physics.nist.gov/PhysRefData/ASD/index.html.

account the hfs, [V/Fe] ≈ 0.01 dex, while without the hfs, [V/Fe] ≈ 0.23 dex. The latter value is closer to the value that Ramírez & Allende Prieto (2011) seemingly derived without taking into account the hyperfine splitting for V (we have five V I lines in common). So the hfs seems to explain the disagreement. In the following, we will derive the V ratios *with* the hfs.

Except for V, our derived elemental ratios are in good agreement, within the errors, with Ramírez & Allende Prieto (2011) or Worley et al. (2009) (difference between the literature and our ratios $\lessapprox 0.15$ dex in absolute value) and are perfectly understandable if we consider all the possible differences between our study and theirs (stellar parameters, atomic data, method to derive the abundances). We refer the reader to Lebzelter et al. (2012) who offer a broad analysis of the effects of models, input data and procedures on the derived stellar parameters and chemical composition; for instance, differences of up to ~ 0.3 dex are observed for [Ca/Fe] between the different works.

In our determinations, we note that, in general, when S/N ratio decreases, [X/Fe] slightly decreases ($\lessapprox 0.05$ dex) and the error increases. This general good agreement between our results for Arcturus and the literature makes us confident for the detailed chemical analysis of our Large Magellanic Cloud (LMC) sample. There is no strong bias and we are able to compare directly the abundance trends of the LMC to those of the Milky Way (MW), at all S/N ratio of our sample.

4.2.4 The LMC bar sample

Computation of the mean abundance As shown in the previous section, for a number of elements, two lines or more are available in the full spectral coverage, and we measured all of them whenever possible.

To combine the abundances from multiple lines, we distinguished three different cases to compute the quantity $\langle$[X/Fe]$\rangle$:

- if $N_{\rm lines} = 1$, then the final elemental abundance is simply equal to the single measurement.
- if $2 \leq N_{\rm lines} < 5$, then we computed the simple mean of the $N_{\rm lines}$ measurements.
- if $N_{\rm lines} \geq 5$, then we applied a 3σ-clipping to remove discrepant measurement, and computed the simple mean of the remaining measurements.

Table B.1 provides the final abundance for our LMC bar stars.

Cleaning of the line lists We tried to identify the lines which systematically led to a discrepant measurement of the corresponding abundance by analysing the mean behaviour (computed over all sample stars) of each absorption line of an element X with respect to the mean abundance (computed over the lines, for a given star). For a given star, we computed the mean abundance $\langle$[X/Fe]$\rangle_{\rm lines}$; to compare the $N_{\rm lines}$ together, we computed the quantity:

$$[{\rm X}_i/\langle {\rm X}\rangle_{\rm lines}] = [{\rm X/Fe}]_i - \langle [{\rm X/Fe}]\rangle_{\rm lines} \tag{4.18}$$

The mean behaviour of a given line is then given by the mean (and standard deviation) of $[X_i/\langle X\rangle_{\rm lines}]$ over the stars $\langle[X_i/\langle X\rangle_{\rm lines}]\rangle_{\rm stars}$. Of course, this was possible only when $N_{\rm lines} \geq 2$. This sanity check was not only useful to identify systematically discrepant lines but above all, it was useful to handle the cases where we do not have enough measurements to apply a 3σ-clipping cleaning: if $N_{\rm lines} = 2$, we could simply check whether the two lines were in agreement; if $N_{\rm lines} \geq 3$, it was also possible to identify systematically discrepant lines. We labelled a line suspicious when it showed a significant departure from the mean ($|\langle[X_i/\langle X\rangle_{\rm lines}]\rangle_{\rm stars}| \gtrapprox 0.3$ dex) and/or a high standard deviation ($\gtrapprox 0.3$ dex). We applied the same kind of analysis on the abundance ratios we derived for the simulated Arcturus spectra; as the literature provides us with accurate abundance measurements, it helps to identify discrepant lines and to quantify biases by confronting each single measurement to the published mean values.

In the end, we discarded a few lines for Ca I (5601 Å, 6162 Å, 6572 Å), Cr I (6362 Å), Na I (5682 Å), Ni I (6314 Å), Sc II (5657 Å, 6245 Å), Si I (5665 Å), V I (6119 Å, 6199 Å, 6357 Å, 6452 Å) and Zr I (6140 Å) and updated the computation of the mean abundances accordingly. We decided to keep in our abundance analysis the Ba line at 6141.713 Å (resp. the La line at 6320.430 Å) for which no hfs data is available since we noted a good agreement with the other Ba (resp. La) line, with a difference of 0.2 dex for Ba (resp. 0.1 dex for La) in the mean (over the whole sample) between the line with and without hfs. Table A.1 gives the final line list. Figures 4.4 to 4.9 show examples of these diagnosis tests.

4.2.5 The LMC disc sample

4.2.5.1 Abundances

To derive the abundances for our LMC disc stars, we used the same EW and the same reduced spectra that were used by Pompéia et al. (2008). The differences between their work and ours lie in the stellar parameters and the methods to derive and compute the final abundances. Table 4.2 gives a comparison of our new abundances for our LMC disc stars and those published in Pompéia et al. (2008). For most of the elements, the agreement between our abundance ratios and those from Pompéia et al. (2008) is good, with a mean difference less than ≈ 0.15 dex, i.e. of the order of the error. Thus, it is reasonable to attribute the observed differences to the differences in the stellar parameters, and in the measurement of the individual abundances and their combination. For six elements, Mg I, Na I, Sc II, V I, Y I, and Zr I, the differences are larger. Those elements, as well as Ca I, are discussed below:

- Mg I: Pompéia et al. (2008) used the Mg I line at 5711 Å while we used in addition two other lines (6318 Å and 6319 Å). If we used only the line at 5711 Å, then $\langle[{\rm Mg/Fe}]_{\rm us} - [{\rm Mg/Fe}]_{\rm Pompeia}\rangle = -0.09$ dex (r.m.s $= 0.12$ dex), instead of -0.23 dex.

- Ca I: we recall that we changed the $\log gf$ of the Ca I lines (Sec. 4.2.3). Consequently, all the abundances are shifted by about 0.2 dex. With the old $\log gf$, $\langle[{\rm Ca/Fe}]_{\rm us} - [{\rm Ca/Fe}]_{\rm P08}\rangle = -0.08$ dex; with the new $\log gf$, $\langle[{\rm Ca/Fe}]_{\rm us} - [{\rm Ca/Fe}]_{\rm P08}\rangle = 0.09$ dex.

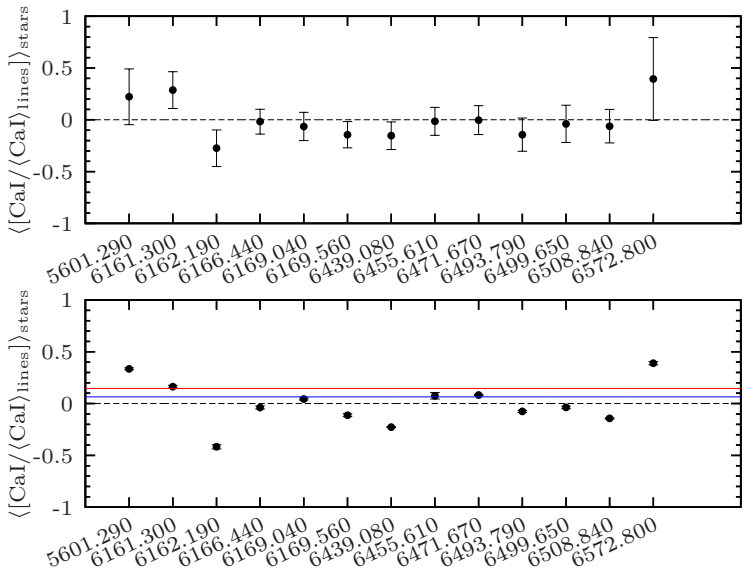

Figure 4.4: **Diagnosis graphs for the cleaning of Ca lines:** mean behaviour of all tested Ca lines for our LMC bar stars (top panel) and our simulated Arcturus (bottom panel). For a given line i, the error bar represents the standard deviation of the difference $[\mathrm{X/Fe}]_i - \langle[\mathrm{X/Fe}]\rangle_{\mathrm{lines}}$. The solid lines indicates the mean disagreement between our Arcturus abundances, on the one hand, and Ramírez & Allende Prieto (2011) and Worley et al. (2009), on the other hand: red solid line: $\langle[\mathrm{X/Fe}]_{\mathrm{Worley}} - \langle[\mathrm{X/Fe}]\rangle_{\mathrm{lines}}\rangle_{\mathrm{Arcturus}}$; blue solid line: $\langle[\mathrm{X/Fe}]_{\mathrm{Ramirez}} - \langle[\mathrm{X/Fe}]\rangle_{\mathrm{lines}}\rangle_{\mathrm{Arcturus}}$. In the mean, the lines at 5601 Å and 6572 Å exhibit a larger scatter than other lines (top panel) and the lines at 5601 Å, 6162 Å and 6572 Å show a larger disagreement with the mean abundance. Those three lines have been removed from the abundance analysis.

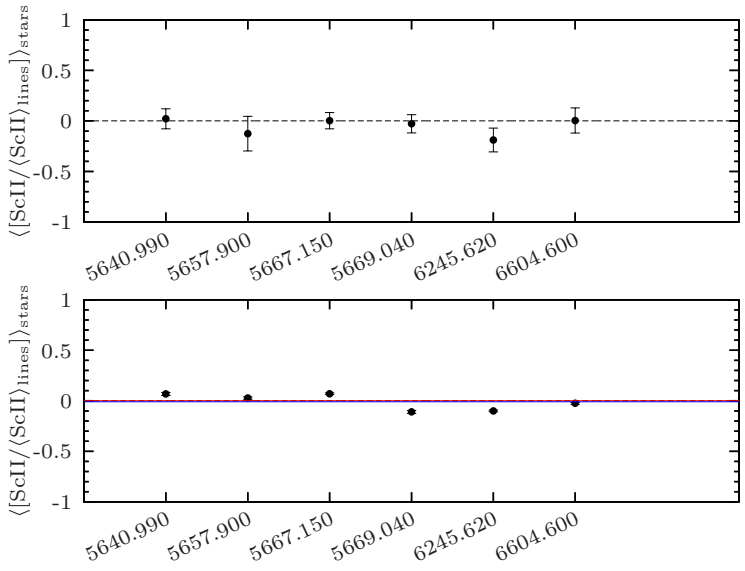

Figure 4.5: **Diagnosis graphs for the cleaning of Sc lines:** mean behaviour of all tested Sc lines for our LMC bar stars (top panel) and our simulated Arcturus (bottom panel). In the mean, the lines at 5657 Å and 6245 Å exhibit a larger disagreement with the mean abundance (top panel). Those two lines have been removed from the abundance analysis.

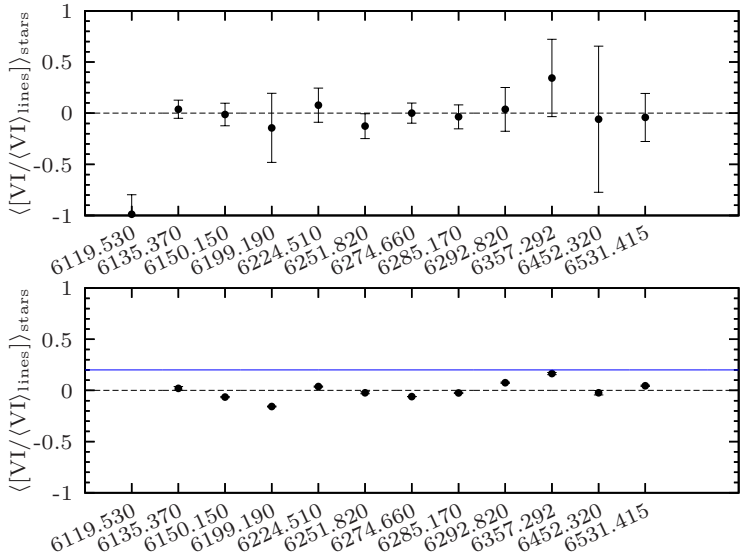

Figure 4.6: **Diagnosis graphs for the cleaning of V lines:** mean behaviour of all tested V lines for our LMC bar stars (top panel) and our simulated Arcturus (bottom panel). The line at 6119 Å could not be detected in our LMC stars (border of the setup HR13). In the mean, the lines at 6199 Å, 6357 Å and 6452 Å exhibit a larger scatter and/or disagreement with the mean abundance (top panel). Those four lines have been removed from the abundance analysis.

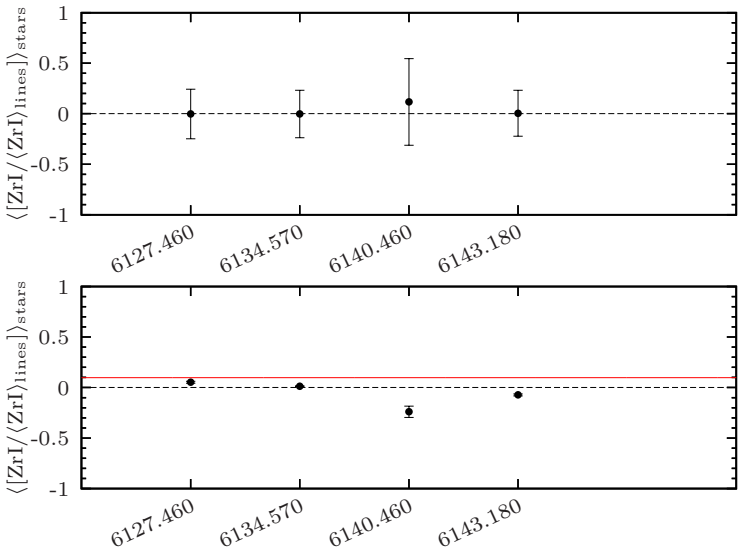

Figure 4.7: **Diagnosis graphs for the cleaning of Zr lines:** mean behaviour of all tested Zr lines for our LMC bar stars (top panel) and our simulated Arcturus (bottom panel). The line at 6140 Å is an outlier in Arcturus abundances (bottom panel) and exhibits a larger scatter than the other lines for LMC bar stars. This line has been removed from the abundance analysis.

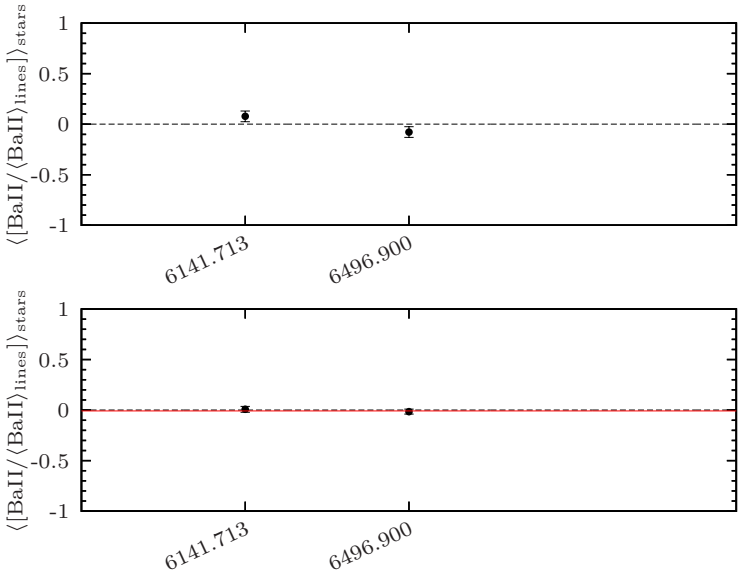

Figure 4.8: **Diagnosis graphs for the cleaning of Ba lines:** mean behaviour of all tested Ba lines for our LMC bar stars (top panel) and our simulated Arcturus (bottom panel). The two lines are in excellent agreement for Arcturus.

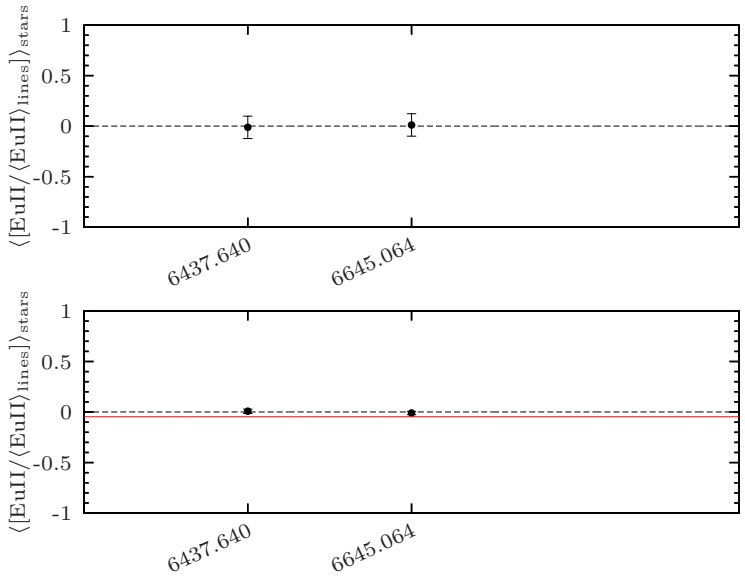

Figure 4.9: **Diagnosis graphs for the cleaning of Eu lines:** mean behaviour of all tested Eu lines for our LMC bar stars (top panel) and our simulated Arcturus (bottom panel). The two lines are in excellent agreement for Arcturus and our LMC bar stars.

- Na I: Pompéia et al. (2008) used four lines and derived the individual abundances from EW while we used only three lines after having discarded the Na I line at 5862 Å (that we found systematically discrepant) and derived the individual abundances from spectrum synthesis (SS). If we had used all four lines, then $\langle[\mathrm{Na/Fe}]_{\rm us} - [\mathrm{Na/Fe}]_{\rm P08}\rangle = 0.03$ dex (r.m.s = 0.18 dex).

- Sc II: Pompéia et al. (2008) used only the Sc II line at 5657 Å instead of four lines and they also took into account the hfs when deriving the abundance. If we limit ourselves to the line at 5657 Å, then $\langle[\mathrm{Sc/Fe}]_{\rm us} - [\mathrm{Sc/Fe}]_{\rm P08}\rangle = 0.05$ dex (r.m.s = 0.11 dex).

- V I: as explained in Section 4.2.3, we took into account the hfs in the abundance measurement, while Pompéia et al. (2008) did not. This explain the disagreement.

- Y I, Zr I: for Y I, Pompéia et al. (2008) and we used the same line and the same method (fitting of line profile) to derive the abundance. For Zr I, Pompéia et al. (2008) used the Zr I line at 6134 Å while we used three lines. But if we restrict the analysis to the same line, we still have $\langle[\mathrm{Zr/Fe}]_{\rm us} - [\mathrm{Zr/Fe}]_{\rm P08}\rangle = 0.46$ dex (r.m.s = 0.21 dex). For those two elements, the lines are weak and difficult to measure. Therefore, the abundance measurement is likely less robust and more sensitive to the method (e.g., the wavelength range where the synthesis is compared to the data, the continuum placement). Furthermore, these lines are extremely $T_{\rm eff}$ sensitive and differences in the stellar parameter determinations between the two studies can explain a large part of the

Table 4.2: **Comparison of our new abundances for our LMC disc stars and those published by Pompéia et al. (2008):** mean m and r.m.s s of the distribution of $[X/Fe]_{us} - [X/Fe]_{Pompeia}$.

Element	m	s
	dex	dex
O I	-0.12	0.13
Mg I	-0.23	0.12
Si I	+0.11	0.12
Ca I	+0.09	0.12
Ti I	+0.12	0.14
Ti II	+0.15	0.11
Na I	-0.19	0.18
Sc II	+0.14	0.15
V I	-0.22	0.14
Cr I	+0.06	0.12
Co I	-0.00	0.14
Ni I	+0.06	0.09
Cu I	-0.04	0.14
Y I	+0.24	0.25
Zr I	+0.43	0.20
Ba II	+0.04	0.17
La II	+0.05	0.11

difference (see Sec. 4.3 § "Stellar parameters").

In addition, we derived the Eu abundances for the LMC disc stars. The wavelength coverage of Pompéia et al. (2008) spectra is not exactly the same as ours since the setup HR14 they used was different (see Footnote 4 and 5). Consequently, the Eu II line at 6645 Å is not available; but the Eu II line at 6437 Å is present. Although this line is weaker than the other, we could use it successfully for most of the LMC disc stars. Table C.1 gives the final abundances for the LMC inner disc stars.

4.2.5.2 Signal-to-noise ratio for our LMC inner disc stars

The minimum value $T^2_{\rm nominal}$ of the function T^2 is related to the S/N ratio according to a power-law. In order to derive a robust S/N–$T^2_{\rm nominal}$ relation, we computed for each LMC bar stars the median of $T^2_{\rm nominal}$ values of all measured lines. Figure 4.10 shows $\widehat{\rm Median}[T^2_{\rm nominal}]$ vs. S/N for the setups HR11, HR13 and HR14 (from left rot right), together with the adjusted power-law function.

Since we do not have S/N ratio for our LMC inner disc stars (Sec. 2.2.3 and 2.2.5), we decided to apply the S/N–$T^2_{\rm nominal}$ relations derived for our LMC bar stars. To this end, we computed for each LMC inner disc stars the median of $T^2_{\rm nominal}$ values of all measured lines, and after inverting the power-law, we obtained a calibrated S/N ratio. As a sanity check, we computed calibrated S/N ratios for

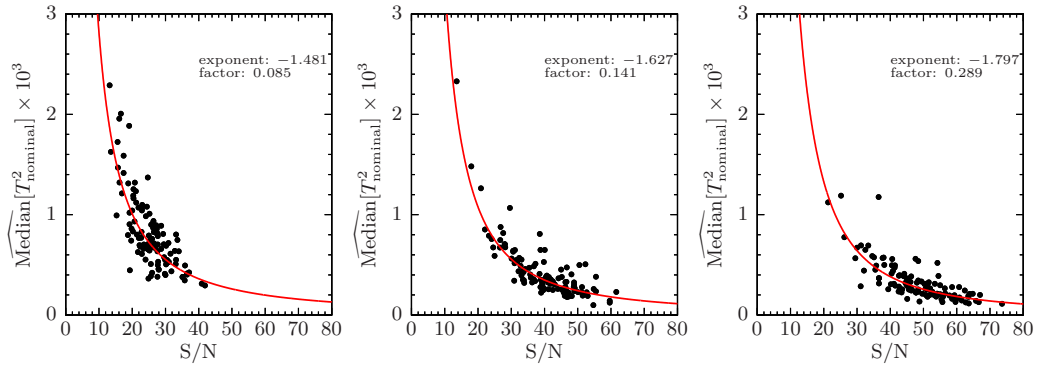

Figure 4.10: S/N–T^2_{nominal} **relations for our LMC bar stars. From left to right panel:** $\widehat{\text{Median}}[T^2_{\text{nominal}}]$ vs. S/N for the setups HR11, HR13 and HR14. Red solid line: power-law fit (whose exponent and multiplying factor are given in the plot).

our LMC bar stars and compared them to the measured ones in Figure 4.11: the agreement between measured and calibrated S/N ratios is rather good, and more importantly, despite the scatter, most stars are classified in the same S/N ratio regime.

4.3 Error budget

Four main sources of uncertainty exist: uncertainties on the atomic data describing the measured lines (systematic from star to star), uncertainties due to the modelling of the absorption line (mostly systematic from star to star in our sample since it is very homogeneous in stellar type), and two stochastic errors (from star to star), namely uncertainties on the abundance measurement (for both EW or SS, due to the noise in the fluxes, the continuum placement, the profile integration or profile fitting, and if the line is blended, the hypothesis on the contaminant abundance), and uncertainties on the stellar parameters.

4.3.1 Abundance measurement

DAOSPEC provides us with an error on the EW, which is obtained during the least-square fit of the line. As mentioned in Stetson & Pancino (2008), this error is not a genuine 1σ confidence interval (e.g., the correlation between the pixels is not taken into account). We checked it using our Arcturus spectra and the set of Fe I lines (51 lines measured which cover a broad range of line strengths and wavelengths). For each S/N ratio hypothesis and for each Fe I line, we computed the sample standard deviation $\widehat{\text{Std}}[W]$ of the EW distribution, as well as the mean $\langle e_{\text{dao}}(W)\rangle$ of the error returned by DAOSPEC. $\widehat{\text{Std}}[W]$ is a good estimator of the error on the EW since it encompasses the effect of the noise in the fluxes and the continuum placement. Figure 4.12a shows the comparison of $\langle e_{\text{dao}}(W)\rangle$ and $\widehat{\text{Std}}[W]$. There is a fairly good agreement between the two: the mean of $(\widehat{\text{Std}}[W] - \langle e_{\text{dao}}(W)\rangle)$ is -0.18 mÅ,

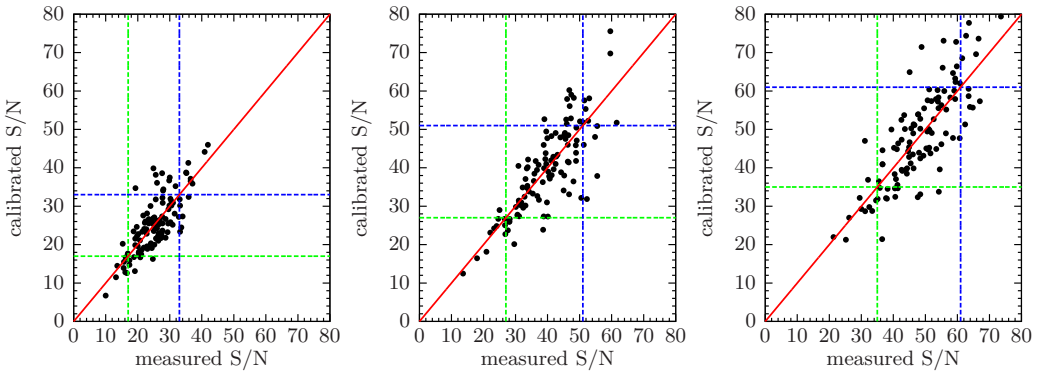

Figure 4.11: **Comparison between measured and calibrated** S/N **ratio for our LMC bar stars.** [**right panel:** From left to] comparison for the setups HR11, HR13 and HR14. Red solid line: 1-to-1 relation; green dashed line: frontier between the low and median S/N ratio regime; blue dashed line: frontier between the median and high S/N ratio regime.

$-0.54\,\mathrm{m\AA}$, $-0.76\,\mathrm{m\AA}$ for the low, median and high S/N ratio respectively; when the Monte-Carlo simulations predicts large errors, DAOSPEC does also; the error decreases when the S/N ratio increases. In the mean, DAOSPEC tends to mildly overestimate the error bar, especially when the S/N ratio gets better. So it is reasonable to use the error computed by DAOSPEC.

Another pitfall is the conversion of the error on the EW into an error on the abundance. Indeed, when we feed *turbospectrum* with the pair $(W, e_{\mathrm{dao}}(W))$, it computes the abundances corresponding to W, and $W \pm e_{\mathrm{dao}}(W)$ and often provides asymmetric (right and left) errors. This is not *a priori* a proper way to find the error on the abundance since we do not know the relationship between [X/Fe] $\pm$ e([X/Fe]) and $W \pm e_{\mathrm{dao}}(W)$. We performed similar tests for the abundances as we did for EW. For each S/N ratio hypothesis and for each Fe I line, we computed the sample standard deviation $\widehat{\mathrm{Std}}$[[Fe/H]] of the [Fe/H] distribution, as well as the mean $\langle e_{\mathrm{turbo}}([\mathrm{Fe/H}])\rangle$ of the error returned by *turbospectrum*. Figure 4.12b shows the comparison of $\langle e_{\mathrm{turbo}}([\mathrm{Fe/H}])\rangle$ and $\widehat{\mathrm{Std}}$[[Fe/H]]. We obtain a similar pattern for the abundances as that for the EW: the agreement is fairly good but the errors tend to be mildly overestimated when the S/N ratio increases (tough the effect is $< 0.05\,\mathrm{dex}$ at high S/N ratio). Here again, we considered safe to keep the error returned by *turbospectrum* (i.e. the mean of the right and left errors).

Unfortunately, for the lines measured by absorption line fitting, we cannot use classical theorems to derive an error on the abundance measurement. Indeed, T^2 is not a random variable which follow a χ^2 distribution since we do not divide each term of the quadratic sum by the error on the flux at pixel i (the GIRAFFE pipeline certainly provides an error for each pixel but it is overestimated and correlated, see Section 2.2.3) and the $\mathcal{O}_i$ are correlated due to the interpolation or rebinning performed during the data reduction. One way to get an estimator of the the 1σ error is to do Monte-Carlo simulations. We used the Arcturus spectra to estimate the error $e_{\mathrm{Arcturus}}([\mathrm{X/Fe}])$ on each single line (by computing the standard deviation

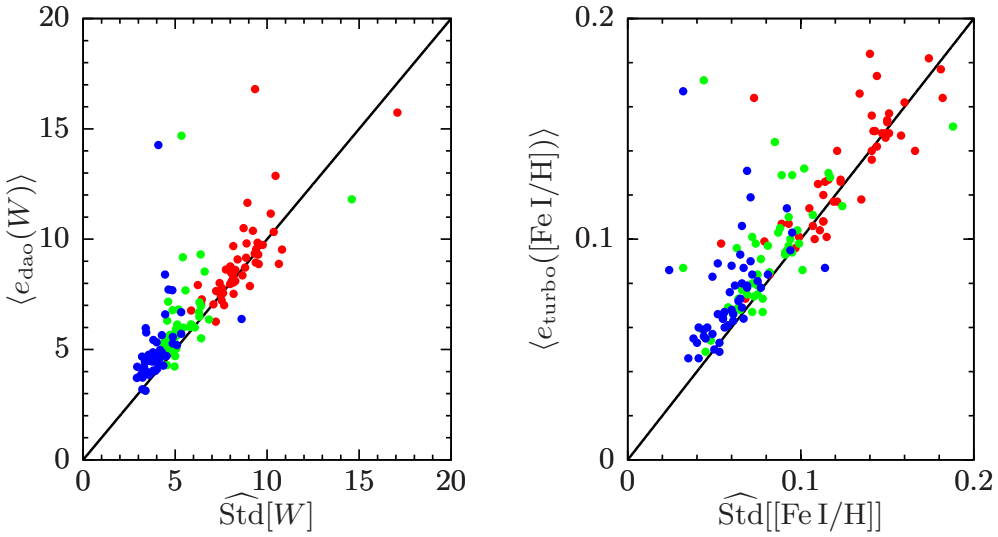

(a) DAOSPEC error (b) *turbospectrum* error

Figure 4.12: Comparison of DAOSPEC and *turbospectrum* errors to standard deviations of Monte-Carlo distributions. **Left panel:** $\langle e_{\rm dao}(W)\rangle$ vs. $\widehat{\rm Std}[W]$. **Right panel:** $\langle e_{\rm turbo}([{\rm Fe\,I/H}])\rangle$ vs. $\widehat{\rm Std}[[{\rm Fe\,I/H}]]$. Red dots: low S/N ratio; green dots: median S/N ratio; blue dots: high S/N ratio.

of the abundance distribution) and to assign the error to the LMC stars depending on the S/N ratio category in which they fall.

For a given element X, we propagated the errors on the individual lines $e_{\rm turbo}([{\rm X/Fe}])$ or $e_{\rm Arcturus}([{\rm X/Fe}])$, which gave us $e_{\rm prop}(\langle[{\rm X/Fe}]\rangle)$.

4.3.2 Atomic data and line modelling

Our capacity to model correctly an absorption line, and thus measure the abundances accurately, depends on the quality of the atomic data describing the radiative transitions but also on our understanding of the underlying physics. Line lists are often a compilation of various sources aiming at giving the best parameters for a given line, and therefore, the precision of these parameters (among which $\log gf$ hold the main role) varies from line to line. The resulting synthetic spectrum is model-dependent (systematic error due to the choice of the grid of model atmospheres, the assumptions on the thermodynamic equilibrium, the atom models) and data-dependent (random error due to the $\log gf$ provided by the line lists). The sample dispersion $\widehat{\rm Std}\,[[{\rm X/Fe}]]$ of the individual abundances about the mean can be used to estimate the combination of these effects (if enough lines are available to estimate it). We derived conservative errors as follows:

- if $N_{\rm lines} < 5$:

$$e_{\rm data}(\langle[{\rm X/Fe}]\rangle) = e_{\rm prop}(\langle[{\rm X/Fe}]\rangle) \tag{4.19}$$

- if $N_{\rm lines} \geq 5$:

$$e_{\rm data}(\langle[{\rm X/Fe}]\rangle) = \max\left(\frac{\widehat{\rm Std}\,[[{\rm X/Fe}]]}{\sqrt{N_{\rm lines}}}, e_{\rm prop}\,(\langle[{\rm X/Fe}]\rangle)\right) \tag{4.20}$$

To assess our method of error estimation, we compared the standard error of the mean to the propagated error for Ca, Ni, Sc and V. We recall that for these elements, we have enough lines to compute a meaningful variance) and that we derived Ca and Ni abundances from EW and Sc and V abundances from SS. We found a median difference of ~ 0.02 dex: thus, this check validates the use of $e_{\rm turbo}([{\rm X/Fe}])$ or $e_{\rm Arcturus}([{\rm X/Fe}])$ for the individual measurements.

4.3.3 Stellar parameters

The error $e_{\rm params}$ on chemical abundances due to the adopted stellar parameters is a thorny question. The four stellar parameters are mutually dependent and changing one of them implies a change of the others (see Johnson et al., 2006; McWilliam et al., 1995a for a discussion on covariance terms). When the propagation of error is not straightforward, a usual practise is to perturb the explanatory variable (input) by $\pm$ its error and to look at the corresponding shift of the dependent variable (output). For the abundances, it would come down to repeat this procedure for each parameter, keeping the other three constant. The pitfall is to work with a set of parameters that do not satisfactorily describe the atmosphere of the star under study. For instance, when the temperature is changed by, say, 150 K, and $\{\log g, [{\rm M/H}], \xi_{\rm micro}\}_{\rm nominal}$ (which were found for the nominal temperature) are kept, it is likely that the spectroscopic criterion used to find $\xi_{\rm micro}$ does not hold anymore and therefore the determination of abundances from strong lines will not be correct. We followed the prescription from Cayrel et al. (2004): as $\rm T_{phot}$ has the major effect on the abundance determination, we change it by $\pm$ its error and determine the three other stellar parameters corresponding to this new temperature $\{\log g, [{\rm M/H}], \xi_{\rm micro}\}_{\pm\sigma({\rm T_{phot}})}$; we derive the chemical abundances corresponding to this perturbed solution (with $\sigma({\rm T_{phot}}) = 150$ K; see Sec. 3.2.3) and compare them to those given by the nominal solution. The final systematic error on [A/B] due to errors on effective temperature is then given by:

$$\begin{aligned} e_{\rm params} = \max\Big(&|[{\rm A/B}]_{+\sigma({\rm T_{phot}})} - [{\rm A/B}]_{\rm nominal}|, \\ &|[{\rm A/B}]_{-\sigma({\rm T_{phot}})} - [{\rm A/B}]_{\rm nominal}|\Big) \end{aligned} \tag{4.21}$$

Table 4.3 gives the typical (mean over the sample) $e_{\rm data}$ and $e_{\rm params}$ (given as $[{\rm A/B}]_{+\sigma({\rm T_{phot}})} - [{\rm A/B}]_{\rm nominal}$ and $[{\rm A/B}]_{-\sigma({\rm T_{phot}})} - [{\rm A/B}]_{\rm nominal}$) for different elemental ratios for our LMC bar stars. In the vast majority of cases, the errors due to stellar parameters dominates over the random measurement errors. Figures 4.13 and 4.14 respectively show the effect of increasing and decreasing the temperature by 150 K on the other stellar parameters; in the mean, we find:

- for $T_{\rm phot} + 150$ K: $\log g$ is increased by 0.15 (r.m.s = 0.06), $\xi_{\rm micro}$ is increased by 0.2 km s^{-1} (r.m.s = 0.08), [M/H] is increased by 0.04 dex (r.m.s = 0.08),

Table 4.3: Mean random $e_{\rm data}$ and systematic errors $e_{\rm params}$ for different elemental ratios for our LMC bar stars. $e_{\rm params}(\pm\sigma(T_{\rm phot})) = [{\rm A/B}]_{\pm\sigma(T_{\rm phot})} - [{\rm A/B}]_{\rm nominal}$.

Elemental ratio	$e_{\rm data}$ dex	$e_{\rm params}$ $(-\sigma(T_{\rm phot}))$ dex	$e_{\rm params}$ $(+\sigma(T_{\rm phot}))$ dex
[Fe I/H]	0.03	0.04	0.04
[Fe II/H]	0.08	0.23	-0.12
[O I/Fe I]	0.04	- 0.10	0.06
[Mg I/Fe I]	0.04	- 0.03	0.01
[OI + MgI /Fe I]	0.03	- 0.07	0.04
[Si I/Fe I]	0.08	0.03	-0.05
[Ca I/Fe I]	0.04	- 0.09	0.05
[Ti I/Fe I]	0.07	- 0.20	0.17
[Ti II/Fe I]	0.04	0.02	-0.04
[Na I/Fe I]	0.04	- 0.14	0.05
[Sc II/Fe I]	0.04	- 0.01	-0.01
[V I/Fe I]	0.04	- 0.27	0.24
[Cr I/Fe I]	0.05	- 0.13	0.11
[Co I/Fe I]	0.04	- 0.12	0.10
[Ni I/Fe I]	0.05	- 0.04	0.03
[Cu I/Fe I]	0.08	- 0.10	0.09
[Y I/Fe I]	0.08	- 0.40	0.31
[Zr I/Fe I]	0.04	- 0.28	0.26
[Ba II/Fe I]	0.07	0.06	-0.06
[La II/Fe I]	0.06	- 0.04	0.04
[YI + ZrI /BaII + LaII]	0.06	- 0.33	0.29
[Eu II/Fe I]	0.07	- 0.05	0.02
[Ba II/Eu II]	0.11	0.08	-0.08
[La II/Eu II]	0.09	- 0.00	0.02

[Fe I/H] is increased by 0.04 dex (r.m.s = 0.08), [Fe II/H] is decreased by 0.12 dex (r.m.s = 0.09);

- for $T_{\rm phot} - 150$ K: $\log g$ is decreased by 0.13 (r.m.s = 0.04), $\xi_{\rm micro}$ is decreased by 0.2 km s^{-1} (r.m.s = 0.15), [M/H] is increased by 0.03 dex (r.m.s = 0.12), [Fe I/H] is increased by 0.04 dex (r.m.s = 0.13), [Fe II/H] is increased by 0.22 dex (r.m.s = 0.11).

We note that the [Fe I/H] (and [M/H]) distribution does not change from a situation to another: it does not mean that [Fe I/H] is not sensitive to the temperature. In fact, in our procedure, $\xi_{\rm micro}$ and [Fe I/H] are correlated and the change in [Fe I/H] is compensated by the change in $\xi_{\rm micro}$. Except for [Fe II/H], the behaviour of the stellar parameters is symmetrical when increasing or decreasing the temperature by 150 K.

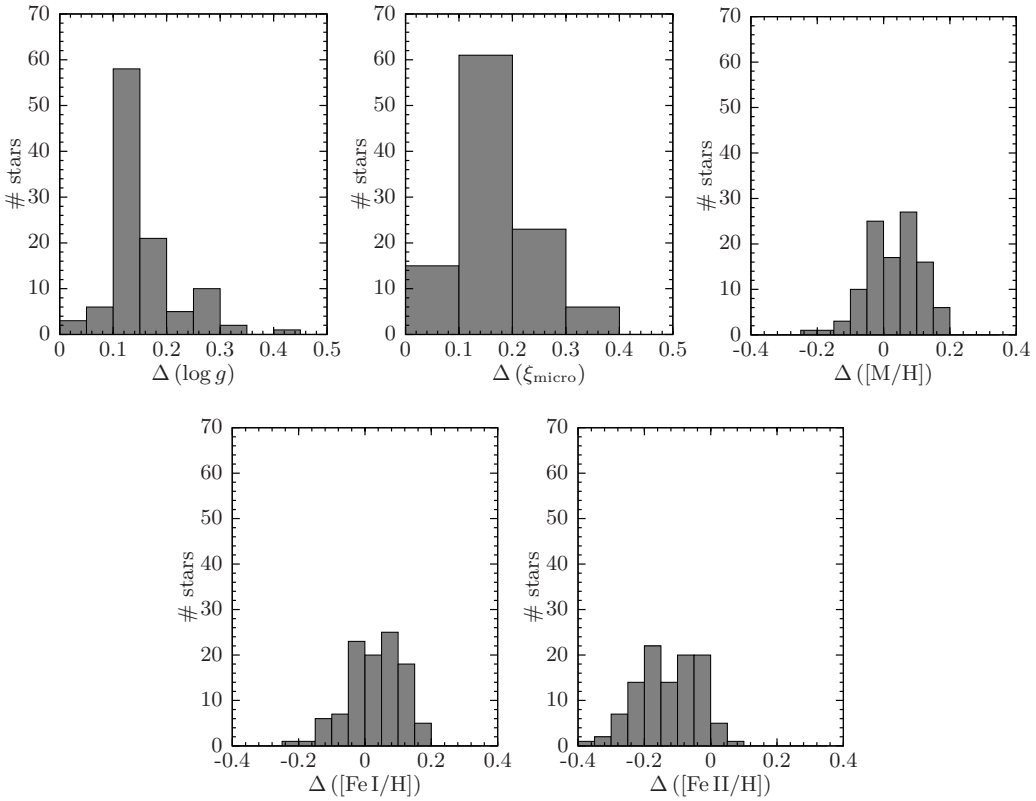

Figure 4.13: Behaviour of $\log g$, ξ_{micro}, [M/H], [Fe I/H] and [Fe II/H] for $T_{\mathrm{phot}} + 150\,\mathrm{K}$. **From top left to bottom right panel:** histogram of $\Delta\,(\log g)$, $\Delta\,(\xi_{\mathrm{micro}})$, $\Delta\,([\mathrm{M/H}])$, $\Delta\,([\mathrm{Fe\,I/H}])$, $\Delta\,([\mathrm{Fe\,II/H}])$, where $\Delta\,(\mathcal{P}) = \mathcal{P}_{+150\,\mathrm{K}} - \mathcal{P}_{\mathrm{nominal}}$.

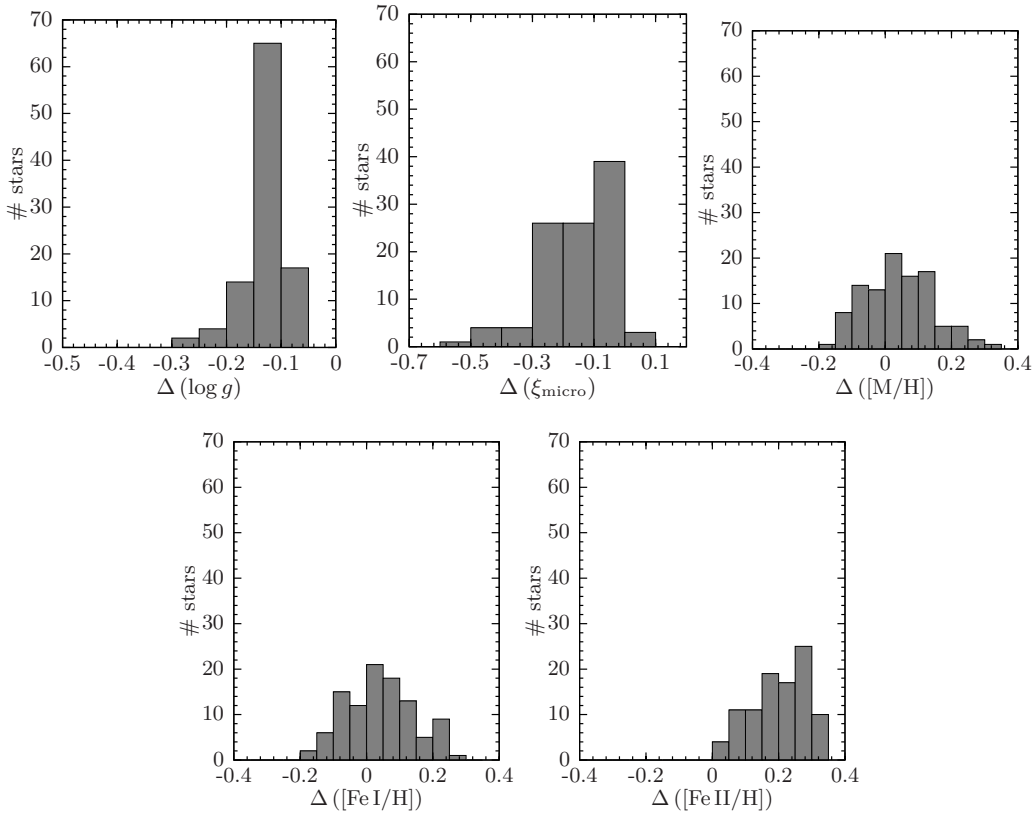

Figure 4.14: Behaviour of $\log g$, ξ_{micro}, [M/H], [Fe I/H] and [Fe II/H] for $T_{\mathrm{phot}} - 150\,\mathrm{K}$. **From top left to bottom right panel:** histogram of $\Delta(\log g)$, $\Delta(\xi_{\mathrm{micro}})$, $\Delta([\mathrm{M/H}])$, $\Delta([\mathrm{Fe\,I/H}])$, $\Delta([\mathrm{Fe\,II/H}])$, where $\Delta(\mathcal{P}) = \mathcal{P}_{-150\,\mathrm{K}} - \mathcal{P}_{\mathrm{nominal}}$.

4.4 Correlations between abundance ratios and stellar parameters

We checked whether there exist correlations between our abundance ratios and stellar parameters. For [FeI/H], we expect a correlation between [FeI/H] and $T_{\rm eff}$ because the location of red giant branch (RGB) isochrones changes with the metallicity. However, Figure 4.15 shows that two regimes exist: there is no significant correlation between [FeI/H] and $T_{\rm eff}$ over the temperature range $[3800\,{\rm K}, 4400\,{\rm K}]$ (metal-rich and cool stars). For higher temperatures, two correlations appear: a negative correlation (hotter stars are more metal-poor), which is the expected one (as described above) and is due to stellar evolution, and a positive correlation (hotter stars are more metal-rich), which means that those stars are very young. On the other hand, there is no significant trend between [FeI/H] and $\xi_{\rm micro}$. Figures 4.16 and 4.17 show respectively the distribution of [X/Fe] with respect to $T_{\rm eff}$ and $\xi_{\rm micro}$. For Na, V, Y and Zr, we found for both fields a clear correlation between [Na, V, Y, Zr/Fe] and $T_{\rm eff}$ and $\xi_{\rm micro}$, i.e. increasing abundance ratio with increasing temperature or microturbulence velocity; for Co and Cr, we found for both fields a marked correlation [Co/Fe] and $\xi_{\rm micro}$ and a mild correlation between [Cr/Fe] and $\xi_{\rm micro}$. Interestingly, LMC GC stars of Mucciarelli et al. (2008, 2010) and LMC disc field stars of Lapenna et al. (2012) follow the same correlation as ours (except V for Mucciarelli et al. (2008)). To finish, if we look at Table 4.3, we see that, in general, elements with a large error due to stellar parameters ($T_{\rm eff}$, $\xi_{\rm micro}$) are those showing a correlation with $T_{\rm eff}$ (it is the case for V, Y and Zr). In Chapter 5, we will take into account these correlations when interpreting the abundance trends.

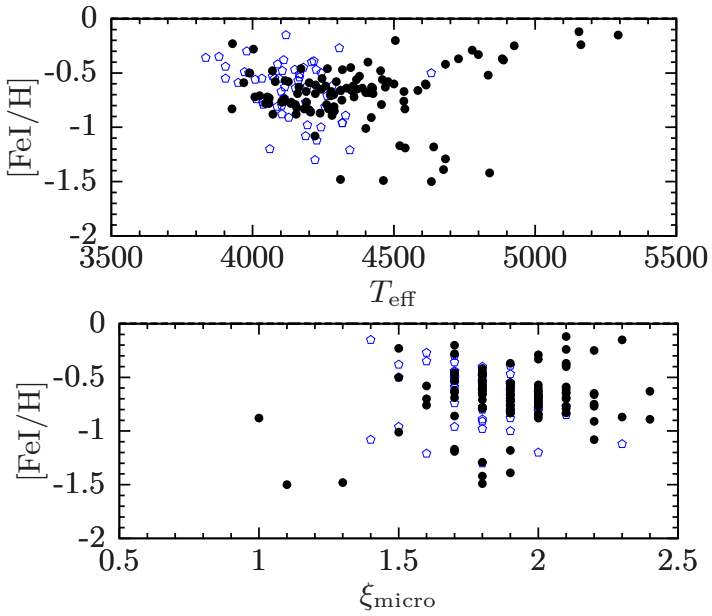

Figure 4.15: **Correlations between** [FeI/H] **and temperatures (top panel) and microturbulence velocities (bottom panel).** Black dots: our LMC bar stars; blue empty pentagons: our LMC inner disc stars.

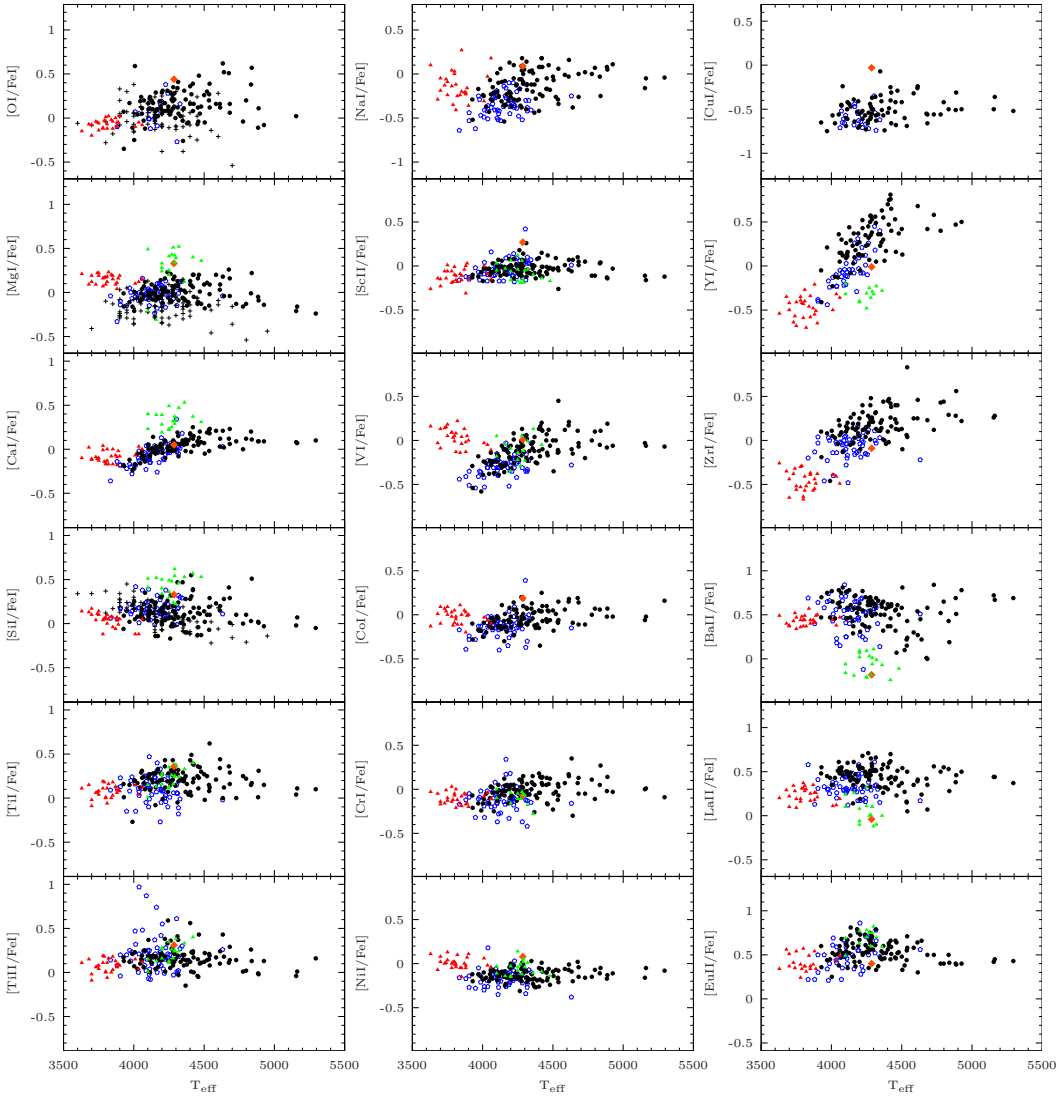

Figure 4.16: Correlations between abundances and temperatures. Black dots: our LMC bar stars; blue empty pentagons: our LMC inner disc stars; red filled diamond: our Arcturus (median S/N ratio); red filled triangles: Mucciarelli et al. (2008) LMC GC stars; green filled triangles: Mucciarelli et al. (2010) LMC GC stars; black plusses: Lapenna et al. (2012) LMC disc field stars.

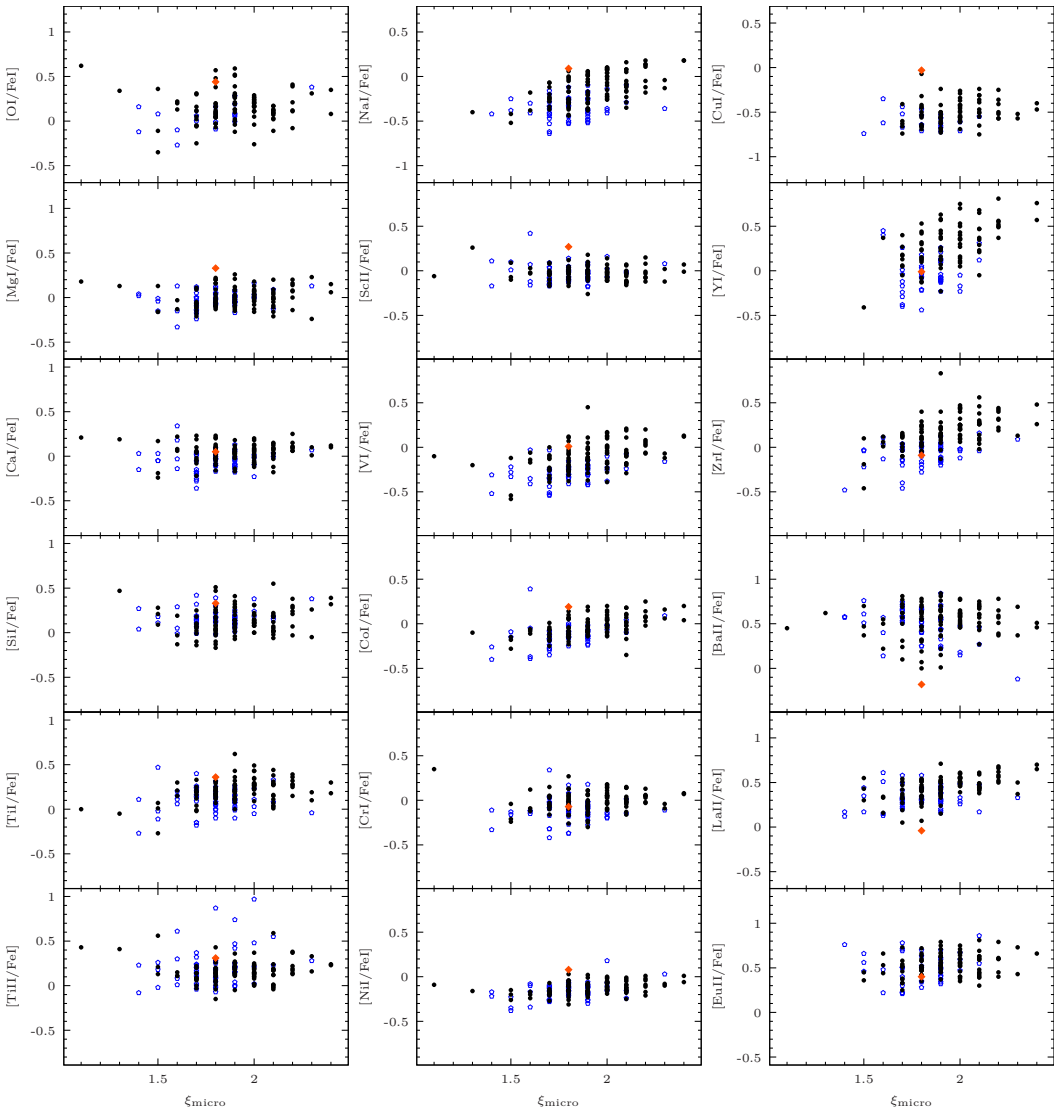

Figure 4.17: Correlations between abundances and microturbulent velocities. Black dots: our LMC bar stars; blue empty pentagons: our LMC inner disc stars; red filled diamond: our Arcturus (median S/N ratio).

Chapter 5

The chemical history of the Large Magellanic Cloud

Contents

5.1 An introduction to galaxy chemical evolution

5.1.1 Stars as chemical element factories

Understanding the structure of the matter around us has been a long quest from the Ancient Greek atomism[1] to the discovery of the electron (Thomson, 1897), the atomic nucleus (Rutherford, 1911), the proton (Rutherford, 1919) and the neutron (Chadwick, 1932). However, the origin of chemical elements and how abundant they are were still mysterious: the advent and development of nuclear and quantum physics at the beginning of the 20th century brought theoretical tools to answer this question.

Until the early 20th century, no satisfactory theory was able to explain the source of energy of stars. Indeed, if the gravitational contraction (proposed by Kelvin and Helmholtz) had been a candidate, Eddington showed that, unfortunately, the total amount of gravitational energy ($E_{gravit} \approx -\frac{3GM_\star^2}{5R_\star}$) was not sufficient for the Sun to

[1] The first appearance of an atomic theory in the European culture is awarded to Leucippus and his disciple Democritus (ca. 450 BC). Atomism was eclipsed by Empedocles' and Aristotle's principles (matter made of a mixture of four elements) until the 19th century. Discoveries in chemistry (Lavoisier, etc.) and gas physics (Boyle, Mariotte, Bernoulli, etc.) rejected Aristotle's vision and in 1803, Dalton proposed a new atomic theory.

shine for billion years, contradicting the age of the Earth estimated by geologists. Nuclear and quantum physics allowed to imagine nuclear energy as a new source of energy: the energy E released by a nuclear reaction is proportional to the mass defect Δm between initial nucleids and nuclear reaction products through the mass–energy equivalence formula[2] $E = \Delta m c^2$. Fusion of H into He was then proposed to explain energy generation in stars. Nevertheless, a conceptual difficulty remained, since in a classical view, the central temperature of stars is too low for fusion reactions to occur (the classic approach requires $T_c \sim 10^{10}$ K while $T_{c\odot} \sim 10^7$ K): two protons cannot get close enough for the strong interaction to dominate the Coulomb interaction. In 1928, Gamow proposed the tunnel effect to explain α radioactivity and thus brought the last ingredient to understand how nuclear fusions can occur at the centre of stars (*Gamow peak*). Houtermans and Atkinson in 1929 made the first calculations of thermonuclear reactions and the conversion of H into He was explained later by the pp chain (Bethe and Critchfield, 1930) and the CNO cycle (von Weizsäcker, 1938; Bethe, 1939). Thus, answering the question of energy generation in stars started to answer the question of the origin of elements. However, since stellar theories still did not explain the origin of all chemical elements (the needed temperatures are higher and higher for fusion reactions involving heavier and heavier elements), Gamow suggested in 1942 that all elements were produced by the Big Bang; unfortunately, the cooling of the Universe allowed to form only elements from H to Li, i.e. the first three elements of the periodic table. In 1952, Merrill discovered Tc lines in the spectra of evolved stars (AGB stars): as all known Tc isotopes are short-lived (longest half-life ~ 4 Myr) and very small compared to the age of an red giant branch (RGB) star (hundreds of million years or more), the presence of Tc in stellar spectra meant that this element had been recently synthesised in the star. Thus, Merrill's spectacular discovery is the experimental confirmation of the then-supposed stellar origin of elements. And, in 1957, Burbidge et al. (1957) published a complete description of the various nucleosynthetic processes occurring in stellar interiors in their seminal paper, the so-called B^{2}FH (see also Wallerstein et al., 1997 for an update 40 years after B^{2}FH). According to the current picture, elements an be divided in three main groups depending on their production site:

- *Big Bang nucleosynthesis*: H (and its isotope D), He and traces of ^{7}Li produced at the beginning of Universe's life;
- *cosmic ray spallation*: ^{6}Li, Be and B produced in the interstellar medium (ISM);
- *stellar nucleosynthesis*: Li, all elements from C to U produced in stellar interiors through various nuclear processes: nuclear fusion reactions; α captures, proton or neutron captures; α, β^+, β^- radioactivity; photo-disintegration.

In Section 5.1.2 and 5.1.4, I will briefly review a selection of nucleosynthetic processes occurring in stars.

[2] In 1919, Rutherford experimentally confirmed this with an experiment turning N into O via α captures.

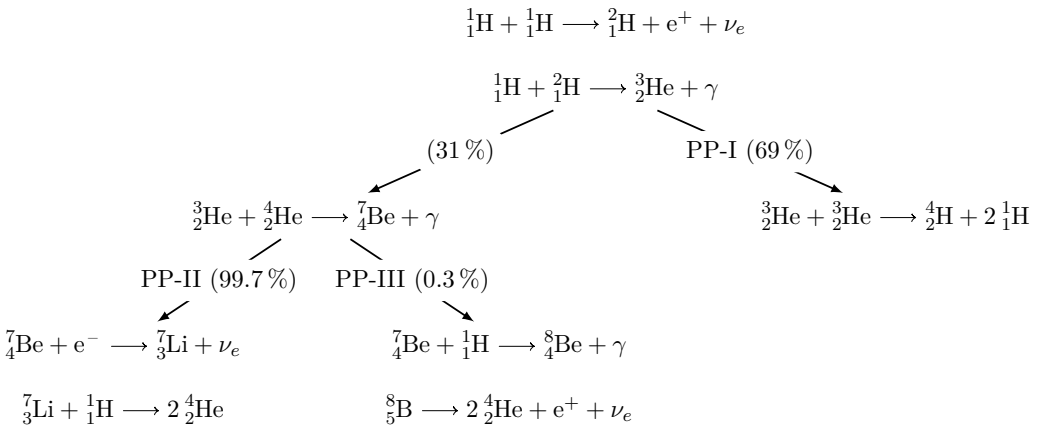

Figure 5.1: **Hydrogen burning through pp chains.** The percentages indicate the occurrence of each chain. *Credits:* Leblanc (2010)

5.1.2 Nucleosynthesis of elements lighter than iron

5.1.2.1 Main sequence evolution

A star forms from the gravitational collapse of a gas cloud and its fate depends mainly on its initial mass $M_{\mathrm{init}\star}$. In the following, we will be interested in stars with $M_{\mathrm{init}\star} \gtrapprox 0.08 M_\odot$, i.e. stars massive enough to ignite hydrogen burning in their core[3]. After its formation, a star lies on the *main sequence (MS)*: during this first phase of the stellar life, the energy supply is ensured by hydrogen burning whose net effect is to turn four H nuclei into one He nucleus. In fact, nuclear reactions involving four reacting particles are highly improbable and the hydrogen burning needs chain reactions. Depending on the central temperatures, i.e. the initial mass of the star, hydrogen burning will predominantly occurs through the pp chains ($T_\mathrm{c} > 10^6$ K for stars with $M_{\mathrm{init}\star} \lessapprox 2 M_\odot$; Fig. 5.1) or the CNO cycles ($T_\mathrm{c} \sim 10^7$ K for stars with $M_{\mathrm{init}\star} \gtrapprox 2 M_\odot$; Fig. 5.2). In the CNO cycles, C, N and O nuclei are catalysts and the total number of nuclei is kept approximately constant: C and N suffer from an isotopic redistribution ($^{12}\mathrm{C} \longrightarrow {}^{13}\mathrm{C}$ and $^{15}\mathrm{N} \longrightarrow {}^{14}\mathrm{N}$); ^{12}C, ^{13}C and ^{15}N are depleted in favour of ^{14}N. The CNO cycles are the main source of energy in massive stars.

5.1.2.2 Post-main sequence evolution

As said, the initial mass of a star will determine its subsequent evolution and thus which nucleosynthesis processes will take place in its interior. The typical lifetime $\tau_{\mathrm{MS}\star}$ of a star on the MS is given by:

$$\frac{\tau_{\mathrm{MS}\star}}{\tau_{\mathrm{MS}\odot}} = \left(\frac{M_\star}{M_\odot}\right)^{-2.5} \tag{5.1}$$

[3]Stars with $M_{\mathrm{init}\star} \lessapprox 0.08 M_\odot$ are called *brown dwarf* and have almost no evolution. Deuterium and lithium burning can occur in their core for a limited period ($\sim$ 1 to 10 Myr).

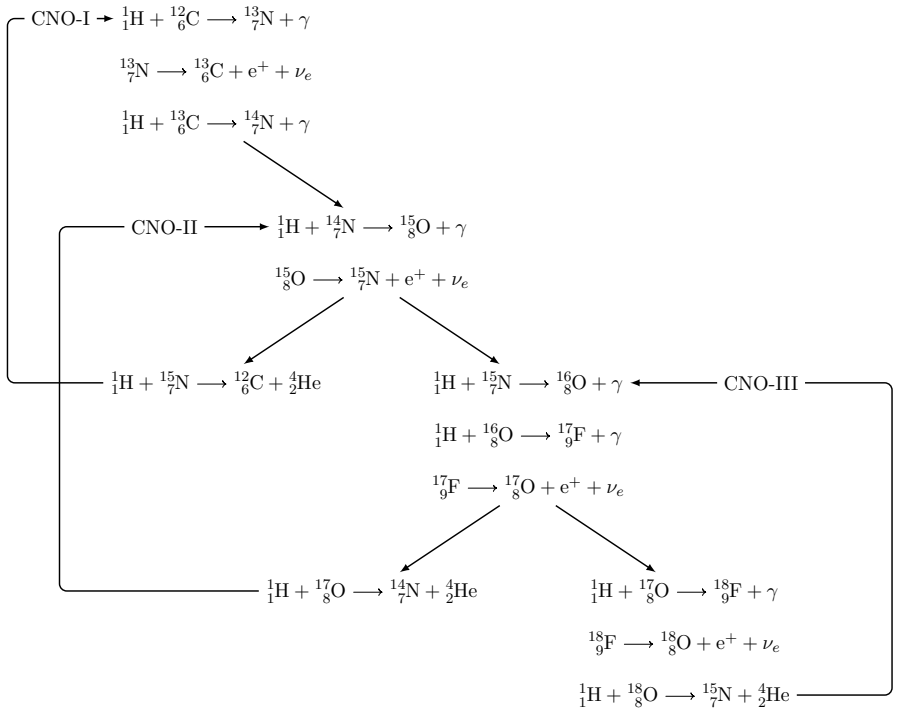

Figure 5.2: **Hydrogen burning through CNO cycles.** *Credits:* Leblanc (2010)

For instance, a $2M_\odot$, $3M_\odot$ and $10M_\odot$ will remain on the MS about 1.8 Gyr, 700 Myr and 30 Myr respectively.

Low mass stars Stars with $M_{\mathrm{init}\star} \lessapprox 2M_\odot$ do not have a convective core: as the pp chains fuse hydrogen nuclei, the stellar core progressively becomes He rich and no more nuclear reactions occur. When H is exhausted in the stellar core, the star leaves the MS and enters the *sub-giant branch (SGB)*. As the number of particles decreases due to hydrogen burning, the core contracts, temperatures increase and nuclear reaction rates increase. To remain in equilibrium, the star adjusts its structure: the envelope expands ($R_\star$ increases), the surface temperature decreases but the luminosity remains constant. The star moves on the SGB, i.e. horizontally and towards the cool side in the Hertzsprung-Russel diagram (HR diagram). On the SGB, the hydrogen fusion is confined in a thick H shell at the rim of the He core: this is the *hydrogen shell burning*. The hydrogen shell becomes thinner and thinner as nuclear reactions consume H nuclei, and therefore, the mass of the He core increases: when the density is high enough, the He core becomes degenerate (i.e. pressure is temperature independent) and the star is at the bottom of the *red giant branch (RGB)*. The hydrogen shell burning continues to add mass to the degenerate He core: the core contracts, central temperature increases, the rate of nuclear reactions in the hydrogen shell increases, the envelope expand. The surface temperature of the stars remains almost constant while the luminosity increases: the star climbs up the RGB. During this phase, two particular events occur:

$$^4_2\mathrm{He} + {}^4_2\mathrm{He} \longrightarrow {}^8_4\mathrm{Be} + \gamma$$

$$^8_4\mathrm{Be} + {}^4_2\mathrm{He} \longrightarrow {}^{12}_6\mathrm{C}^* + \gamma$$

$$^{12}_6\mathrm{C}^* \longrightarrow {}^{12}_6\mathrm{C} + \gamma$$

Figure 5.3: **Helium burning through triple-α reactions.** It occurs when $T_\mathrm{c} \sim 10^8$ K. $^8_4$Be is unstable against β decay but the combination of $^8_4$Be with $^4_2$He is a resonant reaction, with a (relatively) large cross-section.

- the *first dredge-up*: the convective envelope goes deeper in the star interior and dredges up processed material towards the star atmosphere, in particular C and N newly distributed isotopes;
- the *luminosity bump*: as the hydrogen shell moves outwards, it finally meets the deepest region mixed by the convective envelope; the chemical discontinuity decreases the rate of nuclear reactions and causes a decrease of the luminosity; a further mixing of CNO cycled material occurs. In the HR diagram, the star makes a vertical loop.

When the central temperature reaches $T_\mathrm{c} \sim 10^8$ K, He burning is ignited and He nuclei are converted into C through the triple-α reactions (Fig. 5.3). This new energy supply still increases T_c and as the core is degenerate, it cannot expand to cool. In fact, a positive feedback exists: the increase in temperature speeds us nuclear reactions, which increases temperatures. This runaway mechanism leads to the *helium flash* (the star is at the *tip* of the RGB): a huge amount of energy is released (which provokes a sudden increase of the luminosity) and used to remove the degeneracy in the core (the pressure increases again with increasing temperatures). The star reaches a new equilibrium and lies on the *horizontal branch (HB)* or the *red clump (RC)*, depending on the star metallicity and mass: the core expands, the envelope contracts, the luminosity decreases. The energy supply is then ensured by stable core He burning and hydrogen shell burning: the HB is the He burning counterpart of the MS. As the triple-α reactions (see Fig. 5.3) convert the He core into a C core, the amount of He nuclei decreases and progressively, a helium shell burning develops at the core border. At this point, the fate of a low mass star depends on its current mass:

- if the mass is too small, the helium burning shell stops rapidly and the star contracts into a *white dwarf (WD)* (this is an AGB-manqué);
- if the mass is high enough, the helium burning shell develops and adds C to the core, and the star climbs up the *asymptotic giant branch (AGB)* (see § "Intermediate mass stars").

Intermediate mass stars Stars with $2M_\odot \lessapprox M_{\mathrm{init}\star} \lessapprox 8 - 10M_\odot$ have a slightly different evolution path than low mass stars since their He core does not become

degenerate. For stars with $M_{\text{init}\star} \gtrapprox 2M_{\odot}$, the dominant mechanism of H burning is the CNO cycles. A steep temperature gradient exists and leads to a fully convective core, which keeps the core material mixed. Therefore, in the central parts, the fuel reservoir is replenished by H from the core border. When H is exhausted, the H burning suddenly stops: T_{c} decreases, the core contracts and heats up while the luminosity slightly increases. The star performs a small hook in the HR diagram. The core contraction heats up the H material around the core and when the temperature is sufficient, H burning is ignited in a thin hydrogen shell. Then, the star evolves rapidly through the SGB up to the bottom of the RGB. As the He core grows (because of He production through the hydrogen shell burning), it contracts and the envelope expands: the star climbs up the RGB. The envelope becomes unstable against convection and the first dredge-up occurs. As the core is non-degenerate, the temperature increase implies a pressure increase: the core contraction goes on until a new balance is found between pressure and gravity. When T_{c} reaches 10^8 K, the He burning starts: the energy release heats up the core. As the core is not degenerate, it expands while the envelope contracts: the star becomes a *blue loop star*. Unlike the low mass stars, the He ignition occurs in a smooth way in intermediate-mass stars and no helium flash happens. As the amount of C in the convective core increases, a new type of nuclear reactions produces O (α capture onto a C nuclei). When the He fuel is exhausted in the core, the star has reached a maximum surface temperature. He burning in a shell around the core and the envelope expands again: the star moves back in the HR diagram (becomes redder), and then, climbs up the AGB. The CO becomes degenerate and the central temperatures will never reach the threshold needed to ignite C. On the AGB, a *second dredge-up* occurs and brings processed material towards the atmosphere. As the helium burning shell moves outwards, it approaches the He–H discontinuity and the hydrogen shell burning is ignited again. Therefore, two burning shells exists simultaneously and are mutually influenced. As the helium shell burning is thermally unstable, it brightens and fades periodically (*He flashes*), leading to *thermal pulses* (associated to mass losses): the star makes blue excursions in the HR diagram. Between two thermal pulses, mixing occurs and gives rise to the *s*-process (Sec. 5.1.4.1). *s*-process elements are brought to the surface via the *third dredge-up*. Ultimately, the star expels its outer layers and forms WD, surrounded by a *planetary nebulae (PN)*. The enriched material containing C, O and heavy elements is then injected into the ISM and will serve as raw matter to form new generations of stars.

Massive stars The beginning of massive stars' life is similar to that of intermediate stars (H burning in core driven by CNO cycle on the MS, followed by H shell burning on the SGB). Unlike low and intermediate mass stars, massive stars (i.e. stars with $M_{\text{init}} \gtrapprox 10M_{\odot}$) will be able to ignite C, O, etc. burning in their core. Once again, the precise evolution of a massive star depends on its initial mass and the mass loss occurring during its evolution: red giant phase followed by blue loops, *red supergiant (RSG)*, *Wolf-Rayet (WR)* stars or *luminous blue variable (LBV)*.

$$^{12}_{6}\mathrm{C} + ^{4}_{2}\mathrm{He} \longrightarrow ^{16}_{8}\mathrm{O} + \gamma$$

$$^{12}_{6}\mathrm{C} + ^{12}_{6}\mathrm{C} \longrightarrow ^{24}_{12}\mathrm{Mg}^{*} \longrightarrow ^{20}_{10}\mathrm{Ne} + ^{4}_{2}\mathrm{He}$$

$$^{12}_{6}\mathrm{C} + ^{12}_{6}\mathrm{C} \longrightarrow ^{24}_{12}\mathrm{Mg}^{*} \longrightarrow ^{23}_{11}\mathrm{Na} + ^{1}1\,\mathrm{H}$$

Figure 5.4: **Carbon burning.** It occurs when $T_\mathrm{c} \sim 10^9$ K. The latter two reactions occur when significant amount of C are available, i.e. after He burning.

After He burning[4], the C core contracts and heats up so that C burning starts and produces O, Ne and Mg (Fig. 5.4). After exhaustion of C, the core contracts again. For stars with $10M_\odot \lessapprox M_\mathrm{init} \lessapprox 15M_\odot$, the core becomes degenerate and depending on the final core mass and the mass loss, the star will die as *type II supernova (SNII)* or ONeMg WD. For stars with $M_\mathrm{init} \gtrapprox 15M_\odot$, the central temperatures reach $\sim 10^9$ K, and Ne burning is ignited (Fig. 5.5) and produces O and Mg[5]. The next burning reaction converts O into Si and S (Fig. 5.6). C, O, Mg, Si are called α *elements* since their are obtained by successive α captures. Finally, Si burning starts (Fig. 5.7) and produce α (Ca, Ti) and *iron-peak elements* through photo-disintegrations and α captures. These different burning phases are shorter and shorter in time and occur in a smaller and smaller core. At the end, the star has a Fe rich core, surrounded by Si rich, O rich, Ne rich, C rich, and He rich shells: this is the so-called onion-like structure. Isotopes with the highest binding energy (e.g., ^{62}Ni, ^{58}Fe or ^{56}Fe) belongs to iron-peak elements: no more fusion reaction occur since it would cost energy. Therefore, the star has no more energy source to balance the gravitational contraction: the core contracts and heats up until photo-disintegrations are able to break up Fe nuclei and then He nuclei (for an example of such photo-disintegration, see Fig. 5.8). The stellar core is then made of protons, neutrons and free electrons. As the core collapse goes on, protons and electrons fuse and produce neutrons and neutrinos (*neutronisation*). As the density increases, the neutron pool becomes degenerate and the quantum pressure stops the gravitational collapse: the infalling material rebounds, moves outwards and meets the still infalling outermost layers. The shock waves thus generated propagate outwards and, with neutrinos winds, expel the star envelope: this is an *type II supernova (SNII)* explosion (or core-collapse supernova). After the SNII explosion, the stellar remnant can be a *neutron star (NS)* or a *black hole (BH)* (if the gravitational collapse goes on). As for AGB stars, the enriched material containing elements from C to iron-peak elements is injected into the ISM and will serve for new generations of stars.

[4] Minor nucleosynthesis processes occur during He burning and produce $^{18}_{8}$O and $^{22}_{10}$Ne.

[5] A reaction of α capture onto a Mg nucleus can also occur at this temperature range and produce Si.

$$^{20}_{10}\mathrm{Ne} + \gamma \longrightarrow {}^{16}_{8}\mathrm{O} + {}^{4}_{2}\mathrm{He}$$

$$^{20}_{10}\mathrm{Ne} + {}^{4}_{2}\mathrm{He} \longrightarrow {}^{24}_{12}\mathrm{Mg} + \gamma$$

Figure 5.5: **Neon burning.** It occurs when $T_\mathrm{c} \sim 1.2 \times 10^9\,\mathrm{K}$. The Ne burning occurs at lower temperatures than O burning (because O is double magic). The first reaction is a photo-disintegration and is endothermic, i.e. removes energy from the medium. However, it creates α particles than are used in the second reaction. The equivalent reaction is exothermic.

$$^{16}_{8}\mathrm{O} + {}^{16}_{8}\mathrm{O} \longrightarrow {}^{32}_{16}\mathrm{S}^{*} \longrightarrow {}^{28}_{14}\mathrm{Si} + {}^{4}_{2}\mathrm{He}$$

$$^{16}_{8}\mathrm{O} + {}^{16}_{8}\mathrm{O} \longrightarrow {}^{32}_{16}\mathrm{S}^{*} \longrightarrow {}^{31}_{15}\mathrm{P} + {}^{1}_{1}\mathrm{H}$$

$$^{16}_{8}\mathrm{O} + {}^{16}_{8}\mathrm{O} \longrightarrow {}^{31}_{16}\mathrm{S} + \mathrm{n}$$

$$^{16}_{8}\mathrm{O} + {}^{16}_{8}\mathrm{O} \longrightarrow {}^{24}_{12}\mathrm{Mg} + 2\,{}^{4}_{2}\mathrm{He}$$

Figure 5.6: **Oxygen burning.** It occurs when $T_\mathrm{c} \sim 1.5 \times 10^9\,\mathrm{K}$. The last reaction is endothermic.

$$^{28}_{14}\mathrm{Si} + \gamma \longrightarrow {}^{24}_{12}\mathrm{Mg} + {}^{4}_{2}\mathrm{He}$$

$$^{24}_{12}\mathrm{Mg} + \gamma \longrightarrow {}^{20}_{10}\mathrm{Ne} + {}^{4}_{2}\mathrm{He}$$

$$^{20}_{10}\mathrm{Ne} + \gamma \longrightarrow {}^{16}_{8}\mathrm{O} + {}^{4}_{2}\mathrm{He}$$

$$^{16}_{8}\mathrm{O} + \gamma \longrightarrow {}^{12}_{6}\mathrm{C} + {}^{4}_{2}\mathrm{He}$$

$$^{12}_{6}\mathrm{C} + \gamma \longrightarrow 3\,{}^{4}_{2}\mathrm{He}$$

$$^{28}_{14}\mathrm{Si} + {}^{4}_{2}\mathrm{He} \longrightarrow {}^{32}_{16}\mathrm{S} + \gamma$$

$$^{32}_{16}\mathrm{S} + {}^{4}_{2}\mathrm{He} \longrightarrow {}^{36}_{18}\mathrm{Ar} + \gamma$$

$$^{36}_{18}\mathrm{Ar} + {}^{4}_{2}\mathrm{He} \longrightarrow {}^{40}_{20}\mathrm{Ca} + \gamma$$

$$^{40}_{20}\mathrm{Ca} + {}^{4}_{2}\mathrm{He} \longrightarrow {}^{44}_{22}\mathrm{Ti} + \gamma$$

$$^{44}_{22}\mathrm{Ti} + {}^{4}_{2}\mathrm{He} \longrightarrow {}^{48}_{24}\mathrm{Cr} + \gamma$$

$$^{48}_{24}\mathrm{Cr} + {}^{4}_{2}\mathrm{He} \longrightarrow {}^{52}_{26}\mathrm{Fe} + \gamma$$

$$^{52}_{26}\mathrm{Fe} + {}^{4}_{2}\mathrm{He} \longrightarrow {}^{56}_{28}\mathrm{Ni} + \gamma$$

Figure 5.7: **Silicon burning.** It occurs when $T_\mathrm{c} \sim 3 \times 10^9\,\mathrm{K}$ through photo-disintegration (left columns) or successive α captures (right columns). $^{56}_{28}\mathrm{Ni}$ is unstable: it decays into $^{56}_{27}\mathrm{Co}$, which decay into $^{56}\mathrm{Fe}$ (radiogenic element).

$$^{56}_{26}\mathrm{Fe} + 13\,\gamma \longrightarrow 13\,^{4}_{2}\mathrm{He} + 4\,\mathrm{n}$$

$$^{4}_{2}\mathrm{He} + \gamma \longrightarrow 2\,\mathrm{p} + 2\,\mathrm{n}$$

$$\mathrm{p} + \mathrm{e}^{-} \longrightarrow \mathrm{n} + \nu_e$$

Figure 5.8: **Photo-disintegration reactions and neutronisation after Si exhaustion.** After exhaustion of Si, no more energy supply balance the gravitational contraction: Fe and He nuclei are destroyed through photo-disintegration (first two reactions) and protons and electrons fuse to form neutrons and neutrinos.

5.1.3 Iron-peak elements production by type Ia supernova

If iron-peak elements are produced in the core of massive stars, a more efficient mechanism to form them exists: *type Ia supernova*. It occurs when a WD, in a binary system, accretes the envelope of its companion while it enters a giant phase. When the WD reaches a critical mass, a thermonuclear explosion occurs. During the explosion, iron-peak elements are produced in huge amounts (e.g., Timmes et al., 2003) compared to those of massive stars.

5.1.4 Nucleosynthesis of elements heavier than the iron-peak

The previous section showed that hydrostatic nucleosynthesis only produces elements lighter than the iron-peak. As nuclear fusion cannot be used to form heavier elements (see Fig. 5.9), other mechanisms are needed. It appears that neutron captures allow to easily build up heavier elements than iron: unlike charged particles, neutrons do not suffer from the Coulomb barrier. Depending on the ratio between the timescale of a neutron capture event τ_{neutron} and the timescale of β^- decay τ_{β^-}, one distinguishes the *slow neutron capture process* ($\tau_{\mathrm{neutron}} \ll \tau_{\beta^-}$) — *s*-process — and the *rapid neutron capture process* ($\tau_{\mathrm{neutron}} \gg \tau_{\beta^-}$) — *r*-process.

5.1.4.1 AGB nucleosynthesis: *s*-process

Principle For the *s*-process, the probability of a neutron capture by an unstable isotope is very small compared to the probability of a β^- decay. Therefore, the *s*-process allows to move by small jumps in the (N, Z) plane (where N is the number of neutrons and Z the atomic number), close to the band of stability (Fig. 5.10):

- as long as stable isotopes are involved in neutron capture reactions, the neutron capture goes on and heavier and heavier isotopes of a given element X are built:

$$\begin{aligned} ^{\mathrm{A}}_{\mathrm{Z}}\mathrm{X} + \mathrm{n} &\longrightarrow ^{\mathrm{A+1}}_{\mathrm{Z}}\mathrm{X} + \gamma \\ ^{\mathrm{A+1}}_{\mathrm{Z}}\mathrm{X} + \mathrm{n} &\longrightarrow ^{\mathrm{A+2}}_{\mathrm{Z}}\mathrm{X} + \gamma \end{aligned} \tag{5.2}$$

- when the created isotope is far from the band of stability, it is β^- unstable:

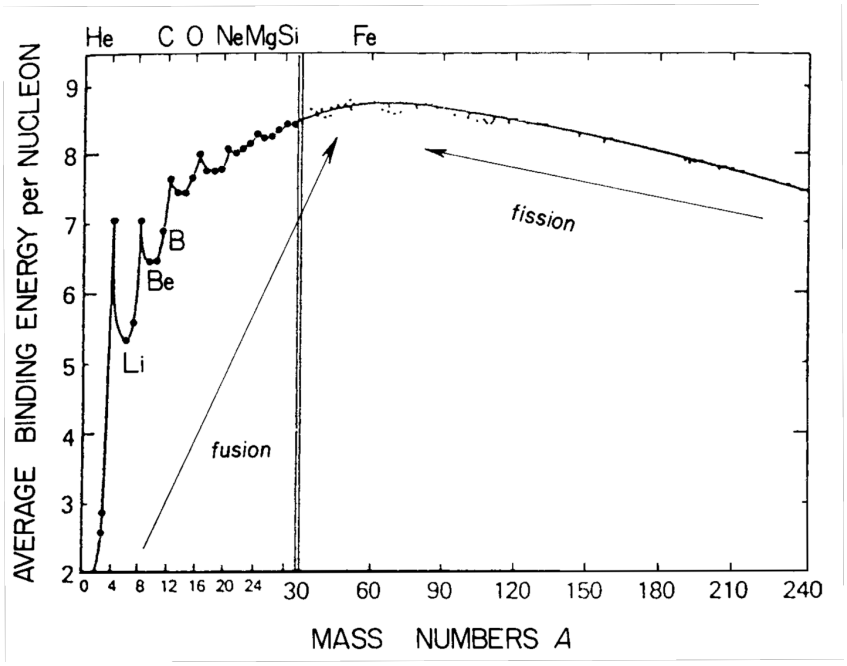

Figure 5.9: **Aston curve.** This curve gives the binding energy per nucleons as a function of mass number. It shows that the most stable elements are those of the iron-peak, especially Fe and Ni. For nuclei lighter than iron, fusion reactions release energy; for nuclei heavier than iron, fission reactions release energy. *Credits:* Pagel (2009)

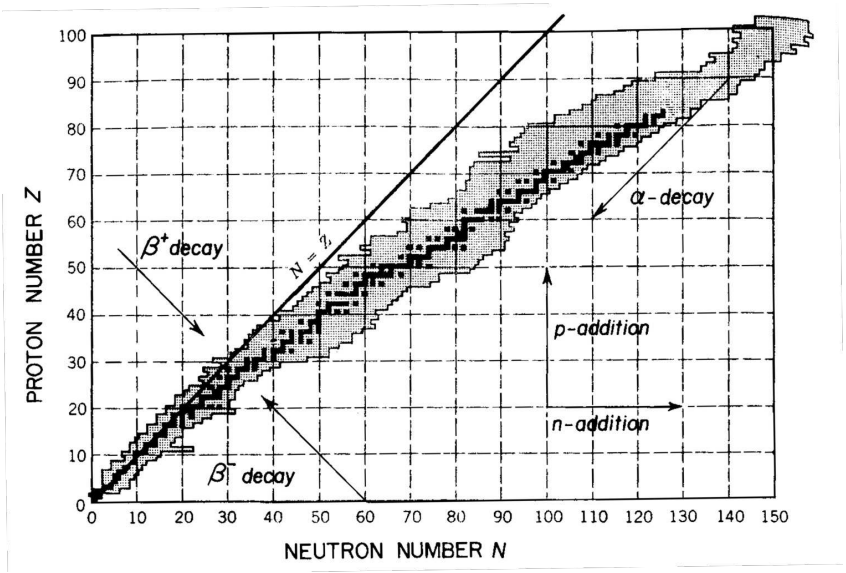

Figure 5.10: **Valley of stability.** Dark shades: stable isotope; light shades: known radioactive nuclei. Arrows indicate several radioactive disintegration or particule capture processes. *Credits:* Pagel (2009)

a β^- decay occurs before the next neutron capture

$$^{A+1}_{Z}X \longrightarrow ^{A+1}_{Z+1}X + e^- + \nu_e \tag{5.3}$$

and then the *s*-path resumes.

The *s*-elements are called *secondary elements* since they cannot be formed from H or He: iron-peak nuclei that have not been synthesised in-situ are needed and used as seeds to initiate the *s*-process.

Branching point A *branching point* (Fig. 5.11) is a particular element for which $\tau_{\text{neutron}} \approx \tau_{\beta^-}$ and the outcome depends on the neutron density:

- if the neutron density is below a critical value, the β^- decay will occur before the next neutron capture;
- if the neutron density is above the critical value, a new neutron capture occur before the β^- decay, i.e. the *s*-path goes through the β^- unstable isotope and continues building up heavier isotopes of element X until the next β^- unstable isotope.

Thus, at a branching point, two possible paths exists, which has an influence on the final products of the *s*-process (if the *s*-process goes through the branching point, some isotopes will not be produced at all).

Peaks of the *s*-process The *s*-process brings an explanation to the shape of the solar system abundance distribution (Fig. 5.12). Indeed, for particular number of nucleons, called *magic numbers* (2, 8, 20, 28, 50, 82, 126), the nuclei are extremely stable[6]. Close to a magic number (e.g., $N = 82$ or $N = 126$), the neutron-capture cross-section drops suddenly and magic isotopes act as bottleneck: they stop the *s*-process and elements accumulate. This is the reason why we observe a peak around $Z = 40$, $Z = 56$ and $Z = 86$ in the solar system abundance distribution. For instance, Y and Zr belong to the first peak of the *s*-process while Ba and La belong to the second peak. Of course, the probability of neutron captures around a magic isotope is not zero, and the *s*-process continues to build higher nuclei.

End of the *s*-process The *s*-process produces only elements up to $^{209}_{83}$Bi (the heaviest stable isotope): there the *s*-process reaches an impasse since another neutron capture creates unstable $^{210}_{83}$Bi which disintegrates towards $^{209}_{83}$Bi (Fig. 5.13).

Sites for the *s*-process and neutron sources The *main* s-*process* occurs in the envelope of AGB stars (*e.g.*, Busso et al., 1999) during mixing events (dredges-up between thermal pulses; § "Intermediate mass stars"). Observations of Tc absorption lines in spectra of AGB stars has been an empirical proof: Tc has only

[6] A nucleus is called *magic* if Z or (exclusively) N is magic and *double magic* if both Z and N are magic.

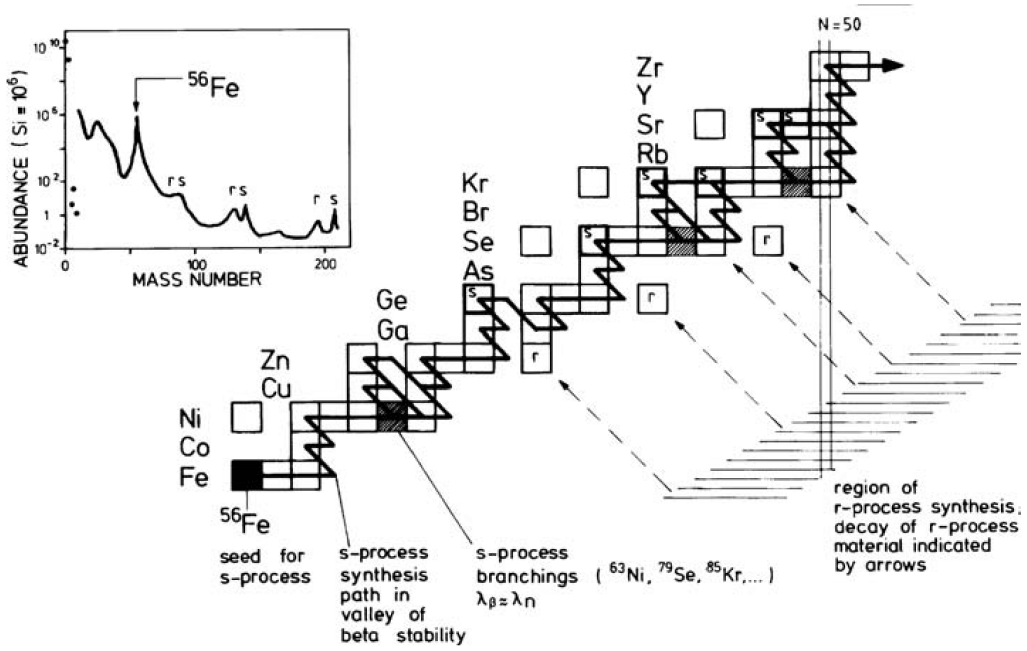

Figure 5.11: **Paths of the *s*- and *r*-processes.** The thick line represents the path of the *s*-process along the valley of stability. Shaded boxes indicate some branching points. The *r*-process allows to form neutron-rich unstable isotopes far from the valley of stability (horizontal lines); when the neutron flow ceases, multiple β-decays occur to form stable isotopes. Some isotopes are marked "s" or "r" when they are respectively pure *s*- and *r*-isotopes. The two vertical lines indicate a magic number of neutrons ($N = 50$) and corresponds to an *s*-process peak. *Credits:* Pagel (2009)

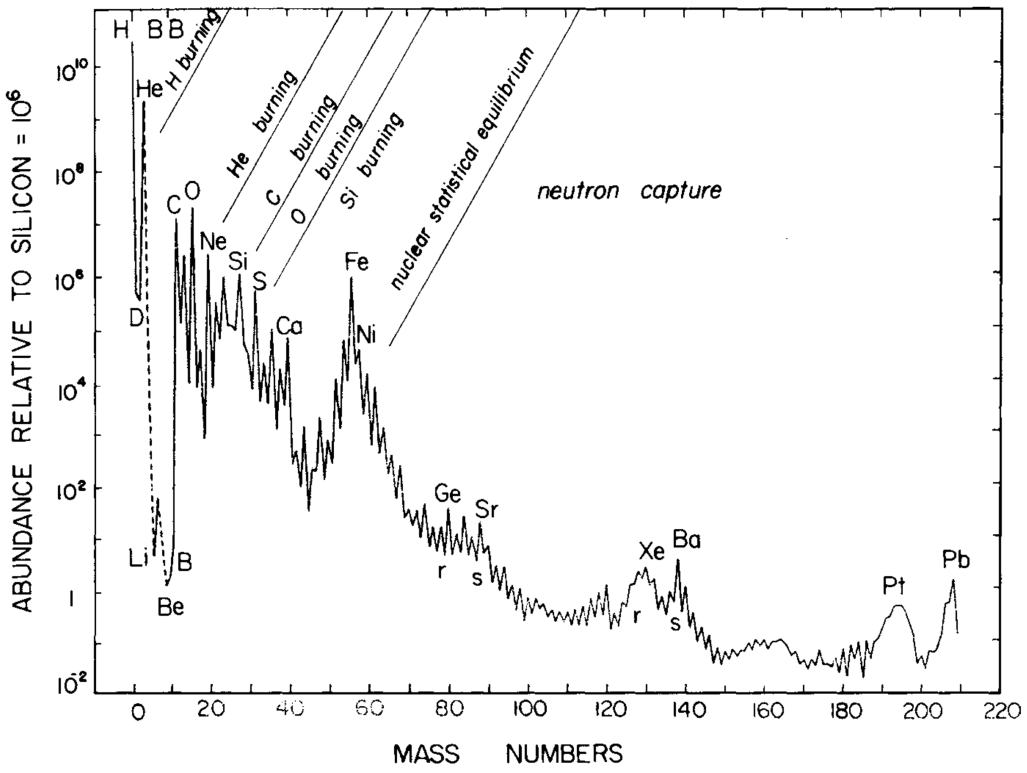

Figure 5.12: **Cosmic abundances.** Solar abundance distributions of all elements nomalised to Si. H and He are the most abundant elements, followed by C, O and Fe. For the nuclei heavier than iron, we clearly remark the presence of two systems of peaks: they are due to magic numbers and are associated to the *s*- and *r*-processes. *Credits:* Pagel (2009)

$$^{209}_{83}\mathrm{Bi} + \mathrm{n} \longrightarrow {}^{210}_{83}\mathrm{Bi} + \gamma$$

$$^{210}_{83}\mathrm{Bi}^{*} \longrightarrow {}^{210}_{84}\mathrm{Po} + \mathrm{e}^{-} + \bar{\nu}_e$$

$$^{210}_{84}\mathrm{Po}^{*} \longrightarrow {}^{206}_{82}\mathrm{Pb} + {}^{4}_{2}\mathrm{He}$$

$$^{206}_{82}\mathrm{Pb} + \mathrm{n} \longrightarrow {}^{207}_{82}\mathrm{Pb} + \gamma$$

$$^{207}_{82}\mathrm{Pb} + \mathrm{n} \longrightarrow {}^{208}_{82}\mathrm{Pb} + \gamma$$

$$^{208}_{82}\mathrm{Pb} + \mathrm{n} \longrightarrow {}^{209}_{82}\mathrm{Pb} + \gamma$$

$$^{208}_{82}\mathrm{Pb} + \mathrm{n} \longrightarrow {}^{209}_{82}\mathrm{Pb} + \gamma$$

$$^{209}_{82}\mathrm{Pb}^{*} \longrightarrow {}^{209}_{83}\mathrm{Bi} + \mathrm{e}^{-} + \bar{\nu}_e$$

Figure 5.13: **End of the *s*-process.**

short-lived isotopes and it is on the *s*-process path. $^{13}_{6}\mathrm{C}$ is the source of free neutrons ($^{13}_{6}\mathrm{C} + {}^{4}_{2}\mathrm{He} \longrightarrow {}^{16}_{8}\mathrm{O} + \mathrm{n}$) in AGB stars: the reactions occurs in $^{13}_{6}\mathrm{C}$ pockets in the He inter-shell, i.e. the zone between the H and He burning shells. $^{22}_{10}\mathrm{Ne}$ is another neutron donor ($^{22}_{10}\mathrm{Ne} + {}^{4}_{2}\mathrm{He} \longrightarrow {}^{25}_{12}\mathrm{Mg} + \mathrm{n}$), especially in the core of massive stars where the *weak* s-*process* is thought to occur and to produce the lightest *s*-elements[7] (e.g., see Frischknecht et al., 2012, which show the positive effect of rotation in metal-poor massive stars on the efficiency on the weak *s*-process).

5.1.4.2 Explosive nucleosynthesis: *r*-process

Principle As mentioned in Section 5.1.4.1, the *s*-process is not able to produce all known elements: it stops with $^{209}_{83}\mathrm{Bi}$, and therefore, does not form elements from Po to U. Thus, another nucleosynthetic process is required[8]. For the *r*-process, the probability of a neutron capture by an unstable isotope is very large compared to the probability of a β^- decay. Therefore, the *r*-process allows to quickly move horizontally in the (N, Z) plane (where N is the number of neutrons and Z the atomic number), creating neutron-rich unstable isotopes, far from the valley of stability (Fig. 5.10). When a magic neutron number is reached, the neutron capture cross-section drops and the β^- decay dominates. Numerous β^- decays occur, which provokes a vertical move in the (N, Z) plane (Z increases at constant N): this is a *waiting point*. At a certain point, the probability to capture a neutron is again larger than the probability of a β^- decay: the course of the *r*-process resumes. When the neutron flow ceases, the neutron-rich β^- unstable isotopes decay towards the valley of stability. Most of the heavy isotopes are produced by both *s*- and *r*-neutron

[7] Weak *s*-process elements can behave like primary elements (see Sec. 5.1.4.2).

[8] In fact, there also exist rare proton rich isotopes which can not be made neither by the *s*-process nor the *r*-process: they are produced by the *p*-process.

capture processes. However, some are pure *s*- or pure *r*-isotopes:

- *pure* r-*isotope*: while the *r*-process can produce an isotope ${}^{\rm A}_{\rm Z}{\rm X}$, the *s*-process cannot since one of the lighter isotope of ${}^{\rm A}_{\rm Z}{\rm X}$ is β^- unstable, with $\tau_{\rm neutron} \ll \tau_{\beta^-}$ (i.e. it is not a branching point);

- *pure* s-*isotope*: while the *s*-process can produce an isotope ${}^{\rm A}_{\rm Z}{\rm X}$, the *r*-process cannot since it produces a β^- stable isotope ${}^{\rm A}_{\rm Z'}{\rm Y}$ ($Z' < Z$) along the same isobar (i.e. elements with the same total number of nucleons).

Formally, *r*-process elements are secondary elements since the seeds of the *r*-process are iron-peak nuclei; however, observationally, they behave as *primary* elements since the seeds may be produced in-situ (in principle, *r*-process elements could be produced by massive metal-free stars while *s*-process elements cannot be produced in metal-free AGB stars).

Peaks of the *r*-process Similarly to the *s*-process, the *r*-process brings an explanation to the shape of the solar system abundance distribution (Fig. 5.12). A fine look at the curve shows that there are two system of peaks, slightly horizontally shifted: the *r*-process leads to enhanced heavy element abundances at slightly lower Z compared to the *s*-process. As the *r*-process produces enhancements of neutron-rich *unstable* elements for magic N, after β^- decays, the enhancements appears at lower Z (Fig. 5.11).

Sites for the *r*-process There is no consensus as to where the *r*-process is made, except that it should be linked to massive stars since (1) neutron-rich environments are needed, and (2) *r*-elements behave like an α-elements in the observed Galactic chemical evolution (Truran, 1981). The more promising candidates (providing the needed high neutron fluxes) are SNII (Wasserburg et al., 1996) (see neutronisation in § "Massive stars"), but neutron star (Freiburghaus et al., 1999) also enter the list (see Qian, 2012 for a more exhaustive list and their pros and cons). McWilliam et al. (1995a,b) showed that *r*- and α-elements are decoupled for [Fe/H] ≤ -3 dex, i.e. they do not track each other: assuming that *r*-process occurs in SNeII, which are also the production site of α-elements, then it means that the *r*-process occurs in less massive SNII progenitors (8-10 $M_\odot$) than α-elements (more than 15 $M_\odot$). Qian et al. (1998) that the large scatter observed in the elemental trends of *r*-elements means that the production of *r*-elements is a rare event at very low metallicity.

5.1.5 From stellar nucleosynthesis to galactic chemical evolution

Sections 5.1.2 and 5.1.4 showed that stars are the main actors of the chemical evolution of a galaxy since they produce new elements through various nucleosynthesis processes. As the production site is different from element to element, the typical timescale needed for an element to be produced and released into the ISM depends on the element. For instance, α elements are produced in short-lived stars and will be among the first to appear in a given galactic environment. Therefore, the time evolution of chemical abundances can be used to track and date the main events

that drove the chemical evolution of a system. Fortunately, the atmosphere of stars are the access door to the chemical composition of the ISM from which they formed as long as the chemical composition has not been altered by self-enrichment. This statement holds for our LMC RGB stars, except for some elements as C or N (our stars underwent the first dredge-up and bump; Sec. 5.1.2). To further discuss the chemical evolution of a galaxy, four fundamental concepts are needed:

- *initial mass function (IMF)*: the initial mass function $\phi(M)$ gives the mass distribution of stars born from a single stellar burst. Although still debated, the initial mass function (IMF) is thought to be universal (Calzetti et al., 2010; Elmegreen, 2004; Kroupa, 2001). It is a power-law of the mass $\phi(M) \propto M^{-\alpha}$ (or a combination of power-laws with a different exponent from a mass range to another): the higher the mass, the less stars formed. A steeper IMF, i.e. a larger α, will favour intermediate and low mass stars. Salpeter (1955) derived the slope α for the first time and found $\alpha = 2.35$ for $0.4M_{\odot} < M < 10M_{\odot}$ but other determinations have been made since then (Kroupa et al., 1993; Miller & Scalo, 1979; see also Kroupa et al., 2011 for a broad review). In a chemical evolution point-of-view, the shape of the IMF at high masses (i.e., the relative number of intermediate-mass and massive stars) is the most important since the low-mass stars contribute to the chemical evolution on timescales larger than a Hubble time.

- *star formation rate (SFR)*: the star formation rate is a time-dependent function giving the mass of gas turned into stellar mass during dt. The star formation rate (SFR) changes from galaxy to galaxy. It gives the history of the stellar formation, i.e. if the stellar formation was quiescent, bursty (how many bursts? which intensity? when and how long?) etc. The SFR can be determined observationally (e.g. star count in CMD).

- *stellar yield*: the stellar yield of an element X gives the mass of the element X ejected by a star of mass $M_{\star}$. Stellar yields are probably metallicity-dependent and difficult to determine accurately (theoretical predictions).

- *gas inflow and outflow*: the chemical evolution of a galaxy will also be influenced by the external supply of pristine or evolved material (gas inflow) and its ability to retain AGB and SNII ejecta (gas outflow due to energetic stellar winds).

5.2 The chemical evolution of the LMC

In the subsequent sections, we present the results for the following key elements and interpret them in terms of LMC chemical evolution: O, Mg, Si, Ca, Ti (α-elements), Na (light odd element), Sc, V, Cr, Co, Ni, Cu (iron-peak elements), Y, Zr, Ba, La and Eu (s- and r-elements). We compare our results for the Large Magellanic Cloud (LMC) field stars (bar and inner disc) to LMC GC stars (Johnson et al., 2006; Mucciarelli et al., 2008, 2010), and to the Milky Way (MW) stellar populations (thin and thick disc Bensby et al., 2005; Reddy et al., 2006, 2003; halo Fulbright,

2000; Reddy et al., 2006; Stephens & Boesgaard, 2002; Eu and La ratios: Brewer & Carney, 2006; Simmerer et al., 2004; O ratios of halo stars: Carretta et al., 2000). Our results for Arcturus are plotted as well to check our abundance scale (Arcturus) versus the literature abundance scales (the MW thick disc compilation).

5.2.1 A slow chemical evolution, driven by type Ia supernovae and metal-poor AGB winds

α-elements Figures 5.14 and 5.15 show the abundance trends for [O/Fe], [Mg/Fe], [Si/Fe], [Ca/Fe] and [Ti/Fe]. O, Mg, Si, Ca and Ti belong to the α-elements and are used to track the epoch where SNIIs drove the chemical evolution of the galaxy. Indeed, α-elements are formed by successive α captures occurring in massive stars interiors and are released to the ISM through SNII explosions (§ "Massive stars" in Sec. 5.1.2.2). As iron-peak elements are also processed in massive stars, it results in a constant [α/Fe] ratio. When type Ia supernovae (SNeIa) start to dominate the chemical enrichment and release huge amount of iron-peak elements (see Sec. 5.1.3 and e.g., Timmes et al., 2003), [α/Fe] decreases (SNeIa efficiently produce iron-peak elements without producing α-elements).

The bottom panel of Figure 5.14 shows [α/Fe] = [O + Mg/2Fe] for the LMC and the MW (when O, Mg ratios were available, we computed [α/Fe] the same way for MW). We clearly see that compared to the MW, the LMC exhibits deficient [α/Fe] for [Fe/H] ≥ -1.3 dex. Those low [α/Fe] ratios can be explained by a higher contribution of SNIa to the chemical enrichment of the LMC, compared to the MW (e.g. Pagel & Tautvaisiene, 1998).

To illustrate the slower chemical enrichment of the LMC compared to the MW, we overplotted some theoretical elemental trends in Figure 5.14. In the middle panels of Figure 5.14, we overplotted theoretical [Mg/Fe]–[Fe/H] relations computed for the LMC by Pagel & Tautvaisiene (1998) for their smooth star formation history (SFH) and their two-burst SFH (initial burst 14 Gyr ago and second burst 3 Gyr ago; see Fig. 5.16), theoretical [Mg/Fe]–[Fe/H] relations computed for the MW by Pagel & Tautvaisiene (1995) assuming instantaneous and delayed production approximations, theoretical [Mg/Fe]–[Fe/H] relation computed for the LMC by Bekki & Tsujimoto (2012a) for a smooth model, similar to the smooth model of Pagel & Tautvaisiene (1998) (with Salpeter's IMF; their model S1) and a model with steeper IMF and strong winds (their model W2). We see that for a given metallicity, the slower enrichment experienced by the LMC leads to lower [Mg/Fe] ratios. For the LMC trends predicted by Pagel & Tautvaisiene (1998) in the case of a two-burst model, the jump observed in [Mg/Fe] is associated to the second burst: we see that the expected increase of [Mg/Fe] is small and comparable to our observational dispersion. All models fail at reproducing the observed trends. However, we can notice that the wind model of Bekki & Tsujimoto (2012a), i.e. with a steeper IMF ($\alpha = 2.55$) and strong winds, is closer to the observed ratios than any other (see Sec. 5.2.2 for a discussion on the IMF).

Finally, we note that Lapenna et al. (2012) have measured O, Mg and Si for 89 stars in a field in the LMC disc (around the globular cluster NGC 1786, some 3° North-West of the bar centre) and found similar trends as ours.

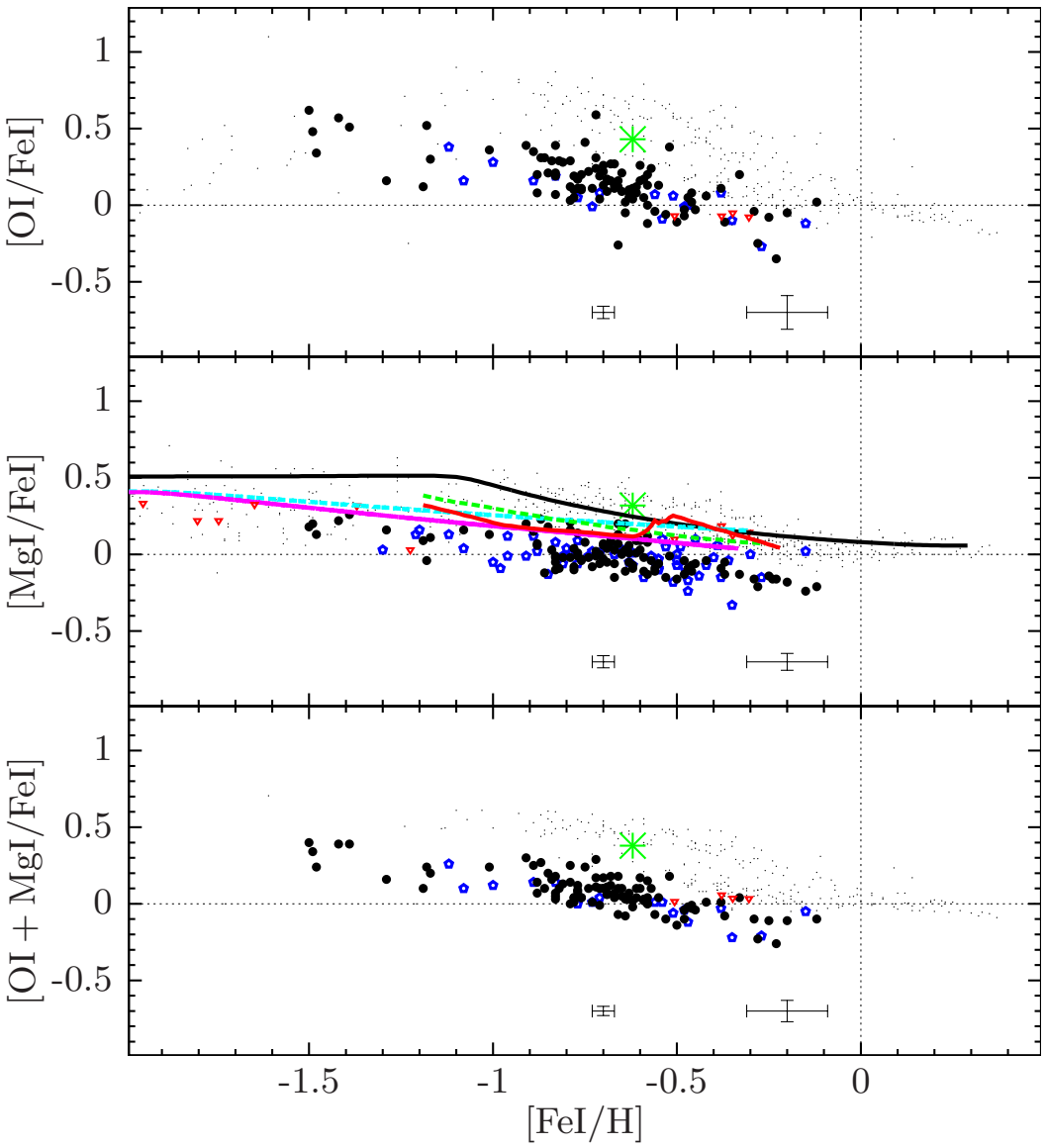

Figure 5.14: **From top to bottom panel:** [OI/FeI] **vs.** [FeI/H]**,** [MgI/FeI] **vs.** [FeI/H]**,** [OI + MgI/2FeI] **vs.** [FeI/H]**.** Black filled circles: LMC bar (this work); blue open pentagons: LMC inner disc (this work); green asterisk: Arcturus (this work, data for median S/N ratio); red downward triangle: LMC GC (Johnson et al., 2006; Mucciarelli et al., 2008, 2010); black tiny dots: MW thin and thick disc (Bensby et al., 2005; Reddy et al., 2006, 2003), halo (Fulbright, 2000; Reddy et al., 2006; Stephens & Boesgaard, 2002), and additional MW data for O from Carretta et al. (2000). Solid red line: two-burst model of Pagel & Tautvaisiene (1998); green dashed line: smooth model of Pagel & Tautvaisiene (1998); magenta solid line: wind model of Bekki & Tsujimoto (2012a); cyan dashed line: smooth model of Bekki & Tsujimoto (2012a). Typical random (left) and systematic (right) error bars on both coordinates are provided for our LMC samples.

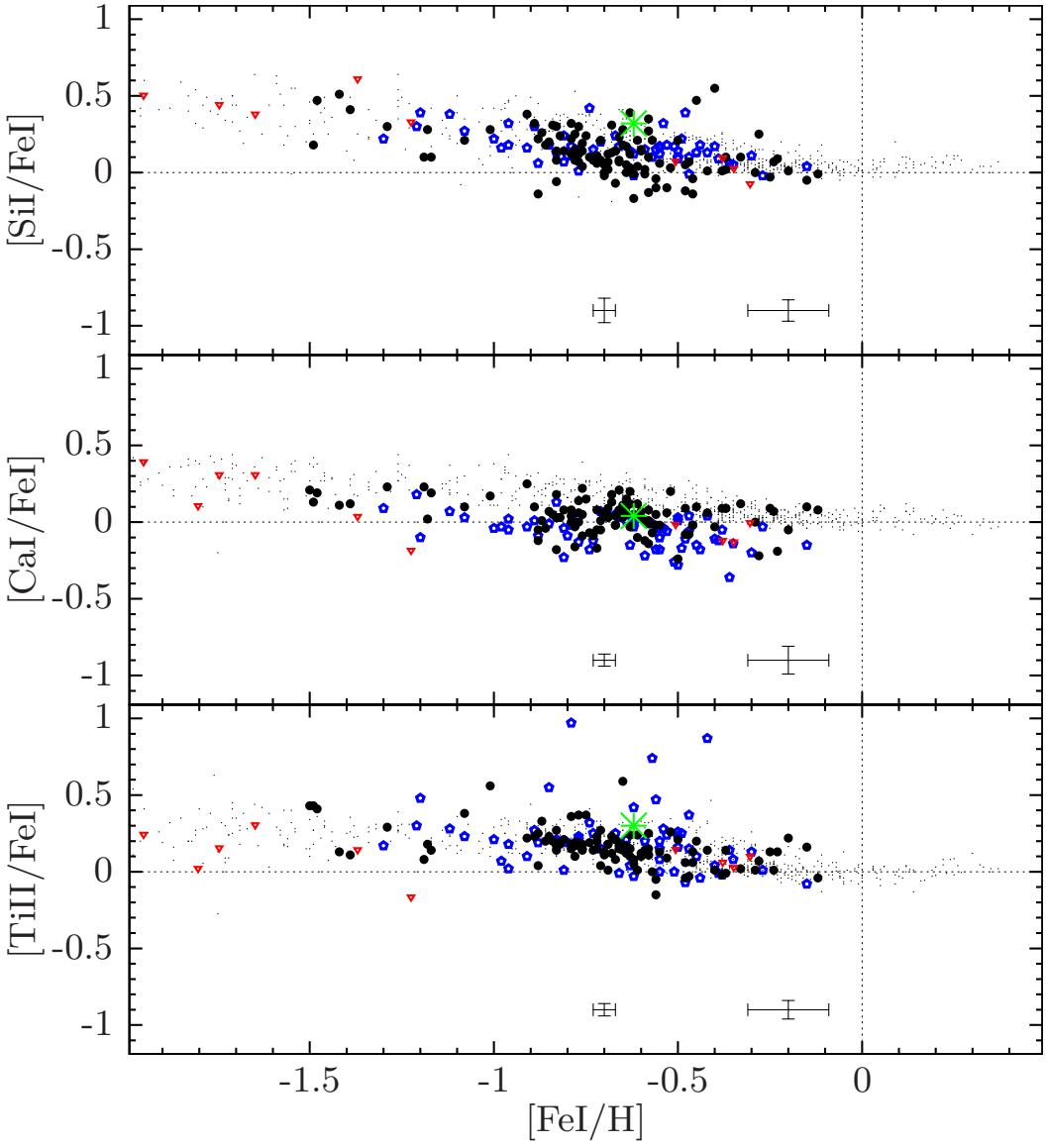

Figure 5.15: **From top to bottom panel:** [SiI/FeI] **vs.** [FeI/H], [CaI/FeI] **vs.** [FeI/H], [TiII/FeI] **vs.** [FeI/H]**.** Same legend as Figure 5.14.

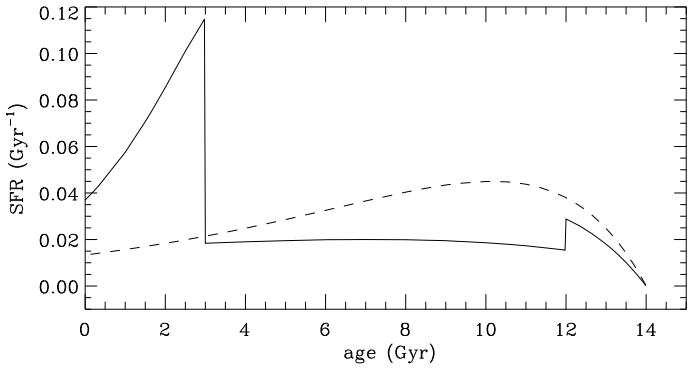

Figure 5.16: **LMC SFR corresponding to the two-burst and smooth models proposed by Pagel & Tautvaisiene (1998).** Solid line: two-burst model; dashed line: smooth model. *Credits:* Pagel & Tautvaisiene (1998)

Barium and lanthanum Figure 5.17 shows the elemental distributions for Ba and La. Ba and La are heavy elements (Sec. 5.1.4), thought to be mainly produced by the *s*-process with a minor contribution from the *r*-process (e.g., $\approx 85\,\%$ of the solar Ba and $\approx 75\,\%$ of the solar La were produced by the *s*-process Burris et al., 2000; Sneden et al., 2008). While the MW has constant solar [Ba/Fe] and [La/Fe] ratios (with a weak increase towards high metallicities), both LMC fields exhibit a dramatic increase of [Ba/Fe] and [La/Fe] with increasing metallicity (first and third panels of Fig. 5.17): the LMC distributions agree with MW halo trends, i.e. for [Fe/H] ≤ -1.0 dex, and are above the MW elsewhere. The bar and disc field distributions overlap for both Ba and La. Ba has the strongest increase, starting from solar value at [Fe/H] $= -1.5$ dex and reaching 0.8 dex for [Fe/H] ≥ -0.3 dex. La, on the other hand, remains approximately constant from [Fe/H] ≈ -0.7 dex ([La/Fe] ≈ 0.5 dex for the LMC bar and ≈ 0.4 dex for the LMC disc). Furthermore, there is an excellent match between LMC field population and LMC GC population. This indicates that the production of Ba and La has been much more efficient in the LMC than in the MW, i.e. that AGB stars have played a strong role in the chemical evolution of the LMC while the $\approx$ solar [Ba/Fe] and [La/Fe] MW ratios indicate that SNeIa are the main driver (relatively to AGB stars) of the chemical evolution. In top panel of Figure 5.17, we overplotted theoretical [Ba/Fe]–[Fe/H] relation computed for the LMC by Bekki & Tsujimoto (2012a) for a smooth model (with Salpeter's IMF; their model S1) and a model with steeper IMF and strong winds (IMF slope: $\alpha = 2.55$; their model W2). We see that a standard model fails at reproducing the Ba trends; a steeper IMF and strong winds are needed to reproduce the observed ratios.

To identify the process responsible for this high production, we examine [Ba/Eu] and [La/Eu] in second and fourth panels of Figure 5.17. We see that for LMC GC and field metal-poor stars (from -2.0 dex to -0.8 dex), [Ba, La/Eu] is constant and compatible (within uncertainties) with a pure *r*-process source (Arlandini et al., 1999: [Ba$_r$/Eu$_r$] $= -0.69$ dex and [La$_r$/Eu$_r$] $= -0.4$ dex; Sneden et al., 2008: [Ba$_r$/Eu$_r$] $= -0.82$ dex and [La$_r$/Eu$_r$] $= -0.59$ dex). On the other hand, for [Fe/H] ≥ -0.8 dex, the increase of the LMC [Ba, La/Eu] is interpreted as the rise

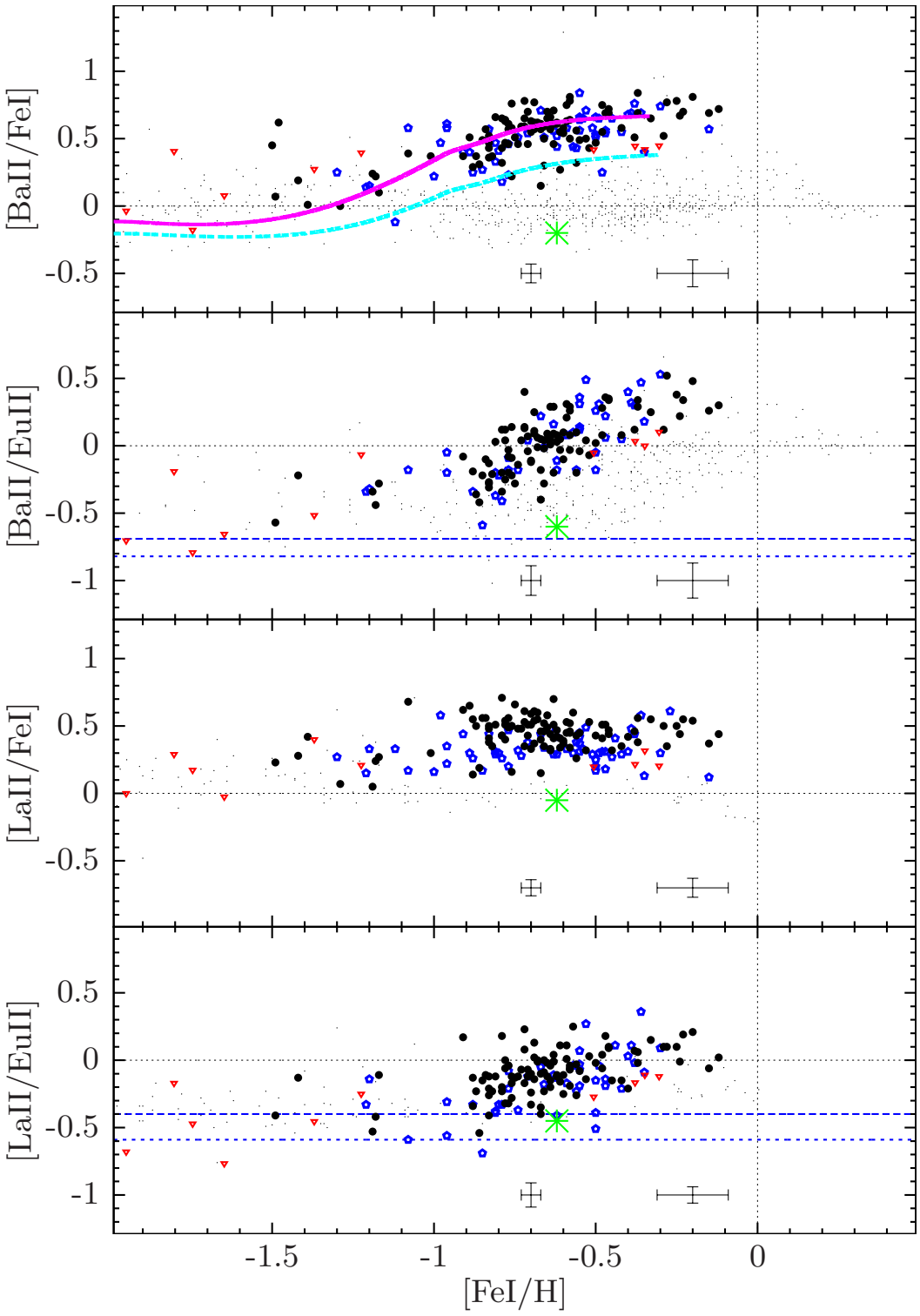

Figure 5.17: **From top to bottom panel:** [BaII/FeI] **vs.** [FeI/H], [BaII/EuII] **vs.** [FeI/H], [LaII/FeI] **vs.** [FeI/H], [LaII/EuII] **vs.** [FeI/H]. Same legend as Figure 5.14; additional MW data for Eu and La from Brewer & Carney (2006); Simmerer et al. (2004); horizontal blue dashed line: $[Ba_r/Eu_r] = -0.69$ dex and $[La_r/Eu_r] = -0.4$ dex (Arlandini et al., 1999); horizontal blue dotted line: $[Ba_r/Eu_r] = -0.82$ dex and $[La_r/Eu_r] = -0.59$ dex (Sneden et al., 2008); magenta solid line: wind model of Bekki & Tsujimoto (2012a); cyan dashed line: smooth model of Bekki & Tsujimoto (2012a).

of a new source of Ba and La, i.e. the *s*-process. The MW exhibits similar patterns (constant ratio at low metallicity, then an increase) but two differences exist with the LMC: first, the increase of [Ba, La/Eu] starts at lower metallicity in the LMC ([Fe/H] ≈ -0.8 dex) than in the MW ([Fe/H] ≈ -0.4 dex), reflecting the slower metal-enrichment in the LMC; secondly, while for the MW, [Ba/Eu] reaches a solar value, for the LMC, [Ba/Eu] reaches a much higher value ([Ba/Eu] ≈ 0.4 dex). This suggest that the production of Ba and La by the *s*-process has been much more efficient in the LMC than in the MW, and thus it indicates that AGB stars played a stronger role in the chemical enrichment of the LMC compared to the MW.

Light and heavy *s*- & *r*-elements Figure 5.18 shows [Y + Zr/Ba + La]. Like Ba and La, Y and Zr are heavy elements thought to be mainly produced by the *s*-process (e.g., $\approx 70\,\%$ of the solar Y and $\approx 80\,\%$ of the solar Zr were produced by the *s*-process Burris et al., 2000; Sneden et al., 2008). However, Y and Zr belong to the first peak of the *s*-process (light *s*-elements; see Sec. 5.1.4.1) while Ba and La belong to the second peak (heavy *s*-elements). Thus the ratio [ls/hs] informs us on the relative importance of metal-poor and metal-rich AGB since the second peak is favoured, relatively to the first peak, when metal-poor AGB stars dominate the chemical enrichment (e.g., theoretical predictions Cristallo et al., 2011; abundances determinations of first and second peak *s*-elements: Abia et al., 2008; de Laverny et al., 2006). For [Fe/H] $\gtrapprox -0.8$ dex, we know from above that the *s*-process dominates the chemical enrichment. We remark that the LMC trend is below that of the MW, which suggests that the AGB stars which dominated the LMC enrichment were more metal-poor than those of the MW. While the bar distribution is flat, the disc distribution seems to slightly decrease with increasing metallicity. Colucci et al. (2012) also found a decrease of [Y/Ba] in intermediate-age clusters. This could be a mass effect: in the LMC disc, metal-poor low mass AGB stars, i.e. whose nucleosynthesis favours Ba and La production relatively to Y and Zr production and whose products are released later, still contribute significantly to the enrichment, which leads to a decrease of [Y + Zr/Ba + La]; however, only a consistent chemical evolution modelling can confirm this explanation. We remark that the match between LMC GC and our LMC fields is again excellent.

5.2.2 Is the LMC IMF different?

There has been a long debate on the claimed universality of the IMF (see Kroupa et al., 2011 for a broad review on the IMF) and the LMC can be used to test this assumption (e.g., Bekki & Tsujimoto, 2012a; Holtzman et al., 1997). Since standard models fail to reproduce the steep increase of [Ba/Fe] in the LMC (see Fig. 5.17), Bekki & Tsujimoto (2012a) tested different chemical evolution models changing the IMF, the number of bursts and the characteristics of the winds. They found that models with selective winds (i.e. only SNeII products are removed by the galactic winds) and steep IMF better reproduce [Mg/Fe] and [Ba/Fe] trends (see Fig. 5.14 and 5.17). For instance, at [Fe/H] $= -0.3$ dex, increasing the fraction of ejected SNII products and steepening the IMF ($\alpha = 2.55$ instead of Salpeter's exponent $\alpha = 2.35$) change [Ba/Fe] by ≈ 0.25 dex. Since a steeper IMF will favour

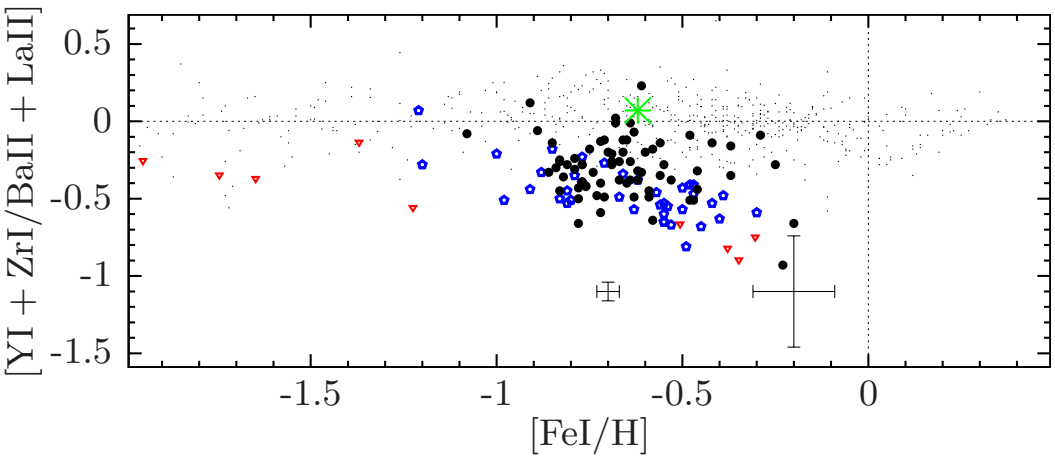

Figure 5.18: [YI + ZrI/BaII + LaII] **vs.** [FeI/H]**.** Same legend as Figure 5.14.

intermediate mass SNeII (8-10 $M_\odot$) relatively to massive SNeII (15-25 $M_\odot$), we tried to identify this mass effect in our elemental abundances.

α-elements The comparison of the LMC trends to those of the MW shows that the α-elements can be divided in two groups: on the one hand, O and Mg, and on the other hand, Si, Ca and Ti. Indeed, the LMC distributions of O and Mg (Fig. 5.14) are below those of the MW at all metallicities (except for the very most metal poor stars), while the LMC distribution of Si, Ca and Ti (Fig. 5.15) completely or partially overlap the MW distributions. Although O, Mg, Si, Ca and Ti are all α-elements, their production efficiency depends on the mass of the SNII progenitor: while O (and somewhat Mg) are predicted to be mainly produced in very massive SNII progenitors (Woosley & Weaver, 1995), Si, Ca and Ti are predicted to be produced in intermediate mass SNII and, in smaller quantity, by SNIa (Thielemann et al., 2002; Tsujimoto et al., 1995). The discrepancy between Galactic and LMC trends for O and Mg is not an artifact of the abundance analysis: for instance, for a 1 dex metallicity bin centred around Arcturus, we have $\langle[O/Fe]_{LMCBar}\rangle = 0.1$ dex, $\langle[O/Fe]_{MWDiscs}\rangle = 0.47$ dex, $[O/Fe]_{Arcturus} = 0.44$ dex, hence $\Delta(MW - LMC) \approx \Delta(Arcturus - LMC)$ (the same is true for Mg). This result is compatible with the assumption that the LMC formed high mass stars less efficiently than the MW. However, the decreasing part of the [α/Fe] (where α stands for O, Mg, Si, Ca or Ti) trends corresponds to the SNIa-dominated regime, i.e. the epoch where Si, Ca, Ti, iron-peak elements are released by both SNII and SNIa: the differences between O and Mg, on the one hand, and Si, Ca and Ti, and on the other hand could be accounted for because of different SNIa contributions. In fact, only the α plateau, i.e. the SNII-dominated regime, is purely sensitive to the IMF. In order to get rid of the SNIa contribution, we look at the trends [Ca/Mg] vs. [Mg/H] (Fig. 5.19) and [O/Mg] vs. [Mg/H] (Fig. 5.20). [Ca/Mg] can be seen as a proxy for the ratio between intermediate-mass and high mass stars: if the LMC IMF is steeper than that of the MW, the LMC will have higher [Ca/Mg] than the MW. Figure 5.19

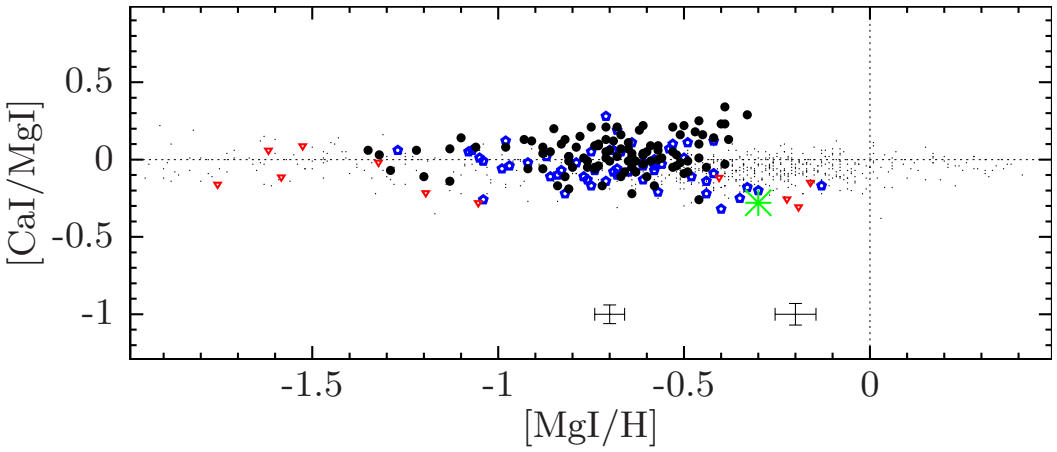

Figure 5.19: [CaI/MgI] **vs.** [MgI/H]**.** Same legend as Figure 5.14.

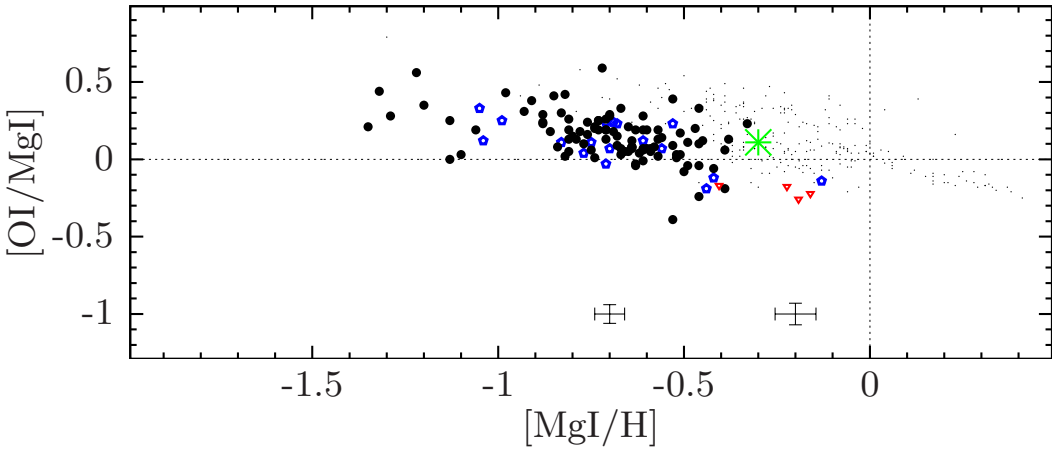

Figure 5.20: [OI/MgI] **vs.** [MgI/H]**.** Same legend as Figure 5.14.

shows that the MW and the LMC have a flat [Ca/Mg] ≈ 0 dex, i.e. no evidence for a steeper IMF. Similarly, [O/Mg] can be seen as a proxy for the ratio between very high and high mass stars: if the LMC IMF is steeper than that of the MW, the LMC will have lower [O/Mg] than the MW. Figure 5.20 shows that the MW and the LMC exhibit a similar [O/Mg] trend, but shifted one to each other: that of the LMC is horizontally shifted by [Mg/H] ≈ -0.5 dex. We recall that [Mg/H] is a proxy for time, but because of different chemical enrichment histories a given [Mg/H] ratio does not correspond to the same age for the MW and LMC. Thus, Figure 5.20 tells us that at a given metallicity (i.e. a given [Mg/H] ratio), the contribution from very massive stars, relatively to massive stars, is lower in the LMC than in the MW but it does not point necessarily towards a different IMF.

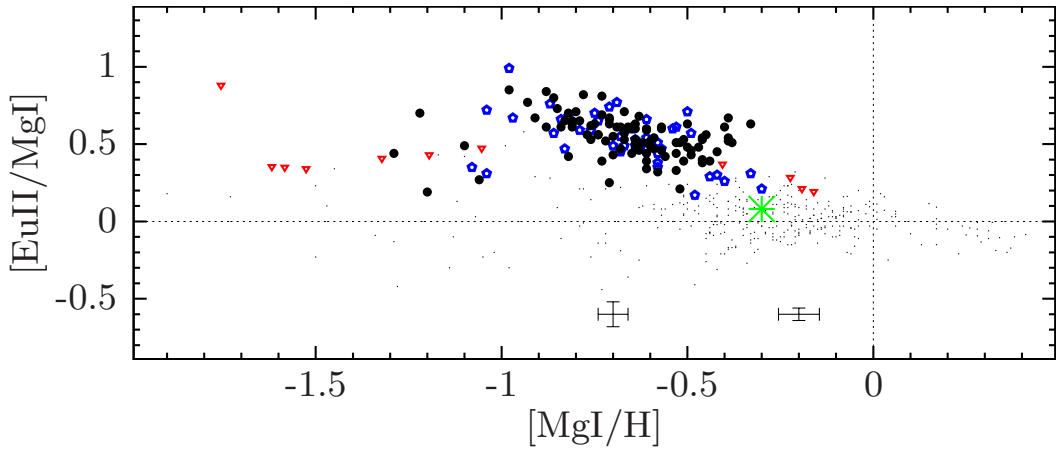

Figure 5.21: [EuII/MgI] **vs.** [MgI/H]**.** Same legend as Figure 5.14.

Europium Assuming that Eu is mainly produced by the r-process occurring in intermediate mass SNeII, the ratio [Eu/Mg] can also be used as an IMF proxy: a steeper IMF should produce a higher [Eu/Mg]. Figure 5.21 shows [Eu/Mg] as a function of [Mg/H]. While the MW trends are flat and have a constant solar value, the LMC trends exhibit for both fields a higher [Eu/Mg] ratio at any [Mg/H] (0.5 dex higher, in the mean): this can be an evidence of a steeper IMF for the LMC.

On the one hand, the α trends indicate no variation of the IMF between the MW and the LMC while, on the other hand, the Eu trend seems to point towards a steeper IMF for the LMC compared to the MW. How can we reconcile the two points of view? In Section 5.3, we will see that, for the LMC, a stronger contribution from the s-process to the production of Eu is a more promising route to explain the enhanced [Eu/Fe] ratios. Therefore, the high [Eu/Mg] ratios observed for the LMC might be ascribable to the s-process (i.e. we see the effect of an additional source of Eu in the LMC trends compared to those of the MW) and not to a steeper IMF. We conclude that no clear evidence exists in favour of a steeper IMF for the LMC.

5.2.3 Do we need prompt type Ia supernovae?

α-elements Unlike the MW, the plateau corresponding to the SNII-dominated regime is not clearly visible in our LMC field stars distribution of α-elements (Fig. 5.14 and 5.15). Two possibilities can lead to this: either there is a plateau but it appears at a lower metallicity, which means that the chemical evolution has been very slow compared to the MW (when the SNeIa start to explode in the LMC, the metallicity has reached a lower value than in the MW). Or there is no plateau, which Tsujimoto & Shigeyama (2012) explain by prompt SNeIa, for which the onset of SNIas occurs as soon as 100 Myr after the formation of the progenitors. Since the lowest metallicity of our samples is only ≈ -1.6 dex, we cannot draw firm conclusions about the presence or absence of a plateau in the LMC. However, LMC glob-

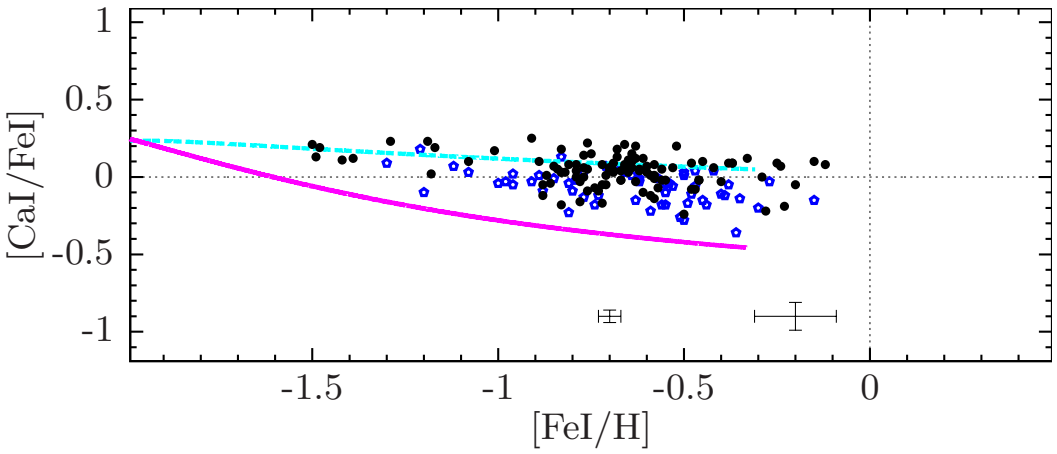

Figure 5.22: [CuI/FeI] **vs.** [FeI/H]**.** Same legend as Figure 5.14; magenta solid line: wind model of Bekki & Tsujimoto (2012a); cyan dashed line: smooth model of Bekki & Tsujimoto (2012a).

ular clusters can also be used to infer the [α/Fe] in the metal-poor regime. Except for O (for which metal-poor LMC GC stars exhibit chemical anomalies due to self-enrichment), there is a good agreement between LMC GC and LMC field stars at both low ($-1.5\,\mathrm{dex} \leq$ [Fe/H] $\leq -1.2\,\mathrm{dex}$) and high ($-0.5\,\mathrm{dex} \leq$ [Fe/H] $\leq -0.2\,\mathrm{dex}$) metallicities. The metal-poor LMC GC populate the metallicity range $[-2, -1.2]$ and line up along a MW-like plateau at low metallicity ([Fe/H] $\lessapprox -1.6\,\mathrm{dex}$). Furthermore, Haschke et al. (2012c) also find that extremely metal-poor RR Lyrae stars in the LMC populate a plateau similar to that of the MW.

Let us note that Bekki & Tsujimoto (2012b) also used prompt SNIas in their models to reproduce the LMC trends of Mg and Ca (based on abundances of LMC field stars and GC stars) and conclude that prompt SNIa have influenced the chemical evolution of the LMC. We remark that to fully explain the low LMC [Ca/Fe], Bekki & Tsujimoto (2012a) had to invoke galactic winds which remove Ca more efficiently than the others α-elements (their model W6). Figure 5.22 shows that the smooth model of Bekki & Tsujimoto (2012a) reproduce relatively well the Ca LMC trends while their wind model W5, i.e. *without* efficient Ca removal, predicts deficient abundances; therefore, according to our revised abundances (Bekki & Tsujimoto, 2012a used abundance measurements from Pompéia et al., 2008 and our revised abundances are $\approx 0.1\,\mathrm{dex}$ higher), it seems useless to invoke more efficient removal for Ca. We conclude that an α plateau is likely to exist at lower metallicities than those probed by our LMC RGB stars, and therefore, prompt SNeIa are not needed to explain the LMC elemental trends.

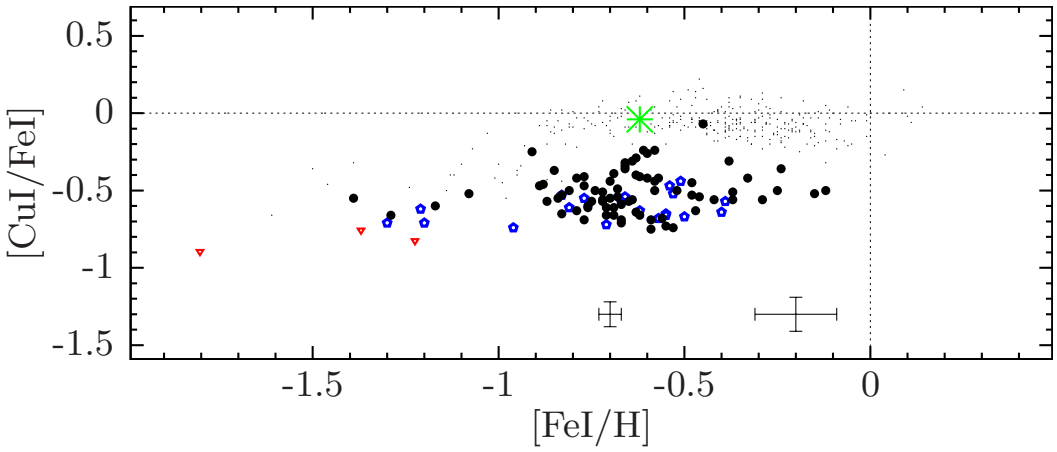

Figure 5.23: [CuI/FeI] **vs.** [FeI/H]**.** Same legend as Figure 5.14.

5.3 Chemical anomalies: new lights on nucleosynthesis models

Copper Figure 5.23 shows the abundance trends of Cu. While the LMC bar and disc ratios match those of the MW for [Fe/H] ≤ -1.1 dex, the LMC ratios are significantly lower than those of the MW for higher metallicities: $\langle$[Cu/Fe]$\rangle = -0.5$ dex for the bar and $\langle$[Cu/Fe]$\rangle = -0.6$ dex for the disc. Since we found an expected value for the Arcturus abundance (i.e. Arcturus behaves like MW thick disc stars), the observed deficiency for Cu is not an artifact of our abundance analysis. The origin of Cu is still heavily debated since Cu is thought to have both primary and secondary production: Romano & Matteucci (2007) see the origin of Cu in neutron captures occurring in massive stars dying as SNeII (primary production), Travaglio et al. (2004) invoke a minor contribution from *s*-process in AGB (secondary production) and Mishenina et al. (2002) consider the thermonuclear nucleosynthesis in SNeIa as the main source (secondary production). We saw in Section 5.2.1 that a stronger contribution of SNeIa is needed to explain the low α ratios and that a stronger contribution of AGB is needed to explain the high Ba and La ratios. In addition, Pignatari et al. (2010) found that more than half of the solar copper is produced through weak *s*-process occurring in massive stars ($25 M_{\odot}$). Therefore, SNIa and AGB stars cannot be the main site of Cu production in the LMC and the hypothesis of massive stars being the main source of Cu seems to be more plausible: Cu in the LMC has mainly a primary origin.

Europium Eu is another heavy element, often considered as a pure *r*-process element (the *r*-process contribution to the solar Eu is of 94 % according to Arlandini et al., 1999 and 97 % according to Sneden et al., 2008). In Figure 5.24, we see that the LMC bar and disc Eu distributions agree very well: they both exhibit a constant [Eu/Fe] ≈ 0.5 dex for [Fe/H] ≤ -0.8 dex, then a decreasing trend with increasing metallicity. While for the metal-poor stars the abundance ratios of the LMC and

the MW halo overlap, it is clear that for [Fe/H] ≥ -1 dex the LMC trend is above that of MW. This enhancement for metal-rich stars is not an artifact of our analysis since Arcturus has the expected Eu abundance (i.e. it falls on top of the MW thick disc). This is in fact a chemical anomaly already noticed in LMC supergiant stars (Hill et al., 1995; Russell & Bessell, 1989) and LMC GC stars (Colucci et al., 2012; Mucciarelli et al., 2008) and its origin still remains unclear. Different mechanisms can help in maintaining a high Eu ratio in late stages of the chemical evolution:

1. new star bursts will form a high number of massive stars which will, in turn, inject fresh Eu in the ISM;
2. another source of *r*-processed Eu;
3. a stronger contribution of *s*-processed Eu.

Explanation (1) is not supported by the SFH of our two LMC fields (Smecker-Hane et al., 2002): although recent star bursts (about 5 Gyr ago and less than 1 Gyr ago) are expected in the bar, they are not expected in the inner disc; so it cannot explain the high ratios observed in both fields. Moreover, they would produce similar α enhancements, which are not observed (Sec. 5.2.1). Reasons (2) or (3) are more likely to explain the differences between the LMC and the MW. The contribution of the *s*-process to the solar system Eu is estimated to be of few percents (3 % according to Sneden et al., 2008) and therefore, it is dubious that the *s*-process could be responsible for the Eu enhancement. In the MW, the presence of *s*-process at very low metallicity has been found in stars called CEMP-*s*: CEMP stars are carbon enhanced metal-poor stars and they are furthermore classified as *s* when they exhibit *s*-process enhancements. This class of stars is thought to acquire its C and *s* enhancements from a binary interaction with a (now deceased) AGB companion. A small fraction of CEMP-*s* stars also exhibit enhanced *r*-process products (CEMP-*r*/*s* stars). In their study of CEMP-*s* and CEMP-*r*/*s* stars, Allen et al. (2012) found a correlation between [Ba/Fe] and [Eu/Fe] and that [Eu/Fe] is coupled to the degree of C over-abundance (i.e. Eu tracks the binary mass transfer from the AGB companion). So, while it was thought that Ba and Eu in CEMP-*r*/*s* originated in two distinct processes (through three mass-transfer in a binary system, see Cohen et al., 2003; through two successive mass-accretion of a 8-10 $M_\odot$ companion, see Wanajo et al., 2006; through pre-*r* enrichment followed by *s*-material accretion, see Bisterzo et al., 2012), Allen et al. (2012) claim that Ba and Eu have the same origin in CEMP-*s* and CEMP-*r*/*s*, *i.e.* produced by the *s*-process occurring during the AGB phase of the more massive star of a binary system. In essence, the CEMP-*r*/*s* stars would be stars polluted by metal-poor AGB with significant Eu production. Thus, those new results and the dominant role played by AGB stars in the chemical evolution of the LMC (see Sec. 5.2.1) support explanation (3).

Scandium Figure 5.25 shows the LMC bar and disc Sc distributions. The bar and disc have similar [Sc/Fe]. They overlap the MW halo but are below the MW discs. As noticed for the MW (Nissen et al., 2000; Reddy et al., 2006, 2003), the Sc in the LMC behaves approximately like Ca or Ti (while Sc is an odd element):

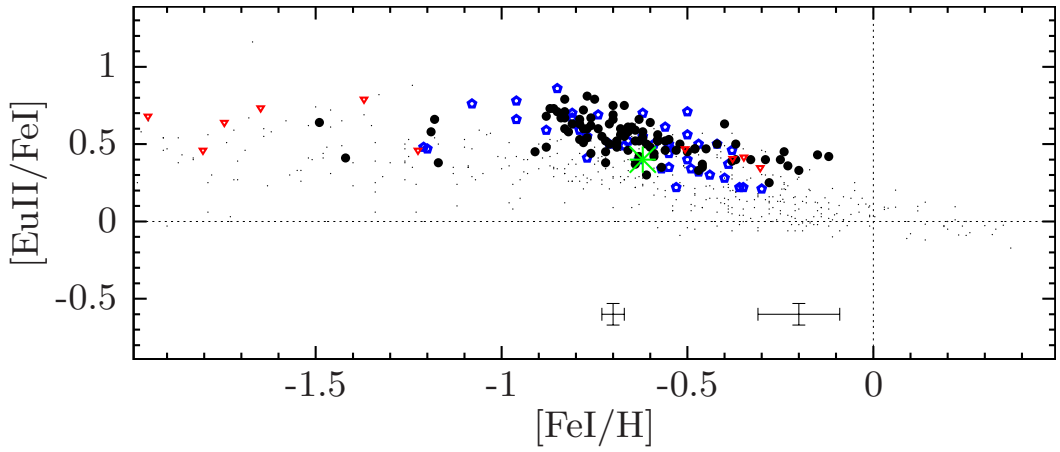

Figure 5.24: [EuII/FeI] **vs.** [FeI/H]**.** Same legend as Figure 5.14.

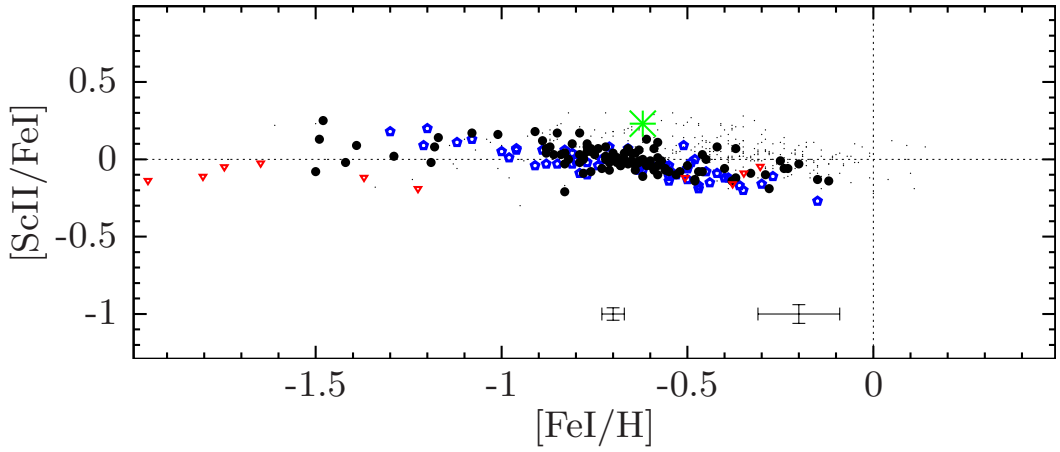

Figure 5.25: [ScII/FeI] **vs.** [FeI/H]**.** Same legend as Figure 5.14.

small scatter at all metallicities; [Sc/Fe] decreases with increasing metallicity; the distribution for the most metal-poor stars ([Fe/H] ≤ -1 dex) is compatible with a plateau (especially for the bar); the amplitude of the decrease between the metal-poor edge and the metal-rich edge is of 0.2 dex. Prochaska & McWilliam (2000) claimed that the α-like pattern of Sc could be due to poor hyperfine structure (hfs) data but Reddy et al. (2006, 2003) used weak Sc II lines in dwarf stars for which the hfs has little effect on the derived abundances. For our giant stars, the hfs must be taken into account since Sc II lines are strengthened; and we see that Arcturus [Sc/Fe] lies on the top of the thick disc distribution, as expected. To conclude, we also found that Sc behaves like an α-elements for our LMC RGB stars, and therefore, its nucleosynthetic origin remains unclear.

Other iron-peak elements Figure 5.26 presents the abundance distributions of V, Cr, Co and Ni. Although they all belong to the iron-peak and are mainly produced by SNeIa, these elements exhibit different patterns. The abundance distributions of V, Cr and Co are characterised by a rather large scatter, V being the most dramatic case. Cr and Co have flat distributions overlapping those of the MW for both LMC fields while Ni is sub-solar at all metallicities for both LMC fields.

On the other hand, for V, the bar and disc distributions agree only for [Fe/H] ≤ -1.1 dex. For [Fe/H] ≥ -1.1 dex, in the mean, the bar has higher [V/Fe] than the disc (bar: $\langle$[V/Fe]$\rangle = -0.11$ dex; disc: $\langle$[V/Fe]$\rangle = -0.30$ dex). Among the iron-peak elements, V is the one with the highest number of measured lines (7 lines, most of the time) but it exhibits the larger scatter, which should be in principle a sign that the scatter is astrophysical. Interestingly, like for Na (Sec. 5.4), the disagreement between the two LMC fields appears at -1 dex. In Section 4.4, we found a correlation between the derived [V/Fe] and $T_{\rm eff}$ or $\xi_{\rm micro}$, i.e. increasing abundance ratio with increasing temperature or microturbulence velocity. In addition, our two samples do not have the same temperature coverage (3900 K to 5200 K for the bar, 3800 K to 4600 K for the inner disc). We performed the following sanity check for V in order to verify that the correlations are not responsible for the differences between our two fields: we select only stars in the temperature range $[4000, 4400]$ (common to our two samples), and compute for both fields the mean and standard deviation of the [V/Fe] distributions and compare them. We found that the dispersion slightly decreases in each field, but the two fields remain significantly different. To finish, the typical random and systematic error are respectively 0.04 dex and 0.29 dex and can explain the scatter but not the offset between the two fields.

To conclude, the differences observed between the iron-peak elements between the MW and LMC distributions indicate that we are still missing a detailed understanding of their production (production efficiency metallicity dependent or dependent on the mass of the progenitors etc.).

5.4 A new picture for the formation of the LMC bar

α-elements and europium Our two fields do not exhibit strong differences in their α trends: for O, Mg, Si and Ti, the trends of the bar and the disc overlap at all metallicities. On the other hand, we observe a larger scatter for the bar [α/Fe] = [O + Mg/2Fe] for -0.8 dex $\leq$ [Fe/H] ≤ -0.4 dex: over this range of metallicities, $\widehat{\rm Std}$([α/Fe]) = 0.08 dex for the bar, $\widehat{\rm Std}$([α/Fe]) = 0.05 dex for the disc. For the most metal-rich stars (above -0.5 dex), we notice also small differences in the Eu trends of our two LMC fields (see Fig. 5.24). Indeed, while the disc [Eu/Fe] still decreases and reaches lower values than the bar, the bar [Eu/Fe] seems to remain constant ([Eu/Fe] ≈ 0.4 dex). According to the age-metallicity relation (Cole et al., 2005), the metallicity range $[-0.8, -0.4]$ corresponds to ages between 2 Gyr to 6 Gyr ago, thus the suspected epoch of the bar formation. The slight increase of the scatter in the [α/Fe] and the slightly higher [Eu/Fe] ratios for the bar field can be understood in the scenario where a new population is formed. Indeed, if the bar is the result of a new population formation, sustained by gas inflow, then

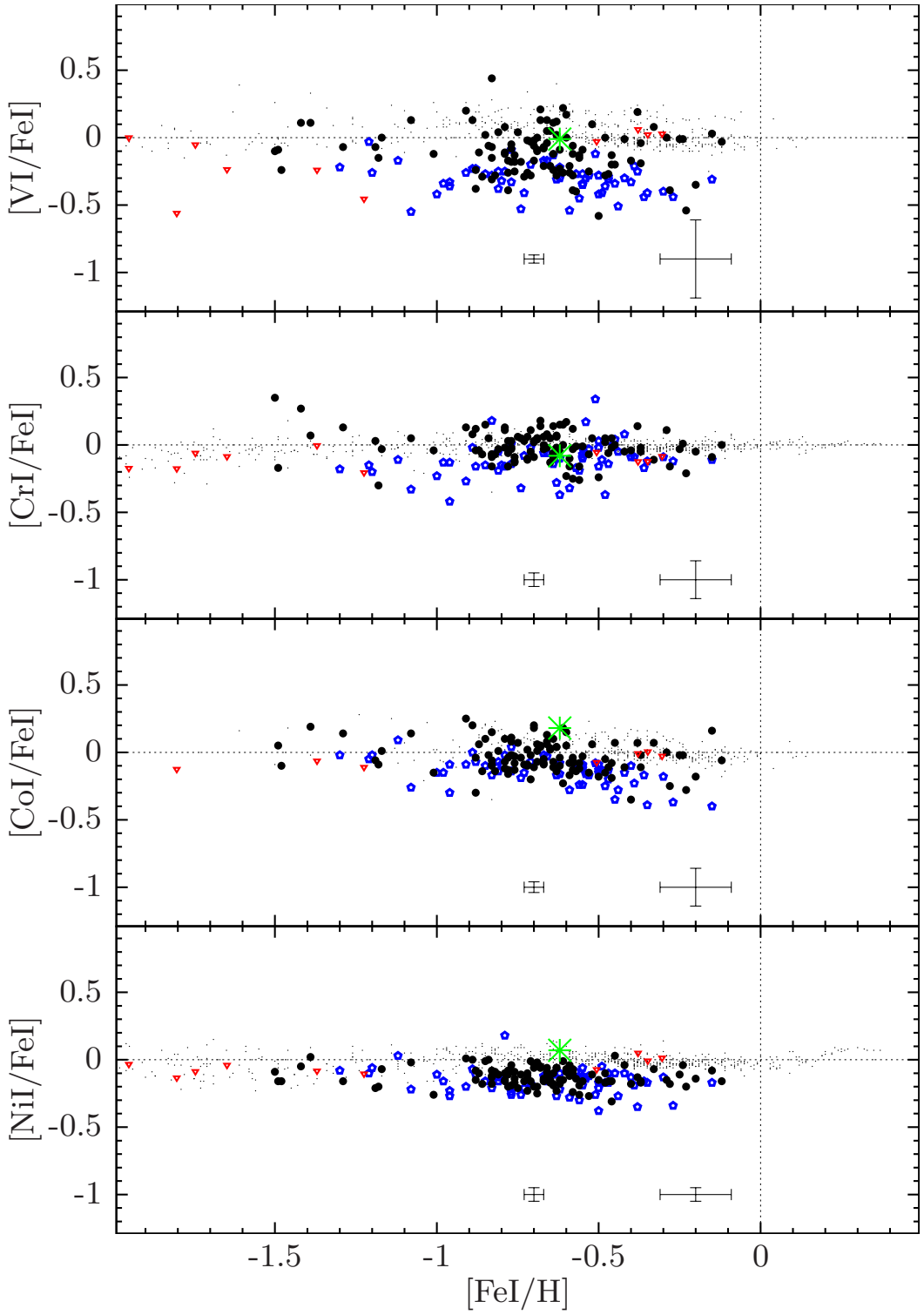

Figure 5.26: [VI/FeI] **vs.** [FeI/H], [CrI/FeI] **vs.** [FeI/H], [CoI/FeI] **vs.** [FeI/H], [NiI/FeI] **vs.** [FeI/H]**.** Same legend as Figure 5.14.

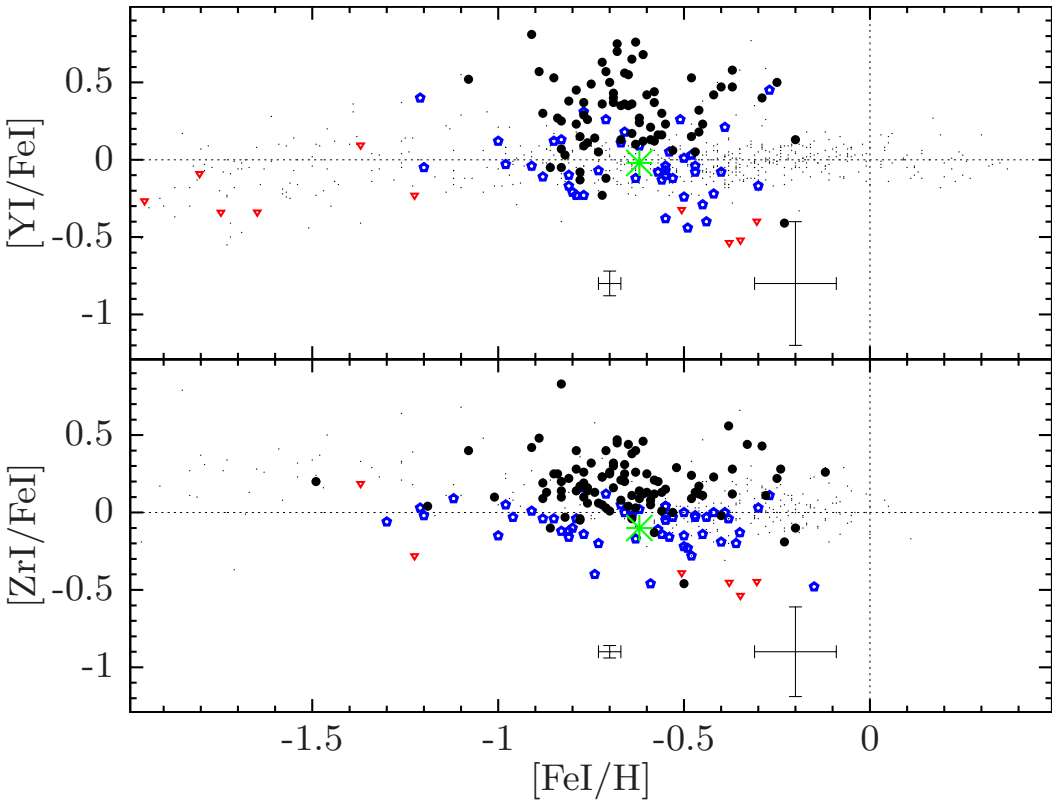

Figure 5.27: **[YI/FeI] vs. [FeI/H], [ZrI/FeI] vs. [FeI/H].** Same legend as Figure 5.14.

the number of massive stars will increase and they will release significant amounts of freshly formed α-elements and Eu into the ISM. We should then expect an increase of [α/Fe] and [Eu/Fe] a few Myr after the start of the star burst (Gilmore & Wyse, 1991; Pagel & Tautvaisiene, 1998; Tsujimoto et al., 1995). In fact, this increase would be too small to be clearly identifiable in our data because of uncertainties in both [Fe/H] and [α/Fe] or [Eu/Fe]: instead, we see a larger scatter for [α/Fe] and a fading of the decreasing trend for [Eu/Fe]. These features support the scenario of a new stellar population instead of a dynamically-driven bar.

AGB products: yttrium and zirconium For [Fe/H] ≤ -1 dex, the LMC bar and disc seem to have a solar Zr ratio (Figure 5.27) and a solar Y ratio (at least for the disc field; we do not have enough data point for the bar field). For [Fe/H] > -1 dex, the two LMC fields have a flat Y and Zr distribution with a large scatter but the LMC disc and bar exhibit a different mean behaviour in their Y and Zr trends: in the mean, the bar has higher [Y/Fe] and [Zr/Fe] than the disc (bar: $\langle$[Y/Fe]$\rangle = 0.31$ dex, $\langle$[Zr/Fe]$\rangle = 0.19$ dex; disc: $\langle$[Y/Fe]$\rangle = -0.04$ dex, $\langle$[Zr/Fe]$\rangle = -0.08$ dex).

We checked for possible systematic effects explaining the differences but found

none (same kind of stars, same instrument and observing setups, similar data reduction procedure, same procedures to derive stellar parameters and abundances). In particular, we checked whether one of the three Zr lines used could be responsible for the difference. In the mean, each line gives higher Zr abundances for the bar than for the disc: for the bar, $\langle$[Zr/Fe]$\rangle = 0.22$ dex, 0.20 dex and 0.14 dex; for the disc, $\langle$[Zr/Fe]$\rangle = -0.04$ dex, 0.0 dex, and -0.14 dex (resp. for the line at 6127 Å, 6134 Å and 6143 Å). In Section 4.4, we found for both fields a clear correlation between [Y, Zr/Fe] and $T_{\rm eff}$ or $\xi_{\rm micro}$. LMC GC stars of Mucciarelli et al. (2008, 2010) follow the same correlation as ours (Fig. 4.16), and since they are colder than our stars, they have Y and Zr abundances lower than those of our stars. If we perform a sanity check similar to what we did for V (i.e. selecting only stars in the temperature range $[4000, 4400]$ and comparing the two fields distributions for those stars), then we find that the dispersion slightly decreases in each field, but the two fields remain significantly different: $\langle$[Y/Fe]$\rangle = 0.25$ dex, $\langle$[Zr/Fe]$\rangle = 0.15$ dex for the bar, and $\langle$[Y/Fe]$\rangle = 0.0$ dex, $\langle$[Zr/Fe]$\rangle = -0.07$ dex for the disc.

The typical random error (due to pixel noise) on the final Y or Zr abundances are respectively 0.08 dex and 0.04 dex while the typical systematic error (due to errors on effective temperature) are 0.4 dex and 0.29 dex respectively. Thus, errors can explain the observed scatter but cannot explain the offset between our two LMC populations.

Such a discrepancy is not seen for Ba and La for which the distributions of our two LMC fields agree rather well. Interestingly, Y and Zr, on the one hand, Ba and La, on the other hand respectively belong to the first peak and the second peak of the *s*-process (the position of the peaks correspond to magic number of nucleons for which the nucleus is more stable). The observed differences can be an effect of metallicity of the AGB stars producing the *s*-elements since the second peak is favoured, relatively to the first peak, when metal-poor AGB stars dominate the chemical enrichment (e.g., Cristallo et al., 2011; see Sec. 5.2.1). This suggests that AGB stars were more metal-poor in the disc than in the bar of the LMC. We note that the metal-rich LMC GC have [Y/Fe] and [Zr/Fe] clearly lower than those of the LMC bar, and probably similar to the LMC inner disc, which is understandable since their projected locations lie in the LMC disc. Thus, the differences observed between the LMC bar and disc for Y and Zr for [Fe/H] $\gtrapprox -1$ dex speak in favour of a different chemical evolution path: unlike the disc, the bar experienced a recent episode of stellar formation (a few Gyr ago) which generated metal-rich AGB that explain the present Y an Zr ratios.

Sodium: another AGB product? In Figure 5.28, for stars whose metallicity is below -1.1 dex, we see that the LMC bar and disc [Na/Fe] agree rather well within uncertainties (bar: $\langle$[Na/Fe]$\rangle = -0.28$ dex; disc: $\langle$[Na/Fe]$\rangle = -0.37$ dex) and they overlap the MW halo distribution. On the other hand, for [Fe/H] ≥ -1.1 dex, the two LMC distributions become different. The bar [Na/Fe] seems to increase with increasing metallicity and reaches solar values ($\langle$[Na/Fe]$\rangle = -0.13$ dex, r.m.s = 0.17 dex), thus overlapping the Galactic trends. On the other hand, the disc [Na/Fe] remains subsolar with a flat distribution ($\langle$[Na/Fe]$\rangle = -0.35$ dex, r.m.s = 0.13 dex). Both fields exhibit a large scatter in this metallicity regime: although only five bar

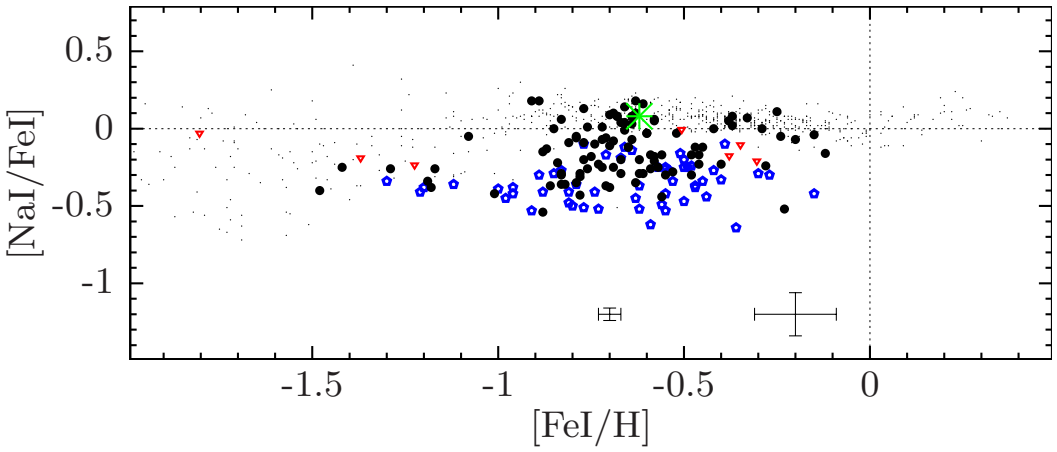

Figure 5.28: [NaI/FeI] **vs.** [FeI/H]**.** Same legend as Figure 5.14.

stars and four disc stars are observed for [Fe/H] ≤ -1.1 dex, we can guess that the scatter is smaller than for [Fe/H] ≥ -1.1 dex (if the scatter were the same, it would be unlikely to have five or four measures concentrated within 0.2 dex). None of the three Na lines used is responsible for the difference; in the mean, each line gives higher Na abundances for the bar than for the disc: for the bar, $\langle$[Na/Fe]$\rangle = -0.11$ dex, -0.15 dex and 0.12 dex; for the disc, $\langle$[Na/Fe]$\rangle = -0.31$ dex, -0.35 dex, and -0.36 dex (respectively for the line at 5688 Å, 6154 Å and 6160 Å).

As for Y and Zr, there is a correlation between [Na/Fe] and $T_{\rm eff}$ and again, if we select only the stars in the temperature range $[4000, 4400]$, the dispersion slightly decreases but we still see the different mean behaviour. We note that there is an excellent agreement at both low an high metallicity between the LMC GC and our LMC fields. As for Y and Zr, the typical random and systematic error on the final Na abundance are respectively 0.04 dex and 0.14 dex and can explain the scatter but not the offset between the two fields.

The production of Na is still uncertain and is thought to occur in high-mass SNeII (Woosley & Weaver, 1995) and AGB stars (Bisterzo et al., 2010; Cristallo et al., 2006; Goriely & Mowlavi, 2000). Issues on the abundance measurement have been reported, e.g. in Pasquini et al. (2004) where the authors find a disagreement between Na abundances of giant and dwarf stars belonging to the same cluster. Different explanations are quoted to explain these issues: departure from local thermodynamic equilibrium, surface Na abundances modified by the first dredge-up or uncertainties on atomic data (Smiljanic, 2012). It is therefore difficult to understand the LMC trends relatively to those of the MW (most of the MW abundances were measured in dwarf stars) but comparing the two LMC fields is still valid. The discrepancy between the LMC bar and disc fields tells us that the production of Na has been more efficient in the bar than in the disc: once again, it can be the result of the star burst that gave birth to the new population in the central parts of the LMC.

To conclude, our two LMC fields exhibit differences in their Na, Y and Zr

trends, which support the scenario of a burst-born bar. There is evidence for a recent stellar activity, which leads to the formation of a new generation of metal-rich AGB stars in the LMC bar; those metal-rich AGB bar stars increased the ratios [Na, Y, Zr/Fe] while in the LMC disc, more metal-poor AGB stars were driving the chemical evolution and kept those ratios at a lower level. Our results show that a one-zone modelling of the LMC is not relevant: at least, a two-zone modelling is needed to handle separately the LMC bar and the LMC disc. I intend to build a two-zone chemical evolution model of the LMC (see Sec. 6.3) in order to explain the chemical differences between the LMC bar and disc.

Chapter 6

Conclusion & future works

Contents

6.1 Main developments for this thesis work

To perform a detailed chemical analysis of Large Magellanic Cloud (LMC) giant stars (106 stars in a field centred on the LMC bar, and reanalysed in a homogeneous manner the 58 RGB stars observed by Pompéia et al. (2008) in a field situated in the inner LMC disc field some ∼2 deg South of the bar, using high resolution and mid signal-to-noise ratio (S/N ratio) spectra obtained at ESO/VLT. We took great care to insure the homogeneity of the two samples, and furthermore used the local thick disc giant Arcturus to insure a proper comparison to Milky Way (MW) disc samples. To this end, I developed a number of tools dealing with data reduction, stellar parameters and abundance measurements. The first step of this work consisted in the preparation of the spectra (Chapter 2): as the GIRAFFE pipeline stopped at the spectrum extraction step, I developed my own tools to perform sky subtraction, telluric correction, radial velocity correction (based on my own cross-correlation algorithm and masks). I set up a pipeline to determine the stellar parameters of our LMC RGB stars (Chapter 3). I used three kinds of methods: photometric $T_{\rm eff}$–calibrations to obtain $T_{\rm eff}$, isochrone fitting to obtain $\log g$ and a spectroscopic criterion to obtain $\xi_{\rm micro}$ and [M/H] simultaneously. My pipeline relies on and uses pre-exiting tools: photometric calibrations from Ramírez & Meléndez (2005b), DAOSPEC (Stetson & Pancino, 2008) to measure equivalent width (EW) and fit the stellar continuum, *turbospectrum* (Alvarez & Plez, 1998) and the Bayesian estimation algorithm of stellar parameters of da Silva et al. (2006). I wrote a pipeline to derive elemental abundances using both EW and absorption line fitting (Chapter 4). I adopted a differential analysis using the MW thick disc star Arcturus to allow a comparison between our LMC elemental trends and those of the MW; this also allowed me to offer a new homogeneous detailed chemical composition of Arcturus. In order to secure the abundance ratios, I performed different sanity checks: looking for suspicious atomic lines (too weak lines, outliers), determination of random and systematic errors, and looking for correlations between abundance

ratios and stellar parameters. This allowed me to build a catalogue of 17 elemental abundances for 164 LMC RGB stars (106 newly analysed and 58 re-analysed from Pompéia et al., 2008).

6.2 Main results of this thesis work

We compared the chemical history of the LMC to that of the MW and disentangled the chemical evolution of the LMC bar and disc, based on the data that I obtained in this work. The main findings of this thesis work can be summarised as follows:

- The two samples cover the metallicity range [Fe/H] from -1.5 to -0.1 dex, covering the full LMC disc metallicity distribution (Carrera et al., 2008b; Cole et al., 2005), albeit leaving out the most metal-poor (and less numerous) tail of the distribution despite our deliberate overpopulation of this tail in the target selection. 80% of the sample is comprised between -1.1 and -0.4 dex. we stress the fact that this metallicity-biased sample cannot be used for metallicity distribution studies.

- In the metallicity range covered by both types of objects, the LMC field and GC elemental abundances exhibit an excellent agreement for all elements (except for O and Na at low metallicity where the clusters experienced self-enrichment creating anti-correlated O-Na star to star variations).

- The α-elements ratios [Mg/Fe] and [O/Fe] are lower in the LMC than in the MW suggesting a slower enrichment. The presence of a plateau for [α/Fe] is not convincingly probed by our samples (that lack the statistics at low metallicities), although the most metal-poor globular cluster (GC) do seem to lie on a plateau. [Ba, La/Eu] exhibit a strong increase from [Fe/H] ≈ -0.8 dex with increasing metallicity showing that the chemical enrichment of the LMC has been slower than that of the MW, and that the neutron-capture elements were dominated by AGB stars strongly contributing to the *s*-process. The LMC has lower [Y + Zr/Ba + La] ratios than the MW indicating that these asymptotic giant branchs (AGBs) were more metal-poor in the LMC.

- Eu does not follow the expected trend which could be an indication of an efficient *s*-production of this element, despite the usually assumed almost pure *r*-process origin of this element. This finding is supported by the recent work by (Allen et al., 2012) who advocate a strong *s*-process contribution to Eu in a certain category of extremely metal-poor carbon and *s*-process enhanced stars (the so-called *sr*-stars).

- Cu is almost constant over the metallicity range and about 0.5 dex lower in the LMC than in the MW showing that in the LMC Cu has mainly a primary origin (through weak *s*-process in massive stars).

- The LMC bar and disc exhibit subtle differences in their [α/Fe] (slightly larger scatter for the bar in the metallicity range $[-1, -0.5]$), their [Eu/Fe] (the bar trend is above the disc trend for [Fe/H] ≥ -0.5 dex, their Y and Zr, their

Na and their V (offset between the bar and the disc distributions). These differences are possibly related to the formation of a new stellar population in the central part of the LMC: the resulting new generation of massive stars will inject freshly synthesised α-elements (hence the increased scatter observed in the bar) and Eu (hence the higher [Eu/Fe] ratios in the bar) and the new generation of metal-rich AGB stars will produce Na, Y and Zr (hence the offset). These findings strengthen a scenario where the LMC bar is not a mere dynamically-driven (or interaction driven) over-density, but implied a fresh episode of star formation. This scenario also supported by the star formation history derived in the bar, that highlights an increased star formation 2-5 Gyr ago, with no clear counterparts in other locations in the LMC disc (Smecker-Hane et al., 2002). More globally, (Harris & Zaritsky, 2009) have established a map of star formation histories across the whole LMC and find again that the dominant star formation episode that occurred some 5 Gyr is more pronounced in the bar than anywhere else in the LMC. Even younger bursts of star formation seem to follow the bar morphology, around 500 and 100 Myr ago. Gallart et al. (2008), although their sample does not include the bar per say, also highlight that the younger populations in the LMC are found closer to the centre together with a positive age-gradient of the youngest star formation episode towards the outskirts. All these findings regarding the star formation history of the LMC bar and disc strengthen a scenario where the bar is the strongest manifestation of the higher recent star formation activity in the central parts of the LMC.

6.3 Future works

Our LMC project aims at chemically tagging the stellar populations at various location of the LMC. My thesis work concentrated on the two fields, one located in the LMC bar, and one located in the LMC inner disc. We have GIRAFFE spectroscopic data ($\sim$ 100 RGB stars observed with three setups HR11, HR13 and HR14) for a third field, located in outer parts of the LMC disc, at 4° from the bar. To extend this thesis work, a first step will be to perform a similar chemical analysis of the LMC outer disc RGB sample. It will be interesting to see if the chemical peculiarities of the bar are confirmed, i.e. if the LMC outer field exhibits similar trends as those of the inner disc field, in particular for α-elements, Eu, Na, Y, and Zr. I reduced the data in the same fashion as for the LMC bar spectra, i.e. with the GIRAFFE pipeline and my own tools. In order to derive abundances homogeneous with those of our LMC bar and disc, I will apply the same procedures as developed for this thesis work. For the time being, we are missing VI photometry for this LMC outer disc field: we will use images of the EIS program to complete our photometric catalogue.

The next step will be to propose a chemical evolution modelling of the LMC, in close collaboration with Donatella Romano (Osservatorio di Bologna), using — at least — a two-zone model (the bar on the one hand, the disc on the other hand). I will use the chemical evolution developed by Romano et al. (2007), which

is currently designed for one-zone modelling. I will be actively involved in the modification of the code to allow multi-zone modelling. Stellar yields for elements up to Zn have already been selected by Romano et al. (2010a) for their adequacy with MW elemental trends. We plan to use empirical star formation rate (SFR) (Smecker-Hane et al., 2002) for the LMC bar and disc, and test various hypotheses: gas exchange between the bar and the disc, pristine gas infall etc. First runs that I made with this model show that we can expect to reproduce the chemical evolution of the LMC.

Appendix A

Final line lists

Table A.1: Final line lists. [Available electronically]

Appendix B

Final abundances for LMC bar stars

Table B.1: Final abundances for LMC RGB bar stars. [Available electronically]

Appendix C

Final abundances for LMC inner disc stars

Table C.1: Final abundances for LMC RGB disc stars. [Available electronically]

Appendix D

Publications

Astronomy & Astrophysics manuscript no. aeta2012
January 15, 2013

Chemical abundances in LMC stellar populations.

II. The bar sample⋆

M. Van der Swaelmen[1], V. Hill[1], F. Primas[2], and A. A. Cole[3]

[1] Observatoire de la Côte d'Azur, CNRS UMR6202, BP4229, 06304, Nice Cedex 4, France
e-mail: Mathieu.Van-der-Swaelmen@oca.eu
e-mail: Vanessa.Hill@oca.eu
[2] European Southern Observatory, Karl Schwarzschild Str. 2, 85748 Garching b. München, Germany
e-mail: fprimas@eso.org
[3] School of Mathematics & Physics, University of Tasmania, Private Bag 37, Hobart, Tasmania 7001, Australia
e-mail: andrew.cole@utas.edu.au

Received ??; accepted ??

ABSTRACT

Aims. This paper compares the chemical evolution of the Large Magellanic Cloud (LMC) to that of the Milky Way (MW) and investigates the relation between the bar and the inner disc of the LMC in the context of the bar formation.
Methods. We obtained high-resolution and mid signal-to-noise ratio spectra with FLAMES/GIRAFFE at ESO/VLT and performed a detailed chemical analysis of 106 and 58 LMC field red giant stars (mostly older than 1 Gyr), respectively located in the bar and the disc of the LMC. To validate our stellar parameter determination and our abundance measurement procedures, we performed thorough tests using the well-known mildly metal-poor Milky-Way thick disc giant Arcturus (HD 124 897, α Boo). We measured elemental abundances for O, Mg, Si, Ca, Ti (α-elements), Na (light odd element), Sc, V, Cr, Co, Ni, Cu (iron-peak elements), Y, Zr, Ba, La and Eu (s- and r-elements).
Results. We found that the α-elements ratios [Mg/Fe] and [O/Fe] are lower in the LMC than in the MW while the LMC has similar [Si/Fe] [Ca/Fe] and [Ti/Fe] to the MW. As for the heavy elements, [Ba, La/Eu] exhibit a strong increase with increasing metallicity starting from [Fe/H] ≈ -0.8 dex, and the LMC has lower [Y + Zr/Ba + La] ratios than the MW. Cu is almost constant over the metallicity range and about 0.5 dex lower in the LMC than in the MW. The LMC bar and inner disc exhibit differences in their [α/Fe] (slightly larger scatter for the bar in the metallicity range $[-1, -0.5]$), their Eu (the bar trend is above the disc trend for [Fe/H] ≥ -0.5 dex, their Y and Zr, their Na and their V (offset between the bar and the disc distributions).
Conclusions. Our results show that the chemical history of the LMC experienced a strong contribution by type Ia supernovae as well as a strong s-process enrichment from metal-poor AGB winds. Massive stars had a smaller contribution to the chemical enrichment compared to the MW. The differences observed between the bar and the disc speak in favour of a new episode of star formation a few Gyr ago, occurring in the central parts of the LMC and leading to the formation of the bar. This is in agreement with the derived star formation histories.

Key words. Stars: abundances - Galaxies: Magellanic Clouds - Galaxies: abundances - Galaxies: evolution

1. Introduction

Despite decades of intensive observational and theoretical works, we are still far from a complete and clear understanding of our close universe, the MW and its neighbours. Among the satellites of the MW, the Small Magellanic Cloud (SMC) and the LMC are of particular interest since they form the closest example of galaxies in gravitational and chemical interactions and, therefore, constitute a unique laboratory to study the effect of gravitational tides and matter exchange on the chemical evolution and the star formation history of a galaxy.

The LMC is an almost face-on, gas-rich galaxy with regions of active stellar formation located at 50 kpc (Alves 2004). It has a mass of $10^{10} M_{\odot}$ (van der Marel et al. 2002), which is intermediate between massive spirals and dwarf galaxies. Because of its bar-like feature embedded in a disc and its single spiral arm, the LMC is classified as a Barred Magellanic Spiral (SBm) (de Vaucouleurs & Freeman 1972). The young population exhibits an irregular morphology, likely the stigmata of the very recent interaction with the SMC while the old and intermediate-age population are located within a regular disc and a prominent and luminous off-centre bar. However, the morphology of the LMC is not well understood. For instance, the GC population of the LMC is intriguing since no object of age between 3 and 10 Gyr is found: this is the age gap (e.g. Da Costa 1991; Rich et al. 2001), which is not observed in the SMC GC population. We still do not know the origin and the true nature of the asymmetric bar-like structure: is it a dynamical bar driven by disc instabilities like the one found at the centre of the MW or is it a new stellar population? In addition, distance measurements based on Red Clump stars or RR Lyrae variables located in the LMC bar suggest that the bar is about 5 kpc above the disc plane (Haschke et al. 2012a). This feature is also puzzling and difficult to understand: is it a deformation of the LMC disc due to gravitational interaction with the SMC? Another interesting feature is that the bar is off-centre: the centroid of the bar and the disc differs (van der Marel 2001). Zaritsky (2004) showed that these features can be explained by a triaxial stellar bulge embedded in a highly obscuring thin disc: unfortunately, this solution is not

⋆ Proposals 072.B-0293(B) and 078.B-0323(A), P.I. Vanessa Hill

completely satisfactory since it requires a strong reddening (or a very inclined disc which has equivalent effect). If this were the case, one would then have to understand the origin of such a stellar bulge (driven by a dynamical instability in the past or similar to early-type bulges?). The Magellanic Bridge, made of gas and stars, connects the LMC and the SMC and is the site of matter exchange between the two Clouds.

Numerous authors (e.g Besla et al. 2007; Bekki & Chiba 2005; Bekki 2009) have tried to reproduce consistently the large-scale and/or small-scale structure of the LMC (asymmetric off-centre bar, GC age gap, Magellanic Bridge...) in their dynamical models, taking into account the interaction with the SMC and/or with the MW. However, because of uncertainties on the proper motions (Kallivayalil et al. 2006b,a), we still do not know whether the {LMC+SMC} system is performing its first passage about the MW, or whether the two Magellanic Clouds formed as separate entities and have become gravitationally bounded later on... Hence a variety of models. Besla et al. (2012) tested two first infall models: at the beginning, the MC are a binary pair, evolving in isolation until their first passage close to the MW. Their model 2 reproduces most of the morphological and dynamical features. In particular, Besla et al. (2012) explains the asymmetric off-centre bar: as the LMC disc is bar unstable, the bar is present from the beginning; it becomes asymmetric off-centre due to a close encounter of the LMC and SMC a few Myr ago. On the other hand, Smecker-Hane et al. (2002) have derived from deep colour-magnitude diagram (CMD) the star formation histories for field stars located in the LMC bar and the inner part of the LMC disc. They show that the star formation history (SFH) of the bar and the inner disc were similar at old epochs (between 7 and 14 Gyr); but while the SFH of the inner disc has remained rather constant, the bar has experienced a dramatic increase of its SFH, 4 to 6 Gyr ago. Thus, the SFH supports the scenario of a new burst of stellar formation at the centre of the LMC, which could lead to the appearance of the bar-like structure.

Kinematical and chemical tagging of stellar populations is a powerful tool helping in reconstructing the past history of a given galactic environment. Pompéia et al. (2008) provided for the first time a detailed chemical analysis of a large sample of LMC red giant branch (RGB) stars located in the LMC disc, ∼2 degrees South of the LMC bar, hereafter the inner disc. Lapenna et al. (2012) measured the [α/Fe] of 89 stars in a field close to the LMC globular cluster NGC 1786, some 3° North-West of the bar. The present work aims at bringing new light on the nature of the bar: to this end, we provide a detailed chemical tagging of a large sample of LMC bar RGB stars and compare the elemental trends to the reanalysed trends of the inner disc. Section 2 describes the sample selection and the data reduction. Section 3 and 4 explain the stellar parameter and abundance measurement methods. Section 5 provides the results and their interpretation. Section 6 summarises the main results of this work.

2. Observations and data reduction

2.1. Sample selection

Cole et al. (2005) observed 373 RGB stars in the field of the LMC bar and derived radial velocities and metallicities from low-resolution infrared Ca II triplet spectra. We used their metallicity distribution to select 113 RGB stars (maximum number of a single multi-object fiber configuration with FLAMES) belonging to the LMC bar, taking care to sample as evenly as possible the whole metallicity range from $[Fe/H]_{CaT} = -1.69$ dex to $[Fe/H]_{CaT} = 0.14$ dex. Indeed since metal-poor stars ($[Fe/H] \leq -1$ dex) are rare, a random selection would not provide enough metal-poor stars; hence this metallicity selection, a necessary precaution to trace the early epochs of the LMC history (which populate the low-metallicity tail of the metallicity distribution). Figure 1 shows the location of the 373 stars from Cole et al. (2005) and our 113 targets on a I,(V-I) CMD and the metallicity distribution function of these two samples. We obtained high resolution spectra of our 113 stars at VLT/ESO with the FLAMES/GIRAFFE multifibre spectrograph (Pasquini et al. 2002). In order to measure numerous elemental abundances, we used three setups HR11 ($\lambda_{central} = 572.8$ nm, $R_{\lambda_{central}} \simeq 24\,200$), HR13 ($\lambda_{central} = 627.3$ nm, $R_{\lambda_{central}} \simeq 22\,500$) and HR14 ($\lambda_{central} = 651.5$ nm, $R_{\lambda_{central}} \simeq 17\,740$)[1], covering a total of ≈ 1000 Å. The spectra thus cover lines belonging to the α- (Ca, O, Mg, Ti, Si), iron-peak (Sc, V, Cr, Co, Ni, Cu), *s*-process and *r*-process elements (Ba, La, Zr, Y, Eu). Thanks to the MEDUSA mode of the GIRAFFE spectrograph up to 135 objects can be observed simultaneously in a single exposure. For our purposes, around 10 to 20 fibres were allocated to sky positions and the other remaining fibres were devoted to the observation of LMC bar stars. In addition, three hot (O-B type) stars in the LMC were allocated to fibres, to allow an accurate correction for telluric absorption lines.

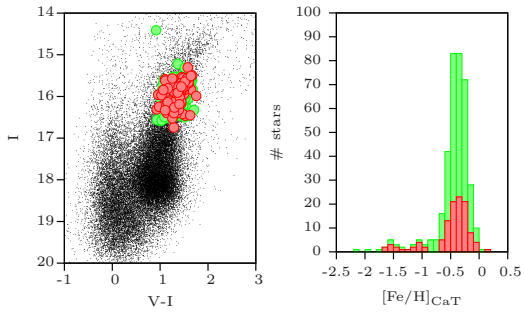

Fig. 1. Colour-Magnitude diagram (left panel) and metallicity distribution (right panel) of Cole et al. (2005) RGB sample (green) and our selected RGB stars (red). V and I magnitude are from the OGLE catalogue Udalski et al. (1997, 2000); Szymanski (2005) for the samples of Cole et al. (2005) and the present paper, while black dots in the CMD are photometric data from Zaritsky et al. (2004) catalogue. Metallicities in the right panel are those derived from the infrared Ca II triplet index by Cole et al. (2005).

2.2. Data reduction

We carried out the data reduction with the help of the ESO GIRAFFE pipeline (built upon the Geneva Giraffe pipeline described in Blecha et al. 2000), part of the *esorex* framework[2]. The reduction steps include the bias and dark current correction, wavelength calibration (using a Th-Ar lamp), spectrum extraction and flat fielding. As the pipeline does not support sky subtraction nor radial velocity correction, we carried out those operations separately.

[1] for technical details see `http://www.eso.org/sci/facilities/paranal/instruments/flames/doc/VLT-MAN-ESO-13700-2994_v86.0.pdf`

[2] pipeline available at `http://www.eso.org/projects/dfs/dfs-shared/web/vlt/vlt-instrument-pipelines.html`

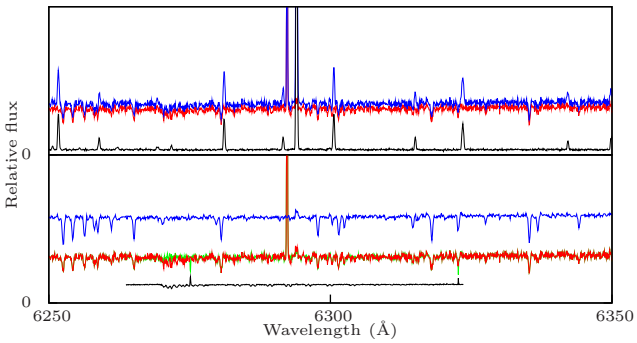

Fig. 2. Top panel: an example of raw spectrum (blue) for the star 05244301-6943412 and the corresponding master-sky (black) we used to obtain the sky-subtracted spectrum (red). In the red spectrum sky emission lines have been correctly removed. A cosmic ray remains at $\sim$ 6290 Å. Bottom panel: the sky-subtracted spectrum of 05244301-6943412 before (red) and after (green) the correction for the telluric lines. The spectrum of the fast rotator is plotted in black to show the position of telluric features. The blue spectrum is the co-added spectrum: the σ-clipping has removed the remaining cosmic rays and the signal-to-noise ratio is clearly improved compared to the single exposure. All spectra are plotted in the same scale, except for the fast rotator spectrum (it has been scaled for legibility).

Sky subtraction We visually sorted out the sky spectra to check for their quality and discarded those showing the lowest signal-to-noise ratio (S/N ratio) or spectral contamination: jump in fluxes due to polluting light (stellar light, CCD glow, simultaneous calibration lamp) or a CCD defect. After this quality selection, we ended up with a handful of sky spectra (at least five to eight) in most cases. The selected sky spectra were averaged with k-σ clipping rejection and the resulting master-sky was subtracted to each stellar spectrum (see Fig. 2). This procedure was repeated for each observation of the 113 bar stars and for each setup.

Correction of telluric absorption band around 6300 Å Among the two oxygen lines (at 6300 Å and 6363 Å) that are available in the optical wavelength range, the first is the strongest line and is more appropriate for abundance measurements. Unfortunately, it is in a region contaminated by atmospheric spectral features (from 6270 Å to 6330 Å). To measure abundance reliably, it is mandatory to correct for the telluric lines. Three hot stars were observed simultaneously to our science targets for that purpose: 05235121-6934233, 05235885-6952357, 05242945-6937236. We inspected the spectra of the three stars. As the star 05235885-6952357 showed the broadest stellar spectral features (highest rotation) and the highest S/N ratio, we used its spectrum for a telluric correction: in the wavelength region [6270 Å, 6330 Å], we divided our individual stellar spectra by the hot star spectrum. We checked that no discontinuities were introduced (see Fig. 2).

Radial velocities measurements and correction We obtained multiple observations of the same star in a given setup: 10 exposures with HR11, 5 exposures with HR13 and 4 exposures with HR14, which represents a total of more than 2000 spectra. Table 1 lists the observations, the dates and the total exposure times. We wrote a cross-correlation routine using our own

Table 1. For each setup, the exposures, the total exposure times and the observation dates are given.

Setups	#	Total exp. time	Dates
HR11	10	7 h 42 min	2006-10-[6, 7, 10, 26]
			2006-11-[8, 22]
HR13	5	5 h 50 min	2004-01-15
			2004-02-[16, 21]
			2004-03-26
HR14	4	4 h 08 min	2004-02-[16, 17, 18, 20]

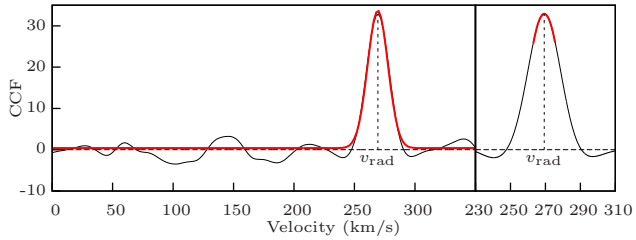

Fig. 3. Left panel: example of cross-correlation function (black line) and its Gaussian fit (red thick line). Right panel: Zoom in on the maximum of the cross-correlation function and its parabolic fit (red thick line). We first used a Gaussian fit to locate the position of the maximum and then defined a smaller velocity range (Gaussian fit FWHM) and compute the cross-correlation function over a finer grid to improve the determination of the radial velocity.

Gaussian masks to perform the radial velocity measurement. In order to build Gaussian masks resembling our spectra in terms of stellar parameters (temperature, gravity, metallicity, microturbulent velocity) and spectral resolution, we used a set of our LMC spectra: in each spectrum, we selected a high number ($\geq$ 30) of strong spectral features (iron, calcium... lines), fitted them with a Gaussian profile, computed an average absorption line profile, and then built a mask for each setup. The cross-correlation routine returned the radial velocity in the Earth frame; to correct it for the Earth motion and obtain the barycentric velocity $v_{\rm rad}$, we used the MIDAS task *barycor*. Using a k-σ clipping rejection (over the radial velocity) allowed us to point out suspicious spectra requiring a special investigation, and we discarded them if justified (*e.g.* low S/N ratio leading to a poor determination of the radial velocity). For instance, in the setup HR14, for the star 05231321-6946382, we measured four radial velocities: 270.2 km s^{-1}, 270.3 km s^{-1}, 270.5 km s^{-1} and 275.4 km s^{-1}; based on the above procedure, we flagged the observation leading to a velocity of 275.4 km s^{-1}. As the poor S/N ratio ($\sim$ 2) explains the disagreement, we discarded this observation. We only excluded a few spectra with this test. Figure 3 shows an example of a cross-correlation function and the parabolic fit used to determine the radial velocity.

In order to detect any systematic effect (from one setup to the other) or possible variations of the radial velocity, we computed a mean barycentric radial velocity for each star in each setup. For a given setup s, we used the N_s estimates to compute the mean radial velocity $v_{{\rm rad},s}$. As the setup HR11 provides the highest number of exposures, the standard deviation of the radial velocity distribution is better defined in this setup; we therefore employed it to estimate the precision on a single velocity measurement by computing the mean of the standard deviations over the sample and found 0.6 km s^{-1}. For each setup s, we compute

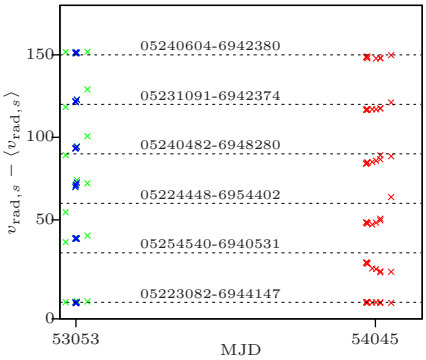

Fig. 4. Radial velocity curves for six stars. The relative radial velocities $v_{\mathrm{rad},s} - \langle v_{\mathrm{rad},s} \rangle$ determined for each exposure are plotted as a function of MJD for five stars where the T-test failed and we suspect a variability in the radial velocity. The curves were shifted for legibility (the solid line represents the offset). The bottom curve (star 05223082-6944147) is a star with no radial velocity variability and shown here for reference. In red: HR11, in green: HR13, in blue: HR14 (for HR13 data and HR14 data obtained at the same epoch, the green crosses are below the blue ones).

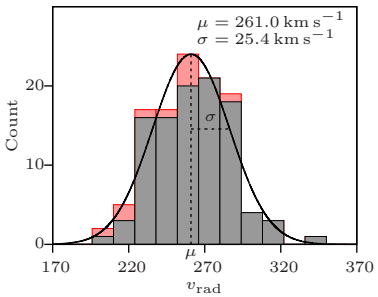

Fig. 5. Distribution of the radial velocities of the LMC bar stars. The histogram overplotted in red denote the stars for which we suspect a radial velocity variability. The mean and the standard deviation of the distribution are respectively 261 km s^{-1} and 25 km s^{-1}. A Gaussian curve (μ; σ) is plotted over the histogram.

the standard error of the mean radial velocity per setup $v_{\mathrm{rad},s}$ as $e_{\mathrm{rad},s} = \max(\sqrt{\mathrm{var}(v_{\mathrm{rad},s})/\mathrm{N}_s}, 0.6/\sqrt{\mathrm{N}_s})$. We performed a T-test to compare $v_{\mathrm{rad,HR11}}$, $v_{\mathrm{rad,HR13}}$, and $v_{\mathrm{rad,HR14}}$, taken two by two (H_0: the two mean radial velocities are equal; H_1: they are different; significance level: 1%; hypothesis of equal variance). For 103 stars (91% of the sample), we conclude that the three mean radial velocities are equal at the significance level of 1%. For those stars, the radial velocity measurements in the various setups are remarkably similar: $\langle v_{\mathrm{rad,HR11}} - v_{\mathrm{rad,HR13}} \rangle = -0.1\,\mathrm{km\,s^{-1}}$, r.m.s $= 0.6\,\mathrm{km\,s^{-1}}$, $\langle v_{\mathrm{rad,HR11}} - v_{\mathrm{rad,HR14}} \rangle = 0.3\,\mathrm{km\,s^{-1}}$, r.m.s $= 0.7\,\mathrm{km\,s^{-1}}$ and $\langle v_{\mathrm{rad,HR13}} - v_{\mathrm{rad,HR14}} \rangle = 0.4\,\mathrm{km\,s^{-1}}$, r.m.s $= 0.3\,\mathrm{km\,s^{-1}}$. For the 10 stars reported in Table 2 however, at least one of the three T-tests failed. We remark that for all reported cases, the radial velocities measured for HR13 and HR14 agree rather well, while the radial velocity measured for HR11 is discrepant with the two others. The stars 05240482-6948280, 05254540-6940531, and 05224448-6954402 show the most dramatic disagreement with differences of about 8, 17, 18 km s^{-1} (respectively) between HR11 and HR13 or between HR11 and HR14. The mean epoch and time span of the observations for each setup are given in the last columns of the Table 2: the observations in HR13 and HR14 were run at similar epochs (for HR13, more than two months separate the first and the last observation, which explains the large values of standard deviations observed for this setup for stars with a variable v_{rad}) while those in HR11 were carried out two years later. The discrepancies between setups for those stars therefore reveal a true radial velocity variation, most probably due to an internal stellar variability or a binary system. Figure 4 displays the radial velocity curves for the five stars with the most extreme variations. The period of variation seems to be large, which is expected for giant stars.

Table 3 provides the weighted mean radial velocity defined by $\langle v_{\mathrm{rad}} \rangle = \sum_s \omega_s v_{\mathrm{rad},s}$, where the sum is over the three setups s and $\omega_s = ({e_{\mathrm{rad},s}}^2)^{-1} / \sum_s ({e_{\mathrm{rad},s}}^2)^{-1}$, together with the associated error defined by $e_{\mathrm{rad}} = \sqrt{\sum_s \omega_s^2 {e_{\mathrm{rad},s}}^2}$. The typical error on the final radial velocity is $\sim 0.16\,\mathrm{km\,s^{-1}}$. Figure 5 shows the distribution of the radial velocities in the LMC bar; the mean of the $\langle v_{\mathrm{rad}} \rangle$ distribution is 261 km s^{-1} and the standard deviation of the distribution is 25 km s^{-1}, in good agreement with values reported in Cole et al. (2005) (257 km s^{-1}, σ =24.7 km s^{-1}).

Co-addition and S/N ratio To compute the S/N ratio, we used the error spectrum produced by the ESO GIRAFFE pipeline, so that the S/N ratio at pixel i is given by $\mathrm{SNR}_i = \mathrm{flux}_i/\mathrm{error}_i$ (actually, this estimator of the S/N ratio underestimates the S/N ratio because the errors are overestimated in the GIRAFFE pipeline; but it is still a good index to compare the quality of a spectrum to another). Before co-adding multiple exposures, we selected the spectra according to their median S/N ratio, requiring it to be higher than $\sim$ 3. Some observations were taken with the old FLAMES CCD, affected by the so-called glow (polluting light in one corner of the CCD); when necessary, we removed the part of a given spectrum altered by this extra source of light. Some observations were obtained with the simultaneous calibration (simcal) lamp turned on: the light of a Th-Ar lamp feeds 5 MEDUSA fibres and allows for small corrections to the wavelength calibration. However, some well-known strong emission lines of the Th-Ar gas leak and contaminate the stellar light of the $\sim$ 5 science fibres adjacent to a given simcal fibre; we removed these wavelength regions when needed. Once all exposures of the same star were in the same frame, we averaged them with k-σ clipping rejection (over the fluxes at a given wavelength) to clean for cosmic rays and increase S/N ratio. We ended up with a typical final S/N ratio of around 25 for HR11, 40 for HR13 and 48 for HR14. Table 4 lists the typical lowest, median and highest values of S/N ratio as well as an empirically corrected S/N ratio (see Sec. 2.3).

2.3. Arcturus as a benchmark star

To control any systematic effect that could hamper the comparison of our derived abundances to literature measurements, we have tested and applied our methods to the well-known mildly metal-poor Milky-Way thick disc giant Arcturus (HD 124 897, α Boo). Indeed, well-known stars such as the Sun, or the giant stars μLeo or Arcturus are often chosen (*e.g.,* Ramírez et al. 2009; Meléndez et al. 2009; Lecureur et al. 2007; Worley et al. 2009; Alves-Brito et al. 2010) as reference stars for differential analysis, since the literature is broad and provides a good knowledge of their stellar parameters and atmospheric chemical composition (from independent and less model-dependent methods). Arcturus, with $\mathrm{T_{eff}} = 4286\,\mathrm{K}$, $\log g = 1.66$ and $[\mathrm{Fe/H}] = -0.52$ dex (Ramírez & Allende Prieto 2011, and see

Table 2. Stars showing a disagreement in their mean radial velocities from one setup to another.

2MASS ID	HR11			HR13			HR14		
	$v_{\rm rad}$ km s^{-1}	$\sigma(v_{\rm rad})$ km s^{-1}	#	$v_{\rm rad}$ km s^{-1}	$\sigma(v_{\rm rad})$ km s^{-1}	#	$v_{\rm rad}$ km s^{-1}	$\sigma(v_{\rm rad})$ km s^{-1}	#
05223316-6951389	220.9	0.9	8	219.3	0.8	5	219.1	0.6	4
05224448-6954402	243.8	5.2	9	262.2	8.0	5	264.7	1.2	4
05230867-6956329	266.6	0.6	7	262.7	1.2	5	262.5	0.6	4
05231074-6939184	201.2	0.6	9	204.1	0.6	5	203.7	0.6	4
05231091-6942374	248.9	1.4	9	254.4	3.9	5	253.4	0.7	4
05240482-6948280	222.1	1.9	9	230.7	4.1	5	229.9	0.6	4
05240604-6942380	255.3	0.7	8	258.2	0.6	5	258.1	0.6	4
05240613-6953529	217.7	1.2	9	215.8	0.6	5	216.1	0.7	4
05254540-6940531	269.3	2.6	9	286.8	1.4	5	286.7	0.6	4
05255801-6937309	257.5	0.6	9	256.9	0.6	5	256.4	0.6	4
$\langle$MJD$\rangle$ (d)	54045.347			53054.700			53053.109		
MJD$_{\rm max}$ − MJD$_{\rm min}$ (d)	82.94			71.84			4.86		

Table 3. Radial velocities of LMC bar stars. 2MASS identifiers, $v_{\rm rad}$, $\sigma(v_{\rm rad})$, number of independent measurements and S/N ratio for each setup, final mean $v_{\rm rad}$ and its error. Be aware that the table provides $\sigma(v_{\rm rad})$ and not $e_{{\rm rad},s}$. The exponents l, m and h of the S/N ratio indicate respectively whether the spectrum was classified as low, median or high S/N.

2MASS ID	HR11				HR13				HR14				Average	
	$v_{\rm rad}$ km s^{-1}	$\sigma(v_{\rm rad})$ km s^{-1}	#	S/N	$v_{\rm rad}$ km s^{-1}	$\sigma(v_{\rm rad})$ km s^{-1}	#	S/N	$v_{\rm rad}$ km s^{-1}	$\sigma(v_{\rm rad})$ km s^{-1}	#	S/N	$v_{\rm rad}$ km s^{-1}	$e_{\rm rad}$ km s^{-1}
05223082-6944147	250.0	0.1	9	28$^{\rm m}$	250.4	0.1	5	38$^{\rm m}$	249.7	0.1	4	50$^{\rm m}$	250.0	0.1
05223112-6945292	263.1	0.1	9	32$^{\rm m}$	262.9	0.2	5	48$^{\rm m}$	262.5	0.2	4	59$^{\rm m}$	262.9	0.1
05223186-6947159	271.2	0.1	9	25$^{\rm m}$	271.7	0.2	5	36$^{\rm m}$	271.2	0.1	4	43$^{\rm m}$	271.3	0.1
05223309-6946595	258.3	0.1	9	35$^{\rm h}$	258.2	0.5	5	45$^{\rm m}$	258.1	0.1	4	51$^{\rm m}$	258.3	0.2
...	...	...	...	...	...	...	...	...	...	...	...	...	...	...

Notes. Excerpt of the full table shown here for guidance regarding its form and content. Full table available online at CDS.

references therein), is very similar to the stars of our LMC sample, hence the choice of this star as a benchmark for our sample.

We sliced the Hinkle et al. (2000) spectral atlas of Arcturus (high resolution $R \sim 150\,000$, high S/N ratio $\sim$ 1000) into three pieces to simulate an HR11 (550 nm to 589 nm), an HR13 (609 nm to 641 nm) and an HR14 (629 nm to 671 nm) spectrum. We then degraded the resolution (according to the setup, see Sec. 2.1) and sampling of these spectra to reach a best quality spectrum for each setup (referred to as {low-resolution, low sampling, ∞ S/N} in the following). We finally added gaussian noise according to the typical noise encountered in our LMC sample for each setup, to match four assumptions of S/N ratio: an ∞ S/N, which is the original quality of the Hinkle et al. (2000) atlas; a high S/N, which corresponds to the median of the ninth decile of the S/N ratio distribution (the best 10% of the sample); a median S/N, which corresponds to the ∼ median of the S/N ratio distribution; a low S/N, which corresponds to the median of the first decile of the S/N ratio distribution (the worse 10% of the sample).

As mentioned in Section 2.2, the S/N ratio computed from the GIRAFFE pipeline products (as the ratio of the flux over its propagated error) is not accurate and likely underestimated. Indeed, if we inject in our {low-resolution, low sampling, ∞ S/N} Arcturus spectrum a Gaussian noise described by the variance ${\sigma_{\rm noise}}^2$, and if we compare this noisy spectrum to a GIRAFFE LMC spectrum with a S/N = ${\sigma_{\rm noise}}^{-1}$ (measured as described in Sec. 2.2), the quality of the GIRAFFE spectrum will appear better than the quality of the noisy Arcturus spectrum. In order to empirically find a correspondence between the measured S/N and the genuine S/N, we employed the automated tool DAOSPEC (Stetson & Pancino 2008), designed to measure equivalent width (EW): when it performs this task, the software splits the input spectrum S into a fitted continuum component C_f and a fitted line component L_f and returns a number $\sigma_{\rm residual}$ called "relative flux dispersion in residual spectrum", which is the dispersion (expressed in percentage) of $|S_i - (C_{f_i} + L_{f_i})|/C_{f_i}$ (where i is the pixel index). Therefore, $\sigma_{\rm residual}$ depends on the S/N ratio with an observed dependence as shown in Figure 6. The saturation of the residuals at high values of S/N ratio is probably due to the residual not being dominated by the noise anymore but by the mismatch (between the observed absorption lines and the fitted profiles). For each setup and S/N ratio regime (low, median or high) observed in our LMC spectra, we investigated various values of ${\sigma_{\rm noise}}^2$ until the $\sigma_{\rm residual}$ matched the targeted S/N ratio. Table 4 gives for each setup, the values of S/N ratio (measured and corrected values) corresponding to the qualifiers high, median, and low.

Thus we added a Gaussian noise (with zero-mean and variance ${\sigma_{\rm noise}}^2 = ({\rm S/N}^*)^{-2}$) in the three {low-resolution, low sampling, ∞ S/N} spectra according to S/N ratio values listed in Table 4. We drew 101 realisations for each high, median and low S/N ratio version of the Arcturus spectra. In the following, we will employ the single ∞ S/N, the 101 high S/N, the 101 median S/N, and the 101 low S/N spectra when we determine the stellar parameters (Sec. 3) and when we measure the chemical abundances (Sec. 4).

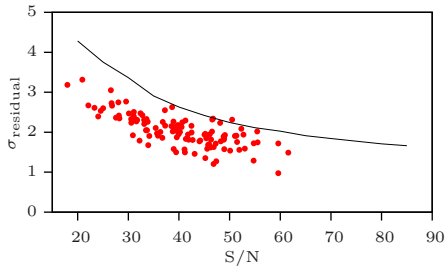

Fig. 6. $\sigma_{residual}$ vs. S/N. Black solid line: we measured $\sigma_{residual}$ of the Arcturus HR13 spectrum for different values of artificially added noise ${\sigma_{noise}}^2 = (S/N)^{-2}$. Red dots: LMC HR13 spectra. For Arcturus with artificial noise, $\sigma_{residual} \simeq 2$ when S/N $\simeq 55$ while for our LMC spectra, $\sigma_{residual} \simeq 2$ when S/N $\simeq 40$.

Table 4. Values of S/N ratio corresponding to the qualifiers high (best 10% of the sample), median and low (worse 10% of the sample). S/N is the S/N ratio measured with the pipeline products and S/N* is the empirically corrected S/N ratio.

Qualifier	HR11		HR13		HR14	
	S/N	S/N*	S/N	S/N*	S/N	S/N*
low	16	25	24	35	31	35
median	25	40	40	55	48	60
high	36	55	55	75	64	75

3. Stellar parameters

To derive the stellar parameters of our LMC stars (the temperature T_{phot}, the gravity $\log g$, the overall metallicity [M/H] and the microturbulent velocity ξ_{micro}), we used a combination of photometric and spectroscopic methods. We used our set of Arcturus spectra to assess our iterative procedure and estimate the errors on [M/H] and ξ_{micro}.

3.1. Photometric temperature T_{phot}

For our stars, visible (V and I magnitude, from the OGLE catalogue Udalski et al. 1997, 2000; Szymanski 2005) and infrared (J, H and K magnitude, from the 2MASS catalogue Skrutskie et al. 2006) photometry is available. Table 5 gives the V magnitude, the four colour indices we used and the CaT metallicity index for our LMC bar stars. We used the Ramírez & Meléndez (2005a,b) photometric calibrations for giants (the calibrations are functions of the colour index and the [Fe/H]; they are available for our photometric systems, so no conversion of magnitude from one photometric system to another is needed) to compute four scales of photometric temperatures, using the de-reddened $(V-I)_0$, $(V-J)_0$, $(V-H)_0$ and $(V-K)_0$ colour indices. Table 6 shows that the agreement between the four photometric temperature scales is very good with a mean difference always smaller than 100 K (in absolute value), therefore we simply averaged the four estimates to derive our final T_{phot}.

The photometric calibrations are subject to, at least, four sources of uncertainties: the dispersion σ_{calib} of the calibration relation itself, the uncertainty σ_{colour} of the two magnitudes combined to form the colour index, the uncertainty σ(E(B − V)) of the reddening E(B − V), and the uncertainty σ([Fe/H]) of the [Fe/H] ratio. The dispersion of the calibration relations can be taken from Ramírez & Meléndez (2005b) (their Table 3); they are smaller than 50 K and account for less than 20 K in the error on the final temperature (for the colour indices we used in this study). The errors on the magnitudes were taken from the OGLE and 2MASS catalogues. The typical error is of the order of 0.05 mag, and the error on the colour index translates in a typical error of $\sim$ 35 K on the final mean T_{phot}. We used the Ca II triplet (CaT) metallicity from Cole et al. (2005) as the initial estimator of the [Fe/H] ratio. Although the CaT metallicity is not a very precise estimator of [Fe/H] (mean error of $\sim$ 0.20 dex), the calibrations are not very sensitive to this parameter (typical error of < 5 K on the final mean T_{phot}). For the reddening, we used E(B − V) = 0.14 mag and a conservative relative error of 50 %, σ(E(B − V)) = 0.07 mag (see Sec. 3.5). It results in a typical error on the final mean T_{phot} of the order of 130 K. Among the four sources of uncertainty denoted above, the reddening is the least constrained quantity and accounts for most of the final error on the final mean temperature. After propagating all the errors, we end up with a typical error on the mean photometric temperature T_{phot} of about 150 K.

3.2. Surface gravity $\log g$

The surface gravities $\log g$ were derived using the Bayesian estimation algorithm of stellar parameters of da Silva et al. (2006), based on evolutionary tracks[3]. The required input parameters (and their associated errors) are: the effective temperature, [Fe/H], the dereddened V magnitude V_0, and the parallax π_{LMC}. We used the photometric temperature as the effective temperature, and the CaT metallicity index as an initial guess of [Fe/H]. The V magnitude was taken from the OGLE catalogue, and was dereddened using the reddening value defined above. The parallax of the LMC was set to $(20 \pm 1) \times 10^{-6}$ arcsec which corresponds to a distance modulus of (18.5 ± 0.1)mag (Alves 2004). The typical error returned by the method on $\log g$ is of the order of 0.16 dex.

3.3. Overall metallicity [M/H] and microturbulent velocity ξ_{micro}

The overall metallicity and the microturbulent velocity were derived simultaneously by requiring that different Fe I lines of different EW give the same iron abundance [Fe I/H]. We used the automated tool DAOSPEC (Stetson & Pancino 2008) to measure the EW and their associated error, and we used the grid of OSMARCS model atmospheres[4] (Gustafsson et al. 2008) together with the code of spectrum synthesis *turbospectrum* (*turbospectrum* is described in Alvarez & Plez 1998 and improved along the years by B. Plez) to convert the EW into abundances. Since our stars are giants, atmosphere models and radiative transfer were both in spherical geometry. We built the atmosphere model for a given set of stellar parameters by interpolation onto the OSMARCS grid with the interpolation routine written by Masseron (2006, PhD thesis).

The iterative procedure is as follows:

1. for a given set of stellar parameters $\{T_{phot}, \log g, \xi_{micro}, [M/H]\}$, abundances of around 45 Fe I lines are derived from their EW.
2. the mean [Fe I/H] is computed and compared to the input metallicity; if $|\langle[Fe\,I/H]\rangle - [M/H]| > 0.01$ dex, then the global metallicity is updated ($[M/H] \leftarrow \langle[Fe\,I/H]\rangle$) and we go back to step 1. If the convergence is not reached after 10

[3] web interface at `http://stev.oapd.inaf.it/cgi-bin/param`
[4] models available at `http://marcs.astro.uu.se/`

Table 5. Photometry and Cat metallicity of LMC bar stars. 2MASS identifiers, V, (V − I), (V − J), (V − H) and (V − K) (Udalski et al. 1997, 2000; Szymanski 2005) and $[Fe/H]_{CaT}$ (Cole et al. 2005). Errors are provided for each quantity.

2MASS ID	V	e(V)	V − I	e(V − I)	V − J	e(V − J)	V − H	e(V − H)	V − K	e(V − K)	$[Fe/H]_{CaT}$	$e([Fe/H]_{CaT})$
	mag	mag	mag	mag	mag	mag	mag	mag	mag	mag	dex	dex
05223082-6944147	17.228	0.031	1.554	0.038	2.702	0.053	3.519	0.053	3.663	0.052	-0.14	0.14
05223112-6945292	17.163	0.021	1.584	0.025	2.729	0.051	3.524	0.059	3.676	0.050	-0.41	0.14
05223186-6947159	17.450	0.030	1.385	0.037	2.349	0.064	3.129	0.066	3.323	0.085	-0.35	0.14
05223309-6946595	17.106	0.037	1.342	0.041	2.268	0.061	3.027	0.070	2.945	0.094	-0.40	0.14
...	...	...	...	...	...	...	...	...	...	...	...	...

Notes. Excerpt of the full table shown here for guidance regarding its form and content. Full table available online at CDS.

Table 6. Mean difference between the four photometric scales and standard deviation.

	$T((V_{Johnson} - J_{2MASS})_0)$ K	$T((V_{Johnson} - H_{2MASS})_0)$ K	$T((V_{Johnson} - K_{2MASS})_0)$ K
$T(V_{Johnson,0} - I_{Cousins,0})$	−40 ± 110	−95 ± 80	−90 ± 100
$T(V_{Johnson,0} - J_{2MASS,0})$	–	−50 ± 110	−50 ± 120
$T(V_{Johnson,0} - H_{2MASS,0})$	–	–	10 ± 100

iterations, we release the previous criterion and increase the threshold by 0.01 dex.

3. the linear regression of [Fe I/H] vs. EW′ is made, where EW′ is the reduced equivalent width ($\log EW/\lambda$). As said before, the errors on the EW are given by DAOSPEC and are turned into errors on [Fe I/H] abundances by *turbospectrum*. There is no analytical solution to the problem of linear regression with errors on both coordinates, and a few recipes exist to answer this question. Besides, in our cases, the errors of the EW (explanatory variable) and the abundances (dependent variable) are correlated because we used the former to derive the latter. In order to handle as properly as possible the errors on both coordinates, we used a linear regression algorithm based on bootstrapping, as it turns out that the low statistics (number of Fe I lines) dominate the uncertainty on the slope of the regression.

This procedure is repeated for each value of ξ_{micro} in the range $\{1.0, 1.1, ..., 2.5\}$ ($km\,s^{-1}$). We then selected the set of parameters which gives a minimum slope, smaller than its error (in absolute value). The estimate of the error on the metallicity [M/H] and the microturbulent velocity ξ_{micro} is not a straightforward task and a method is proposed in Section 3.4.

Table 7 gives the final stellar parameters for our LMC bar stars. For the stars 05223316-6951389, 05225632-6942269, 05225980-6954368, 05224240-6940567, 05232554-6943388, 05244301-6943412, 05253235-6943137, the procedure did not converge onto a satisfactory solution. Figure 7 (left panel) shows the location of the LMC bar stars in the Hertzsprung-Russel diagram.

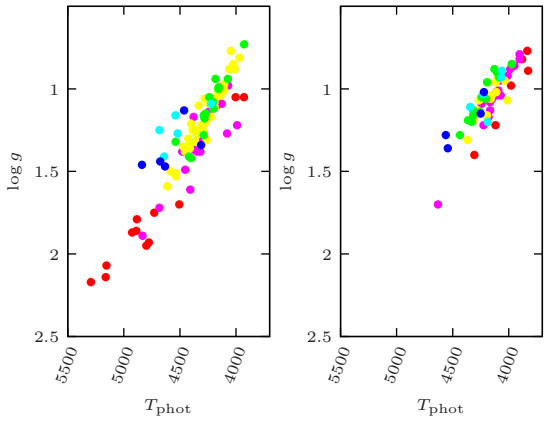

Fig. 7. Location of the LMC bar (left panel) and disc (right panel) stars in the Hertzsprung-Russel diagram. Legend: blue: −2 dex ≤ [Fe I/H] ≤ −1.3 dex, cyan: −1.3 dex ≤ [Fe I/H] ≤ −1 dex, green: −1 dex ≤ [Fe I/H] ≤ −0.8 dex, yellow: −0.8 dex ≤ [Fe I/H] ≤ −0.6 dex, magenta: −0.6 dex ≤ [Fe I/H] ≤ −0.4 dex, red: −0.4 dex ≤ [Fe I/H] ≤ 0 dex,

3.4. Arcturus

Our set of Arcturus spectra served to perform tests on our iterative procedure giving the overall metallicity [M/H] and the microturbulent velocity ξ_{micro}. To this end, we used the effective temperature and the gravity published by Ramírez & Allende Prieto (2011): T_{eff} = 4286 K (spectral energy distribution fitting) and $\log g$ = 1.66 (isochrone fitting) and kept them constant and we applied the iterative procedure described in Section 3.3 on the 101 realisations of high, median and low S/N version of the Arcturus spectra. Table 8 gives the mean [M/H], [Fe I/H], [Fe II/H] and ξ_{micro} and the standard deviation around the mean; results for the ∞ S/N are also given for reference. As could be anticipated, results differ according to the S/N, but the differences are mild: the lower the S/N ratio, the higher the metallicity (or [Fe I/H], or [Fe II/H]), the higher the difference Δ = [Fe I/H] - [Fe II/H], and the lower the microturbulent velocity. We can notice that the standard deviation around the mean value increases when the S/N ratio decreases, which is again an expected behaviour. Our procedure tends to lead to lower metallicities and higher microturbulent velocity than the reference values in the literature (in fact, in our procedure, the bias in [Fe I/H] varies linearly with the bias in ξ_{micro}), although this effect is paradoxically alleviated at the median and low S/N of our LMC sample: Worley et al. (2009) found [Fe I/H] = −0.6 dex and ξ_{micro} = 1.5 $km\,s^{-1}$; Ramírez & Allende Prieto (2011) found [Fe I/H] = −0.52 dex and ξ_{micro} = 1.74 $km\,s^{-1}$.

Table 7. Stellar parameters of LMC bar stars. 2MASS identifiers, $T_{\rm phot}$, $\log g$, [M/H], $\xi_{\rm micro}$, [Fe I/H], [Fe II/H]. Errors are given for each quantity.

2MASS ID	$T_{\rm phot}$ K	$\sigma(T_{\rm phot})$ K	$\log g$	$\sigma(\log g)$	[M/H] dex	σ([M/H]) dex	$\xi_{\rm micro}$ km s^{-1}	$\sigma(\xi_{\rm micro})$ dex	[Fe I/H] dex	σ([Fe I/H]) dex	[Fe II/H] dex	σ([Fe II/H])
05223082-6944147	4070	102	0.98	0.15	-0.49	0.10	1.80	0.15	-0.48	0.04	-0.49	0.15
05223112-6945292	4025	98	0.85	0.14	-0.71	0.10	1.80	0.15	-0.71	0.03	-0.65	0.11
05223186-6947159	4277	134	1.21	0.16	-0.70	0.10	1.90	0.15	-0.71	0.03	-0.78	0.13
05223309-6946595	4401	151	1.21	0.19	-0.68	0.10	2.00	0.15	-0.68	0.03	-0.90	0.10
...	...	...	...	...	...	...	...	...	...	...	...	...

Notes. Excerpt of the full table shown here for guidance regarding its form and content. Full table available online at CDS.

Table 8. Mean and standard deviation of the distribution of [M/H], [Fe I/H], [Fe II/H] and $\xi_{\rm micro}$ for the 101 realisations of high, median and low S/N version of the Arcturus spectra. The bottom line give the results for the ∞ S/N spectrum.

S/N	⟨[M/H]⟩ dex	⟨[FeI/H]⟩ dex	⟨[FeII/H]⟩ dex	$\langle\xi_{\rm micro}\rangle$ km s^{-1}
low	-0.58 ± 0.11	-0.58 ± 0.11	-0.49 ± 0.11	1.82 ± 0.15
median	-0.65 ± 0.06	-0.65 ± 0.06	-0.59 ± 0.07	1.83 ± 0.09
high	-0.69 ± 0.05	-0.69 ± 0.05	-0.63 ± 0.05	1.87 ± 0.07
∞	-0.71	-0.72	-0.70	1.9

Standard deviations reported in Table 8 can also be used as an estimator of the (random) error on the determined metallicity and microturbulent velocity in the LMC sample, due to the (random) error on the EW measurements (itself originating in the noise present in the stellar spectra). In the following, we will keep the conservative estimates: σ([M/H]) = 0.1 dex and $\sigma(\xi_{\rm micro}) = 0.15$ km s^{-1}.

3.5. Choice of the reddening

The mapping of the reddening in the LMC has been a longstanding issue, and depending on the targeted stars and the technique used, different reddenings are derived. Zaritsky et al. (2004) published a reddening map of the LMC based on a colour decomposition. We estimated the reddening for our LMC bar field from their catalogue[5]. As all of our stars were not studied by Zaritsky et al. (2004) and as individual reddening values are reported to be too uncertain, we extracted all of the Zaritsky et al. (2004) stars located in our field of view, and computed a median value of the extinction A_V: $A_V = 0.44$ mag, hence a median reddening E(B − V) = $A_V/3.24 \approx 0.14$ mag (4287 extracted stars). This value of reddening is similar to what was found by Udalski et al. (1999) from Red Clump (RC) stars (comparison of the observed and the theoretical RC colour): E(B − V) $\simeq$ 0.13 mag in the bar region. Haschke et al. (2012b) have derived optical reddening maps using two different techniques: RC stars and RR Lyrae (comparison of the apparent and the absolute colour, the latter being computed with the period and the metallicity). They found similar results with the two techniques and their reddening map gives E(B−V) $\simeq$ 0.06 mag and σ (E(B − V)) = 0.05 mag for our bar field. They found good agreement with other works from Subramaniam (2005, RC stars) and Pejcha & Stanek (2009, RR Lyrae). Based on these variations for the reddening in our region, we decided to use a conservative error of 50 %, σ (E(B − V)) = 0.07 mag to propagate the errors on our stellar parameters (see Sec. 3), which covers all the range of possible reddenings in this field.

To investigate further the most probable reddening for our field, we tested the two following hypothesis of reddening: E(B − V) = 0.06 mag and E(B − V) = 0.14 mag. The choice of the reddening has a strong effect on the photometric temperature scale and somewhat more moderate on the microturbulent velocity (comparable to the typical error on the parameter) and a small effect on the gravity and overall metallicity (lower than the typical error): $\langle T_{\rm phot}[E(B-V) = 0.14] - T_{\rm phot}[E(B-V) = 0.06]\rangle$ = 140 K, with a r.m.s of 40 K; $\langle \log g[E(B-V) = 0.14] - \log g[E(B-V) = 0.06]\rangle$ = 0.03, with a r.m.s of 0.07; ⟨[M/H][E(B − V) = 0.14] − [M/H][E(B − V) = 0.06]⟩ = −0.02 dex, with a r.m.s of 0.12 dex; $\langle \xi_{\rm micro}[E(B-V) = 0.14] - \xi_{\rm micro}[E(B-V) = 0.06]\rangle = 0.17$ km s^{-1}, with a r.m.s of 0.13 km s^{-1}. Figure 8 shows the results of the determination of the stellar parameters for the LMC bar stars (first row: E(B − V) = 0.06 mag; second row: E(B − V) = 0.14 mag) and for the median S/N Arcturus spectra (third row). The choice of reddening has a small effect on the distribution of the slopes ([Fe I/H] | log(EW/λ)) (first column): for E(B − V) = 0.06 mag and 0.14 mag respectively, the medians are −0.008 dex and −0.017 dex, the semi-interquartile ranges are 0.037 dex and 0.030 dex respectively. We note however that the distribution is narrower when the reddening is higher. Similarly, the effect on the distribution of the slopes ([Fe I/H] | $\chi_{\rm ex}$) (excitation equilibrium, second column) is also small: the medians are similar in both cases and close to zero ($\simeq -0.023$ dex eV^{-1}), but the distribution is narrower when the reddening is higher: the semi-interquartile ranges are 0.023 dex eV^{-1} and 0.020 dex eV^{-1} for E(B − V) = 0.06 mag and 0.14 mag respectively. Whatever the assumed reddening, we see that our photometric scales do not break dramatically the excitation equilibrium and that the highest reddening seems to improve slightly the general trend. The largest effect is observed for the ionisation equilibrium: changing the reddening will shift the distribution of the difference Δ(Fe) = [Fe I/H] − [Fe II/H] (ionisation equilibrium, third column). Indeed, the medians are −0.12 dex (over-ionisation) and 0.06 dex (under-ionisation) for E(B − V) = 0.06 mag and 0.14 mag respectively, with similar semi-interquartile ranges of 0.12 dex and 0.11 dex respectively. The last column of Figure 8 shows that the reddening (thus the temperature) has a small effect on the distribution of the standard deviations of Fe I abundances (though the situation improves slightly for E(B − V) = 0.14 mag: smaller median, distribution queue less populated): therefore, the change of reddening has negligible effect on the agreement of Fe I lines (when the pipeline has converged). As the high reddening tends to slightly improve the determination of parameters (distribution of slopes are narrower, the departure

[5] online LMC reddening estimator at `http://ngala.as.arizona.edu/dennis/lmcext.html`

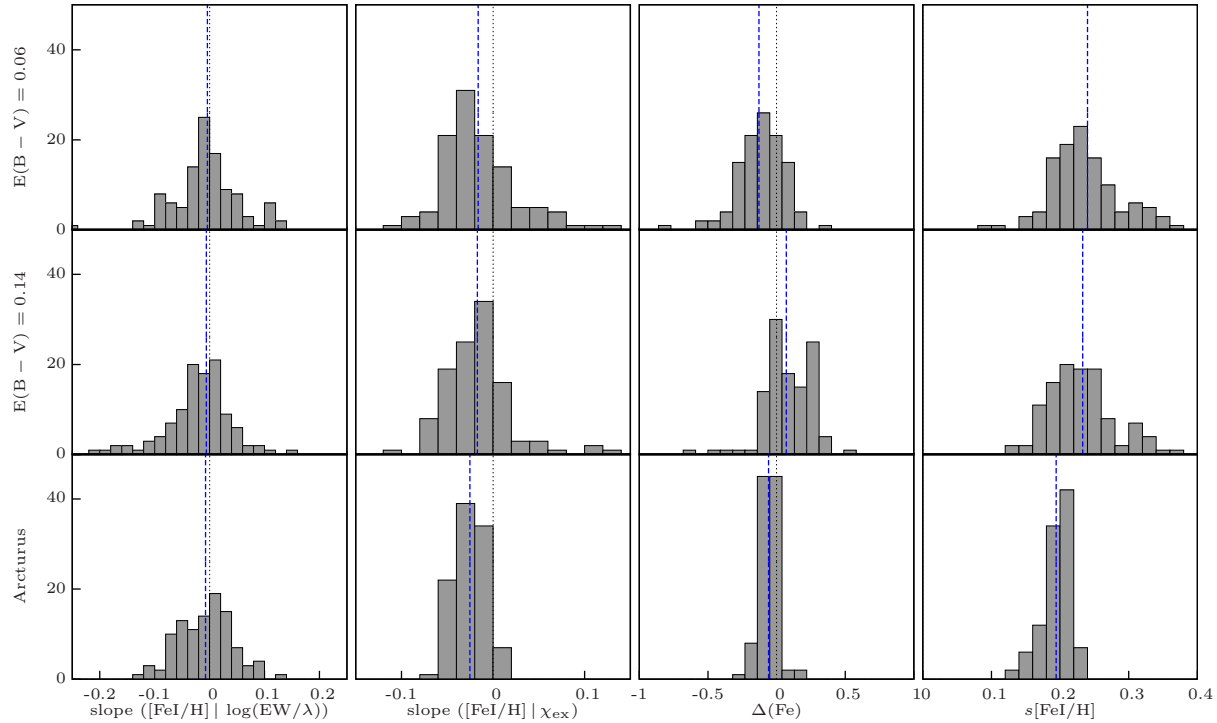

Fig. 8. First and second row: distribution of a given quantity for our LMC stars assuming E(B − V) = 0.06 mag and E(B − V) = 0.14 mag respectively. Third row: distribution of a given quantity for the 101 median S/N Arcturus spectra. First column: distributions of the slopes ([Fe I/H] | log(EW/λ)) (spectroscopic criterion used to derive $\xi_{\rm micro}$). Second column: distributions of the slopes ([Fe I/H] | $\chi_{\rm ex}$) (excitation equilibrium). Third column: distribution of the difference Δ(Fe) = [Fe I/H] − [Fe II/H] (ionisation equilibrium). Fourth column: distribution of the sample standard deviation of [Fe I/H].

from the ionisation equilibrium is reduced), we decided to use this hypothesis.

We checked that results obtained for the 101 median S/N Arcturus spectra share the same properties: the distribution of the slopes ([Fe I/H] | log(EW/λ)) is centred around zero; the excitation equilibrium is not exactly fulfilled (the median of the distribution is -0.024 dex eV^{-1}, similar to the median of our LMC sample), and we found a small over-ionisation (the median of Δ(Fe) is -0.05 dex).

3.6. Re-analysis of Pompéia et al. (2008) sample

In the following, we will compare our results for the LMC bar to the results for the LMC inner disc published by Pompéia et al. (2008). In order to remove systematic effects due to differences in the analysis procedures, we re-analysed the 59 stars of the inner disc field and derived a new set of stellar parameters, assuming a reddening E(B − V) = 0.12 mag (computed from Zaritsky et al. (2004) catalogue as for the bar). We found a good agreement, within the error bars, between our newly derived stellar parameters and those of Pompéia et al. (2008): $\langle T_{\rm spec,Pompeia} - T_{\rm phot}\rangle = -25$ K (r.m.s = 65 K); $\langle \log g_{\rm spec,Pompeia} - \log g\rangle = -0.13$ (r.m.s = 0.14); $\langle$[Fe I/H]$_{\rm Pompeia}$ − [Fe I/H]$\rangle = -0.06$ dex (r.m.s = 0.15 dex); $\langle$[Fe II/H]$_{\rm Pompeia}$ − [Fe II/H]$\rangle = -0.11$ dex (r.m.s = 0.17 dex); $\langle \xi_{\rm micro,Pompeia} - \xi_{\rm micro}\rangle = 0.05$ km s^{-1} (r.m.s = 0.22 km s^{-1}). It is remarkable to find such a good agreement between physical quantities (temperature, gravity) derived by different methods (photometry/spectroscopy, isochrone/spectroscopy respectively).

Table 9 gives the final stellar parameters for the LMC disc stars. Compared to Pompéia et al. (2008), our procedure did not converge onto a satisfactory solution for the star 0758. Figure 7 (right panel) shows the location of the LMC disc stars in the Hertzsprung-Russel diagram. In Section 4.4, we will use our new set of stellar parameters to re-derive the abundances for the inner disc stars.

3.7. [Fe/H]$_{\rm CaT}$ *vs.* [Fe/H]$_{\rm spectro}$

Figure 9 compares for both bar and inner disc fields the [Fe I/H] ratio derived from high-resolution spectroscopy to the metallicity derived from the infrared Ca II triplet (CaT) index. The typical error bar on [Fe/H]$_{\rm CaT}$ is 0.1-0.2 dex (Cole et al. 2005), and the typical error bar on [Fe/H]$_{\rm spectro}$ is 0.11 dex (quadratic sum of the typical random and systematic errors on the mean Fe abundance). We see a rather good agreement, within the errors, between the two indices up to [Fe/H]$_{\rm CaT} \approx -0.5$ dex; then, for higher [Fe/H]$_{\rm CaT}$, we have [Fe/H]$_{\rm CaT} \geq$ [Fe/H]$_{\rm spectro}$. A possible explanation is that for metal-rich stars the continuum placement in the CaT region becomes difficult and leads to poor abundance determinations. A possible contribution to the discrepancy could also be due to the presence of stars in the 0.8-1.2 Gyr age range in the field samples, where the Red Clump magnitude is changing very quickly and few calibrators of the CaT method are available. Based on the trends in the Padova stellar isochrones and with reference to the empirical data in Cole et al. (2004) there might be a bias of order 0.1 dex in the CaT abundances for stars aged $\sim$ 1 Gyr. Good agreement between CaT metallicities (Grocholski et al. 2006; Olszewski et al. 1991, *e.g.*,) and spectroscopic abundances (Mucciarelli et al. 2008, *e.g.*,) has been seen for LMC GC with [Fe/H] = -0.4 ± 0.1 and ages around $\sim$2 Gyr.

Table 9. Stellar parameters of LMC disc stars. Star identifiers, $T_{\rm phot}$, $\log g$, [M/H], $\xi_{\rm micro}$, [Fe I/H], [Fe II/H]. Errors are given for each quantity.

2MASS ID	$T_{\rm phot}$	$\sigma(T_{\rm phot})$	$\log g$	$\sigma(\log g)$	[M/H]	σ([M/H])	$\xi_{\rm micro}$	$\sigma(\xi_{\rm micro})$	[Fe I/H]	σ([Fe I/H])	[Fe II/H]	σ([Fe II/H])
	K	K			dex	dex	km s^{-1}	dex	dex	dex	dex	
0499	4264	117	1.07	0.15	-0.69	0.10	1.90	0.15	-0.71	0.03	-0.78	0.07
0512	4128	99	0.88	0.13	-0.91	0.10	1.80	0.15	-0.91	0.03	-0.78	0.04
0522	4101	97	0.91	0.15	-0.66	0.10	1.90	0.15	-0.67	0.03	-0.73	0.09
0533	4188	107	0.96	0.15	-0.78	0.10	2.10	0.15	-0.77	0.04	-0.81	0.09
...	...	...	...	...	...	...	...	...	...	...	...	...

Notes. Excerpt of the full table shown here for guidance regarding its form and content. Full table available online at CDS.

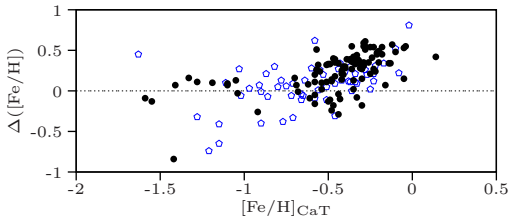

Fig. 9. Comparison of $[Fe/H]_{CaT}$ and $[Fe/H]_{spectro}$. $\Delta([Fe/H]) = [Fe/H]_{CaT} - [Fe/H]_{spectro}$ vs. $[Fe/H]_{CaT}$. Legend: black filled circles: LMC bar; blue open pentagons: LMC disc.

Very few to no LMC GC with abundances [Fe/H] > −0.3 are known, so we have no direct tests of the correspondence between the two methods for LMC stars. For the remainder of this paper we take the spectroscopic [Fe I/H] to be the true metallicity.

In the metal-poor range, one LMC bar star (05232680-6953109) and four LMC disc stars (0606, 0633, 0699, 1105) have very discrepant $[Fe/H]_{CaT}$ and $[Fe/H]_{spectro}$ ($|\Delta| \geq 0.4$ dex). Except for the disc star 0606, we could not find any anomaly in the stellar parameters determination or the abundance measurements. The star 0606 with [Fe/H] = −2.07 dex has normal α-ratios ([Ca/Fe] = 0.39 dex) but overabundant *s*- and *r*-ratios ([Ba/Fe] = 0.57 dex, [La/Fe] = 0.51 dex). This is in agreement with Pompéia et al. (2008) who found [Fe/H] = −1.74 dex, [Ca/Fe] = 0.13 dex (our LMC disc Ca ratios are 0.1 dex higher in the mean, see Sec. 4), [Ba/Fe] = 0.80 dex, [La/Fe] = 0.30 dex. The high fraction of *s*-process in this star could be the sign that it is part of a binary system (the *s*-process elements would have been transfer from a former AGB companion).

4. Abundance analysis

4.1. Abundance measurements

Methods We used both equivalent widths and fitting of absorption profiles to measure elemental abundances. As mentioned in Section 3.3, we used DAOSPEC to measure the EW. We converted EW into abundances, and computed spectrum syntheses with *turbospectrum* (in spherical geometry, with LTE spherical radiative transfer) together with the grid of OSMARCS spherical model atmospheres.

The fitting of absorption profile consists in computing a grid of theoretical spectra by varying the abundance of an element and comparing them to an observed absorption line of this specific element and search for the best fit, which gives us the abundance. We set up the following procedure:

1. for a given absorption line $\mathcal{L}$ of an element X, with a central wavelength λ_0, we define a small wavelength interval I in which the profile fitting is performed. The definition of the interval resulted from the compromise between three contradictory requirements: covering as many pixels as possible, avoiding neighbouring lines and including continuum on both sides of the line. The typical width of the wavelength interval considered ranged from 3 to 5 Å.
2. we compute a grid of theoretical spectra by varying the abundance ratio [X/Fe][6] with *turbospectrum*, from −1 dex up to 1 dex, by increments of 0.1 dex. We compute the spectra over a wavelength range centred on λ_0 and convolve them by a Gaussian profile to take into account the combined effects of rotation, macroturbulence and instrumental response.
3. we normalise the theoretical spectra and the observed spectrum in the same way and then compute the quantity:

$$T^2([X/Fe]) = \frac{1}{\sum_{i=1}^{n} \hat{\mathcal{S}}_i} \sum_{i=1}^{n} \hat{\mathcal{S}}_i (\mathcal{S}([X/Fe])_i - O_i)^2$$

where i is the pixel index, n is the number of pixel in the interval I, $\hat{\mathcal{S}}$ is the (normalised) theoretical spectrum *without* the element X, $\mathcal{S}([X/Fe])$ is the (normalised) theoretical spectrum for a given value of [X/Fe], and O is the (normalised) observed spectrum. $\hat{\mathcal{S}}$ allows to weight each pixel by its contamination: if the flux at pixel i is only due to the absorption by the element X, then $\hat{\mathcal{S}}_i = 1$; if the flux at pixel i is the result of the absorption by the element X and by one or more other chemical entities, then $\hat{\mathcal{S}}_i < 1$. Therefore, the more contaminated, the less it counts in $T^2([X/Fe])$.
4. T^2 is (generally) a convex function of [X/Fe], the position of the minimum $T^2_{\rm nominal} = T^2([X/Fe]_{\rm nominal})$ gives us the best-fit abundance $[X/Fe]_{\rm nominal}$. $T^2([X/Fe])$ is not a genuine χ^2 since we do not divide the quadratic difference $(\mathcal{S}([X/Fe])_i - O_i)^2$ by the error at pixel i (the errors returned by the pipeline do not take into account the correlation) but we can still use it to find the best fit.
5. the last step aims at accepting or rejecting the solution. Once again, as $T^2([X/Fe])$ is not a genuine χ^2, we cannot apply usual statistics theorems, and for instance, we cannot check the goodness of fit. Therefore, to decide whether the solution has to be rejected, we checked the shape of the T^2 curve thanks to simple geometrical criteria. Indeed, the shape of the T^2 curve is not accidental and reveals the curve of growth of the measured line. For instance, a saturated line is likely to produce a very open curve; a weak line is likely to produce a curve with a well defined minimum, but with a left branch that becomes flat for the smallest abundance ; the match between the synthesis and the observed spectrum will influence the value of $T^2_{\rm nominal}$. So it is easier to work with the

[6] [X/Fe] = [X/H] − [Fe/H]

normalised T^2 given by

$$\hat{T}^2([\mathrm{X/Fe}]) = \frac{T^2([\mathrm{X/Fe}]) - T^2_{\mathrm{nominal}}}{T^2_{\mathrm{nominal}}}$$

Non-detection: as we cover a broad abundance range ([X/Fe] varies from −1 to 1 dex), we expect (in general) a strong variation of T^2 over this interval. A flat T^2 curve (or at least, if the curve has a completely flat left branch) is the symptom of a non-detection of the line. If the line is very weak, then the profile of the absorption line will slightly change from one abundance point of the grid to the next, at least as long as [X/Fe] is small (say $\lessapprox -0.3$ dex). Therefore, $(\mathcal{S}([\mathrm{X/Fe}])_i - O_i)^2 \approx$ cst, thus $T^2([\mathrm{X/Fe}]) \approx$ cst. For larger abundances, the line appears in the synthesis and T^2 (or $\hat{T}^2$) steeply increases. We can detect a flat left (right) branch with this criterion: $\hat{T}^2(-1.0) < \epsilon_1$ ($\hat{T}^2(+1.0) < \epsilon_1$, respectively). We empirically fixed ϵ_1 to 4.0. In other words, we require T^2 to be five times as high as T^2_{nominal} at the grid border for the solution to be meaningful. It may happen that the nominal abundance is close to the grid edge; thus the left (right) branch will not be complete and the solution will be mistakenly rejected. So, in that case, we checked the local symmetry of the $\hat{T}^2$ curve around the nominal abundance. If the curve is non-symmetric, the solution is rejected. In the mean, the rejection rate is of about ten lines/star; the rejection is minimum for stars with a metallicity between −1 and −0.5 dex and tends to be higher for metallicities lower than −1 dex or larger than −0.5 dex.

We used the EW or the fitting of absorption profile depending on the line: if the number of lines was high (≥ 5), we privileged the EW; if only few lines were available or if a blend was present or if the element has a hyperfine structure (hfs), we privileged the fitting of absorption profile.

List of elements In our broad wavelength coverage, we are in position to measure elemental abundances for 17 elements (the method used, equivalent width (EW) or spectrum synthesis (SS), and the number of available lines are given in parenthesis): O I (SS, 1), Mg I (SS, 3), Si I (EW, 3), Ca I (EW, 13), Ti I (EW, 8), Ti II (EW, 3), Na I (SS, 4), Sc II (SS, 6), V I (SS, 12), Cr I (SS, 4), Co I (SS, 3), Ni I (EW, 7), Cu I (SS, 1), Y I (SS, 1), Zr I (SS, 4), Ba II (SS, 2), La II (SS, 3), Eu II (SS, 2). We compiled the atomic line lists from the line database VALD[7] (Kupka et al. 1999, 2000); for the measured lines, we used the $\log gf$ quoted in Pompéia et al. (2008). We took into account the hyperfine structure (hfs) for Sc II (Wiese et al. 1966: 5640 Å, 5667 Å, 5669 Å, 6245 Å; Martin et al. 1988: 5657 Å, 6604 Å), V I (Martin et al. 1988: 6119 Å, 6135 Å, 6150 Å, 6199 Å, 6224 Å, 6274 Å, 6285 Å, 6292 Å, 6357 Å, 6452 Å, 6531 Å; Kurucz 1988: 6224 Å), Co I (Fuhr et al. 1988: 5647.240 Å, 6117.000 Å, 6282.600 Å), Cu I (Bielski 1975: 5782.127 Å), Ba II (Rutten 1978: 6496.912 Å; no hfs data for 6141.713 Å), La II (Lawler et al. 2001a: 6262.287 Å, 6390.477 Å; no hfs data for 6320.430 Å), and Eu II (Lawler et al. 2001b: 6437.640 Å, 6645.064 Å). We extracted the hfs data from the Kurucz database[8] (Kurucz 1995) for Sc, V, Co, and Cu; we computed the hyperfine splitting for Ba, La and Eu using the published hyperfine constants. As our stars are cold ($T_{\mathrm{phot}} \sim 4500$ K), molecules form in the stellar atmospheres and form absorption lines in the stellar spectra: we included the molecular line lists of $^{12}C^{14}N$, $^{13}C^{14}N$ (Plez, private communication) and TiO (Plez 1998) in the spectrum synthesis. We consider the solar composition from Grevesse & Sauval (1998). For all our LMC stars, we fixed the carbon and nitrogen abundances: [C/Fe] = −0.65 dex and [N/Fe] = 0.3 dex (values derived from Smith et al. 2002).

Calibration of the line lists When a line of interest is blended by another chemical specie (atom or molecule), the abundance measurement becomes more difficult. Especially, if the absorption profile of the contaminant is poorly predicted (lack of accurate experimental quantum data or reliable theoretical predictions), as it is the case for the CN lines. We therefore calibrated a number of CN lines contaminating crucial lines of Eu, La, Y, Ba, and Zr using Arcturus.

4.2. Arcturus

In the following, we will derive the abundances for Arcturus so that it will provide the zero-point of our abundance scale. In order to have a unique Arcturus atmosphere model for any S/N hypothesis, we chose as stellar parameters $T_{\mathrm{eff}} = 4286$ K, $\log g = 1.66$, [M/H] = −0.65 dex and $\xi_{\mathrm{micro}} = 1.8\,\mathrm{km\,s^{-1}}$: the former two are from Ramírez & Allende Prieto (2011) while we determined the latter two in Section 3.4 (median S/N ratio hypothesis).

We followed the same procedure described above to derive the abundances for our Arcturus spectra. For the high (respectively median and low) S/N hypothesis, we computed a mean abundance and dispersion (over the 101 realisations) for each individual line of a given element, and then we computed the final mean abundance ratio (over the N_{lines}) following the procedure described in Section 4.3. The error on the individual line abundance (dispersion over the 101 realisations) was propagated when we computed the final mean abundance. We did the same for the ∞ S/N hypothesis (except for the averaging over the realisations); as we have only one realisation for this S/N hypothesis, we used the standard error of the mean as an error estimator (hence the lack of error bar when only one line was used). Table 10 gives the results for the ∞, high, median and low S/N version of the Arcturus spectra as well as the abundance ratios (and their errors) published by Ramírez & Allende Prieto (2011) and Worley et al. (2009).

Chemical differences appeared for two elements: calcium and vanadium. When we first computed [Ca/Fe], we obtained ≈ -0.12 dex which is not the expected ratio for a disc star and is very different from the Ramírez & Allende Prieto (2011) and Worley et al. (2009) ratios. The $\log gf$ we used had been taken from the NIST[9] database and used in Pompéia et al. (2008). We tested two other sets of $\log gf$: the Kurucz $\log gf$ gave also ≈ -0.12 dex (the Kurucz and the NIST $\log gf$ of our Ca I lines are almost equal); the VALD $\log gf$ gave ≈ 0.05 dex, which is closer to the quoted [Ca/Fe]. We decided to keep the VALD $\log gf$ (Drozdowski et al. 1988; Smith & Raggett 1981; Smith 1981, 1988) in order to alleviate the disagreement. Vanadium has an hyperfine structure: when we take into account the hfs, [V/Fe] ≈ 0.01 dex, while without the hfs, [V/Fe] ≈ 0.23 dex. The latter value is closer to the value that Ramírez & Allende Prieto (2011) seemingly derived without taking into account the hyperfine splitting for V (we have five V I lines in common). So

[7] http://www.astro.uu.se/~vald/php/vald.php

[8] http://kurucz.harvard.edu

[9] http://physics.nist.gov/PhysRefData/ASD/index.html

Table 10. Elemental abundances and errors for our ∞, high, median and low S/N version of the Arcturus spectra as well as abundance ratios (and their errors) published by Ramírez & Allende Prieto (2011) and Worley et al. (2009). The number of lines used and the method to derive the abundances are recalled.

[X/Fe]	∞ S/N	high S/N	median S/N	low S/N	#	Method	Ramirez et al.	Worley et al.
	dex	dex	dex	dex			dex	dex
O I	0.46	0.47 ± 0.03	0.44 ± 0.04	0.41 ± 0.06	1	SS	0.50 ± 0.03	0.57 ± 0.02
Mg I	0.34 ± 0.06	0.33 ± 0.03	0.33 ± 0.04	0.30 ± 0.07	3	SS	0.37 ± 0.03	0.34 ± 0.15
Si I	0.32 ± 0.04	0.33 ± 0.05	0.33 ± 0.06	0.33 ± 0.11	2	EW	0.33 ± 0.04	0.24 ± 0.14
Ca I	0.04 ± 0.04	0.06 ± 0.02	0.05 ± 0.02	0.03 ± 0.04	10	EW	0.11 ± 0.04	0.19 ± 0.06
Ti I	0.36 ± 0.07	0.38 ± 0.02	0.36 ± 0.03	0.34 ± 0.04	8	EW	0.27 ± 0.05	0.35 ± 0.12
Ti II	0.32 ± 0.07	0.33 ± 0.04	0.31 ± 0.04	0.32 ± 0.08	3	EW	0.21 ± 0.04	0.33 ± 0.10
Na I	0.11 ± 0.04	0.11 ± 0.03	0.09 ± 0.04	0.06 ± 0.07	3	SS	0.11 ± 0.03	0.15 ± 0.04
Sc II	0.29 ± 0.02	0.29 ± 0.03	0.27 ± 0.04	0.25 ± 0.07	4	SS	0.23 ± 0.04	0.24 ± 0.01
V I	0.03 ± 0.02	0.03 ± 0.02	0.01 ± 0.02	−0.03 ± 0.03	7	SS	0.20 ± 0.05	-
Cr I	−0.05 ± 0.06	−0.05 ± 0.04	−0.07 ± 0.05	−0.09 ± 0.08	3	SS	−0.05 ± 0.04	-
Co I	0.21 ± 0.11	0.20 ± 0.03	0.19 ± 0.04	0.15 ± 0.07	2	SS	0.09 ± 0.04	-
Ni I	0.08 ± 0.04	0.10 ± 0.03	0.08 ± 0.03	0.07 ± 0.05	6	EW	0.06 ± 0.03	-
Cu I	−0.02	−0.03 ± 0.06	−0.03 ± 0.08	−0.05 ± 0.15	1	SS	-	-
Y I	0.02	0.01 ± 0.07	−0.01 ± 0.08	−0.02 ± 0.13	1	SS	-	0.07 ± 0.24
Zr I	−0.06 ± 0.03	−0.07 ± 0.03	−0.09 ± 0.04	−0.13 ± 0.05	3	SS	-	0.01 ± 0.07
Ba II	−0.18 ± 0.03	−0.16 ± 0.06	−0.18 ± 0.07	−0.22 ± 0.11	2	SS	-	−0.19 ± 0.08
La II	−0.03 ± 0.05	−0.02 ± 0.04	−0.04 ± 0.06	−0.06 ± 0.09	3	SS	-	0.04 ± 0.08
Eu II	0.41 ± 0.02	0.42 ± 0.07	0.40 ± 0.07	0.38 ± 0.18	2	SS	-	0.36 ± 0.04

the hfs seems to explain the disagreement. In the following, we will derive the V ratios *with* the hfs.

Except for V, our derived elemental ratios are in good agreement within the errors with Ramírez & Allende Prieto (2011) or Worley et al. (2009) and are perfectly understandable if we consider all the possible differences between our study and theirs (stellar parameters, atomic data, method to derive the abundances). We refer the reader to Lebzelter et al. (2012) who offer a broad analysis of the effects of models, input data and procedures on the derived stellar parameters and chemical composition; for instance, differences of up to ∼ 0.3 dex are observed for [Ca/Fe] between the different works.

In our determinations, we note that, in general, when S/N decreases, [X/Fe] slightly decreases ($\lessapprox$ 0.05 dex) and the error increases. This general good agreement between our results for Arcturus and the literature makes us confident of the detailed chemical analysis of our LMC sample. There is no strong bias and we are able to compare directly the abundance trends of the LMC to those of the MW, at all S/N ratio of our sample.

4.3. Final elemental abundances

Computation of the mean abundance As shown in the previous section, for a number of elements, two lines or more are available in the full spectral coverage, and we measured all of them whenever possible.

To combine the abundances from multiple lines, we distinguished three different cases to compute the quantity ⟨[X/Fe]⟩. If $N_{\rm lines} = 1$, then the final elemental abundance is simply equal to the single measurement. If $2 \leq N_{\rm lines} < 5$, then we computed the simple mean of the $N_{\rm lines}$ measurements. If $N_{\rm lines} \geq 5$, then we applied a 3σ-clipping to remove discrepant measurement, and computed the simple mean of the remaining measurements. The complete abundance table for our LMC bar stars is available online at CDS and provides the reader with all abundance ratios and their corresponding random and systematic errors.

Cleaning of the line lists We tried to identify the lines which systematically led to a discrepant measurement of the corresponding abundance by analysing the mean behaviour (computed over all sample stars) of each absorption line of an element X with respect to the mean abundance (computed over the lines, for a given star). For a given star, we computed the mean abundance $\langle[{\rm X/Fe}]\rangle_{\rm lines}$; to compare the $N_{\rm lines}$ together, we computed the quantity $[{\rm X}_i/\langle{\rm X}\rangle_{\rm lines}] = [{\rm X/Fe}]_i - \langle[{\rm X/Fe}]\rangle_{\rm lines}$. The mean behaviour of a given line is then given by the mean (and standard deviation) of $[{\rm X}_i/\langle{\rm X}\rangle_{\rm lines}]$ over the stars $\langle[{\rm X}_i/\langle{\rm X}\rangle_{\rm lines}]\rangle_{\rm stars}$. Of course, this was possible only when $N_{\rm lines} \geq 2$. This sanity check was not only useful to identify systematically discrepant lines but above all, it was useful to handle the cases where we do not have enough measurements to apply a 3σ-clipping cleaning: if $N_{\rm lines} = 2$, we could simply check whether the two lines were in agreement; if $N_{\rm lines} \geq 3$, it was also possible to identify systematically discrepant lines. We labeled a line suspicious when it showed a significant departure from the mean ($|\langle[{\rm X}_i/\langle{\rm X}\rangle_{\rm lines}]\rangle_{\rm stars}| \gtrapprox 0.3$ dex) and/or a high standard deviation ($\gtrapprox 0.3$ dex).

We applied the same kind of analysis on the abundance ratios we derived for the simulated Arcturus spectra; as the literature provides us with accurate abundance measurements, it helps to identify discrepant lines and to quantify biases by confronting each single measurement to the published mean values. In the end, we discarded a few lines for Ca I (5601 Å, 6162 Å, 6572 Å), Cr I (6362 Å), Na I (5682 Å), Ni I (6314 Å), Sc II (5669 Å, 6245 Å), Si I (5665 Å), V I (6119 Å, 6150 Å, 6199 Å, 6357 Å, 6452 Å) and Zr I (6140 Å) and updated the computation of the mean abundances accordingly. We decided to keep in our abundance analysis the Ba line at 6141.713 Å (resp. the La line at 6320.430 Å) for which no hfs data is available since we noted a good agreement with the other Ba (resp. La) line, with a difference of 0.2 dex for Ba (resp. 0.1 dex for La) in the mean (over the whole sample) between the line with and without hfs. Table 11 gives the final line list.

Table 11. Line list. For each line, the wavelength λ (column 4), excitation potential $\chi_{\rm exc}$ (column 5), oscillator strength $\log gf$ (column 6) and literature reference (column 9) are given. The abundance measurement method is recalled (column 7). If a line has hyperfine structure, the label *equivalent* appear across the column 2 and 3: we provide first the wavelength and oscillator strength of the equivalent line, and below the detailed hyperfine structure for the different isotopes (isotope in column 2, isotopic fraction f in column 6, isotope-scaled $\log gf$ in column 6). The column before the last indicates lines identical to Pompéia et al. (2008).

Element	Isotope	f	λ Å	$\chi_{\rm exc}$ eV	$\log gf$	Method		Source
$_{8}$O I			6300.304	0.000	-9.819	SS		VALD
$_{12}$Mg I			5711.088	4.346	-1.833	SS		VALD
$_{12}$Mg I			6318.717	5.108	-1.730	SS		VALD
$_{12}$Mg I			6319.237	5.108	-1.950	SS		VALD
$_{14}$Si I			5690.425	4.930	-1.870	EW	x	Smith et al. (2000)
...	...	...	...	...	...	...	...	...

Notes. Excerpt of the full table shown here for guidance regarding its form and content. Full table available online at CDS.

4.4. Re-analysis of Pompéia et al. (2008) sample

To derive the abundances for the LMC disc stars, we used the same EW and the same reduced spectra that were used by Pompéia et al. (2008). The differences between their work and ours lie in the stellar parameters and the methods to derive and compute the final abundances. Table 12 gives a comparison of our new abundances for the LMC disc stars and those published in Pompéia et al. (2008). For most of the elements, the agreement between our abundance ratios and those from Pompéia et al. (2008) is good, with a mean difference less than ≈ 0.15 dex, *i.e.* of the order of the error. Thus, it is reasonable to attribute the observed differences to the differences in the stellar parameters, and in the measurement of the individual abundances and their combination. For six elements, Mg I, Na I, Sc II, V I, Y I, and Zr I, the differences are larger. Those elements, as well as Ca I, are discussed below:

- Mg I: Pompéia et al. (2008) used the Mg I line at 5711 Å while we used in addition two other lines (6318 Å and 6319 Å). If we had used only the line at 5711 Å, then $\langle[{\rm Mg/Fe}]_{\rm us} - [{\rm Mg/Fe}]_{\rm P08}\rangle = -0.09$ dex (r.m.s = 0.12 dex), instead of −0.23 dex.
- Ca I: we recall that we changed the $\log gf$ of the Ca I lines (see Section 4.2). Consequently, all the abundances are shifted by about 0.2 dex. With the old $\log gf$, $\langle[{\rm Ca/Fe}]_{\rm us} - [{\rm Ca/Fe}]_{\rm P08}\rangle = -0.08$ dex; with the new $\log gf$, $\langle[{\rm Ca/Fe}]_{\rm us} - [{\rm Ca/Fe}]_{\rm P08}\rangle = 0.09$ dex.
- Na I: Pompéia et al. (2008) used four lines and derived the individual abundances from EW while we used only three lines after having discarded the Na I line at 5862 Å (that we found systematically discrepant) and derived the individual abundances from SS. If we had used all four lines, then $\langle[{\rm Na/Fe}]_{\rm us} - [{\rm Na/Fe}]_{\rm P08}\rangle = 0.03$ dex (r.m.s = 0.18 dex).
- Sc II: Pompéia et al. (2008) used only the Sc II line at 5657 Å instead of four lines and took into account the hfs when deriving the abundance. If we limit ourselves to the line at 5657 Å, then $\langle[{\rm Sc/Fe}]_{\rm us} - [{\rm Sc/Fe}]_{\rm P08}\rangle = 0.05$ dex (r.m.s = 0.11 dex).
- V I: as explained in Section 4.2, we took into account the hfs in the abundance measurement, while Pompéia et al. (2008) did not. This explain the disagreement.
- Y I, Zr I: for Y I, and we used the same line and the same method (fitting of line profile) to derive the abundance. For Zr I, Pompéia et al. (2008) used the Zr I line at 6134 Å while we used three lines. But if we restrict the analysis to the same line, we still have $\langle[{\rm Zr/Fe}]_{\rm us} - [{\rm Zr/Fe}]_{\rm P08}\rangle = 0.46$ dex (r.m.s = 0.21 dex). For those two elements, the lines are weak and difficult to measure. Therefore, the abundance measurement is likely less robust and more sensitive to the method (*e.g.* the wavelength range where the synthesis is compared to the data, the continuum placement).

Table 12. Comparison of our new abundances for the LMC disc stars and those published in Pompéia et al. (2008): mean m and r.m.s s of the distribution of $[{\rm X/Fe}]_{\rm us} - [{\rm X/Fe}]_{\rm P08}$.

Element	m dex	s dex
O I	-0.12	0.13
Mg I	-0.23	0.12
Si I	+0.11	0.12
Ca I	+0.09	0.12
Ti I	+0.12	0.14
Ti II	+0.15	0.11
Na I	-0.19	0.18
Sc II	+0.14	0.15
V I	-0.22	0.14
Cr I	+0.06	0.12
Co I	-0.00	0.14
Ni I	+0.06	0.09
Cu I	-0.04	0.14
Y I	+0.24	0.25
Zr I	+0.43	0.20
Ba II	+0.04	0.17
La II	+0.05	0.11

In addition, we derived the Eu abundances for the LMC disc stars. The wavelength coverage of Pompéia et al. (2008)'s spectra is not exactly the same as ours since the setup HR14 they used was different. Consequently, the Eu II line at 6645 Å is not available; but the Eu II line at 6437 Å is present. Although this line is weaker than the other, we could use it successfully for most of the LMC disc stars. The complete abundance table for our LMC disc stars is available online at CDS and provides the reader with all abundance ratios and their corresponding random and systematic errors.

4.5. Error budget

Four main sources of uncertainty exist: uncertainties on the atomic data describing the measured lines, uncertainties due to the modelling of the absorption line, uncertainties on the abundance measurement (for both EW or SS, due to the noise in the fluxes, the continuum placement, the profile integration or profile fitting, and if the line is blended, the hypothesis on the contaminant abundance), and uncertainties on the stellar parameters.

Abundance measurement DAOSPEC provides us with an error on the EW, which is obtained during the least-square fit of the line. As mentioned in Stetson & Pancino (2008), this error is not a genuine 1σ confidence interval (*e.g.*, the correlation between the pixels is not taken into account). We checked it using our Arcturus spectra and the set of Fe I lines (51 lines measured which cover a broad range of line strengths and wavelengths). For each S/N hypothesis and for each Fe I line, we computed the sample standard deviation s[EW] of the EW distribution, as well as the mean $m[e_{\rm dao}({\rm EW})]$ of the error returned by DAOSPEC. s[EW] is a good estimator of the error on the EW since it encompasses the effect of the noise in the fluxes and the continuum placement. Figure 10 shows the comparison of $m[e_{\rm dao}({\rm EW})]$ and s[EW]. There is a fairly good agreement between the two: the mean of $(s[{\rm EW}] - m[e_{\rm dao}({\rm EW})])$ is -0.18 mÅ, -0.54 mÅ, -0.76 mÅ for the low, median and high S/N respectively; when the Monte-Carlo simulations predicts large errors, DAOSPEC does also; the error decreases when the S/N ratio increases. In the mean, DAOSPEC tends to mildly overestimate the error bar, especially when the S/N ratio gets better. So it is reasonable to use the error computed by DAOSPEC.

Another pitfall is the conversion of the error on the EW into an error on the abundance. Indeed, when we feed *turbospectrum* with the pair (EW, $e_{\rm dao}$(EW)), it computes the abundances corresponding to EW, and EW $\pm$ $e_{\rm dao}$(EW) and often provides asymmetric (right and left) errors. This is not *a priori* a proper way to find the error on the abundance since the relationship between [X/Fe] $\pm$ e([X/Fe]) and EW $\pm$ $e_{\rm dao}$(EW) is not known. We performed similar tests for the abundances as we did for EW in the previous paragraph. For each S/N hypothesis and for each Fe I line, we computed the sample standard deviation s[[Fe/H]] of the [Fe/H] distribution, as well as the mean $m[e_{\rm turbo}([{\rm Fe/H}])]$ of the error returned by *turbospectrum*. Figure 10 shows the comparison of $m[e_{\rm turbo}([{\rm Fe/H}])]$ and s[[Fe/H]]. We obtain a similar pattern for the abundances as that for the EW: the agreement is fairly good but the errors tend to be mildly overestimated when the S/N ratio increases (tough the effect is < 0.05 dex at high S/N). Here again, we considered safe to keep the error returned by *turbospectrum* (*i.e.*, the mean of the right and left errors).

Unfortunately, for the lines measured by absorption line fitting, we cannot use classical theorems to derive an error on the abundance measurement. Indeed, T^2 is not a random variable which follows a χ^2 distribution since we do not divide each term of the quadratic sum by the error on the flux at pixel i (the GIRAFFE pipeline certainly provides an error for each pixel but it is overestimated and correlated, see Section 2.2) and the O_i are correlated due to the interpolation or rebinning performed during the data reduction. One way to get an estimator of the the 1σ error is to do Monte-Carlo simulations. We used the Arcturus spectra to estimate the error $e_{\rm Arcturus}$([X/Fe]) on each single line (by computing the standard deviation of the abundance distribution) and to assign the error to the LMC stars depending on the S/N ratio category in which they fall.

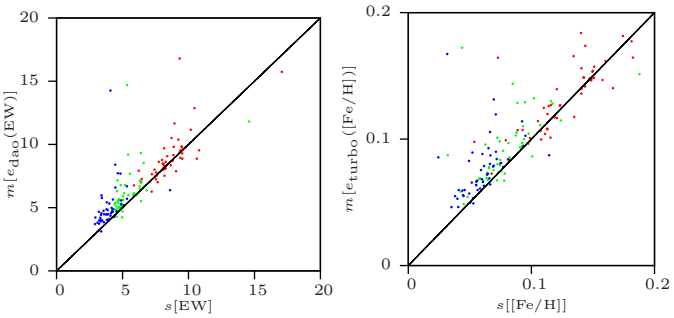

Fig. 10. Left panel: $m[e_{\rm dao}({\rm EW})]$ vs. s[EW]. Righ panel: $m[e_{\rm turbo}([{\rm Fe/H}])]$ vs. s[[Fe/H]]. Red dots: low S/N; green dots: median S/N; Blue dots: high S/N.

For a given element X, we propagated the errors on the individual lines $e_{\rm turbo}$([X/Fe]) or $e_{\rm Arcturus}$([X/Fe]), which gave us $e_{\rm prop}(\langle[{\rm X/Fe}]\rangle)$.

Atomic data and line modelling Our capacity to model correctly an absorption line, and thus measure the abundances accurately, depends on the quality of the atomic data describing the radiative transitions but also on our understanding of the underlying physics. Line lists are often a compilation of various sources aiming at giving the best parameters for a given line, and therefore, the precision of these parameters (among which $\log gf$ hold the main role) varies from line to line. The resulting synthetic spectrum is model-dependent (systematic error due to the choice of the grid of model atmospheres, the assumptions on the thermodynamic equilibrium, the atom models) and data-dependent (random error due to the $\log gf$ provided by the line lists). The sample dispersion s[[X/Fe]] of the individual abundances about the mean can be used to estimate the combination of these effects (if enough lines are available to estimate it). We derived conservative errors as follows:

- if $N_{\rm lines} < 5$:

$$e_{\rm data}(\langle[{\rm X/Fe}]\rangle) = e_{\rm prop}(\langle[{\rm X/Fe}]\rangle)$$

- if $N_{\rm lines} \geq 5$:

$$e_{\rm data}(\langle[{\rm X/Fe}]\rangle) = \max\left(\frac{s[[{\rm X/Fe}]]}{\sqrt{N_{\rm lines}}}, e_{\rm prop}(\langle[{\rm X/Fe}]\rangle)\right)$$

To assess our method of error estimation, we compared the standard error of the mean to the propagated error for Ca, Ni, Sc and V. We recall that for these elements, we have enough lines to compute a meaningful variance, and that we derived Ca and Ni abundances from EW and Sc and V abundances from SS. We found a median difference of ~ 0.02 dex: thus, this check validates the use of $e_{\rm turbo}$([X/Fe]) or $e_{\rm Arcturus}$([X/Fe]) for the individual measurements.

Stellar parameters The error $e_{\rm params}$ on chemical abundances due to the adopted stellar parameters is a thorny question. The four stellar parameters are mutually dependent and changing one of them will imply a change of the others (see McWilliam et al. 1995; Johnson et al. 2006 for a discussion on covariance terms). When the propagation of error is not straightforward, a usual practise is to perturb the explanatory variable (input) by $\pm$ its error and to look at the corresponding shift of the dependent variable (output). For the abundances, it would come down to repeat

Table 13. Typical $e_{\rm data}$ and $e_{\rm params}$, given as $[A/B]_{-\sigma(T_{phot})} - [A/B]_{nominal}$ and $[A/B]_{+\sigma(T_{phot})} - [A/B]_{nominal}$, for different elemental ratios for our LMC bar stars.

Elemental ratio	$e_{\rm data}$ dex	$e_{\rm params}(-\sigma(T_{phot}))$ dex	$e_{\rm params}(+\sigma(T_{phot}))$ dex
[Fe I/H]	0.03	0.04	0.04
[Fe II/H]	0.08	0.23	-0.12
[O I/Fe I]	0.04	- 0.10	0.06
[Mg I/Fe I]	0.04	- 0.03	0.01
[OI + MgI /Fe I]	0.03	- 0.07	0.04
[Si I/Fe I]	0.08	0.03	-0.05
[Ca I/Fe I]	0.04	- 0.09	0.05
[Ti I/Fe I]	0.07	- 0.20	0.17
[Ti II/Fe I]	0.04	0.02	-0.04
[Na I/Fe I]	0.04	- 0.14	0.05
[Sc II/Fe I]	0.04	- 0.01	-0.01
[V I/Fe I]	0.04	- 0.27	0.24
[Cr I/Fe I]	0.05	- 0.13	0.11
[Co I/Fe I]	0.04	- 0.12	0.10
[Ni I/Fe I]	0.05	- 0.04	0.03
[Cu I/Fe I]	0.08	- 0.10	0.09
[Y I/Fe I]	0.08	- 0.40	0.31
[Zr I/Fe I]	0.04	- 0.28	0.26
[Ba II/Fe I]	0.07	0.06	-0.06
[La II/Fe I]	0.06	- 0.04	0.04
[YI + ZrI /BaII + LaII]	0.06	- 0.33	0.29
[Eu II/Fe I]	0.07	- 0.05	0.02
[Ba II/Eu II]	0.11	0.08	-0.08
[La II/Eu II]	0.09	- 0.00	0.02

this procedure for each parameter, keeping the other three constant. The pitfall is to work with a set of parameters that do not satisfactorily describe the atmosphere of the star under study. For instance, when the temperature is changed by, say, 150 K, and $\{\log g, [M/H], \xi_{\rm micro}\}_{\rm nominal}$ (which were found for the nominal temperature) are kept, it is likely that the spectroscopic criterion used to find $\xi_{\rm micro}$ does not hold anymore and therefore the determination of abundances from strong lines will not be correct. We followed the prescription from Cayrel et al. (2004): as $T_{\rm phot}$ has the major effect on the abundance determination, we change it by ± its error and determine the three other stellar parameters corresponding to this new temperature $\{\log g, [M/H], \xi_{\rm micro}\}_{\pm\sigma(T_{phot})}$; we derive the chemical abundances corresponding to this perturbed solution and compare them to those given by the nominal solution. The final systematic error on [A/B] due to errors on effective temperature is then given by:

$$e_{\rm params} = \max\Big(|[A/B]_{+\sigma(T_{phot})} - [A/B]_{nominal}|, \\ |[A/B]_{-\sigma(T_{phot})} - [A/B]_{nominal}|\Big)$$

and the total error by:

$$e_{\rm total} = \sqrt{e^2_{\rm data} + e^2_{\rm params}}$$

Table 13 gives the typical (i.e. the mean over the sample) $e_{\rm data}$ and $e_{\rm params}$ (given as $[A/B]_{+\sigma(T_{phot})} - [A/B]_{nominal}$ and $[A/B]_{-\sigma(T_{phot})} - [A/B]_{nominal}$) for different elemental ratios for our LMC bar stars. In the vast majority of cases, the errors due to stellar parameters dominates over the random measurement errors. Both these sources of errors are plotted in Fig. 11-20.

5. Results and discussion

In this section, we present the results for the key elements: O, Mg, Si, Ca, Ti (α-elements), Na (light odd element), Sc, V, Cr, Co, Ni, Cu (iron-peak elements), Y, Zr, Ba, La and Eu (*s*- and *r*-elements). We compare our results for the LMC field stars (bar and inner disc) to LMC globular cluster (GC) stars (Johnson et al. 2006; Mucciarelli et al. 2008, 2010), and to the MW stellar populations (thin and thick disc Bensby et al. 2005; Reddy et al. 2003, 2006; halo Fulbright 2000; Stephens & Boesgaard 2002; Reddy et al. 2006; Eu and La ratios: Simmerer et al. 2004; Brewer & Carney 2006; O ratios of halo stars: Carretta et al. 2000). Our results for Arcturus are plotted as well to check our abundance scale (Arcturus) versus the literature abundance scales (the MW thick disc compilation).

5.1. α-elements

Figure 11 and 12 show the abundance trends for [O/Fe], [Mg/Fe], [Si/Fe], [Ca/Fe] and [Ti/Fe]. O, Mg, Si, Ca and Ti belong to the α-elements and are used to track the epoch where type II supernovae (SNII) drove the chemical evolution of the galaxy. Indeed, α-elements are formed by successive α captures occurring in massive stars interiors and are released to the intestellar medium (ISM) through SNII explosions (Burbidge et al. 1957). As iron-peak elements are also processed in massive stars, it results in a constant [α/Fe] ratio. When type Ia supernovae (SNIa) start to dominate the chemical enrichment and release huge amount of iron-peak elements (Timmes et al. 2003), [α/Fe] decreases (SNIa efficiently produce iron-peak elements without producing α-elements).

Bottom panel of Figure 11 shows [α/Fe] = [O + Mg/2Fe] for the LMC and the MW (when O, Mg ratios were available, we computed [α/Fe] the same way for MW). We clearly see that compared to the MW, the LMC exhibits deficient [α/Fe] for [Fe/H] ≥ -1.3 dex. Those low [α/Fe] ratios can be explained by a higher contribution of type Ia supernova (SNIa) to the chemical enrichment of the LMC, compared to the MW (e.g. Pagel & Tautvaisiene 1998).

The comparison of the LMC trends to those of the MW shows that the α-elements can be divided in two groups: on one hand, O and Mg, and on the other hand, Si, Ca and Ti. Indeed, the LMC distributions of O and Mg (Figure 11) are below those of the MW at all metallicities (except for the very most metal poor stars), while the LMC distribution of Si, Ca and Ti (Fig. 12) completely or partially overlap the MW distributions. Although O, Mg, Si, Ca and Ti are all α-elements, their production efficiency depends on the mass of the type II supernova (SNII) progenitor: while O and Mg are predicted to be mainly produced in very massive SNII progenitors (Woosley & Weaver 1995), Si, Ca and Ti are predicted to be produced in intermediate mass SNII and, in smaller quantity, by SNIa (Tsujimoto et al. 1995; Thielemann et al. 2002). The discrepancy between Galactic and LMC trends for O and Mg is not an artifact of the abundance analysis: for instance, for a 1 dex metallicity bin centered around Arcturus, we have $\langle[O/Fe]_{\rm LMCBar}\rangle = 0.1$ dex, $\langle[O/Fe]_{\rm MWDiscs}\rangle = 0.47$ dex, $[O/Fe]_{\rm Arcturus} = 0.44$ dex, hence Δ(MW − LMC) ≈ Δ(Arcturus − LMC) (the same is true for Mg). Therefore, it suggests that the LMC formed high mass stars less efficiently than the MW.

Our two fields do not exhibit strong differences in their α trends: for O, Mg, Si and Ti, the trends of the bar and the disc overlap at all metallicities. On the other hand, we observe a larger scatter for the bar [α/Fe] for -0.8 dex ≤ [Fe/H] ≤ -0.4 dex: over this range of metallicities, r.m.s([α/Fe]) = 0.08 dex for the bar, r.m.s([α/Fe]) = 0.05 dex for the disc. According to the age-metallicity relation (Cole et al. 2005), this metallicity range corresponds to ages between 2 Gyr to 6 Gyr

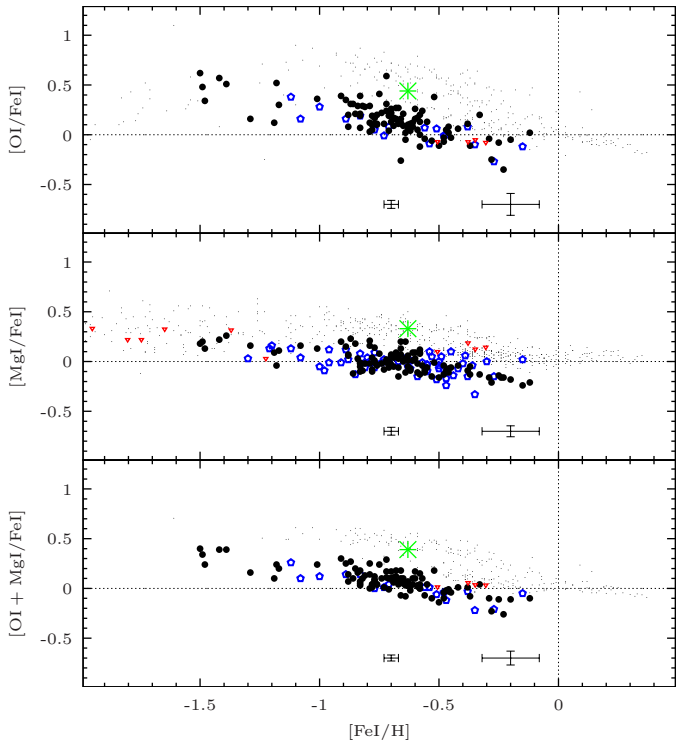

Fig. 11. First row: [O I/Fe I] vs. [Fe I/H]. Second row: [Mg I/Fe I] vs. [Fe I/H]. Third row: [O I + Mg I/2Fe I] vs. [Fe I/H]. Legend: black filled circles: LMC bar (this work); blue open pentagons: LMC inner disc (this work); green asterisk: Arcturus (this work, data for median S/N ratio); red downward triangle: LMC GC (Johnson et al. 2006; Mucciarelli et al. 2008, 2010); black tiny dots: MW thin and thick disc (Bensby et al. 2005; Reddy et al. 2003, 2006), halo (Fulbright 2000; Stephens & Boesgaard 2002; Reddy et al. 2006), and additional MW data for O from Carretta et al. (2000). Typical random (left) and systematic (right) error bars on both coordinates are provided for our LMC samples.

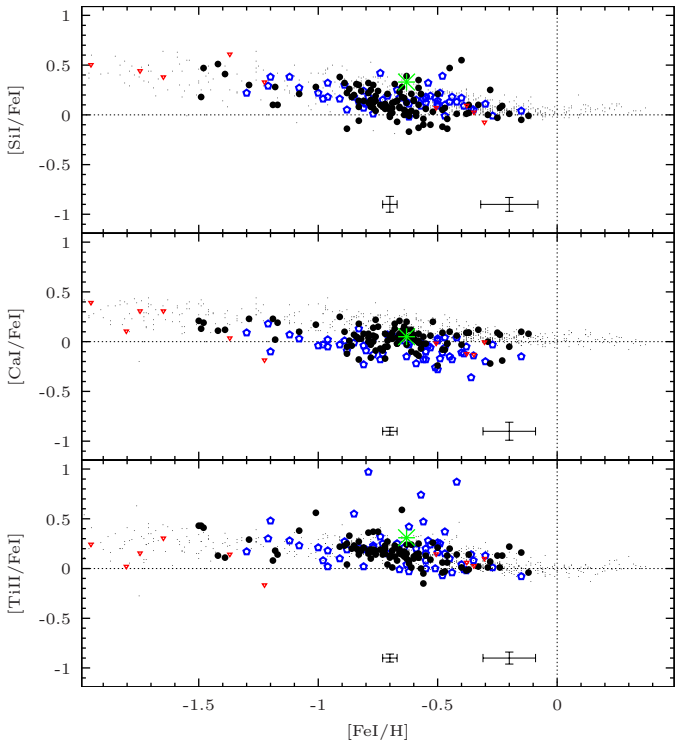

Fig. 12. First row: [Si I/Fe I] vs. [Fe I/H]. Second row: [Ca I/Fe I] vs. [Fe I/H]. Third row: [Ti II/Fe I] vs. [Fe I/H]. Legend: same as Figure 11.

ago, thus the suspected epoch of the bar formation. The slight increase of the scatter between the two fields can be understood in the scenario where a new population is formed. Indeed, if the bar is the result of a new population formation, sustained by gas inflow, then the number of massive stars will increase and they will release significant amounts of freshly formed α-elements into the ISM. We should then expect an increase of [α/Fe] a few Myr after the start of the star burst (Gilmore & Wyse 1991; Tsujimoto et al. 1995; Pagel & Tautvaisiene 1998). In fact, this increase would be too small to be clearly identifiable in our data because of uncertainties in both [Fe/H] and [α/Fe], but a larger scatter should appear instead. So, if the observed scatter is true, then it supports the scenario of a new stellar population instead of a dynamically-driven bar.

Unlike the MW, the plateau corresponding to the SNII-dominated regime is not clearly visible in the LMC field stars distribution. Two possibilities can lead to this: either there is a plateau but it appears at a much lower metallicity, which means that the chemical evolution has been very slow compared to the MW (when the SNIa start to explode in the LMC, the metallicity has reached a lower value than in the MW). Or there is no plateau, which Tsujimoto & Shigeyama (2012) explain by prompt SNIa, for which the onset of SNIa occurs as soon as 100 Myr after the formation of the progenitors. Since the lowest metallicity of our samples is only ≈ -1.6 dex, we cannot draw firm conclusions about the presence or absence of a plateau in the LMC. However, LMC globular clusters can also be used to infer the [α/Fe] in the metal-poor regime. Except for O (for which metal-poor LMC GC stars exhibit chemical anomalies due to self-enrichment), there is a good agreement between LMC GC and LMC field stars at both low (-1.5 dex $\leq$ [Fe/H] $\leq$ -1.2 dex) and high (-0.5 dex $\leq$ [Fe/H] $\leq$ -0.2 dex) metallicity. The metal-poor LMC GC populate the metallicity range $[-2, -1.2]$ and line up along a MW-like plateau at low metallicity ([Fe/H] $\lessapprox -1.6$ dex). Furthermore, Haschke et al. (2012c) also find that extremely metal-poor RR-Lyrae stars in the LMC populate a plateau similar to that of the MW.

Let us note that Bekki & Tsujimoto (2012) also used prompt SNIa in their models to reproduce the LMC trends of Mg and Ca (based on abundances of LMC field stars and GC stars) and conclude that prompt SNIa have influenced the chemical evolution of the LMC. We remark that to fully explain the low LMC [Ca/Fe], Bekki & Tsujimoto (2012) had to invoke galactic winds which remove Ca more efficiently than the others α-elements, but this may not be necessary with our revised abundances (they used abundance measurements from Pompéia et al. 2008 and our revised abundances are ≈ 0.1 dex higher).

Finally, we note that Lapenna et al. (2012) have measured O, Mg and Si for 89 stars in a filed in the LMC disc (around the globular cluster NGC 1786, some 3 degree North-West of the bar center) and found similar trends as ours.

5.2. Heavy elements

Figures 13 to 16 present the elemental distributions for the heavy elements Eu, Y, Zr, Ba, La. Unlike the elements lighter than iron, the heavy elements are produced by neutron captures through *s*-

and *r*-processes. The naming of the two nucleosynthetic channels refers to the neutron flow: the *slow*-process (*s*-process) refers to neutron captures where only a few neutron captures happen before a radioactive β-decay ($\tau_{\rm capture} > \tau_{\rm decay}$ with $\tau_{\rm capture}$ the timescale of a neutron capture event and $\tau_{\rm decay}$ the timescale of β-decay) while the *rapid*-process (*r*-process) refers to processes where numerous neutron captures occur before a radioactive β-decay ($\tau_{\rm capture} < \tau_{\rm decay}$). While it is known that the envelopes of asymptotic giant branch (AGB) stars are the place of the *s*-process (*e.g.*, Busso et al. 1999), there is no consensus as to where the *r*-process is made, except that it should be linked to massive stars. The more promising candidates (providing the needed high neutron fluxes) are SNII (Wasserburg et al. 1996), but neutron stars (Freiburghaus et al. 1999) also enter the lists (Qian 2012). Unlike Y, Zr, Ba, and La which can be mainly produced by the *s*-process (more than 60 % in the solar system) with a minor contribution from the *r*-process (*e.g.*, $\approx$ 85 % of the solar Ba was produced by the *s*-process Burris et al. 2000; Sneden et al. 2008), Eu is often considered as a pure *r*-process element (the *r*-process contribution to the solar Eu is of 94 % according to Arlandini et al. 1999 and 97 % according to Sneden et al. 2008).

Europium In Figure 13, we see that the LMC bar and disc Eu distributions agree very well: they both exhibit a constant [Eu/Fe] $\approx$ 0.5 dex for [Fe/H] ≤ -0.8 dex, then a decreasing trend with increasing metallicity. While for the metal-poor stars the abundance ratios of the LMC and the MW halo overlap, it is clear that for [Fe/H] ≥ -1 dex the LMC trend is above that of MW. This enhancement for metal-rich stars is not an artifact of our analysis since Arcturus has the expected Eu abundance (*i.e.* it falls on top of the MW thick disc). This is in fact a chemical anomaly already noticed in LMC supergiant stars (Russell & Bessell 1989; Hill et al. 1995) and LMC GC stars (Mucciarelli et al. 2008; Colucci et al. 2012) and its origin still remains unclear. Different mechanisms can help in maintaining a high Eu ratio in late stages of the chemical evolution: (1) new star bursts will form a high number of massive stars which will, in turn, inject fresh Eu in the ISM; (2) another source of *r*-processed Eu; (3) a stronger contribution of *s*-processed Eu. Explanation (1) is not supported by the SFH of our two LMC fields (Smecker-Hane et al. 2002): although recent star bursts (about 5 Gyr ago and less than 1 Gyr ago) are expected in the bar, they are not expected in the inner disc; so it cannot explain the high ratios observed in both fields. Moreover, they would produce similar α enhancements, which are not observed. But it can explain the small difference between the LMC bar and disc observed for the most metal-rich stars (above -0.5 dex). Indeed, while the disc [Eu/Fe] still decreases and reaches lower values than the bar, the bar [Eu/Fe] seems to remain constant ([Eu/Fe] $\approx$ 0.4 dex). (2) or (3) are more likely to explain the differences between the LMC and the MW. The contribution of the *s*-process to the solar system Eu is estimated to be of few percents (3 % according to Sneden et al. 2008) and therefore, it is dubious that the *s*-process could be responsible for the Eu enhancement. But in their study of CEMP-*s* and CEMP-*r*/*s* stars, Allen et al. (2012) found a correlation between [Ba/Fe] and [Eu/Fe] and that [Eu/Fe] is coupled to the degree of C over-abundance; so, while it was thought that Ba and Eu in CEMP-*r*/*s* originated in two distinct processes (through three mass-transfer in a binary sytem, see Cohen et al. 2003; through two successive mass-accretion of a 8-10 $M_\odot$ companion, see Wanajo et al. 2006; through pre-*r* enrichment followed by *s*-material accretion, see Bisterzo et al. 2012), Allen et al. (2012) claim that Ba and Eu have the same origin in CEMP-*s* and CEMP-*r*/*s*, *i.e.* produced by the *s*-process occurring during the AGB phase of the more massive star of a binary system. In essence, the CEMP-*r*/*s* stars would be stars polluted by metal-poor AGB with significant Eu production. Thus, those new results and the dominant role played by AGB stars in the chemical evolution of the LMC (see below) support explanation (3).

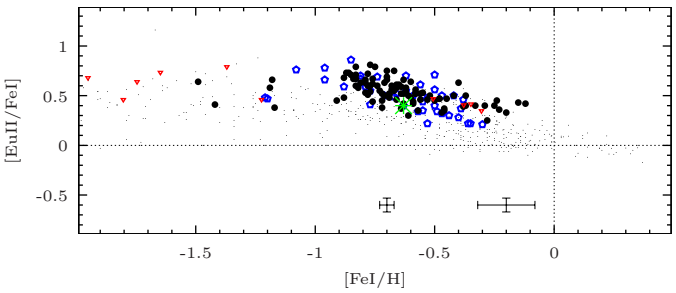

Fig. 13. [Eu II/Fe I] vs. [Fe I/H]. Legend: same as Figure 11.

Barium and lanthanum While the MW has constant solar [Ba/Fe] and [La/Fe] ratios (with a weak increase towards high metallicities), both LMC fields exhibit a dramatic increase of [Ba/Fe] and [La/Fe] with increasing metallicity (first and third panels of Figure 14): the LMC distributions agree with MW halo trends, *i.e.* for [Fe/H] ≤ -1 dex, and are above the MW elsewhere. The bar and disc field distributions overlap for both Ba and La. Ba has the strongest increase, starting from solar value at [Fe/H] $= -1.5$ dex and reaching 0.8 dex for [Fe/H] ≥ -0.3 dex. La, on the other hand, remains approximately constant from [Fe/H] ≈ -0.7 dex ([La/Fe] $\approx$ 0.5 dex for the LMC bar and $\approx$ 0.4 dex for the LMC disc). Furthermore, there is an excellent match between LMC field population and LMC GC population. This indicates that the production of Ba and La has been much more efficient in the LMC than in the MW.

To identify the process responsible for this high production, we examine [Ba/Eu] and [La/Eu] in second and fourth panels of Figure 14. We see that for LMC GC and field metal-poor stars (from -2 dex to -0.8 dex), [Ba, La/Eu] is constant and compatible (within uncertainties) with a pure *r*-process source (Arlandini et al. 1999: $[{\rm Ba_r/Eu_r}] = -0.69$ dex and $[{\rm La_r/Eu_r}] = -0.4$ dex; Sneden et al. 2008: $[{\rm Ba_r/Eu_r}] = -0.82$ dex and $[{\rm La_r/Eu_r}] = -0.59$ dex). On the other hand, for [Fe/H] ≥ -0.8 dex, the increase of the LMC [Ba, La/Eu] is interpreted as the rise of a new source of Ba and La, *i.e.* the *s*-process. The MW exhibits similar patterns (constant ratio at low metallicity, then an increase) but two differences exist with the LMC: first, the increase of [Ba, La/Eu] starts at lower metallicity in the LMC ([Fe/H] ≈ -0.8 dex) than in the MW ([Fe/H] ≈ -0.4 dex), reflecting the slower metal-enrichment in the LMC; secondly, while for the MW, [Ba/Eu] reaches a solar value, for the LMC, [Ba/Eu] reaches a much higher value ([Ba/Eu] $\approx$ 0.4 dex). This suggest that the production of Ba and La by the *s*-process has been much more efficient in the LMC than in the MW, and thus it indicates that AGB stars played a stronger role in the chemical enrichment of the LMC compared to the MW.

Yttrium and zirconium For [Fe/H] ≤ -1 dex, the LMC bar and disc seem to have a solar Zr ratio (Figure 15) and a solar Y ratio (at least for the disc field; we do not have enough data point for the bar field). For [Fe/H] > -1 dex, the two LMC fields have a flat Y and Zr distribution with a large scatter but the LMC disc and bar exhibit a different mean behaviour in their Y and Zr

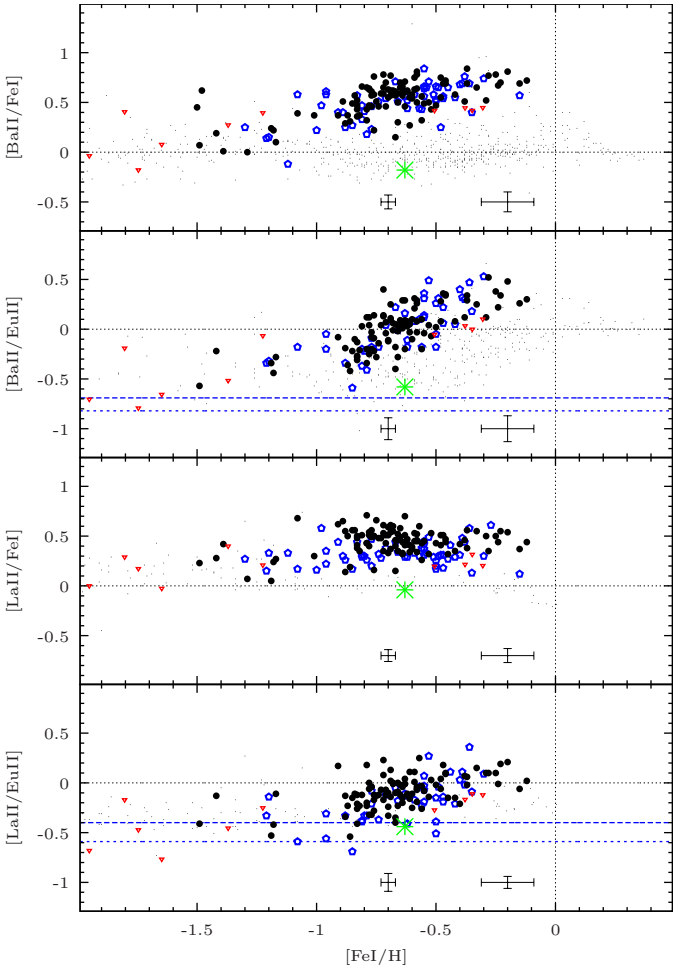

Fig. 14. First row: [Ba II/Fe I] vs. [Fe I/H]. Second row: [Ba II/Eu II] vs. [Fe I/H]. Third row: [La II/Fe I] vs. [Fe I/H]. Fourth row: [La II/Eu II] vs. [Fe I/H]. Legend: same legend as Figure 11; additional MW data for Eu and La from Simmerer et al. (2004); Brewer & Carney (2006); horizontal blue dashed line: $[Ba_r/Eu_r] = -0.69$ dex and $[La_r/Eu_r] = -0.4$ dex (Arlandini et al. 1999); horizontal blue dotted line: $[Ba_r/Eu_r] = -0.82$ dex and $[La_r/Eu_r] = -0.59$ dex (Sneden et al. 2008).

trends: in the mean, the bar has higher [Y/Fe] and [Zr/Fe] than the disc (bar: $\langle[Y/Fe]\rangle = 0.31$ dex, $\langle[Zr/Fe]\rangle = 0.19$ dex; disc: $\langle[Y/Fe]\rangle = -0.04$ dex, $\langle[Zr/Fe]\rangle = -0.08$ dex). We checked for possible systematic effects explaining the differences but found none (same kind of stars, same instrument and observing setups, similar data reduction procedure, same procedures to derive stellar parameters and abundances). In particular, we checked whether one of the three Zr lines used could be responsible for the difference. In the mean, each line gives higher Zr abundances for the bar than for the disc: for the bar, $\langle[Zr/Fe]\rangle = 0.22$ dex, 0.20 dex and 0.14 dex; for the disc, $\langle[Zr/Fe]\rangle = -0.04$ dex, 0 dex, and -0.14 dex (respectively for the line at 6127 Å, 6134 Å and 6143 Å). We also looked for possible correlations between the derived abundances and the stellar parameters and found for both fields a clear correlation between [Y, Zr/Fe] and T_{eff} or ξ_{micro}, *i.e* increasing abundance ratio with increasing temperature or microturbulence velocity. LMC GC stars of Mucciarelli et al. (2008, 2010) follow the same correlation as ours, and since they are colder than our stars, they have Y and Zr abundances

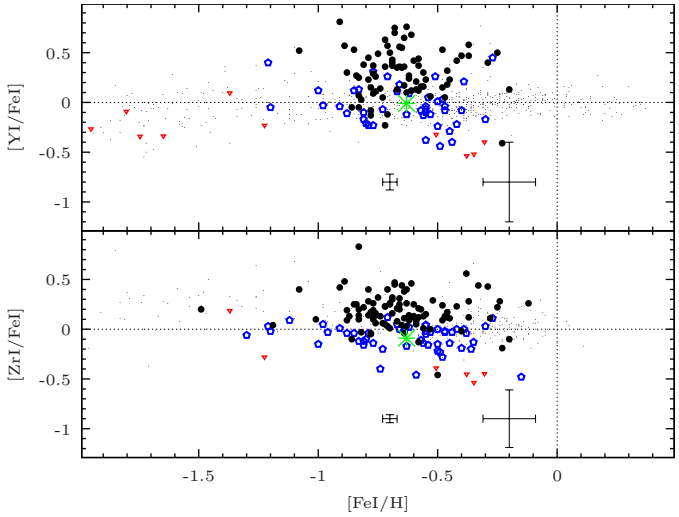

Fig. 15. First row: [Y I/Fe I] vs. [Fe I/H]. Second row: [Zr I/Fe I] vs. [Fe I/H]. Legend: same as Figure 11.

lower than those of our stars. Furthermore, our two samples do not have the same temperature coverage (3900 K to 5200 K for the bar, 3800 K to 4600 K for the inner disc). But if we select only stars in the temperature range [4000, 4400], the dispersion slightly decreases in each field, but the two fields remain significantly different: $\langle[Y/Fe]\rangle = 0.25$ dex, $\langle[Zr/Fe]\rangle = 0.15$ dex for the bar, and $\langle[Y/Fe]\rangle = 0$ dex, $\langle[Zr/Fe]\rangle = -0.07$ dex for the disc. The typical random error (due to pixel noise) on the final Y or Zr abundances are respectively 0.08 dex and 0.04 dex while the typical systematic error (due to errors on effective temperature) are 0.4 dex and 0.29 dex respectively. Thus, errors can explain the observed scatter but cannot explain the offset between our two LMC populations.

Such a discrepancy is not seen for Ba and La for which the distributions of our two LMC fields agree rather well. Interestingly, Y and Zr, on the one hand, Ba and La, on the other hand respectively belong to the first peak and the second peak of the *s*-process (the position of the peaks correspond to magic number of nucleons for which the nucleus is more stable). The observed differences can be an effect of metallicity of the AGB producing the *s*-elements since the second peak is favoured, relatively to the first peak, when metal-poor AGB stars dominate the chemical enrichment (Cristallo et al. 2011). This suggests that AGB stars were more metal-poor in the disc than in the bar of the LMC. We note that the metal-rich LMC GC have [Y/Fe] and [Zr/Fe] clearly lower than those of the LMC bar, and probably similar to the LMC inner disc, which is understandable since their projected locations lie in the LMC disc. Thus, the differences observed between the LMC bar and disc for Y and Zr for $[Fe/H] \gtrapprox -1$ dex speak in favour of a different chemical evolution path: unlike the disc, the bar experienced a recent episode of stellar formation (a few Gyrs ago) which generated metal-rich AGB that explain the present Y an Zr ratios.

Figure 16 shows [Y + Zr/Ba + La]. We recall that Y and Zr belong to the first peak of the *s*-process while Ba and La belong to the second peak. Thus the ratio [ls/hs] informs us on the relative importance of metal-poor and metal-rich AGB. For $[Fe/H] \gtrapprox -0.8$ dex, we know from above that the *s*-process dominates the chemical enrichment. We remark that the LMC trend is below that of the MW, which suggests that the AGB stars which dominated the LMC enrichment were more metal-poor than those of the MW. While the bar distribution is flat,

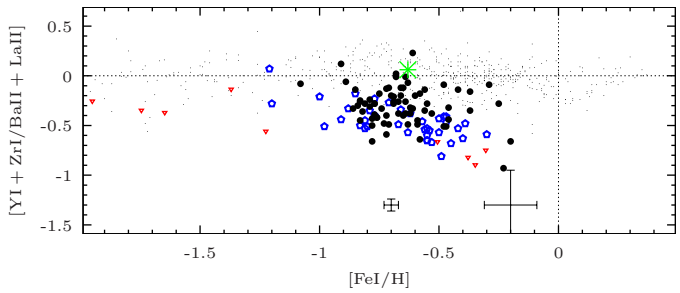

Fig. 16. [Y I + Zr I/Ba II + La II] vs. [Fe I/H]. Legend: same as Figure 11.

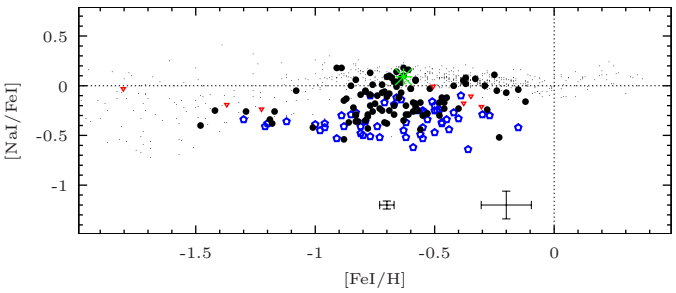

Fig. 17. [Na I/Fe I] vs. [Fe I/H]. Legend: same as Figure 11.

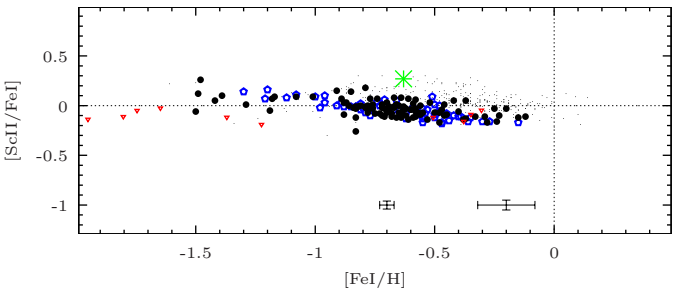

Fig. 18. [Sc II/Fe I] vs. [Fe I/H]. Legend: same as Figure 11.

the disc distribution seems to slightly decrease with increasing metallicity. Colucci et al. (2012) also found a decrease of [Y/Ba] in intermediate-age clusters. This could be a mass effect (in the LMC, metal-poor low mass AGB stars still contribute significantly to the enrichment) but only a consistent chemical evolution modeling can confirm this explanation. We remark that the match between LMC GC and our LMC fields is again excellent.

5.3. Sodium and iron-peak elements

Figures 17 to 19 show the elemental distributions of Na and iron-peak elements Sc, V, Cr, Co and Ni.

Sodium In Figure 17, for stars whose metallicity is below -1.1 dex, we see that the LMC bar and disc [Na/Fe] agree rather well within uncertainties (bar: $\langle$[Na/Fe]$\rangle = -0.28$ dex; disc: $\langle$[Na/Fe]$\rangle = -0.37$ dex) and they overlap the MW halo distribution. On the other hand, for [Fe/H] ≥ -1.1 dex, the two LMC distributions become different. The bar [Na/Fe] seems to increase with increasing metallicity and reaches solar values ($\langle$[Na/Fe]$\rangle = -0.13$ dex, r.m.s $= 0.17$ dex), thus overlapping the Galactic trends. On the other hand, the disc [Na/Fe] remains subsolar with a flat distribution ($\langle$[Na/Fe]$\rangle = -0.35$ dex, r.m.s = 0.13 dex). Both fields exhibit a large scatter in this metallicity regime: although only five bar stars and four disc stars are observed for [Fe/H] ≤ -1.1 dex, we can guess that the scatter is smaller than for [Fe/H] ≥ -1.1 dex (if the scatter were the same, it would be unlikely to have five or four measures concentrated within 0.2 dex). None of the three Na lines used is responsible for the difference; in the mean, each line gives higher Na abundances for the bar than for the disc: for the bar, $\langle$[Na/Fe]$\rangle = -0.11$ dex, -0.15 dex and 0.12 dex; for the disc, $\langle$[Na/Fe]$\rangle = -0.31$ dex, -0.35 dex, and -0.36 dex (respectively for the line at 5688 Å, 6154 Å and 6160 Å). As for Y and Zr, there is a correlation between [Na/Fe] and $T_{\rm eff}$ and again, if we select only the stars in the temperature range [4000, 4400], the dispersion slightly decreases but we still see the different mean behaviour. We note that there is an excellent agreement at both low an high metallicity between the LMC GC and our LMC fields. As for Y and Zr, the typical random and systematic error on the final Na abundance are respectively 0.04 dex and 0.14 dex and can explain the scatter but not the offset between the two fields.

The production of Na is still uncertain and is thought to occur in high-mass SNII (Woosley & Weaver 1995) and AGB stars (Goriely & Mowlavi 2000; Cristallo et al. 2006; Bisterzo et al. 2010). Issues on the abundance measurement have been reported, *e.g.* in Pasquini et al. (2004) where the authors find a disagreement between Na abundances of giant and dwarf stars belonging to the same cluster. Different explanations are quoted to explain these issues: departure from local thermodynamic equilibrium, surface Na abundances modified by the first dredge-up or uncertainties on atomic data (Smiljanic 2012). It is therefore difficult to understand the LMC trends relatively to those of the MW (most of the MW abundances were measured in dwarf stars) but comparing the two LMC fields is still valid. The discrepancy between the LMC bar and disc fields tells us that the production of Na has been more efficient in the bar than in the disc: it can be the result of the star burst that gave birth to the new population in the central parts of the LMC.

Scandium Figure 18 shows the LMC bar and disc Sc distributions. The bar and disc have similar [Sc/Fe]. They overlap the MW halo but are below the MW discs. As noticed for the MW (Nissen et al. 2000; Reddy et al. 2003, 2006), the Sc in the LMC behaves approximately like Ca or Ti: small scatter at all metallicities; [Sc/Fe] decreases with increasing metallicity; the distribution for the most metal-poor stars ([Fe/H] ≤ -1 dex) is compatible with a plateau (especially for the bar); the amplitude of the decrease between the metal-poor edge and the metal-rich edge is of 0.2 dex. Prochaska & McWilliam (2000) claimed that the α-like pattern of Sc could be due to poor hfs data but Reddy et al. (2003, 2006) used weak Sc II lines in dwarf stars for which the hfs has little effect on the derived abundances. For our giant stars, the hfs must be taken into account since Sc II lines are strengthened; and we see that Arcturus [Sc/Fe] lies on the top of the thick disc distribution, as expected.

Other iron-peak elements Figure 19 presents the abundance distributions of V, Cr, Co and Ni. Although they all belong to the iron-peak and are mainly produced by SNIa, these elements exhibit different patterns. The abundance distributions of V, Cr and Co are characterised by a rather large scatter, V being the most dramatic case. Cr and Co have flat distributions overlapping those of the MW for both LMC fields while Ni is subsolar at all metallicities for both LMC fields.

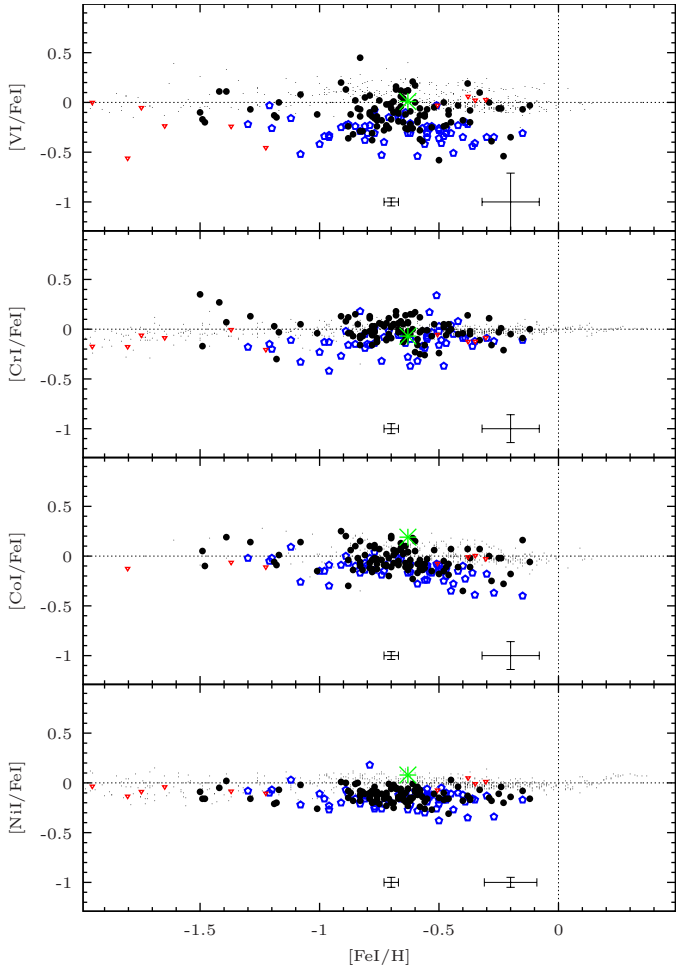

Fig. 19. First row: [V I/Fe I] vs. [Fe I/H]. Second row: [Cr I/Fe I] vs. [Fe I/H]. Third row: [Co I/Fe I] vs. [Fe I/H]. Fourth row: [Ni I/Fe I] vs. [Fe I/H]. Legend: same as Figure 11.

On the other hand, for V, the bar and disc distributions agree only for [Fe/H] ≤ -1.1 dex. For [Fe/H] ≥ -1.1 dex, in the mean, the bar has higher [V/Fe] than the disc (bar: $\langle$[V/Fe]$\rangle = -0.11$ dex; disc: $\langle$[V/Fe]$\rangle = -0.30$ dex). Among the iron-peak elements, V is the one with the highest number of measured lines (7 lines, most of the time) but it exhibits the larger scatter, which should be in principle a sign that the scatter is astrophysical. Interestingly, like for Na, the disagreement between the two LMC fields appears to reach -1 dex. We performed similar sanity checks for V as we did for Y, Zr and Na, and found a correlation between the derived abundance and the temperature; but a selection on temperature leaves the discrepancy unchanged. The typical random and systematic error respectively 0.04 dex and 0.29 dex and can explain the scatter but not the offset between the two fields.

5.4. Copper

Figure 20 shows the abundance trends of Cu. While the LMC bar and disc ratios match those of the MW for [Fe/H] ≤ -1.1 dex, the LMC ratios are significantly lower than those of the MW for higher metallicities: $\langle$[Cu/Fe]$\rangle = -0.5$ dex for the bar and $\langle$[Cu/Fe]$\rangle = -0.6$ dex for the disc. Since we found an expected value for the Arcturus' abundance, the observed deficiency for Cu is not an artifact of our abundance analysis. The origin of

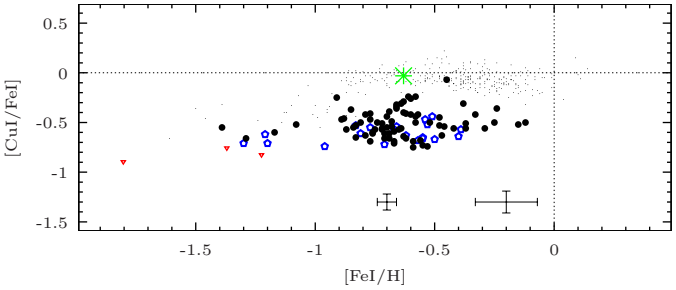

Fig. 20. [Cu I/Fe I] vs. [Fe I/H]. Legend: same as Figure 11.

Cu is still heavily debated since Cu is thought to have both primary and secondary production: Romano & Matteucci (2007) see the origin of Cu in neutron captures occurring in massive stars dying as SNII (primary production), Travaglio et al. (2004) invoke a minor contribution from *s*-process in AGB (secondary production) and Mishenina et al. (2002) consider the thermonuclear nucleosynthesis in SNIa as the main source (secondary production). We saw in Section 5.1 that a stronger contribution of SNIa is needed to explain the low α ratios and in Section 5.2, that a stronger contribution of AGB is needed to explain the high Ba and La ratios. In addition, Pignatari et al. (2010) found that more than half of the solar copper is produced through weak *s*-process occurring in massive stars ($25 M_{\odot}$). Therefore, SNIa and AGB stars cannot be the main site of Cu production in the LMC and the hypothesis of massive stars being the main source of Cu seems to be more plausible: Cu in the LMC has mainly a primary origin. Like for the α elements O and Mg, our results for Cu supports the scenario of a chemical enrichment dominated by intermediate mass AGB stars and SNIa, with a smaller contribution from very massive stars (compared to the MW).

6. Summary and conclusions

To compare the chemical history of the LMC to that of the MW and disentangle the chemical evolution of the LMC bar and disc, we performed a detailed chemical analysis of LMC giant stars (106 stars in a field centered on the LMC bar, and reanalysed in a homogeneous manner the 58 RGB stars observed by Pompéia et al. (2008) in a field situated in the inner LMC disc field some $\sim$2 deg South of the bar, using high resolution and mid S/N ratio spectra obtained at ESO/VLT. We took great care to insure the homogeneity of the two samples, and furthermore used the local thick disc giant Arcturus to insure a proper comparison to Milky-Way disc samples. The main findings of the paper can be summarised as follows:

- The two samples cover the metallicity range [Fe/H] from -1.5 to -0.1 dex, covering the full LMC disc metallicity distribution (Cole et al. 2005; Carrera et al. 2008), albeit leaving out the most metal-poor (and less numerous) tail of the distribution despite our deliberate overpopulation of this tail in the target selection. 80% of the sample is comprised between -1.1 and -0.4 dex. As this sample is metallicity-biased, it cannot be used for metallicity distribution studies.
- In the metallicity range covered by both types of objects, the LMC field and GC elemental abundances exhibit an excellent agreement for all elements (except for O and Na at low metallicity where the clusters experienced self-enrichment creating anticorrelated O-Na star to star variations).
- The α-elements ratios [Mg/Fe] and [O/Fe] are lower in the LMC than in the MW suggesting a smaller contribution of

massive stars (with respect to SNIa) in the LMC, or a slower enrichment. The presence of a plateau for [α/Fe] is not convincingly probed by our samples (that lack the statistics at low metallicities), although the most metal-poor GC do seem to lie on a plateau. [Ba, La/Eu] exhibit a strong increase from [Fe/H] ≈ -0.8 dex with increasing metallicity showing that the chemical enrichment of the LMC has been slower than that of the MW, and that the neutron-capture elements were dominated by AGB stars strongly contributing *s*-process. The LMC has lower [Y + Zr/Ba + La] ratios than the MW indicating that these AGBs were more metal-poor in the LMC.

- Eu does not follow the expected trend which could be an indication of an efficient *s*-production of this element, despite the usually assumed almost pure *r*-process origin of this element. This finding is supported by the recent work by Allen et al. (2012) who advocate a strong *s*-process contribution to Eu in a certain category of extremely metal-poor carbon and *s*-process enhanced stars (the so-called *sr*-stars).
- Cu is almost constant over the metallicity range and about 0.5 dex lower in the LMC than in the MW showing that in the LMC Cu has mainly a primary origin (through weak *s*-process in massive stars).
- The LMC bar and disc exhibit subtle differences in their [α/Fe] (slightly larger scatter for the bar in the metallicity range $[-1, -0.5]$), their [Eu/Fe] (the bar trend is above the disc trend for [Fe/H] ≥ -0.5 dex, their Y and Zr, their Na and their V (offset between the bar and the disc distributions). These differences are possibly related to the formation of a new stellar population in the central part of the LMC: the resulting new generation of massive stars will inject freshly synthesised α-elements (hence the increased scatter observed in the bar) and Eu (hence the higher [Eu/Fe] ratios in the bar) and the new generation of metal-rich AGB stars will produce Na, Y and Zr (hence the offset). These findings strengthen a scenario where the LMC bar is not a mere dynamically driven (or interaction driven) overdensity, but implied a fresh episode of star formation. This scenario also supported by the star formation history derived in the bar, that highlights an increased star formation 2-5 Gyr ago, with no clear counterparts in other locations in the LMC disc (Smecker-Hane et al. 2002). More globally, Harris & Zaritsky (2009) have established a map of star formation histories across the whole LMC and find again that the dominant star formation episode that occurred some 5 Gyr is more pronounced in the bar than anywhere else in the LMC. Even younger bursts of star formation seem to follow the bar morphology, around 500 and 100 Myr ago. Gallart et al. (2008), although their sample does not include the bar per say, also highlight that the younger populations in the LMC are found closer to the center together with a positive age-gradient of the youngest star formation episode towards the outskirts. All these findings regarding the star formation history of the LMC bar and disc strengthen a scenario where the bar is the strongest manifestation of the higher recent star formation activity in the central parts of the LMC.

Acknowledgements. M. Van der Swaelmen thanks ESO and the CNRS for funding his PhD work. DAOSPEC has been written by P. B. Stetson for the Dominion Astrophysical Observatory of the Herzberg Institute of Astrophysics, National Research Council, Canada. This research made use of the VALD database. M. Van der Swaelmen and V. Hill thank the support of the french Programme National Galaxies (INSU) which allowed this research to be carried out.

References

Allen, D. M., Ryan, S. G., Rossi, S., Beers, T. C., & Tsangarides, S. A. 2012, A&A, 548, A34
Alvarez, R. & Plez, B. 1998, A&A, 330, 1109
Alves, D. R. 2004, New A Rev., 48, 659
Alves-Brito, A., Meléndez, J., Asplund, M., Ramírez, I., & Yong, D. 2010, A&A, 513, A35
Arlandini, C., Käppeler, F., Wisshak, K., et al. 1999, ApJ, 525, 886
Bekki, K. 2009, MNRAS, 393, L60
Bekki, K. & Chiba, M. 2005, MNRAS, 356, 680
Bekki, K. & Tsujimoto, T. 2012, ArXiv e-prints
Bensby, T., Feltzing, S., Lundström, I., & Ilyin, I. 2005, A&A, 433, 185
Besla, G., Kallivayalil, N., Hernquist, L., et al. 2007, ApJ, 668, 949
Besla, G., Kallivayalil, N., Hernquist, L., et al. 2012, MNRAS, 421, 2109
Bielski, A. 1975, J. Quant. Spec. Radiat. Transf., 15, 463
Biemont, E., Baudoux, M., Kurucz, R. L., Ansbacher, W., & Pinnington, E. H. 1991, A&A, 249, 539
Bisterzo, S., Gallino, R., Straniero, O., Cristallo, S., & Käppeler, F. 2010, MNRAS, 404, 1529
Bisterzo, S., Gallino, R., Straniero, O., Cristallo, S., & Käppeler, F. 2012, MNRAS, 422, 849
Blecha, A., Cayatte, V., North, P., Royer, F., & Simond, G. 2000, in Society of Photo-Optical Instrumentation Engineers (SPIE) Conference Series, Vol. 4008, Society of Photo-Optical Instrumentation Engineers (SPIE) Conference Series, ed. M. Iye & A. F. Moorwood, 467–474
Brewer, M.-M. & Carney, B. W. 2006, AJ, 131, 431
Burbidge, E. M., Burbidge, G. R., Fowler, W. A., & Hoyle, F. 1957, Reviews of Modern Physics, 29, 547
Burris, D. L., Pilachowski, C. A., Armandroff, T. E., et al. 2000, ApJ, 544, 302
Busso, M., Gallino, R., & Wasserburg, G. J. 1999, ARA&A, 37, 239
Carrera, R., Gallart, C., Hardy, E., Aparicio, A., & Zinn, R. 2008, AJ, 135, 836
Carretta, E., Gratton, R. G., & Sneden, C. 2000, A&A, 356, 238
Cayrel, R., Depagne, E., Spite, M., et al. 2004, A&A, 416, 1117
Cohen, J. G., Christlieb, N., Qian, Y.-Z., & Wasserburg, G. J. 2003, ApJ, 588, 1082
Cole, A. A., Smecker-Hane, T. A., Tolstoy, E., Bosler, T. L., & Gallagher, J. S. 2004, MNRAS, 347, 367
Cole, A. A., Tolstoy, E., Gallagher, III, J. S., & Smecker-Hane, T. A. 2005, AJ, 129, 1465
Colucci, J. E., Bernstein, R. A., Cameron, S. A., & McWilliam, A. 2012, ApJ, 746, 29
Cristallo, S., Gallino, R., Straniero, O., Piersanti, L., & Domınguez, I. 2006, Mem. Soc. Astron. Italiana, 77, 774
Cristallo, S., Piersanti, L., Straniero, O., et al. 2011, ApJS, 197, 17
Da Costa, G. S. 1991, in IAU Symposium, Vol. 148, The Magellanic Clouds, ed. R. Haynes & D. Milne, 183–+
da Silva, L., Girardi, L., Pasquini, L., et al. 2006, A&A, 458, 609
de Vaucouleurs, G. & Freeman, K. C. 1972, Vistas in Astronomy, 14, 163
Drozdowski, R., Ignaciuk, M., Kwela, J., & Heldt, J. 1988, Z. Phys., 21, 2827
Freiburghaus, C., Rosswog, S., & Thielemann, F.-K. 1999, ApJ, 525, L121
Fuhr, J. R., Martin, G. A., & Wiese, W. L. 1988, Journal of Physical and Chemical Reference Data, 17
Fulbright, J. P. 2000, AJ, 120, 1841
Gallart, C., Stetson, P. B., Meschin, I. P., Pont, F., & Hardy, E. 2008, ApJ, 682, L89
Gilmore, G. & Wyse, R. F. G. 1991, ApJ, 367, L55
Goriely, S. & Mowlavi, N. 2000, A&A, 362, 599
Grevesse, N. & Sauval, A. J. 1998, Space Sci. Rev., 85, 161
Grocholski, A. J., Cole, A. A., Sarajedini, A., Geisler, D., & Smith, V. V. 2006, AJ, 132, 1630
Gustafsson, B., Edvardsson, B., Eriksson, K., et al. 2008, A&A, 486, 951
Harris, J. & Zaritsky, D. 2009, AJ, 138, 1243
Haschke, R., Grebel, E. K., & Duffau, S. 2012a, AJ, 144, 106
Haschke, R., Grebel, E. K., Duffau, S., & Jin, S. 2012b, AJ, 143, 48
Haschke, R., Grebel, E. K., Frebel, A., et al. 2012c, AJ, 144, 88
Hill, V., Andrievsky, S., & Spite, M. 1995, A&A, 293, 347
Hinkle, K., Wallace, L., Valenti, J., & Harmer, D. 2000, Visible and Near Infrared Atlas of the Arcturus Spectrum 3727-9300 A
Johnson, J. A., Ivans, I. I., & Stetson, P. B. 2006, ApJ, 640, 801
Kallivayalil, N., van der Marel, R. P., & Alcock, C. 2006a, ApJ, 652, 1213
Kallivayalil, N., van der Marel, R. P., Alcock, C., et al. 2006b, ApJ, 638, 772
Kupka, F., Piskunov, N., Ryabchikova, T. A., Stempels, H. C., & Weiss, W. W. 1999, A&AS, 138, 119
Kupka, F. G., Ryabchikova, T. A., Piskunov, N. E., Stempels, H. C., & Weiss, W. W. 2000, Baltic Astronomy, 9, 590
Kurucz, R. L. 1988, in Trans. IAU XXB
Kurucz, R. L. 1995, in Astronomical Society of the Pacific Conference Series,

Vol. 78, Astrophysical Applications of Powerful New Databases, ed. S. J. Adelman & W. L. Wiese, 205
Lapenna, E., Mucciarelli, A., Origlia, L., & Ferraro, F. R. 2012, ApJ, 761, 33
Lawler, J. E., Bonvallet, G., & Sneden, C. 2001a, ApJ, 556, 452
Lawler, J. E., Wickliffe, M. E., den Hartog, E. A., & Sneden, C. 2001b, ApJ, 563, 1075
Lebzelter, T., Heiter, U., Abia, C., et al. 2012, ArXiv e-prints
Lecureur, A., Hill, V., Zoccali, M., et al. 2007, A&A, 465, 799
Martin, G. A., Fuhr, J. R., & Wiese, W. L. 1988, Atomic transition probabilities. Scandium through Manganese
McWilliam, A., Preston, G. W., Sneden, C., & Searle, L. 1995, AJ, 109, 2757
Meléndez, J., Asplund, M., Gustafsson, B., & Yong, D. 2009, ApJ, 704, L66
Mishenina, T. V., Kovtyukh, V. V., Soubiran, C., Travaglio, C., & Busso, M. 2002, A&A, 396, 189
Mucciarelli, A., Carretta, E., Origlia, L., & Ferraro, F. R. 2008, AJ, 136, 375
Mucciarelli, A., Origlia, L., & Ferraro, F. R. 2010, ApJ, 717, 277
Nave, G., Johansson, S., Learner, R. C. M., Thorne, A. P., & Brault, J. W. 1994, ApJS, 94, 221
Nissen, P. E., Chen, Y. Q., Schuster, W. J., & Zhao, G. 2000, A&A, 353, 722
Olszewski, E. W., Schommer, R. A., Suntzeff, N. B., & Harris, H. C. 1991, AJ, 101, 515
Pagel, B. E. J. & Tautvaisiene, G. 1998, MNRAS, 299, 535
Pasquini, L., Avila, G., Blecha, A., et al. 2002, The Messenger, 110, 1
Pasquini, L., Randich, S., Zoccali, M., et al. 2004, A&A, 424, 951
Pejcha, O. & Stanek, K. Z. 2009, ApJ, 704, 1730
Pignatari, M., Gallino, R., Heil, M., et al. 2010, ApJ, 710, 1557
Plez, B. 1998, A&A, 337, 495
Pompéia, L., Hill, V., Spite, M., et al. 2008, A&A, 480, 379
Prochaska, J. X. & McWilliam, A. 2000, ApJ, 537, L57
Qian, Y.-Z. 2012, ArXiv e-prints
Ramírez, I. & Allende Prieto, C. 2011, ApJ, 743, 135
Ramírez, I. & Meléndez, J. 2005a, ApJ, 626, 446
Ramírez, I. & Meléndez, J. 2005b, ApJ, 626, 465
Ramírez, I., Meléndez, J., & Asplund, M. 2009, A&A, 508, L17
Reddy, B. E., Lambert, D. L., & Allende Prieto, C. 2006, MNRAS, 367, 1329
Reddy, B. E., Tomkin, J., Lambert, D. L., & Allende Prieto, C. 2003, MNRAS, 340, 304
Rich, R. M., Shara, M. M., & Zurek, D. 2001, AJ, 122, 842
Romano, D. & Matteucci, F. 2007, MNRAS, 378, L59
Russell, S. C. & Bessell, M. S. 1989, ApJS, 70, 865
Rutten, R. J. 1978, Sol. Phys., 56, 237
Shetrone, M., Venn, K. A., Tolstoy, E., et al. 2003, AJ, 125, 684
Simmerer, J., Sneden, C., Cowan, J. J., et al. 2004, ApJ, 617, 1091
Skrutskie, M. F., Cutri, R. M., Stiening, R., et al. 2006, AJ, 131, 1163
Smecker-Hane, T. A., Cole, A. A., Gallagher, III, J. S., & Stetson, P. B. 2002, ApJ, 566, 239
Smiljanic, R. 2012, MNRAS, 422, 1562
Smith, G. 1981, A&A, 103, 351
Smith, G. 1988, Journal of Physics B Atomic Molecular Physics, 21, 2827
Smith, G. & Raggett, D. S. J. 1981, Journal of Physics B Atomic Molecular Physics, 14, 4015
Smith, V. V., Hinkle, K. H., Cunha, K., et al. 2002, AJ, 124, 3241
Smith, V. V., Suntzeff, N. B., Cunha, K., et al. 2000, AJ, 119, 1239
Sneden, C., Cowan, J. J., & Gallino, R. 2008, ARA&A, 46, 241
Stephens, A. & Boesgaard, A. M. 2002, AJ, 123, 1647
Stetson, P. B. & Pancino, E. 2008, PASP, 120, 1332
Subramaniam, A. 2005, A&A, 430, 421
Szymanski, M. K. 2005, Acta Astron., 55, 43
Thielemann, F.-K., Argast, D., Brachwitz, F., et al. 2002, Ap&SS, 281, 25
Timmes, F. X., Brown, E. F., & Truran, J. W. 2003, ApJ, 590, L83
Travaglio, C., Gallino, R., Arnone, E., et al. 2004, ApJ, 601, 864
Tsujimoto, T., Nomoto, K., Yoshii, Y., et al. 1995, MNRAS, 277, 945
Tsujimoto, T. & Shigeyama, T. 2012, ArXiv e-prints
Udalski, A., Kubiak, M., & Szymanski, M. 1997, Acta Astron., 47, 319
Udalski, A., Soszynski, I., Szymanski, M., et al. 1999, Acta Astron., 49, 223
Udalski, A., Szymanski, M., Kubiak, M., et al. 2000, Acta Astron., 50, 307
van der Marel, R. P. 2001, AJ, 122, 1827
van der Marel, R. P., Alves, D. R., Hardy, E., & Suntzeff, N. B. 2002, AJ, 124, 2639
Wanajo, S., Nomoto, K., Iwamoto, N., Ishimaru, Y., & Beers, T. C. 2006, ApJ, 636, 842
Wasserburg, G. J., Busso, M., & Gallino, R. 1996, ApJ, 466, L109
Wiese, W. L., Smith, M. W., & Glennon, B. M. 1966, Atomic transition probabilities. Vol.: Hydrogen through Neon. A critical data compilation
Woosley, S. E. & Weaver, T. A. 1995, ApJS, 101, 181
Worley, C. C., Cottrell, P. L., Freeman, K. C., & Wylie-de Boer, E. C. 2009, MNRAS, 400, 1039
Zaritsky, D. 2004, ApJ, 614, L37
Zaritsky, D., Harris, J., Thompson, I. B., & Grebel, E. K. 2004, AJ, 128, 1606

Table 14. Radial velocities of LMC bar stars. 2MASS identifiers, $v_{\rm rad}$, $\sigma(v_{\rm rad})$, number of independent measurements and S/N ratio for each setup, final mean $v_{\rm rad}$ and its error. Be aware that the table provides $\sigma(v_{\rm rad})$ and not $e_{{\rm rad},s}$. The exponents l, m and h of the S/N ratio indicate respectively whether the spectrum was classified as low, median or high S/N.

2MASS ID	HR11				HR13				HR14				Average	
	$v_{\rm rad}$ km s^{-1}	$\sigma(v_{\rm rad})$ km s^{-1}	#	S/N	$v_{\rm rad}$ km s^{-1}	$\sigma(v_{\rm rad})$ km s^{-1}	#	S/N	$v_{\rm rad}$ km s^{-1}	$\sigma(v_{\rm rad})$ km s^{-1}	#	S/N	$v_{\rm rad}$ km s^{-1}	$e_{\rm rad}$ km s^{-1}
05223082-6944147	250.0	0.1	9	28$^{\rm m}$	250.4	0.1	5	38$^{\rm m}$	249.7	0.1	4	50$^{\rm m}$	250.0	0.1
05223112-6945292	263.1	0.1	9	32$^{\rm m}$	262.9	0.2	5	48$^{\rm m}$	262.5	0.2	4	59$^{\rm m}$	262.9	0.1
05223186-6947159	271.2	0.1	9	25$^{\rm m}$	271.7	0.2	5	36$^{\rm m}$	271.2	0.1	4	43$^{\rm m}$	271.3	0.1
05223309-6946595	258.3	0.1	9	35$^{\rm h}$	258.2	0.5	5	45$^{\rm m}$	258.1	0.1	4	51$^{\rm m}$	258.3	0.2
05223316-6951389	220.9	0.3	8	19$^{\rm m}$	219.3	0.4	5	27$^{\rm m}$	219.1	0.2	4	38$^{\rm m}$	219.7	0.2
05223318-6937044	259.9	0.1	8	20$^{\rm m}$	260.4	0.2	5	29$^{\rm m}$	259.5	0.3	4	32$^{\rm l}$	259.9	0.1
05223416-6944433	230.8	0.4	9	28$^{\rm m}$	230.4	0.5	5	45$^{\rm m}$	229.9	0.1	4	50$^{\rm m}$	230.3	0.2
05223487-6938057	217.0	0.1	9	22$^{\rm m}$	217.2	0.2	5	31$^{\rm m}$	216.8	0.1	4	29$^{\rm l}$	217.0	0.1
05223506-6937279	268.2	0.1	9	25$^{\rm m}$	268.5	0.1	5	37$^{\rm m}$	267.5	0.3	4	40$^{\rm m}$	268.2	0.1
05223557-6943373	226.9	0.4	9	24$^{\rm m}$	225.6	0.1	5	38$^{\rm m}$	225.7	0.2	4	42$^{\rm m}$	225.9	0.2
05223701-6936166	263.4	0.1	9	30$^{\rm m}$	263.7	0.2	5	42$^{\rm m}$	263.2	0.3	4	44$^{\rm m}$	263.5	0.1
05223787-6954562	260.1	0.1	8	16$^{\rm l}$	259.6	0.2	5	26$^{\rm l}$	259.2	0.2	4	40$^{\rm m}$	259.8	0.1
05223895-6945007	228.3	0.1	9	36$^{\rm h}$	228.3	0.1	5	51$^{\rm h}$	228.0	0.2	4	59$^{\rm m}$	228.2	0.1
05223988-6946110	232.2	0.1	9	31$^{\rm m}$	232.3	0.1	5	45$^{\rm m}$	232.0	0.2	4	54$^{\rm m}$	232.2	0.1
05224062-6953310	240.9	0.1	9	25$^{\rm m}$	241.1	0.2	5	30$^{\rm m}$	240.6	0.1	4	38$^{\rm m}$	240.9	0.1
05224164-6935518	268.0	0.1	8	15$^{\rm l}$	267.4	0.1	5	30$^{\rm m}$	267.6	0.1	4	35$^{\rm m}$	267.8	0.1
05224195-6941099	291.9	0.1	9	27$^{\rm m}$	292.0	0.1	5	40$^{\rm m}$	291.8	0.1	4	47$^{\rm m}$	291.9	0.1
05224240-6940567	276.3	0.1	9	33$^{\rm h}$	276.1	0.1	5	46$^{\rm m}$	276.1	0.2	4	51$^{\rm m}$	276.2	0.1
05224276-6940109	250.8	0.1	9	33$^{\rm h}$	251.5	0.1	5	50$^{\rm m}$	250.6	0.1	4	54$^{\rm m}$	251.0	0.1
05224309-6940275	314.1	1.6	9	27$^{\rm m}$	309.8	1.6	5	38$^{\rm m}$	308.7	0.1	4	41$^{\rm m}$	308.9	0.3
05224321-6952397	232.8	0.1	9	22$^{\rm m}$	233.3	0.2	5	33$^{\rm m}$	232.6	0.1	4	41$^{\rm m}$	232.9	0.1
05224448-6954402	243.8	1.7	9	20$^{\rm m}$	262.2	3.6	5	22$^{\rm l}$	264.7	0.6	4	26$^{\rm l}$	262.5	0.5
05224854-6940010	231.3	0.2	8	16$^{\rm l}$	232.0	0.1	5	28$^{\rm m}$	231.1	0.1	4	31$^{\rm l}$	231.5	0.2
05225062-6936580	265.9	0.1	9	23$^{\rm m}$	265.9	0.1	5	39$^{\rm m}$	265.7	0.1	4	46$^{\rm m}$	265.8	0.1
05225069-6955486	274.3	0.2	8	17$^{\rm m}$	273.7	0.1	5	20$^{\rm l}$	273.6	0.2	4	29$^{\rm l}$	274.0	0.1
05225632-6942269	296.6	0.5	9	29$^{\rm m}$	296.3	0.1	5	43$^{\rm m}$	296.2	0.2	4	45$^{\rm m}$	296.3	0.2
05225877-6938172	225.7	0.1	9	18$^{\rm m}$	226.4	0.2	5	28$^{\rm m}$	225.7	0.2	4	32$^{\rm l}$	225.9	0.1
05225980-6954368	234.9	0.2	8	13$^{\rm l}$	235.9	0.4	5	17$^{\rm l}$	234.5	0.2	4	25$^{\rm l}$	234.9	0.2
05230009-6935251	293.8	0.1	9	24$^{\rm m}$	294.3	0.2	5	39$^{\rm m}$	293.9	0.2	4	42$^{\rm m}$	293.9	0.1
05230011-6946353	249.2	0.2	9	25$^{\rm m}$	249.0	0.2	5	35$^{\rm m}$	248.8	0.2	4	45$^{\rm m}$	249.1	0.1
05230203-6935557	258.5	0.4	9	22$^{\rm m}$	258.4	0.2	5	32$^{\rm m}$	258.7	0.1	4	36$^{\rm m}$	258.5	0.2
05230230-6939587	285.5	0.1	9	27$^{\rm m}$	285.3	0.1	5	44$^{\rm m}$	285.2	0.2	4	50$^{\rm m}$	285.4	0.1
05230353-6952441	344.7	0.1	9	27$^{\rm m}$	344.9	0.1	5	41$^{\rm m}$	344.7	0.2	4	49$^{\rm m}$	344.8	0.1
05230370-6944219	278.8	0.4	8	23$^{\rm m}$	279.0	0.3	5	41$^{\rm m}$	278.2	0.3	4	48$^{\rm m}$	278.7	0.2
05230589-6944122	257.0	0.2	9	40$^{\rm h}$	256.9	0.2	5	59$^{\rm h}$	257.0	0.2	4	66$^{\rm h}$	257.0	0.1
05230606-6951113	280.8	0.2	9	24$^{\rm m}$	281.0	0.2	5	40$^{\rm m}$	280.6	0.1	4	52$^{\rm m}$	280.8	0.1
05230647-6944394	236.0	0.5	8	25$^{\rm m}$	235.9	0.1	5	41$^{\rm m}$	235.5	0.2	4	48$^{\rm m}$	235.8	0.2
05230776-6946082	279.7	0.7	9	35$^{\rm h}$	279.4	1.5	5	54$^{\rm h}$	277.8	0.2	4	59$^{\rm m}$	278.1	0.3
05230867-6956329	266.6	0.2	7	10$^{\rm l}$	262.7	0.5	5	13$^{\rm l}$	262.5	0.2	4	21$^{\rm l}$	264.8	0.2
05231074-6939184	201.2	0.2	9	29$^{\rm m}$	204.1	0.2	5	47$^{\rm m}$	203.7	0.1	4	48$^{\rm m}$	202.6	0.1
05231091-6942374	248.9	0.5	9	35$^{\rm h}$	254.4	1.7	5	54$^{\rm h}$	253.4	0.4	4	63$^{\rm h}$	251.9	0.3
05231221-6938166	280.7	0.1	9	27$^{\rm m}$	281.0	0.1	5	48$^{\rm m}$	280.4	0.2	4	54$^{\rm m}$	280.7	0.1
05231315-6945212	283.6	0.2	8	15$^{\rm l}$	283.4	0.0	5	31$^{\rm m}$	283.1	0.1	4	44$^{\rm m}$	283.4	0.1
05231321-6946382	270.6	0.1	9	29$^{\rm m}$	270.6	0.2	5	51$^{\rm h}$	270.4	0.1	3	56$^{\rm m}$	270.5	0.1
05231411-6948546	309.7	0.2	6	26$^{\rm m}$	309.8	0.1	5	48$^{\rm m}$	309.3	0.1	4	58$^{\rm m}$	309.6	0.2
05231484-6950196	266.8	0.1	9	26$^{\rm m}$	266.7	0.1	5	39$^{\rm m}$	266.1	0.2	4	45$^{\rm m}$	266.6	0.1
05231562-6955430	311.9	0.1	9	24$^{\rm m}$	312.0	0.1	5	38$^{\rm m}$	311.5	0.1	4	52$^{\rm m}$	311.8	0.1
05231631-6942507	281.4	0.1	9	24$^{\rm m}$	281.6	0.1	5	50$^{\rm m}$	281.3	0.0	4	57$^{\rm m}$	281.4	0.1
05231634-6951332	260.0	0.1	9	22$^{\rm m}$	260.3	0.3	5	39$^{\rm m}$	260.2	0.2	4	47$^{\rm m}$	260.1	0.1
05231962-6943309	260.0	0.1	9	24$^{\rm m}$	260.7	0.2	5	41$^{\rm m}$	260.3	0.3	4	53$^{\rm m}$	260.3	0.1
05232020-6954561	223.2	0.1	9	36$^{\rm h}$	223.9	0.1	5	47$^{\rm m}$	223.9	0.2	4	63$^{\rm h}$	223.5	0.1
05232148-6952155	287.5	0.1	9	29$^{\rm m}$	287.7	0.1	5	48$^{\rm m}$	287.5	0.2	4	59$^{\rm m}$	287.6	0.1
05232181-6945429	277.4	0.1	9	27$^{\rm m}$	277.7	0.2	5	46$^{\rm m}$	277.5	0.1	4	53$^{\rm m}$	277.5	0.1
05232554-6943388	227.5	0.1	9	27$^{\rm m}$	226.9	0.1	5	45$^{\rm m}$	226.7	0.1	4	51$^{\rm m}$	227.2	0.1
05232624-6943558	221.3	0.1	9	26$^{\rm m}$	221.4	0.3	5	45$^{\rm m}$	221.0	0.1	4	50$^{\rm m}$	221.2	0.1
05232680-6953109	268.0	0.1	9	29$^{\rm m}$	268.0	0.2	5	45$^{\rm m}$	267.9	0.2	4	51$^{\rm m}$	268.0	0.1
05232845-6944158	275.5	0.1	9	33$^{\rm h}$	276.4	0.1	5	55$^{\rm h}$	275.6	0.1	4	65$^{\rm h}$	275.8	0.1
05232892-6947486	264.9	0.1	9	25$^{\rm m}$	265.3	0.2	5	44$^{\rm m}$	265.0	0.1	4	53$^{\rm m}$	265.0	0.1
05233236-6948257	224.0	0.2	9	18$^{\rm m}$	224.7	0.2	5	33$^{\rm m}$	224.4	0.3	4	34$^{\rm l}$	224.3	0.1
05235653-6947387	244.1	0.2	9	31$^{\rm m}$	244.2	0.1	5	48$^{\rm m}$	243.7	0.1	4	48$^{\rm m}$	244.0	0.1
05235851-6945519	286.7	0.1	9	30$^{\rm m}$	286.8	0.1	5	52$^{\rm h}$	286.3	0.1	4	58$^{\rm m}$	286.6	0.1
05240317-6953036	265.5	0.2	9	21$^{\rm m}$	265.0	0.1	5	31$^{\rm m}$	265.0	0.2	4	40$^{\rm m}$	265.3	0.1
05240482-6948280	222.1	0.6	9	23$^{\rm m}$	230.7	1.8	5	38$^{\rm m}$	229.9	0.3	4	44$^{\rm m}$	228.5	0.3
05240604-6942380	255.3	0.2	8	16$^{\rm l}$	258.2	0.2	5	32$^{\rm m}$	258.1	0.1	4	39$^{\rm m}$	257.0	0.2
05240613-6953529	217.7	0.4	9	24$^{\rm m}$	215.8	0.2	5	33$^{\rm m}$	216.1	0.4	4	42$^{\rm m}$	216.3	0.2
05240672-6947130	280.4	0.1	9	19$^{\rm m}$	280.6	0.1	5	35$^{\rm m}$	280.1	0.2	4	44$^{\rm m}$	280.4	0.1
05240803-6956250	230.1	0.1	9	22$^{\rm m}$	230.2	0.2	5	26$^{\rm l}$	230.1	0.2	4	36$^{\rm m}$	230.1	0.1

Continued on next page

2MASS ID	HR11				HR13				HR14				Average	
	$v_{\rm rad}$ km s^{-1}	$\sigma(v_{\rm rad})$ km s^{-1}	#	S/N	$v_{\rm rad}$ km s^{-1}	$\sigma(v_{\rm rad})$ km s^{-1}	#	S/N	$v_{\rm rad}$ km s^{-1}	$\sigma(v_{\rm rad})$ km s^{-1}	#	S/N	$v_{\rm rad}$ km s^{-1}	$e_{\rm rad}$ km s^{-1}
05240830-6944428	282.6	0.1	9	33^{h}	283.1	0.3	5	55^{h}	282.6	0.1	4	64^{h}	282.7	0.1
05241033-6944374	292.2	0.1	9	25^{m}	292.5	0.2	5	46^{m}	292.1	0.1	4	54^{m}	292.3	0.1
05241341-6945303	248.9	0.1	9	26^{m}	249.4	0.2	5	46^{m}	249.1	0.1	4	59^{m}	249.1	0.1
05241479-6946323	262.9	0.1	9	35^{h}	263.5	0.3	5	51^{h}	263.2	0.1	4	61^{h}	263.2	0.1
05241699-6942158	251.6	0.2	9	26^{m}	251.9	0.1	5	46^{m}	251.4	0.1	4	55^{m}	251.6	0.1
05241794-6951317	277.0	0.1	9	19^{m}	277.0	0.1	5	31^{m}	276.6	0.1	4	40^{m}	276.9	0.1
05242161-6942097	259.7	0.1	9	27^{m}	260.3	0.1	5	48^{m}	259.5	0.1	4	56^{m}	259.8	0.1
05242198-6943579	251.4	0.2	3	16^{l}	250.4	0.4	2	33^{m}	249.8	0.1	4	63^{h}	250.5	0.2
05242240-6944344	230.5	0.2	9	31^{m}	230.3	0.1	5	52^{h}	229.9	0.1	4	60^{m}	230.3	0.1
05242409-6942051	259.0	0.1	9	30^{m}	258.8	0.2	5	51^{h}	258.6	0.1	4	62^{h}	258.8	0.1
05242542-6955188	244.3	0.1	9	26^{m}	244.2	0.3	5	35^{m}	243.9	0.2	4	46^{m}	244.2	0.1
05242687-6943577	263.9	0.1	9	41^{h}	264.2	0.1	5	61^{h}	263.9	0.1	4	67^{h}	264.0	0.1
05242702-6956445	243.8	0.2	8	15^{l}	243.3	0.1	5	23^{l}	243.0	0.1	4	31^{l}	243.4	0.1
05242811-6947467	287.1	0.1	9	27^{m}	287.1	0.2	5	46^{m}	286.9	0.0	4	47^{m}	287.0	0.1
05243272-6955362	273.7	0.1	9	27^{m}	274.1	0.2	5	36^{m}	273.9	0.1	4	49^{m}	273.9	0.1
05243734-6945496	241.9	0.1	9	21^{m}	241.9	0.1	5	36^{m}	241.3	0.1	4	42^{m}	241.8	0.1
05243901-6948426	257.7	0.1	8	29^{m}	258.4	0.2	5	45^{m}	258.1	0.2	4	62^{h}	258.0	0.1
05244189-6954427	241.6	0.1	9	19^{m}	241.7	0.2	5	25^{l}	241.4	0.1	4	36^{m}	241.6	0.1
05244210-6942596	267.6	0.2	8	13^{l}	267.4	0.2	5	28^{m}	267.0	0.2	4	36^{m}	267.4	0.1
05244301-6943412	300.8	0.4	9	37^{h}	299.9	0.4	5	59^{h}	299.3	0.5	4	73^{h}	300.1	0.2
05244340-6950004	295.1	0.1	9	20^{m}	295.3	0.2	5	33^{m}	294.9	0.1	4	41^{m}	295.1	0.1
05244408-6942423	303.0	0.2	9	25^{m}	302.5	0.2	5	46^{m}	302.6	0.1	4	55^{m}	302.8	0.1
05244600-6946017	224.2	0.1	9	22^{m}	225.2	0.2	5	37^{m}	224.8	0.1	4	46^{m}	224.6	0.1
05244637-6947340	257.6	0.2	9	27^{m}	257.8	0.1	5	42^{m}	257.4	0.2	4	53^{m}	257.6	0.1
05244698-6956141	231.6	0.1	9	19^{m}	231.9	0.2	5	24^{l}	231.5	0.2	4	35^{m}	231.7	0.1
05244878-6948359	235.7	0.1	9	33^{h}	236.7	0.1	5	49^{m}	236.4	0.2	4	59^{m}	236.1	0.1
05244976-6943230	272.0	0.1	9	30^{m}	272.4	0.2	5	53^{h}	272.1	0.1	4	63^{h}	272.1	0.1
05245212-6948184	272.7	0.1	9	25^{m}	273.0	0.1	5	40^{m}	272.8	0.1	4	48^{m}	272.8	0.1
05245859-6952257	196.8	0.2	9	19^{m}	196.9	0.3	5	30^{m}	196.8	0.2	4	37^{m}	196.8	0.2
05252428-6939311	261.9	0.1	9	22^{m}	262.1	0.2	5	41^{m}	261.7	0.1	4	54^{m}	261.9	0.1
05252899-6939078	254.8	0.1	9	20^{m}	255.4	0.2	5	33^{m}	254.9	0.2	4	46^{m}	255.0	0.1
05253039-6940288	272.9	0.1	9	20^{m}	273.0	0.2	5	39^{m}	272.6	0.2	4	47^{m}	272.8	0.1
05253040-6936261	288.1	0.2	9	23^{m}	287.8	0.1	5	33^{m}	287.7	0.1	4	43^{m}	287.9	0.1
05253235-6943137	279.1	0.8	9	21^{m}	277.6	0.2	5	39^{m}	276.3	0.4	4	44^{m}	277.3	0.2
05253522-6937078	284.4	0.1	9	26^{m}	284.5	0.2	5	31^{m}	284.2	0.1	4	43^{m}	284.4	0.1
05254540-6940531	269.3	0.9	9	20^{m}	286.8	0.6	5	31^{m}	286.7	0.1	4	41^{m}	285.1	0.3
05254864-6940501	248.2	0.1	9	21^{m}	248.5	0.1	5	40^{m}	248.0	0.1	4	51^{m}	248.2	0.1
05255000-6942466	244.0	0.1	9	28^{m}	244.5	0.2	5	42^{m}	243.8	0.1	4	55^{m}	244.1	0.1
05255267-6943155	270.5	0.1	9	27^{m}	270.7	0.3	5	46^{m}	270.2	0.1	4	60^{m}	270.5	0.1
05255625-6941243	287.6	0.1	9	30^{m}	287.0	0.1	5	41^{m}	287.0	0.1	4	51^{m}	287.3	0.1
05255801-6937309	257.5	0.1	9	22^{m}	256.9	0.2	5	32^{m}	256.4	0.1	4	45^{m}	257.1	0.1
05255812-6942522	250.2	0.1	9	21^{m}	250.0	0.1	5	26^{l}	249.7	0.1	4	35^{m}	250.1	0.1
05260124-6939268	289.6	0.1	9	23^{m}	290.1	0.3	5	34^{m}	289.4	0.1	4	46^{m}	289.7	0.1
05260720-6942342	291.5	0.2	9	17^{m}	292.2	0.4	5	24^{l}	291.5	0.1	4	33^{l}	291.6	0.2
05260784-6938341	241.2	0.1	9	20^{m}	242.0	0.4	5	30^{m}	241.6	0.2	4	40^{m}	241.4	0.2
05261339-6940590	269.9	0.1	9	24^{m}	270.6	0.1	5	38^{m}	270.3	0.1	4	54^{m}	270.2	0.1

Table 15. Photometry and Cat metallicity of LMC bar stars. 2MASS identifiers, V, (V – I), (V – J), (V – H) and (V – K) (Udalski et al. 1997, 2000; Szymanski 2005) and $[Fe/H]_{CaT}$ (Cole et al. 2005). Errors are provided for each quantity.

2MASS ID	V	e(V)	V – I	e(V – I)	V – J	e(V – J)	V – H	e(V – H)	V – K	e(V – K)	$[Fe/H]_{CaT}$	$e([Fe/H]_{CaT})$
	mag	mag	mag	mag	mag	mag	mag	mag	mag	mag	dex	dex
05223082-6944147	17.228	0.031	1.554	0.038	2.702	0.053	3.519	0.053	3.663	0.052	-0.14	0.14
05223112-6945292	17.163	0.021	1.584	0.025	2.729	0.051	3.524	0.059	3.676	0.050	-0.41	0.14
05223186-6947159	17.450	0.030	1.385	0.037	2.349	0.064	3.129	0.066	3.323	0.085	-0.35	0.14
05223309-6946595	17.106	0.037	1.342	0.041	2.268	0.061	3.027	0.070	2.945	0.094	-0.40	0.14
05223316-6951389	17.664	0.024	1.347	0.031	2.204	0.078	3.008	0.078	3.091	0.120	-1.69	0.15
05223318-6937044	17.492	0.024	1.311	0.030	2.228	0.066	2.950	0.070	3.042	0.109	-0.18	0.14
05223416-6944433	17.411	0.046	1.242	0.049	1.969	0.097	2.600	0.108	2.856	0.113	-1.05	0.12
05223487-6938057	17.455	0.017	1.394	0.022	2.247	0.066	3.155	0.085	3.199	0.087	-0.37	0.13
05223506-6937279	17.372	0.039	1.486	0.044	2.472	0.069	3.264	0.070	3.339	0.084	-0.34	0.14
05223557-6943373	17.439	0.023	1.182	0.027	1.952	0.088	2.658	0.101	2.789	0.138	-1.28	0.11
05223701-6936166	16.898	0.031	1.179	0.033	2.013	0.057	2.518	0.066	2.780	0.092	-0.35	0.14
05223787-6954562	17.487	0.019	1.651	0.025	2.799	0.052	3.599	0.052	3.773	0.064	+0.14	0.15
05223895-6945007	16.976	0.013	1.388	0.019	2.345	0.035	3.111	0.042	3.332	0.059	-0.42	0.14
05223988-6946110	16.992	0.013	1.458	0.018	2.450	0.039	3.305	0.043	3.423	0.054	-0.51	0.13
05224062-6953310	17.350	0.016	1.476	0.022	2.603	0.050	3.335	0.062	3.451	0.065	-0.35	0.14
05224164-6935518	17.590	0.013	1.373	0.018	2.165	0.071	3.067	0.080	3.524	NaN	-0.30	0.14
05224195-6941099	17.316	0.014	1.448	0.021	2.481	0.053	3.342	0.070	3.266	0.073	-0.31	0.14
05224240-6940567	16.917	0.021	0.960	0.028	1.604	0.087	2.160	0.093	2.280	0.123	-0.28	0.14
05224276-6940109	16.986	0.016	1.318	0.020	2.245	0.048	3.020	0.053	3.160	0.065	-0.58	0.13
05224309-6940275	17.266	0.025	1.477	0.030	2.570	0.045	3.363	0.050	3.367	0.067	-0.28	0.14
05224321-6952397	17.392	0.016	1.399	0.020	2.380	0.063	3.124	0.059	3.267	0.083	-0.40	0.15
05224448-6954402	17.482	0.020	1.155	0.026	2.132	0.057	2.775	0.088	2.912	0.107	-0.92	0.13
05224854-6940010	17.984	0.017	1.526	0.021	2.583	0.076	3.494	0.076	3.616	0.108	-0.05	0.15
05225062-6936580	17.334	0.021	1.245	0.028	2.234	0.072	2.861	0.073	3.027	0.092	-0.36	0.14
05225069-6955486	17.438	0.031	1.500	0.034	2.584	0.053	3.308	0.064	3.529	0.071	-0.30	0.14
05225632-6942269	17.151	0.015	1.177	0.021	2.023	0.063	2.718	0.076	2.767	0.096	-1.19	0.13
05225877-6938172	17.536	0.023	1.181	0.027	1.988	0.086	2.673	0.128	3.092	NaN	-0.48	0.14
05225980-6954368	17.893	0.021	1.473	0.027	2.536	0.072	3.425	0.064	3.461	0.108	-0.96	0.12
05230009-6935251	17.234	0.016	1.426	0.021	2.427	0.053	3.173	0.055	3.276	0.063	-0.20	0.15
05230011-6946353	17.240	0.012	0.930	0.017	1.701	0.061	2.065	0.119	2.287	0.155	-0.44	0.14
05230203-6935557	17.252	0.017	1.255	0.021	2.105	0.067	2.836	0.058	2.932	0.089	-1.10	0.11
05230230-6939587	17.293	0.017	1.362	0.022	2.510	0.086	3.238	0.090	3.381	0.086	-0.57	0.13
05230353-6952441	17.350	0.019	1.499	0.024	2.641	0.062	3.405	0.053	3.504	0.067	-0.33	0.14
05230370-6944219	17.600	0.027	1.344	0.035	2.331	0.076	3.183	0.106	3.201	0.123	-1.41	0.11
05230589-6944122	16.696	0.015	1.106	0.021	1.935	0.065	2.471	0.080	2.464	0.100	-0.50	0.13
05230606-6951113	17.742	0.067	1.757	0.069	2.939	0.080	3.739	0.079	3.871	0.091	-0.16	0.14
05230647-6944394	17.282	0.022	1.070	0.029	1.908	0.072	2.466	0.073	2.625	0.118	-1.55	0.10
05230776-6946082	16.964	0.015	1.242	0.019	2.112	0.049	2.770	0.053	2.924	0.077	-1.10	0.12
05230867-6956329	18.028	0.017	1.287	0.024	2.138	0.104	3.115	0.088	3.345	NaN	-0.44	0.14
05231074-6939184	16.980	0.014	1.260	0.018	2.271	0.047	2.886	0.050	2.940	0.077	-1.33	0.11
05231091-6942374	16.910	0.015	1.285	0.019	2.422	0.067	3.099	0.063	3.160	0.059	-0.46	0.13
05231221-6938166	17.182	0.016	1.228	0.021	2.317	0.052	2.878	0.052	2.956	0.083	-0.05	0.15
05231315-6945212	17.212	0.016	1.189	0.021	2.156	0.102	2.802	0.094	2.972	0.100	-0.50	0.13
05231321-6946382	17.128	0.017	1.540	0.020	2.685	0.046	3.431	0.045	3.666	0.059	-0.34	0.14
05231411-6948546	17.169	0.025	1.673	0.029	2.926	0.044	3.712	0.038	3.863	0.047	-0.28	0.14
05231484-6950196	17.439	0.016	1.331	0.020	2.322	0.053	3.069	0.069	3.120	0.089	-0.31	0.16
05231562-6955430	17.275	0.024	1.601	0.029	2.729	0.078	3.587	0.069	3.709	0.083	-0.34	0.14
05231631-6942507	17.153	0.015	1.390	0.018	2.473	0.047	3.153	0.051	3.321	0.064	-0.31	0.14
05231634-6951332	17.612	0.045	1.440	0.048	2.313	0.123	3.177	0.099	3.137	0.127	-0.46	0.13
05231962-6943309	17.227	0.012	0.980	0.017	1.684	0.097	2.113	0.106	2.599	NaN	-0.48	0.14
05232020-6954561	16.881	0.020	1.578	0.026	2.694	0.068	3.474	0.064	3.625	0.070	-0.44	0.14
05232148-6952155	17.284	0.018	1.514	0.022	2.541	0.053	3.422	0.041	3.537	0.062	-0.36	0.14
05232181-6945429	17.329	0.013	1.289	0.018	2.196	0.066	2.867	0.072	3.205	0.080	-0.58	0.13
05232554-6943388	17.293	0.019	1.151	0.022	1.974	0.066	2.801	0.064	2.814	0.100	-0.52	0.14
05232624-6943558	17.278	0.019	1.425	0.022	2.402	0.062	3.758	NaN	3.985	NaN	-0.29	0.14
05232680-6953109	17.282	0.013	1.301	0.021	2.130	0.052	2.909	0.057	2.965	0.086	-1.42	0.13
05232845-6944158	17.226	0.017	1.442	0.023	2.500	0.058	3.181	0.059	3.271	0.078	-0.20	0.14
05232892-6947486	17.342	0.028	1.372	0.033	2.279	0.063	3.078	0.058	3.057	0.095	-0.48	0.13
05233236-6948257	17.749	0.027	1.262	0.035	2.234	0.082	2.915	0.084	3.281	0.107	-1.04	0.12
05235653-6947387	16.933	0.024	1.183	0.029	2.065	0.069	2.754	0.055	2.643	0.086	-0.58	0.15
05235851-6945519	17.321	0.019	1.439	0.022	2.522	0.051	3.212	0.073	3.412	0.084	-0.23	0.15
05240317-6953036	17.723	0.018	1.296	0.022	2.191	0.070	2.896	0.080	3.181	0.105	-0.36	0.14
05240482-6948280	17.536	0.025	1.313	0.038	2.127	0.087	2.931	0.077	3.019	0.106	-0.55	0.14
05240604-6942380	18.082	0.017	1.630	0.021	2.686	0.067	3.661	0.063	3.778	0.091	-0.23	0.15
05240613-6953529	17.538	0.022	1.143	0.026	2.148	0.064	2.655	0.080	2.793	0.124	-1.59	0.11
05240672-6947130	17.642	0.030	1.279	0.034	2.164	0.088	2.760	0.096	3.009	0.132	-0.29	0.14
05240803-6956250	17.387	0.011	1.410	0.015	2.403	0.049	3.053	0.048	3.246	0.075	-0.28	0.14
05240830-6944428	17.140	0.029	1.556	0.035	2.671	0.046	3.476	0.046	3.606	0.055	-0.39	0.14
05241033-6944374	17.405	0.018	1.417	0.025	2.487	0.076	3.235	0.076	3.418	0.085	-0.29	0.14
05241341-6945303	17.285	0.014	1.394	0.019	2.419	0.058	3.236	0.052	3.209	0.076	-0.51	0.14
05241479-6946323	16.997	0.014	1.030	0.018	1.737	0.064	2.144	0.093	2.353	0.120	-0.30	0.14

Continued on next page

2MASS ID	V	e(V)	V − I	e(V − I)	V − J	e(V − J)	V − H	e(V − H)	V − K	e(V − K)	[Fe/H]$_{CaT}$	e([Fe/H]$_{CaT}$)
	mag	mag	mag	mag	mag	mag	mag	mag	mag	mag	dex	dex
05241699-6942158	17.366	0.016	1.389	0.021	2.364	0.050	3.108	0.047	3.113	0.079	-0.21	0.14
05241794-6951317	17.748	0.027	1.346	0.036	2.459	0.072	3.230	0.064	3.240	0.107	-0.25	0.14
05242161-6942097	17.321	0.016	1.421	0.020	2.326	0.059	3.188	0.055	3.263	0.065	-0.57	0.14
05242198-6943579	17.231	0.015	1.472	0.020	2.575	0.045	3.313	0.046	3.523	0.059	-0.22	0.14
05242240-6944344	17.281	0.018	1.517	0.025	2.547	0.047	3.430	0.040	3.500	0.062	-0.34	0.14
05242409-6942051	17.138	0.019	1.467	0.022	2.577	0.055	3.267	0.060	3.398	0.073	-0.42	0.14
05242542-6955188	17.188	0.026	1.296	0.030	2.140	0.080	2.847	0.074	3.139	0.080	-0.42	0.13
05242687-6943577	16.730	0.015	1.110	0.020	1.880	0.046	2.467	0.052	2.404	0.091	-0.33	0.14
05242702-6956445	17.606	0.013	1.373	0.018	2.196	0.100	3.041	0.091	3.164	0.117	-0.54	0.13
05242811-6947467	17.302	0.017	1.375	0.023	2.376	0.059	3.149	0.050	3.213	0.078	-0.46	0.14
05243272-6955362	17.044	0.019	1.489	0.024	2.593	0.040	3.269	0.050	3.520	0.053	-0.58	0.13
05243734-6945496	17.641	0.015	1.261	0.022	1.907	0.122	2.929	0.079	2.757	0.155	-0.26	0.15
05243901-6948426	17.006	0.015	1.288	0.020	2.460	NaN	2.849	0.069	3.079	NaN	-0.54	0.13
05244189-6954427	17.644	0.021	1.343	0.027	2.187	0.080	2.997	0.078	2.962	0.119	-0.35	0.14
05244210-6942596	17.787	0.017	1.259	0.021	2.161	0.090	2.723	0.111	2.909	NaN	-0.69	0.13
05244301-6943412	16.825	0.017	1.256	0.021	2.149	0.042	2.791	0.043	2.851	0.061	-1.54	0.10
05244340-6950004	17.708	0.016	1.391	0.020	2.283	0.079	3.206	0.057	3.264	0.091	-0.13	0.16
05244408-6942423	16.967	0.011	1.161	0.016	2.031	0.049	2.659	0.055	2.684	0.082	-1.19	0.12
05244600-6946017	17.507	0.020	1.366	0.024	2.241	0.064	2.917	0.082	3.227	0.092	-0.24	0.15
05244637-6947340	17.283	0.013	1.183	0.019	1.882	0.071	2.597	0.075	2.698	0.104	-0.47	0.14
05244698-6956141	17.564	0.016	1.442	0.019	2.406	0.061	3.079	0.057	3.118	0.093	-0.32	0.14
05244878-6948359	17.121	0.018	1.440	0.022	2.400	0.037	3.234	0.058	3.282	0.057	-0.25	0.14
05244976-6943230	17.201	0.014	1.470	0.018	2.569	0.049	3.308	0.055	3.406	0.055	-0.49	0.13
05245212-6948184	17.379	0.025	1.364	0.032	2.309	0.089	2.929	0.067	3.164	0.074	-0.36	0.15
05245859-6952257	17.686	0.014	1.290	0.021	1.986	0.083	2.790	0.084	3.061	0.107	-0.68	0.13
05252428-6939311	17.265	0.010	1.473	0.015	2.504	0.037	3.249	0.031	3.543	0.051	-0.12	0.14
05252899-6939078	17.347	0.013	1.134	0.018	1.983	0.066	2.506	0.082	2.645	0.117	-0.43	0.14
05253039-6940288	17.432	0.017	1.297	0.023	2.236	0.052	2.882	0.063	3.117	0.073	-0.29	0.14
05253040-6936261	17.314	0.014	1.392	0.020	2.499	0.061	3.238	0.053	3.428	0.066	-0.70	0.12
05253235-6943137	17.298	0.012	1.160	0.021	2.007	0.073	2.658	0.073	2.777	0.107	-1.64	0.12
05253522-6937078	17.153	0.014	1.389	0.021	2.471	0.049	3.201	0.044	3.290	0.057	-0.47	0.19
05254540-6940531	17.563	0.027	1.301	0.032	2.260	0.064	3.012	0.063	3.012	0.104	-0.21	0.14
05254864-6940501	17.426	0.016	1.410	0.024	2.475	0.074	3.119	0.075	3.442	0.072	-0.41	0.14
05255000-6942466	17.254	0.034	1.597	0.038	2.567	0.067	3.368	0.062	3.460	0.069	-0.37	0.14
05255267-6943155	17.137	0.017	1.561	0.021	2.698	0.046	3.495	0.042	3.587	0.044	-0.18	0.14
05255625-6941243	16.912	0.011	1.068	0.019	1.926	0.051	2.496	0.050	2.528	0.096	-0.49	0.14
05255801-6937309	17.163	0.018	1.518	0.023	2.613	0.054	3.378	0.061	3.459	0.066	-0.30	0.14
05255812-6942522	17.588	0.025	1.405	0.027	2.447	0.061	3.016	0.062	3.160	0.092	-0.10	0.15
05260124-6939268	17.278	0.014	1.370	0.017	2.323	0.047	3.156	0.040	3.375	0.064	-0.62	0.13
05260720-6942342	17.435	0.017	1.105	0.024	1.818	0.085	2.599	0.079	2.650	0.121	-0.61	0.13
05260784-6938341	17.209	0.032	1.445	0.035	2.552	0.059	3.266	0.054	3.547	0.062	-0.56	0.13
05261339-6940590	17.150	0.019	1.647	0.025	2.817	0.040	3.591	0.033	3.813	0.043	-0.04	0.15

Table 16. Stellar parameters of LMC bar stars. 2MASS identifiers, $T_{\rm phot}$, $\log g$, [M/H], $\xi_{\rm micro}$, [Fe I/H], [Fe II/H]. Errors are given for each quantity.

2MASS ID	$T_{\rm phot}$	$\sigma(T_{\rm phot})$	$\log g$	$\sigma(\log g)$	[M/H]	σ([M/H])	$\xi_{\rm micro}$	$\sigma(\xi_{\rm micro})$	[Fe I/H]	σ([Fe I/H])	[Fe II/H]	σ([Fe II/H])
	K	K			dex	dex	km s^{-1}	dex	dex	dex	dex	
05223082-6944147	4070	102	0.98	0.15	-0.49	0.10	1.80	0.15	-0.48	0.04	-0.49	0.15
05223112-6945292	4025	98	0.85	0.14	-0.71	0.10	1.80	0.15	-0.71	0.03	-0.65	0.11
05223186-6947159	4277	134	1.21	0.16	-0.70	0.10	1.90	0.15	-0.71	0.03	-0.78	0.13
05223309-6946595	4401	151	1.21	0.19	-0.68	0.10	2.00	0.15	-0.68	0.03	-0.90	0.10
05223316-6951389	NaN	NaN	NaN	NaN	NaN	NaN	NaN	NaN	NaN	NaN	NaN	NaN
05223318-6937044	4421	152	1.36	0.18	-0.63	0.10	2.40	0.15	-0.63	0.06	-0.87	0.16
05223416-6944433	4641	187	1.41	0.17	-1.18	0.10	1.90	0.15	-1.18	0.03	-1.16	0.06
05223487-6938057	4316	137	1.24	0.16	-0.74	0.10	2.20	0.15	-0.75	0.04	-0.75	0.11
05223506-6937279	4190	123	1.11	0.16	-0.68	0.10	1.90	0.15	-0.67	0.05	-0.70	0.09
05223557-6943373	4676	185	1.44	0.16	-1.40	0.10	1.90	0.15	-1.39	0.03	-1.38	0.09
05223701-6936166	4729	186	1.75	0.14	-0.37	0.10	1.90	0.15	-0.37	0.03	-0.41	0.09
05223787-6954562	4003	93	1.05	0.14	-0.29	0.10	1.70	0.15	-0.28	0.04	-0.31	0.11
05223895-6945007	4279	130	1.06	0.17	-0.66	0.10	2.00	0.15	-0.67	0.03	-0.82	0.07
05223988-6946110	4183	117	0.94	0.16	-0.82	0.10	1.90	0.15	-0.83	0.04	-0.78	0.15
05224062-6953310	4137	112	1.04	0.14	-0.78	0.10	2.10	0.15	-0.77	0.04	-0.75	0.14
05224164-6935518	4347	137	1.38	0.18	-0.44	0.10	1.80	0.15	-0.45	0.03	-0.68	0.13
05224195-6941099	4200	121	1.12	0.16	-0.62	0.10	1.80	0.15	-0.59	0.03	-0.66	0.13
05224240-6940567	NaN	NaN	NaN	NaN	NaN	NaN	NaN	NaN	NaN	NaN	NaN	NaN
05224276-6940109	4378	144	1.17	0.20	-0.57	0.10	1.70	0.15	-0.53	0.03	-0.77	0.04
05224309-6940275	4151	114	1.02	0.15	-0.80	0.10	2.10	0.15	-0.79	0.04	-0.79	0.12
05224321-6952397	4275	131	1.19	0.16	-0.68	0.10	2.00	0.15	-0.70	0.03	-0.80	0.15
05224448-6954402	4585	174	1.50	0.23	-0.66	0.10	1.80	0.15	-0.66	0.03	-0.81	0.17
05224854-6940010	4080	108	1.27	0.12	-0.58	0.10	1.90	0.15	-0.58	0.05	-0.45	0.16
05225062-6936580	4470	158	1.35	0.20	-0.62	0.10	2.00	0.15	-0.63	0.03	-0.91	0.09
05225069-6955486	4127	113	1.09	0.15	-0.58	0.10	1.80	0.15	-0.58	0.05	-0.55	0.19
05225632-6942269	NaN	NaN	NaN	NaN	NaN	NaN	NaN	NaN	NaN	NaN	NaN	NaN
05225877-6938172	4612	181	1.63	0.26	-0.60	0.10	2.00	0.15	-0.60	0.03	-0.83	0.05
05225980-6954368	NaN	NaN	NaN	NaN	NaN	NaN	NaN	NaN	NaN	NaN	NaN	NaN
05230009-6935251	4246	127	1.14	0.17	-0.56	0.10	1.90	0.15	-0.55	0.04	-0.75	0.11
05230011-6946353	5294	269	2.17	0.08	-0.15	0.10	2.30	0.15	-0.15	0.03	-0.43	0.06
05230203-6935557	4521	161	1.27	0.16	-1.17	0.10	1.70	0.15	-1.17	0.03	-1.37	0.10
05230230-6939587	4221	124	1.09	0.13	-1.10	0.10	2.20	0.15	-1.08	0.04	-1.09	0.06
05230353-6952441	4104	108	1.01	0.14	-0.76	0.10	2.00	0.15	-0.77	0.04	-0.66	0.13
05230370-6944219	4311	135	1.34	0.09	-1.50	0.10	1.30	0.15	-1.48	0.02	-1.10	0.11
05230589-6944122	4884	205	1.79	0.14	-0.36	0.10	2.10	0.15	-0.37	0.03	-0.59	0.03
05230606-6951113	3929	90	1.05	0.14	-0.26	0.10	1.50	0.15	-0.23	0.05	-0.13	0.18
05230647-6944394	4839	205	1.46	0.20	-1.43	0.10	1.80	0.15	-1.42	0.02	-1.54	0.05
05230776-6946082	4540	162	1.16	0.17	-1.17	0.10	1.70	0.15	-1.19	0.03	-1.20	0.02
05230867-6956329	4408	148	1.61	0.20	-0.41	0.10	2.10	0.15	-0.40	0.05	-0.45	0.20
05231074-6939184	4463	150	1.13	0.14	-1.49	0.10	1.80	0.15	-1.49	0.02	-1.51	0.07
05231091-6942374	4333	139	1.10	0.19	-0.64	0.10	1.90	0.15	-0.64	0.03	-0.91	0.09
05231221-6938166	4505	154	1.70	0.17	-0.19	0.10	1.70	0.15	-0.20	0.03	-0.15	0.07
05231315-6945212	4539	168	1.32	0.20	-0.82	0.10	1.90	0.15	-0.83	0.05	-1.21	0.12
05231321-6946382	4059	102	0.88	0.14	-0.72	0.10	2.00	0.15	-0.73	0.04	-0.74	0.13
05231411-6948546	3927	84	0.73	0.12	-0.86	0.10	2.10	0.15	-0.83	0.05	-0.55	0.14
05231484-6950196	4350	141	1.28	0.17	-0.66	0.10	2.00	0.15	-0.66	0.04	-0.70	0.10
05231562-6955430	4008	97	0.88	0.13	-0.73	0.10	1.90	0.15	-0.72	0.05	-0.60	0.13
05231631-6942507	4243	126	1.09	0.16	-0.62	0.10	2.10	0.15	-0.65	0.04	-0.66	0.14
05231634-6951332	4289	141	1.28	0.15	-0.84	0.10	2.00	0.15	-0.85	0.03	-0.89	0.07
05231962-6943309	5162	250	2.14	0.09	-0.24	0.10	2.10	0.15	-0.24	0.03	-0.47	0.05
05232020-6954561	4046	101	0.77	0.15	-0.79	0.10	1.80	0.15	-0.78	0.04	-0.74	0.08
05232148-6952155	4112	109	0.99	0.14	-0.74	0.10	2.00	0.15	-0.74	0.03	-0.78	0.14
05232181-6945429	4426	151	1.30	0.18	-0.69	0.10	1.70	0.15	-0.69	0.03	-0.93	0.06
05232554-6943388	NaN	NaN	NaN	NaN	NaN	NaN	NaN	NaN	NaN	NaN	NaN	NaN
05232624-6943558	4072	106	0.94	0.13	-0.88	0.10	2.00	0.15	-0.88	0.03	-0.83	0.10
05232680-6953109	4479	158	1.38	0.22	-0.57	0.10	1.60	0.15	-0.58	0.03	-0.90	0.08
05232845-6944158	4222	123	1.09	0.16	-0.70	0.10	2.00	0.15	-0.69	0.04	-0.87	0.12
05232892-6947486	4356	144	1.26	0.17	-0.61	0.10	1.70	0.15	-0.62	0.03	-0.88	0.05
05233236-6948257	4401	150	1.42	0.14	-0.95	0.10	1.50	0.15	-1.01	0.06	-0.80	0.11
05235653-6947387	4683	179	1.72	0.16	-0.42	0.10	1.80	0.15	-0.42	0.03	-0.62	0.05
05235851-6945519	4191	120	1.08	0.15	-0.78	0.10	2.20	0.15	-0.77	0.03	-0.78	0.12
05240317-6953036	4420	150	1.41	0.15	-0.90	0.10	2.20	0.15	-0.91	0.04	-0.96	0.09
05240482-6948280	4456	158	1.38	0.17	-0.79	0.10	1.80	0.15	-0.79	0.03	-1.03	0.05
05240604-6942380	3990	95	1.22	0.11	-0.49	0.10	1.50	0.15	-0.50	0.05	-0.07	0.06
05240613-6953529	4633	176	1.47	0.14	-1.50	0.10	1.10	0.15	-1.50	0.03	-1.45	0.04
05240672-6947130	4500	166	1.48	0.20	-0.60	0.10	1.90	0.15	-0.60	0.04	-0.72	0.07
05240803-6956250	4281	129	1.18	0.15	-0.90	0.10	2.40	0.15	-0.89	0.04	-0.93	0.14
05240830-6944428	4058	103	0.88	0.14	-0.77	0.10	1.80	0.15	-0.78	0.04	-0.78	0.08
05241033-6944374	4200	122	1.12	0.14	-0.83	0.10	2.00	0.15	-0.84	0.03	-0.89	0.10
05241341-6945303	4259	129	1.15	0.16	-0.60	0.10	1.80	0.15	-0.62	0.04	-0.80	0.06
05241479-6946323	5155	245	2.07	0.09	-0.10	0.10	2.10	0.15	-0.12	0.03	-0.41	0.04

Continued on next page

2MASS ID	$T_{\rm phot}$	$\sigma(T_{\rm phot})$	$\log g$	$\sigma(\log g)$	[M/H]	σ([M/H])	$\xi_{\rm micro}$	$\sigma(\xi_{\rm micro})$	[Fe I/H]	σ([Fe I/H])	[Fe II/H]	σ([Fe II/H])
	K	K			dex	dex	km s^{-1}	dex	dex	dex	dex	
05241699-6942158	4312	135	1.22	0.16	-0.66	0.10	2.20	0.15	-0.66	0.04	-0.89	0.07
05241794-6951317	4262	131	1.31	0.14	-0.78	0.10	1.90	0.15	-0.79	0.04	-0.71	0.08
05242161-6942097	4269	129	1.15	0.15	-0.82	0.10	1.90	0.15	-0.83	0.03	-0.93	0.06
05242198-6943579	4171	112	1.10	0.16	-0.46	0.10	1.70	0.15	-0.46	0.04	-0.76	0.16
05242240-6944344	4114	109	0.99	0.14	-0.75	0.10	2.00	0.15	-0.76	0.04	-0.75	0.12
05242409-6942051	4164	116	1.01	0.16	-0.63	0.10	1.80	0.15	-0.63	0.03	-0.71	0.12
05242542-6955188	4459	158	1.38	0.24	-0.56	0.10	1.90	0.15	-0.56	0.03	-0.77	0.06
05242687-6943577	4926	210	1.87	0.13	-0.25	0.10	2.20	0.15	-0.25	0.03	-0.50	0.04
05242702-6956445	4368	147	1.37	0.17	-0.56	0.10	1.80	0.15	-0.56	0.03	-0.82	0.04
05242811-6947467	4288	132	1.16	0.16	-0.81	0.10	1.90	0.15	-0.81	0.03	-0.99	0.07
05243272-6955362	4135	111	0.92	0.15	-0.80	0.10	1.80	0.15	-0.78	0.04	-0.85	0.04
05243734-6945496	4614	185	1.59	0.24	-0.61	0.10	2.10	0.15	-0.61	0.04	-0.84	0.10
05243901-6948426	4388	144	1.25	0.22	-0.63	0.10	1.70	0.15	-0.64	0.03	-0.65	0.07
05244189-6954427	4453	151	1.49	0.20	-0.47	0.10	1.80	0.15	-0.48	0.03	-0.72	0.10
05244210-6942596	4535	166	1.53	0.18	-0.78	0.10	1.60	0.15	-0.76	0.05	-0.68	0.10
05244301-6943412	NaN	NaN	NaN	NaN	NaN	NaN	NaN	NaN	NaN	NaN	NaN	NaN
05244340-6950004	4318	133	1.38	0.17	-0.48	0.10	1.70	0.15	-0.47	0.03	-0.66	0.12
05244408-6942423	4683	180	1.25	0.19	-1.29	0.10	1.80	0.15	-1.29	0.03	-1.33	0.04
05244600-6946017	4369	144	1.32	0.17	-0.66	0.10	2.20	0.15	-0.65	0.03	-0.83	0.11
05244637-6947340	4777	192	1.93	0.16	-0.29	0.10	2.00	0.15	-0.29	0.03	-0.63	0.04
05244698-6956141	4287	132	1.26	0.15	-0.71	0.10	2.10	0.15	-0.70	0.04	-0.72	0.08
05244878-6948359	4265	125	1.17	0.18	-0.48	0.10	1.80	0.15	-0.46	0.03	-0.73	0.13
05244976-6943230	4156	114	1.00	0.15	-0.83	0.10	1.90	0.15	-0.82	0.03	-0.79	0.07
05245212-6948184	4359	143	1.25	0.17	-0.73	0.10	1.90	0.15	-0.72	0.04	-0.76	0.06
05245859-6952257	4536	168	1.51	0.20	-0.68	0.10	1.90	0.15	-0.67	0.03	-0.56	0.22
05252428-6939311	4159	114	1.04	0.15	-0.70	0.10	2.10	0.15	-0.69	0.04	-0.93	0.12
05252899-6939078	4799	194	1.95	0.17	-0.33	0.10	2.00	0.15	-0.33	0.03	-0.60	0.06
05253039-6940288	4425	150	1.34	0.18	-0.63	0.10	2.10	0.15	-0.64	0.04	-0.84	0.13
05253040-6936261	4205	121	1.08	0.15	-0.85	0.10	1.70	0.15	-0.86	0.03	-0.79	0.10
05253235-6943137	NaN	NaN	NaN	NaN	NaN	NaN	NaN	NaN	NaN	NaN	NaN	NaN
05253522-6937078	4239	124	1.05	0.15	-0.88	0.10	2.30	0.15	-0.87	0.04	-0.76	0.14
05254540-6940531	4410	151	1.36	0.17	-0.69	0.10	2.00	0.15	-0.68	0.04	-0.93	0.05
05254864-6940501	4223	125	1.17	0.16	-0.61	0.10	1.80	0.15	-0.61	0.03	-0.79	0.02
05255000-6942466	4104	109	0.97	0.14	-0.76	0.10	1.90	0.15	-0.76	0.04	-0.80	0.11
05255267-6943155	4052	101	0.88	0.14	-0.72	0.10	2.00	0.15	-0.72	0.04	-0.83	0.08
05255625-6941243	4888	205	1.86	0.14	-0.39	0.10	2.10	0.15	-0.38	0.04	-0.71	0.04
05255801-6937309	4115	110	0.98	0.16	-0.59	0.10	2.00	0.15	-0.57	0.04	-0.69	0.14
05255812-6942522	4296	134	1.30	0.16	-0.58	0.10	1.90	0.15	-0.58	0.04	-0.80	0.06
05260124-6939268	4277	131	1.15	0.16	-0.70	0.10	1.60	0.15	-0.70	0.03	-0.83	0.08
05260720-6942342	4834	211	1.89	0.22	-0.52	0.10	1.80	0.15	-0.52	0.04	-0.52	0.07
05260784-6938341	4154	116	0.99	0.14	-0.88	0.10	1.00	0.15	-0.88	0.05	-0.77	0.20
05261339-6940590	3969	90	0.81	0.14	-0.66	0.10	2.10	0.15	-0.59	0.06	-0.60	0.19

Table 17. Stellar parameters of LMC disc stars. Star identifiers, $T_{\rm phot}$, $\log g$, [M/H], $\xi_{\rm micro}$, [Fe I/H], [Fe II/H]. Errors are given for each quantity.

2MASS ID	$T_{\rm phot}$	$\sigma(T_{\rm phot})$	$\log g$	$\sigma(\log g)$	[M/H]	σ([M/H])	$\xi_{\rm micro}$	$\sigma(\xi_{\rm micro})$	[Fe I/H]	σ([Fe I/H])	[Fe II/H]	σ([Fe II/H])
	K	K			dex	dex	km s^{-1}	dex	dex	dex	dex	
0499	4264	117	1.07	0.15	-0.69	0.10	1.90	0.15	-0.71	0.03	-0.78	0.07
0512	4128	99	0.88	0.13	-0.91	0.10	1.80	0.15	-0.91	0.03	-0.78	0.04
0522	4101	97	0.91	0.15	-0.66	0.10	1.90	0.15	-0.67	0.03	-0.73	0.09
0533	4188	107	0.96	0.15	-0.78	0.10	2.10	0.15	-0.77	0.04	-0.81	0.09
0534	4344	124	1.11	0.13	-1.21	0.10	1.60	0.15	-1.21	0.02	-1.18	0.08
0546	4194	107	0.96	0.14	-0.97	0.10	1.80	0.15	-0.98	0.02	-0.88	0.07
0548	4114	100	0.96	0.15	-0.63	0.10	1.90	0.15	-0.63	0.03	-0.61	0.05
0564	NaN	NaN	NaN	NaN	NaN	NaN	NaN	NaN	NaN	NaN	NaN	NaN
0565	4104	97	0.90	0.14	-0.89	0.10	1.90	0.15	-0.88	0.03	-0.73	0.06
0576	4221	109	1.02	0.11	-1.33	0.10	1.80	0.15	-1.30	0.03	-1.10	0.04
0593	4061	90	0.89	0.10	-1.19	0.10	2.00	0.15	-1.20	0.02	-0.85	0.07
0599	4103	98	0.94	0.13	-0.79	0.10	1.80	0.15	-0.80	0.03	-0.71	0.04
0601	4217	106	1.15	0.16	-0.40	0.10	1.90	0.15	-0.39	0.04	-0.55	0.09
0606	4304	107	1.09	0.05	-2.07	0.10	1.60	0.15	-2.09	0.02	-1.72	0.08
0611	4078	95	0.95	0.15	-0.56	0.10	1.80	0.15	-0.55	0.03	-0.58	0.11
0614	4110	101	1.02	0.16	-0.38	0.10	1.50	0.15	-0.38	0.05	-0.59	0.15
0620	4166	106	1.08	0.15	-0.57	0.10	1.80	0.15	-0.54	0.05	-0.71	0.09
0625	4038	90	0.86	0.13	-0.80	0.10	2.00	0.15	-0.79	0.03	-0.62	0.16
0629	4242	112	1.05	0.14	-0.98	0.10	1.90	0.15	-1.00	0.03	-0.79	0.04
0631	4243	115	1.09	0.16	-0.49	0.10	1.70	0.15	-0.50	0.04	-0.66	0.09
0633	4149	100	1.06	0.15	-0.47	0.10	1.70	0.15	-0.47	0.04	-0.68	0.17
0640	4227	111	1.03	0.12	-1.08	0.10	2.30	0.15	-1.12	0.04	-0.85	0.16
0646	4282	118	1.13	0.16	-0.62	0.10	1.80	0.15	-0.62	0.04	-0.80	0.08
0651	4209	106	1.16	0.16	-0.40	0.10	1.80	0.15	-0.40	0.04	-0.55	0.09
0655	4093	90	1.01	0.14	-0.55	0.10	1.90	0.15	-0.55	0.03	-0.52	0.13
0656	4161	105	1.06	0.15	-0.61	0.10	1.90	0.15	-0.57	0.04	-0.47	0.15
0658	4152	104	1.04	0.15	-0.64	0.10	2.00	0.15	-0.64	0.05	-0.70	0.16
0664	3971	82	0.85	0.14	-0.49	0.10	1.80	0.15	-0.49	0.04	-0.37	0.06
0666	4317	121	1.13	0.15	-0.96	0.10	1.70	0.15	-0.96	0.03	-0.83	0.05
0671	4087	95	0.93	0.13	-0.82	0.10	2.00	0.15	-0.81	0.03	-0.77	0.10
0672	3987	85	0.88	0.14	-0.50	0.10	1.70	0.15	-0.50	0.04	-0.47	0.04
0679	4033	90	0.93	0.14	-0.57	0.10	1.90	0.15	-0.55	0.04	-0.56	0.02
0690	3904	80	0.82	0.14	-0.44	0.10	1.70	0.15	-0.44	0.04	-0.43	0.12
0699	4632	162	1.70	0.22	-0.50	0.10	1.50	0.15	-0.50	0.03	-0.58	0.06
0700	4105	99	1.04	0.15	-0.51	0.10	1.80	0.15	-0.48	0.05	-0.66	0.18
0701	4089	90	1.04	0.14	-0.40	0.10	1.80	0.15	-0.42	0.05	-0.40	0.21
0705	4311	123	1.19	0.16	-0.66	0.10	1.80	0.15	-0.66	0.03	-0.68	0.04
0706	NaN	NaN	NaN	NaN	NaN	NaN	NaN	NaN	NaN	NaN	NaN	NaN
0710	3949	80	0.86	0.13	-0.59	0.10	1.70	0.15	-0.59	0.04	-0.45	0.11
0720	4329	124	1.20	0.15	-0.89	0.10	1.80	0.15	-0.89	0.03	-0.95	0.11
0721	NaN	NaN	NaN	NaN	NaN	NaN	NaN	NaN	NaN	NaN	NaN	NaN
0728	4203	109	1.06	0.14	-0.85	0.10	2.10	0.15	-0.85	0.04	-0.67	0.02
0731	3881	77	0.82	0.14	-0.35	0.10	1.60	0.15	-0.35	0.04	-0.21	0.10
0748	4166	102	1.13	0.15	-0.49	0.10	1.70	0.15	-0.51	0.05	-0.32	0.21
0752	3979	89	0.98	0.14	-0.31	0.10	1.70	0.15	-0.30	0.04	-0.41	0.06
0756	3904	75	0.79	0.13	-0.55	0.10	1.70	0.15	-0.55	0.04	-0.34	0.07
0758	NaN	NaN	NaN	NaN	NaN	NaN	NaN	NaN	NaN	NaN	NaN	NaN
0766	4118	95	1.22	0.16	-0.21	0.10	1.40	0.15	-0.15	0.05	-0.05	0.09
0773	4009	88	0.92	0.14	-0.57	0.10	1.90	0.15	-0.56	0.04	-0.32	0.14
0775	4318	121	1.16	0.14	-0.96	0.10	1.50	0.15	-0.96	0.02	-0.85	0.04
0776	4256	115	1.14	0.15	-0.81	0.10	1.90	0.15	-0.81	0.03	-0.74	0.07
0782	4180	104	1.17	0.15	-0.50	0.10	1.70	0.15	-0.45	0.04	-0.40	0.10
0789	3834	72	0.77	0.13	-0.36	0.10	1.70	0.15	-0.36	0.04	-0.05	0.15
0790	NaN	NaN	NaN	NaN	NaN	NaN	NaN	NaN	NaN	NaN	NaN	NaN
0793	4111	99	1.02	0.13	-0.74	0.10	1.90	0.15	-0.73	0.03	-0.60	0.08
0808	NaN	NaN	NaN	NaN	NaN	NaN	NaN	NaN	NaN	NaN	NaN	NaN
0834	4037	90	0.95	0.12	-0.78	0.10	1.90	0.15	-0.77	0.03	-0.53	0.15
0835	NaN	NaN	NaN	NaN	NaN	NaN	NaN	NaN	NaN	NaN	NaN	NaN
0854	4194	109	1.16	0.15	-0.63	0.10	1.90	0.15	-0.62	0.04	-0.70	0.13
0855	4196	108	1.12	0.13	-0.80	0.10	1.90	0.15	-0.83	0.04	-0.71	0.07
0859	4071	94	1.04	0.14	-0.55	0.10	1.70	0.15	-0.53	0.04	-0.51	0.10
0879	NaN	NaN	NaN	NaN	NaN	NaN	NaN	NaN	NaN	NaN	NaN	NaN
0900	4225	109	1.22	0.15	-0.51	0.10	1.90	0.15	-0.47	0.04	-0.57	0.09
0937	NaN	NaN	NaN	NaN	NaN	NaN	NaN	NaN	NaN	NaN	NaN	NaN
1055	4188	107	1.20	0.10	-1.08	0.10	1.40	0.15	-1.08	0.02	-0.75	0.07
1105	4013	88	1.07	0.10	-0.73	0.10	1.70	0.15	-0.74	0.04	-0.28	0.08
1118	4307	118	1.40	0.17	-0.26	0.10	1.60	0.15	-0.27	0.04	-0.65	0.12

Table 18. Line list. For each line, the wavelength λ (column 4), excitation potential $\chi_{\rm exc}$ (column 5), oscillator strength $\log gf$ (column 6) and literature reference (column 9) are given. The abundance measurement method is recalled (column 7). If a line has hyperfine structure, the label *equivalent* appear across the column 2 and 3: we provide first the wavelength and oscillator strength of the equivalent line, and below the detailed hyperfine structure for the different isotopes (isotope in column 2, isotopic fraction f in column 3, isotope-scaled $\log gf$ in column 6). The column before the last indicates lines identical to Pompéia et al. (2008).

Element	Isotope	f	λ Å	$\chi_{\rm exc}$ eV	$\log gf$	Method		Source
$_{8}$O I			6300.304	0.000	-9.819	SS		VALD
$_{12}$Mg I			5711.088	4.346	-1.833	SS		VALD
$_{12}$Mg I			6318.717	5.108	-1.730	SS		VALD
$_{12}$Mg I			6319.237	5.108	-1.950	SS		VALD
$_{14}$Si I			5690.425	4.930	-1.870	EW	x	Smith et al. (2000)
$_{14}$Si I			5793.073	4.930	-2.060	EW	x	Smith et al. (2000)
$_{20}$Ca I			6161.300	2.523	-1.266	EW		VALD
$_{20}$Ca I			6166.440	2.521	-1.142	EW		VALD
$_{20}$Ca I			6169.040	2.520	-0.797	EW		VALD
$_{20}$Ca I			6169.560	2.520	-0.478	EW		VALD
$_{20}$Ca I			6439.080	2.526	0.390	EW		VALD
$_{20}$Ca I			6455.610	2.523	-1.340	EW		VALD
$_{20}$Ca I			6471.670	2.526	-0.686	EW		VALD
$_{20}$Ca I			6493.790	2.521	-0.109	EW		VALD
$_{20}$Ca I			6499.650	2.523	-0.818	EW		VALD
$_{20}$Ca I			6508.840	2.526	-2.162	EW		VALD
$_{22}$Ti I			5648.580	2.490	-0.250	EW	x	NIST
$_{22}$Ti I			6126.220	1.070	-1.420	EW	x	NIST
$_{22}$Ti I			6258.100	1.443	-0.350	EW	x	Smith et al. (2000)
$_{22}$Ti I			6261.110	1.430	-0.480	EW	x	NIST
$_{22}$Ti I			6303.770	1.440	-1.570	EW	x	NIST
$_{22}$Ti I			6554.240	1.440	-1.220	EW	x	NIST
$_{22}$Ti I			6556.080	1.460	-1.080	EW	x	NIST
$_{22}$Ti I			6599.110	0.900	-2.085	EW	x	NIST
$_{22}$Ti II			6491.561	2.061	-1.793	EW	x	VALD
$_{22}$Ti II			6559.588	2.048	-2.190	EW	x	VALD
$_{22}$Ti II			6606.949	2.061	-2.790	EW	x	VALD
$_{11}$Na I			5688.205	2.104	-0.460	SS	x	Shetrone et al. (2003)
$_{11}$Na I			6154.226	2.102	-1.530	SS	x	NIST
$_{11}$Na I			6160.747	2.104	-1.230	SS	x	NIST
$_{21}$Sc II	*equivalent*		5641.001	1.500	-1.131	SS		Kurucz (with $\log gf$ from VALD)
	$^{45}_{21}$Sc II	1	5640.989	1.500	-1.654	–		–
	–	–	5640.996	1.500	-2.143	–		–
	–	–	5641.001	1.500	-1.947	–		–
	–	–	5641.001	1.500	-2.842	–		–
	–	–	5641.006	1.500	-2.027	–		–
	–	–	5641.010	1.500	-2.402	–		–
	–	–	5641.010	1.500	-2.402	–		–
	–	–	5641.014	1.500	-2.147	–		–

Continued on next page

Element	Isotope	f	λ Å	$\chi_{\rm exc}$ eV	log gf	Method	Source
	–	–	5641.016	1.500	-2.131	–	–
$_{21}$Sc II	*equivalent*		5657.896	1.500	-0.603	SS	Kurucz (with log gf from VALD)
	$^{45}_{21}$Sc II	1	5657.886	1.500	-1.229	–	–
	–	–	5657.888	1.500	-1.799	–	–
	–	–	5657.893	1.500	-1.799	–	–
	–	–	5657.894	1.500	-1.627	–	–
	–	–	5657.895	1.500	-1.641	–	–
	–	–	5657.899	1.500	-1.641	–	–
	–	–	5657.901	1.500	-2.323	–	–
	–	–	5657.902	1.500	-1.652	–	–
	–	–	5657.904	1.500	-1.652	–	–
	–	–	5657.906	1.500	-1.825	–	–
	–	–	5657.906	1.500	-3.749	–	–
	–	–	5657.908	1.500	-1.825	–	–
	–	–	5657.909	1.500	-2.001	–	–
$_{21}$Sc II	*equivalent*		5667.149	1.500	-1.309	SS	Kurucz (with log gf from VALD)
	$^{45}_{21}$Sc II	1	5667.136	1.500	-1.903	–	–
	–	–	5667.141	1.500	-2.099	–	–
	–	–	5667.148	1.500	-2.099	–	–
	–	–	5667.154	1.500	-3.284	–	–
	–	–	5667.157	1.500	-2.103	–	–
	–	–	5667.163	1.500	-2.103	–	–
	–	–	5667.167	1.500	-2.358	–	–
$_{21}$Sc II	*equivalent*		6604.601	1.357	-1.309	SS	Kurucz (with log gf from VALD)
	$^{45}_{21}$Sc II	1	6604.582	1.357	-2.505	–	–
	–	–	6604.590	1.357	-2.347	–	–
	–	–	6604.594	1.357	-1.935	–	–
	–	–	6604.596	1.357	-2.358	–	–
	–	–	6604.599	1.357	-2.333	–	–
	–	–	6604.602	1.357	-2.531	–	–
	–	–	6604.604	1.357	-3.029	–	–
	–	–	6604.607	1.357	-4.455	–	–
	–	–	6604.609	1.357	-2.707	–	–
	–	–	6604.611	1.357	-2.505	–	–
	–	–	6604.613	1.357	-2.347	–	–
	–	–	6604.615	1.357	-2.531	–	–
	–	–	6604.615	1.357	-2.358	–	–
$_{23}$V I	*equivalent*		6135.361	1.051	-0.746	SS	Kurucz
	$^{50}_{23}$V I	0.0025	6135.361	1.051	-3.348	–	–
	$^{51}_{23}$V I	0.9975	6135.338	1.051	-1.553	–	–
	–	–	6135.338	1.051	-1.532	–	–
	–	–	6135.338	1.051	-1.678	–	–
	–	–	6135.378	1.051	-2.009	–	–

Continued on next page

Element	Isotope	f	λ Å	$\chi_{\rm exc}$ eV	log gf	Method	Source
	–	–	6135.378	1.051	-1.532	–	–
	–	–	6135.379	1.051	-1.211	–	–
$_{23}$V I	*equivalent*		6224.529	0.287	-2.010	SS	Kurucz
	$^{50}_{23}$V I	0.0025	6224.529	0.287	-4.612	–	–
	$^{51}_{23}$V I	0.9975	6224.465	0.287	-3.817	–	–
	–	–	6224.468	0.287	-3.537	–	–
	–	–	6224.470	0.287	-4.838	–	–
	–	–	6224.471	0.287	-3.817	–	–
	–	–	6224.475	0.287	-3.399	–	–
	–	–	6224.478	0.287	-4.139	–	–
	–	–	6224.480	0.287	-3.537	–	–
	–	–	6224.486	0.287	-3.333	–	–
	–	–	6224.490	0.287	-3.692	–	–
	–	–	6224.493	0.287	-3.399	–	–
	–	–	6224.501	0.287	-3.326	–	–
	–	–	6224.506	0.287	-3.361	–	–
	–	–	6224.510	0.287	-3.333	–	–
	–	–	6224.520	0.287	-3.391	–	–
	–	–	6224.526	0.287	-3.098	–	–
	–	–	6224.531	0.287	-3.326	–	–
	–	–	6224.543	0.287	-3.595	–	–
	–	–	6224.550	0.287	-2.879	–	–
	–	–	6224.555	0.287	-3.391	–	–
	–	–	6224.577	0.287	-2.692	–	–
	–	–	6224.584	0.287	-3.595	–	–
$_{23}$V I	*equivalent*		6251.827	0.287	-1.340	SS	Kurucz
	$^{50}_{23}$V I	0.0025	6251.827	0.287	-3.942	–	–
	$^{51}_{23}$V I	0.9975	6251.771	0.287	-2.925	–	–
	–	–	6251.788	0.287	-2.721	–	–
	–	–	6251.804	0.287	-2.656	–	–
	–	–	6251.806	0.287	-2.022	–	–
	–	–	6251.817	0.287	-2.663	–	–
	–	–	6251.818	0.287	-2.209	–	–
	–	–	6251.829	0.287	-2.729	–	–
	–	–	6251.829	0.287	-2.428	–	–
	–	–	6251.837	0.287	-2.691	–	–
	–	–	6251.839	0.287	-2.867	–	–
	–	–	6251.844	0.287	-3.022	–	–
	–	–	6251.848	0.287	-3.147	–	–
	–	–	6251.849	0.287	-3.469	–	–
	–	–	6251.853	0.287	-4.168	–	–
	–	–	6251.853	0.287	-2.925	–	–
	–	–	6251.859	0.287	-3.147	–	–
	–	–	6251.859	0.287	-2.721	–	–

Continued on next page

Element	Isotope	f	λ Å	$\chi_{\rm exc}$ eV	log gf	Method	Source
	–	–	6251.862	0.287	-2.656	–	–
	–	–	6251.863	0.287	-2.867	–	–
	–	–	6251.864	0.287	-2.729	–	–
	–	–	6251.864	0.287	-2.663	–	–
$_{23}$V I	*equivalent*		6274.649	0.267	-1.670	SS	Kurucz
	$^{50}_{23}$V I	0.0025	6274.649	0.267	-4.272	–	–
	$^{51}_{23}$V I	0.9975	6274.607	0.267	-2.933	–	–
	–	–	6274.629	0.267	-2.456	–	–
	–	–	6274.641	0.267	-2.477	–	–
	–	–	6274.655	0.267	-2.153	–	–
	–	–	6274.657	0.267	-2.456	–	–
	–	–	6274.678	0.267	-2.602	–	–
$_{23}$V I	*equivalent*		6285.150	0.275	-1.510	SS	Kurucz
	$^{50}_{23}$V I	0.0025	6285.150	0.275	-4.112	–	–
	$^{51}_{23}$V I	0.9975	6285.098	0.275	-3.569	–	–
	–	–	6285.117	0.275	-3.141	–	–
	–	–	6285.122	0.275	-2.704	–	–
	–	–	6285.134	0.275	-2.891	–	–
	–	–	6285.137	0.275	-2.543	–	–
	–	–	6285.148	0.275	-2.715	–	–
	–	–	6285.149	0.275	-2.551	–	–
	–	–	6285.152	0.275	-2.078	–	–
	–	–	6285.157	0.275	-2.715	–	–
	–	–	6285.162	0.275	-2.294	–	–
	–	–	6285.168	0.275	-2.577	–	–
	–	–	6285.172	0.275	-3.016	–	–
$_{23}$V I	*equivalent*		6292.825	0.287	-1.470	SS	Kurucz
	$^{50}_{23}$V I	0.0025	6292.825	0.287	-4.072	–	–
	$^{51}_{23}$V I	0.9975	6292.759	0.287	-4.055	–	–
	–	–	6292.777	0.287	-3.645	–	–
	–	–	6292.790	0.287	-2.941	–	–
	–	–	6292.792	0.287	-3.423	–	–
	–	–	6292.802	0.287	-2.745	–	–
	–	–	6292.805	0.287	-3.298	–	–
	–	–	6292.812	0.287	-2.691	–	–
	–	–	6292.816	0.287	-3.247	–	–
	–	–	6292.820	0.287	-2.713	–	–
	–	–	6292.825	0.287	-2.101	–	–
	–	–	6292.826	0.287	-3.277	–	–
	–	–	6292.827	0.287	-2.804	–	–
	–	–	6292.831	0.287	-2.992	–	–
	–	–	6292.832	0.287	-2.242	–	–
	–	–	6292.837	0.287	-2.406	–	–
	–	–	6292.841	0.287	-3.247	–	–

Continued on next page

Element	Isotope	f	λ Å	$\chi_{\rm exc}$ eV	log gf	Method		Source
	–	–	6292.841	0.287	-2.604	–		–
	–	–	6292.842	0.287	-2.859	–		–
$_{23}$V I	*equivalent*		6531.415	1.218	-0.840	SS		Kurucz
	$^{50}_{23}$V I	0.0025	6531.415	1.218	-3.442	–		–
	$^{51}_{23}$V I	0.9975	6531.382	1.218	-2.492	–		–
	–	–	6531.385	1.218	-2.237	–		–
	–	–	6531.385	1.218	-2.237	–		–
	–	–	6531.388	1.218	-4.145	–		–
	–	–	6531.392	1.218	-2.038	–		–
	–	–	6531.393	1.218	-2.038	–		–
	–	–	6531.397	1.218	-2.902	–		–
	–	–	6531.402	1.218	-1.974	–		–
	–	–	6531.403	1.218	-1.974	–		–
	–	–	6531.408	1.218	-2.185	–		–
	–	–	6531.415	1.218	-2.005	–		–
	–	–	6531.416	1.218	-2.005	–		–
	–	–	6531.423	1.218	-1.779	–		–
	–	–	6531.430	1.218	-2.186	–		–
	–	–	6531.432	1.218	-2.186	–		–
	–	–	6531.440	1.218	-1.487	–		–
$_{24}$Cr I			5783.063	3.323	-0.500	SS		VALD
$_{24}$Cr I			5787.918	3.322	-0.083	SS		VALD
$_{24}$Cr I			6330.091	0.941	-2.920	SS		VALD
$_{26}$Fe I			5618.633	4.209	-1.260	EW	x	Smith et al. (2000)
$_{26}$Fe I			5619.610	4.390	-1.700	EW	x	Nave et al. (1994)
$_{26}$Fe I			5633.950	4.990	-0.270	EW	x	Nave et al. (1994)
$_{26}$Fe I			5635.823	4.256	-1.740	EW	x	Smith et al. (2000)
$_{26}$Fe I			5638.270	4.220	-0.870	EW	x	Nave et al. (1994)
$_{26}$Fe I			5641.450	4.260	-1.180	EW	x	Nave et al. (1994)
$_{26}$Fe I			5679.023	4.651	-0.770	EW	x	Smith et al. (2000)
$_{26}$Fe I			5691.497	4.301	-1.370	EW	x	Smith et al. (2000)
$_{26}$Fe I			5701.560	2.560	-2.220	EW	x	Nave et al. (1994)
$_{26}$Fe I			5705.465	4.301	-1.360	EW	x	Smith et al. (2000)
$_{26}$Fe I			5717.833	4.284	-0.980	EW	x	Smith et al. (2000)
$_{26}$Fe I			5806.725	4.607	-0.900	EW	x	Smith et al. (2000)
$_{26}$Fe I			5809.218	3.883	-1.690	EW	x	Smith et al. (2000)
$_{26}$Fe I			5814.808	4.283	-1.820	EW	x	Smith et al. (2000)
$_{26}$Fe I			6137.700	2.590	-1.400	EW	x	Nave et al. (1994)
$_{26}$Fe I			6151.620	2.180	-3.300	EW	x	Nave et al. (1994)
$_{26}$Fe I			6157.728	4.076	-1.110	EW	x	Smith et al. (2000)
$_{26}$Fe I			6165.360	4.142	-1.470	EW	x	Smith et al. (2000)
$_{26}$Fe I			6173.340	2.220	-2.880	EW	x	Nave et al. (1994)
$_{26}$Fe I			6180.210	2.730	-2.650	EW	x	Nave et al. (1994)
$_{26}$Fe I			6188.020	3.940	-1.720	EW	x	Nave et al. (1994)

Continued on next page

Element	Isotope	f	λ Å	χ_{exc} eV	log gf	Method		Source
$_{26}$Fe I			6200.320	2.610	-2.440	EW	x	Nave et al. (1994)
$_{26}$Fe I			6297.800	2.220	-2.740	EW	x	Nave et al. (1994)
$_{26}$Fe I			6301.510	3.650	-0.600	EW	x	adjusted in Pompéia et al. (2008)
$_{26}$Fe I			6302.500	3.690	-0.910	EW	x	Nave et al. (1994)
$_{26}$Fe I			6322.690	2.590	-2.430	EW	x	Nave et al. (1994)
$_{26}$Fe I			6335.340	2.200	-2.180	EW	x	Nave et al. (1994)
$_{26}$Fe I			6336.830	3.690	-1.050	EW	x	Nave et al. (1994)
$_{26}$Fe I			6344.160	2.430	-2.920	EW	x	Nave et al. (1994)
$_{26}$Fe I			6355.040	2.840	-2.290	EW	x	Nave et al. (1994)
$_{26}$Fe I			6358.690	0.860	-4.470	EW	x	Nave et al. (1994)
$_{26}$Fe I			6380.750	4.190	-1.380	EW	x	Nave et al. (1994)
$_{26}$Fe I			6380.750	4.190	-1.380	EW	x	Nave et al. (1994)
$_{26}$Fe I			6392.540	2.280	-4.030	EW	x	Nave et al. (1994)
$_{26}$Fe I			6393.610	2.430	-1.580	EW	x	Nave et al. (1994)
$_{26}$Fe I			6408.030	3.690	-1.000	EW	x	adjusted in Pompéia et al. (2008)
$_{26}$Fe I			6411.660	3.650	-0.720	EW	x	Nave et al. (1994)
$_{26}$Fe I			6421.351	2.279	-2.010	EW	x	Smith et al. (2000)
$_{26}$Fe I			6430.860	2.180	-2.010	EW	x	Nave et al. (1994)
$_{26}$Fe I			6469.193	4.835	-0.620	EW	x	Smith et al. (2000)
$_{26}$Fe I			6475.630	2.560	-2.940	EW	x	Nave et al. (1994)
$_{26}$Fe I			6481.880	2.280	-2.980	EW	x	Nave et al. (1994)
$_{26}$Fe I			6494.990	2.400	-1.270	EW	x	Nave et al. (1994)
$_{26}$Fe I			6498.950	0.960	-4.700	EW	x	Nave et al. (1994)
$_{26}$Fe I			6518.370	2.830	-2.300	EW	x	Nave et al. (1994)
$_{26}$Fe I			6574.250	0.990	-5.020	EW	x	Nave et al. (1994)
$_{26}$Fe I			6575.040	2.590	-2.710	EW	x	Nave et al. (1994)
$_{26}$Fe I			6581.220	1.480	-4.860	EW	x	Nave et al. (1994)
$_{26}$Fe I			6593.871	2.437	-2.420	EW	x	Smith et al. (2000)
$_{26}$Fe I			6597.561	4.795	-0.920	EW	x	Smith et al. (2000)
$_{26}$Fe I			6608.040	2.280	-4.030	EW	x	Nave et al. (1994)
$_{26}$Fe I			6609.120	2.560	-2.690	EW	x	Nave et al. (1994)
$_{26}$Fe II			6149.246	3.889	-2.724	EW	x	Biemont et al. (1991)
$_{26}$Fe II			6247.560	3.890	-2.329	EW	x	Biemont et al. (1991)
$_{26}$Fe II			6416.921	3.891	-2.740	EW	x	Biemont et al. (1991)
$_{26}$Fe II			6432.680	2.890	-3.708	EW	x	Biemont et al. (1991)
$_{26}$Fe II			6456.390	3.900	-2.075	EW	x	Biemont et al. (1991)
$_{26}$Fe II			6516.080	2.890	-3.450	EW	x	Biemont et al. (1991)
$_{27}$Co I	*equivalent*		5647.234	2.280	-1.560	SS		Kurucz
	$^{59}_{27}$Co I	1	5647.207	2.280	-2.127	–		–
	–	–	5647.220	2.280	-2.343	–		–
	–	–	5647.232	2.280	-2.626	–		–
	–	–	5647.239	2.280	-2.753	–		–
	–	–	5647.243	2.280	-3.065	–		–
	–	–	5647.246	2.280	-2.592	–		–

Continued on next page

Element	Isotope	f	λ Å	$\chi_{\rm exc}$ eV	log gf	Method		Source
	–	–	5647.253	2.280	-2.600	–		–
	–	–	5647.259	2.280	-2.764	–		–
	–	–	5647.265	2.280	-3.618	–		–
	–	–	5647.267	2.280	-3.190	–		–
	–	–	5647.269	2.280	-2.764	–		–
	–	–	5647.269	2.280	-2.940	–		–
$_{27}$Co I	*equivalent*		6117.000	1.785	-2.490	SS		Kurucz
	$^{59}_{27}$Co I	1	6116.957	1.785	-3.120	–		–
	–	–	6116.992	1.785	-2.974	–		–
	–	–	6116.998	1.785	-2.974	–		–
	–	–	6117.033	1.785	-3.451	–		–
$_{27}$Co I	*equivalent*		6282.634	1.740	-2.160	SS		Kurucz
	$^{59}_{27}$Co I	1	6282.576	1.740	-2.727	–		–
	–	–	6282.610	1.740	-2.943	–		–
	–	–	6282.632	1.740	-3.353	–		–
	–	–	6282.639	1.740	-3.226	–		–
	–	–	6282.655	1.740	-3.192	–		–
	–	–	6282.664	1.740	-3.665	–		–
	–	–	6282.676	1.740	-3.200	–		–
	–	–	6282.677	1.740	-4.218	–		–
	–	–	6282.692	1.740	-3.364	–		–
	–	–	6282.692	1.740	-3.790	–		–
	–	–	6282.703	1.740	-3.540	–		–
	–	–	6282.710	1.740	-3.364	–		–
$_{28}$Ni I			6128.980	1.680	-3.330	EW	x	NIST
$_{28}$Ni I			6175.370	4.090	-0.530	EW	x	NIST
$_{28}$Ni I			6327.600	1.680	-3.150	EW	x	NIST
$_{28}$Ni I			6482.810	1.930	-2.630	EW	x	NIST
$_{28}$Ni I			6532.890	1.935	-3.390	EW	x	Smith et al. (2000)
$_{28}$Ni I			6586.320	1.950	-2.810	EW	x	NIST
$_{29}$Cu I	*equivalent*		5782.127	1.642	-1.720	SS		Kurucz
	$^{63}_{29}$Cu I	0.6917	5782.059	1.642	-2.924	–		–
	–	–	5782.066	1.642	-3.225	–		–
	–	–	5782.078	1.642	-2.526	–		–
	–	–	5782.106	1.642	-2.526	–		–
	–	–	5782.117	1.642	-2.526	–		–
	–	–	5782.170	1.642	-2.079	–		–
	$^{64}_{29}$Cu I	0.3083	5782.127	1.642	-1.720	–		–
$_{39}$Y I			6435.004	0.066	-1.070	SS		VALD
$_{40}$Zr I			6127.475	0.154	-1.060	SS		VALD
$_{40}$Zr I			6134.570	0.000	-1.280	SS		VALD
$_{40}$Zr I			6143.180	0.071	-1.100	SS		VALD
$_{56}$Ba II			6141.713	0.704	-0.076	SS		VALD

Continued on next page

Element	Isotope	f	λ Å	χ_{exc} eV	log gf	Method	Source
$_{56}$Ba II	*equivalent*		6496.912	0.604	-0.180	SS	Rutten (1978)
	$^{130}_{56}$Ba II	0.00106	6496.912	0.604	-3.155	–	–
	$^{132}_{56}$Ba II	0.00101	6496.912	0.604	-3.176	–	–
	$^{134}_{56}$Ba II	0.02417	6496.912	0.604	-1.797	–	–
	$^{135}_{56}$Ba II	0.06592	6496.918	0.604	-2.565	–	–
	–	–	6496.920	0.604	-2.167	–	–
	–	–	6496.900	0.604	-2.866	–	–
	–	–	6496.923	0.604	-2.167	–	–
	–	–	6496.903	0.604	-2.167	–	–
	–	–	6496.908	0.604	-1.720	–	–
	$^{136}_{56}$Ba II	0.07854	6496.912	0.604	-1.285	–	–
	$^{137}_{56}$Ba II	0.1123	6496.918	0.604	-2.334	–	–
	–	–	6496.920	0.604	-1.936	–	–
	–	–	6496.900	0.604	-2.635	–	–
	–	–	6496.923	0.604	-1.936	–	–
	–	–	6496.903	0.604	-1.936	–	–
	–	–	6496.908	0.604	-1.489	–	–
	$^{138}_{56}$Ba II	0.7170	6496.912	0.604	-0.324	–	–
$_{57}$La II	*equivalent*		6262.287	0.403	-1.220	SS	Lawler et al. (2001a)
	$^{138}_{57}$La II	0.00089	6262.287	0.403	-4.271	–	–
	$^{139}_{57}$La II	0.99911	6262.114	0.403	-2.901	–	–
	–	–	6262.113	0.403	-3.047	–	–
	–	–	6262.135	0.403	-3.378	–	–
	–	–	6262.134	0.403	-2.718	–	–
	–	–	6262.132	0.403	-2.705	–	–
	–	–	6262.169	0.403	-3.269	–	–
	–	–	6262.166	0.403	-2.596	–	–
	–	–	6262.164	0.403	-2.471	–	–
	–	–	6262.215	0.403	-3.290	–	–
	–	–	6262.212	0.403	-2.535	–	–
	–	–	6262.208	0.403	-2.286	–	–
	–	–	6262.275	0.403	-3.400	–	–
	–	–	6262.271	0.403	-2.531	–	–
	–	–	6262.266	0.403	-2.130	–	–
	–	–	6262.348	0.403	-3.612	–	–
	–	–	6262.343	0.403	-2.597	–	–
	–	–	6262.338	0.403	-1.994	–	–
	–	–	6262.434	0.403	-4.015	–	–
	–	–	6262.429	0.403	-2.802	–	–
	–	–	6262.422	0.403	-1.873	–	–
$_{57}$La II			6320.376	0.173	-1.562	SS	VALD
$_{57}$La II	*equivalent*		6390.477	0.321	-1.410	SS	Lawler et al. (2001a)
	$^{138}_{57}$La II	0.00089	6390.477	0.321	-4.461	–	–
	$^{139}_{57}$La II	0.99911	6390.506	0.321	-2.857	–	–

Continued on next page

Element	Isotope	f	λ Å	$\chi_{\rm exc}$ eV	log gf	Method	Source
	–	–	6390.503	0.321	-2.778	–	–
	–	–	6390.498	0.321	-3.079	–	–
	–	–	6390.502	0.321	-2.954	–	–
	–	–	6390.497	0.321	-2.595	–	–
	–	–	6390.490	0.321	-2.661	–	–
	–	–	6390.496	0.321	-3.100	–	–
	–	–	6390.489	0.321	-2.536	–	–
	–	–	6390.480	0.321	-2.390	–	–
	–	–	6390.489	0.321	-3.334	–	–
	–	–	6390.479	0.321	-2.570	–	–
	–	–	6390.468	0.321	-2.183	–	–
	–	–	6390.479	0.321	-3.752	–	–
	–	–	6390.468	0.321	-2.752	–	–
	–	–	6390.455	0.321	-2.012	–	–
$_{63}$Eu II	*equivalent*		6437.640	1.319	-0.320	SS	Lawler et al. (2001b)
	$^{151}_{63}$Eu II	0.478	6437.611	1.319	-1.281	–	–
	–	–	6437.619	1.319	-2.512	–	–
	–	–	6437.629	1.319	-2.512	–	–
	–	–	6437.636	1.319	-1.391	–	–
	–	–	6437.643	1.319	-2.319	–	–
	–	–	6437.650	1.319	-2.319	–	–
	–	–	6437.656	1.319	-1.502	–	–
	–	–	6437.662	1.319	-2.277	–	–
	–	–	6437.666	1.319	-2.277	–	–
	–	–	6437.672	1.319	-1.608	–	–
	–	–	6437.676	1.319	-2.331	–	–
	–	–	6437.679	1.319	-2.331	–	–
	–	–	6437.684	1.319	-1.698	–	–
	–	–	6437.687	1.319	-2.528	–	–
	–	–	6437.689	1.319	-2.528	–	–
	–	–	6437.692	1.319	-1.749	–	–
	$^{153}_{63}$Eu II	0.522	6437.610	1.319	-1.242	–	–
	–	–	6437.613	1.319	-2.473	–	–
	–	–	6437.624	1.319	-2.473	–	–
	–	–	6437.627	1.319	-1.352	–	–
	–	–	6437.630	1.319	-2.280	–	–
	–	–	6437.634	1.319	-2.280	–	–
	–	–	6437.637	1.319	-1.463	–	–
	–	–	6437.639	1.319	-2.238	–	–
	–	–	6437.640	1.319	-2.238	–	–
	–	–	6437.641	1.319	-2.292	–	–
	–	–	6437.642	1.319	-1.569	–	–
	–	–	6437.642	1.319	-2.489	–	–
	–	–	6437.643	1.319	-1.710	–	–

Continued on next page

Element	Isotope	f	λ Å	$\chi_{\rm exc}$ eV	log gf	Method	Source
	–	–	6437.644	1.319	-1.659	–	–
	–	–	6437.644	1.319	-2.292	–	–
	–	–	6437.645	1.319	-2.489	–	–
$_{63}$Eu II	*equivalent*		6645.103	1.380	0.120	SS	Lawler et al. (2001b)
	$^{151}_{63}$Eu II	0.478	6645.071	1.379	-0.838	–	–
	–	–	6645.078	1.379	-2.144	–	–
	–	–	6645.085	1.379	-3.788	–	–
	–	–	6645.097	1.379	-0.914	–	–
	–	–	6645.104	1.379	-1.949	–	–
	–	–	6645.112	1.379	-3.470	–	–
	–	–	6645.118	1.379	-0.993	–	–
	–	–	6645.126	1.379	-1.904	–	–
	–	–	6645.133	1.379	-3.398	–	–
	–	–	6645.137	1.379	-1.075	–	–
	–	–	6645.144	1.379	-1.956	–	–
	–	–	6645.150	1.379	-3.566	–	–
	–	–	6645.152	1.379	-1.160	–	–
	–	–	6645.158	1.379	-2.151	–	–
	–	–	6645.163	1.379	-1.242	–	–
	$^{153}_{63}$Eu II	0.522	6645.072	1.379	-2.105	–	–
	–	–	6645.074	1.379	-0.799	–	–
	–	–	6645.074	1.379	-3.749	–	–
	–	–	6645.087	1.379	-0.875	–	–
	–	–	6645.089	1.379	-1.910	–	–
	–	–	6645.094	1.379	-3.431	–	–
	–	–	6645.096	1.379	-0.954	–	–
	–	–	6645.101	1.379	-1.865	–	–
	–	–	6645.104	1.379	-1.036	–	–
	–	–	6645.107	1.379	-3.359	–	–
	–	–	6645.109	1.379	-1.121	–	–
	–	–	6645.110	1.379	-1.917	–	–
	–	–	6645.113	1.379	-1.203	–	–
	–	–	6645.116	1.379	-2.112	–	–
	–	–	6645.116	1.379	-3.527	–	–

Volume Title
ASP Conference Series, Vol. **Volume Number**
Author

α-elements abundances in the Large Magellanic Cloud Bar

Mathieu Van der Swaelmen,[1,2] Vanessa Hill,[1] and Francesca Primas[2]

[1] *Laboratoire Lagrange, UMR 7293, Université de Nice Sophia-Antipolis, CNRS, Observatoire de la Côte d'Azur, Bd. de l'Observatoire BP 4229, F-06304, Nice cedex 4*

[2] *European Southern Observatory, Karl Schwarzschild Str. 2, 85748 Garching b. München, Germany*

Abstract. We carried out a spectroscopy survey of about 110 stars located in the bar of the Large Magellanic Cloud (LMC) that combined with photometry already available allowed us to derive photometric temperatures, surface gravities, microturbulence velocity, overall metallicity, [Fe/H] and [α/Fe] ratios. We compare our results to Galactic stellar populations and to the LMC inner disc sample.

1. Introduction

The LMC is one of the closest satellites of the Milky Way (MW), located at only 50kpc. This low-mass disc galaxy showing a prominent stellar bar is almost face-on, which gives us the possibility to easily distinguish these different components. The LMC is believed to have had an irregular star formation history (SFH). Especially, the central parts that are showing a stronger star formation 2-5 Gyrs ago, maybe related to the formation of the bar (Smecker-Hane et al. 2002). Dynamical simulations by Bekki et al. (2004) and Bekki & Chiba (2005, 2007) are able to explain the increase in star formation activity (new start of star formation, formation of the bar, formation of the Magellanic Stream) with the first close encounter with the Small Magellanic Cloud about 4 Gyr ago.

To investigate the relation between the bar and the disc, we obtained spectra of 110 stars located in the LMC bar at the ESO/VLT with the FLAMES multifibre spectrograph ($R \sim 20,000$) in 3 different wavelength regions covering a total of 600 Å, complementing a similar dataset in the LMC disc, $\sim$ 2 kpc from the center (Pompéia et al. 2008). Equivalent widths (EW) measured with DAOSPEC (Stetson & Pancino 2008) were translated into abundances with *turbospectrum* (Alvarez & Plez 1998) using OSMARCS spherical atmosphere models (Gustafsson et al. 2008). The sample of Pompéia et al. (2008) was reanalysed in exactly the same fashion to insure a homogeneous comparison of bar and disc fields.

2. Results and conclusions

Figure 1 shows that the LMC bar has experienced a chemical enrichment different from that of the Milky Way (MW) disc, with a slower SFH (left panel): 1) while metal-

poor LMC stars possess alpha abundances similar to those of MW halo stars, stars with [Fe/H] ≥ -1 have [α/Fe] smaller than that of the MW; 2) the transition between the SNe II-dominated regime and SNe Ia-dominated regime seems to occur at a lower metallicity in the LMC bar than in the MW. The fields of the bar and the inner disc (Pompéia et al. 2008) show similar [α/Fe] pattern at low metallicity (right plot). Nevertheless, there is a hint that for $-0.3 \leq$ [Fe/H] ≤ -0.6, the [α/Fe] ratio is higher in the inner disc than in the bar, which is also shown by the steeper decrease of the running average of the bar data.

The right panel shows the α age-metallicity relation (AMR) of our two LMC fields. While abundance ratios of the bar and the inner disc are similar for old ages, they become differentiated for intermediate ages, the α-AMR of the bar being surprisingly flat between 1 and 6 Gyr. Theoretical AMRs' proposed by Pagel & Tautvaisiene (1998) are shown for a bursting and a continuous SFH. The smooth model systematically predicts higher abundances than observed, while the bursting model gives ratios closer to our measurements: it suggests that the bar has experienced a bursting SFH, with a weak activity at intermediate ages.

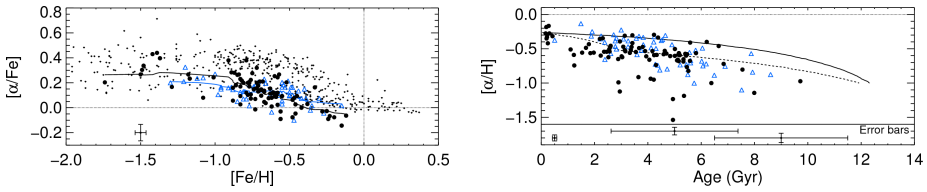

Figure 1. Filled black circles: LMC bar (this work), empty blue triangles: LMC inner disc, small black dots: MW thin and thick disc (Bensby et al. 2005; Reddy et al. 2003, 2006), and halo (Fulbright 2000; Stephens & Boesgaard 2002). [α/Fe] = 1/3([O/Fe] + [Mg/Fe] + [Si/Fe]). Left panel: the data were smoothed with a boxcar average (black and blue continuous lines). Right panel: dashed line: AMR for bursting SFH (bursts 3 and 12 Gyr ago), continuous line: AMR for continuous SFH (Pagel & Tautvaisiene 1998). Typical error bars are given for the bar abundances.

References

Alvarez, R., & Plez, B. 1998, A&A, 330, 1109
Bekki, K., & Chiba, M. 2005, MNRAS, 356, 680
— 2007, MNRAS, 381, L16
Bekki, K., Couch, W. J., Beasley, M. A., Forbes, D. A., Chiba, M., & Da Costa, G. S. 2004, ApJ, 610, L93
Bensby, T., Feltzing, S., Lundström, I., & Ilyin, I. 2005, A&A, 433, 185
Fulbright, J. P. 2000, AJ, 120, 1841
Gustafsson, B., Edvardsson, B., Eriksson, K., Jørgensen, U. G., Nordlund, Å., & Plez, B. 2008, A&A, 486, 951
Pagel, B. E. J., & Tautvaisiene, G. 1998, MNRAS, 299, 535
Pompéia, L., Hill, V., Spite, M., Cole, A., Primas, F., Romaniello, M., Pasquini, L., Cioni, M.-R., & Smecker Hane, T. 2008, A&A, 480, 379
Reddy, B. E., Lambert, D. L., & Allende Prieto, C. 2006, MNRAS, 367, 1329
Reddy, B. E., Tomkin, J., Lambert, D. L., & Allende Prieto, C. 2003, MNRAS, 340, 304
Smecker-Hane, T. A., Cole, A. A., Gallagher, J. S., III, & Stetson, P. B. 2002, ApJ, 566, 239
Stephens, A., & Boesgaard, A. M. 2002, AJ, 123, 1647
Stetson, P. B., & Pancino, E. 2008, PASP, 120, 1332

SF2A 2012
S. Boissier, P. de Laverny, N. Nardetto, R. Samadi, D. Valls-Gabaud and H. Wozniak (eds)

ELEMENTAL ABUNDANCES IN RGB STARS OF THE LARGE MAGELLANIC CLOUD

M. Van der Swaelmen[1], V. Hill[1] and F. Primas[2]

Abstract. The present work is based on a high-resolution spectroscopic survey of two LMC fields located in the bar and the inner disc, observed at ESO/VLT with FLAMES/GIRAFFE. Three setups were used to cover about 1000 Å and enable the measurement of numerous elemental abundances. We confront the results in the inner disc and bar fields and discuss their similarities/differences in the light of the origin of the LMC bar. Both fields show that the LMC has a SFH slower than the MW, resulting in a chemical evolution dominated by SNIa and metal-poor AGB winds. Chemical anomalies for Eu, Ba and La are detected in the most metal-rich field stars, as it has been before in LMC GC stars, and cannot be explained by canonical nucleosynthesis processes.

Keywords: Abundances, Magellanic Clouds, Galaxy: evolution

1 Introduction

Despite decades of intensive observational and theoretical works, we are still far from a complete and clear understanding of our close universe, the Milky Way (MW) and its neighbours. Among the satellites of the MW, the Small and the Large Magellanic Clouds (SMC, LMC) are of particular interest since it is the closest example of galaxies in gravitational (systems: SMC+LMC, SMC+LMC+MW) and chemical interactions (Magellanic Bridge between the clouds, made of stars and gas). Therefore it is a unique laboratory to study the effect of gravitational tides and matter exchange on the chemical evolution and the star formation history of a galaxy. The LMC is an almost face-on, gas-rich galaxy with regions of active stellar formation (distance: 50 kpc (Alves 2004), mass: $10^{10}M_{\odot}$ (van der Marel et al. 2002)). The young population exhibits an irregular morphology, likely the stigmata of the very recent interaction with the SMC. The old and intermediate-age population are located within a regular disc and a prominent and luminous off-centre bar. The morphology of the LMC is not well understood and, in particular, we still do not know the origin and the true nature of the bar-like structure: is it a dynamical bar driven by disc instabilities like the one found at the centre of the MW or is it a stellar overdensity? was the formation of the bar driven by a close encounter with the SMC (Subramaniam & Subramanian 2009; Zaritsky 2004; Bekki 2009)? Smecker-Hane et al. (2002) have derived from deep colour-magnitude diagram (CMD) the star formation histories for field stars located in the LMC bar and the inner part of the LMC disc. They found that the LMC field stars do no exhibit an age gap, unlike the stars of the LMC globular clusters (GC), hence their usefulness to probe the epoch 3 to 13 Gyr (see also Cole et al. 2005). Moreover they show that the star formation history (SFH) of the bar and the inner disc were similar at old epochs (between 7 and 14 Gyr); but while the SFH of the inner disc has remained rather constant, the bar has experienced a dramatic increase of its SFH, 4 to 6 Gyr ago. Interestingly, it corresponds to the epoch of the formation of the bar. This work aims at investigating the chemical history of and the relation between the bar and the disc via a detailed chemical analysis of Red Giant Branch (RGB) stars located in the bar and in the inner disc.

[1] Laboratoire Lagrange, UMR 7293, Université de Nice Sophia-Antipolis, Observatoire de la Côte d'Azur, BP4229, 06304, Nice Cedex 4, France
[2] European Southern Observatory, Karl Schwarzschild Str. 2, 85748 Garching b. München, Germany

2 Data and methods

Cole et al. (2005) observed 373 RGB stars in the field of the LMC bar and derived radial velocities and metallicities for their stars. We used their metallicity distribution to select 113 RGB stars belonging to the LMC bar, taking care to sample each metallicity bin from $[Fe/H]_{CaT} = -1.69$ dex to $[Fe/H]_{CaT} = 0.14$ dex. We obtained high resolution spectra ($R \sim 20,000$) of our 113 stars at VLT/ESO with the FLAMES/GIRAFFE multifibre spectrograph (Pasquini et al. 2002). In order to measure numerous elemental abundances, we used three setups HR11, HR13 and HR14, covering a total of ≈ 1000 Å. The spectra thus cover lines belonging to the α- (Ca, O, Mg, Ti, Si), iron-peak (Sc, V, Cr, Co, Ni, Cu), s-process and r-process elements (Ba, La, Zr, Y, Eu). This complements a similar dataset in the LMC disc, located at ~ 2 kpc from the centre (Pompéia et al. 2008). We carried out the data reduction with the help of the ESO GIRAFFE pipeline (built upon the Geneva Giraffe pipeline described in Blecha et al. 2000), part of the *esorex* framework. The reduction steps include the dark current correction, wavelength calibration (using a Th-Ar lamp), spectrum extraction and flat fielding. As the pipeline does not support sky subtraction nor radial velocity correction, we carried out those operations separately. Once all exposures of the same star were sky-subtracted and in the same frame, we averaged them with k-σ clipping rejection (over the fluxes at a given wavelength) to clean for cosmic rays and increase the signal-to-noise ratio (SNR). We ended with a typical final SNR of around 25 for HR11, 40 for HR13 and 48 for HR14.

3 Stellar parameters and abundances

To derive the stellar parameters of our LMC stars (the temperature T_{phot}, the gravity $\log g$, the overall metallicity [M/H] and the microturbulent velocity ξ_{micro}), we used a combination of photometric and spectroscopic methods. For our stars, visible (V and I magnitude, from the OGLE catalogue Udalski et al. 1997, 2000; Szymanski 2005) and infrared (J, H and K magnitude, from the 2MASS catalogue Skrutskie et al. 2006) photometry is available. We used the Ramírez & Meléndez (2005a,b) photometric calibrations for giants to compute four scales of photometric temperatures, using four de-reddened colour indices. The surface gravities $\log g$ were derived using the Bayesian estimation algorithm of stellar parameters of da Silva et al. (2006), based on evolutionary tracks. The overall metallicity and the microturbulent velocity were derived simultaneously by requiring that different FeI lines of different equivalent widths (EW) give the same iron abundance [FeI/H].

We used the two traditional methods to measure the chemical abundances: EW and fitting of absorption profiles. For the first method, we used the automated tool DAOSPEC (Stetson & Pancino 2008) to measure the EW and we converted them into abundances with *turbospectrum* (*turbospectrum* is described in Alvarez & Plez 1998 and improved along the years by B. Plez) together with the grid of OSMARCS spherical model atmospheres (Gustafsson et al. 2008). The spectrum syntheses, computed by *turbospectrum*, are in spherical geometry, with LTE spherical radiative transfer. The second method, the fitting of absorption profile, consists in computing a grid of theoretical spectra by varying the abundance of an element and comparing them to an observed absorption line of this specific element. We used a χ^2 minimisation to find the best fitting, which gives the value of the elemental abundance. We re-analysed (stellar parameters+abundances) the sample of LMC disc stars of (Pompéia et al. 2008), in exactly the same fashion to insure a homogeneous comparison of bar and disc fields and we used Arcturus as a reference star to determine the zero-point of our chemical abundances scale. The abundances we derived for Arcturus are in good agreement with the literature (Ramírez & Allende Prieto 2011; Worley et al. 2009). The tests we performed on noisy Arcturus spectra (at the same SNR level of GIRAFFE spectra) allowed us to derive typical error bars for our LMC stars.

4 Results

In this section, we present the results for some key elements: O, Mg, Si (α elements), Ba, La and Eu (s- and r-elements). Figure 1 (left panel) shows the [α/Fe] trend (mean of O, Mg and Si ratios) for the LMC bar and disc stars, as well as that of the MW. α elements are thought to be produced in massive stars interiors dying as type II supernovae (SNII) while iron is mainly produced in type Ia supernovae (SNIa). Therefore, the ratio [α/Fe] can track the epoch when SNIa start to dominate the chemical enrichment of a galactic environment. Metal-poor ($[Fe/H] \leq -1.1$ dex) LMC stars possess alpha abundances similar to those of MW halo stars, but we note that stars with higher metallicity have α ratios smaller than that of the MW. Unlike for the MW, we do not see a clearly defined plateau in the LMC trends in the low metallicity regime; but despite the paucity of data, we can

suspect that the transition between the SNe II-dominated regime and SNe Ia-dominated regime seems to occur at a lower metallicity in the LMC bar than in the MW. This tells us that the LMC bar has experienced a chemical enrichment different from that of the Milky Way, with a slower SFH. The LMC bar and disc do not exhibit strong differences, though a larger scatter of [α/Fe] is observed for the bar for $-1\,\mathrm{dex} \leq [\mathrm{Fe/H}] \leq -0.5\,\mathrm{dex}$. Remarkably, we found an excellent agreement between globular clusters (Mucciarelli et al. 2008, 2010) and field stars at both low and high metallicities (we do not have stars at the metallicity of the metal-poor GC but the level of their [α/Fe] is compatible with that of the most metal-poor field stars).

Figure 1 (right panel) shows the [Eu/Fe] trend for the LMC bar and disc stars, and the MW stellar populations. According to chemical composition of the Sun, europium is thought to be an element mainly produced by the r-process occurring during SNII explosive nucleosynthesis. Therefore, we expect it to follow a pattern similar to that of the [α/Fe]. At low metallicity, we have enhanced [Eu/Fe] for the LMC as expected, but we have also enhanced ratios at high metallicities. For the low metallicity regime, the abundance ratios of the LMC and the MW overlap, while for $[\mathrm{Fe/H}] \geq -1\,\mathrm{dex}$ the LMC trend is above the MW's. This chemical anomaly cannot be understood in the canonical nucleosynthesis picture recalled before. To explain it, we may invoke another source of Eu. Asymptotic Giant Branch (AGB) stars may be candidates: they are the place of s-process nucleosynthesis, and so, can produce Eu. Nevertheless, it is not clear whether the production of Eu would be efficient enough to reach such high [Eu/Fe]. Here again, we found an excellent agreement between LMC field and LMC GC stars. It is worth mentioning that this enhancement at high metallicity is not an artifact of our abundance analysis since we found the expected value for Arcturus.

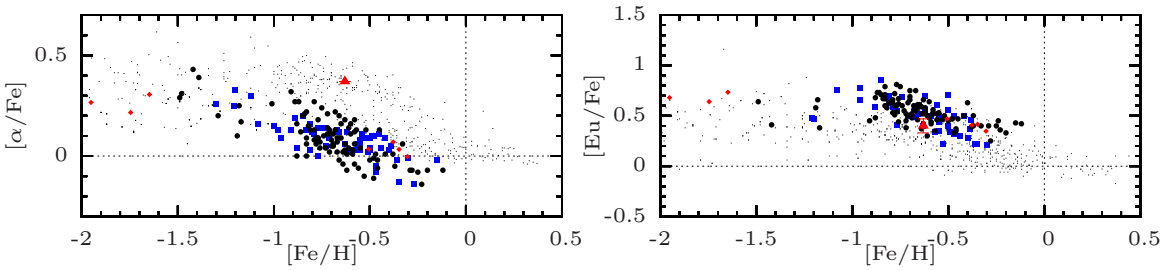

Fig. 1. Left: [α/Fe] vs [Fe/H]. **Right:** [Eu/Fe] vs [Fe/H]. Legend for both: black dots: LMC bar (this study), blue squares: LMC disc (re-analysis of Pompéia et al. 2008), red diamonds: LMC GC (Mucciarelli et al. 2008, 2010), red triangle: Arcturus (reference star of this study), black tiny points: MW thin and thick disc (Bensby et al. 2005; Reddy et al. 2003, 2006), MW halo (Fulbright 2000; Stephens & Boesgaard 2002).

Figure 2 (left panel) shows the [Ba, La/Eu] trend. Ba and La are s- and r-elements, produced by AGB and SNII; the [Ba, La/Eu] allows to track the relative importance of SNII and AGB in the chemical enrichment. For a pure r-process, Arlandini et al. (1999) predict $[\mathrm{Ba/Eu}] = -0.67\,\mathrm{dex}$. This value is reached for the metal-poor stars of LMC GC. The s-process starts to dominate from a metallicity of about $-1\,\mathrm{dex}$ in the LMC bar and disc. Moreover, the [Ba/Eu] and [La/Eu] increase is steeper in the LMC than in the MW: it proves that AGB played a stronger role in the chemical enrichment of the LMC, compared to the MW. Figure 2 (right panel) shows the [Ba/Fe] trend (similar pattern is observed for [La/Fe]). A very steep increase of LMC [Ba/Fe] is observed from $[\mathrm{Fe/H}] \approx -1.1\,\mathrm{dex}$, while the LMC and MW ratios overlap for lower metallicities. This dramatic increase is not expected in the canonical nucleosynthesis picture and clearly contrasts with what is observed for the MW. This is another chemical anomaly, shared by the dwarf galaxies like Fornax or Sagittarius, two galaxies also dominated by intermediate-age stellar populations. We may explain this with very efficient AGB winds.

5 Discussion and conclusion

We performed a detailed chemical analysis of LMC field stars located in the bar and the disc and compared it to LMC GC stars and MW field stars. We found that the LMC had a chemical history different from that of the MW: the SFH of the LMC was slower and the chemical enrichment was dominated by SNIa (α trend) and AGB winds ([Ba, La/Eu] vs [Fe/H]). We found chemical anomalies for Ba, La and Eu compared to the Galactic trends. Those trends are the results of a chemical enrichment occurring in a metal-poor environment and cannot be completely apprehended in the current chemical evolution scheme: they recall the importance of studying external galaxies that followed different enrichment path in order to perfect our understanding of the

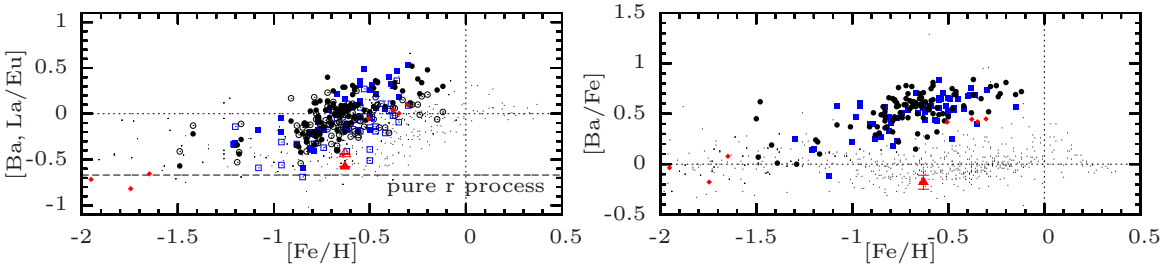

Fig. 2. Left: [Ba/Eu] vs [Fe/H] (filled symbols), [La/Eu] vs [Fe/H] (empty symbols). **Right:** [Ba, La/Fe] vs [Fe/H]. Same legend as Figure 1.

details of galactic chemical evolution. The two LMC fields do not exhibit strong differences in their abundance patterns, except for the α. For the α elements, a larger scatter is observed for the bar stars in the metallicity range $[-1, -0.5]$ and maybe related to the formation of the bar: the start of a new episode of star formation will increase the number of massive stars, in which the α elements originate, and therefore will enrich the interstellar medium with freshly formed α. If this scatter is true, then it is a proof that the bar is a stellar overdensity and not a dynamical structure. We found similar abundance ratios for the LMC field and GC populations, which is rather intriguing since we should expect a different chemical history (no GC formation between $\sim$ 10 and 3 Gyr ago, while the field star formation has never stopped).

References

Alvarez, R. & Plez, B. 1998, A&A, 330, 1109
Alves, D. R. 2004, New A Rev., 48, 659
Arlandini, C., Käppeler, F., Wisshak, K., et al. 1999, ApJ, 525, 886
Bekki, K. 2009, MNRAS, 393, L60
Bensby, T., Feltzing, S., Lundström, I., & Ilyin, I. 2005, A&A, 433, 185
Blecha, A., Cayatte, V., North, P., Royer, F., & Simond, G. 2000, in SPIE Conference Series, Vol. 4008, Society of Photo-Optical Instrumentation Engineers (SPIE) Conference Series, ed. M. Iye & A. F. Moorwood, 467–474
Cole, A. A., Tolstoy, E., Gallagher, III, J. S., & Smecker-Hane, T. A. 2005, AJ, 129, 1465
da Silva, L., Girardi, L., Pasquini, L., et al. 2006, A&A, 458, 609
Fulbright, J. P. 2000, AJ, 120, 1841
Gustafsson, B., Edvardsson, B., Eriksson, K., et al. 2008, A&A, 486, 951
Mucciarelli, A., Carretta, E., Origlia, L., & Ferraro, F. R. 2008, AJ, 136, 375
Mucciarelli, A., Origlia, L., & Ferraro, F. R. 2010, ApJ, 717, 277
Pasquini, L., Avila, G., Blecha, A., et al. 2002, The Messenger, 110, 1
Pompéia, L., Hill, V., Spite, M., et al. 2008, A&A, 480, 379
Ramírez, I. & Allende Prieto, C. 2011, ApJ, 743, 135
Ramírez, I. & Meléndez, J. 2005a, ApJ, 626, 446
Ramírez, I. & Meléndez, J. 2005b, ApJ, 626, 465
Reddy, B. E., Lambert, D. L., & Allende Prieto, C. 2006, MNRAS, 367, 1329
Reddy, B. E., Tomkin, J., Lambert, D. L., & Allende Prieto, C. 2003, MNRAS, 340, 304
Skrutskie, M. F., Cutri, R. M., Stiening, R., et al. 2006, AJ, 131, 1163
Smecker-Hane, T. A., Cole, A. A., Gallagher, III, J. S., & Stetson, P. B. 2002, ApJ, 566, 239
Stephens, A. & Boesgaard, A. M. 2002, AJ, 123, 1647
Stetson, P. B. & Pancino, E. 2008, PASP, 120, 1332
Subramaniam, A. & Subramanian, S. 2009, ApJ, 703, L37
Szymanski, M. K. 2005, Acta Astron., 55, 43
Udalski, A., Kubiak, M., & Szymanski, M. 1997, Acta Astron., 47, 319
Udalski, A., Szymanski, M., Kubiak, M., et al. 2000, Acta Astron., 50, 307
van der Marel, R. P., Alves, D. R., Hardy, E., & Suntzeff, N. B. 2002, AJ, 124, 2639
Worley, C. C., Cottrell, P. L., Freeman, K. C., & Wylie-de Boer, E. C. 2009, MNRAS, 400, 1039
Zaritsky, D. 2004, ApJ, 614, L37

Mem. S.A.It. Vol. 75, 282

Memorie della

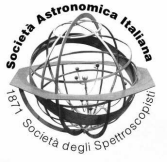

Elemental abundances in RGB stars of the Large Magellanic Cloud

M. Van der Swaelmen[1,2], V. Hill[1], and F. Primas[2]

[1] Laboratoire Lagrange, UMR 7293, Université de Nice Sophia-Antipolis, Observatoire de la Côte d'Azur, BP4229, 06304, Nice Cedex 4, France
[2] European Southern Observatory, Karl Schwarzschild Str. 2, 85748 Garching b. München, Germany
e-mail: swaelmen@oca.eu

Abstract. The present work is based on a high-resolution spectroscopic survey of two LMC fields located in the bar and the inner disc, observed at ESO/VLT with FLAMES/GIRAFFE. We confront the results in the LMC inner disc and bar fields and discuss their similarities/differences in the light of the origin of the LMC bar. Both fields show that the LMC has a SFH slower than the MW, resulting in a chemical evolution dominated by SNIa and metal-poor AGB winds. Chemical anomalies for Eu, Ba and La are detected in the most metal-rich field stars, as it has been before in LMC GC stars, and cannot be explained by canonical nucleosynthesis processes.

Key words. Stars: abundances - Galaxies: Magellanic Clouds - Galaxies: abundances - Galaxies: evolution

1. Introduction

Despite decades of intensive observational and theoretical works, we are still far from a complete and clear understanding of our close universe, the Milky Way (MW) and its neighbours. Among the satellites of the MW, the Small and the Large Magellanic Clouds (SMC, LMC) are of particular interest since it is the closest example of galaxies in gravitational (systems: SMC+LMC, SMC+LMC+MW) and chemical interactions (Magellanic Bridge between the clouds, made of stars and gas). The LMC is an almost face-on, gas-rich galaxy with regions of active stellar formation (distance: 50 kpc (Alves 2004), mass: $10^{10}M_{\odot}$ (van der Marel et al. 2002)). The young population exhibits an irregular morphology, likely the stigmata of the very recent interaction with the SMC. The old and intermediate-age population are located within a regular disc and a prominent and luminous off-centre bar. The morphology of the LMC is not well understood and, in particular, we still do not know the origin and the true nature of the bar-like structure (dynamical bar driven by disc instabilities or new stellar population) (Subramaniam & Subramanian 2009; Zaritsky 2004; Bekki 2009). Smecker-Hane et al. (2002) have derived from deep colour-magnitude diagram (CMD) the star formation histories (SFH) for field stars located in the LMC bar and the inner part of the LMC disc. They found that the LMC field stars do no ex-

Send offprint requests to: M. Van der Swaelmen

hibit an age gap, unlike the stars of the LMC globular clusters (GC), hence their usefulness to probe the epoch 3 to 13 Gyr (see also Cole et al. 2005). Moreover they show that the SFH of the bar and the inner disc were similar at old epochs (between 7 and 14 Gyr); but while the SFH of the inner disc has remained rather constant, the bar has experienced a dramatic increase of its SFH, 4 to 6 Gyr ago, corresponding to the epoch of the formation of the bar. This work aims at investigating the chemical history of and the relation between the bar and the disc via a detailed chemical analysis of Red Giant Branch (RGB) stars located in the bar and in the inner disc.

2. Data and methods

We obtained high resolution spectra ($R \sim 20,000$) for 113 LMC bar stars at VLT/ESO with the FLAMES/GIRAFFE multifibre spectrograph (Pasquini et al. 2002). This complements a similar dataset in the LMC disc, located at ~ 2 kpc from the centre (Pompéia et al. 2008). We carried out the data reduction with the help of the ESO GIRAFFE pipeline (built upon the Geneva Giraffe pipeline described in Blecha et al. 2000) and with our own reduction routines: our reduced averaged spectra have a typical final SNR of around 25 for HR11, 40 for HR13 and 48 for HR14.

We derived the temperature T_{phot} from VIJHK photometry (Udalski et al. 1997, 2000; Szymanski 2005) using photometric calibrations for giants (Ramírez & Meléndez 2005a,b), the surface gravities $\log g$ using the Bayesian estimation algorithm of stellar parameters of da Silva et al. (2006), and the overall metallicity and the microturbulent velocity simultaneously by requiring that different FeI lines of different equivalent widths (EW) give the same iron abundance [FeI/H].

We used both EW and fitting of absorption profiles to derive abundances. We measured EW with DAOSPEC (Stetson & Pancino 2008) and converted them into abundances. We computed synthetic spectra with *turbospectrum* (Alvarez & Plez 1998), together with the grid of OSMARCS spherical model atmospheres (Gustafsson et al. 2008) and used a χ^2 minimisation to find the best fit abundance. We reanalysed (stellar parameters+abundances) the sample of LMC disc stars of (Pompéia et al. 2008), in exactly the same fashion to insure a homogeneous comparison of bar and disc fields and we used Arcturus as a reference star to determine the zero-point of our chemical abundances scale. The abundances we derived for Arcturus are in good agreement with the literature (Ramírez & Allende Prieto 2011; Worley et al. 2009).

3. Results and discussion

In this section, we present the results for some key elements: O, Mg, (α elements), Ba, La and Eu (s- and r-elements). α-elements are used to track the epoch where SNeII drove the chemical evolution of the galaxy since at early epochs, α elements and iron are produced in massive stars interiors and are released to the ISM through SNeII explosions (Burbidge et al. 1957) (α-plateau) while later, iron is mainly produced in type Ia supernovae (SNIa). Figure 1 shows the [α/Fe] trend (mean of O and Mg) for the LMC bar and disc stars, as well as that of the MW. We clearly see that compared to the MW, the LMC has deficient [α/Fe] for [Fe/H] ≥ -1.3 dex. Those low [α/Fe] ratios can be explained by a higher contribution of SNIa to the chemical enrichment of the LMC, compared to the MW. Unlike for the MW, we do not see a plateau until [Fe/H] ≈ -1.5 dex in the LMC trends; despite the paucity of data, we can suspect that the plateau pops up for [Fe/H] $\lessapprox -1.6$ dex. This indicates that the SFH has been slower in the LMC than in the MW.

Unlike the elements lighter than iron, the heavy elements are produced by neutron captures through s- and r-processes. While it is known that the s-process takes place in the envelopes of AGB stars (*e.g.*, Busso et al. 1999), the r-process can in principle take place in several sites (Qian 2012), such as SNII (Wasserburg et al. 1996) or neutron stars (Freiburghaus et al. 1999). In Figure 1, we see that the LMC bar and disc Eu distributions agree very well: they both exhibit a constant [Eu/Fe] ≈ 0.5 dex for [Fe/H] ≤ -0.8 dex, then

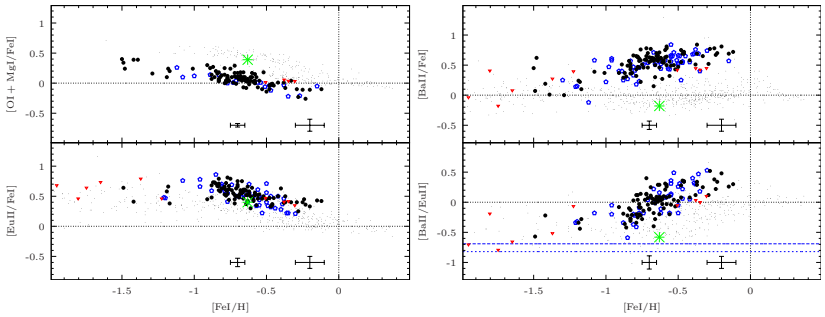

Fig. 1. Top left: [O I + Mg I/2Fe I] vs. [Fe I/H]. **Bottom left:** [Eu II/Fe I] vs. [Fe I/H]. **Top Right:** [Ba II/Fe I] vs. [Fe I/H]. **Bottom right:** [Ba II/Eu II] vs. [Fe I/H]. **Legend:** black filled circles: LMC bar (this work); blue open pentagons: LMC inner disc (this work); green asterisk: Arcturus (this work, data for median SNR); red downward triangle: LMC GC (Johnson et al. 2006; Mucciarelli et al. 2008, 2010); black tiny dots: MW thin and thick disc (Bensby et al. 2005; Reddy et al. 2003, 2006), halo (Fulbright 2000; Stephens & Boesgaard 2002; Reddy et al. 2006), MW data for Eu and La from Simmerer et al. (2004); Brewer & Carney (2006); blue dashed and dotted lines: $[Ba_r/Eu_r]$ (Arlandini et al. 1999 and Sneden et al. 2008, respectively). Typical random (left) and systematic (right) error bars on both coordinates are provided for our LMC samples.

a decreasing trend with increasing metallicity. The LMC Eu distribution does not match that of the MW: while for the metal-poor stars the abundance ratios of the LMC and the MW halo overlap, for [Fe/H] ≥ -1 dex the LMC trend is above that of MW. This enhancement for metal-rich stars is not an artifact of our analysis since Arcturus has the expected Eu abundance (*i.e.* it falls in the MW thick disc): this is a chemical anomaly already noticed in LMC supergiant stars (Russell & Bessell 1989; Hill et al. 1995) and LMC GC stars (Mucciarelli et al. 2008; Colucci et al. 2012) and its origin still remains unclear. However, recent work on CEMP-*r*/*s* by Allen et al. (2012) suggests that metal-poor AGB stars could have significant Eu production through *s*-process.

While the MW has constant solar [Ba/Fe] ratios (with a weak increase towards high metallicities), both LMC fields exhibit a dramatic increase of [Ba/Fe] with increasing metallicity. This indicates that the production of Ba and La has been much more efficient in the LMC than in the MW. To identify the process responsible for this high production, we examine [Ba/Eu]. We see that for LMC GC and field metal-poor stars (from -2. dex to -0.8 dex), [Ba/Eu] is constant and compatible (within uncertainties) with a pure *r*-process source (see Fig. 1). On the other hand, for [Fe/H] ≥ -0.8 dex, the increase of the LMC [Ba/Eu] is interpreted as the rise of a new source of Ba and La, *i.e.* the *s*-process. The differences between the LMC and the MW (the increase starts at lower metallicity, the LMC has higher ratios) suggest that the production of Ba by the *s*-process has been much more efficient in the LMC than in the MW, and thus it indicates that AGB stars played a stronger role in the chemical enrichment of the LMC compared to the MW. Furthermore, the LMC has lower [Y + Zr/Ba + La] ([1^{st} peak/2^{nd} peak]) than the MW, which shows that the AGB stars that contributed to the chemical enrichment were more metal-poor (Cristallo et al. 2011).

4. Conclusion

We found that the LMC had a chemical history different from that of the MW: the SFH of the LMC was slower and the chemical enrichment was dominated by SNIa (α trend) and AGB winds ([Ba/Eu] vs [Fe/H]). We found chemical anomalies in Eu compared to the Galactic

trends, which probably indicate that Eu can be significantly produced by *s*-process. For these elements, the two LMC fields do not exhibit strong differences in their abundance patterns, except for the α, where a slightly larger scatter of [α/Fe] is observed for the bar for -0.8 dex $\leq$ [Fe/H] ≤ -0.5 dex. According to the age-metallicity relation (Cole et al. 2005), this metallicity range corresponds to the age range 2 Gyr to 6 Gyr ago, thus the suspected epoch of the bar formation and it can be understood in a scenario where a new population is formed (new burst of star formation).

References

Allen, D. M., Ryan, S. G., Rossi, S., Beers, T. C., & Tsangarides, S. A. 2012, A&A, 548, A34

Alvarez, R. & Plez, B. 1998, A&A, 330, 1109

Alves, D. R. 2004, New A Rev., 48, 659

Arlandini, C., Käppeler, F., Wisshak, K., et al. 1999, ApJ, 525, 886

Bekki, K. 2009, MNRAS, 393, L60

Bensby, T., Feltzing, S., Lundström, I., & Ilyin, I. 2005, A&A, 433, 185

Blecha, A., Cayatte, V., North, P., Royer, F., & Simond, G. 2000, in SPIE, ed. M. Iye & A. F. Moorwood, Vol. 4008, 467–474

Brewer, M.-M. & Carney, B. W. 2006, AJ, 131, 431

Burbidge, E. M., Burbidge, G. R., Fowler, W. A., & Hoyle, F. 1957, Reviews of Modern Physics, 29, 547

Busso, M., Gallino, R., & Wasserburg, G. J. 1999, ARA&A, 37, 239

Cole, A. A., Tolstoy, E., Gallagher, III, J. S., & Smecker-Hane, T. A. 2005, AJ, 129, 1465

Colucci, J. E., Bernstein, R. A., Cameron, S. A., & McWilliam, A. 2012, ApJ, 746, 29

Cristallo, S., Piersanti, L., Straniero, O., et al. 2011, ApJS, 197, 17

da Silva, L., Girardi, L., Pasquini, L., et al. 2006, A&A, 458, 609

Freiburghaus, C., Rosswog, S., & Thielemann, F.-K. 1999, ApJ, 525, L121

Fulbright, J. P. 2000, AJ, 120, 1841

Gustafsson, B., Edvardsson, B., Eriksson, K., et al. 2008, A&A, 486, 951

Hill, V., Andrievsky, S., & Spite, M. 1995, A&A, 293, 347

Johnson, J. A., Ivans, I. I., & Stetson, P. B. 2006, ApJ, 640, 801

Mucciarelli, A., Carretta, E., Origlia, L., & Ferraro, F. R. 2008, AJ, 136, 375

Mucciarelli, A., Origlia, L., & Ferraro, F. R. 2010, ApJ, 717, 277

Pasquini, L., Avila, G., Blecha, A., et al. 2002, The Messenger, 110, 1

Pompéia, L., Hill, V., Spite, M., et al. 2008, A&A, 480, 379

Qian, Y.-Z. 2012, ArXiv e-prints

Ramírez, I. & Allende Prieto, C. 2011, ApJ, 743, 135

Ramírez, I. & Meléndez, J. 2005a, ApJ, 626, 446

Ramírez, I. & Meléndez, J. 2005b, ApJ, 626, 465

Reddy, B. E., Lambert, D. L., & Allende Prieto, C. 2006, MNRAS, 367, 1329

Reddy, B. E., Tomkin, J., Lambert, D. L., & Allende Prieto, C. 2003, MNRAS, 340, 304

Russell, S. C. & Bessell, M. S. 1989, ApJS, 70, 865

Simmerer, J., Sneden, C., Cowan, J. J., et al. 2004, ApJ, 617, 1091

Smecker-Hane, T. A., Cole, A. A., Gallagher, III, J. S., & Stetson, P. B. 2002, ApJ, 566, 239

Sneden, C., Cowan, J. J., & Gallino, R. 2008, ARA&A, 46, 241

Stephens, A. & Boesgaard, A. M. 2002, AJ, 123, 1647

Stetson, P. B. & Pancino, E. 2008, PASP, 120, 1332

Subramaniam, A. & Subramanian, S. 2009, ApJ, 703, L37

Szymanski, M. K. 2005, Acta Astron., 55, 43

Udalski, A., Kubiak, M., & Szymanski, M. 1997, Acta Astron., 47, 319

Udalski, A., Szymanski, M., Kubiak, M., et al. 2000, Acta Astron., 50, 307

van der Marel, R. P., Alves, D. R., Hardy, E., & Suntzeff, N. B. 2002, AJ, 124, 2639

Wasserburg, G. J., Busso, M., & Gallino, R. 1996, ApJ, 466, L109

Worley, C. C., Cottrell, P. L., Freeman, K. C., & Wylie-de Boer, E. C. 2009, MNRAS, 400, 1039

Zaritsky, D. 2004, ApJ, 614, L37

Acronyms

ΛCDM Λ cold dark matter.

AGB asymptotic giant branch.

AMR age-metallicity relation.

BH black hole.

CaT Ca II triplet.

CCD coupled-charged device.

CEMP carbon enhanced metal-poor.

CMD color-magnitude diagram.

dSph dwarf spheroidal.

ESO European Southern Observatory.

EW equivalent width.

FLAMES Fibre Large Array Multi Element Spectrograph.

FWHM full width at half maximum.

GC globular cluster.

HB horizontal branch.

hfs hyperfine structure.

HR diagram Hertzsprung-Russel diagram.

HST Hubble Space Telescope.

IMF initial mass function.

IRFM InfraRed Flux Method.

ISM interstellar medium.

LA Leading Arm.

LBV luminous blue variable.

LG Local Group.

LMC Large Magellanic Cloud.

LTE local thermodynamic equilibrium.

MB Magellanic Bridge.

MC Magellanic Cloud.

MS Magellanic Stream.

MS main sequence.

MW Milky Way.

NS neutron star.

OGLE Optical Gravitational Lensing Experiment.

PN planetary nebulae.

r.m.s root mean square.

RC red clump.

RGB red giant branch.

RSG red supergiant.

SBm Barred Magellanic spiral.

SFH star formation history.

SFR star formation rate.

SGB sub-giant branch.

S/N **ratio** signal-to-noise ratio.

SMC Small Magellanic Cloud.

SN supernova.

SNIa type Ia supernova.

SNII type II supernova.

SS spectrum synthesis.

UT unit telescope.

VLT Very Large Telescope.

WD white dwarf.

WR Wolf-Rayet.

Bibliographies

Articles

Abia, C., de Laverny, P., & Wahlin, R. 2008, *Chemical analysis of carbon stars in the Local Group. II. The Carina dwarf spheroidal galaxy*, Astron. Astrophys., 481, 161 170

Allen, D. M., Ryan, S. G., Rossi, S., Beers, T. C., & Tsangarides, S. A. 2012, *Elemental abundances and classification of carbon-enhanced metal-poor stars*, Astron. Astrophys., 548, A34 176, 186

Allende Prieto, C., García López, R. J., Lambert, D. L., & Gustafsson, B. 1999, *A Consistency Test of Spectroscopic Gravities for Late-Type Stars*, Astrophys. J., 527, 879 92

Allende Prieto, C. & Lambert, D. L. 1999, *Fundamental parameters of nearby stars from the comparison with evolutionary calculations: masses, radii and effective temperatures*, Astron. Astrophys., 352, 555 92

Allende Prieto, C., Lambert, D. L., Tull, R. G., & MacQueen, P. J. 2002, *Convective Wavelength Shifts in the Spectra of Late-Type Stars*, Astrophys. J., Lett., 566, L93 48

Alonso, A., Arribas, S., & Martinez-Roger, C. 1994a, *A semi-empirical absolute flux calibration in the near infrared: Direct stellar diameters vs. IRFM determinations*, Astron. Astrophys., 282, 684 83

Alonso, A., Arribas, S., & Martinez-Roger, C. 1994b, *Broad band JHK infrared photometry of an extended sample of late type dwarfs and subdwarfs.*, Astron. Astrophys. Suppl. Ser., 107, 365 84

Alonso, A., Arribas, S., & Martinez-Roger, C. 1996a, *Determination of effective temperatures for an extended sample of dwarfs and subdwarfs (F0-K5).*, Astron. Astrophys. Suppl. Ser., 117, 227 83

Alonso, A., Arribas, S., & Martinez-Roger, C. 1996b, *The empirical scale of temperatures of the low main sequence (F0V-K5V).*, Astron. Astrophys., 313, 873 84

Alonso, A., Arribas, S., & Martínez-Roger, C. 1999a, *The effective temperature scale of giant stars (F0-K5). I. The effective temperature determination by means of the IRFM*, Astron. Astrophys. Suppl. Ser., 139, 335 83

Alonso, A., Arribas, S., & Martínez-Roger, C. 1999b, *The effective temperature scale of giant stars (F0-K5). II. Empirical calibration of T_{eff} versus colours and [Fe/H]*, Astron. Astrophys. Suppl. Ser., 140, 261 84

Alvarez, R. & Plez, B. 1998, *Near-infrared narrow-band photometry of M-giant and Mira stars: models meet observations*, Astron. Astrophys., 330, 1109 95, 125, 185

Alves, D. R. 2004a, *A review of the distance and structure of the Large Magellanic Cloud*, New A Rev., 48, 659 4, 92

Alves, D. R. 2004b, *The Stellar Halo in the Large Magellanic Cloud: Mass, Luminosity, and Microlensing Predictions*, Astrophys. J., Lett., 601, L151 5, 8

Alves-Brito, A., Meléndez, J., Asplund, M., Ramírez, I., & Yong, D. 2010, *Chemical similarities between Galactic bulge and local thick disk red giants: O, Na, Mg, Al, Si, Ca, and Ti*, Astron. Astrophys., 513, A35 58

Arlandini, C., Käppeler, F., Wisshak, K., et al. 1999, *Neutron Capture in Low-Mass Asymptotic Giant Branch Stars: Cross Sections and Abundance Signatures*, Astrophys. J., 525, 886 168, 169, 175

Asplund, M., Nordlund, Å., Trampedach, R., Allende Prieto, C., & Stein, R. F. 2000, *Line formation in solar granulation. I. Fe line shapes, shifts and asymmetries*, Astron. Astrophys., 359, 729 48

Athanassoula, E., Lambert, J. C., & Dehnen, W. 2005, *Can bars be destroyed by a central mass concentration?- I. Simulations*, Mon. Not. R. Astron. Soc., 363, 496 20

Bailer-Jones, C. A. L. 2011, *Bayesian inference of stellar parameters and interstellar extinction using parallaxes and multiband photometry*, Mon. Not. R. Astron. Soc., 411, 435 22

Baranne, A., Queloz, D., Mayor, M., et al. 1996, *ELODIE: A spectrograph for accurate radial velocity measurements.*, Astron. Astrophys. Suppl. Ser., 119, 373 28

Barklem, P. S., Stempels, H. C., Allende Prieto, C., et al. 2002, *Detailed analysis of Balmer lines in cool dwarf stars*, Astron. Astrophys., 385, 951 81

Battaglia, G., Irwin, M., Tolstoy, E., et al. 2008, *Analysis and calibration of CaII triplet spectroscopy of red giant branch stars from VLT/FLAMES observations*, Mon. Not. R. Astron. Soc., 383, 183 94

Bedin, L. R., Piotto, G., Anderson, J., et al. 2004, *ω Centauri: The Population Puzzle Goes Deeper*, Astrophys. J., Lett., 605, L125 9

Bekki, K. 2009, *Formation of the off-centre bar in the Large Magellanic Cloud: a collision with a dark satellite?*, Mon. Not. R. Astron. Soc., 393, L60 21

Bekki, K. 2011, *When was the Large Magellanic Cloud accreted on to the Galaxy?*, Mon. Not. R. Astron. Soc., 416, 2359 17

Bekki, K., Beasley, M. A., Forbes, D. A., & Couch, W. J. 2004a, *Formation of Star Clusters in the Large Magellanic Cloud and Small Magellanic Cloud. I. Preliminary Results on Cluster Formation from Colliding Gas Clouds*, Astrophys. J., 602, 730 18

Bekki, K. & Chiba, M. 2005, *Formation and evolution of the Magellanic Clouds - I. Origin of structural, kinematic and chemical properties of the Large Magellanic Cloud*, Mon. Not. R. Astron. Soc., 356, 680 17, 21

Bekki, K., Couch, W. J., Beasley, M. A., et al. 2004b, *Explaining the Mysterious Age Gap of Globular Clusters in the Large Magellanic Cloud*, Astrophys. J., Lett., 610, L93 17, 21

Bekki, K. & Tsujimoto, T. 2012a, *Chemical Evolution of the Large Magellanic Cloud*, Astrophys. J., 761, 180 16, 165, 166, 168, 169, 170, 174

Bekki, K. & Tsujimoto, T. 2012b, *Chemical evolution of the Large Magellanic Cloud*, ArXiv e-prints 174

Bell, R. A., Edvardsson, B., & Gustafsson, B. 1985, *The surface gravity of Arcturus from MgH lines, strong metal lines and the ionization equilibrium of iron*, Mon. Not. R. Astron. Soc., 212, 497 91

Bensby, T., Feltzing, S., Lundström, I., & Ilyin, I. 2005, *α-, r-, and s-process element trends in the Galactic thin and thick disks*, Astron. Astrophys., 433, 185 164, 166

Bergemann, M., Lind, K., Collet, R., Magic, Z., & Asplund, M. 2012, *Non-LTE line formation of Fe in late-type stars - I. Standard stars with 1D and $\langle 3D \rangle$ model atmospheres*, Mon. Not. R. Astron. Soc., 427, 27 91

Bertelli, G., Bressan, A., Chiosi, C., Fagotto, F., & Nasi, E. 1994, *Theoretical isochrones from models with new radiative opacities*, Astron. Astrophys. Suppl. Ser., 106, 275 92

Besla, G., Kallivayalil, N., Hernquist, L., et al. 2007, *Are the Magellanic Clouds on Their First Passage about the Milky Way?*, Astrophys. J., 668, 949 17, 18

Besla, G., Kallivayalil, N., Hernquist, L., et al. 2010, *Simulations of the Magellanic Stream in a First Infall Scenario*, Astrophys. J., Lett., 721, L97 5, 18

Besla, G., Kallivayalil, N., Hernquist, L., et al. 2012, *The role of dwarf galaxy interactions in shaping the Magellanic System and implications for Magellanic Irregulars*, Mon. Not. R. Astron. Soc., 421, 2109 18, 19, 20

Bessell, M. S. 2005, *Standard Photometric Systems*, Ann. Rev. Astron. Astrophys., 43, 293 84

Bessell, M. S. & Brett, J. M. 1988, *JHKLM photometry - Standard systems, passbands, and intrinsic colors*, PASP, 100, 1134 84

Bessell, M. S., Castelli, F., & Plez, B. 1998, *Model atmospheres broad-band colors, bolometric corrections and temperature calibrations for O - M stars*, Astron. Astrophys., 333, 231 83

Bica, E., Geisler, D., Dottori, H., et al. 1998, *Ages and Metallicities of Star Clusters and Surrounding Fields in the Outer Disk of the Large Magellanic Cloud*, Astron. J., 116, 723 9

Bica, E. L. D. & Schmitt, H. R. 1995, *A Revised and Extended Catalog of Magellanic System Clusters, Associations, and Emission Nebulae. I. Small Magellanic Cloud and Bridge*, Astrophys. J., Suppl. Ser., 101, 41 9

Bica, E. L. D., Schmitt, H. R., Dutra, C. M., & Oliveira, H. L. 1999, *A Revised and Extended Catalog of Magellanic System Clusters, Associations, and Emission Nebulae. II. The Large Magellanic Cloud*, Astron. J., 117, 238 9

Bielski, A. 1975, *A critical survey of atomic transition probabilities for Cu I.*, J. Quant. Spec. Radiat. Transf., 15, 463 128

Bisterzo, S., Gallino, R., Straniero, O., Cristallo, S., & Käppeler, F. 2010, *s-Process in low-metallicity stars - I. Theoretical predictions*, Mon. Not. R. Astron. Soc., 404, 1529 182

Bisterzo, S., Gallino, R., Straniero, O., Cristallo, S., & Käppeler, F. 2012, *The s-process in low-metallicity stars - III. Individual analysis of CEMP-s and CEMP-s/r with asymptotic giant branch models*, Mon. Not. R. Astron. Soc., 422, 849 176

Blackwell, D. E., Petford, A. D., & Shallis, M. J. 1980, *Use of the infra-red flux method for determining stellar effective temperatures and angular diameters - The stellar temperature scale*, Astron. Astrophys., 82, 249 83

Blackwell, D. E. & Shallis, M. J. 1977, *Stellar angular diameters from infrared photometry - Application to Arcturus and other stars; with effective temperatures*, Mon. Not. R. Astron. Soc., 180, 177 83

Blackwell, D. E., Shallis, M. J., & Selby, M. J. 1979, *The infrared flux method for determining stellar angular diameters and effective temperatures*, Mon. Not. R. Astron. Soc., 188, 847 83

Blackwell, D. E. & Willis, R. B. 1977, *Stellar gravities from metallic line profiles, with application to Arcturus - The effective temperature of Arcturus*, Mon. Not. R. Astron. Soc., 180, 169 91

Blecha, A., Cayatte, V., North, P., Royer, F., & Simond, G. 2000, in Society of Photo-Optical Instrumentation Engineers (SPIE) Conference Series, Vol. 4008, Society of Photo-Optical Instrumentation Engineers (SPIE) Conference Series, ed. M. Iye & A. F. Moorwood, 467–474 31

Bonnell, J. T. & Bell, R. A. 1993, *The Gravities of K Giant Stars Determined from OI and OH Features*, Mon. Not. R. Astron. Soc., 264, 319 91

Bournaud, F. & Combes, F. 2002, *Gas accretion on spiral galaxies: Bar formation and renewal*, Astron. Astrophys., 392, 83 20

Bournaud, F., Combes, F., & Semelin, B. 2005, *The lifetime of galactic bars: central mass concentrations and gravity torques*, Mon. Not. R. Astron. Soc., 364, L18 20

Boylan-Kolchin, M., Besla, G., & Hernquist, L. 2011, *Dynamics of the Magellanic Clouds in a Lambda cold dark matter universe*, Mon. Not. R. Astron. Soc., 414, 1560 4

Brewer, M.-M. & Carney, B. W. 2006, *A Comparison of the Chemical Evolutionary Histories of the Galactic Thin Disk and Thick Disk Stellar Populations*, Astron. J., 131, 431 165, 169

Bruntt, H., Bedding, T. R., Quirion, P.-O., et al. 2010, *Accurate fundamental parameters for 23 bright solar-type stars*, Mon. Not. R. Astron. Soc., 405, 1907 92

Burbidge, E. M., Burbidge, G. R., Fowler, W. A., & Hoyle, F. 1957, *Synthesis of the Elements in Stars*, Reviews of Modern Physics, 29, 547 150

Burris, D. L., Pilachowski, C. A., Armandroff, T. E., et al. 2000, *Neutron-Capture Elements in the Early Galaxy: Insights from a Large Sample of Metal-poor Giants*, Astrophys. J., 544, 302 168, 170

Busso, M., Gallino, R., & Wasserburg, G. J. 1999, *Nucleosynthesis in Asymptotic Giant Branch Stars: Relevance for Galactic Enrichment and Solar System Formation*, Ann. Rev. Astron. Astrophys., 37, 239 159

Calzetti, D., Chandar, R., Lee, J. C., et al. 2010, *A Method for Measuring Variations in the Stellar Initial Mass Function*, Astrophys. J., Lett., 719, L158 164

Carrera, R., Gallart, C., Aparicio, A., et al. 2008a, *The Chemical Enrichment History of the Small Magellanic Cloud and its Gradients*, Astron. J., 136, 1039 13

Carrera, R., Gallart, C., Aparicio, A., & Hardy, E. 2011, *Metallicities, Age-Metallicity Relationships, and Kinematics of Red Giant Branch Stars in the Outer Disk of the Large Magellanic Cloud*, Astron. J., 142, 61 7, 8, 13, 14, 15, 16

Carrera, R., Gallart, C., Hardy, E., Aparicio, A., & Zinn, R. 2008b, *The Chemical Enrichment History of the Large Magellanic Cloud*, Astron. J., 135, 836 7, 8, 13, 14, 16, 186

Carretta, E., Gratton, R. G., & Sneden, C. 2000, *Abundances of light elements in metal-poor stars. III. Data analysis and results*, Astron. Astrophys., 356, 238 165, 166

Casagrande, L., Portinari, L., & Flynn, C. 2006, *Accurate fundamental parameters for lower main-sequence stars*, Mon. Not. R. Astron. Soc., 373, 13 83, 84

Casagrande, L., Ramírez, I., Meléndez, J., Bessell, M., & Asplund, M. 2010, *An absolutely calibrated T_{eff} scale from the infrared flux method. Dwarfs and subgiants*, Astron. Astrophys., 512, A54 83

Cayrel, R., Depagne, E., Spite, M., et al. 2004, *First stars V - Abundance patterns from C to Zn and supernova yields in the early Galaxy*, Astron. Astrophys., 416, 1117 141

Cayrel, R., van't Veer-Menneret, C., Allard, N. F., & Stehlé, C. 2011, *The Hα Balmer line as an effective temperature criterion. I. Calibration using 1D model stellar atmospheres*, Astron. Astrophys., 531, A83 81

Chabrier, G. 2001, *The Galactic Disk Mass Budget. I. Stellar Mass Function and Density*, Astrophys. J., 554, 1274 92

Chiappini, C., Matteucci, F., & Gratton, R. 1997, *The Chemical Evolution of the Galaxy: The Two-Infall Model*, Astrophys. J., 477, 765 13

Chiappini, C., Matteucci, F., & Romano, D. 2001, *Abundance Gradients and the Formation of the Milky Way*, Astrophys. J., 554, 1044 13

Chiavassa, A., Bigot, L., Thévenin, F., et al. 2011, *3-D hydrodynamical model atmospheres: a tool to correct radial velocities and parallaxes for Gaia*, Journal of Physics Conference Series, 328, 012012 48

Cioni, M.-R. L., Habing, H. J., & Israel, F. P. 2000, *The morphology of the Magellanic Clouds revealed by stars of different age: results from the DENIS survey*, Astron. Astrophys., 358, L9 5

Cohen, J. G., Christlieb, N., Qian, Y.-Z., & Wasserburg, G. J. 2003, *Abundance Analysis of HE 2148-1247, A Star with Extremely Enhanced Neutron Capture Elements*, Astrophys. J., 588, 1082 176

Cole, A. A., Smecker-Hane, T. A., Tolstoy, E., Bosler, T. L., & Gallagher, J. S. 2004, *The effects of age on red giant metallicities derived from the near-infrared CaII triplet*, Mon. Not. R. Astron. Soc., 347, 367 94, 103

Cole, A. A., Tolstoy, E., Gallagher, III, J. S., & Smecker-Hane, T. A. 2005, *Spectroscopy of Red Giants in the Large Magellanic Cloud Bar: Abundances, Kinematics, and the Age-Metallicity Relation*, Astron. J., 129, 1465 8, 14, 16, 19, 20, 27, 28, 29, 53, 62, 85, 86, 103, 178, 186

Colin, J. & Athanassoula, E. 1989, *Asymmetrical barred galaxies*, Astron. Astrophys., 214, 99 5, 20

Colucci, J. E., Bernstein, R. A., Cameron, S. A., & McWilliam, A. 2012, *Globular Cluster Abundances from High-resolution, Integrated-light Spectroscopy. IV. The Large Magellanic Cloud: α, Fe-peak, Light, and Heavy Elements*, Astrophys. J., 746, 29 170, 176

Combes, F., Debbasch, F., Friedli, D., & Pfenniger, D. 1990, *Box and peanut shapes generated by stellar bars*, Astron. Astrophys., 233, 82 20

Combes, F. & Elmegreen, B. G. 1993, *Bars in Early Type and Late Type Galaxies*, Astron. Astrophys., 271, 391 20

Combes, F. & Sanders, R. H. 1981, *Formation and properties of persisting stellar bars*, Astron. Astrophys., 96, 164 20

Cristallo, S., Gallino, R., Straniero, O., Piersanti, L., & Domınguez, I. 2006, *Short-lived isotopes and ^{23}Na production in low mass AGB Stars*, Mem. Soc. Astron. Italiana, 77, 774 182

Cristallo, S., Piersanti, L., Straniero, O., et al. 2011, *Evolution, Nucleosynthesis, and Yields of Low-mass Asymptotic Giant Branch Stars at Different Metallicities. II. The FRUITY Database*, Astrophys. J., Suppl. Ser., 197, 17 170, 181

Da Costa, G. S. 1991, in IAU Symposium, Vol. 148, The Magellanic Clouds, ed. R. Haynes & D. Milne, 183 9, 10

da Silva, L., Girardi, L., Pasquini, L., et al. 2006, *Basic physical parameters of a selected sample of evolved stars*, Astron. Astrophys., 458, 609 92, 185

de Laverny, P., Abia, C., Domínguez, I., et al. 2006, *Chemical analysis of carbon stars in the Local Group*, Astron. Astrophys., 446, 1107 170

de Medeiros, J. R., Da Rocha, C., & Mayor, M. 1996, *The distribution of rotational velocity for evolved stars.*, Astron. Astrophys., 314, 499 120

de Vaucouleurs, G. 1964, in IAU Symposium, Vol. 20, The Galaxy and the Magellanic Clouds, ed. F. J. Kerr, 269 3

de Vaucouleurs, G., de Vaucouleurs, A., & Freeman, K. C. 1968, *Photometry, kinematics and dynamics of the Magellanic-type barred spiral galaxy NGC 4027*, Mon. Not. R. Astron. Soc., 139, 425 3

de Vaucouleurs, G. & Freeman, K. C. 1972, *Structure and dynamics of barred spiral galaxies, in particular of the Magellanic type*, Vistas in Astronomy, 14, 163 3

Diaz, J. & Bekki, K. 2011, *Constraining the orbital history of the Magellanic Clouds: a new bound scenario suggested by the tidal origin of the Magellanic Stream*, Mon. Not. R. Astron. Soc., 413, 2015 18

Diaz, J. D. & Bekki, K. 2012, *The Tidal Origin of the Magellanic Stream and the Possibility of a Stellar Counterpart*, Astrophys. J., 750, 36 5, 18

Dixon, M. E. & Ford, V. L. 1972, *An Observational Approach to the Problem of Spiral Structure. II*, Astrophys. J., 173, 35 5

Dottori, H., Bica, E., Claria, J. J., & Puerari, I. 1996, *Spatial Distributions of Young Large Magellanic Cloud Clusters as Tracers of a Bar Perturbation*, Astrophys. J., 461, 742 5

Driver, S. P., Hill, D. T., Kelvin, L. S., et al. 2011, *Galaxy and Mass Assembly (GAMA): survey diagnostics and core data release*, Mon. Not. R. Astron. Soc., 413, 971 4

Drozdowski, R., Ignaciuk, M., Kwela, J., & Heldt, J. 1988, Z. Phys., 21, 2827 130

Edvardsson, B. 1988, *Spectroscopic surface gravities and chemical compositions for 8 nearby single sub-giants*, Astron. Astrophys., 190, 148 91

Elmegreen, B. G. 2004, *Variability in the stellar initial mass function at low and high mass: three-component IMF models*, Mon. Not. R. Astron. Soc., 354, 367 164

Elson, R. A. & Fall, S. M. 1988, *LMC clusters - Age calibration and age distribution revisited*, Astron. J., 96, 1383 9

Ferraro, F. R., Sollima, A., Pancino, E., et al. 2004b, *The Discovery of an Anomalous Subgiant Branch in the Color-Magnitude Diagram of ω Centauri*, Astrophys. J., Lett., 603, L81 9

Fossati, L., Ryabchikova, T., Shulyak, D. V., et al. 2011, *The accuracy of stellar atmospheric parameter determinations: a case study with HD 32115 and HD 37594*, Mon. Not. R. Astron. Soc., 417, 495 91

Freeman, K. C. 1999, in IAU Symposium, Vol. 192, The Stellar Content of Local Group Galaxies, ed. P. Whitelock & R. Cannon, 383 8

Freiburghaus, C., Rosswog, S., & Thielemann, F.-K. 1999, *R-Process in Neutron Star Mergers*, Astrophys. J., Lett., 525, L121 163

Frischknecht, U., Hirschi, R., & Thielemann, F.-K. 2012, *Non-standard s-process in low metallicity massive rotating stars*, Astron. Astrophys., 538, L2 162

Fuhr, J. R., Martin, G. A., & Wiese, W. L. 1988, *Atomic transition probabilities. Iron through Nickel*, Journal of Physical and Chemical Reference Data, 17 128

Fuhrmann, K., Axer, M., & Gehren, T. 1993, *Balmer lines in cool dwarf stars. 1. Basic influence of atmospheric models*, Astron. Astrophys., 271, 451 81

Fuhrmann, K., Axer, M., & Gehren, T. 1994, *Balmer lines in cool dwarf stars II. Effective temperatures and calibration of colour indices*, Astron. Astrophys., 285, 585 81

Fuhrmann, K., Pfeiffer, M., Frank, C., Reetz, J., & Gehren, T. 1997, *The surface gravities of cool dwarf stars revisited.*, Astron. Astrophys., 323, 909 91

Fulbright, J. P. 2000, *Abundances and Kinematics of Field Halo and Disk Stars. I. Observational Data and Abundance Analysis*, Astron. J., 120, 1841 164, 166

Gallart, C., Stetson, P. B., Hardy, E., Pont, F., & Zinn, R. 2004, *Surface Brightness and Stellar Populations at the Outer Edge of the Large Magellanic Cloud: No Stellar Halo Yet*, Astrophys. J., Lett., 614, L109 7, 13

Gallart, C., Stetson, P. B., Meschin, I. P., Pont, F., & Hardy, E. 2008, *Outside-In Disk Evolution in the Large Magellanic Cloud*, Astrophys. J., Lett., 682, L89 13, 187

Gardiner, L. T. & Noguchi, M. 1996, *N-body simulations of the Small Magellanic Cloud and the Magellanic Stream*, Mon. Not. R. Astron. Soc., 278, 191 5, 17

Gardiner, L. T., Turfus, C., & Putman, M. E. 1998, *Numerical Simulation of Asymmetric Spiral Structure in the Large Magellanic Cloud*, Astrophys. J., Lett., 507, L35 5, 19, 21

Gehren, T., Liang, Y. C., Shi, J. R., Zhang, H. W., & Zhao, G. 2004, *Abundances of Na, Mg and Al in nearby metal-poor stars*, Astron. Astrophys., 413, 1045 81

Gehren, T., Shi, J. R., Zhang, H. W., Zhao, G., & Korn, A. J. 2006, *Na, Mg and Al abundances as a population discriminant for nearby metal-poor stars*, Astron. Astrophys., 451, 1065 81

Geisler, D., Bica, E., Dottori, H., et al. 1997, *A Search for Old Star Clusters in the Large Magellanic Cloud*, Astron. J., 114, 1920 9

Geisler, D., Piatti, A. E., Bica, E., & Clariá, J. J. 2003, *Ages and metallicities of eight star clusters and their surrounding fields in the inner disc of the Large Magellanic Cloud*, Mon. Not. R. Astron. Soc., 341, 771 9

Gilmore, G. & Wyse, R. F. G. 1991, *Chemical evolution with bursts of star formation - Element ratios in dwarf galaxies*, Astrophys. J., Lett., 367, L55 180

Girard, T. M., Wu, H., Lee, J. T., et al. 2000, *A Redetermination of the Mass of Procyon*, Astron. J., 119, 2428 89

Girardi, L., Bressan, A., Bertelli, G., & Chiosi, C. 2000, *Evolutionary tracks and isochrones for low- and intermediate-mass stars: From 0.15 to 7 M_{sun}, and from Z=0.0004 to 0.03*, Astron. Astrophys. Suppl. Ser., 141, 371 92

Goriely, S. & Mowlavi, N. 2000, *Neutron-capture nucleosynthesis in AGB stars*, Astron. Astrophys., 362, 599 182

Gray, D. F. 1981, *Rotation and turbulence in G giant stars*, Astrophys. J., 251, 155 120

Gray, D. F. & Toner, C. G. 1986, *Rotation and macroturbulence in bright giants*, Astrophys. J., 310, 277 120

Grevesse, N. & Sauval, A. J. 1998, *Standard Solar Composition*, Space Sci. Rev., 85, 161 93, 129

Grocholski, A. J., Cole, A. A., Sarajedini, A., Geisler, D., & Smith, V. V. 2006, *Ca II Triplet Spectroscopy of Large Magellanic Cloud Red Giants. I. Abundances and Velocities for a Sample of Populous Clusters*, Astron. J., 132, 1630 103

Gullberg, D. & Lindegren, L. 2002, *Determination of accurate stellar radial-velocity measures*, Astron. Astrophys., 390, 383 47

Gustafsson, B., Edvardsson, B., Eriksson, K., et al. 2008, *A grid of MARCS model atmospheres for late-type stars. I. Methods and general properties*, Astron. Astrophys., 486, 951 95

Hall, J. C., Fulton, E. E., Huenemoerder, D. P., Welty, A. D., & Neff, J. E. 1994, *The reduction of fiber-fed echelle spectrograph data: Methods and an IDL-based solution procedure*, PASP, 106, 315 28

Harris, J. & Zaritsky, D. 2001, *A Method for Determining the Star Formation History of a Mixed Stellar Population*, Astrophys. J., Suppl. Ser., 136, 25 11

Harris, J. & Zaritsky, D. 2004, *The Star Formation History of the Small Magellanic Cloud*, Astron. J., 127, 1531 12

Harris, J. & Zaritsky, D. 2009, *The Star Formation History of the Large Magellanic Cloud*, Astron. J., 138, 1243 5, 11, 12, 15, 20, 187

Haschke, R., Grebel, E. K., & Duffau, S. 2012a, *Three-dimensional Maps of the Magellanic Clouds using RR Lyrae Stars and Cepheids. I. The Large Magellanic Cloud*, Astron. J., 144, 106 7

Haschke, R., Grebel, E. K., Duffau, S., & Jin, S. 2012b, *Metallicity Distribution Functions of the Old Populations of the Magellanic Clouds from RR Lyrae Stars*, Astron. J., 143, 48 100

Haschke, R., Grebel, E. K., Frebel, A., et al. 2012c, *Chemical Abundances of Metal-poor RR Lyrae Stars in the Magellanic Clouds*, Astron. J., 144, 88 174

Hidalgo, S. L., Marín-Franch, A., & Aparicio, A. 2003, *Spatial Distribution of Stellar Populations in the Dwarf Irregular Galaxies DDO 165 and DDO 181*, Astron. J., 125, 1247 12

Hill, V. 1995, in IAU Symposium, Vol. 164, Stellar Populations, ed. P. C. van der Kruit & G. Gilmore, 416 14, 15

Hill, V. 1997, *Chemical composition of six K supergiants in the Small Magellanic Cloud.*, Astron. Astrophys., 324, 435 14

Hill, V. 1999, *Abundances of cool supergiants in the SMC young cluster NGC 330*, Astron. Astrophys., 345, 430 14

Hill, V., Andrievsky, S., & Spite, M. 1995, *Chemical evolution of the Magellanic Clouds. VI. Chemical composition of nine F supergiants from different regions of the large Magellanic Cloud.*, Astron. Astrophys., 293, 347 176

Hill, V., Barbuy, B., & Spite, M. 1997, *Carbon, nitrogen, oxygen and lithium abundances of six cool supergiants in the SMC.*, Astron. Astrophys., 323, 461 14

Hinkle, K., Wallace, L., Valenti, J., & Harmer, D. 2000, Visible and Near Infrared Atlas of the Arcturus Spectrum 3727-9300 A 59

Hodge, P. 1986, *Clusters of the Small Magellanic Cloud. I - A catalog of 213 new clusters*, PASP, 98, 1113 9

Hodge, P. 1988a, *A catalog of 255 new clusters in the Large Magellanic Cloud*, PASP, 100, 1051 9

Hodge, P. 1988b, *The age distribution and history of formation of Large Magellanic Cloud clusters*, PASP, 100, 576 9

Holtzman, J. A., Gallagher, III, J. S., Cole, A. A., et al. 1999, *Observations and Implications of the Star Formation History of the Large Magellanic Cloud*, Astron. J., 118, 2262 11

Holtzman, J. A., Mould, J. R., Gallagher, III, J. S., et al. 1997, *Stellar Populations in the Large Magellanic Cloud:Evidence for a Significant Number of Older Stars or a Steeper IMF?*, Astron. J., 113, 656 170

Horne, K. 1986, *An optimal extraction algorithm for CCD spectroscopy*, PASP, 98, 609 38

Houdashelt, M. L., Bell, R. A., & Sweigart, A. V. 2000, *Improved Color-Temperature Relations and Bolometric Corrections for Cool Stars*, Astron. J., 119, 1448 83

James, P. A. & Ivory, C. F. 2011, *On the scarcity of Magellanic Cloud like satellites*, Mon. Not. R. Astron. Soc., 411, 495 4

Janes, K. A. 1979, *Evidence for an abundance gradient in the galactic disk*, Astrophys. J., Suppl. Ser., 39, 135 13

Johnson, J. A., Ivans, I. I., & Stetson, P. B. 2006, *Chemical Compositions of Red Giant Stars in Old Large Magellanic Cloud Globular Clusters*, Astrophys. J., 640, 801 15, 141, 164, 166

Jørgensen, B. R. & Lindegren, L. 2005, *Determination of stellar ages from isochrones: Bayesian estimation versus isochrone fitting*, Astron. Astrophys., 436, 127 92

Kallivayalil, N., van der Marel, R. P., & Alcock, C. 2006a, *Is the SMC Bound to the LMC? The Hubble Space Telescope Proper Motion of the SMC*, Astrophys. J., 652, 1213 17

Kallivayalil, N., van der Marel, R. P., Alcock, C., et al. 2006b, *The Proper Motion of the Large Magellanic Cloud Using HST*, Astrophys. J., 638, 772 12, 17, 18

Kennicutt, Jr., R. C., Bresolin, F., Bomans, D. J., Bothun, G. D., & Thompson, I. B. 1995, *Large scale structure of the ionized gas in the magellanic clouds*, Astron. J., 109, 594 7

Kim, S., Staveley-Smith, L., Dopita, M. A., et al. 1998, *An H i Aperture Synthesis Mosaic of the Large Magellanic Cloud*, Astrophys. J., 503, 674 5, 6, 7, 21

Klypin, A., Kravtsov, A. V., Valenzuela, O., & Prada, F. 1999, *Where Are the Missing Galactic Satellites?*, Astrophys. J., 522, 82 3

Koerwer, J. F. 2009, *Large Magellanic Cloud Distance and Structure from Near-Infrared Red Clump Observations*, Astron. J., 138, 1 7

Kordopatis, G., Recio-Blanco, A., de Laverny, P., et al. 2011, *Automatic stellar spectra parameterisation in the IR Ca ii triplet region*, Astron. Astrophys., 535, A106 22

Kormendy, J. & Kennicutt, Jr., R. C. 2004, *Secular Evolution and the Formation of Pseudobulges in Disk Galaxies*, Ann. Rev. Astron. Astrophys., 42, 603 20

Kroupa, P. 2001, *On the variation of the initial mass function*, Mon. Not. R. Astron. Soc., 322, 231 164

Kroupa, P., Tout, C. A., & Gilmore, G. 1993, *The distribution of low-mass stars in the Galactic disc*, Mon. Not. R. Astron. Soc., 262, 545 164

Kroupa, P., Weidner, C., Pflamm-Altenburg, J., et al. 2011, *The stellar and sub-stellar IMF of simple and composite populations*, ArXiv e-prints 164, 170

Kupka, F., Piskunov, N., Ryabchikova, T. A., Stempels, H. C., & Weiss, W. W. 1999, *VALD-2: Progress of the Vienna Atomic Line Data Base*, Astron. Astrophys. Suppl. Ser., 138, 119 128

Kupka, F. G., Ryabchikova, T. A., Piskunov, N. E., Stempels, H. C., & Weiss, W. W. 2000, *VALD-2 – The New Vienna Atomic Line Database*, Baltic Astronomy, 9, 590 128

Kurucz, R. L. 1988, in Trans. IAU XXB 128

Kurucz, R. L. 1995, in Astronomical Society of the Pacific Conference Series, Vol. 78, Astrophysical Applications of Powerful New Databases, ed. S. J. Adelman & W. L. Wiese, 205 128

Lah, P., Kiss, L. L., & Bedding, T. R. 2005, *Red variables in the OGLE-II data base - III. Constraints on the three-dimensional structures of the Large and Small Magellanic Clouds*, Mon. Not. R. Astron. Soc., 359, L42 7

Lapenna, E., Mucciarelli, A., Origlia, L., & Ferraro, F. R. 2012, *Tagging the Chemical Evolution History of the Large Magellanic Cloud Disk*, Astrophys. J., 761, 33 15, 145, 147, 165

Lawler, J. E., Bonvallet, G., & Sneden, C. 2001a, *Experimental Radiative Lifetimes, Branching Fractions, and Oscillator Strengths for La II and a New Determination of the Solar Lanthanum Abundance*, Astrophys. J., 556, 452 128

Lawler, J. E., Wickliffe, M. E., den Hartog, E. A., & Sneden, C. 2001b, *Improved Laboratory Transition Parameters forEu II and Application to the Solar Europium Elemental and Isotopic Composition*, Astrophys. J., 563, 1075 128

Lebzelter, T., Heiter, U., Abia, C., et al. 2012, *Comparative Modelling of the Spectra of Cool Giants*, ArXiv e-prints 131

Lecureur, A., Hill, V., Zoccali, M., et al. 2007, *Oxygen, sodium, magnesium, and aluminium as tracers of the galactic bulge formation*, Astron. Astrophys., 465, 799 58, 82, 129

Lin, D. N. C. & Lynden-Bell, D. 1982, *On the proper motion of the Magellanic Clouds and the halo mass of our galaxy*, Mon. Not. R. Astron. Soc., 198, 707 16

Lin, D. N. C. & Richer, H. B. 1992, *Young globular clusters in the Milky Way Galaxy*, Astrophys. J., Lett., 388, L57 10

Lind, K., Bergemann, M., & Asplund, M. 2012, *Non-LTE line formation of Fe in late-type stars - II. 1D spectroscopic stellar parameters*, Mon. Not. R. Astron. Soc., 427, 50 91

Lindegren, L. & Dravins, D. 2003, *The fundamental definition of "radial velocity"*, Astron. Astrophys., 401, 1185 47

Luck, R. E. & Lambert, D. L. 1992, *The chemical composition of Magellanic Cloud Cepheids and nonvariable supergiants*, Astrophys. J., Suppl. Ser., 79, 303 14, 15

Luks, T. & Rohlfs, K. 1992, *Structure and kinematics of neutral hydrogen gas in the Large Magellanic Cloud*, Astron. Astrophys., 263, 41 5

Mackey, A. D., Broby Nielsen, P., Ferguson, A. M. N., & Richardson, J. C. 2008, *Multiple Stellar Populations in Three Rich Large Magellanic Cloud Star Clusters*, Astrophys. J., Lett., 681, L17 9

Majewski, S. R., Nidever, D. L., Muñoz, R. R., et al. 2009, in IAU Symposium, Vol. 256, IAU Symposium, ed. J. T. Van Loon & J. M. Oliveira, 51–56 5, 8

Martin, G. A., Fuhr, J. R., & Wiese, W. L. 1988, Atomic transition probabilities. Scandium through Manganese 128

Mateo, M., Hodge, P., & Schommer, R. A. 1986, *CCD photometry of Large Magellanic Cloud clusters. III - The unique, remote cluster ESO 121-SC03*, Astrophys. J., 311, 113 9

Mathewson, D. S., Cleary, M. N., & Murray, J. D. 1974, *The Magellanic stream*, Astrophys. J., 190, 291 5

Mayor, M. 1976, *Chemical evolution of the galactic disk and the radial metallicity gradient*, Astron. Astrophys., 48, 301 13

McWilliam, A., Preston, G. W., Sneden, C., & Searle, L. 1995a, *Spectroscopic Analysis of 33 of the Most Metal Poor Stars. II.*, Astron. J., 109, 2757 141, 163

McWilliam, A., Preston, G. W., Sneden, C., & Shectman, S. 1995b, *A Spectroscopic Analysis of 33 of the Most Metal-Poor Stars.I.*, Astron. J., 109, 2736 163

Meléndez, J., Asplund, M., Gustafsson, B., & Yong, D. 2009, *The Peculiar Solar Composition and Its Possible Relation to Planet Formation*, Astrophys. J., Lett., 704, L66 58

Miller, G. E. & Scalo, J. M. 1979, *The initial mass function and stellar birthrate in the solar neighborhood*, Astrophys. J., Suppl. Ser., 41, 513 164

Milone, A. P., Bedin, L. R., Cassisi, S., et al. 2013, *Multiple stellar populations in Magellanic Cloud clusters. II. Evidence also in the young NGC1844?*, ArXiv e-prints 9

Milone, A. P., Bedin, L. R., Piotto, G., & Anderson, J. 2009, *Multiple stellar populations in Magellanic Cloud clusters. I. An ordinary feature for intermediate age globulars in the LMC?*, Astron. Astrophys., 497, 755 9

Minniti, D., Borissova, J., Rejkuba, M., et al. 2003, *Kinematic Evidence for an Old Stellar Halo in the Large Magellanic Cloud*, Science, 301, 1508 5, 8

Mishenina, T. V., Kovtyukh, V. V., Soubiran, C., Travaglio, C., & Busso, M. 2002, *Abundances of Cu and Zn in metal-poor stars: Clues for Galaxy evolution*, Astron. Astrophys., 396, 189 175

Mizuno, N., Yamaguchi, R., Mizuno, A., et al. 2001, *A CO Survey of the LMC with NANTEN: II. Catalog of Molecular Clouds*, PASJ, 53, 971 7

Moore, B., Ghigna, S., Governato, F., et al. 1999, *Dark Matter Substructure within Galactic Halos*, Astrophys. J., Lett., 524, L19 3

Morel, T. & Miglio, A. 2012, *Assessing the accuracy of the surface gravity determination in late-type stars with solar-like pulsators*, Mon. Not. R. Astron. Soc., 419, L34 90

Mucciarelli, A., Carretta, E., Origlia, L., & Ferraro, F. R. 2008, *The Chemical Composition of Red Giant Stars in Four Intermediate-Age Clusters of the Large Magellanic Cloud*, Astron. J., 136, 375 15, 103, 145, 147, 164, 166, 176, 181

Mucciarelli, A., Cristallo, S., Brocato, E., et al. 2011, *NGC 1866: a milestone for understanding the chemical evolution of stellar populations in the Large Magellanic Cloud*, Mon. Not. R. Astron. Soc., 413, 837 15

Mucciarelli, A., Origlia, L., & Ferraro, F. R. 2010, *Chemical Composition of the Old Globular Clusters NGC 1786, NGC 2210, and NGC 2257 in the Large Magellanic Cloud*, Astrophys. J., 717, 277 15, 145, 147, 164, 166, 181

Murai, T. & Fujimoto, M. 1980, *The Magellanic Stream and the Galaxy with a Massive Halo*, PASJ, 32, 581 16

Nidever, D. L., Majewski, S. R., Butler Burton, W., & Nigra, L. 2010, *The 200 Long Magellanic Stream System*, Astrophys. J., 723, 1618 6

Nidever, D. L., Majewski, S. R., Muñoz, R. R., et al. 2011, *Discovery of a Large Stellar Periphery Around the Small Magellanic Cloud*, Astrophys. J., Lett., 733, L10 9

Nikolaev, S., Drake, A. J., Keller, S. C., et al. 2004, *Geometry of the Large Magellanic Cloud Disk: Results from MACHO and the Two Micron All Sky Survey*, Astrophys. J., 601, 260 5, 7

Nissen, P. E., Chen, Y. Q., Schuster, W. J., & Zhao, G. 2000, *Sc and Mn abundances in disk and metal-rich halo stars*, Astron. Astrophys., 353, 722 176

Olsen, K. A. G. 1999, *Star Formation Histories from Hubble Space Telescope Color-Magnitude Diagrams of Six Fields of the Large Magellanic Cloud*, Astron. J., 117, 2244 11

Olszewski, E. W., Schommer, R. A., Suntzeff, N. B., & Harris, H. C. 1991, *Spectroscopy of giants in LMC clusters. I - Velocities, abundances, and the age-metallicity relation*, Astron. J., 101, 515 9, 103

Olszewski, E. W., Suntzeff, N. B., & Mateo, M. 1996, *Old and Intermediate-Age Stellar Populations in the Magellanic Clouds*, Ann. Rev. Astron. Astrophys., 34, 511 8, 9, 10

Pagel, B. E. J. & Tautvaisiene, G. 1995, *Chemical evolution of primary elements in the Galactic disc: an analytical model*, Mon. Not. R. Astron. Soc., 276, 505 165

Pagel, B. E. J. & Tautvaisiene, G. 1998, *Chemical evolution of the Magellanic Clouds: analytical models*, Mon. Not. R. Astron. Soc., 299, 535 16, 165, 166, 168, 180

Panagia, N. & Tosi, M. 1980, *The chemical abundance gradient in the galaxy derived from an analysis of the H-R diagrams of open clusters*, Astron. Astrophys., 81, 375 13

Pancino, E., Ferraro, F. R., Bellazzini, M., Piotto, G., & Zoccali, M. 2000, *New Evidence for the Complex Structure of the Red Giant Branch in ω Centauri*, Astrophys. J., Lett., 534, L83 9

Pancino, E., Mucciarelli, A., Bonifacio, P., Monaco, L., & Sbordone, L. 2011, *The subgiant branch of ω Centauri seen through high-resolution spectroscopy. II. The most metal-rich population*, Astron. Astrophys., 534, A53 9

Pancino, E., Seleznev, A., Ferraro, F. R., Bellazzini, M., & Piotto, G. 2003, *The multiple stellar population in ω Centauri: spatial distribution and structural properties*, Mon. Not. R. Astron. Soc., 345, 683 9

Pasquini, L., Avila, G., Allaert, E., et al. 2000, in Society of Photo-Optical Instrumentation Engineers (SPIE) Conference Series, Vol. 4008, Society of Photo-Optical Instrumentation Engineers (SPIE) Conference Series, ed. M. Iye & A. F. Moorwood, 129–140 24, 26

Pasquini, L., Avila, G., Blecha, A., et al. 2002, *Installation and commissioning of FLAMES, the VLT Multifibre Facility*, The Messenger, 110, 1 27

Pasquini, L., Melo, C., Chavero, C., et al. 2011, *Gravitational redshifts in main-sequence and giant stars*, Astron. Astrophys., 526, A127 48

Pasquini, L., Randich, S., Zoccali, M., et al. 2004, *Detailed chemical composition of the open cluster IC 4651: The iron peak, α elements, and Li*, Astron. Astrophys., 424, 951 182

Pejcha, O. & Stanek, K. Z. 2009, *The Structure of the Large Magellanic Cloud Stellar Halo Derived using Ogle-III RR Lyr Stars*, Astrophys. J., 704, 1730 5, 8, 100

Piatti, A. E., Bica, E., Geisler, D., & Clariá, J. J. 2003, *Fundamental parameters of the LMC clusters NGC 1836, NGC 1860, NGC 1865, SL 444, LW 224 and SL 548*, Mon. Not. R. Astron. Soc., 344, 965 9

Piatti, A. E., Sarajedini, A., Geisler, D., Bica, E., & Clariá, J. J. 2002, *Constraining the LMC cluster age gap: Washington photometry of NGC 2155 and SL 896 (LW 480)*, Mon. Not. R. Astron. Soc., 329, 556 9, 10, 15

Pignatari, M., Gallino, R., Heil, M., et al. 2010, *The Weak s-Process in Massive Stars and its Dependence on the Neutron Capture Cross Sections*, Astrophys. J., 710, 1557 175

Pilkington, K., Few, C. G., Gibson, B. K., et al. 2012, *Metallicity gradients in disks. Do galaxies form inside-out?*, Astron. Astrophys., 540, A56 13

Pipino, A., Matteucci, F., & Chiappini, C. 2006, *The Outside-In Formation of Elliptical Galaxies*, Astrophys. J., 638, 739 12

Platais, I., Melo, C., Mermilliod, J.-C., et al. 2007, *WIYN open cluster study. XXVI. Improved kinematic membership and spectroscopy of IC 2391*, Astron. Astrophys., 461, 509 40

Plez, B. 1998, *A new TiO line list*, Astron. Astrophys., 337, 495 129

Pompéia, L., Hill, V., Spite, M., et al. 2008, *Chemical abundances in LMC stellar populations. I. The inner disk sample*, Astron. Astrophys., 480, 379 15, 21, 28, 30, 55, 88, 89, 93, 94, 99, 103, 128, 130, 132, 136, 137, 174, 185, 186

Pont, F. & Eyer, L. 2004, *Isochrone ages for field dwarfs: method and application to the age-metallicity relation*, Mon. Not. R. Astron. Soc., 351, 487 92

Posbic, H., Katz, D., Caffau, E., et al. 2012, *SPADES: a stellar parameters determination software*, Astron. Astrophys., 544, A154 81

Pourbaix, D., Nidever, D., McCarthy, C., et al. 2002, *Constraining the difference in convective blueshift between the components of alpha Centauri with precise radial velocities*, Astron. Astrophys., 386, 280 89

Prantzos, N. & Boissier, S. 2000, *Chemo-spectrophotometric evolution of spiral galaxies - III. Abundance and colour gradients in discs*, Mon. Not. R. Astron. Soc., 313, 338 13

Prochaska, J. X. & McWilliam, A. 2000, *On the Perils of Hyperfine Splitting: A Reanalysis of MN and SC Abundance Trends*, Astrophys. J., Lett., 537, L57 177

Putman, M. E., Gibson, B. K., Staveley-Smith, L., et al. 1998, *Tidal disruption of the Magellanic Clouds by the Milky Way*, Nature, 394, 752 5

Qian, Y.-Z. 2012, *Astrophysical Models of r-Process Nucleosynthesis: An Update*, ArXiv e-prints 163

Qian, Y.-Z., Vogel, P., & Wasserburg, G. J. 1998, *Diverse Supernova Sources for the r-Process*, Astrophys. J., 494, 285 163

Rafelski, M. & Zaritsky, D. 2005, *The Star Clusters of the Small Magellanic Cloud: Age Distribution*, Astron. J., 129, 2701 10

Ramírez, I. & Allende Prieto, C. 2011, *Fundamental Parameters and Chemical Composition of Arcturus*, Astrophys. J., 743, 135 59, 99, 100, 129, 130, 131, 133

Ramírez, I. & Meléndez, J. 2005a, *The Effective Temperature Scale of FGK Stars. I. Determination of Temperatures and Angular Diameters with the Infrared Flux Method*, Astrophys. J., 626, 446 83

Ramírez, I. & Meléndez, J. 2005b, *The Effective Temperature Scale of FGK Stars. II. T_{eff}:Color:[Fe/H] Calibrations*, Astrophys. J., 626, 465 84, 85, 86, 87, 88, 185

Ramírez, I., Meléndez, J., & Asplund, M. 2009, *Accurate abundance patterns of solar twins and analogs. Does the anomalous solar chemical composition come from planet formation?*, Astron. Astrophys., 508, L17 58

Recio-Blanco, A., Bijaoui, A., & de Laverny, P. 2006, *Automated derivation of stellar atmospheric parameters and chemical abundances: the MATISSE algorithm*, Mon. Not. R. Astron. Soc., 370, 141 22

Reddy, B. E., Lambert, D. L., & Allende Prieto, C. 2006, *Elemental abundance survey of the Galactic thick disc*, Mon. Not. R. Astron. Soc., 367, 1329 164, 165, 166, 176, 177

Reddy, B. E., Tomkin, J., Lambert, D. L., & Allende Prieto, C. 2003, *The chemical compositions of Galactic disc F and G dwarfs*, Mon. Not. R. Astron. Soc., 340, 304 164, 166, 176, 177

Regan, M. W. & Teuben, P. J. 2004, *Bar-driven Mass Inflow: How Bar Characteristics Affect the Inflow*, Astrophys. J., 600, 595 20

Rich, R. M., Shara, M., Fall, S. M., & Zurek, D. 2000, *Two Groups of Nearly Coeval Star Clusters in the Small Magellanic Cloud*, Astron. J., 119, 197 10

Rich, R. M., Shara, M. M., & Zurek, D. 2001, *New Photometry for the Intermediate-Age Large Magellanic Cloud Globular Cluster NGC 2121 and the Nature of the LMC Age Gap*, Astron. J., 122, 842 9, 10

Robertson, J. G. 1986, *Optimal extraction of single-object spectra from observations with two-dimensional detectors*, PASP, 98, 1220 38

Robles-Valdez, F., Carigi, L., & Peimbert, M. 2013, *Outside-in stellar formation in the spiral galaxy M33?*, Mon. Not. R. Astron. Soc., 429, 2351 12

Robotham, A. S. G., Baldry, I. K., Bland-Hawthorn, J., et al. 2012, *Galaxy And Mass Assembly (GAMA): in search of Milky Way Magellanic Cloud analogues*, Mon. Not. R. Astron. Soc., 424, 1448 4

Romano, D., Karakas, A. I., Tosi, M., & Matteucci, F. 2010a, *Quantifying the uncertainties of chemical evolution studies. II. Stellar yields*, Astron. Astrophys., 522, A32 188

Romano, D. & Matteucci, F. 2007, *Contrasting copper evolution in ω Centauri and the Milky Way*, Mon. Not. R. Astron. Soc., 378, L59 175

Romano, D., Matteucci, F., Tosi, M., et al. 2007, *The chemical evolution of Omega Centauri's progenitor system*, Mon. Not. R. Astron. Soc., 376, 405 187

Romano, D., Tosi, M., Cignoni, M., et al. 2010b, *On the origin of the helium-rich population in ωCentauri*, Mon. Not. R. Astron. Soc., 401, 2490 9

Roškar, R., Debattista, V. P., Stinson, G. S., et al. 2008, *Beyond Inside-Out Growth: Formation and Evolution of Disk Outskirts*, Astrophys. J., Lett., 675, L65 13

Russell, S. C. & Bessell, M. S. 1989, *Abundances of the heavy elements in the Magellanic Clouds. I - Metal abundances of F-type supergiants*, Astrophys. J., Suppl. Ser., 70, 865 14, 176

Rutten, R. J. 1978, *Empirical NLTE analyses of solar spectral lines. II - The formation of the BA II lambda 4554 resonance line*, Sol. Phys., 56, 237 128

Saha, A., Olszewski, E. W., Brondel, B., et al. 2010, *First Results from the NOAO Survey of the Outer Limits of the Magellanic Clouds*, Astron. J., 140, 1719 7

Salpeter, E. E. 1955, *The Luminosity Function and Stellar Evolution.*, Astrophys. J., 121, 161 164

Sellwood, J. A. & Wilkinson, A. 1993, *Dynamics of barred galaxies*, Reports on Progress in Physics, 56, 173 20

Shaver, P. A., McGee, R. X., Newton, L. M., Danks, A. C., & Pottasch, S. R. 1983, *The galactic abundance gradient*, Mon. Not. R. Astron. Soc., 204, 53 13

Simmerer, J., Sneden, C., Cowan, J. J., et al. 2004, *The Rise of the s-Process in the Galaxy*, Astrophys. J., 617, 1091 165, 169

Skillman, E. D., Tolstoy, E., Cole, A. A., et al. 2003, *Deep Hubble Space Telescope Imaging of IC 1613. II. The Star Formation History*, Astrophys. J., 596, 253 12

Skrutskie, M. F., Cutri, R. M., Stiening, R., et al. 2006, *The Two Micron All Sky Survey (2MASS)*, Astron. J., 131, 1163 27, 28, 62, 65, 85, 88

Smecker-Hane, T. A., Cole, A. A., , et al. Private communication, *Chemical abundances, kinematics and ages of Red Giant stars in the Large Magellanic Cloud: II. The inner disk fields* 28, 30, 55

Smecker-Hane, T. A., Cole, A. A., Gallagher, III, J. S., & Stetson, P. B. 2002, *The Star Formation History of the Large Magellanic Cloud*, Astrophys. J., 566, 239 11, 12, 14, 15, 16, 20, 28, 30, 65, 88, 176, 187, 188

Smiljanic, R. 2012, *On the sodium overabundance of giants in open clusters: the case of the Hyades*, Mon. Not. R. Astron. Soc., 422, 1562 182

Smith, G. 1981, *Non-resonance lines of neutral calcium in the spectra of the sun and Procyon*, Astron. Astrophys., 103, 351 130

Smith, G. 1988, Journal of Physics B Atomic Molecular Physics, 21, 2827 130

Smith, G. & Raggett, D. S. J. 1981, *Oscillator strengths and collisional damping parameters for lines of neutral calcium*, Journal of Physics B Atomic Molecular Physics, 14, 4015 130

Smith, V. V., Hinkle, K. H., Cunha, K., et al. 2002, *Chemical Abundances in 12 Red Giants of the Large Magellanic Cloud from High-Resolution Infrared Spectroscopy*, Astron. J., 124, 3241 129

Sneden, C., Cowan, J. J., & Gallino, R. 2008, *Neutron-Capture Elements in the Early Galaxy*, Ann. Rev. Astron. Astrophys., 46, 241 168, 169, 170, 175, 176

Spite, F., Spite, M., & Francois, P. 1989, *Chemical evolution of the Magellanic Clouds. I - Metal abundance in three young supergiants of the Small Cloud*, Astron. Astrophys., 210, 25 14

Staveley-Smith, L., Kim, S., Calabretta, M. R., Haynes, R. F., & Kesteven, M. J. 2003, *A new look at the large-scale HI structure of the Large Magellanic Cloud*, Mon. Not. R. Astron. Soc., 339, 87 5, 7, 13

Stephens, A. & Boesgaard, A. M. 2002, *Abundances from High-Resolution Spectra of Kinematically Interesting Halo Stars*, Astron. J., 123, 1647 165, 166

Stetson, P. B. & Pancino, E. 2008, *DAOSPEC: An Automatic Code for Measuring Equivalent Widths in High-Resolution Stellar Spectra*, PASP, 120, 1332 60, 95, 125, 138, 185

Subramaniam, A. 2003, *Large Magellanic Cloud Bar: Evidence of a Warped Bar*, Astrophys. J., Lett., 598, L19 5, 7

Subramaniam, A. 2005, *Reddening map of the Large Magellanic Cloud bar region*, Astron. Astrophys., 430, 421 100

Subramaniam, A. & Subramanian, S. 2009a, *RR Lyrae stars in the inner LMC: Where did they form?*, Astron. Astrophys., 503, L9 5, 8

Subramaniam, A. & Subramanian, S. 2009b, *The Mysterious Bar of the Large Magellanic Cloud: What Is It?*, Astrophys. J., Lett., 703, L37 7

Szymanski, M. K. 2005, *The Optical Gravitational Lensing Experiment. Internet Access to the OGLE Photometry Data Set: OGLE-II BVI maps and I-band data*, Acta Astron., 55, 43 27, 29, 62, 85

Thielemann, F.-K., Argast, D., Brachwitz, F., et al. 2002, *Nucleosynthesis and Stellar Evolution*, Astrophys. Space. Sci., 281, 25 171

Thorén, P., Edvardsson, B., & Gustafsson, B. 2004, *Subgiants as probes of galactic chemical evolution*, Astron. Astrophys., 425, 187 91

Timmes, F. X., Brown, E. F., & Truran, J. W. 2003, *On Variations in the Peak Luminosity of Type Ia Supernovae*, Astrophys. J., Lett., 590, L83 157, 165

Tollerud, E. J., Boylan-Kolchin, M., Barton, E. J., Bullock, J. S., & Trinh, C. Q. 2011, *Small-scale Structure in the Sloan Digital Sky Survey and ΛCDM: Isolated ˜L ∗ Galaxies with Bright Satellites*, Astrophys. J., 738, 102 4

Travaglio, C., Gallino, R., Arnone, E., et al. 2004, *Galactic Evolution of Sr, Y, And Zr: A Multiplicity of Nucleosynthetic Processes*, Astrophys. J., 601, 864 175

Truran, J. W. 1981, *A new interpretation of the heavy element abundances in metal-deficient stars*, Astron. Astrophys., 97, 391 163

Tsujimoto, T., Nomoto, K., Yoshii, Y., et al. 1995, *Relative frequencies of Type Ia and Type II supernovae in the chemical evolution of the Galaxy, LMC and SMC*, Mon. Not. R. Astron. Soc., 277, 945 16, 171, 180

Tsujimoto, T. & Shigeyama, T. 2012, *Diversity of Type Ia Supernovae Imprinted in Chemical Abundances*, ArXiv e-prints 173

Udalski, A., Kubiak, M., & Szymanski, M. 1997, *Optical Gravitational Lensing Experiment. OGLE-2 – the Second Phase of the OGLE Project*, Acta Astron., 47, 319 27, 29, 62, 85

Udalski, A., Soszynski, I., Szymanski, M., et al. 1999, *The Optical Gravitational Lensing Experiment. Cepheids in the Magellanic Clouds. IV. Catalog of Cepheids from the Large Magellanic Cloud*, Acta Astron., 49, 223 100

Udalski, A., Szymanski, M., Kubiak, M., et al. 2000, *The Optical Gravitational Lensing Experiment. BVI Maps of Dense Stellar Regions. II. The Large Magellanic Cloud*, Acta Astron., 50, 307 27, 29, 62, 85

van den Bergh, S. 1998, *Star and Cluster Formation in the Large Magellanic Cloud*, Astrophys. J., Lett., 507, L39 9

van den Bergh, S. 2006, *The Dwarf Satellites of M31 and the Galaxy*, Astron. J., 132, 1571 18

van der Marel, R. P. 2001, *Magellanic Cloud Structure from Near-Infrared Surveys. II. Star Count Maps and the Intrinsic Elongation of the Large Magellanic Cloud*, Astron. J., 122, 1827 7

van der Marel, R. P., Alves, D. R., Hardy, E., & Suntzeff, N. B. 2002, *New Understanding of Large Magellanic Cloud Structure, Dynamics, and Orbit from Carbon Star Kinematics*, Astron. J., 124, 2639 4

van der Marel, R. P. & Cioni, M.-R. L. 2001, *Magellanic Cloud Structure from Near-Infrared Surveys. I. The Viewing Angles of the Large Magellanic Cloud*, Astron. J., 122, 1807 7

van't Veer-Menneret, C. & Megessier, C. 1996, *Effective temperature of A and F stars from Balmer line profiles, and the Infrared Flux Method. I. Two AM stars: the Sun and Procyon as standards.*, Astron. Astrophys., 309, 879 81

Venn, K. A. 1999, *A-Type Supergiant Abundances in the Small Magellanic Cloud: Probes of Evolution*, Astrophys. J., 518, 405 14

Villanova, S., Piotto, G., King, I. R., et al. 2007, *The Multiplicity of the Subgiant Branch of ω Centauri: Evidence for Prolonged Star Formation*, Astrophys. J., 663, 296 9

Walborn, N. R. 1991, in IAU Symposium, Vol. 148, The Magellanic Clouds, ed. R. Haynes & D. Milne, 145 7

Wallerstein, G., Iben, Jr., I., Parker, P., et al. 1997, *Synthesis of the elements in stars: forty years of progress*, Reviews of Modern Physics, 69, 995 150

Wanajo, S., Nomoto, K., Iwamoto, N., Ishimaru, Y., & Beers, T. C. 2006, *Enrichment of Very Metal Poor Stars with Both r-Process and s-Process Elements from 8-10 M_{solar} Stars*, Astrophys. J., 636, 842 176

Wannier, P. & Wrixon, G. T. 1972, *An Unusual High-Velocity Hydrogen Feature*, Astrophys. J., Lett., 173, L119 5

Wasserburg, G. J., Busso, M., & Gallino, R. 1996, *Abundances of Actinides and Short-lived Nonactinides in the Interstellar Medium: Diverse Supernova Sources for the r-Processes*, Astrophys. J., Lett., 466, L109 163

Weinberg, M. D. 2000, *Effect of the Milky Way on Magellanic Cloud Structure*, Astrophys. J., 532, 922 7

Wiese, W. L., Smith, M. W., & Glennon, B. M. 1966, Atomic transition probabilities. Vol.: Hydrogen through Neon. A critical data compilation 128

Wilcots, E. M. & Prescott, M. K. M. 2004, *H I Observations of Barred Magellanic Spirals. II. The Frequency and Impact of Companions*, Astron. J., 127, 1900 21

Woosley, S. E. & Weaver, T. A. 1995, *The Evolution and Explosion of Massive Stars. II. Explosive Hydrodynamics and Nucleosynthesis*, Astrophys. J., Suppl. Ser., 101, 181 171, 182

Worley, C. C., Cottrell, P. L., Freeman, K. C., & Wylie-de Boer, E. C. 2009, *Differential chemical abundance analysis of a 47 Tucanæ asymptotic giant branch star with respect to Arcturus*, Mon. Not. R. Astron. Soc., 400, 1039 58, 99, 130, 131, 133

Zaritsky, D. 2004, *The Case of the Off-Center, Levitating Bar in the Large Magellanic Cloud*, Astrophys. J., Lett., 614, L37 7, 19

Zaritsky, D., Harris, J., Thompson, I. B., & Grebel, E. K. 2004, *The Magellanic Clouds Photometric Survey: The Large Magellanic Cloud Stellar Catalog and Extinction Map*, Astron. J., 128, 1606 29, 30, 88, 100

Zhang, H.-X., Hunter, D. A., Elmegreen, B. G., Gao, Y., & Schruba, A. 2012, *Outside-in Shrinking of the Star-forming Disk of Dwarf Irregular Galaxies*, Astron. J., 143, 47 12

Zhao, H. & Evans, N. W. 2000, *The So-called "Bar" in the Large Magellanic Cloud*, Astrophys. J., Lett., 545, L35 7

Books

Boehm-Vitense, E. 1989, Introduction to stellar astrophysics. Volume 1 - Basic stellar observations and data. Volume 2 - Stellar atmospheres

Böhm-Vitense, E. 1989, Introduction to stellar astrophysics. Vol. 2. Stellar atmospheres.

Böhm-Vitense, E. 1992, Introduction to stellar astrophysics. Volume 3. Stellar structure and evolution.

de Boer, K. & Seggewiss, W. 2008, Stars and Stellar Evolution

Gray, D. F. 2008, The Observation and Analysis of Stellar Photospheres

Leblanc, F. 2010, An Introduction to Stellar Astrophysics 151, 152

Léna, P., Rouan, D., Lebrun, F., Mignard, F., & Pelat, D. 2008, L'observation en astrophysique

Monier, R. 2006, Les étoiles et le milieu interstellaire : Introduction à l'astrophysique

Pagel, B. E. J. 2009, Nucleosynthesis and Chemical Evolution of Galaxies 158, 160, 161

Westerlund, B. E. 1997, The Magellanic Clouds 2

Webography & miscellaneous online ressources

Frommert, H. & Kronberg, C. Observatoire de Paris-Meudon. *Al Sufi* (HTML, English) [Online]. Available: http://messier.obspm.fr/xtra/Bios/alsufi.html. Last revision: 17 Jul. 2006. Last access: 1 Dec. 2012 2

Frommert, H. & Kronberg, C. Observatoire de Paris-Meudon. *The Large Magellanic Cloud* (HTML, English) [Online]. Available: http://messier.obspm.fr/xtra/ngc/lmc.html. Last revision: 5 Sep. 2007. Last access: 1 Dec. 2012 2

GIRAFFE Quality Control group. ESO. *FLAMES/GIRAFFE pipeline: calibration recipes* (HTML, English) [Online]. Available: http://www.eso.org/observing/dfo/quality/GIRAFFE/pipeline/recipe_calib.html. Last revision: 8 Nov. 2011. Last access: 25 Oct. 2012 39

GIRAFFE Quality Control group. ESO. *FLAMES/GIRAFFE: reduction of science data* (HTML, English) [Online]. Available: http://www.eso.org/observing/dfo/quality/GIRAFFE/pipeline/pipe_reduc.html. Last revision: 23 Apr. 2012. Last access: 25 Oct. 2012 36

Kaufer, A., Martayan, C., & Melo, C. ESO. *FLAMES User Manual* (PDF, English) [Online]. Available: http://www.eso.org/sci/facilities/paranal/instruments/flames/doc/VLT-MAN-ESO-13700-2994_v91.pdf. Last revision: 01 Sep. 2012. Last access: 25 Oct. 2012 25, 33

Melo, C. & Smoker, J. ESO. *GIRAFFE data reduction cookbook* (PDF, English) [Online]. Available: http://www.eso.org/sci/facilities/paranal/instruments/flames/doc/VLT-MAN-ESO-13700-4034_v85.pdf. Last revision: 29 Aug. 2009. Last access: 25 Oct. 2012 28, 36